Nucleation mechanisms of volatile particles in aircraft engine emissions and their links with fuel composition

Rafaël Barrellon-Vernay

Doctoral Thesis

Doctoral school: Science of Matter, Radiation and Environment
Discipline: Energetic, Thermic and Combustion

Nucleation mechanisms of volatile particles in aircraft engine emissions and their links with fuel composition

by

Rafaël Barrellon--Vernay

Thesis submitted for the degree of Doctor of the University of Lille
Defended on December 20th, 2023 in front of the defense committee composed of:

Reviewers:	Prof. Beatriz Cabañas Galán	University of Castilla La Mancha, Spain
	Dr. Richard Miake-Lye	Vice President of AERODYNE RESEARCH, USA
President of jury:	Dr. Xavier Mercier	Research director, PC2A, Villeneuve d'Ascq
Examiners:	Dr. Yoann Méry	Head of SAFRAN AE Combustion Team, Villaroche
	Prof. Tuukka Petäjä	University of Helsinki, Finland
Thesis Director:	Prof. Cristian Focsa	University of Lille, PhLAM, Villeneuve d'Ascq
Thesis Supervisors:	Dr. David Delhaye	Research engineer, ONERA, Palaiseau
	Dr. Ismael K.Ortega	Research engineer, ONERA, Palaiseau

This work benefited from the support of the project UNREAL ANR-18-CE22-0019 of the French National Research Agency (ANR).

This page is intentionally left blank

Thèse de Doctorat

École Doctorale: Sciences de la Matière, du Rayonnement
et de l'Environnement
Discipline: Énergétique, thermique, combustion

Mécanismes de nucléation des particules volatiles dans les émissions des moteurs d'avions et leurs liens avec la composition du carburant

par
Rafaël Barrellon-Vernay

Thèse présentée pour l'obtention du grade de docteur de l'Université de Lille.
Soutenue le 20 Décembre 2023 devant la commission d'examen:

Rapporteurs:	Pr. Beatriz Cabañas Galán	Université de Castille - La Manche, Espagne
	Dr. Richard Miake-Lye	Vice-Président AERODYNE RESEARCH, USA
Président de jury :	Dr. Xavier Mercier	Directeur de Recherche, PC2A, Villeneuve d'Ascq
Examinateurs:	Dr. Yoann Méry	Chef du département de Combustion, SAFRAN, Villaroche
	Prof. Tuukka Petäjä	Université d'Helsinki, Finlande
Directeur de thèse:	Pr. Cristian Focsa	Université de Lille, PhLAM, Villeneuve d'Ascq
	Dr. David Delhaye	Ingénieur de Recherche, ONERA, Palaiseau
Co-encadrants :	Dr. Ismael K.Ortega	Ingénieur de Recherche, ONERA, Palaiseau

Ce travail a bénéficié du soutien du projet UNREAL ANR-18-CE22-0019 de l'Agence Nationale de la Recherche française (ANR).

This page is intentionally left blank

NUCLEATION MECHANISMS OF VOLATILE PARTICLES IN AIRCRAFT ENGINE EMISSIONS AND THEIR LINKS WITH FUEL COMPOSITION

ABSTRACT

One of the actual concerns of the aviation industry is to reduce fuel consumption and environmental footprint. Indeed, aviation emissions impact air quality in and around airports. As other transport sectors, aviation effluents need to be addressed to reduce greenhouse gases contribution (2% of these emissions are related to air transport worldwide), volatile and non-volatile Particulate Matter (vPM and nvPM) and indirect impact as condensation trails.

To reduce these emissions, different approaches have been investigated, in particular the use of Sustainable Aviation Fuels (SAF). Aims of SAF are to decrease the net CO_2 emissions and nvPM. However, combustion of these fuels may lead to new pollutants that can react with atmosphere by formation of secondary aerosols. As part of the UNREAL project (Unveiling Nucleation mechanism in aiRcraft Engine exhAust and its Link with fuel composition), the objective of this work was to study the different molecular mechanisms of new particle formation from the exhausts of aircraft engines fed by fuels with different composition, from the standard Jet A-1 to 100 % SAF fuel.

The physicochemical characterisation of the particulate emissions from aircraft engines in real conditions is challenging both from the technical and economical point of view. Thus, a mini-CAST burner, suitable for the combustion of aeronautic liquid fuels, has been used as an alternative to obtain emissions comparable to some extent to those from aircraft engines. A decrease in nvPM emissions (number concentration, mass concentration and size distribution) can be observed in correlation with the quantity of aromatic compounds in the fuel. Moreover, the analysis by mass spectrometry revealed a decrease in the relative intensity of PAHs when alternative fuels were employed. Emissions from the burner have been injected, with and without soot filtration, into an atmospheric chamber for ageing (CESAM chamber reproducing atmospheric conditions at ground level – LISA). For all fuels tested formation of vPM by homogeneous nucleation has been observed in the atmospheric chamber in absence of nvPM. This phenomenon is particularly highlighted for fuels with high amounts of sulphur in their compositions. However, in real cases (presence of soot), the formation of vPM is only observed for the fuels containing high amounts of sulphur. The concentration of gaseous precursors formed for other fuels was not enough to produce vPM after being adsorbed on soot surface (heterogeneous nucleation). On-line characterisation techniques were completed by filter sampling and off-line mass spectrometry analysis, highlighting the presence of PAHs, oxygenated hydrocarbons, sulphur and nitrogen compounds. By employing semi-quantitative methods, it was possible to link the relative chemical composition (sulphur and PAH relative intensity) with vPM formation and their repartitions in particulate and gaseous phases.

Keywords: Aeronautic emissions, volatile (vPM) and non-volatile (nvPM) Particulate Matter, formation of particles, atmospheric chamber, homogeneous nucleation, aeronautical fuels, liquid laboratory burner.

MÉCANISMES DE NUCLÉATION DES PARTICULES VOLATILES DANS LES ÉMISSIONS DES MOTEURS D'AVIONS ET LEURS LIENS AVEC LA COMPOSITION DU CARBURANT

RESUME

L'une des préoccupations actuelles de l'industrie aéronautique est la diminution de la consommation de carburant et de l'empreinte environnementale. En effet, les émissions aéronautiques ont un impact sur la qualité de l'air et notamment au niveau des zones aéroportuaires. Comme d'autres secteurs du transport, le trafic aérien génère des gaz à effet de serre (2 % du total dans le monde), des traînées de condensation ainsi que des particules volatiles et non volatiles (vPM et nvPM).

Pour réduire ces émissions, différentes approches ont été pensées avec en particulier l'usage de carburants aéronautiques durables (SAF - Sustainable Aviation Fuels). L'objectif des SAF est de réduire les émissions nettes de CO_2 et de nvPM. Cependant, la combustion de ces carburants peut entraîner la formation de nouveaux polluants qui réagissent avec l'atmosphère en formant des aérosols secondaires (SA). Dans le cadre du projet UNREAL (Unveiling Nucleation mechanism in aiRcraft Engine exhAust and its Link with fuel composition), l'objectif de ce travail était d'étudier les différents mécanismes au niveau moléculaire à l'origine de la formation de nouvelles particules à partir des rejets moteurs alimentés par des carburants de compositions différentes, allant du Jet A-1 standard à du carburant 100 % SAF.

La caractérisation physico-chimique des émissions en conditions réelles en sortie moteur est un défi à la fois d'un point de vue technique et économique. Pour pallier à cela un brûleur mini-CAST, adapté à la combustion de carburants liquides aéronautiques, a été utilisé comme alternative pour obtenir des émissions comparables, dans une certaine mesure, à celles des moteurs aéronautiques. Une diminution des émissions de nvPM (concentration en nombre, concentration en masse et distribution de tailles) peut être observée en corrélation avec la quantité de composés aromatiques présents dans le carburant. De plus, l'analyse par spectrométrie de masse a révélé une diminution de l'intensité relative des HAP lors de l'emploi de carburants alternatifs. Les émissions du brûleur ont été injectées, avec ou sans filtration des suies, dans une chambre atmosphérique de vieillissement (chambre CESAM reproduisant les conditions atmosphériques au niveau du sol - LISA). Pour tous les carburants testés, la formation de vPM par nucléation homogène a été observée dans la chambre atmosphérique en l'absence de nvPM. Ce phénomène est particulièrement prononcé pour les carburants comprenant de grandes quantités de soufre dans leur composition. Cependant, dans les cas réels (présence de suies), la formation de vPM n'est observée que pour les carburants contenant de fortes quantités de soufre. La concentration de précurseurs gazeux formés pour les autres carburants n'est pas suffisante pour produire des vPM, notamment avec l'adsorption des gaz à la surface des particules de suies (nucléation hétérogène). Les techniques de caractérisation en ligne ont été complétées par des prélèvements sur filtre et une analyse par spectrométrie de masse, mettant en évidence la présence de HAP, d'hydrocarbures oxygénés, de composés soufrés et azotés. En utilisant des méthodes semi-quantitatives, il a été possible de mettre en relation la composition chimique (intensité relative de soufre et de HAP) avec la formation de vPM et leur répartition dans les phases particulaires et gazeuses des émissions.

Mots-clés: Émissions aéronautique, particules volatiles (vPM) et non-volatiles (nvPM), formation de particules, chambre atmosphérique, nucléation homogène, carburant aéronautique, brûleur de laboratoire pour carburant liquide.

ACKNOWLEDGEMENTS

Arrivé au bout de ce voyage, je peux maintenant me retourner et regarder tout le chemin fait pour en arriver là. Ce parcours a été instructif, surprenant, difficile et c'est pourquoi je souhaite remercier tous ceux qui de près ou de loin m'ont apporté leur soutien et leurs conseils au cours de ce périple. Cette section est la seule qui ne sera pas corrigée donc autant en profiter.

Tout d'abord je voudrais remercier mon directeur de thèse M. Cristian Focsa pour avoir accepté de diriger ces travaux. Ses conseils, son expérience et nos échanges ont permis de canaliser et de mener à bien ces recherches. Ma thèse s'étant déroulée en très grande partie à l'ONERA, je voudrais ensuite remercier mes encadrants sans qui rien n'aurait été possible : M. David Delhaye et M. Ismaël K. Ortega. Ils m'ont accueilli dans leur monde des émissions il y a de cela maintenant presque 4 ans. J'ai pu apprendre énormément à leur contact et toujours avec leur soutien, entre David le rodé des émissions et Kenty le roi de la nucléation. Alternant échanges constructifs et ludiques, cette thèse s'est faite petit à petit et je ne peux que vous remercier pour votre encadrement quotidien et votre patience. Merci à vous trois !

Je tiens ensuite à remercier mon unité CMEI pour toute cette période de thèse. Merci à M. Frédéric Ser, chef de l'unité, pour son accueil et sa gentillesse. Merci à tous ceux qui m'ont aidé et permis d'avancer Antoine, Louise, Bruno, Yanis, Mickaël. Merci à Ségolène, Alaric (je n'aurai jamais vu tes plantes), Lucie, Soraya, Margaux, Nathalie, Matthieu et Mathieu pour votre présence quotidienne, pour cette bonne humeur, pour nos discussions houleuses et réfléchies lors des pauses cafés. Je tiens particulièrement à remercier mon ancienne maître de stage Cornelia Irimiea pour ses conseils toujours avisés et sa gentillesse ainsi que pour m'avoir mis le pied à l'étrier du monde des suies et m'avoir encouragé à me lancer dans cette thèse. Je retiens également tous les doctorants que j'ai côtoyés et notamment Jean Pierre qui m'a permis de m'accrocher et de ne pas me laisser distancer. Merci également à tous les membres de l'ONERA non cités ici et qui m'ont accompagné au cours de ces années de recherche.

Je souhaite également remercier le personnel du laboratoire PhLAM pour leur accueil et leur disponibilité. Apprendre de nouvelles techniques expérimentales complexes telle que la spectrométrie de masse ne peut se faire sans conseils avisés, que ce soit sur la technique d'analyse ou la méthodologie de traitement des données. Pour cela un grand merci particulièrement à M. Dmitrii Egorov et Mitra Tirthankar qui se sont relayés pour m'accompagner et me guider : plusieurs journées d'analyses et des frigos regorgeant de filtres.

Je tiens enfin à remercier toutes les personnes avec qui j'ai eu la chance de travailler durant mes essais dans le cadre du projet UNREAL. Je pense notamment au personnel du LISA en la présence de Mathieu et Antonin qui m'ont permis de m'ouvrir à CESAM, à Alexandre d'INERIS, à Matti et Miikka venus de Finlande pour m'expliquer la nucléation et à tous les autres qui m'ont aidé durant ces travaux.

J'adresse mes remerciements à tous les membres du comité de défense de m'avoir fait l'honneur d'accepter et d'évaluer mon travail : Mme Beatriz Cabañas Galán, M. Richard Miake-Lye, M. Xavier Mercier, M . Yoann Méry et M. Tuukka Petäjä.

Et pour finir, car rien de tout cela n'aurait été possible sans eux, je souhaiterais remercier tous ceux qui m'ont soutenu dans la vie de tous les jours. Il est impossible de quantifier votre soutien et de citer tout le monde mais on a fait un bout de chemin ensemble et je vous suis grandement reconnaissant de m'avoir aidé et encouragé durant tout ce temps. Merci à mes amis qui m'ont supporté dans tous les sens du terme. Un grand merci également à celle qui a su me soutenir tous les jours. Merci d'avoir eu la patience d'attendre que je rende ce manuscrit en restant positive et en me motivant.

Enfin je tiens à remercier mes parents et mes frères qui m'ont toujours encouragé. Merci à ma famille qui a toujours cru en moi, même dans les moments difficiles. Je vous dédie cette thèse comme cadeau de Noël.

Bonne lecture!

This page is intentionally left blank

TABLE OF CONTENTS

LIST OF ACRONYMS

AAFEX :	Alternative Aviation Fuel EXperiment
ACSM :	Aerosol Chemical Speciation Monitor
aDBD :	Annular Dielectric Barrier Discharge
AIC :	Aircraft-induced clouds
AMS :	Aerosol Mass Spectrometer
ANR :	French National Agency for Research
API-ToF :	Atmospheric Pressure Interface Mass Spectrometer
APU :	Auxiliary Power Unit
AQG :	Air Quality Guideline
ASTM :	American Society for Testing and Materials
AtJ :	Alcohol-to-Jet
AVIATOR :	Assessing aViation emission Impact on local Air quality at airports: TOwards Regulation CESAM Multiphase Atmospheric Experimental Simulation Chamber
BVOCs :	Biogenic volatile organic compounds
CAEP :	Committee on Aviation Environmental Protection of the International Civil Aviation Organization
CAST :	Combustion Aerosol STandard Generator
CCN :	Cloud Condensation Nuclei
CESAM :	Multiphase Atmospheric Experimental Simulation Chamber
CIMS :	Chemical Ionisation Mass Spectrometer
CLD :	Semi decompression chemi-luminescence method
CLOUD :	Cosmics Leaving Outdoor Droplets
CMEI :	Chemistry of energetic Materials, Emissions and environmental Impact
CN :	Cetane Number
CNRS :	French National Centre for Scientific Research
CPC :	Condensation Particle Counter
CS :	Catalytic Stripper
d_a :	aerodynamic diameter
d_{agg} :	agglomerate diameter
DCN :	Derived Cetane Number
DEED :	Dekati Engine Exhaust Diluter
d_{ev} :	equivalent volume diameter
DF :	Dilution Factor
d_g :	turning diameter
DLR :	German Aerospace Centre
d_m :	electric mobility diameter
DMA :	DiMethylAmine
DMA_P :	Differential Mobility Analyser for Particles
DMPE :	Multi-Physics Department for Energy
d_{pp} :	primary particle diameter
EASA :	European Union Safety Agency
eBC :	equivalent Black Carbon
ELVOC :	Extremely Low Volatility Organic Compounds
FCE:	Faraday Cup Electrometer
FPS :	Fine Particles Sampler (Dekati)
FTIR :	Fourier Transform Infrared (Spectroscopy)
FT-SPK :	Fischer-Tropsch Synthetic Paraffinic Kerosene
GC-FID :	Gas Chromatography - Flame Ionisation Detection
GIFAS :	French Aerospace Industries Association

GMD :	Geometric Mean Diameter
GR :	Growth Rate
GSD :	Geometric Standard Deviation
HACA :	Hydrogen Abstraction-C_2H_2 Addition
HC :	Hydrocarbons
HEFA :	Hydroprocessed Esters and Fatty Acids
HFS-SIP :	Hydroprocessed Fermented Sugars Synthesised Iso-Paraffins
HOA :	Hydrocarbon Organic Aerosols
HOMs :	Highly Oxidised Organic
HR-AMS :	High Resolution Aerosol Mass Spectrometry
HR-L2MS :	High-Resolution Two-Step Laser Mass Spectrometry
IARC :	International Agency for Research on Cancer
ICAO :	International Civil Aviation Organisation
INAR :	INstitut for Atmospheric and earth system Research (Helsinki)
INERIS :	French National Institute for Industrial Environment and RISks
INTA :	National Institute of Aerospace Technology (Spain)
IPCC :	Intergovernmental Panel on Climate Change
JETSCREEN :	JET Fuel SCREENing and Optimisation
L2MS :	Two-Step Laser Mass Spectrometry
LDI :	Laser Desorption Ionisation
LII :	Laser Induced Incandescence
LISA :	Inter-university Laboratory of Atmospheric Systems (France)
LSCE :	Climate and Environment Sciences Laboratory (France)
LTAG :	Long Term global Aspirational Goal
LVOC :	Low Volatility Organic Compounds
NASA :	National Aeronautics and Space Administration
NOAA :	National Oceanic and Atmospheric Administration
NOC :	Nitrogen-Containing Organic compounds
nvPM :	non-volatile Particulate Matter
ONERA :	French National Aerospace Research Centre
OOA:	Oxygenated Organic Aerosols
PAH :	Polycyclic Aromatic Hydrocarbons
PAM-OFR :	Potential Aerosol Mass Oxidation Flow Reactor
PC2A :	Physico-Chimie des Processus de Combustion et de l'Atmosphère
PhLAM :	Laboratory of Laser, Atom and Molecule Physics
PM_1 :	Particulate Matter ≤1 µm
$PM_{2.5}$:	Particulate Matter ≤2.5 µm
PM_{10} :	Particulate Matter ≤10 µm
POA :	Primary Organic Aerosols
PTR-MS :	Proton-Transfer-Reaction Mass Spectrometry
RAPTOR :	Research of Aviation PM Technologies mOdelling and Regulation
RF :	Radiative Forcing
RH :	Relative Humidity
RIVM :	National Institute for Public Health and the Environment (Netherlands)
ROI :	Regions Of Interest
RSR :	Radical chain reaction mechanisms and Stabilised by Resonance
SA :	Secondary Aerosols
SAF :	Sustainable Aviation Fuel
SIA :	Secondary Inorganic Aerosols
SIMS :	Secondary Ions Mass Spectrometry
SMPS :	Scanning Mobility Particle Sizer

S/N :	Signal to Noise ratio
SOA :	Secondary Organic Aerosols
TNO :	Netherlands Organisation for Applied Scientific Research
ToF-MS :	Time of Flight Mass Spectrometer
TUT :	Tampere University of Technology
UCAR :	University Corporation for Atmospheric Research
UFP :	Ultrafine Particles
UNREAL :	Unveiling Nucleation mechanism in aiRcraft Engine exhAust and its Link with fuel composition
VOC :	Volatile Organic Compounds
VOLCAN :	VOL avec Carburants Alternatifs Nouveaux (Fly with Alternative Fuels)
vPM :	volatile Particulate Matter
WHO :	World Health Organisation

LIST OF FIGURES

LIST OF TABLES

LIST OF ANNEXES

Chapter I. General introduction

I.1 Context of the study

This PhD thesis has been funded by the French National Research Agency (ANR) and through the project Unveiling Nucleation mechanism in aiRcraft Engine exhAust and its Link with fuel composition (UNREAL project, 2019). The goal of this project (https://anr.fr/Project-ANR-18-CE22-0019) has been to study, from a molecular point of view, the mechanisms of formation of volatile particles in aircraft engines exhaust depending on fuel composition, to understand the impact of biofuels on aircraft engine emissions and their evolution in the atmosphere. This is a topic of high current interest, especially given the real concern of the aviation industry to reduce its impact on climate and air quality.

The UNREAL project was led by Dr. Ismael Kenneth Ortega from the ONERA CESAM laboratory and involved the following partners:

- the National Centre for Scientific Research (CNRS, France) and the Inter-university Laboratory for Atmospheric Systems (LISA, France) allowed the study of the vPM formation in detail with the experimental CESAM chamber;
- the Laboratory of Climate and Environmental Sciences (LSCE, France) and the National Institute for industrial Environment and RISks (INERIS, France - subcontract) provide the PAM oxidation flow reactor to induce the formation of vPM from the exhaust of CAST;
- the Mines-Télécom Nord Europe Institute (University of Lille, France) has participated to the characterisation of chemical composition with a High Resolution Aerosol Mass Spectrometer (HR-AMS);
- the Tampere University of Technology (TUT) allows the study of molecular clusters emitted by CAST with an Atmospheric Pressure Interface Time of Flight Mass spectrometer (API-ToF);
- the Netherlands Organisation for Applied Scientific Research (TNO, Netherlands) and the National Institute for Public Health and the Environment (RIVM, Netherlands) for the study of the impact of emissions on health within the framework of the Research of Aviation PM Technologies mOdelling and Regulation (RAPTOR: Cleansky 2 project);
- the Institute for Atmospheric and earth system Research (INAR, University of Helsinki) has been added, as part of the TNO project, for the study of ice nucleation.

The UNREAL project was divided into four work packages (Figure I-1): WP1 involved the use of a laboratory burner to observe the impact of the composition of various fuels on emissions: physical properties (size, number, mass, etc.) and chemical composition; WP2 addressed the study of the formation of volatile particles and the evolution of aircraft aerosols within an atmospheric simulation chamber (CESAM); WP3 was carried out on an engine test bench to characterise emissions for various engine regimes, while WP4 developed theoretical simulations focused on the formation of volatile particles. This thesis work mainly contributes to WP1 and WP2, with the aim of studying the transformation of the aeronautical emissions during interaction with the atmosphere, taking into account the formation of secondary aerosols, the nature of the fuel and its impact on the resulting emissions. A particular attention has been paid to volatile particles (vPM) emitted from aeronautical combustion sources to measure them as well as understand and propose reaction mechanisms related to their formation and interaction in the atmosphere. Moreover, this study addressed the effect of the chemical composition of the fuels on the properties and chemical composition of the emitted volatile (vPM) and non-volatile (nvPM) particles, with the aim of helping future development of alternative fuels (Zheng et al., 2019).

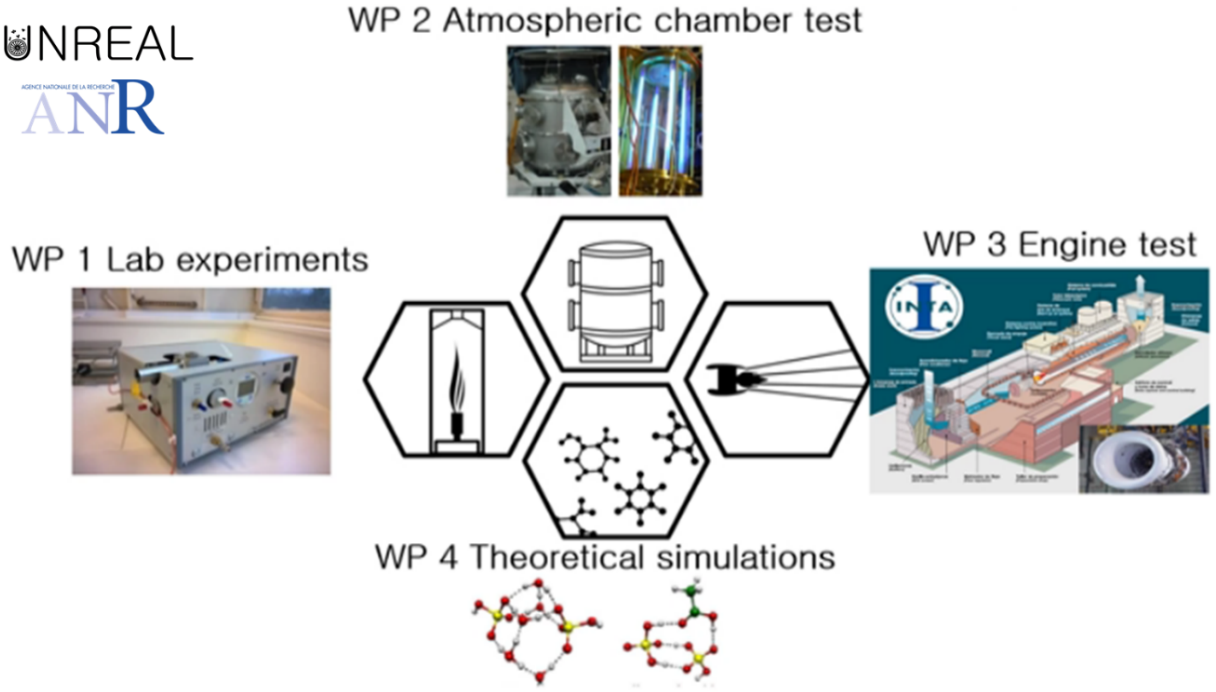

Figure I-1: Work packages of the UNREAL project: from the laboratory measurement to modelling studies, passing by tests on simulation chamber and engine.

The study has been carried out through experiments that investigated the emissions produced by an aeronautical fuel burner to observe the evolution of emitted particles in the atmosphere at ground level. A reliable emission source has been used with various types of liquid fuels ranging from classic Jet A-1 to 100% alternative fuel, such as Alcohol to Jet (AtJ). The use of an atmospheric simulation chamber allowed to reproduce real atmospheric conditions, such as pressure, temperature, and UV irradiation, found in the airport area. During experiments physico-chemical characterisation of nvPM and vPM has been done by using a wide panel of analytical techniques. A particular attention has been given to the impact on these particles of the sulphur and aromatic contents of the fuels. Sampling of emissions was also performed on filters for each experiment to obtain a chemical characterisation of the elements present in the atmospheric chamber and to propose hypotheses regarding their formation.

The supervision of this thesis was jointly provided by Dr. David Delhaye and Dr. Ismael K. Ortega within the Chemistry of energetic Materials, Emissions and environmental Impact unit (CMEI) of the Multi-Physics Department for Energy (DMPE) of the French National Office for Aerospace Studies and Research (ONERA, Paris) and by Prof. Cristian Focsa within the Laboratory of Physics of Lasers, Atoms and Molecules (PhLAM, University of Lille). The two collaborating entities each have their own scientific and technological specificities, which have proven complementary over the years and through common projects (MERMOSE, JETSCREEN, UNREAL...). Although this work was mostly carried out within ONERA, the thesis project once again highlights the emissions characterisation techniques developed by these two entities, by applying them to the particular case of aeronautical emissions, bringing out the technological aspect of this study.

I.2 Atmosphere structure and composition

I.2.1 Atmospheric layers

The composition of the atmosphere, defined as the gaseous layer that surrounds our planet, has evolved over the centuries (Seinfeld, & Pandis, 2006). The interactions between its components and suspended particles coming from various sources play a fundamental role for the Earth's balance: absorption of UV radiation, warming by the greenhouse effect...

The atmosphere is subdivided into several layers (Figure I-2) according to the altitude, which is slightly different depending on the location: at the poles or at the equator. The layers above 50 km are considered as the upper atmosphere (mesosphere and thermosphere) and those below as the lower atmosphere (troposphere and stratosphere). From the Earth to space, the temperature increases slightly in the stratosphere before decreasing in the upper layers (in red) and the gases become increasingly scarce: for example, ozone disappears in the mesosphere and oxygen in the thermosphere. It should be noted that air traffic is mainly taking place in the troposphere and in particular at the boundary between the upper troposphere and the lower stratosphere.

Furthermore, the atmosphere plays an important role in the Earth's radiative balance (Hatfield et al., 2005; Stuhlmann, 1995), being a key agent in the exchange of heat and radiation between the Sun and the Earth's surface. The regulation of Earth's temperature involves the oceans and the winds, and the atmosphere adapts quickly to these changes. It is within the atmospheric layer that some species will affect the exchanges between the Earth and Space.

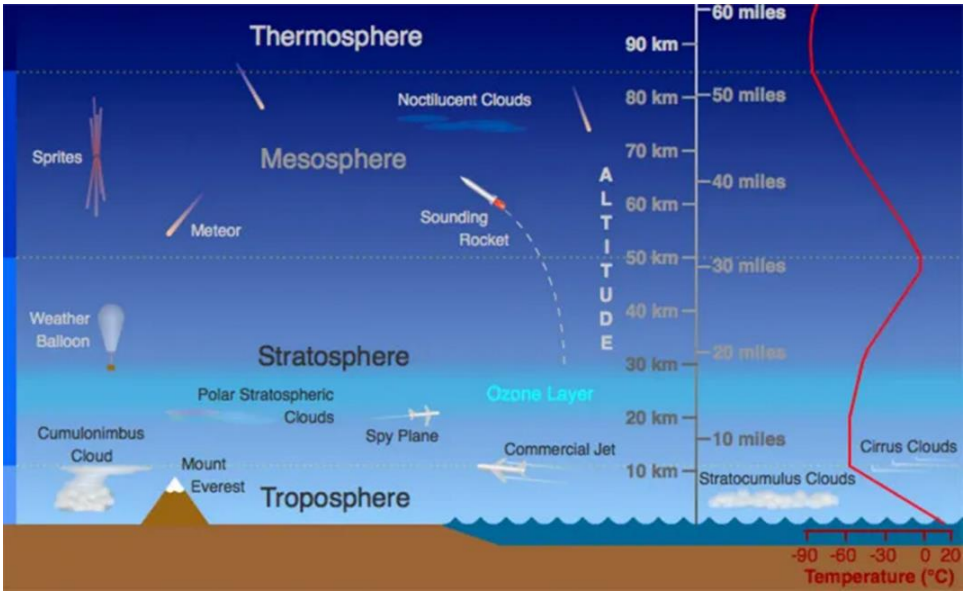

Figure I-2: Layers of the atmosphere: troposphere, stratosphere, mesosphere and thermosphere (UCAR).

I.2.2 Atmospheric gases

The atmosphere is composed of various gases such as nitrogen N_2, oxygen O_2, carbon dioxide CO_2 (0.04% in 2017), water vapour H_2O, rare gases in small amounts such as neon (Ne), helium (He), xenon (Xe), and aerosol particles. Depending on the water vapour contribution, the repartition of these gases is different: for example 78% of N_2 and 21% of O_2 for dry winds (i.e. 0% of H_2O) but 76% of N_2 and 20% of O_2 for extremely hot/humid days (water vapour contribution climbs to near 3%).

It can be noted that in recent years, the concentration of CO_2 has increased from 345 ppm in 1998 (Pomerol et al., 2011) to 404 ppm in 2017 (NOAA, 2021). All of these species evolve in the

atmosphere depending on their lifetime and spatial distribution (Figure I-3). The lifetime refers to the time required for a considered species to reach a negligible concentration in the atmosphere (Seinfeld, & Pandis, 2006). This lifetime in the atmosphere varies greatly, ranging from several centuries for long-lived species (methane CH_4 or nitrous oxide N_2O) to a few seconds for short-lived species (nitrate NO_3 or hydroperoxyl radical HO_2). In addition, the spatial and temporal variabilities of the species are inversely related to the lifetime. Long-lived species tend to be mixed relatively uniformly in the troposphere, while short-lived species show much more variability (National Academies of Sciences, 1998).

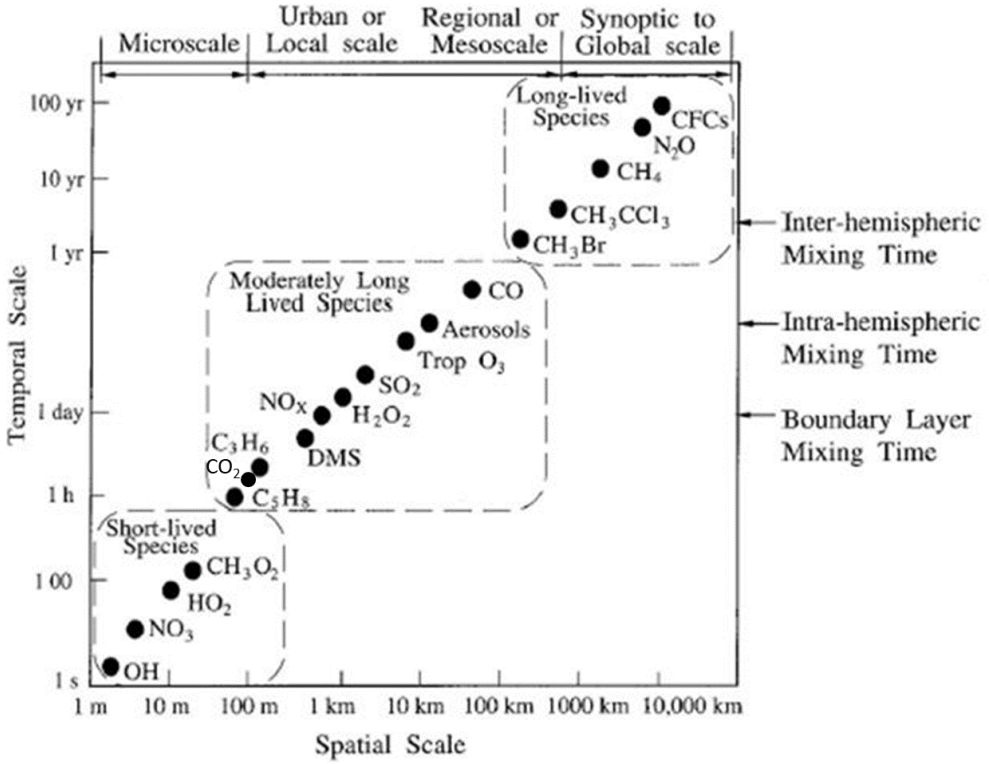

Figure I-3: Spatial and temporal scales of variability of a number of key constituents in the atmosphere (National Academies of Sciences, 1998). Details of the notations: C_3H_6 = propene; C_5H_8 = isoprene; CH_3Br = methyl bromide; CH_3CCl_3 = methyl chloroform; CH_3O_2 = methyl peroxy radical; DMS = dimethyl sulphide; H_2O_2 = hydrogen peroxide; NO_3 = nitrogen trioxide; OH = hydroxyl radical; SO_2 = sulphur dioxide; Trop = tropospheric (Lakey et al., 2021; National Academies of Sciences, 1998; Seinfeld, & Pandis, 2006).

These species evolve through physico-chemical transformations, playing a major role in the composition of the atmosphere. Their evolution depends on their lifetime and the majority of these species are eliminated by chemical reactions. The gas phase contains radical species (hydroxyls OH, hydroperoxyls HO_2, and alkylperoxyls RO_2) which are the main actors in these chemical transformations (Albrecht et al., 2019; Stone et al., 2012). However, these reactions can lead to the oxidation of the gas phase generating compounds that are not initially present or only slightly emitted into the atmosphere. Transformations such as the progressive oxidation of hydrogen (H), carbon (C), nitrogen (N), or sulphur (S) atoms by molecular oxygen lead in the atmosphere to the formation of ozone (O_3), nitric acid (HNO_3), sulphuric acid (H_2SO_4), and carbon dioxide (CO_2). These transformations require complex reaction mechanisms involving many species and including many steps, not necessarily all controlled or known, in particular when catalysis is involved (Baron & Klaus, 2002; Seinfeld, & Pandis, 2006). In recent decades, an increase in the concentration of these gases (CO_2, N_2O, CH_4 and O_3) has been recorded at low altitudes in the atmosphere and at ground level (notably due to the development of industry) impacting the climate and air quality (Lee et al., 2021; NOAA, 2021; Pascal, 2013).

I.2.3 Atmospheric aerosols

I.2.3.1 Definition

Aerosols are defined as solid or liquid particles in suspension in a gas and are typically found in the troposphere and stratosphere (Baron & Klaus, 2002). The particle size can vary from nanometres to micrometres. Aerosols are generally differentiated according to whether they are emitted directly into the atmosphere, in which case they are called primary aerosols, or whether they are formed in the atmosphere, in which case they are called secondary aerosols.

Primary particles can be divided into two categories:

- Natural sources such as erupting volcanoes, desert dust, oceans, pollen, and the nucleation of biogenic vapours emitted by forests;
- Anthropogenic or artificial sources such as industrial activity, transportation (road, railway, maritime, aviation), and intensive agriculture.

Secondary particles come from nucleation of gaseous vapours leading to the formation of new solid particles. Precursors of this transition from the gaseous state to the solid state come from oxidation (oxidation by ozone and/or hydroxyl radicals). After that, different physical processes will modify the characteristics of this population of aerosols (condensation, coagulation...).

All these aerosols present in the atmosphere have a direct or indirect impact on radiative exchanges between the Earth and space and affect the composition of the atmosphere and therefore air quality (Baron & Klaus, 2002). In urban areas, for example, aerosols are a mixture of primary particles emitted from industry, transportation, and energy production facilities and secondary particles resulting from gas-to-particle conversion mechanisms (nucleation). The repartition of these aerosols in the atmosphere depends on the source's location and on their properties such as lifetime or volatility.

I.2.3.2 Size of atmospheric particles

One of the challenges raised by the detection of aerosols concerns their small size, making them difficult to measure. The size of these particles changes (Figure I-4) from a few nanometres for the smallest ones like viruses, to several hundred micrometres for the largest such as pollen or dust (Alvarez-Láinez et al., 2014; Berruyer, 2017).

To physically describe the phenomena regulating the evolution of aerosols, larger particles are modelled according to the laws of general physics and smaller particles according to the kinetic theory of gases. Aerosols are distributed over significant size ranges and are classified according to their aerodynamic diameter. They are then divided between those with a size less than 10 µm (PM_{10}), less than 2.5 µm ($PM_{2.5}$), less than 1 µm (PM_1), and less than 100 nm called ultrafine particles. These small sizes allow the particles to remain in the air and to travel long distances, as they are characterised by a relatively low settling velocity (i.e. sedimentation - Baron & Klaus, 2002). The size of the particles will depend on the formation process: initially ultrafine and fine particles will evolve into larger particles through various mechanical processes (explained in detail in I.3.1.2).

These particles can also have different structures and various shapes: fibres, agglomerates, droplets, crystals, rarely spherical, possibly fractal.... These characteristics depend on the source, the evolution environment, the maturation and the transport between the formation area and the deposition or disappearance zone. For example, pollen can be spherical to subprolate (Babayi et al., 2012) but not fractal. Primary particles, known as soot precursors, are almost spherical, but with aggregation they form fresh soot aggregates with a more or less branched three-dimensional fractal morphology (Ess et al., 2021). Mature soot aggregates can collide or condense to form aerosols with spherical shapes, while mineral aerosols are neither fractal nor spherical (Maugendre, 2009).

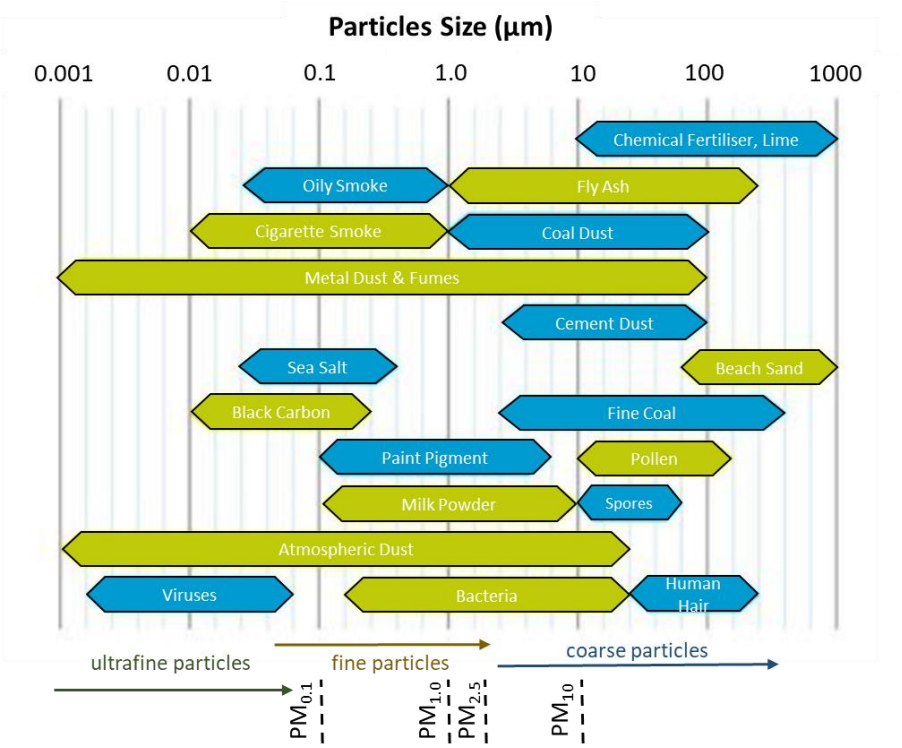

Figure I-4: Size of atmospheric particles (adapted from Alvarez-Láinez et al., 2014).

It is therefore necessary to define parameters to approach particle size as closely as possible while facilitating their study with more adapted shapes (Figure I-5). An aerosol particle can simply be assimilated to a spherical shape allowing a simple description by a single parameter: its diameter. Thus, the diameter of a particle is assimilated to an equivalence diameter corresponding to the diameter of a sphere with a specific physical characteristic common to the non-spherical shape of the particle to be measured, such as a sphere of the same surface area (Figure I-5) or the same volume (D_{ev}, Figure I-6). It is also possible to use other atmospheric models to describe aerosols based on fractal descriptions: mathematical approaches allowing a description of apparently disordered branched structures (Maugendre, 2009).

The reference diameter to describe particle sedimentation and their inertial behaviour in the respiratory organs is the aerodynamic diameter D_a (Figure I-5 and Figure I-6). This diameter of an irregularly shaped particle is defined as the diameter of a spherical particle with a standard density of 1000 kg/m³ and the same gravity settling velocity as the irregularly shaped particle considered (Hinds & Zhu, 1982).

There is also the optical diameter (Figure I-5). It allows the representation of the interaction between matter and light, i.e. diffraction and absorption of light. It is determined using techniques of static and dynamic light diffraction that belong to the field of microscopy.

In addition, it is possible to define the size of a particle with the electric mobility diameter noted D_m (Figure I-6). It corresponds to the diameter of a mono-charged particle, having the same speed of movement in a constant electric field as the considered particle (Baron & Klaus, 2002). The mobility of spherical particles is usually calculated from the Millikan model based on the Stokes equation and the electric mobility of the particles (Tammet, 2017). This model applies to particles with a sufficiently large diameter, but it is limited for the detection of fine nanoscale particles. This model is improved by the Tammet algorithm, which updates the Millikan model and overcomes this problem (Tammet, 2012).

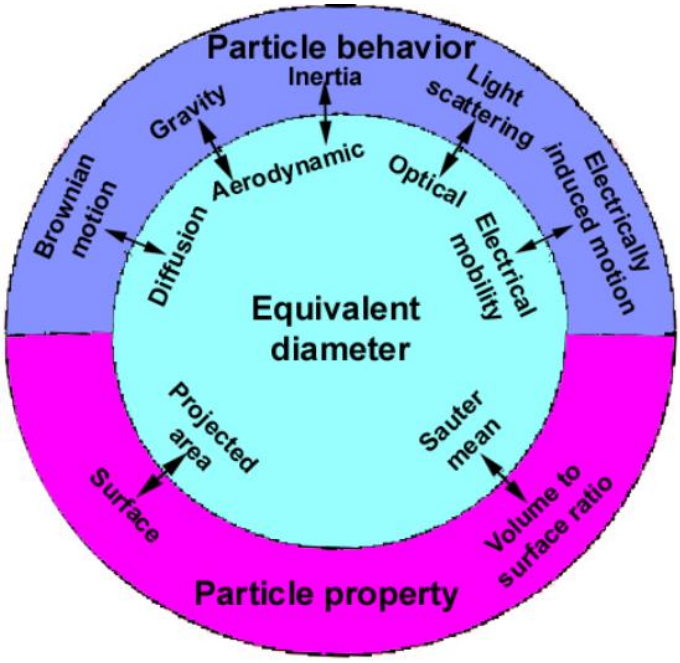

Figure I-5 : Definition of the size of particles according to their properties or behaviour (Baron & Klaus, 2002).

It is also possible to consider a diameter that provides an estimation of the mass distribution of aggregates, called the gyration or turning diameter D_g (Figure I-6). It depends on the distance between the primary particles and the mass centre of the aggregate. This approximation can be seen as a hollow sphere of the same inertia as the considered particle (Yon, 2014). This diameter is obtained by analysing electron microscopy images and provides information about the distribution of primary particles in the aggregate. It is also involved in the fractal relationship that characterises the aggregate.

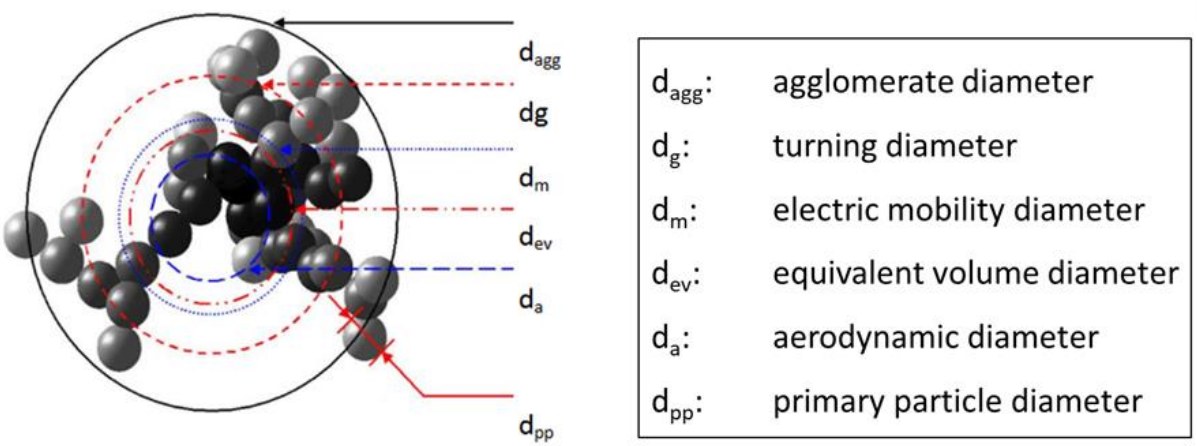

Figure I-6 : Equivalent diameters used for nanoparticle agglomerates (Ouf, 2006).

All these diameters (Figure I-6) are defined by precise equations allowing them to be calculated or related (Ouf, 2006). The determination of aerodynamic, electrical mobility, and aggregate diameters is notably linked to the turning diameter (Rogak & Flagan, 1990). In our study, most of the measurement instruments are using the electrical mobility diameter to study aeronautical particles; therefore, this diameter will be reported unless otherwise specified.

Once it is possible to estimate the size of particles in the atmosphere, a distinction is done according to different modes (Figure I-7):

- the nucleation mode (1 nm to 10 nm) for aerosols newly formed by nucleation and with a negligible mass;
- the Aitken mode (10 nm to 100 nm) concerning primary particles and related the condensation of organic gases and vapours on their surface increasing their diameter;
- the accumulation mode (0.1 to 2.5 µm) resulting from the condensation, coagulation, and coalescence of particles and corresponding to slow evolution;
- the coarse mode (2.5 to 50 µm) resulting from coagulation and impacted by erosion and abrasion phenomena.

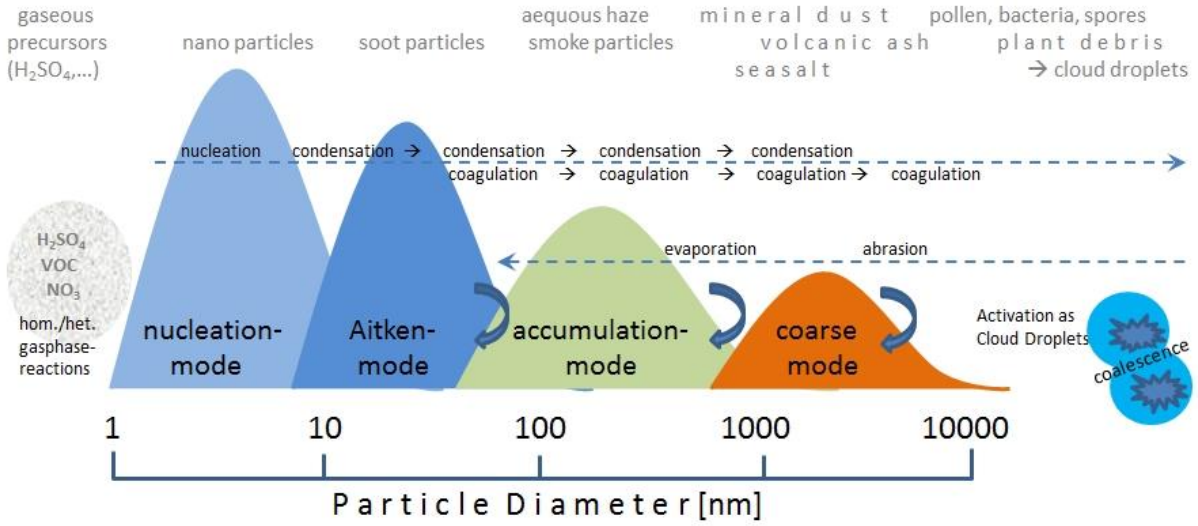

Figure I-7 : Particle evolution based on multimodal particle size distribution illustrating the different growth and decay processes of particle diameters (Deutscher Wetterdienst, 2015).

These modes overlap because particle dimensions constantly evolve due to phenomena such as condensation, coagulation, fragmentation, and evaporation. The smallest particles are produced from gas conversion into particles, which is known as homogeneous nucleation. They rapidly develop with gas condensation on their surface, followed by coagulation and coalescence. When particle diameters exceed 100 nm, thermodynamic mechanisms such as evaporation and sublimation, as well as mechanical steps such as sedimentation and deposition, take the lead (Figure I-7). At the same time, particle fragmentation and evaporation processes counterbalance diameter growth. Activation of cloud condensation nuclei, associated with an increase of the solubility by oxidation, as well as incorporation into cloud and rain droplets followed by wet deposition, are the main factors that affect and remove particles from the atmosphere.

I.2.3.3 Impact on climate

Aerosols affect the atmosphere in different ways at different levels: greenhouse gases, formation of induced cirrus clouds, climate warming… For example, the white trails observed after a plane flying overhead are called "contrails". These condensation trails from air traffic are generated by the condensation of water vapours on particles ("ice nuclei particles") emitted by aircraft engines at very high altitudes (Schumann, 2005). This phenomenon mainly occurs in the upper troposphere and is favoured by humid and cold air.

Due to the presence of natural and anthropogenic aerosols in the different layers of the atmosphere, the radiative exchanges received and emitted between the Earth's surface and Space are no longer balanced, which generates variations in atmospheric temperatures: we speak about Radiative Forcing (RF). It depends on the exchange of energy between the Sun, the atmosphere, and the Earth's surface, as well as the vertical distribution and properties of scattering and absorption of

clouds formed of ice crystals. For example, contrail cirrus have both cooling effects due to their impact on short-wave radiation and warming effects due to their influence on long-wave radiation. It can be noted that the warming effect predominates during night-time (IPCC, 1999; Lee et al., 2021; Shine, 2015). RF contributions due to the thickening of natural cirrus clouds by embedded contrail have not yet been determined, making the distinction between natural cirrus and contrail cirrus more difficult.

The presence of ice crystals in high-altitude clouds, i.e. thin cirrus clouds and contrails with long lifetimes, contributes to reduce thermal emission to space (radiant energy with $\lambda > 4$ µm) by absorbing and re-emitting infrared radiation at lower temperatures (Schumann et al., 2016). It involves an increase of the atmospheric temperature under the clouds at the surface of the Earth (Kärcher, 2018; Schumann et al., 2016) due to the forcing of the cloud greenhouse effect (Figure I-8-a). By contrast with low-altitude clouds mainly composed of water droplets (Figure I-8-b), high-altitude ice clouds are optically thin (Figure I-8-c and -d), i.e. partially transparent to solar radiation ($\lambda \approx 0.2$-4 µm). This implies that their ability to scatter shortwave radiation toward space (albedo forcing) is weak. Thus the RF is stronger for higher and colder clouds where ice crystals are more abundant (Kärcher, 2018). At low altitudes, these cirrus induce a lower degree of reflection of solar radiation back into space, resulting in a slight cooling effect. Thus, modifications of the local radiative flux due to condensation trails can reach up to 100 W/m² (Vázquez-Navarro et al., 2015). Aerosols are therefore considered as agents of climate change at different scales, whether local, regional or global, due to their impact on Earth's radiative balance (Seinfeld, & Pandis, 2006).

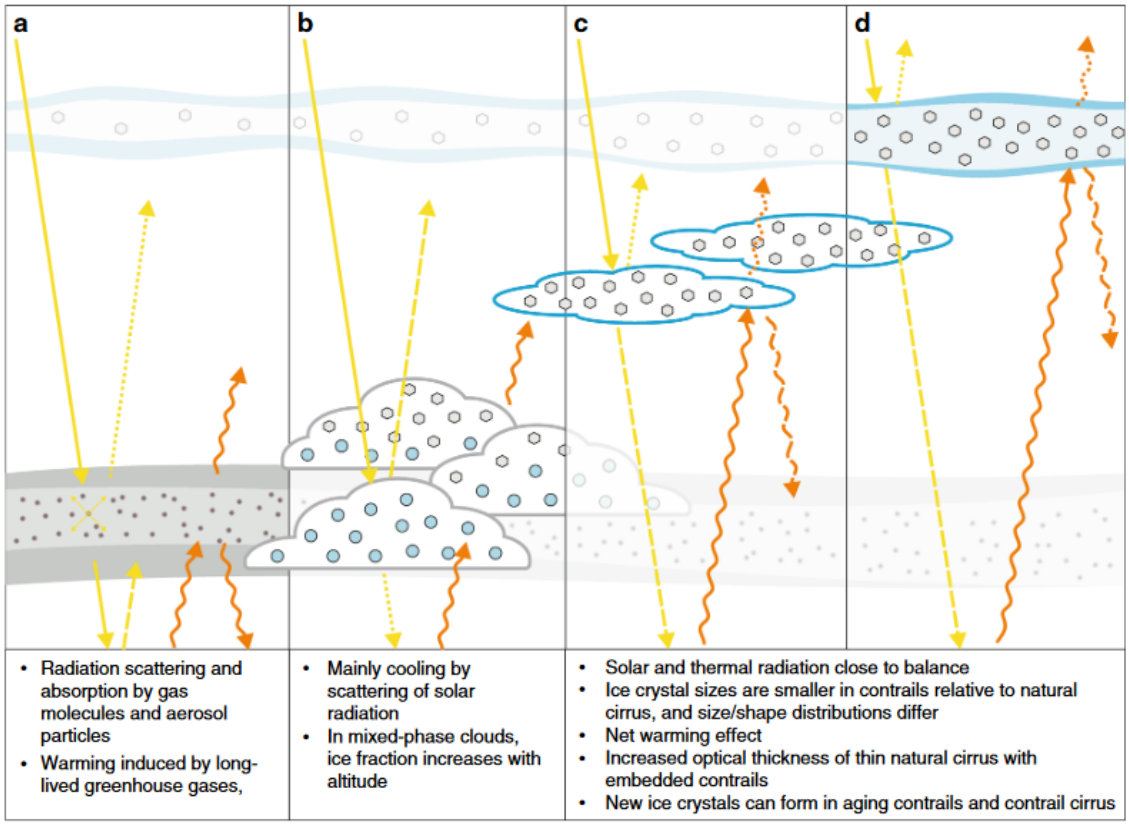

Figure I-8 : Impact of clouds with the formation and evolution of contrails depending on the altitude in the atmosphere on the Earth's radiation balance (Kärcher, 2018).

I.2.3.4 Impact on air quality and health

Air pollution has an impact on air quality and on the health of the population, particularly in urban areas (European Commission, 2021). The WHO estimates that approximately 7 million

premature deaths worldwide are caused by ambient air pollution (WHO, 2018). The most significant air pollutants are Particulate Matter (PM), nitrogen oxides (NO_x) and ground-level ozone (O_3).

Aerosols such as $PM_{2.5}$ are the cause of health problems for humans such as respiratory and cardiovascular diseases in the case of short or prolonged exposure: obstruction of the pulmonary airways due to inhalation of fine particles, internal and cutaneous irritation, cancer, a probable cause of Alzheimer's disease (Lentini, 2018; Pascal et al., 2013; Pope et al., 2011). The potential danger represented by these aerosols is related to the transport of toxic molecules on their surface combined with their small sizes. Some species, such as polycyclic aromatic hydrocarbons (PAHs), are classified as carcinogenic (Pandey et al., 2011) by the International Agency for Research on Cancer (IARC). Moreover, these particles are small enough (on the order of nanometres or micrometres) to penetrate the lungs (Figure I-9) and deep into the respiratory tract, where they can then block them or cause breathing difficulties (Jonsdottir et al., 2019). The smallest particles can cause lung cancer as well as cardiovascular, allergic, and respiratory problems, due to their significant reactivity surface area and potential toxicity (Kim et al., 2013). They can also stay in the lungs for a long time and release dangerous chemical species absorbed on their surface, such as PAHs or sulphur dioxide (Guo et al., 2021).

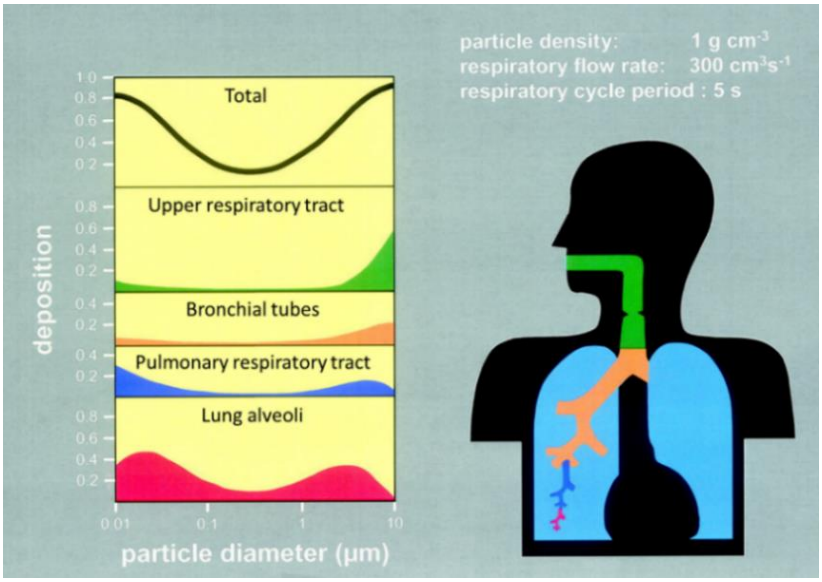

Figure I-9: Total and regional deposition of unit-density spheres in the human respiratory tract predicted by the International Commission on Radiological Protection deposition model for oral inhalation at rest (Heyder, 2004).

Exposure limits to pollutants have been set to protect populations. A global Air Quality Guideline (AQG) from the WHO has defined six key atmospheric pollutants (Table I-1) for different alert thresholds (WHO, 2021). Two types of fine particulate matter are considered here: those with a diameter less than 10µm (PM_{10}) and those with a diameter less than 2.5µm ($PM_{2.5}$). In addition, ozone (O_3), nitrogen dioxide (NO_2), sulphur dioxide (SO_2), and carbon monoxide (CO) are included.

Air quality has gradually improved in high-income countries, while it has deteriorated in low- and middle-income countries due to economic development and industrialisation, thus increasing disparities in exposure to air pollution. Pollutant concentrations still exceed air quality limit values set by the WHO (2005) in many regions. In 2019, over 90% of the world's population lived in areas where concentrations exceeded the WHO (2005) air quality guidelines for long-term exposure to $PM_{2.5}$.

Achieving recommended levels for air quality criteria would result in considerable global health benefits. Based on WHO scenarios and AQG recommendations, it is estimated that about 80% of deaths attributed to $PM_{2.5}$ exposure worldwide could be avoided. The greatest impact would be seen in the Southeast Asia and Africa regions (57% and 60% reduction respectively).

Pollutant	Averaging time	2005 AQGs	2021 AQG level
$PM_{2.5}$ (µg/m³)	Annual	10	5
	24-hours[a]	25	15
PM_{10} (µg/m³)	Annual	20	15
	24-hours[a]	50	45
O_3 (µg/m³)	Peak season[b]	-	60
	24-hours[a]	100	100
NO_2 (µg/m³)	Annual	40	10
	24-hours[a]	-	25
SO_2 (µg/m³)	24-hours[a]	20	40
CO (mg/m³)	24-hours[a]	-	4

Table I-1: Air quality Guidelines (AQG) recommended in 2021 compared to 2005 by the World Health Organisation (WHO, 2021). [a] 99th percentile (i.e. 3–4 exceedance days per year). [b] Average of daily maximum 8-hours mean O_3 concentration in the six consecutive months with the highest six-month running-average O_3 concentration. Note: Annual and peak season is long-term exposure, while 24 hours and 8 hours is short-term exposure.

Some air pollutants such as black carbon or ground-level ozone are short-lived climate pollutants. Reducing their impact has beneficial effects on both health and climate.

I.3 Formation of non-volatile and volatile Particulate Matter

I.3.1 Main mechanisms of nvPM formation in combustion

Non-volatile particulate emissions mainly consist of soot particles or black carbon emissions. They are present at high temperatures in engine exhaust and have a geometric mean diameter extremely small from 15nm to 60nm (ICAO, 2016). To reduce emissions of these particles, detailed knowledge of their characteristics (properties, problems generated) and an understanding of their formation in the combustion chamber is necessary.

Soot particles are formed from the incomplete combustion of hydrocarbons (HCs) (Burg, 2014; Kohse-Höinghaus, 2019; Smallwood et al., 2000). These particles are generally observed in high-temperature flames with high local richness (Baron & Klaus, 2002; Borghi & Destriau, 1995). Their elemental chemical composition is mostly made up of carbon and hydrogen atoms, allowing them to be classified based on this ratio as nascent soot or as mature/carbonised soot. These particles have a complex quasi-fractal morphology and are composed of primary particles with a nearly spherical shape and a diameter of a few nanometres (Figure I-10). It should be noted that the detection limit of nascent soot particles is around 2-4 nm (Betrancourt et al., 2017; Carbone et al., 2016; Desgroux et al., 2013). This diameter evolves within a flame depending on the combustion parameters. Indeed, at the surface of the soot particles, the presence of radical areas allows reactions between radicals (Johansson et al., 2016). It happens that they retain by absorption molecules or poly-aromatic radicals during the combustion processes but also in the exhaust (Lentini, 2018; Michelsen et al., 2015a). The main stages of formation and evolution of soot are nucleation (to get primary particles), surface growth by agglomeration and coalescence (to get soot particles), coagulation (to get soot aggregates), and decrease by oxidation (Figure I-10).

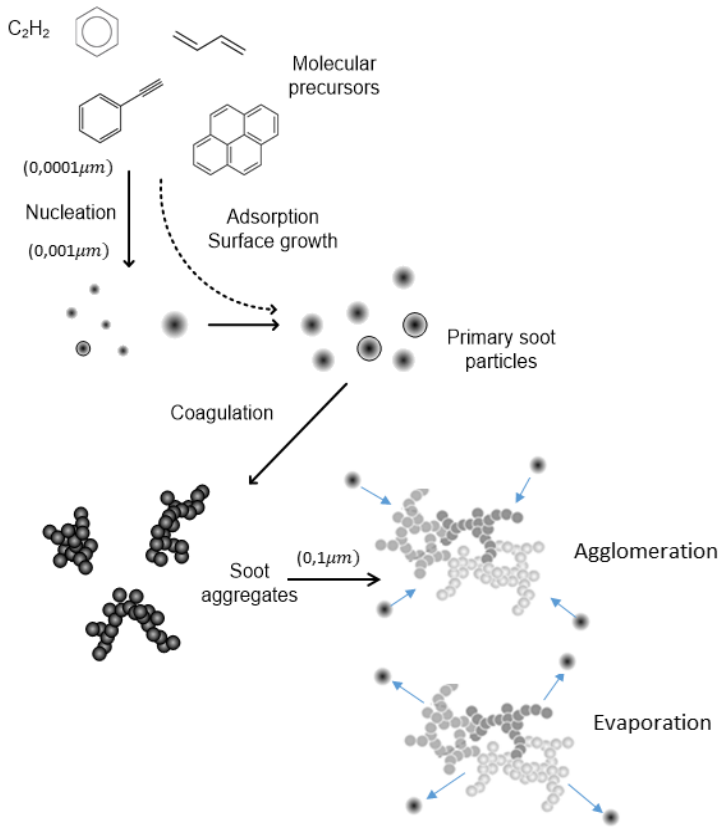

Figure I-10 : General mechanism of soot particle formation (Bockhorn & Schäfer, 1994).

I.3.1.1 Nucleation principle

The formation of the first soot particles called nuclei, with a diameter of a few nanometres (Desgroux et al., 2017), is obtained through nucleation from gaseous precursors. The transition of gaseous compounds, corresponding to the precursors of soot called Polycyclic Aromatic Hydrocarbons (PAHs), into solid nuclei is still not entirely understood in the combustion process (Desgroux et al., 2013). It is difficult to experimentally detect the species involved in these reactions and to identify the molecular phenomena involved (Johansson et al., 2017; Veshkini et al., 2016).

There are various studies proposing mechanisms for the formation of soot particles in the literature. One of them describes the formation of fullerenes (polyhedral carbon structures) obtained by bimolecular reactions between two PAHs, involving a coordinated detachment of hydrogen atoms or closure mechanisms (Homann & Wagner, 1996). A second version involves the coagulation of PAHs by collision forming compact clusters governed by Van der Waals interactions (Frenklach, 2002), resulting in dimers of PAHs considered as the very first solid particles. These dimers continue to increase in size by undergoing new collisions with other similar species, while the PAHs continue to grow in size individually through molecular reactions. Another mechanism describes the formation of the first soot nuclei from the coalescence of PAHs with C-C bonds resulting in a three-dimensional structure (Richter & Howard, 2000). It should also be noted that the formation of soot particles in flames is faster than the increase of PAHs in aromatic rings from the HACA H-Abstraction and C_2H_2-Addition mechanism (Frenklach & Wang, 1991). Recent studies propose another main reaction leading to the formation of soot particles based on rapid chain reactions of resonance-stabilised radicals (Johansson et al., 2018). The radicals react with other hydrocarbon species (Figure I-11-A) to form covalently linked clusters of PAHs. Growth and grouping are favoured by successive couplings of radicals (Figure I-11-B), and the clusters of PAHs are stabilised by resonance through hydrogen abstraction and absorption reactions (HACA mechanism).

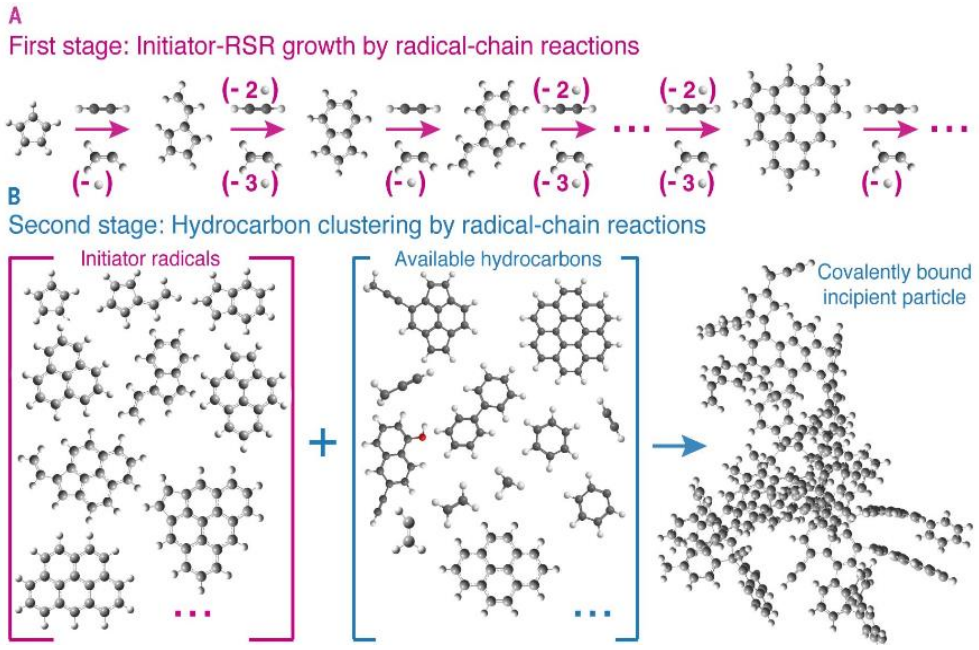

Figure I-11 : Hydrocarbon clustering by radical chain reaction mechanisms and stabilised by resonance (RSR) (Johansson et al., 2018).

I.3.1.2 Growth and reduction of the particles surface

The surface of the particles thus created then grows by chemisorption of hydrocarbons (Johansson et al., 2018). These experimental and theoretical works also suggest that structures containing 5 non-aromatic carbon atom cycles play an important role in the formation and growth of soot particles (Irimiea et al., 2019). These clusters are indeed stable enough to be present in the gas phase or absorbed by young soot particles at potentially high concentrations (Figure I-12).

When the first nuclei are thus formed, their surface increases rapidly through various processes. One of them is based on the condensation of PAHs on the carbon matrix of soot according to collision theory (Balthasar, 2000). Another process involves heterogeneous reactions between the carbon matrices of soot and surrounding gaseous precursors. In this case, the precursor primarily responsible for increasing particle size is acetylene, according to the HACA mechanism (Balthasar, 2000; Frenklach & Wang, 1991).

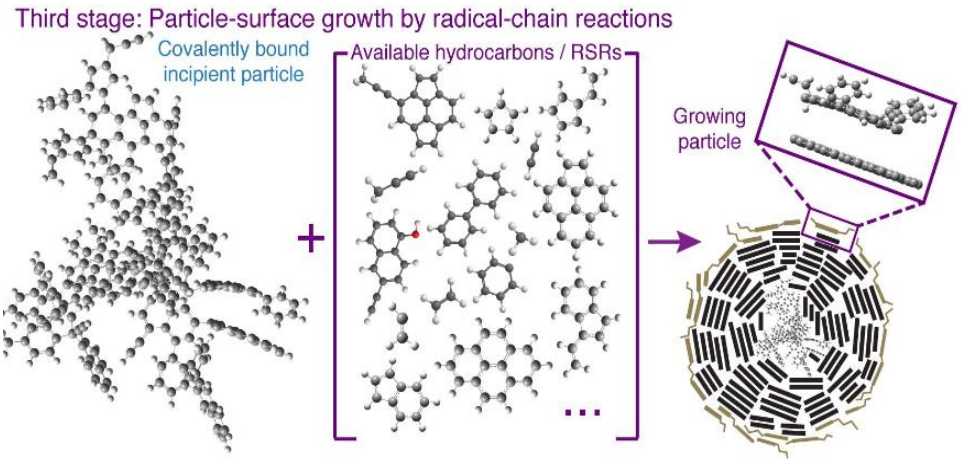

Figure I-12 : Particles Surface growth by radical chain reaction mechanisms leading to cluster size increase and primary soot particles formation (Johansson et al., 2018).

Physical and chemical processes, such as coagulation, automatically lead to an increase in the diameter of soot particles, especially the mobility diameter D_m (Kelesidis et al., 2017). With soot coagulation, particles produced through different nucleation stages merge and form aggregates that are quickly covered by an outer shell from deposition of gas-phase materials. This process increases particle size (Figure I-13) but decreases the number of particles without changing the soot volume fraction (Irimiea, 2017).

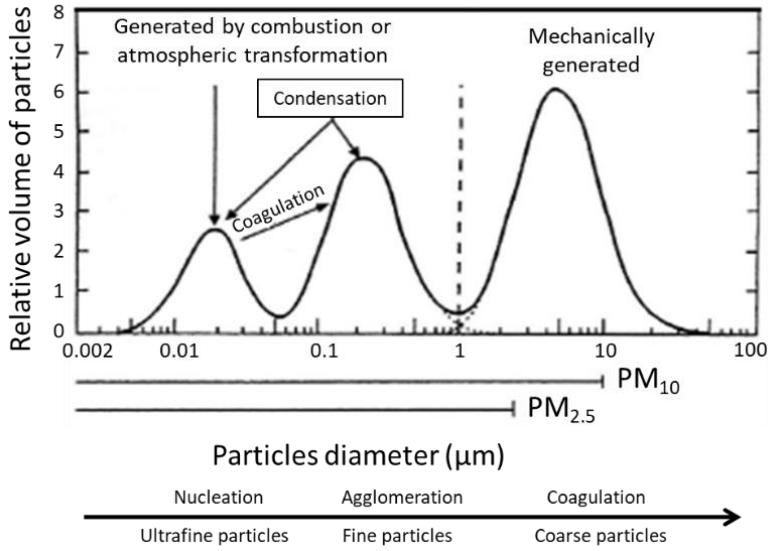

Figure I-13: Formation of atmospheric particles typical of an urban aerosol (Berruyer, 2017).

During coagulation, there is a progressive reduction in the number of hydrogen atoms and a rearrangement of the internal structure of soot particles, giving them a spherical shape. The size and structure of the particles change as the soot grows. After coagulation and surface development, the size of the particles can reach around a hundred nanometres in diameter depending on the experimental conditions. Furthermore, the particles can undergo surface reactions resulting in particle aggregation.

During the collision process, mature soot no longer coagulates but particles can still merge. These aggregation reactions allow the formation of complex-shaped soot aggregates (Ono et al., 2015), as shown in Figure I-12. Mature soot particles continue to grow in size by agglomeration before the phenomenon of oxidation, which takes place both on the surface and inside the particle, takes over (Kelesidis & Pratsinis, 2019). Oxidation corresponds to the partial combustion of aggregates by oxygen and OH radicals. Oxygen penetrates inside the particles due to its low collision efficiency. This leads to internal oxidation that contributes to particle rupture. OH radicals, having a higher collision efficiency, lead to surface oxidation that tends to reduce the mass and size of aggregates (Ouf, 2006).

I.3.2 Factors affecting secondary aerosol formation

The formation and ageing mechanisms of secondary aerosol (SA) attracted more and more attention in recent years due to aerosol-cloud-climate interactions and their impact on human health. A large amount of studies are dealing with the properties of the atmospheric SA to understand how particles are formed and grown under atmospheric conditions (Almeida et al., 2013; Kirkby et al., 2011, 2016; Kulmala et al., 2013; Kulmala & Wagner, 1996; Lehtipalo et al., 2016a; Riccobono et al., 2014; M. Wang et al., 2022). This aerosol formation process is complex and involves different chemical and physical mechanisms (Figure I-14): aerosol nucleation and growth (Kulmala et al., 1996; Sipila et al., 2010), gas/ particle partitioning (Odabasi et al., 2005), and heterogeneous reactions (Tolbert et al.,

2013). It also depends on many factors such as gas composition or presence of pollutants as well as temperature, humidity or light exposure (Zhang et al., 2023).

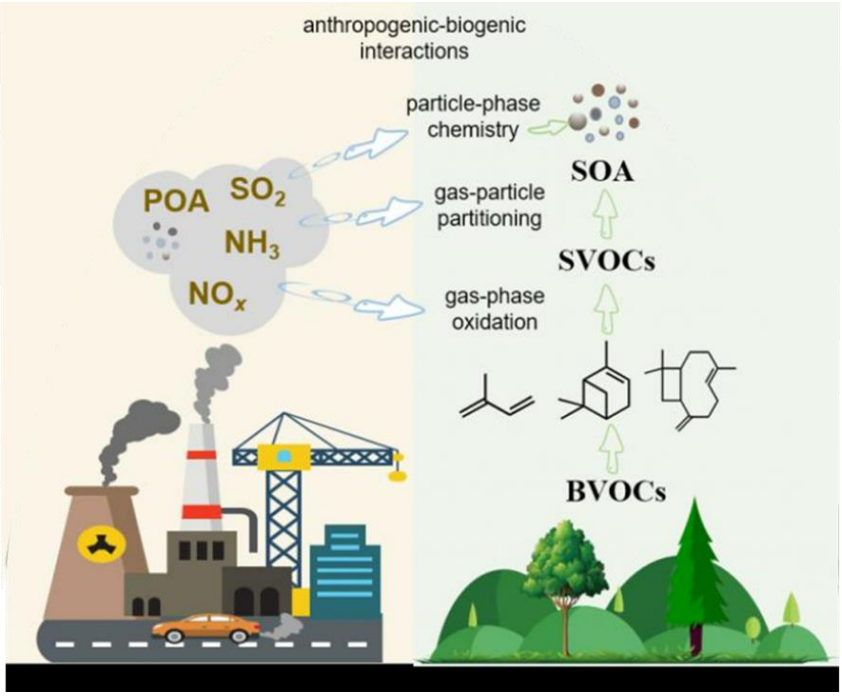

Figure I-14: Schematic process of Secondary Organic Aerosol (SOA) formation through anthropogenic-biogenic interactions (adapted from L. Xu et al., 2021). Human activities generate Primary Organic Aerosols (POA), sulphur dioxide (SO_2), Ammonia (NH_3), or nitrogen oxides (NO_x). Biogenic volatile organic compounds (BVOCs) are produced by terrestrial vegetation.

Secondary aerosols can be classified in two categories: Secondary Organic Aerosols (SOAs) and Secondary Inorganic Aerosols (SIAs) that are formed in the atmosphere through different mechanisms (Peng et al., 2022). SOAs come from the oxidation of volatile organic compounds (VOCs) emitted from anthropogenic and natural sources, such as engine exhaust, industrial processes, and vegetation. The oxidation products of VOCs can condense and form SOAs, which can contribute significantly to fine particulate matter (PM) in the atmosphere. Model predictions have shown that the atmospheric concentrations of SOAs will exceed the one of sulphate by the end of the century (Tsigaridis & Kanakidou, 2007), which suggests that the role of SOA in the atmosphere is likely to become increasingly important in the future. On the other hand, SIAs are formed through the oxidation products from the condensation of inorganic gases, such as sulphur dioxide (SO_2) and nitrogen oxides (NO_x), which are emitted primarily from anthropogenic sources (power plants, industrial processes, transportation). These gases can react in the atmosphere to form sulphuric acid (H_2SO_4) and nitric acid (HNO_3), which can lead to the formation of aerosols by condensation. It should be noted that most condensed compounds are organics leading more generally to the formation of SOA. Both categories contribute to PM in the atmosphere and have significant impacts on the environment and the human health (Sokan-Adeaga et al., 2019; B. Zhang, 2020).

SA formation has been studied for several years and at the beginning, only the heterogeneous process between gas and particles was taken into account. Since 1996, the possibility of a homogeneous nucleation process has been considered with (Kulmala & Wagner, 1996). Nowadays, thanks to the development of cutting edge experimental (Junninen et al., 2010) and theoretical techniques (McGrath et al., 2012; I. K. Ortega et al., 2012) as well as experiments on atmospheric simulation chambers (Kirkby et al., 2011; Lehtipalo et al., 2016a; Y. Zhang et al., 2023), our knowledge about this phenomenon has been deeply improved. Currently, sulphuric acid is considered as the main driving component involved in the formation of SA (Kulmala et al., 2013). Other compounds are also envisaged in atmospheric nucleation such as ammonia (Kirkby et al., 2011), organic compounds like

amines (Almeida et al., 2013) or highly oxidised organic compounds (HOMs - Riccobono et al., 2014), but also chemi-ions (Kirkby et al., 2016). The principle of nucleation reaction to obtain SA is based on the presence of an acid (H_2SO_4, HNO_3, HOMs…) assisted by a base (ammonia, water, DMA…) to stabilise the cluster formed. The following subsections will present in more detail and chronologically the different pathways considered in the formation and growth of secondary aerosols.

I.3.2.1 Implication of sulphuric acid on SOA formation

Sulphuric acid has been considered as the first candidate to explain the formation of SA (Donahue et al., 2013; Kulmala et al., 1996, 2013; Riipinen et al., 2007; Sipila et al., 2010). It is linked in particular to the formation of sulphate aerosols that are one of the main components of volatile particles in the atmosphere. Initially, sulphur oxides (SO_x), including sulphur dioxide (SO_2) are emitted into the atmosphere from anthropogenic sources (power plants, industrial processes, aircraft engines). SO_2 can be oxidised by hydroxyl radicals (OH) or ozone (O_3) to form sulphur trioxide (SO_3 – cf. eq. I.3 to I.5). This reaction is catalysed by some transition metal ions like iron and manganese that are present in atmospheric particles. SO_3 can then react with water vapour (eq. I.6) to form sulphuric acid (H_2SO_4).

$$SO_2 + OH \rightarrow HOSO_2 \quad \text{(eq. I.3)}$$
$$HOSO_2 + O_2 \rightarrow HO_2 + SO_3 \quad \text{(eq. I.4)}$$
$$SO_2 + O_3 \rightarrow SO_3 + O_2 \quad \text{(eq. I.5)}$$
$$SO_3 + H_2O \rightarrow H_2SO_4 \quad \text{(eq. I.6)}$$

H_2SO_4 is a key precursor for secondary aerosols formation and responsible for the nanoparticle growth in the atmosphere (Donahue et al., 2013). Once formed, sulphuric acid molecules can cluster together (homogeneous nucleation - Sipila et al., 2010) or with other compounds such as water or ammonia (hetero-molecular homogeneous nucleation) to form first small particles. It happens when the concentration of sulphuric acid vapours exceeds a certain threshold. The nuclei are small and they are referred to as "molecular clusters." Once the nuclei are formed, other gases and particles in the atmosphere can condense onto their surface, causing them to grow in size. Sulphuric acid molecules can also be absorbed onto pre-existing particles in the atmosphere through an acid-catalytic mechanism (Liggio & Li, 2006; Surratt et al., 2007), which can act as nuclei for further growth and promote the formation of SOA. For example in Figure I-15, sulphuric acid can react with organic compounds, such as volatile organic compounds (VOCs) to stabilise sulphuric acid clusters. The reaction of sulphuric acid with organic compounds is complex and can involve several pathways, including photo-oxidation, ozonolysis, and heterogeneous reactions on aerosol surfaces.

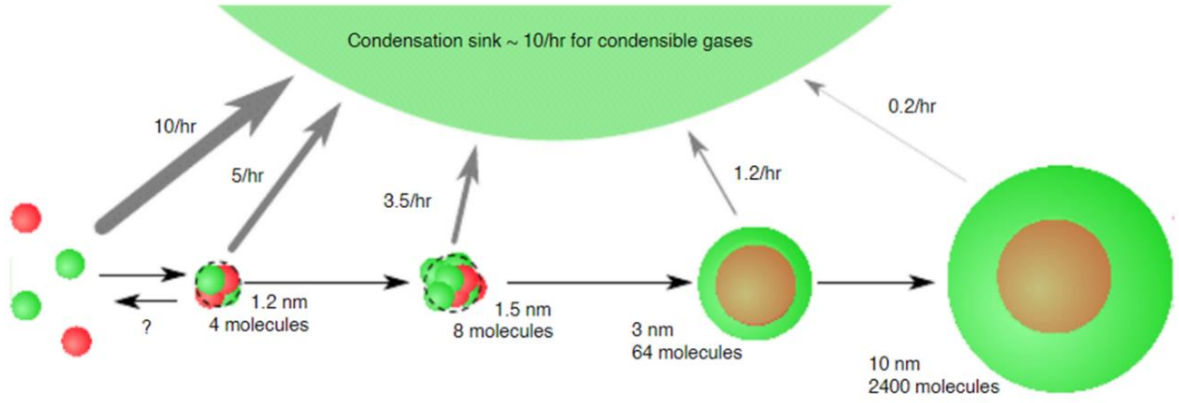

Figure I-15: Nucleation process leading to particle formation from organics (in green) and sulphuric acid (in red) (Donahue et al., 2013). Typical growth rates are of the order 1-2nm/hr. Only a small fraction of small clusters reach the operational threshold for particle formation (1.2nm ≤ physical diameter ≤ 1.5nm).

The effect of sulphur oxides on secondary aerosol formation depends on several factors, including the concentration of SO_x and other precursor gases, temperature, humidity, light, and the availability of other reactants (Y. Zhang et al., 2023). Additionally, the impact of SO_x emissions on secondary aerosol formation can vary depending on the location and time of year, as well as other local factors such as topography and atmospheric circulation patterns (Pan, 2011). Sulphur functional groups can also make aerosol PM significantly acidic, which significantly enhances the hygroscopicity of particulate matter and improves the Cloud Condensation Nuclei (CCN) activity (Merikanto et al., 2009; Nguyen et al., 2012; Pye et al., 2020). However, only sulphuric acid is not sufficient to explain the complete conversion of gaseous precursors into secondary aerosol (Kuang et al., 2012; Kulmala et al., 2013). Therefore, there are other mechanisms and contributions involved such as organic particles (for example nucleation of biogenic vapours emitted by forests) and ammonia produced by natural sources or human activities.

I.3.2.2 Effect of basis: ammonia and amines

As mentioned before, the reaction of nucleation can be completed by a base to help the acid in aerosols formation (Chen et al., 2012). Ammonia (NH_3) has been considered at first as involved in atmospheric SOA formation (Kirkby et al., 2011; Paulot & Jacob, 2014; Updyke et al., 2012). For example, ammonium aerosols are produced by the reaction of ammonia with sulphuric acid. When ammonia mixing ratios in the atmosphere reach 100 parts per trillion by volume or less, they significantly increase the nucleation rate of sulphuric acid particles by 100 to 1,000 times, according to (Kirkby et al., 2011). This nucleation process is driven by a base-stabilisation mechanism, which involves the gradual accumulation of ammonia molecules (based on molecular measurements that are time-resolved).

NH_3 can also react with carbonyl species and other secondary organic compounds to produce highly conjugated, light-absorbing, nitrogen-containing organic (NOC) compounds, which are an important component of brown carbon (Huanget al., 2018; Updyke et al., 2012; Wang et al., 2018). SOA change colour from white (fresh aerosols) to brown (aged aerosols) in presence of ammonia (Figure I-16) and this secondary brown carbon may contribute to absorption of solar radiation by the aerosols (Updyke et al., 2012). It can be noted that aqueous reaction with ammonium ions is equally efficient in producing brown carbon. NOC are generated through two pathways: reaction of NH_3 with carbonyl-containing compounds to generate organic amines (Wang et al., 2010), or reaction of NH_3 with organic/inorganic acids in particulate matter under acidic conditions (Kuwata & Martin, 2012). The addition of NH_3 can either promote or inhibit SOA generation, depending on the initial concentration of NH_3 and the reaction system.

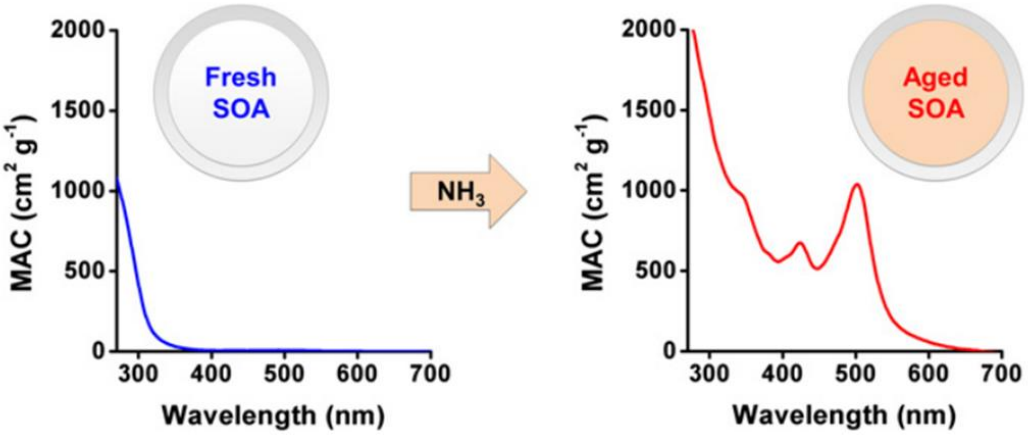

Figure I-16: Wavelength-dependent mass absorption coefficients (MAC) of the aged SOA. Reactions of SOA compounds with Ammonia (NH_3) result in production of light-absorbing "brown carbon" compounds (Updyke et al., 2012).

When NH_3 is oxidised by NO_x and O_3, it can form ammonium nitrate (NH_4NO_3) and ammonium sulphate (NH_4SO_4). Ammonium salts can then act as aerosol nuclei, facilitating particle formation and growth by condensation onto existing aerosol particles (J. Smith et al., 2010). The reaction of ammonia and nitric acid occurs in two steps. At first, ammonia reacts with nitric acid (HNO_3) to form ammonium nitrate (eq. I.7). Then, the ammonium nitrate can react with other acids or bases in the atmosphere, leading to the formation of different types of aerosols. For example, if the ammonium nitrate reacts with organic compounds, it can form organic nitrates. If the ammonium nitrate reacts with sulphuric acid, it can form ammonium sulphate (eq. I.8). Nitric acid is considered in recent studies to complete sulphuric acid in aerosol formation. Generally, the nitric acid is negligible compared to sulphuric acid concentrations, but at high altitude and low temperatures, the nitric acid becomes more relevant in the nucleation process (M. Wang et al., 2022). Synergistic nucleation of HNO_3, H_2SO_4 and NH_3 generates CCN and ice nuclei in the upper troposphere (M. Wang et al., 2022) and is closely linked with anthropogenic ammonia emissions (Nault et al., 2021).

$$NH_3 + HNO_3 \rightarrow NH_4NO_3 \qquad \text{(eq. I.7)}$$
$$NH_4NO_3 + H_2SO_4 \rightarrow (NH_4)_2SO_4 + HNO_3 \qquad \text{(eq. I.8)}$$

The formation of secondary aerosols from ammonia is influenced by several factors, including the concentration of the gases in the atmosphere, the temperature (higher temperatures can increase the rate of chemical reactions and aerosol formation) and the presence of other chemical species. High concentrations of ammonia can lead to more rapid formation of ammonium nitrate and other SOA (Lehtipalo et al., 2016a). However, atmospheric concentrations of ammonia and sulphuric acid are insufficient to account for observed boundary-layer nucleation (Kirkby et al., 2011).

Observations in the field and quantum chemical calculations have suggested that organic amine compounds, in addition to ammonia, may play an important role in the formation of new particles involving H_2SO_4 (Chen et al., 2012; Erupe et al., 2011; Kürten et al., 2014; Kurtén et al., 2008; Loukonen et al., 2010; J. Smith et al., 2010; H. Yu et al., 2012). To investigate this further, researchers have examined the structure and formation thermodynamics of dimer clusters containing H_2SO_4 with ammonia and different amines that may exist in the atmosphere (Kurtén et al., 2008). The results indicate that all studied amine-H_2SO_4 complexes bind more strongly than NH_3-H_2SO_4 and that amines assist the growth of both neutral and ionic clusters along the H_2SO_4 coordinate more efficiently than ammonia. This suggests that amines may play a more significant role than ammonia in enhancing neutral and particularly ion-induced sulphuric acid-water nucleation in the atmosphere. Furthermore, when assessing the impact of human activities on particle formation, both amines and sulphur dioxide should be considered in areas close to amine sources. Amines and NH_3 are important nucleation species, but under dry atmospheric conditions, amines may have stronger effects on H_2SO_4 nucleation than NH_3 (Erupe et al., 2011; Loukonen et al., 2010).

According to Almeida et al. (2013) and Kürten et al. (2014), new particle formation rates in the atmospheric boundary layer can be explained in particular by the presence of DiMethylAmine (DMA). Indeed, concentrations of DMA at levels above 3 parts per trillion by volume (pptv) can enhance particle formation rates more than 1,000 times compared with ammonia, which is sufficient to account for the observed rates of particle formation in the atmosphere. The mechanism behind the accelerated nucleation is a base-stabilisation process involving pairs of acid-amine molecules that decrease evaporation. The Figure I-17 presents the concentration of the neutral acid dimer and monomer measured using a chemical ionisation mass spectrometer (CIMS) before and after the addition of DMA (only neutral clusters in the CLOUD chamber - Almeida et al., 2013). The results demonstrate that the nucleation process in the atmospheric boundary layer is highly sensitive to small amounts of amine (few pptv). Sulphuric acid-amine nucleation follows the same base-stabilisation mechanism as observed with ammonia, in which each additional acid molecule in the cluster is stabilised by one or two base molecules (Kirkby et al., 2011). However, acid-base pairs with amines are more tightly bound

than with ammonia, resulting in cluster formation rates approaching the kinetic limit. The concentration of DMA above 5 pptv does not show a significant increase, indicating that nucleation at atmospheric H_2SO_4 concentrations is limited by the availability of H_2SO_4 and not by DMA (Almeida et al., 2013).

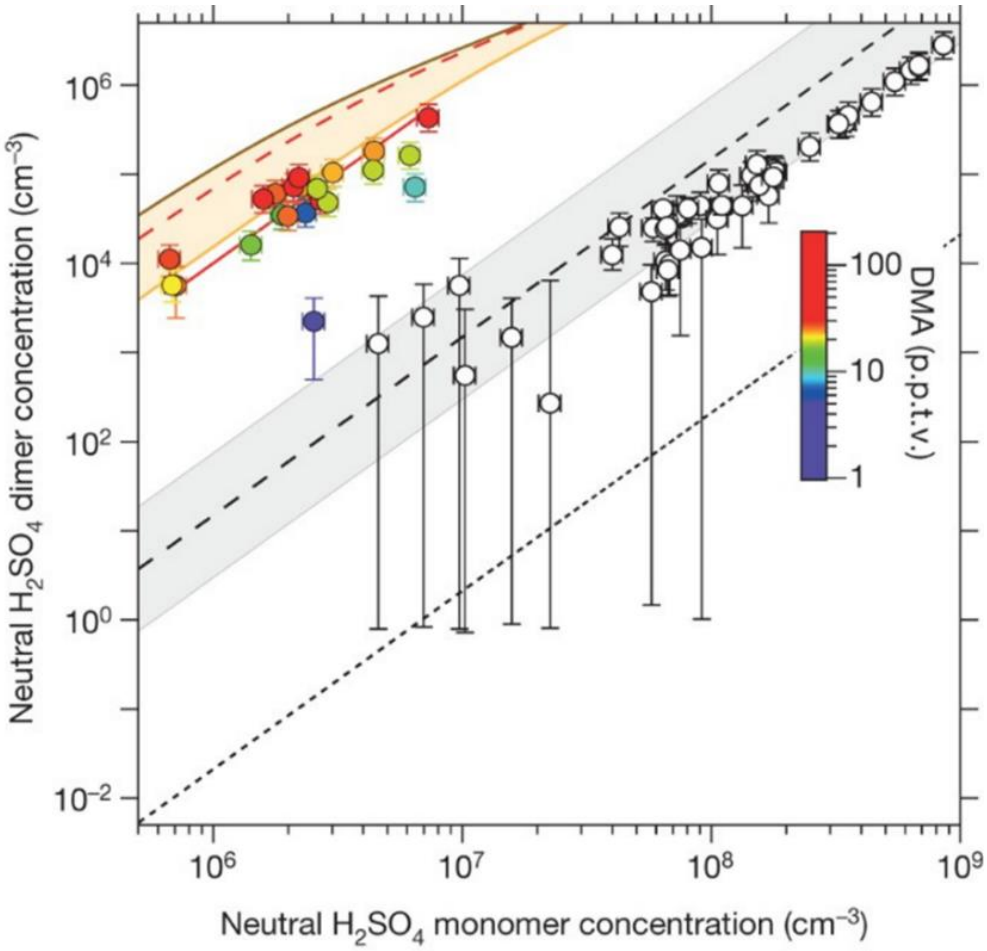

Figure I-17: Evolution of neutral H_2SO_4 dimer depending on monomer concentrations before and after the addition of DMA (Almeida et al., 2013). Concentrations have been measured by CIMS in CLOUD chamber without (blank circles) and with DMA (3–140 pptv) and 10 pptv NH_3 (coloured circles), at 38% RH and 278 K. The fitted red curve corresponds to the quadratic dependence on monomer concentration, associated with a model of uncertainty (orange band) and an upper limit (brown curve). The other curves show the expected neutral dimer concentrations for the binary H_2SO_4–H_2O system (short-dashed black line), for production in the CIMS ion source (dashed black line and grey uncertainty band) and for 10 pptv DMA in the ACDC model (dashed red line).

I.3.2.3 Contributions of Highly Oxidised organic Molecules to atmospheric aerosols

In some cases, for example nucleation of biogenic vapours emitted by forests, H_2SO_4 concentrations are really low and insufficient to explain the formation of SOA, implying that something else contributes to the nucleation process. As seen for the case of sulphur oxides (I.3.2.1), atmospheric oxidation reactions have an impact on the formation of secondary aerosols. When primary pollutants as volatile organic compounds (VOCs) are emitted into the atmosphere, they undergo oxidation reactions with atmospheric oxidants, such as hydroxyl radicals (OH), ozone (O_3), and nitrate radicals (NO_3), to form secondary aerosols. In the troposphere, OH radicals and O_3 are the main removal pathways for VOCs during the daytime, while NO_3 is the main oxidant at night (Atkinson, 2000). A particular attention is given to the oxidation of organic compounds such as terpenes $(C_5H_8)_n$, benzene (C_6H_6) or toluene (C_7H_8) by OH radicals, that leads to the formation of Highly Oxidised organic

Molecules (HOMs – examples Figure I-18). These molecules have been identified as large contributors to atmospheric SOA in forested environments (Bianchi et al., 2019). HOMs are highly functionalised molecules with large variety of functional groups, such as nitrates, alcohols, carboxylic acids, peroxides. They can condense onto pre-existing aerosol particles and thus be involved in secondary organic aerosol formation (Pospisilova et al., 2020; Riccobono et al., 2014).

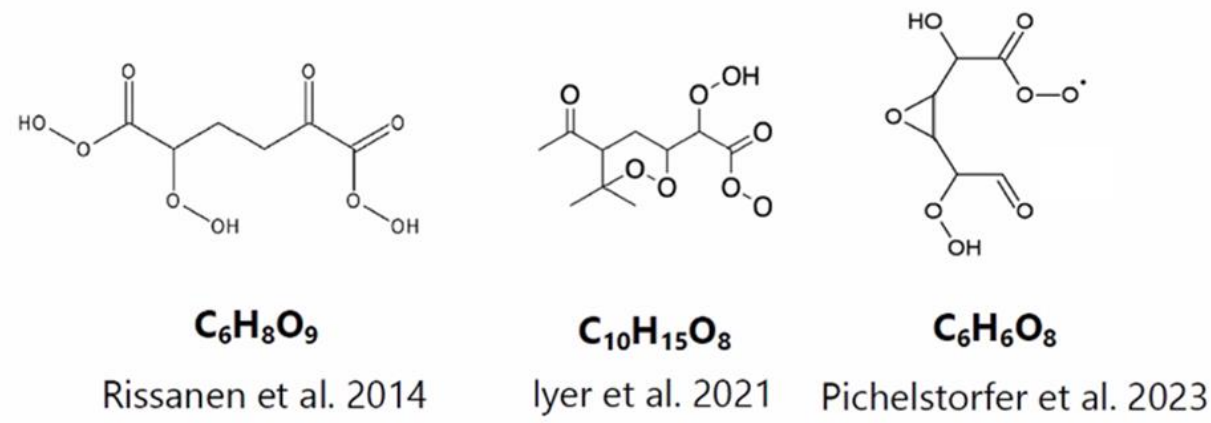

Figure I-18: Example of HOMs particles. HOMs correspond to particles with an O/C ratio close to 1.

HOMs mainly come from the oxidation of biogenic and anthropogenic gases. Their formation is a complex process and there are different possible ways that VOCs can be transformed in the atmosphere into HOMs due to reaction with atmospheric oxidants. Recent studies have suggested that reactions involving multi-generation OH oxidation steps, followed by subsequent reactions with oxygen, may be an important pathway for the formation of HOMs (Garmash et al., 2020).

A first method involves the creation of alkyl radicals (R) and water through the removal of hydrogen atoms from various C-H bonds in VOCs, including C-H bonds in aldehydes (CHO groups) and C-H bonds in substituents in alkene and aromatic compounds. However, hydrogen atoms cannot be easily removed from vinyl C-H bonds, C=C bonds or C-H bonds in aromatic rings.

A second method involves oxidants attacking double bonds. The compounds obtained then break down into carbonyl oxide (by ozonolysis of alkene), which can undergo additional reactions with other molecules such as CO, NO_2 or H_2O leading to the formation of alkyl radicals R and then peroxy radicals RO_2 (Figure I-19). These products are typically highly reactive and unstable compounds that can undergo further reactions (Bianchi et al., 2019; Cheng et al., 2021) which lead to the formation of highly oxygenated or nitrated products (Pospisilova et al., 2020; Zhao et al., 2021). For example Figure I-20 presents the formation process leading to peroxy radicals more oxidised through autoxidation (Bianchi et al., 2019). At the end, the new peroxy radical formed is heavier and less volatile. First HOMs are obtained after different reactions (Hoyle et al., 2011; Kroll & Seinfeld, 2008): hydroperoxides (ROOH), carboxylic acids (RC(O)OH), peroxycarboxylic acids (RC(O)OOH), peroxynitrates (ROONO2), nitrates (RONO2), alcohols (ROH), and carbonyls (RC(O)R').

Depending on the oxidation process, the contributions of HOMs will be different: HOMs from monoterpene oxidation dominate the growth of ultra-fine particles while HOMs (with sulphuric acid) from aromatics oxidation play a more important role in particle growth (Qi et al., 2018). Furthermore, the experimental conditions have an impact on product distributions. For example, high-NO_x conditions enhance the formation of organonitrates while the HOMs composition is changed and their formation is suppressed (Cheng et al., 2021; Garmash et al., 2020).

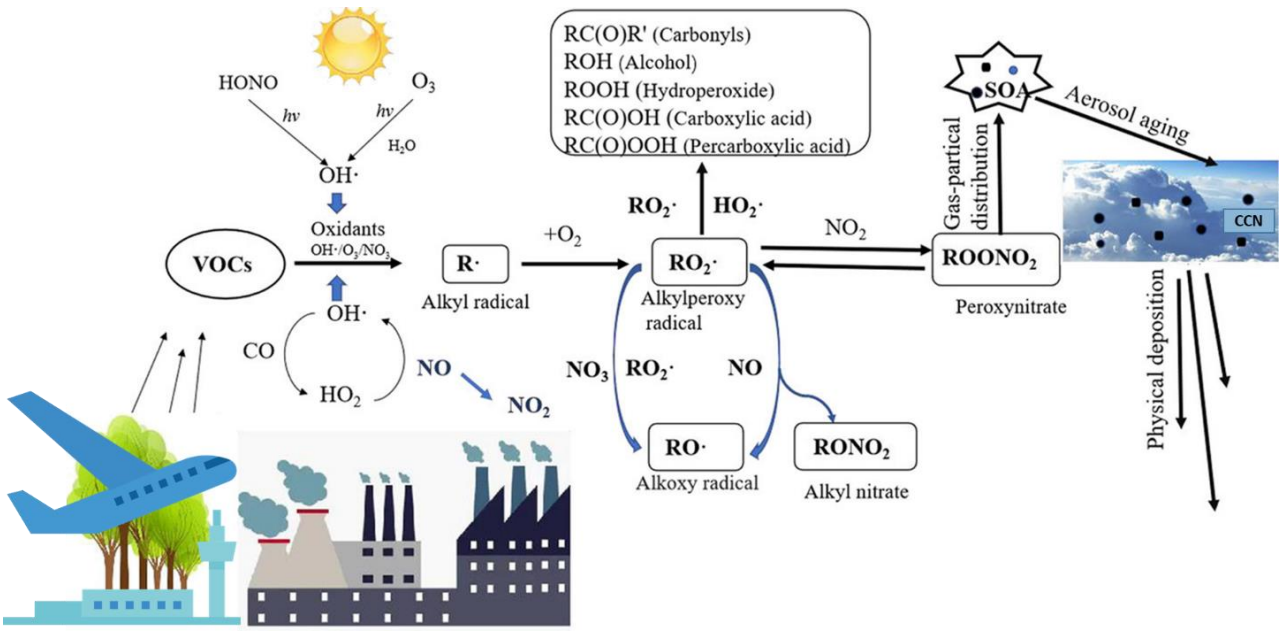

Figure I-19: SOA formations based on the alkyl oxidation mechanism (Y. Zhang et al., 2023). Alkyl radicals R quickly react with O_2 to produce alkyl peroxy radicals (RO_2). These newly formed radicals can react with NO, NO_2, NO_3, HO_2 or through cross-reaction between two RO_2 radicals, which converts them into steady-state compounds like alkoxy radicals (RO). VOCs correspond to Volatile Organic Compounds, CCN to Cloud Condensation Nuclei.

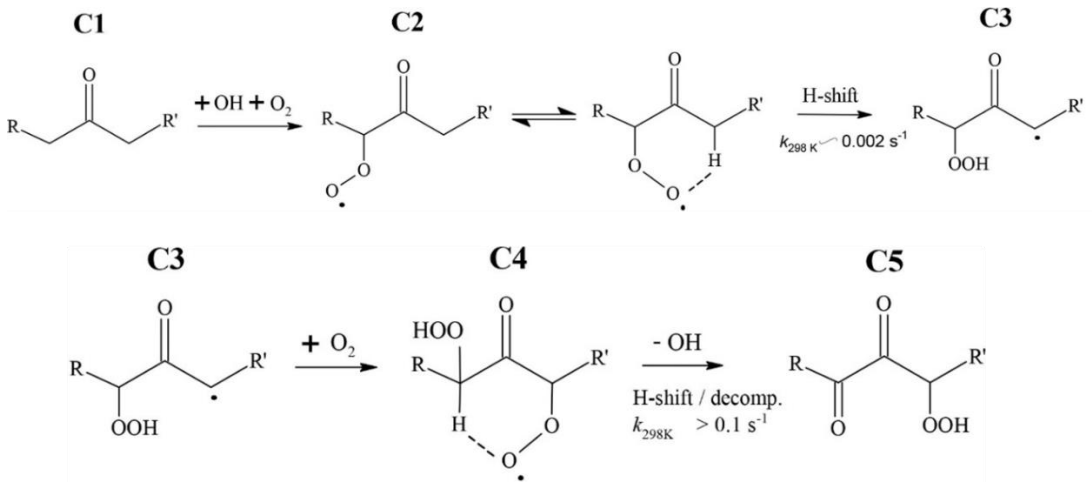

Figure I-20: Autoxidation of peroxy radical in OH-initiated oxidation (adapted from Crounse et al., 2013). Ketone (C1) reacts with OH to create a peroxy radical (C2) that undergoes an H-shift isomerisation. This reaction forms a hydroperoxide with a radical centre on the carbon atom from which the hydrogen atom was removed (C3). Rapid addition of O_2 to (C3) produces a new RO_2 radical (C4) that goes through another H-shift, leading to the termination of the autoxidation process by losing an OH radical. This results in a dicarbonyl hydroperoxide. The steps between (C2) and (C4) define the autoxidation process.

The partitioning of HOM compounds into the particulate phase depends on their vapour pressure. Larger molecules with more functional groups have lower vapour pressure and are more likely to form SOAs (Pankow & Asher, 2008). Indeed according to Bianchi et al. (2019), HOMs are related to the oxidised ELVOC area and in particular to the nucleation region, where organics can assist sulphuric-acid nucleation (Donahue et al., 2013). Studies show that HOMs can make strong hydrogen bonds with sulphuric acid and form stable molecular clusters (Figure I-21). Extremely low volatility organics can stabilise clusters with sulphuric acid before more volatile compounds participate in the

growth of the molecule (Donahue et al., 2013). Conversely, cleavage reactions can reduce SOA by increasing volatility and restoring gas-particle equilibrium (Robinson et al., 2007).

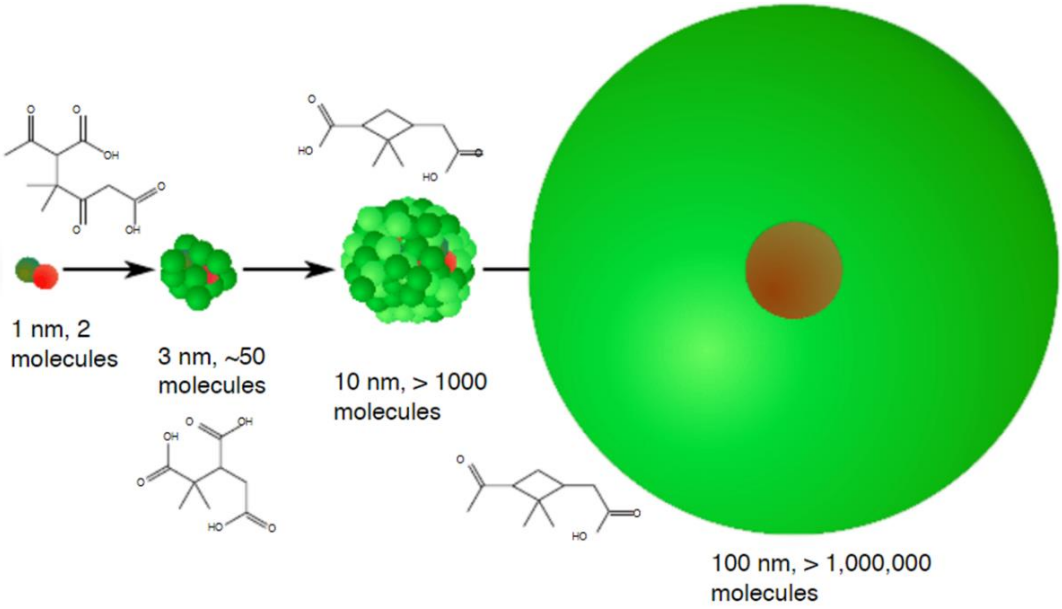

Figure I-21: New-particles formation and growth involving oxidised organics (green) and sulphuric acid (red) (Donahue et al., 2013). At the beginning, clusters of sulphuric acid are stabilised by HOMs (C_{10} keto-diacid). Then, more volatile species (pinic acid or cis-pinonic acid) contribute to the growth with the increase of the particle size.

Thus, high atmospheric oxidation reactions play a non-negligible role in the formation of secondary aerosols in the atmosphere, in particular concerning biogenic vapours. Synergistic effects from HOMs with sulphuric acid and ammonia participate in new particle formation (Lehtipalo et al., 2018). It should be also noted that HOMs can form on their own new particles in the atmosphere without sulphuric acid presence (Kirkby et al., 2016). In this way, HOMs can play a comparable role compared to sulphuric acid in atmospheric particle nucleation. In the lower atmosphere, they can form new particles at vapour concentrations near 10^7 cm^{-3} (corresponding to 0.4 pptv) with the help of a suitable stabilising agent (Kirkby et al., 2016). For pure biogenic particles, the stabilising agent is a suitable ion, while for sulphuric acid particles, amines or oxidised organics with ammonia act as stabilising agents. The nucleation of pure biogenic particles induced by ions could have significant implications for unpolluted environments since it offers a way for natural processes to generate particles with low sulphuric acid pollution.

I.3.2.4 Ion-induced nucleation

Ions also have a role to play in SOA formation and can interact in nucleation reactions involving acid/base pairs (Kirkby et al., 2016; Lehtipalo et al., 2016a). Indeed, electric charge of the initial clusters can have an impact on the formation and the growth process, in particular on smallest particles, affecting the neutral and charged particles formation pathways (Leppä et al., 2011; Nadykto & Yu, 2003). The particle sizes can increase by condensation of polar vapours on the charged clusters (increased collision rate) or by making the clusters more stable (decreased evaporation rate) to obtain secondary aerosol.

The formation of ionic aerosols depends on various factors, including the concentration of ions in the atmosphere. Charged particles are produced by the photo-ionisation of gas molecules, by atmospheric pollution or by the reaction of gas with cosmic rays (Kirkby et al., 2011, 2016). These ions condense onto aerosol particles to form ionic aerosols and affect their stability and their growth by attracting particles of opposite charge on their surface. This process, known as ion-induced nucleation,

can lead to the formation of new particles and facilitate the formation of secondary aerosols that can continue to grow by forming aggregates through further condensation and coagulation. Additionally, electric charges can affect the stability of aerosol particles (Kirkby et al., 2011), particularly in the presence of high humidity. Charged particles form clusters that are more stable and less likely to coagulate or evaporate than uncharged particles. This can lead to the formation of larger and more persistent aerosol particles.

However, the role of ions can be limited. According to previous studies (Almeida et al., 2013), the faster nucleation reaction is due to a base-stabilisation mechanism that involves acid-amine pairs, which results in decreased evaporation. The ion-induced contribution is typically small, suggesting that the formation of sulphuric acid-dimethylamine clusters is highly stable and galactic cosmic rays have only a minor impact on their formation, except when the overall formation rates are low. The presence of ions can increase nucleation in two ways: by increasing the collision rate between a charged cluster and polar molecules like H_2SO_4 or H_2SO_4·DMA, or by increasing the cluster binding energy, leading to a decreased evaporation rate. Because neutral clusters of H_2SO_4 and DMA are already highly stable, charge offers little competitive advantage. More recently, (Kirkby et al., 2016) indicates that ions produced by Galactic cosmic rays can significantly increase the nucleation rate, ranging from one to two orders of magnitude, in comparison to neutral nucleation. These findings are further supported by quantum chemical calculations of the cluster binding energies of representative HOMs. This suggests that ion-induced nucleation of pure organic particles could be a common source of aerosol particles in environments with low levels of sulphuric acid pollution (if associated neutral particles have sufficient evaporation rate). However, this effect is only observed when the nucleation rate is below the limiting ion-pair production rate. Ion-induced binary nucleation of H_2SO_4–H_2O can occur in the mid-troposphere, but it is not significant in the boundary layer (Kirkby et al., 2011).

I.3.2.5 Growth rate of atmospheric SOA

Multiple parameters and mechanisms can be considered in the secondary aerosol formation, as well as in the growth process of these particles. Indeed, their size can increase by condensing other gases and particles onto their surface. This particle growth is influenced by several factors, such as the concentration of aerosol precursors, ambient conditions and availability of aerosol nuclei. The evolution of the particle size can be related to the particle growth rate (GR - in nm/h). It refers to the rate at which small particles in the atmosphere grow in size due to the condensation of gases and particles onto their surfaces. Particle growth rates are important in understanding the dynamics of atmospheric aerosols.

New particle formation contributes to 50-90% of cloud condensation nuclei (CCN - Merikanto et al., 2009). Growth rate in 1-3 nm is key to know how many tiny particles will survive to be able to form CCN (Kulmala et al., 2013). To complete the formation and the growth of secondary aerosols from sulphuric acid vapour, the remaining fraction of growth has usually been attributed to condensation of low-volatility organic vapours (Kuang et al., 2012; Kulmala et al., 2013; Metzger et al., 2010; Riipinen et al., 2012; J. N. Smith et al., 2008). Recently, amines and alkaline vapours have been also considered in the growth process of the vPM in particular with the formation of salt (Erupe et al., 2011; H. Yu et al., 2012). Some experiments have been already done about the influence of such precursors on SOA formation processes, as for example in (Lehtipalo et al., 2016a).

Figure I-22 presents experimental results from the study of nanoparticle growth under well-controlled conditions in the CLOUD atmospheric chamber (Lehtipalo et al., 2016a). In the experiment, particles with diameters ranging from 1 to 100 nm were analysed, and the GR of particles with mobility diameters of approximately 1.5 to 2.5 nm were determined as a function of the measured concentration of H_2SO_4 monomers. The impact of different vapour concentrations such as sulphuric acid H_2SO_4, water H_2O, ammonia NH_3 (35-14000 pptv) and dimethylamine DMA (5-70 pptv) has been tested. More details about parameters of these experiments are indicated in the Figure I-22 legend. The main observation is that GRs increased almost linearly with the H_2SO_4 concentration (red line),

regardless of the NH_3 or DMA concentration. Any shift above the red line (for example collision enhancement lines) must be related to other compounds rather than H_2SO_4 and it provides an idea of how many condensable vapour are available for each test performed. If alkaline vapours are introduced into the system, the GR at a given H_2SO_4 monomer concentration increases. The addition of >100 pptv NH_3 resulted in a 2-3 times increase in the GR, while the addition of >5 pptv DMA further increased the GR by approximately 10 times.

To complete these observations, other studies have shown that when DMA is present, sulphuric acid forms clusters rapidly (Almeida et al., 2013; Kürten et al., 2014), suppressing cluster evaporation and leading to clustering occurring near or at the kinetic limit (Kürten et al., 2014; McGrath et al., 2012). This implies that a large portion of the available sulphuric acid for growth is bound to larger clusters (Lehtipalo et al., 2016a). The cluster formation rate was found to be lower in experiments with sulphuric acid and ammonia compared to DMA (Almeida et al., 2013). As a result, a larger proportion of sulphuric acid was available in the form of free or hydrated monomers. It is important to note that these experiments did not take into account extremely low-volatility organic compounds that participate in secondary aerosol formation in continental boundary layers (Kulmala et al., 2013), and that organics are still likely to dominate growth at larger particle sizes in these environments (Riipinen et al., 2012).

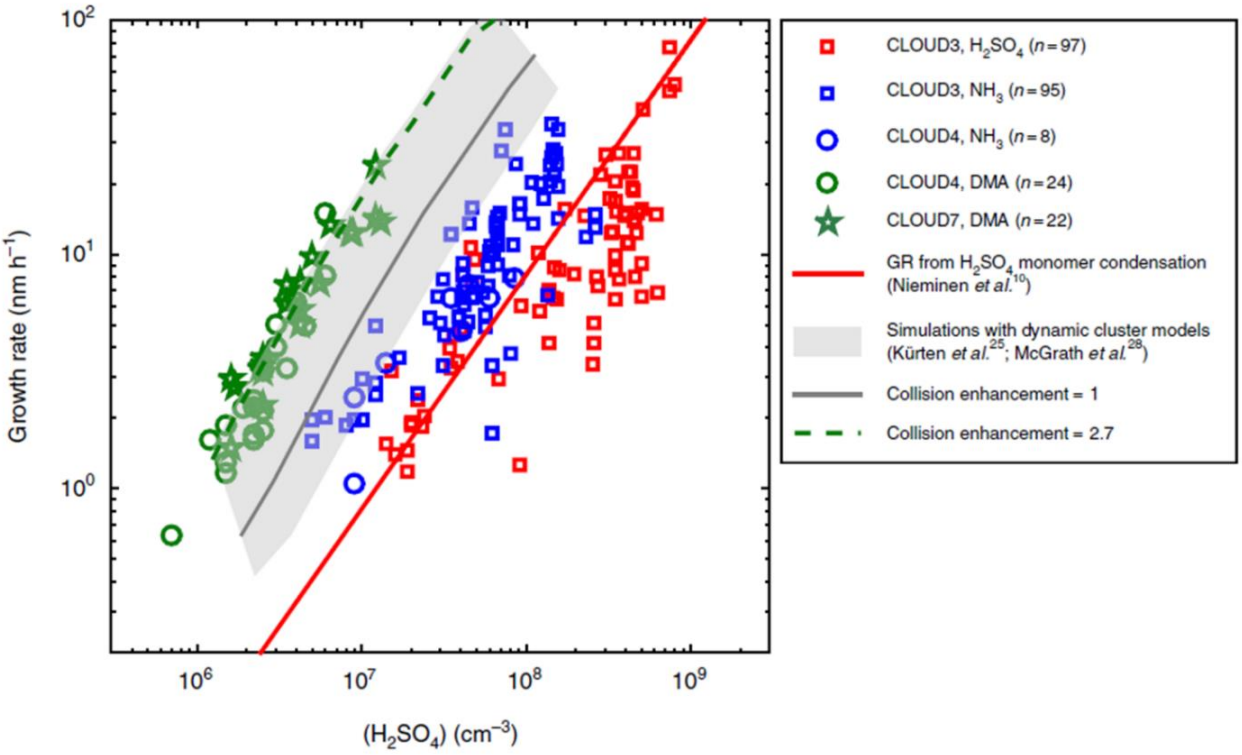

Figure I-22: Growth rates of particles in different systems (Lehtipalo et al., 2016a). Growth rates of 2 nm particles determined with the appearance time method between 1.5 and 2.5 nm as a function of the measured sulphuric acid (H_2SO_4) concentration with different amounts of ammonia (NH_3) and dimethylamine (DMA) in the CLOUD chamber. In the red data points, ammonia was present only as an impurity; for the blue points NH_3 was added, and for green points DMA was added to the chamber. Squares, circles and stars represent experiments at varying temperatures and relative humidity: T=248–293 K and RH=10–40% for squares one, T=278 K and RH=38% for the two others. Sample size (n) for each system is given in the legend. The red line is the mass flux growth rate calculated from the sulphuric acid monomer concentration (at T=278 K - Nieminen et al., 2010), and the grey shaded area represents the appearance time growth rate determined from cluster population simulations (Kürten et al., 2014; McGrath et al., 2012) assuming zero cluster evaporation rates and hard-sphere collision rates. A factor of 0.5–3 uncertainty in the collision rates (giving the limits of the shaded area) arises from the possibly non-unit sticking factors, uncertainty in the geometric cross-section of the clusters, and possible dipole–dipole enhancements in the collision rates. A collision enhancement factor of 2.7 (green dashed line) gives a good match between the simulated and measured data points in the sulphuric-acid–DMA system (Kürten et al., 2012).

To summarise, SOA are in the focus of much attention due to their impact on climate change, air quality and human health. However, due to the complex processes involved in their formation and ageing, understanding the mechanisms and factors that influence them remains a challenge for current atmospheric pollution research. Sulphur oxides play an important role in the formation of secondary aerosols in the atmosphere by reacting with organic particles and ammonia to produce organo-sulphate aerosols and ammonium salts. VOCs, oxidation modes, humidity and inorganic gases (NO_x, NH_3…) also influence SOA formation and ageing to varying degrees. The impact of ion-enhancement on the formation of secondary aerosols is minimal in the atmospheric boundary layer as there are typically sufficient stabilising vapours (Kürten et al., 2014) and it becomes more pronounced in highly unpolluted environments, such as the free troposphere (Lehtipalo et al., 2016a). Reducing emissions of SO_x and other aerosol precursors is an important strategy for improving air quality and mitigating the impacts of air pollution on human health and the environment. For instance, assuming that sulphate is the limiting factor of new particle generation, a reduction in SO_2 emissions by over 50% could significantly decrease SOA concentration and global radiative forcing of SOA, as predicted in an IPCC report (He, 2015).

I.4 Air transport environmental impact and mitigation solutions

I.4.1 The commercial aviation sector today

Before the COVID-19 sanitary crisis, air traffic was constantly increasing (+38% between 2000 and 2007) and was the fastest-growing transportation sector, with an annual growth rate of +5% (ICAO, 2018). In fact, this sector represented up to 128,000 commercial flights per day in 2019 (including freight), with an estimated number of passengers exceeding 4.5 billion worldwide. It was spread across a total of 1,478 commercial airlines, consuming more than 300 million tons of fuel per year (https://aviationbenefits.org/). The air traffic was strongly impacted by the pandemic compared to previous economic and financial crises (Figure I-23). Global passenger traffic experienced an unprecedented drop (EASA, 2022; ICAO, 2022), with a total reduction of more than 2.7 billion passengers (-60%) compared to 2019 levels. However, the crisis has quickly subsided and air traffic levels in 2023 have returned to those achieved in 2019.

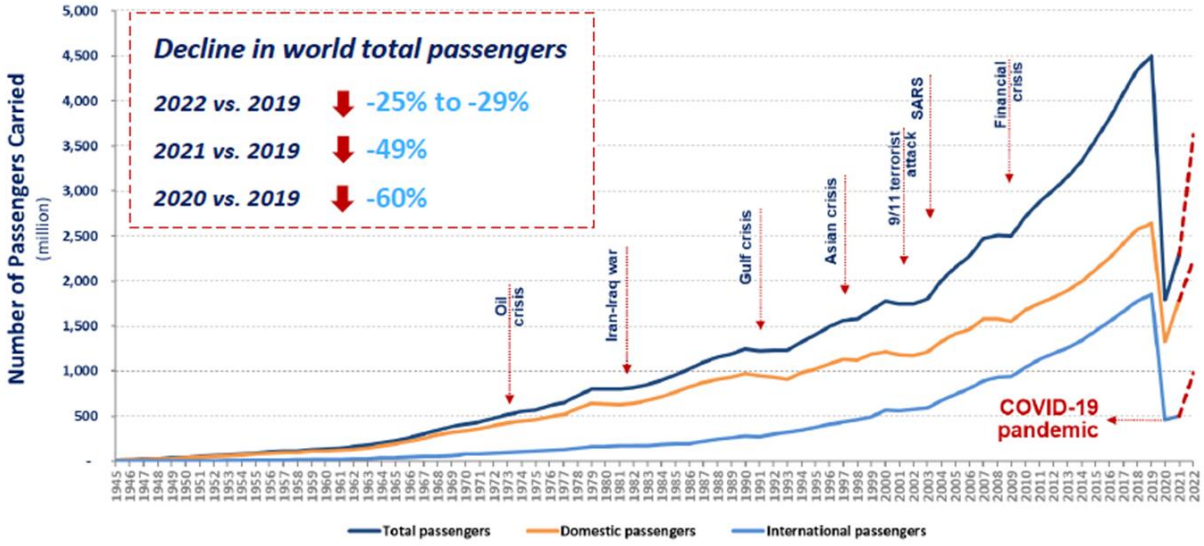

Figure I-23: World passenger traffic evolution from 1945 to 2022 (ICAO, 2022).

First estimations indicated a return to normal air traffic activity in Europe by the end of the decade, according to forecasts from the European Union Safety Agency (EASA, 2022). Different scenarios have been considered to simulate the evolution of the number of flights at the 2050 horizon (Figure I-24), taken into account economic growth, sustainability goals, regulations, airport capacity, as well as the arrival of new aircrafts, new fuels and new propulsion technologies. In the "base traffic" scenario (in blue, Figure I-24), flights are supposed to rebound after the COVID-19 downturn and to increase gradually to 12.2 million flights at EU airports (EU27+AELE) by 2050, representing a relatively low average annual growth rate of 0.9% between 2019 and 2050. In the same time, the average annual growth rate of passenger-kilometres was estimated to be -0.3%, 1.1%, and 1.7%, respectively, for the "low traffic" (cyan), "base traffic" (blue), and "high traffic" (red) recovery scenarios.

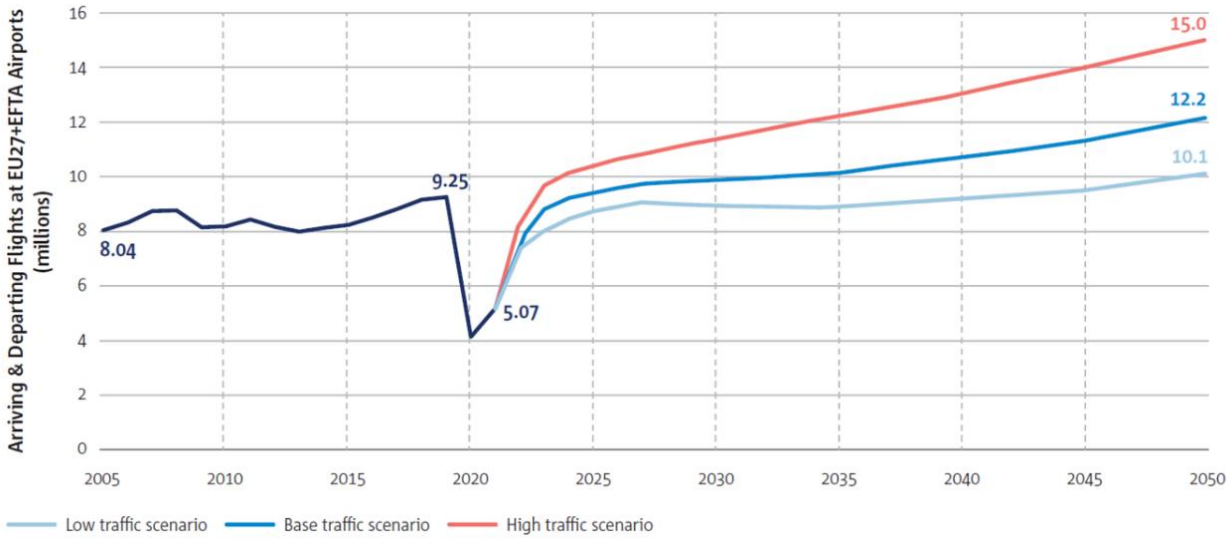

Figure I-24: Evolution of the numbers of flights following the recovery from the COVID-19 pandemic for 2050 depending on the low (cyan), base (blue) and high (red) traffic scenarios (EASA, 2022).

More recently (IATA, 2023), new estimations have confirmed that the projections follow a "high traffic" scenario to complete a return to normal activity before the end of the year. Indeed, it is anticipated that approximately 4.35 billion individuals will travel worldwide in 2023, approaching the number of passengers (4.54 billion) who flew in 2019 (IATA, 2023). Air traffic industry will achieve net profits of $9.8 billion and operating profits of $22.4 billion in 2023, representing more than double of the previous estimates made in December 2022. However, cargo volumes are expected to decline to 57.8 million tonnes, falling below the 61.5 million tonnes transported in 2019 due to a notable slowdown in international trade. Total revenues in the industry are projected to experience a year-over-year growth of 9.7% and reach $803 billion (first time since 2019).

I.4.2 Aviation-related pollutant emissions

Aircraft engine emissions (Figure I-25) are similar to other sources of fossil fuel combustion with nitrogen oxides (NO_X), particulate matter (PM), volatile organic compounds (VOCs), sulphur dioxide (SO_2), carbon monoxide (CO) and unburnt hydrocarbons (HC) being the most significant (EASA, 2022; ICAO, 2022; Schripp et al., 2022). Despite the overall decrease of emissions and recent improvements, air pollutant emissions from aviation have increased, representing 0.4% of premature deaths worldwide (Yim et al., 2015). The increasing growth of air traffic generates effluents impacting the climate, air quality, and health (Cochet et al., 2016; Hudda et al., 2020; Kohse-Höinghaus, 2019; W. Xu et al., 2016). Studies have shown that the growth of aviation has a twice as damaging effect on air

quality compared to its impact on climate change in particular near airport areas (Grobler et al., 2019; Riley et al., 2021; Yim et al., 2015). About 64% of the social impact is due to poor air quality, particularly fine particle emissions and nitrogen oxides. In the presence of heat and sunlight, surface NO_X reacts with VOCs, HC and CO to form ground level ozone or smog that cause health impacts (EEA, 2021).

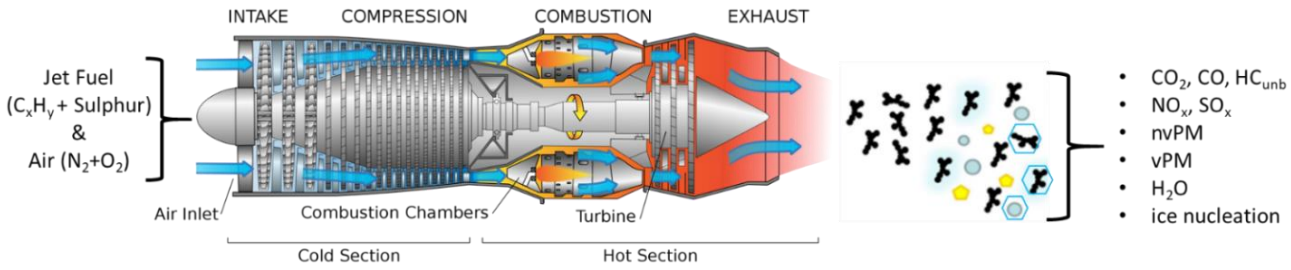

Figure I-25: Aeronautical emissions resulting from the combustion reaction between the jet fuel and the outside air in an aircraft turbojet engine (inspired from Dahl, 2008).

Local air quality is primarily affected by ground-level emissions originating at the airport, whereas the impact of higher-altitude aircraft emissions is relatively lower. While aircraft operations are a major source of air pollution near airports, air quality is also affected by ground support equipment, surface access road transport and on-site energy generation at airports. Aircrafts are responsible for approximately 54% of ground-level emissions, while airport-related traffic accounts for an additional 28% (Zaporozhets & Synylo, 2019). The exhaust gases are related to the operating conditions (Kinsey et al., 2010). Indeed, following the combustion of aviation fuels with outside air, numerous pollutants are released into the atmosphere (Hudda et al., 2014; Unal et al., 2005; Westerdahl et al., 2008) and have a local impact (Z. Yu et al., 2019). In surrounding residential areas, these emissions affect public health and air quality by increasing the concentrations of pollutants such as ultrafine particles (Hudda & Fruin, 2016; Jonsdottir et al., 2019; Lin et al., 2008; WHO, 2021).

With the recovery of the air traffic, issues related to the global environmental impact of emissions from aircraft engines and prerogatives for reducing CO_2 levels by 2050 remain topical environmental concerns (GIFAS, 2023; ICAO, 2022; Neu, 2020; Vorster et al., 2013). Indeed in 2017 in Europe, air transport is responsible for 12% of the amount of CO_2 released into the atmosphere (ICAO, 2018). More broadly, this sector currently accounts for 2% of greenhouse gas emissions worldwide and is expected to reach 5% by 2050 (Neu, 2020). The aeronautical sector represents 4% of the total global radiative forcing (RF) from all human activities (Kärcher, 2018 - Figure I-26-a) and gaseous and particulate aircraft emissions have an impact on air quality and Earth's radiative balance (Figure I-26-b). For example, CO_2 and H_2O emissions accumulated in the upper atmosphere have a positive impact on RF by altering chemical composition of the atmosphere (Lee et al., 2009). The presence of NO_x in the upper layers has a double effect: an increase of the global ozone (O_3) formation by photochemical changes leading to the increase of the RF, but also a reduction of methane lifetimes leading to the decrease of the RF (Lee et al., 2021). Sulphuric acid (H_2SO_4) formed from the oxidation of sulphur dioxide (SO_2) can nucleate homogeneously into droplets or be accumulated on the surface of soot particles (Gysel et al., 2003). The sulphate particles thus emitted have a negative impact on RF. Then nvPM, initially hydrophobic, can become hydrophilic by absorbing sulphuric acid on their surface (Wong & Miake-Lye, 2010). It contributes to form contrails, which have a positive impact on RF (Schumann, 2005; Schumann et al., 2016). Aircraft-induced clouds (AIC) represent the largest aviation RF component (Figure I-26-b and -c) and it is estimated that these contrails already covered in 1999 between 0.1 and 0.5% of the Earth's surface (Penner et al., 1999).

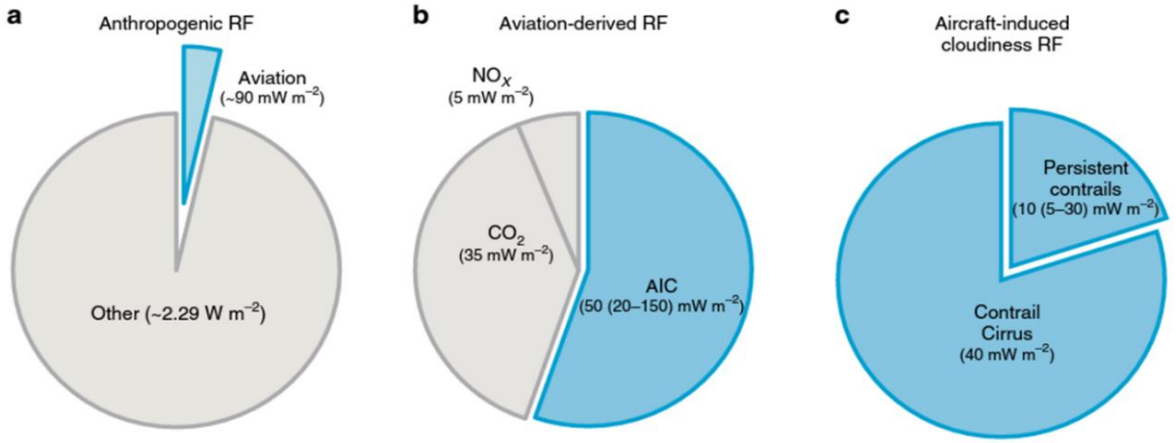

Figure I-26: Aviation radiative forcing (RF) components (Kärcher, 2018). Figure a) represents the part of the aviation sector in global anthropogenic RF (IPCC, 2013). Figure b) corresponds to the RF of the different components within the aviation emissions where aircraft-induced clouds (AIC) account for more than half. Figure c) shows the repartition of RF depending on the kind of contrails (Boucher & Randall, 2013).

I.4.3 Aviation-generated aerosols

During all phases of an airplane flight, aerosols are generated into the atmosphere: cruising phase (condensation trails called “contrails”), take-off, landing and also during ground handling. These aerosols will affect air quality on the ground through their presence, but also by reacting with the surrounding air. Among the species present in aircraft emissions, this study focused on particulate emissions, due to their impact on airport air quality with the objective of understanding their formation processes.

Recent studies have revealed increased levels of $PM_{2.5}$ and ultrafine particles (UFP) in and around airports (Hudda et al., 2020; Riley et al., 2021; Shirmohammadi et al., 2017). Aircraft engine emissions, being a significant source of UFP, can result in increased particle concentrations at ground level over large areas downwind of airports. Particles with a diameter smaller than 2.5 µm (known as $PM_{2.5}$) are particularly dangerous. Indeed, they can transport, e.g., polycyclic aromatic hydrocarbons (PAH) on their surface into the lungs, causing cancer and respiratory difficulties (Kim et al., 2013). Moreover, the emitted nvPM can serve as a core for the condensation of ice crystals in the upper atmosphere, resulting in the formation of contrails that modify the Earth's radiative balance (Penner et al., 2018). Estimations indicate that premature deaths resulting from long-term exposure to $PM_{2.5}$ and O_3 attributed to aviation contribute to an annual cost of approximately $21 billion (Yim et al., 2015). When comparing these costs to other societal expenses associated with aviation, it has been found that they are of a similar magnitude to the global climate costs attributed to aviation and one order of magnitude higher than the costs related to aviation accidents and noise (Yim et al., 2015). Although cruise emissions are primarily responsible for 75% of global premature deaths caused by aviation emissions, around half of these early deaths are attributed to take-off and landing emissions in North America and Europe—regions with relatively high levels of aviation activity and airport fuel consumption (Yim et al., 2015).

In aeronautics, the nvPM / vPM classification is defined by the ability of a particle to survive heating at 350°C (ICAO, 2017; ICAO, 2018). The nvPM are present at the engine exhaust and are mostly represented by soot particles resulting from incomplete fuel combustion. The vPM evaporate at temperatures above 350°C and are produced during the nucleation of gaseous precursors at the engine exhaust (Figure I-27) when emissions are cooled and diluted (Kılıç et al., 2018). They can adhere to pre-existing particles such as soot particles and they can interact with atmosphere components. Their formation mechanisms are still not entirely understood and the objective of this thesis is to focus on the comprehension of these phenomena through the study and measurement of aeronautical vPM and nvPM.

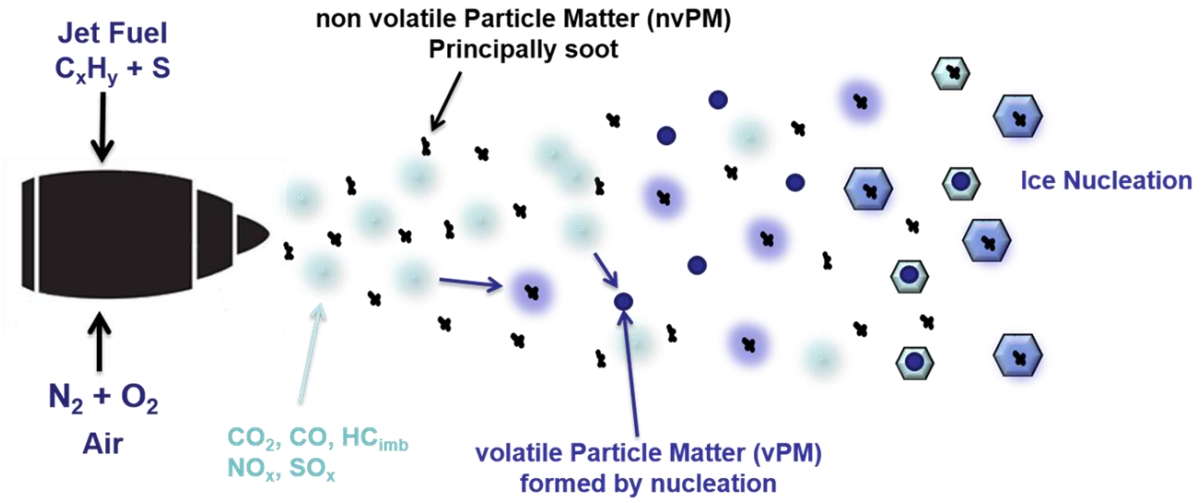

Figure I-27: Aircraft emissions resulting from the incomplete combustion of jet fuel with air.

It is possible to do an analogy between primary aerosols and nvPM and between secondary aerosol and vPM. Nevertheless, it is necessary to make the distinction between the definition of nvPM/ vPM and the atmospheric definition of volatility. Atmospheric compounds are characterised by their ability to easily evaporate/sublimate into the surrounding air and their volatility is related to the partitioning of the compounds between the gas phase and the particulate phase (Donahue et al., 2013; Song et al., 2022; Williams et al., 2010). For example, Intermediate and Semi Volatile Organic Compounds (IVOC and SVOC, respectively) present a large diversity of chemical classes in both gas- and particle phase (Song et al., 2022): acids, alkanes (C_8-C_{25}) and aromatics are dominant in gas phase while esters, alkanes (C_9-C_{34}), acids and siloxanes are abundant in particle phase. Volatility is influenced by the nature of the molecular groups and their ability to form H bonds. Thus, molecules containing carboxylic acids and having a high number of carbon and oxygen atoms constitute heavier molecules and are more likely to be located in the region of non-volatile molecular compounds (Donahue et al., 2013). In the case of polycyclic aromatic hydrocarbon, known as soot precursors (Desgroux et al., 2013), the number of aromatic rings is variable: ranging from two rings for the most volatile compounds to several dozen rings for the heaviest compounds (L. D. Ngo et al., 2020). This will influence the weight of the molecule and its volatility. The lighter ones evaporate quickly (high vapour pressure) and are highly volatile (Volatile Organic Compounds, VOC) (Bianchi et al., 2019). In the case of PAH, VOCs correspond to compounds containing one or two aromatic cycles (Desgroux et al., 2013; Frenklach, 2002) and therefore have a low mass-to-charge ratio (m/z), like naphthalene (128.06 m/z) or fluorene (166.078 m/z). IVOC and SVOC are those containing three to four aromatic cycles and have an intermediate m/z ratio like anthracene (178.07 m/z) and pyrene (202.078 m/z). IVOCs are entirely in the gas phase under ambient conditions and SVOC can be found in both phases (Donahue et al., 2013). Extremely Low and Low Volatility Organic Compounds noted ELVOC and LVOC correspond to PAHs with more than five aromatic cycles with a high m/z ratio, such as coranulene (250.078 m/z) and coronene (300.09 m/z). The gas/particle phase partitioning of volatile compounds can be linked to atmospheric aerosol formation processes and growth rates (see section I.3).

Contrary to nvPM (Agarwal et al., 2019; ICAO, 2016; Kinsey et al., 2010), there are very few studies and insufficient experimental data dealing with the properties of aeronautical vPM to understand how particles are formed and grown under atmospheric conditions. Hitherto, the certification measurements of aviation emissions have been focused only on nvPM (ICAO, 2018). Though vPM is still not included in any certification process, ICAO has started to move towards including vPM in it and more studies are addressing the subject (Z. Yu et al., 2019). The development of a measurement protocol to quantify vPM on the engine exhaust is more complicated than for nvPM.

Indeed, as vPM are formed in the exhaust once the plume has been diluted and cooled down, measurements need to be performed at several metres from the exit plane of the engine and it represents a big constraint on test benches. Furthermore, on the tarmac, the airport ambient conditions would affect the vPM formation process. It will be impossible to compare essays done in different conditions and therefore, hindering the choice of emission limits for future norms. Another problem in the measure of the complete engine emissions (nvPM + vPM) is the potential impact of vPM presence on the certified instruments for measuring nvPM, for example on the soot mass determination by laser incandescence (Michelsen et al., 2015). Air quality models have some difficulties to reproduce field observations. One of the main reasons for this can be the absence of vPM formation and evolution in these models (Zhang et al., 2023).

Mechanisms involving sulphuric acid, organic vapours, ions or ammonium are all contributing to the formation of secondary aerosols. Understanding these mechanisms is crucial for assessing the impacts of vPM on air quality and climate change in the aeronautical field. Aircraft emissions are impacted as well by the atmospheric conditions (temperature, pressure, humidity, UV light) but also by the fuel choice. Indeed, depending on the composition of the kerosene (aromatics/sulphur contents), nvPM and vPM generated at engine exhaust will be different. Sulphuric acid formed at engine exhaust is currently considered as the main driving component involved in the formation of vPM (Brown et al., 1996; Kärcher et al., 1995; Miake-Lye et al., 1994; Wong et al., 2008). By interaction with water, it results in a binary homogeneous nucleation of H_2SO_4/H_2O forming clusters and leading to vPM formation by condensation of vapours. However, from an aeronautical point of view, the amount of sulphur present in the fuel converted to sulphuric acid is not enough (25-60% estimated in Kärcher & Fahey, 1997) to explain the entire amount of vPM observed (Vancassel et al., 2004) and other sources must be considered.

For example, organic components can play an essential role in the growth of volatile particles, initially nucleated from sulphuric acid and water vapours in the aircraft plume (Wong et al., 2013, 2014, 2015; F. Yu et al., 1999). Secondary aerosol formation dominates the total aerosol mass, surpassing primary aerosol by approximately two orders of magnitude, as reported by (Kılıç et al., 2018a). During idling load (thrust 2.5–7%), more than 90% of the secondary particle mass is organic (Figure I-28), mostly due to the oxidation of gaseous aromatic species such as benzene, toluene, xylenes, naphthalene, tri-, tetra-, and pentamethyl-benzene. Additionally, oxygenated-aromatics like phenol and furans contribute to this aromatic fraction, and their oxidation can account for up to 25% of the secondary organic particle mass during idling loads. However, the organic fraction decreases with an increase in thrust level (Z. Yu et al., 2019), and the inorganic fraction becomes dominant (Figure I-28). At cruise load, sulphates make up around 85% of the total secondary particle mass. This role seems significant only when the fuel sulphur content is low (of the order of 100 ppm or less - Schumann et al., 2002).

The possible presence of ammonia in the air can also have an impact on vPM formation, as ammonia is known to lead to ternary nucleation with the sulphuric acid-water mixture (I.3.2.2). With ammonia, nucleation can be enhanced and the sulphur conversion factor is reduced (Vancassel et al., 2004). The impact of ions produced by chemi-ionisation within aircraft engine combustors on the plume can also contribute to vPM formation (Arnold et al., 2000; Kılıç et al., 2018a; F. Yu & Turco, 1997). Ions act as nuclei around which molecular clusters form, facilitating the creation of electrically charged sulphuric acid/water aerosols. These charged micro-particles enhance growth due to condensation and coagulation, in addition to electrostatic effects. Simulations show that such processes can explain the presence of volatile particles behind aircraft, if the initial ion concentration in the exhaust is greater than 10^8 cm^{-3} (F. Yu & Turco, 1997). Ionised plume studies reveal also a bimodal aerosol distribution, with a larger "ion" mode consisting of the activated volatile sulphuric acid particles and a smaller "neutral" mode comprising the residual slowly growing neutral molecular clusters formed in the highly supersaturated region of the plume.

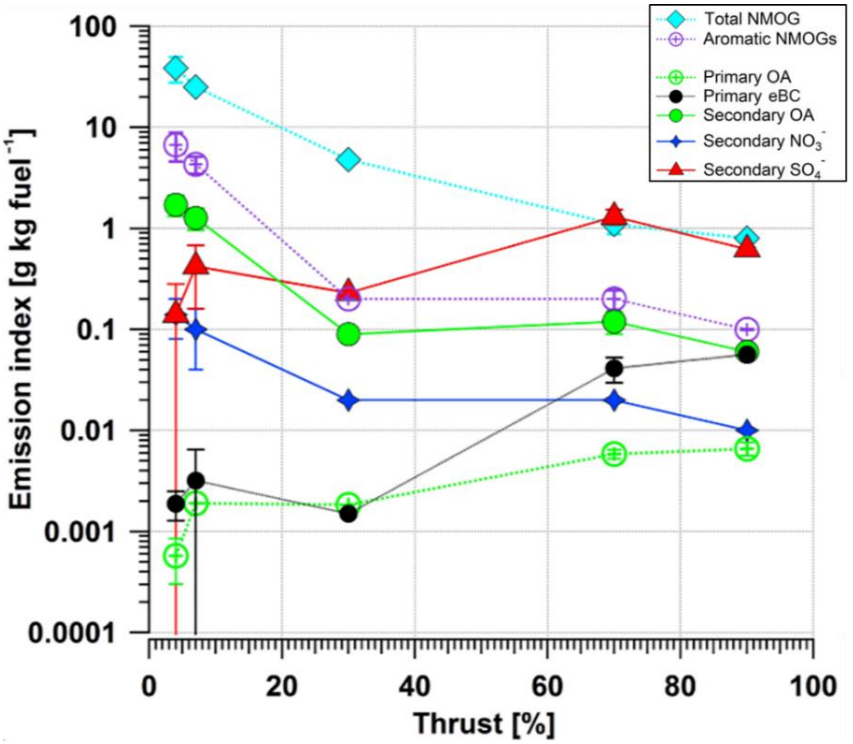

Figure I-28: Average emission indices for primary non-methane organic gases (NMOGs), aromatic gases, primary organic aerosol (POA), equivalent black carbon (eBC), secondary organic aerosol (SOA), nitrate (NO_3), and sulphate (SO_4). Oxidative processing of aircraft turbine-engine exhausts has been studied using a potential aerosol mass (PAM) chamber at different engine loads corresponding to typical flight operations (Kılıç et al., 2018a). The OH exposure was in the range of 91–113 × 10^6 molecules cm^{-3} h for the secondary aerosol cases.

Understanding the mechanisms of formation of these particles and their reaction with atmospheric components is a major challenge (Lee et al., 2021) in order to propose a solution to reduce their impact on air quality over the coming years. Numerous efforts to reduce these emissions and fuel consumption have been done in recent decades in accordance with the standards set by international requirements with improvements in aerodynamics and combustion. In this study, a particular attention is paid to the deployment of sustainable aviation fuels (Kandaramath Hari et al., 2015; Koumelis, 2023; Staples et al., 2018) and their impact on emissions at engine exhaust.

I.4.4 Reduction of aviation emissions

Important efforts have been deployed to reach a consensus among all economic actors in the aviation industry regarding the strategies for reducing the emissions and in particular CO_2 emissions in the medium term (-50% by 2030) and long term (net-zero growth emissions by 2050). Different scenarios have been considered to decarbonise air transport (CORSIA, 2022; EASA, 2022). Recently, the Committee on Aviation Environmental Protection of the International Civil Aviation Organization (CAEP) outlined in its resolution A41-21 the objectives to achieve carbon neutral growth from 2019 and then to achieve a long-term goal of net-zero carbon emissions by 2050 (ICAO, 2023). According to the latest estimates (Figure I-29), the measures taken should reduce CO_2 emissions worldwide by 77% compared to a constant technology scenario, to reach 211 million tons (compared to 915 million tons in 2019). This decrease comes from the improvement of aircraft and engine technology/design (-23%), from the optimisation of air traffic and of the airport infrastructures (-12%), from the development of sustainable fuels (-37%), and from electric or hydrogen-powered aircraft (-5%).

These improvements are partly due to technological advancements. For each new airplane generation, there has been a significant increase in energy efficiency, resulting in gains of 10% to 15%. The most recent generation of airplanes and engines now consume between 2 and 3 Litres per 100 kilometres per passenger, and in some cases, even less than 2 L on specific types of flights (GIFAS, 2023). The other main contribution is the development of Sustainable Aviation Fuel (SAF). The European Council and Parliament have reached a provisional political agreement on a proposal aiming to decarbonise aviation using such new fuels and cleaner energy sources for aviation, including hydrogen and renewable electricity. SAF plays an essential role in achieving this objective and the current agreement lays the foundations for collaboration to achieve the agreed SAF blending shares in kerosene. It is notably the goal of the RefuelEu project and "Fit for 55" package of proposals to reduce emissions by 55% for 2030 (European Commission, 2020; Koumelis, 2023). This agreement is expected to stimulate greater production and widespread use of SAF on a larger scale, leading up to 2050.

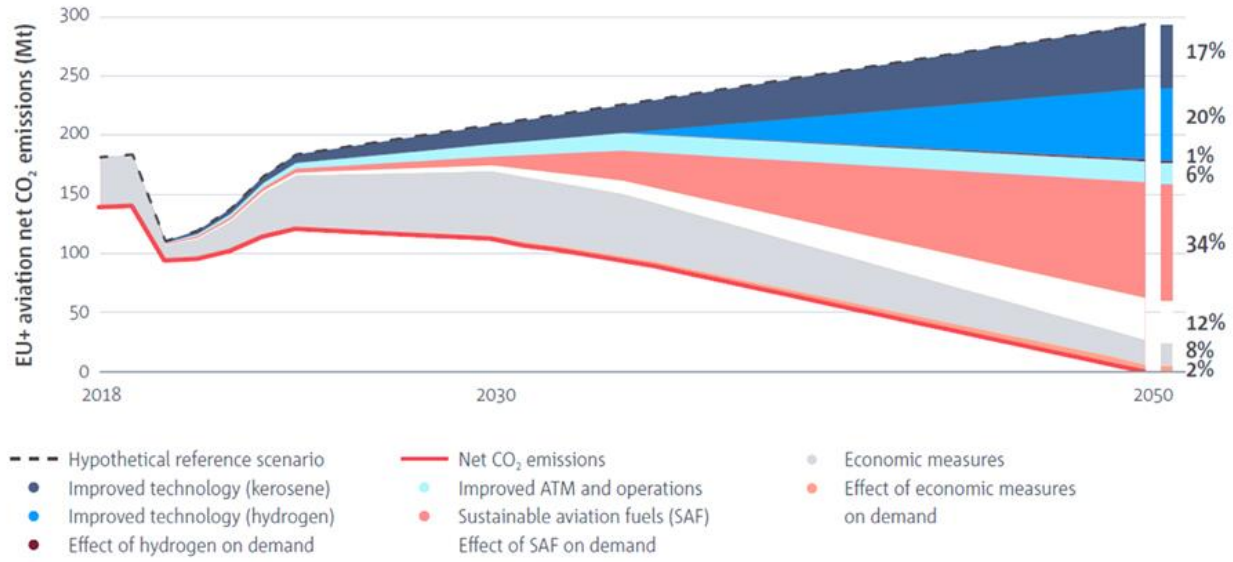

Figure I-29: Estimation of the reduction of CO2 emissions for 2050 (EASA, 2022). Results are presented for all flights within and departing from the EU region (EU27+UK+EFTA). Improving aircraft and engine technology, ATM and aircraft operations, SAF and economic measures all hold decarbonisation potential. Modelled for 2030 and 2050, the impacts are linearly interpolated. The base year for this study is 2018.

Due to the impact of aviation on the climate and air quality combined with the decrease of fossil fuel resources, the aviation industry has developed an interest in new sources of energy currently available (IATA, 2023) and in advanced aircraft configuration for new-generation engines. For example, the power generation industry can turn to wind, hydro, nuclear and solar technologies to produce electricity and reduce CO_2 emissions. In the case of aviation, while solar and electric aircrafts are nowadays underdeveloped, they are still a long way from commercial versions due to aviation's need for high power-to-weight ratio and globally compatible infrastructure.

For example, electric propulsion systems do not generate on-board emissions but the specific energy of electrical energy storage sources (batteries) is much lower compared to fossil fuel. The development of aircraft based on 100% electric propulsion systems is currently limited by the problem of energy storage and these aircrafts will not be able to achieve the same performance as combustion-based aircrafts in the near future. Due to these limitations, the concept of Hybrid Electric Propulsion System (electric powertrain coupled with a conventional combustion engine) has taken strength lately as a solution for, at least, personal or small size aircrafts at regional scale (ICAO: E-HAPI, 2022).

Nowadays there is growing interest in hydrogen as a solution to decarbonised aviation. Hydrogen has a specific energy that is 2.8 times higher than the one for Jet A-1. On the other hand, due to its low density, hydrogen presents a severe volumetric disadvantage compared to the high-

energy storage capability of the hydrocarbon fuels. This makes the use of gaseous hydrogen for combustion not an option for aviation. Liquid hydrogen has only 4.1 times lower volume energy than jet fuel, so it may be an interesting option as fuel. The main drawback is that liquid hydrogen must be kept at temperatures of 20 K, which makes its use in aviation quite challenging. Association between hydrogen and electric engines is one of the alternatives proposed by Airbus (Airbus ZEROe project, 2022), but one more time it is more adapted to regional scale.

I.4.5 Sustainable aviation fuels

Current conventional aviation combustibles are defined as fossil fuels based on the oil refining. The kerosene is not only burned to generate thrust, but is also used for cooling down and lubricating the engine or for the swelling of the joints (Ben Amara et al., 2016). Furthermore, an aviation fuel needs to respect specific criteria to be qualified as a kerosene (Aviation Fuel Quality Requirements for Jointly Operated Systems, 2020). To control its properties (density, composition…) and be certified, kerosene needs to follow the international quality requirements defined by the American Society for Testing Materials (ASTM D1655, 2022) and Defence Standard 91-091 (Defence Standard 91-091, 2019). Some requirements are listed below:

- a high thermal stability to support high temperature (over 150°C) and avoid auto-oxidation;
- a flash point (i.e. combustion temperature) over 38°C;
- a freezing point under -47°C;
- a viscosity under 8 mm^2/s;
- a specific energy (i.e. energy given by the fuel per unit mass) higher than 42.8 MJ/kg.

The standard aeronautic fuels currently used (Jet A-1 for the most common one) are derived from oil refining and are composed of hydrocarbons. Generally, they are formed by a majority of alkanes (75%-90% of C_nH_{2n+2}) regrouping paraffin groups with a high calorific value and a high resistance to low temperature (iso-paraffin). The composition is completed by mono- and di-aromatics (C_nH_m), which are useful to increase the density of the fuel and to facilitate the swelling of joints. They are seen as the precursors of soot particles in exhaust (Bouvier, 2006; Desgroux et al., 2013; Irimiea et al., 2019). Standard fuels must contain between 8% and 25% of total aromatics compounds (ASTM D7566, 2009) to ensure a correct adaptation to the engine. The naphthalene content must not exceed 3%. Furthermore, kerosene incorporates sulphur, which is naturally present in crude oil. In Europe the average content in sulphur is typically around 300 ppm. In the literature, a maximum amount of sulphur concentration in fuel composition is limited at 3000 ppm (ASTM D1655, 2022; Defence Standard 91-091, 2019). On the other hand, there is no specification about the minimum amount of sulphur required. There are fuels being refined today with only a few ppm fuel sulphur content that are satisfactory Jet A/Jet A1 certified fuels (ASTM D1655, 2022).

To complement technological improvements of combustors and to assure an energetic independence regarding fossil fuel foreign sources in the future, the aviation industry has identified the development of biofuels as one of the major tools to tackle its emissions. Actually, research on the field of these synthetic fuels is on-going (Mawhood et al., 2016). A synthetic fuel that fulfils the requirements fixed by ICAO (ICAO: CORSIA, 2022) can be labelled as Sustainable Aviation Fuel (SAF). Last ICAO report is exploring the feasibility of a Long Term global Aspirational Goal (LTAG) for international aviation (ICAO, 2022), through detailed studies assessing the attainability and impacts of any goals proposed: SAF, innovations in aircraft technology (Rich-Burn Quick-Quench Lean Burn, Double Annular Combustor or Lean Direct Injector), hydrogen… This last LTAG report shows that SAF has the greatest potential to reduce CO_2 emissions from International Aviation in the following years (Figure I-30) and this potential is illustrated by different ongoing programs testing 100% SAF like ECLIF (DLR) or VOLCAN (AIRBUS).

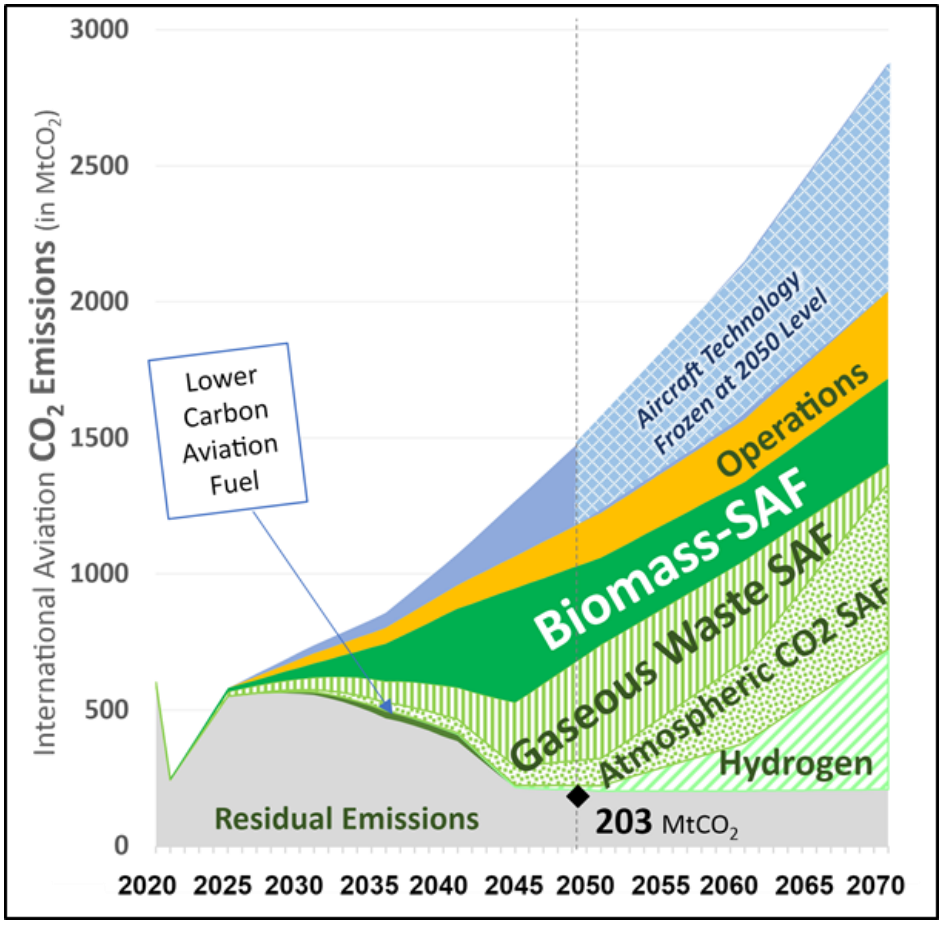

Figure I-30: CO_2 emissions from international aviation associated with Long Term global Aspirational Goal (LTAG) integrated scenarios. In 2050, emissions would be reduced by 87% compared to an IS0 reference scenario: 21% from aircraft technologies, 11% from operations and 55% from fuels (ICAO, 2022).

These synthetic fuels are derived from biomass (Mawhood et al., 2016). They have been obtained in the first instance from the cultivation of cereals (G. Liu et al., 2013). Nowadays it comes from waste oil/ organic urban waste and from the cultivation of micro-algae (Figure I-31). Synthetic fuels willing to replace jet fuel must satisfy different functionalities such as performance properties (thermal stability, flash point, viscosity…) and must also ensure the proper mechanical operation of the engine (to power fueldraulic actuators, to lubricate pumps - Heyne et al., 2021).

The use of such fuels has advantages like the reduction of net CO_2 emissions in the fuel consumption process avoiding a modification of the engine. Indeed, the plants used for the production of SAF have captured atmospheric CO_2 before being used. Thus, the net CO_2 emission is lower and opposite of fossil fuel despite that in terms of combustion, CO_2 emissions are really close to standard Jet fuels. However, they also present some disadvantages (Hileman & Stratton, 2014) including their technical feasibility (high cost of agricultural waste collection) and the economic cost of their production (three times more than for an actual conventional fuel). The question of the durability (encroachment on food crops) and the impact of using such fuels on the overall carbon footprint and air quality are still under evaluation.

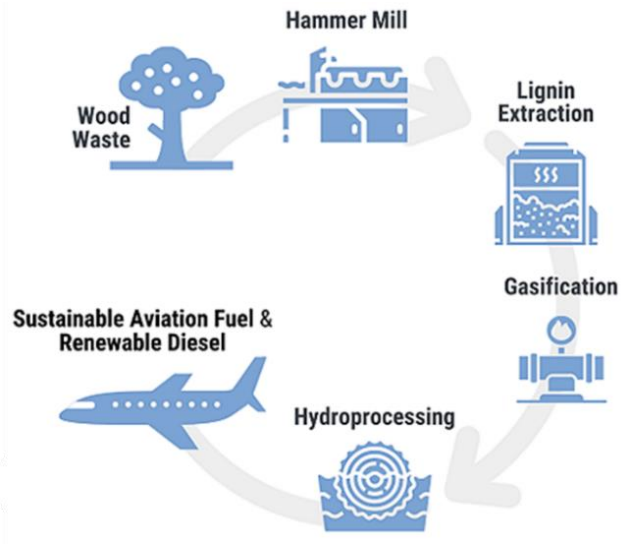

Figure I-31: SAF generation from waste (Aemetis Inc.).

Each synthetic fuel needs to respect the conditions set by the D4054 evaluation process (Evaluation of New Aviation Turbine Fuels Containing Synthesised Hydrocarbons) on fuel properties and engine tests (Vozka et al., 2019). In 2009, the landscape of alternative fuels in aviation has significantly evolved with the approval of a first alternative "drop in" fuel by the ASTM D75566 (Status of Technical Certification of Aviation Alternative Fuels 2017). This first 100% synthetic fuel for aviation is called Fischer-Tropsch Synthetic Paraffinic Kerosene (FT-SPK). However, the need of sulphur and aromatics contents imposes a certain limit on the use of such alternative fuels without sulphur or low aromatics content. Therefore, SAF are seen as an alternative to fossil fuel but a 100% alternative fuel cannot be actually used on a real engine. Some standard jet fuel and synthetic fuel blends are in this way employed. The fossil fuel needs to contain a minimum of 16% of aromatic compounds to avoid a mixed fuel with less than 8% of aromatics contents (to avoid shrinking and fuel leaks, Graham et al., 2013) . Therefore, FT-SPKs are approved for commercial use in a blending ratio up to 50 % (maximum mixing ratio available for this case) with current Jet A-1 (aromatics compounds over 16% in the composition).

In the same way, Hydroprocessed Esters and Fatty Acids (HEFAs), producing synthetic paraffinic kerosene from vegetable/ recycled oils or animal fats, have also been approved in 2011 after blending (up to 50 %) with conventional Jet A-1. In June 2014, the certification body ASTM approved the Hydroprocessed Fermented Sugars Synthesised Iso-Paraffins (HFS-SIP) pathway. The process called Direct Sugar to HydroCarbon (DSHC) uses saccharides (C_5 and C_6 sugars) originating from different feedstocks for fermentation by yeasts directly creating hydrocarbons. This fermentation product is then converted by a standard chemical process into farnesane ($C_{15}H_{24}$) and can be blended as a biobased jet fuel component up to 10 % with Jet A-1 fuel. Between 2015 and 2016, FT Synthesised Paraffinic Kerosene plus Aromatics (SPK/A - blending ratio up to 50 % with Jet A-1) and Alcohol-to-Jet Synthetic Paraffinic Kerosene (AtJ-SPK - blending ratio up to 30 % with Jet A-1) were also approved. The AtJ fuel is a certified synthetic paraffin (approved by ASTM norm in 2016) derived from the polymerisation of plant-based alcohol such as sugar or beet alcohol (Gutiérrez-Antonio et al., 2017; W.-C. Wang & Tao, 2016). Recently (2020), two more pathways have been approved by ASTM, the Catalytic Hydrothermolysis Jet (CHJ) and Hydroprocessed Hydrocarbon synthetic Paraffinic Kerosene (HHC-SPK). CHJ uses processing waste oils or energy oils to produce clean free fatty acids that are then cracked, isomerised, and cyclised into paraffin, isoparaffin, cycloparaffin, and aromatic compounds. CHJ approved blend ratio is 50 % and it has the potential to become drop-in fuel, due to the identical composition to jet-A1. HHC-SPK uses biologically derived hydrocarbons such as algae to produce the synthetic paraffinic kerosene. The blend ratio is only 10% and it is not possible to use it as drop-in fuel.

The use of SAFs in aviation is rather limited due to their recent development. Indeed, the first commercial flight using biofuel was done in 2011 by KLM. The situation from a research point of view is similar. Studies dealing with aviation biofuel emissions are more and more numerous. (Corbin et al., 2022; Corporan et al., 2005, 2007, 2011; DeWitt et al., 2008; Schripp et al., 2022) reported a reduction in nvPM emission when FT fuel was used in substitution of standard jet fuel. On the other hand, these studies were performed on engines that were not representative from those present in the current commercial fleet. (Timko et al., 2011) studied the performance of sustainable fuels in a CFM56 engine, one of the most common in the current commercial fleet. They reported a reduction of NO_x and CO emissions when using a SAF or a blend fuel. Furthermore, a reduction of soot in terms of number and mass concentration is also measured especially in low engine regimes (Figure I-32). It should be noted that the number of particles decreases more than the soot mass, meaning that less particles are generated from SAF/blend combustion compared to conventional Jet A-1.

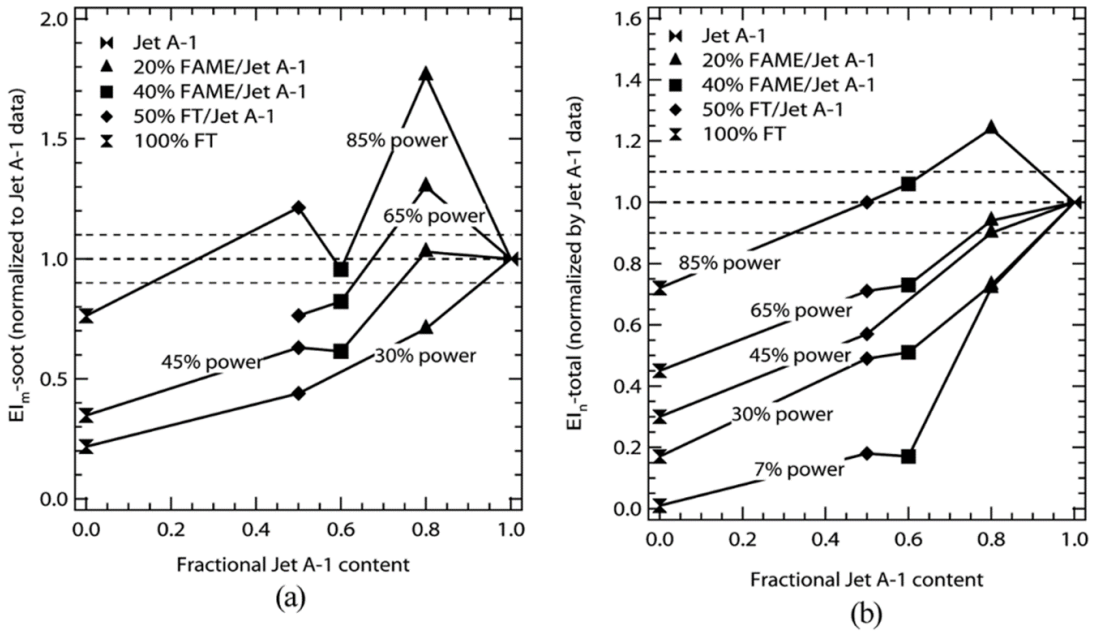

Figure I-32: PM emissions data for soot mass (EI_m- soot – figure a) and particle number (EI_n- total – figure b) depending on the engine thrust from 7% to 85%. FT is a natural gas-derived Fischer–Tropsch synthetic fuel. FAME corresponds to Fatty Acid Methyl Ester. In all cases, data have been normalised using data obtained for Jet A-1 combustion (Timko et al., 2011).

Thereafter, German Space Centre (DLR) performed with the National Aeronautics and Space Administration (NASA) different experimental campaigns to study alternative fuel performance (ACCESS) and to investigate the impact of jet fuel properties on aerosols emitted by CFM56-2-C1 engines on a Douglas DC-8 (ECLIF project). 15 different aviation fuels containing SAF (such as FT and HEFA) were tested in four ground tests to see the impact of their composition on the resulting emissions at different engine regimes (Moore et al., 2015). The results were similar to those found by (Timko et al., 2011). Indeed, it was found that the aromatic and sulphur content of the fuel mainly affects the volatile fraction of aerosols. The linear regression coefficients show that reducing the fuel sulphur and naphthalene content to near-zero levels would result in a reduction of the number of aerosols emitted per kilogram of fuel burned (related to engine power). In a recent work, (Moore, Thornhill, et al., 2017) reported a reduction up to 50% on particle emission in cruise conditions for a 50/50 blend of HEFA fuel and standard jet (Figure I-33). However, certification limitations prevent the use of a 100% alternative fuel. Airbus reported a test flight of an A350 with 100% HEFA SAF in March 2021 (AIRBUS SAF, 2021). United Airlines also performed a commercial flight in December 2021 with one engine using 100% SAF (UNITED airlines SAF, 2021); the measurements seem to point to an important reduction of nvPM emission.

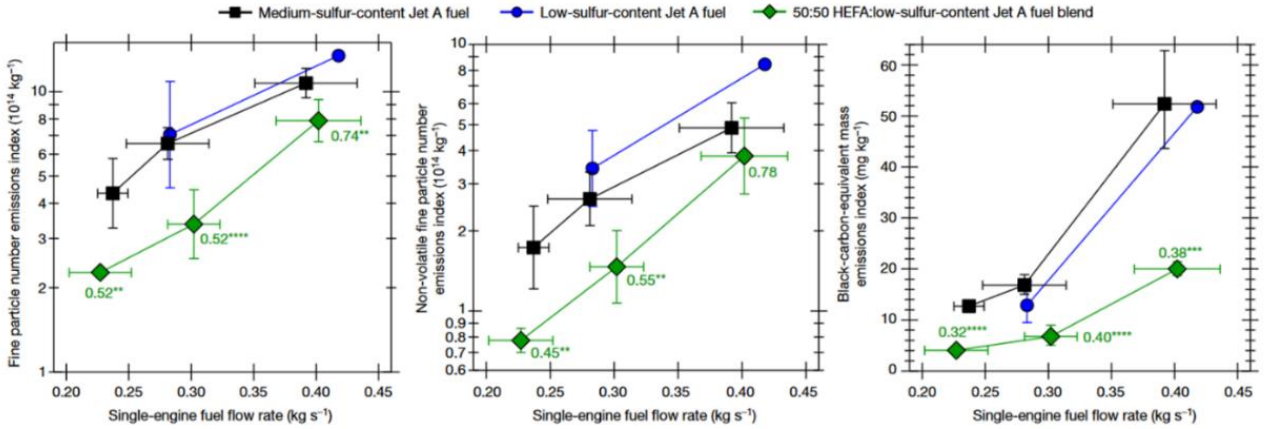

Figure I-33: Summary of particle emission indices depending on engine thrust, cruise conditions and fuel composition (colour legend). The ratio of the emission indices for the 50/50 biofuel blend and the medium-sulphur-content Jet A-1 fuel are indicated on the figure (Moore, Thornhill, et al., 2017).

I.5 Thesis progress

To study the different molecular mechanisms of new particle formation from the exhausts of aircraft engines fed by fuels with different composition under atmospheric ground level conditions, the manuscript is divided into five chapters:

- In this first chapter, we presented the general context of the study and provided a brief state-of-the-art view on the aviation-related emissions and their impact on the atmosphere, with special focus on the evolution of atmospheric aerosols, the characteristics of volatile / non-volatile Particulate Matter and their impact on air quality and human health. A review of the potential mechanisms already known that could be at the origin of the formation of nvPM and vPM is proposed. A section is also dedicated to aviation fuels to better understand the impact of their composition on resulting emissions;
- In the second chapter, the experimental set-ups used during the test campaigns are detailed, along with the investigated fuel matrix. The characteristics of the measuring instruments, as well as the experimental measurement lines deployed or the sampling system associated to the offline chemical analysis are detailed;
- The third chapter presents a characterisation of the emissions of the liquid mini-CAST burner in order to compare the nvPM formed according to the fuel composition at the burner outlet and also to optimise the operating parameters of this burner;
- In the fourth and fifth chapters, the results of experiments on the CESAM atmospheric simulation chamber are presented. A first approach to vPM formation processes is done solely from gaseous precursors to isolate this phenomenon as best as possible (homogeneous nucleation). Then, a second approach is carried out to take into account all interactions between nvPM and vPM corresponding to tarmac conditions (homogeneous and heterogeneous nucleation);
- A general conclusion summarises all these works and presents new research opportunities for the future. Such as promising preliminary results on ageing emissions, focusing on the use of a portable oxidation flow reactor in parallel to the atmospheric simulation chamber.

Chapter II. Materials and Methods

The main aspect of this thesis is to understand the formation of vPM as well as the interaction between aeronautical emissions in aircraft engine exhaust and atmosphere. It should be noted that ICAO only started recently to work on vPM inclusion in certification processes. The development of a measurements protocol to quantify vPM on the engine exhaust is more complicated than for nvPM due to the conditions in which the emissions are produced. Indeed, vPM cannot appear directly at the exhaust where the temperature and the concentration of pre-existing particles are too high to allow vapour nucleation and thus their formation. They are formed in the exhaust once the emissions plume has been diluted and cooled down. Measurement on the tarmac or at high altitudes on a real aircraft engine in these conditions is a big challenge requiring a pre-treatment of the sample.

Actually, it is possible to collect emissions from an on-wing engine using a sampling probe (AVIATOR, 2020) at several metres from the exit plane of the engine or on a cruise flight chasing the aircraft with another airplane (Voigt et al., 2021). However, ambient conditions would affect the formation of vPM process making difficult to understand formation mechanism and to establish certification standards. These problems are also present in measurements on test benches. To adapt the experimentation and work on these interactions, different approaches and options are available.

One of the first elements for a proper research in the combustion exhaust about atmospheric nucleation is to control the conditions for the formation of particles. It is possible to simulate controlled atmospheric processes at ground level using specific installations such as experimental chambers (ATMO-ACCESS, 2020). These are installed in different laboratories (Figure II-1-bottom) and have specificities depending on the study (ice nucleation, VOC degradation mechanism, SOA formation processes…). In this way, aircraft emissions can be injected in the chamber to observe their evolution with atmospheric compounds over the time. Another difficulty is to bring an entire engine or connect a real airplane directly to an experimental chamber (or vice versa due to their large size). The low number of studies reported is not surprising, since experiments involving aircraft engines are extremely demanding, from both a technical and an economic point of view. One of the options is to change and adapt the scale to the study, starting with generating emissions in a laboratory. Indeed, vPM and nvPM can be produced from a simple laboratory burner to simplify a real aircraft engine, before moving on the test bench (Figure II-1-top). In the first instance, laboratory burners are easy to adapt and field use. They present a good alternative to work on a simulation chamber with various operating points and/or different fuels.

To generate, describe and compare emissions from aviation fuel combustion before and after interaction with atmosphere, various experimental set-ups have been carried out and different on- and off-line instruments from different institutions have been used.

This Chapter will be focused on the laboratory experiment description. The first element deployed is a combustion aerosol standard generator giving aeronautical soot particle surrogates (ONERA laboratory). Then different installations to simulate atmospheric processes are introduced. Finally, experimental devices already approved for nvPM analysis (ICAO, 2017) and adaptable for vPM study are presented. In this way, it is possible to collect samples, quantify emissions and analyse their composition to understand interaction between emissions and atmosphere compounds leading to new vPM formation.

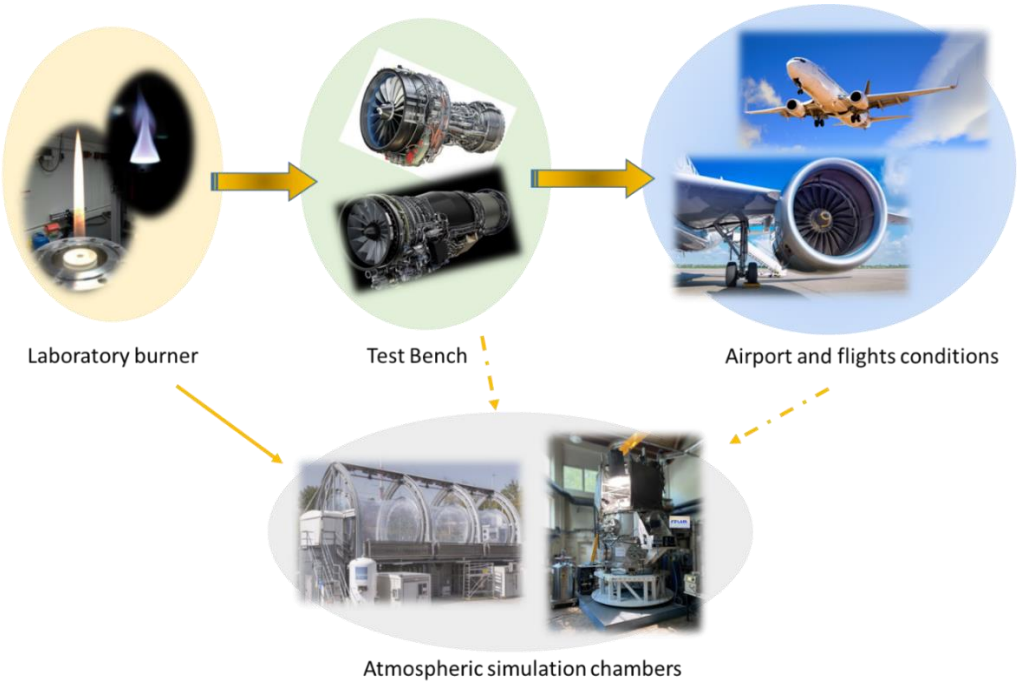

Figure II-1: Source of emissions at various scales: McKenna Burner (ONERA laboratory) generating a stable laminar diffusion flame in a laboratory; LEAP and M-88 engines (SAFRAN) on test bench; aircraft at ground level and at cruise altitude. At the bottom, two examples of atmospheric simulation chamber (ATMO-ACCESS, 2020) are presented: Simulation of Atmospheric Photochemistry in a Large Reaction Chamber (SAPHIR_EUROCHAMP, 2020) in Germany and Experimental Multiphasic Atmospheric Simulation Chamber (CESAM_EUROCHAMP, 2020) in France.

II.1 Emissions source and atmospheric chamber

II.1.1 Source of aeronautical emission surrogates

II.1.1.1 A laboratory burner for liquid fuel

As a first step, it is necessary to have a reliable and stable emission source, capable of producing emissions with properties similar to aircraft ones. For this, a version of a Combustion Aerosol STandard (CAST) Generator (company Jing.Ltd) is used. There are different models of this burner to generate diffusion or premixed flames. For example it is possible to work with a gas or a liquid version, a classic or a compact model... (Jing, 2009). These particle generators can be easily operated in a laboratory to carry out a first experimental approach.

The gas version of the CAST is well referenced in the literature. It can be used to generate soot particles using a laminar diffusion flame of propane. Studies about its operating points and emissions have been already done (Ess & Vasilatou, 2019; Mamakos et al., 2013; Mueller et al., 2015; Ouf et al., 2016; Yon et al., 2018). A characterisation of this burner describing the number concentration of soot particles emitted and their size distribution depending on the input flows (fuel and combustion agent) is presented in (Moore et al., 2014). The particles generated have a mean geometric diameter ranging from 10 nm to over 100 nm depending on the operating points. This aerosol source has also been used in research on the characterisation and formation of soot particles (L. D. Ngo et al., 2020; Ouf et al., 2016).

In the case of the UNREAL project, one of the aims is to understand the formation of volatile Particle Matter related to the combustion of aeronautical fuel. In this sense, it is not possible to work

with a gas CAST version that only uses gas propane and does not allow the ability to burn different liquid fuels. This is the reason why a liquid version of the CAST has been employed (Figure II-2 – left). Furthermore, aeronautical kerosene can have various compositions for example in terms of aromatic contents and sulphur concentrations. As explained previously (I.3.2.1), these compounds play an important role in the process of particle formation (soot and vPM) and will capture our attention in this study. Figure II-2 (right) presents a chemical analysis of filters collected at gas CAST exhaust and at liquid CAST exhaust (Jet A-1 fuel) compared to a filter collected on a Snecma/NPO Saturn SaM146-1S17 turbofan exhaust (Delhaye et al. 2017 - MERMOSE project). These mass spectra represent the normalised intensity of recorded signal corresponding to the detection of compounds at the surface of the sample as a function of mass/charge ratio (m/z). A zoom has been done on the HSO_4 signal (96.959m/z) to compare the answer of each case. It is shown that gas CAST generator is not able to reproduce sulphur content as they use propane gas as fuel. On the contrary, the liquid CAST burner tested with a standard Jet A-1 kerosene presents good similitudes in terms of sulphur compounds compared to the real case corresponding to an aircraft engine. It confirms that the gas CAST burner is not adapted to this study. The second signal corresponds to the hydrocarbon C_8H^+ (97.007m/z) and shows that in terms of nvPM particles the answer obtained is comparable for each test.

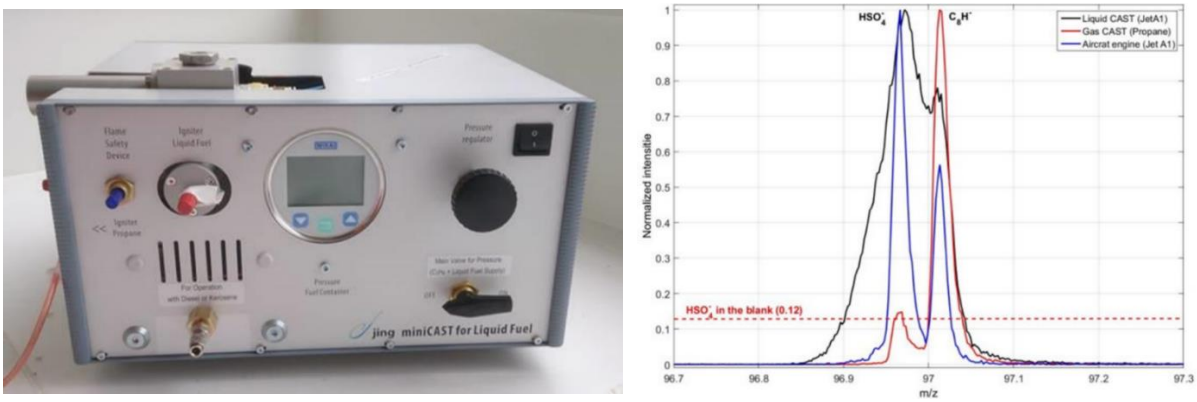

Figure II-2: CAST burner for aeronautic liquid fuel (on the left). On the right, analysis of different CAST emission samples to study the chemical composition (ToF-SIMS – for more details cf. II.2.2.3.2): difference between gas and liquid CAST model for Sulphur compounds (HSO_4) detection in comparison with an aircraft engine.

The compact model of the liquid CAST burner is used in this thesis. It is a modified version of the well-known mini-CAST "gas" (Jing, Series 5200/Series 6200) allowing a combustion under atmospheric conditions (Jing, 2003). This version is designed to work with different fuels according to the standard certification procedures assuming a low fuel consumption (from the order of 100 µL/min). The liquid version of the mini-CAST is less documented in the literature (Daoudi et al., 2023 but it concerns diesel fuels) and it is unfortunately difficult to find points of comparison, as its emissions depend on the composition of the fuel used.

Nevertheless, some precedent studies show that this CAST version is suitable to work with different liquid fuels (Berthier, 2022) and generates PM emissions which can mimic to some extent the aircraft PM emissions, depending on the set point. Indeed, emissions from the burner have been compared to those obtained from complete aircraft engines and present some similar aspects especially regarding the nvPM emission index (Delhaye et al., 2017; Moore, Shook, et al., 2017). Figure II-3 depicts the comparison of the data obtained from JETSCREEN experiments (JETSCREEN Project, 2020) using liquid CAST burner with those obtained in the Generic high-pressure RQL burner combustor rig (https://www.cu-gtrc.co.uk/generic-rql-burner) at Cardiff University and in the Auxiliary Power Unit (APU) test bench at University of Sheffield. It represents the evolution of the fitted particle GMD (left) and of the particle number emissions (right) depending on the fuel hydrogen content. Results are normalised to reference fuel. As it can be seen, CAST results present overall good agreement with APU and generic combustor rig tests for the diameter comparison. For the particle

concentration, the CAST values are closer to the APU and Generic combustor measurement when the fuel hydrogen content increases.

These previous comparisons between soot from a real engine and a liquid miniCAST generator show that the impact of hydrogen content is representative in terms of mass and number concentration as well as size of particles. It should be noted that absolute values are not representative: for example, particles are larger with a CAST burner.

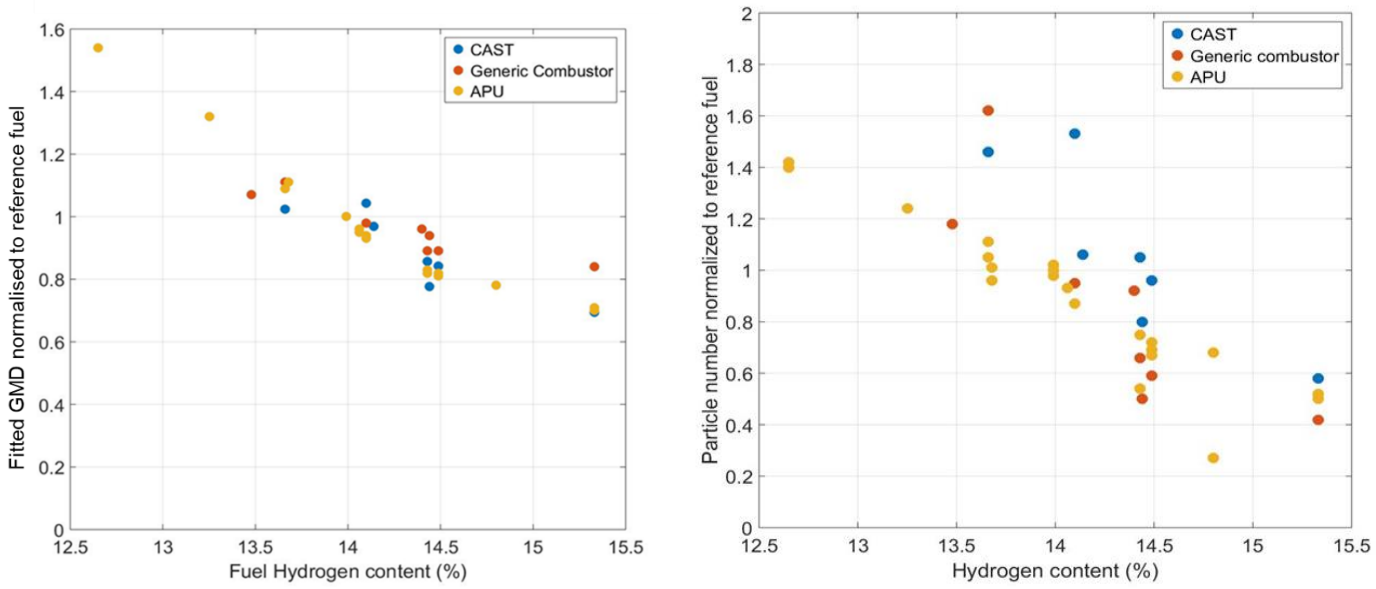

Particles Size Distribution

Particles Number concentration

Figure II-3: Representability of liquid CAST burner in comparison to a Generic Combustor and an Auxiliary Power Unit (APU). Impact of fuel hydrogen content on particle GMD (left) and on the particle number concentration (right) for different tests (JETSCREEN Project, 2020).

The operating principle of the liquid CAST is based on the use of a propane flame, which heats and vaporises the liquid fuel in the combustion chamber to generate a kerosene flame. A first piezo-igniter at the bottom of the CAST starts the ignition of the propane flame and a second one is used to ignite the vapours of kerosene at the top of the chamber (Figure II-4 - left). An airflow feeds the propane flame from the bottom of the burner and goes up to the kerosene flame (Figure II-4 - right).

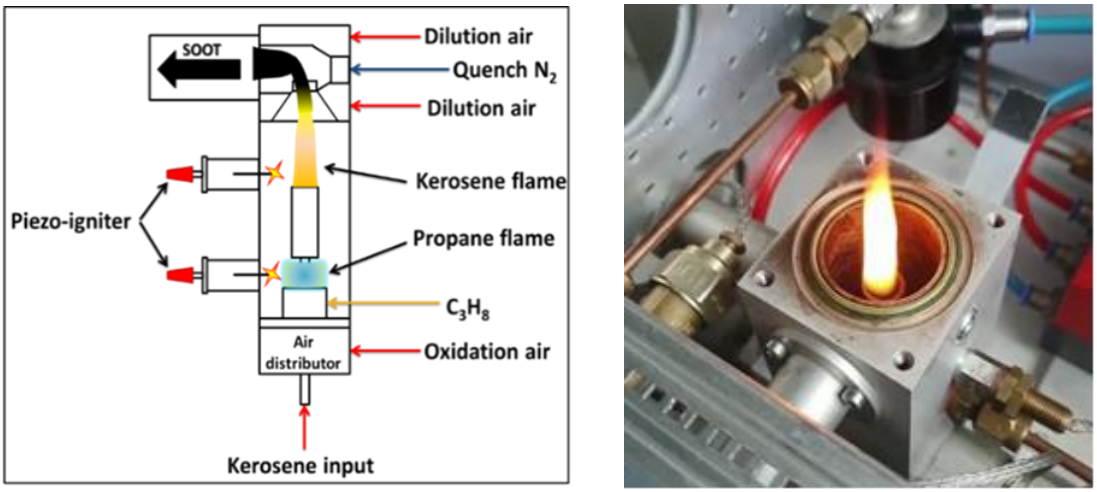

Figure II-4: Description of the combustion process using a propane flame to initiate fuel combustion at the top of the device (on the left - Jing, 2003). Example of kerosene flame inside the liquid CAST burner without exhaust/dilution hat.

Particle emissions resulting from the combustion of propane are negligible (in terms of number and mass concentrations) compared to those emitted from the kerosene flame. Nitrogen injection ("Quench N_2" on Figure II-4 - left) stops the oxidation phenomenon at the top of the flame. Compressed air (filtered and dried) is injected on both sides of the nitrogen injection to dilute the emissions, limit reaction and coagulation, and send them to the measurement line. The nitrogen and the dilution air flows are kept constant during the experiments at their optimum values: 7 L/min and 20 L/min respectively (Berthier, 2022). To get the fuel flow, a mini CORI-FLOW mass flow controller (MFC - model M12V14I, Bronkhorst) is used. Its working principle is based on the Coriolis effect: the liquid fuel passes through a tube subjected to a fixed vibration and the inertia of the mass flow causes the direction of oscillation of the tube to drift. The phase shift is measured and used to estimate the flow (https://www.bronkhorst.com/en-us/service-support/knowledge-base/coriolis-mass-flow-measuring-principle).

By controlling the flow rates (Table II-1) of fuel $Q_{kerosene}$ (µL/min), propane $Q_{propane}$ (mL/min) and air Q_{air} (L/min), it is then possible to modify some physical characteristics of particles emitted such as mass concentration, number concentration and size distribution (Berthier, 2022). Thereafter, flows will be specified as follows: (fuel flow in $\mu L.min^{-1}$ /propane flow in $mL.min^{-1}$ /air flow in $L.min^{-1}$).

Flow	*Values*
$Q_{kerosene}$	0 – 105µL/min
$Q_{propane}$	0 – 50mL/min
$Q_{air,\ oxidation}$	0 – 5L/min
$Q_{air,\ dilution}$	0 – 10L/min
$Q_{nitrogen}$	0 – 7L/min

Table II-1: Liquid CAST burner settings. Fuel flow is regulated with a mass flow controller in the entrance of the CAST; propane and air flows are regulated by internal volumetric flowmeters.

All of these parameters can affect the structure of the soot aggregates measured from the combustion (Ikhenazene et al., 2020; Mamakos et al., 2013; Moore et al., 2014; L. D. Ngo et al., 2020) but also the stability of the flame and experimental reproducibility. By controlling these parameters, it is possible to obtain a very wide range of non-volatile particulate emissions (Berthier, 2022). A description of the fuels used during this thesis is presented in the next section. Furthermore, a study dedicated to the stability, the reproducibility of emissions and the different chosen operating points for UNREAL experimental campaigns are detailed in Chapter III.

II.1.1.2 Fuel matrix of the experimental tests

All the fuels tested in this work are listed in Table II-2. The fuel defined as the reference one is the standard Jet A-1 from JETSCREEN project (fuel comparable to the actual commercial ones). The other fuels present variation in terms of aromatics and sulphur contents (Extreme-, High Aromatics-, High Sulphur-, Low Jet A-1). The Alcohol to Jet (AtJ) fuel is a 100% SAF without sulphur and aromatics content. The result of the blend between the reference Jet A-1 and the AtJ is called Mix E5 and its composition is conformed to fuel restrictions (70% Jet A-1 + 30% AtJ – cf. Chapter I).

All these fuels have been characterised according to the American Society for Testing and Materials (ASTM) standard tests:

- Standard Test Method for Dynamic Viscosity and Density of Liquids by Stabinger Viscometer (ASTM D7042, 2021);

- Standard Test Method for Determination of Aromatic Hydrocarbon Types in Aviation Fuels and Petroleum Distillate;
- High Performance Liquid Chromatography Method with Refractive Index Detection (ASTM D6379, 2021).

Fuels denomination	Aromatics compounds (%)	Including naphthalene (%)	Sulphur contents (ppm)	Comments
Jet A-1 JETSCREEN	20.2	1.8	200	Reference fuel ASTM D7566
Jet A-1 AVIATOR	21.1	Not provided	<430	Aircraft on tarmac
Jet A-1 VOLCAN	17.8	Not provided	417	Aircraft engine on test bench
Extreme Jet A-1	23	3	3000	Limit of certification
High Aromatics Jet A-1	23	3	4	Maximum of aromatics
High Sulphur Jet A-1	16	0.5	3000	Maximum of sulphur
Low Jet A-1	16	0.5	4	Low level of aromatic and sulphur content
Mix E5	14.2	1.3	140	Blend of 70% Jet A-1 ref + 30% AtJ
Alcohol-to-Jet (AtJ-SPK)	0	0	0	Synthetic Paraffinic fuel

Table II-2: UNREAL fuel matrix for experimental tests on CAST burner with the CESAM atmospheric during UNREAL experimental campaigns.

- **Standard Jet A-1 fuels**

The reference fuel employed during these experiments is a standard Jet A-1 from the JETSCREEN Project (JET Fuel SCREENing and Optimisation – HORIZON 2020). This project aims to develop an optimisation platform to assess the risks and benefits of alternative fuels (CORDIS europa 2020). Its objective is to optimise alternative fuels in terms of maximum energy density and minimum pollutant emissions. During the JETSCREEN project, tests at different scales, from the laboratory to the combustion chamber, have been carried out using different fuels including this Jet A-1 (JETSCREEN Project, 2020).

To compare this standard kerosene with other conventional fuels, two Jet A-1 from two other European projects have been used. The first one is provided by the AVIATOR project (Assessing aViation emission Impact on local Air quality at airports: TOwards Regulation - Horizon 2020). The objectives of this project are, inter alia, the improvement of measurement systems for aircraft engine emissions and the interdependencies of air quality and certification (AVIATOR, 2020). The second one is provided by the VOLCAN project (Fly with Alternative Fuels 2021-2024). This project contributes to ongoing efforts to ensure that the aviation sector is ready for the widespread deployment and use of SAF as part of the wider industry decarbonisation initiative. In addition, one of its ultimate goals is to achieve 100% SAF certification in single-aisle commercial aircraft and the new generation of business jets. These two additional Jet A-1 present some differences in terms of aromatic compounds and sulphur contents with respect to the reference Jet A-1 (Table II-2). These fuels are mainly composed of alkanes (iso-paraffins, branched alkanes and cycloalkanes), mono-aromatics (benzene chains and alkyl chains) and di-aromatics (naphthalene content) as well as sulphur (between 200 and 400 ppm).

- **Limits of certification: modified fuels**

In addition to the standard kerosene, we studied different Jet fuels with different aromatic cuts and sulphur compounds to evaluate their impact on emissions (cf. Table II-2). These modified fuels are provided by the ONERA fuel laboratory and are used in parallel with the RAPTOR project (Research of Aviation PM Technologies, mOdelling and Regulation - funding from the Clean Sky 2 – Horizon 2020). This selection of fuels covered the limits of the ASTM requirements for certification in terms of sulphur content and aromatic content. The objective is to see the impact of variations due to aromatics and sulphur contents on emissions.

The first fuel selected is an initial Jet A-1 fuel with low content of aromatics (16% including 0.5% of naphthalene) and low content of sulphur (4 ppm). We will refer to this fuel as “Low Jet A-1”. Using this fuel as base, three other modified fuels have been obtained:

- initial fuel plus an aromatic blend, to set the total aromatic content to 23% (including 3% of naphthalene), we will refer to this fuel as “High Aromatic Jet A-1”;
- initial fuel plus sulphur to set the total sulphur content to 3000 ppm, we will refer to this fuel as “High Sulphur Jet A-1”;
- initial fuel plus aromatic and sulphur added to set the total aromatic content to 23% (including 3% of naphthalene) and the total sulphur content to 3000 ppm, being these the higher limits set by (ASTM D7566, 2009) for both parameters. We will refer to this fuel as “Extreme Jet A-1”.

- **Sustainable Aviation Fuel and blend**

Sustainable fuels are integrated in the class of synthetic fuels. In this study, a fuel presenting neither aromatics nor sulphur compounds is used. This fuel is obtained from the Alcohol to Jet (AtJ) pathway. It is a certified synthetic paraffin (SPK approved by ASTM norm in 2016) derived from the polymerisation of plant-based alcohol such as sugar or beet alcohol (Gutiérrez-Antonio et al., 2017; W.-C. Wang & Tao, 2016). Sugar or starches are converted through fermentation into an intermediate alcohol such as ethanol or iso-butanol. Then a dehydration/ oligomerisation/ hydrogenation/ fractionation process is done (Figure II-5). The final step is the conversion into a hydrocarbon mixture composed of 99% branched alkanes containing neither aromatic nor sulphur compounds. In this way, AtJ-SPK fuels are a blend of hydroprocessed synthesised paraffinic hydrocarbons wholly derived from iso-butanol.

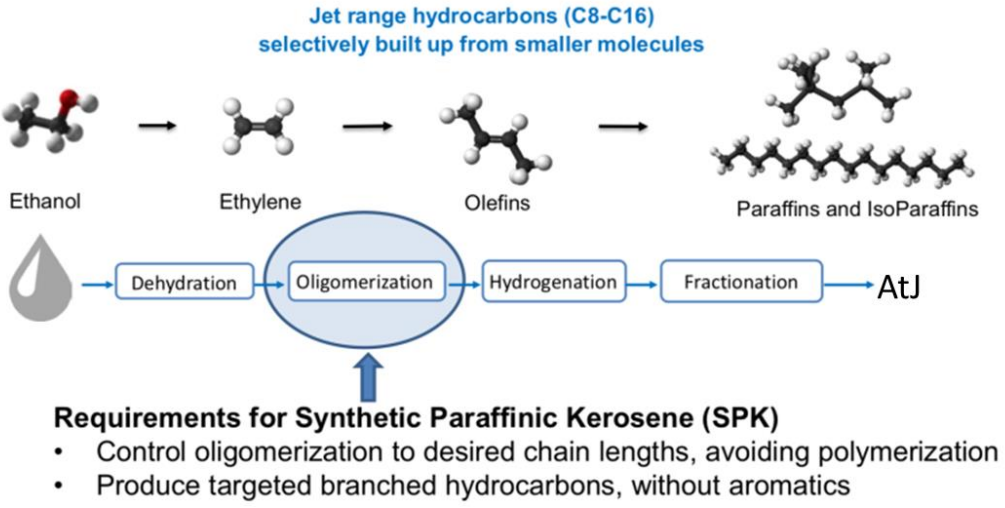

Figure II-5: Alcohol to Jet formation process. The intermediate alcohol is taken through a four-step process to produce jet-range hydrocarbons (Green Car Congress, 2018).

One of the main distinctions between AtJ and conventional aviation fuels is the ignition delay measured by the Cetane Number (CN) and the Derived Cetane Number (DCN). The CN represents the percentage of cetane in a mixture of cetane and methylnaphthalene that has the same ignition quality as the given fuel. The DCN of fuel is determined using an Ignition Quality Tester. In this test, the ignition delay is defined as the time difference between the start of ignition and the recovery of combustion gases. The DCN (easier to perform) provides insights into the combustion speed of fuels and influences various ignition properties, such as for example the required compression, CO emissions, and stability. It is a critical factor in evaluating fuel quality and combustion performance: a higher DCN indicates better ignition properties (McGann et al., 2020; Y. Zhang et al., 2021). For Jet fuel, the DCN is typically around 50-55, while for HEFA, it is around 75. In the case of AtJ, the DCN is approximately 20 (Luning Prak et al., 2021; 2015). This means that the combustion efficiency of AtJ is lower than that of Jet fuel, which may account for some of the observed differences in emissions when comparing the two fuels (cf. results in section III.2.3). This can be a problem for CAST burner that was originally designed for diesel with higher cetane number and this can lead to a bad combustion in the case of the AtJ fuel and affect the stability of the flame generated during combustion with the burner.

The maximum of AtJ authorised on a blend fuel is 30% to keep a sufficient amount of aromatics and sulphur compounds in the blend (i.e. aromatics amount > 8%). The main difference with a standard SPK fuel (used at 50% in a blend fuel) is their distribution of hydrocarbons. As AtJ is derived from iso-butanol, the produced hydrocarbons have chain lengths of C_8, C_{12} and C_{16}, with C_{12} being the most abundant ones. On the other hand, FT-SPK fuels are obtained by cracking synthetic paraffin, producing a Gaussian distribution of hydrocarbons with chain lengths between C_8 and C_{16}, thus much richer than the one found in AtJ. To complete the fuel matrix of this study, a blend fuel has been employed. This one is a mix of the standard Jet A-1 (70%) with AtJ (30%) and is called mixE5 in this study. Its composition is defined as 14.2% of aromatic compounds and 140 ppm of sulphur content.

Figure II-6 presents a repartition of the composition for different fuels (conventional, blend and SAF). The main contents are paraffin (i- and n-) and alkanes. These fuels differ also in terms of H/C ratio. For example, the Jet A-1 presents 200 ppm of sulphur and 14.02% of hydrogen content while the AtJ presents no sulphur but 15.33% of hydrogen content. In comparison the Mix E5 is composed of 140 ppm of sulphur and 14.41% of hydrogen content. As seen previously (cf. Figure II-3 - right), fuels with higher hydrogen content generate emissions more representative of aeronautical ones.

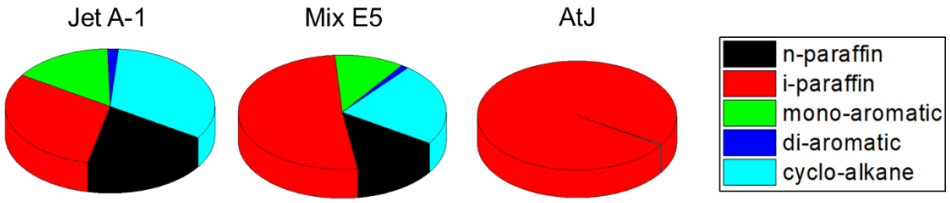

Figure II-6: Comparison of composition for different fuels: a standard Jet A-1, a blend of Jet A-1/ AtJ and a 100% SAF AtJ.

The impact of these alternative fuels on nvPM is already established in the literature for different tests on bench or in flight (Beyersdorf et al., 2014; Lobo et al., 2012). A reduction in soot particle emissions is observed when the concentration of aromatic compounds in the fuel is reduced (Speth et al., 2015). However, the impact of fuel composition on the formation of vPM is not clearly determined.

II.1.2 Simulation of emissions – atmosphere interaction

The main objective of this work is to study the interaction between aeronautic emissions and atmosphere at ground level. The liquid CAST generator has been used as a source of emissions from different aeronautic fuels. To study interactions of these emissions with the atmosphere under controlled conditions, experiments are performed with a simulation chamber.

II.1.2.1 Atmospheric simulation chamber

There are 14 atmospheric simulation chambers in Europe (ATMO-ACCESS, 2020) with different specificities: studies at sub-zero temperatures (AURA Chamber, Denmark), investigations on the gas phase processes and radical chemistry under different conditions (HELIOS Chamber, France), studies on cloud and ice nucleating particle formation (AIDA Chamber, Germany), observations of chemical degradation of pollutants under simulated atmospheric conditions (ESC-Q-UAIC Chamber, Romania) etc.

In this study, the experiments were done in the Multiphase Atmospheric Experimental Simulation Chamber (CESAM - Figure II-7). This smog chamber is able to reproduce atmospheric conditions at ground level (Temperature, Relative Humidity, solar irradiance…). Different studies have been already done on CESAM to work on interaction of atmosphere with different aerosol particles. For example about soot particles (Grimonprez et al., 2021), seeded and non-seeded SOA formation (Duporté et al., 2016; Lamkaddam et al., 2017; Massabò et al., 2018), as well as very early stages of particle formation (Boulon et al., 2013). This chamber is located at the Interuniversity Laboratory for Atmospheric Systems (LISA) in Créteil (France) which is part of the National Centre for Scientific Research (CNRS).

CESAM Chamber (Créteil, France)

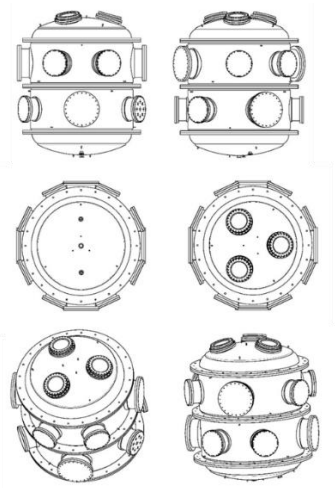

Mechanical description of the chamber (Scale 1:15 - Design: Edouard Pangui / CNRS-LISA)
Diameter: 1.8m / Height: 2.3m

Figure II-7: Multiphase Atmospheric Experimental Simulation Chamber - CESAM is part of the facilities of the European consortium Eurochamp (CESAM_EUROCHAMP, 2020).

This 4.2 m^3 stainless steel simulation chamber (Figure II-8) is dedicated to the study of multiphase atmospheric processes such as the formation of secondary aerosols and ageing processes. The chamber double walls allow the circulation of a coolant liquid connected to a thermostat (LAUDA Integral T 10 000 W), enabling temperature control during the experiments between -10°C and +60°C. The pressure can be controlled as well, with a limit vacuum at 10^{-4} mbar but normally the chamber is operated with a slightly overpressure with respect to atmospheric pressure to avoid contamination and eliminate any memory effects. Relative Humidity (RH) can as well be controlled between 0 and 100%. Three high power xenon arc lamps (6.5 kW) situated above large quartz windows on the top of the installation allow to simulate the solar radiation inside the chamber (Figure II-8 – top). It is comparable to the sunlight at noon on the 21st of June (at 45° lat. N) in terms of intensity (Figure II-9) and spectral distribution (coverage from 280 nm to the infrared). The light can be filtered with Pyrex

filters of different thickness to simulate solar irradiance at different heights in the atmosphere, ranging from the ground level to above the stratospheric ozone layer. For this experiment, the solar spectrum at ground level is reproduced to study photochemical ageing of emissions.

Furthermore, the CESAM chamber is designed to ensure a lifetime of aerosol consistent with the study of its ageing process, for example keeping a very low level of electrostatic charges on the wall. Figure II-10 shows how the lifetime of the particles depends on their size, with a maximum of four days lifetime for particles of about 0.2 µm (Di Biagio et al., 2014).

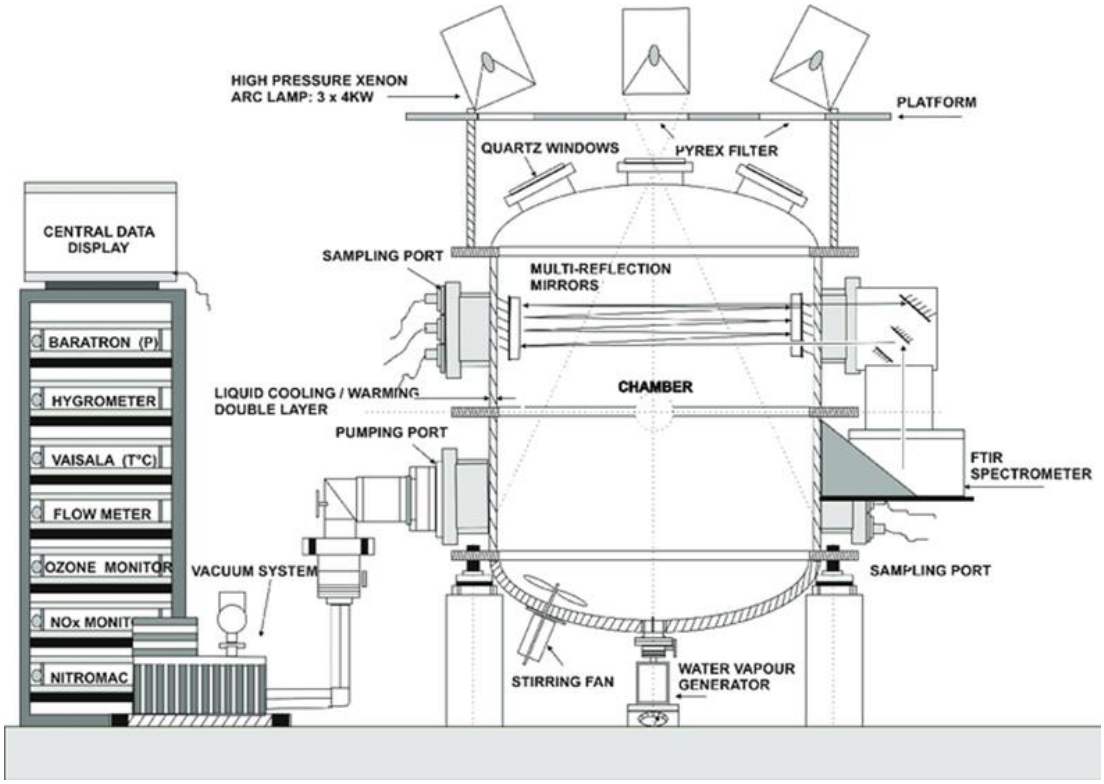

Figure II-8: Schematic front view of atmospheric CESAM facility (J. Wang et al., 2011).

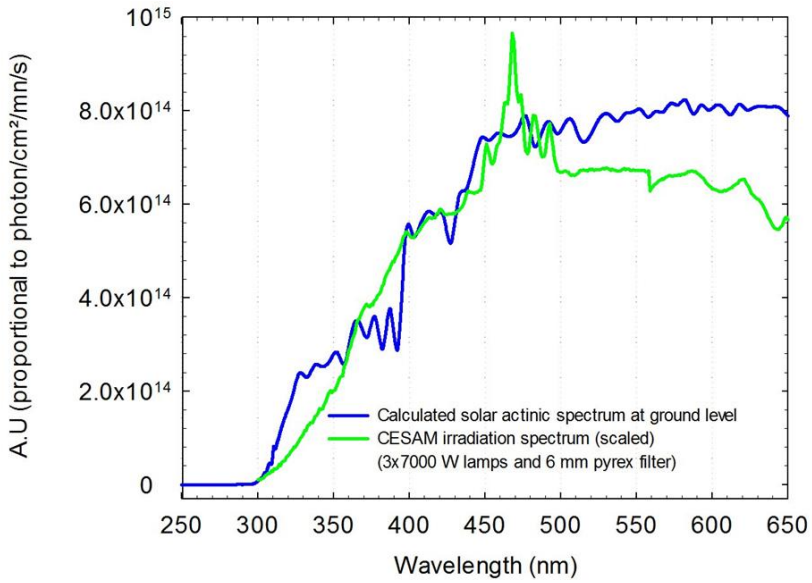

Figure II-9: Comparison of the CESAM irradiation spectrum (from 3 high pressure xenon arc lamps - 6.5 kW) with solar spectrum at ground level (comparable to the sunlight at noon on the 21st of June at 45° lat. N) - measurement from Dr. M. Cazaunau (CNRS/LISA - CESAM_EUROCHAMP, 2020).

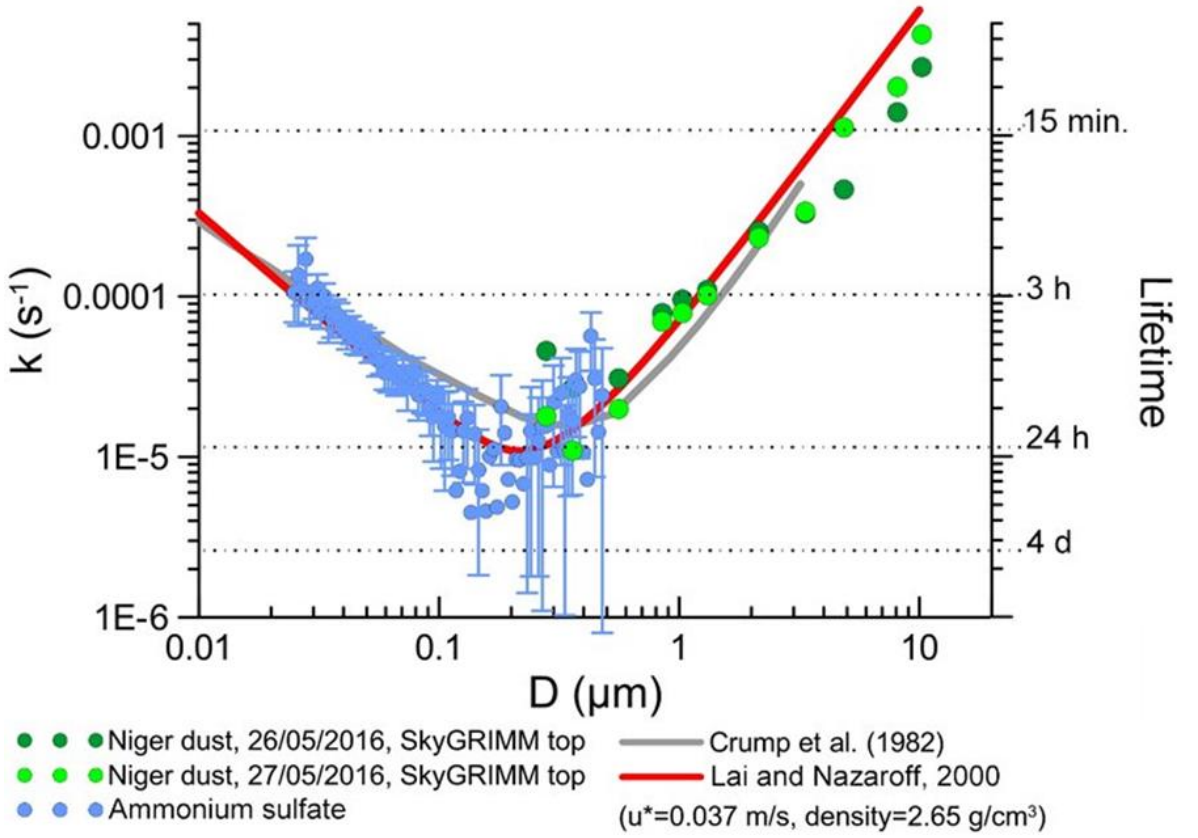

Figure II-10: Size dependent aerosol loss/lifetime inside CESAM chamber: deposition rate constant (k) as a function of particle diameter (D) based on the Lai and Nazaroff model (Crump & Seinfeld, 1981; Di Biagio et al., 2017; Lai & Nazaroff, 2000; Lamkaddam, 2017).

The CESAM facility is hence unique in its capability to both generate photochemical HO_x chemistry and handle injected aerosols of very different natures (soot, dust, salt, etc.). A comprehensive up-to-date set of analytical instruments (Figure II-8, CNRS-LISA) are connected to the atmospheric chamber to characterise emissions and monitor their evolution over time. The main devices available at CESAM are listed in Table II-3 below and the most relevant of them for this work are highlighted and described in detail in sections II.2.2.1, II.2.2.2 and II.2.2.2.4:

	Measurement	Instruments available at CESAM
Gas Phase	**Temperature, Relative Humidity**	**Vaisala HMP 234**
	Pressure	**Pressure gauge – Baratron**
	Actinic flux	Spectrometer LICOR 1800
	CO_2, CO, H_2O	**Picarro 3202**
	O_3, NO_x, SO_2	**On-line analysers**
	VOC	2 **On-line PTR-ToF-MS** (**H_3O^+** and NO^+ mode)
	VOC (alkane etc.)	On-line: automated GC-FID Off-line: ATD GC-MS
	VOC, NO_x, NO_y, O_3	In-situ long path (200m) FTIR
Particulate Phase	**Granulometry (18 - 850nm)** Particle Size Distribution and Concentration Number	**On-line SMPS - TSI 3080**

	Granulometry (0.3- ~20µm)	Grimm OPC – Welas® 2000, Palas TM
	Soot (EC/OC speciation)	Sunset EC/OC inst.
	Aerosol physical properties	On-line: Aethalometer (Absorption), Optical cavities 450 and 630 nm (extinction and scattering), Nephelometer (scattering), HTDMA (Hygroscopicity) Off-line: TEM and SEM microscopy (morphology)
	Chemical composition of aerosols	**On-line: ACSM-ToF** Off-line: SFE-GC-MS (organics), ionic chromatography (inorganic species and organic acids), UPLC-QToF (oligomers and heavy organics species)

Table II-3: Summary of CESAM facilities. Devices used during this study are displayed in bold.

To assure chamber cleanliness after each test, the chamber is pumped down to $5x10^{-4}$ - $10x10^{-4}$ mbar while heating the walls to 60°C to desorb the compounds that might be adsorbed on them. If this process is not enough to completely clean the chamber, it is possible to do that manually to remove all traces from previous tests. At the beginning of each experiment, different blanks are done to check chamber background.

Since the instruments connected to the chamber are continuously sampling from the chamber at a certain flow, a synthetic air flow (N_2 and O_2) is introduced into the chamber to keep the pressure constant. This induces a dilution that increases with time and has to be accounted for. In addition, measurements need to be corrected to account for wall losses (Figure II-11). The low surface/volume ratio (S/V = 4.3 m^{-1}) minimises these wall effects.

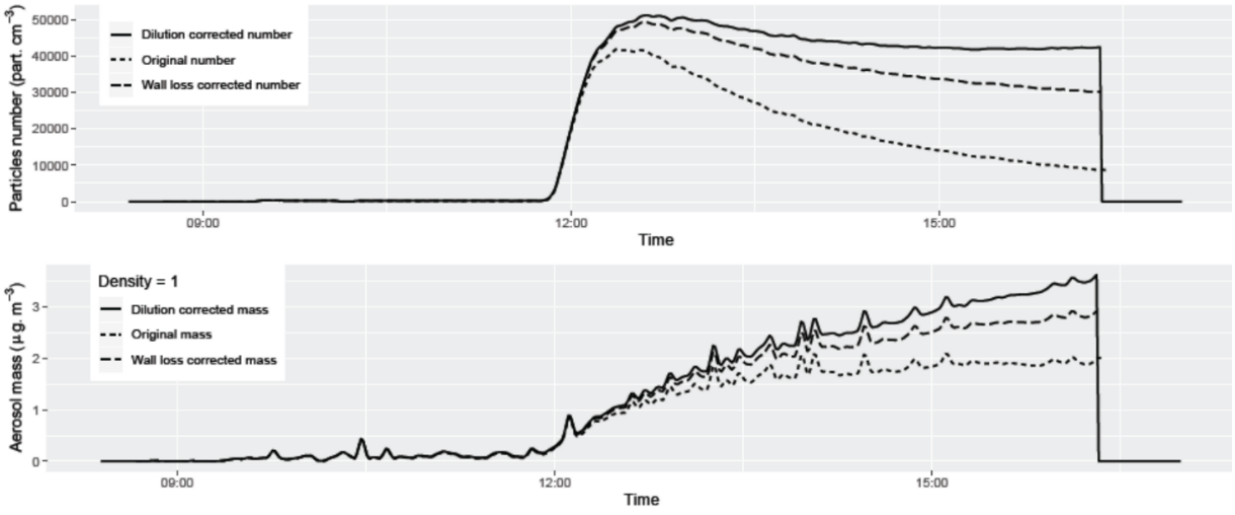

Figure II-11: Example of data from UNREAL experimental campaign (November 2020) corrected with dilution and wall loss factors (Rcode). It corresponds to the injection of emissions from the CAST burner inside the CESAM chamber and the evolution of the particles number and aerosol mass over the time (Lamps started at 11h35).

Taking into account the characteristics described above, the CESAM chamber is perfectly suited for the work proposed in this thesis: to study the interactions between emissions of a laboratory burner and atmosphere at ground level conditions.

II.1.3 Experimental campaigns

During the UNREAL project, different measurement campaigns were performed at CESAM chamber in LISA laboratory facilities (Créteil), gathering different partners (cf. I.1) and based on the set-up presented in this chapter (Figure II-12).

The objective of the first tests was to optimise the experimental protocol for the study of nvPM and vPM. For example the selection of the CAST parameters such as set point depending on the fuel tested. The injection process of emissions into the atmospheric chamber is also to be determined (time, amount of particles…). The main point has been to separate the gas phase from the particulate phase to study the formation of particles independently of the soot presence in the chamber.

Based on these experiments, the productive campaign took place between March and April 2022. In this campaign, specific techniques to study particle formation were deployed to complement the measurements done during the previous tests. The processing and the analysis of the emissions samples are detailed in the following section.

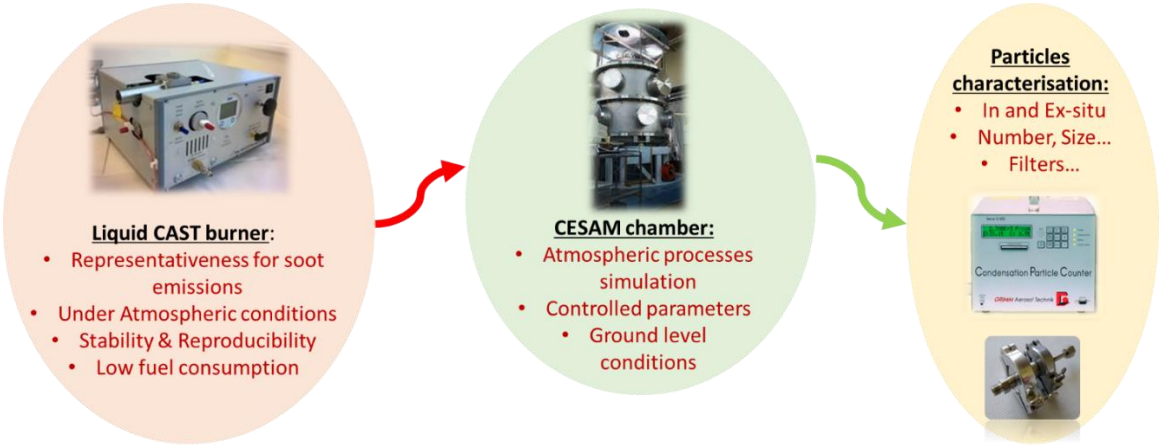

Figure II-12: Summary of set-up for UNREAL campaign: an emission source for injection in parallel inside an atmospheric simulation chamber and connection with instruments to analyse emissions evolution (II.2.2).

II.2 Experimental set-up

The main objective of certification protocols is to define a standard methodology (sample line material, temperature and length, sample flow, dilution ratio, measurement instruments to be used, etc.) to ensure the validity and comparability of all certification measurements worldwide. All these parameters are defined under SAE AIR 6241 procedure (ICAO, 2017). For example, to avoid the formation of vPM, the sample must be collected on the engine exit plane and sampling lines should be heated to 160°C.

In this thesis, a deployable and adaptable experimental line is developed in the CESAR laboratory at ONERA to study the emissions collected in the exhaust of the CAST burner or an engine. The purpose of the line is to keep the emissions as unchanged as possible compared to the exit of the engine or the burner, avoiding interaction with the atmosphere and keeping hot to limit potential condensation or formation of vPM in the line. Figure II-13 represents the standard measurement set-up employed for the various tests performed. This measurement line allows the study of non-volatile Particulate Matter (nvPM) in particular by distinguishing them thanks to the evaporation of vPM at 350°C (cf. vPM definition in I.4.3). This installation also includes different dilution stages and connects each measuring device respecting their technical constraints in terms of sample temperature or pressure. With this

set-up, it is possible to quantify aeronautical emissions in terms of particle size, mass and number concentration and to study the chemical composition of emissions using a sampling method and off-line techniques. Methods and instruments used in this study are described in the following part.

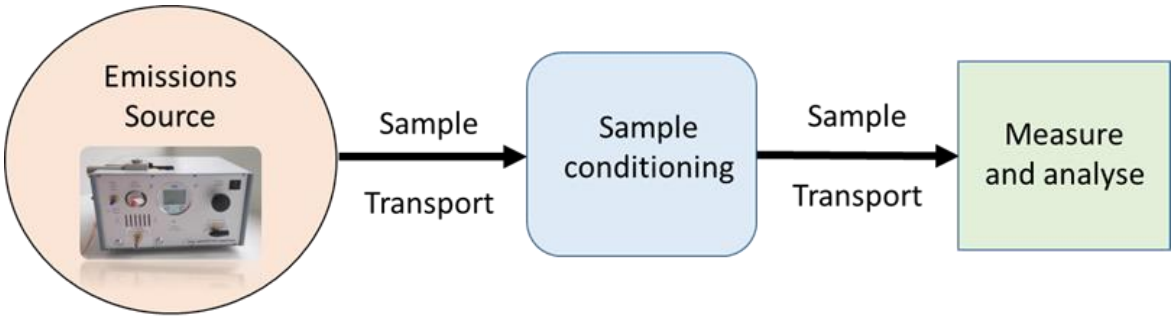

Figure II-13: Typical measurement line adapted to a combustion source and deployed to study emissions for the sampling and characterisation of vPM and nvPM.

II.2.1 Sample conditioning

The sample flow from CAST exhaust needs to be diluted at high temperature to avoid condensation and cooled down (generally at room temperature) before being analysed by the different instruments to respect their measurement range. Thermally controlled lines of different lengths (from 1 to 8m) provide the transport of the sample from burner/engine exhaust until measuring devices avoiding condensation of emissions. Various dilution instruments complete the set-up to limit post-combustion chemical reactions between particles and gases (oxidation, nucleation, homogeneous or heterogeneous reactions) and to condition the sample in temperature and concentration level for the measurement in a second part. In the case of this study, the sampling line between the CAST and the dilution stage has been kept at 160°C to avoid the formation of vPM.

II.2.1.1 First dilution stage

II.2.1.1.1 Dilution Stage at burner outlet

A first dilution step called ejection dilutor DI-1000 (Figure II-14 - left) is positioned directly at the CAST outlet. It is an easy-to-operate system produced by Dekati® and used to control aerosol dilution from different kinds of sources. This device is robust and can operate at high temperatures (Dekati_dilution). To avoid the condensation of water and volatile gases on the soot particles, the instrument is heated at 160°C and the sample is diluted with air (Figure II-14 - right) which is upstream purified, pressurised, heated at the same temperature as the device, filtered and dried. The nominal dilution ratio is 1:8 (can reach more in theory depending on dilution air and sample flows) and the nominal value is given for 2 bar inlet pressure.

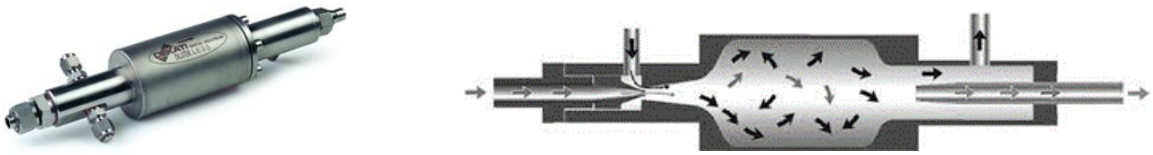

Figure II-14: Dekati Diluter DI-1000 System. Principle (Dekati_dilution) based on the ejection dilution: dilution air introduced by depression at high speed and mixed with the raw sample to obtain a homogenous and stable sample. Only purified air under pressure is required for the diluter - no flow control devices or pumps are needed.

II.2.1.1.2 Dilution stage for fine particle

Another dilution system has been employed in parallel with the one detailed previously to dilute aerosol from combustion. This one is a Dekati® Fine Particle Sampler (FPS - Figure II-15- left) provided by INERIS institute and offers a control in real time of the dilution conditions (Dekati_dilution). It is a robust system (0-600°C for the inlet sample temperature) and has been designed to minimise particle losses. It is composed of two dilution stages (Figure II-15 - right) that can be controlled in terms of temperature by thermocouples (0-350°C) and dilution air pressure (0.1-2bar). For example, it is possible to remove vPM with high temperature or study the nucleation process using cooled dilution with pressurised air. The overall DF can be adjusted between 1:20 and 1:200 setting each stage dilution rate independently, from 1:3 to 1:20 for the first one and from 1:7 to 1:15 for the second one. FPS operates at 4.5bar.

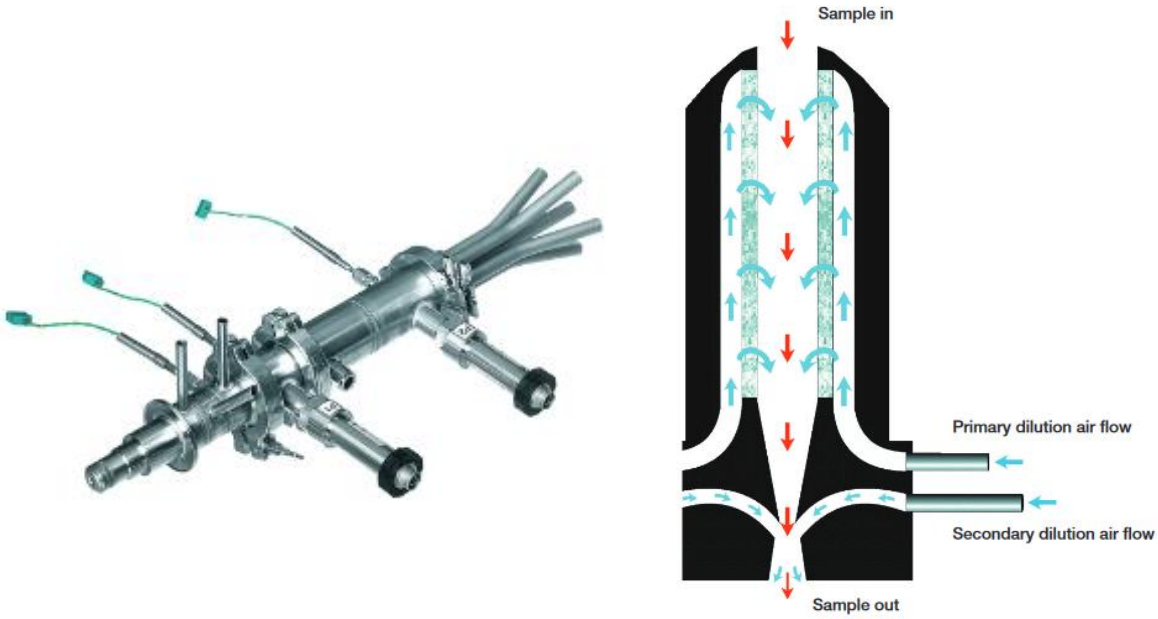

Figure II-15: FPS Dilution System (Dekati_dilution). The first dilution stage forces the dilution by insertion of dilution air through holes in the tube walls. The second stage acts as an ejector type diluter. The temperature is controlled by thermocouples.

II.2.1.2 Additional dilution stage

In addition to the first dilution stage, a second dilution step can be added downstream of the CAST and the DI-1000 to remove vPMs. This system is called a Dekati® Engine Exhaust Diluter (Dekati_dilution) operating at 4 bar. It consists of two DI-1000 dilutors separated by an evaporation chamber (Crayford et al., 2011 - Figure II-16). Emissions are first diluted at 150°C using a DI-1000 system and then heated to 400°C in an evaporation chamber to volatilise the vPMs (efficiency >99% for certification use). An optional dilution stage (VKL - Dekati_dilution) with a dilution factor of 10 can be added after the evaporation chamber leading to a high dilution setting. Finally, emissions reach a second DI-1000 system at ambient temperature to reduce the concentration of gaseous species vaporised in the evaporation chamber thus avoiding unwanted condensation phenomena and nucleation processes. Interactions between the particles are as well avoided.

DEED's Dilution Factor (DF) can be adjusted at 1:100 using the low dilution setting or 1:1000 using the high dilution setting (with VKL) for an inlet flow of 5 L/min. This DF depends on the inlet flow and dilution air flow. In the case of this study, only the low dilution setting is used and the DF has been measured at different moments to be estimated for each test. In theory, this value should be 100 but as it is related to the setting of the two DI-1000 in the instrument and it is possible to get a DF lower than expected. Thus, a DF of 55.84 using the CAST burner in ONERA laboratory has been measured and

an average value of 80 during UNREAL campaigns has been calculated. To ensure an appropriate correction of the emissions measurement by the dilution, the DF is measured for each experiment.

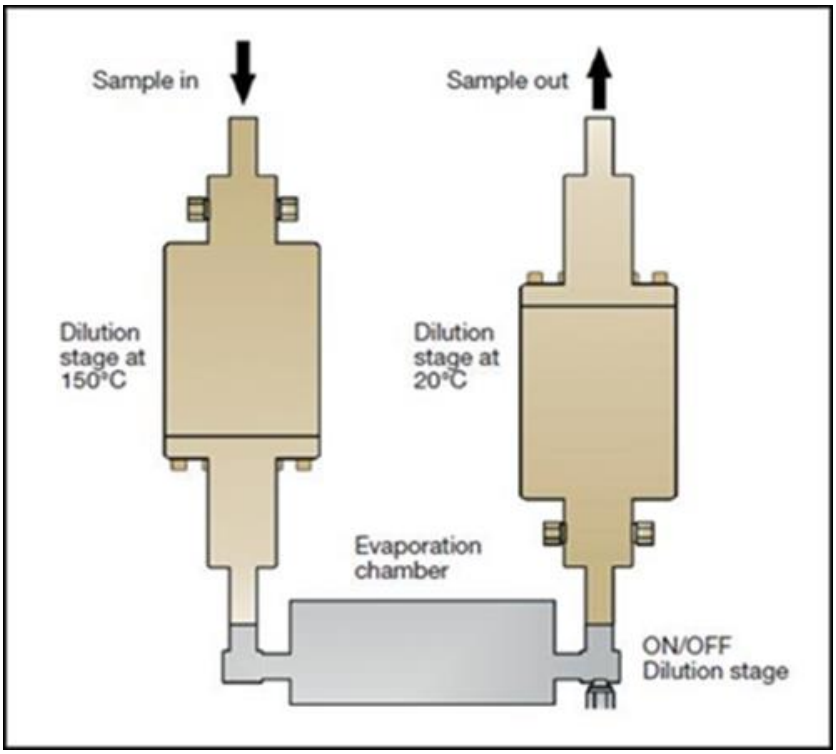

Figure II-16: DEED Dilution System. On the left, a simplified diagram of DEED operation (Crayford et al., 2011) and on the right, an example of variation of the DEED dilution factor as a function of engine speed in % (ANTARES 2020 campaign).

II.2.1.3 vPM removal and nvPM selection

Various instruments allow the characterisation of the emissions in terms of mass or number concentrations, but the measurement of the complete engine emissions (nvPM + vPM) can be a problem. This is due to the potential impact of the presence of vPM on the certified instruments for measuring nvPM. Different methods can be employed to separate vPM and nvPM or remove vPM from emissions using trap or adsorption.

To complete the dilution a Catalytic Stripper (CS) model DCS-100 (Catalytic Instruments GmbH & Co.KG) is used to ensure the full removal of the vPM. This instrument, optimised for an incoming flow of 5L/min, can be placed upstream of the DEED or after another dilution system. This CS is first composed by a catalytic bed heated at 350°C and an oxidation area to remove vPM leaving only nvPM (Amanatidis et al., 2013; Mamakos et al., 2013 - Figure II-17 - left). Unburnt compounds and/or Polycyclic Aromatic Hydrocarbons (PAH) present in the exhaust gases are eliminated by oxidation of volatile organic compounds (VOCs) on the surface of soot particles leading to a decrease in the mass concentration measured subsequently (Berthier, 2022). The formation of vPM is also prevented due to the suppression of potential precursors in the gas phase and the presence of a sulphur-trap (Duca et al. 2021; Giechaskiel et al. 2020 - Figure II-17- right).

Different dilution instruments can therefore be deployed. They all have their specificities and interests depending on the tests performed. In this thesis, both sampling of vPM and nvPM are taken into account. For example, the dilution duo DI-1000 (or FPS)/ DEED coupled with a CS will be used to study emissions characterisation in CAST burner raw exhaust (Chapter III) without vPM. In the case of CESAM chamber, emissions are directly injected inside to work on nvPM and vPM. Corresponding set-ups are detailed in the next Chapter.

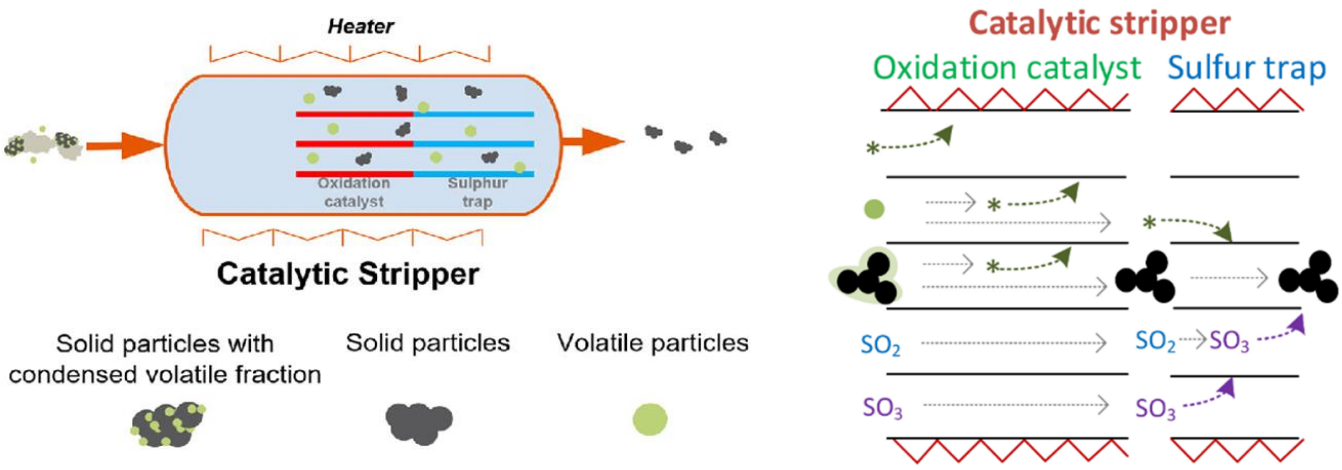

Figure II-17: Catalytic Stripper instrument: On the left, an example of the CS's principle removing vPM from a particle sample (Melas et al., 2020). On the right, zoom on the sulphur trap and SO_2 to SO_3 conversion (Giechaskiel et al., 2020).

II.2.2 Emissions measurement

II.2.2.1 On-line gas measurements

In addition to the experimental line, gas detectors are added to measure evolution of the gas present in emissions sampled over the time.

II.2.2.1.1 Carbon dioxide measurement

To monitor the volume concentration of carbon dioxide in the exhaust gases, a Multi-gas Infra-Red analyser MIR-2M (ENVEA company) is deployed. This detector can be seen as a simple non-dispersive spectroscopic sensor composed of an infrared source (lamp), a sample chamber, a light filter and an infrared detector (Infra-Red Gas Filter Correlation IR GFC principle). Gas phase in the chamber absorbs the infrared of specific wavelengths according to the Beer–Lambert law and this attenuation is recorded through the light filter on the detector to estimate the concentration of CO_2: absorption band at ~4.25 µm on Figure II-18.

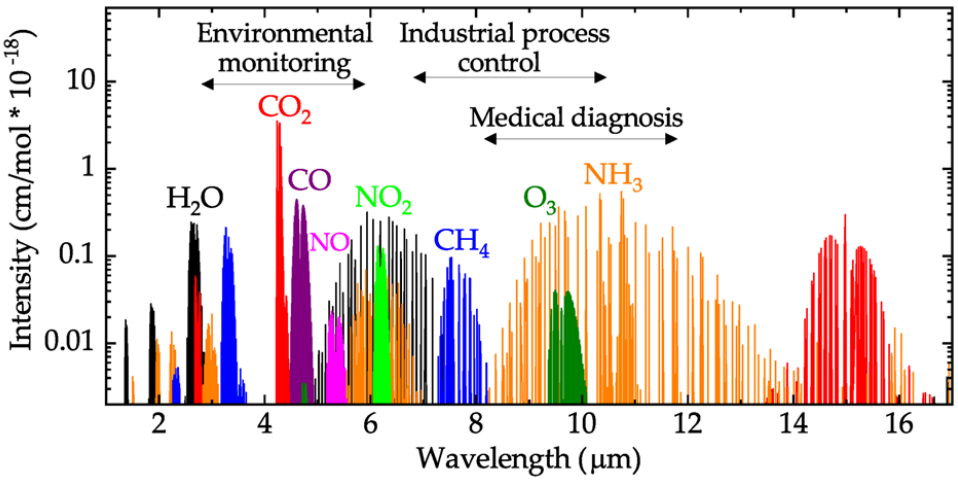

Figure II-18: Some gases and their sensing wavelengths in the mid-infrared absorption spectra (Popa & Udrea, 2019)

The detector has a measurement range from 100 to 250,000 ppm, a response time of less than 2s, and the sample temperature must be between +15°C and +45°C. The CO_2 detector is also a way to indirectly control the combustion efficiency and fuel consumption. Using a second detector installed after the dilution stage, it is possible to evaluate the DF of the DEED or other dilution systems by measuring the ratio of CO_2 before and after the dilution stage.

II.2.2.1.2 Sulphur dioxide measurement

To measure the volume concentration of sulphur dioxide SO_2 in the exhaust gases, a Sulphur Dioxide Analyser Model AF22M SO2 (ENVEA company) is employed. Operating for low sulphur levels in the ambient air (around 100 ppb) with a limit of detection at 0.4ppb, the measuring principle is based on fluorescence radiation in the UV.

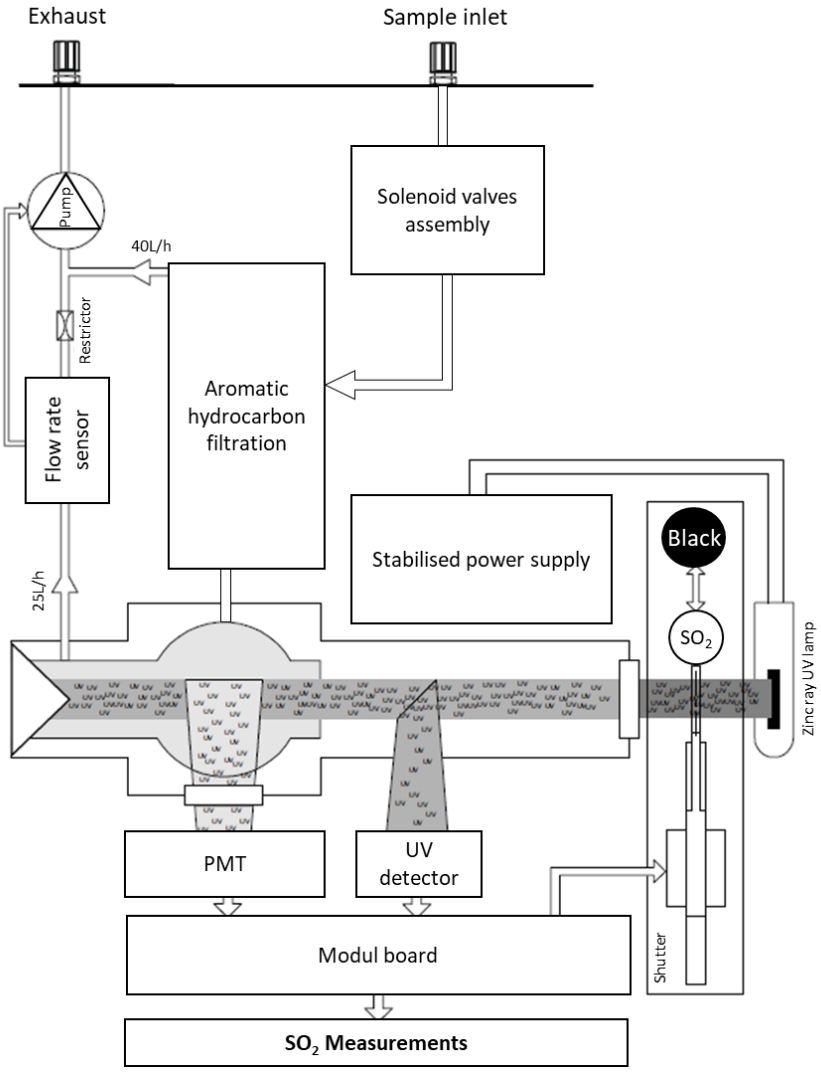

Figure II-19: General principle diagram of SO_2 measurement (adapted from Environment S.A. 2010).

The sample is filtered by a first Teflon filter (5µm) at the inlet, eliminating the particulate phase and allowing only the gas phase to go through before being sent to a block of solenoid valves (calibration/zero/sample switch). The gas phase then passes through an aromatic hydrocarbon removal device (Figure II-19) based on the transfer by permeation of aromatic hydrocarbon molecules between the inner tube and the outer tube (silicones) before being evacuated. Once the aromatic compounds have been eliminated, the emissions arrive in the measurement chamber. A zinc lamp

generates the necessary UV radiation, centred at 214 nm, which is the absorption wavelength of SO_2 molecules. The fluorescence is optically filtered between 300 nm and 400 nm and detected by a photomultiplier tube (PMT) to calculate the concentration of SO_2.

This device operates for a full range from 1 ppb to 10 ppm (typical value of minimum detectable limit is below 0.5ppb) and is equipped with an automatic response time function. It allows working with sample temperatures ranging from 10°C to 35°C (Environment S.A., 2010).

II.2.2.1.3 Nitrogen oxides measurement

To measure continuously the volume concentration of nitrogen oxides in the exhaust gases, an Ambient NO_x Monitor (Model APNA-370, HORIBA) is employed. This device provides NO, NO_2 and NO_x ($NO+NO_2$) concentrations and operates for low levels in the ambient air (between 0-1.0 ppm) with a limit of detection at 1 ppb. An internal dry-method sampling instrument allows the highest levels of sensitivity and accuracy. The measuring principle is based on a cross-flow modulated semi decompression chemi-luminescence method (CLD). The CLD method uses the reaction of NO with O_3:

$$NO + O_3 \rightarrow NO_2^* + O_2 \qquad \text{(eq. II.7)}$$
$$NO_2^* \rightarrow NO_2 + h\nu \qquad \text{(eq. II.8)}$$

When excited molecules return to their ground state, chemi-luminescence is generated (in the spectral range from 600 nm to 3,000 nm). The light intensity is proportional to the concentration of NO molecules and NO can be measured. NO_x concentration is estimated after the sample gas is passed through a de-oxidation converter. The NO_2 concentration is obtained from the difference between NO_x and NO.

The flow rate is 0.8L/min under ambient temperature.

II.2.2.1.4 Composition of the gas phase

Emissions generated by the CAST burner or an engine can be considered as formed by two phases: the gas phase and the particulate phase (cf. II.2.2.2.4). To analyse on-line the chemical composition of the gas compounds present in the emissions, a Proton-Transfer-Reaction Time-of-Flight Mass Spectrometer (PTR-ToF-MS, Kore Ltd), provided by LISA laboratory, is deployed.

This technique is one of the most sensitive (Abis et al., 2018; Haider et al., 2022; Materić et al., 2015) for real-time detection and quantification of Volatile Organic Compounds (VOCs). In this study, it uses soft ionisation by proton transfer (with hydronium ions, H_3O^+) to reduce fragmentation and spectral complexity:

$$H_3O^+ + VOC \rightarrow HCOV^+ + H_2O \qquad \text{(eq. II.9 - Blake, Monks, and Ellis 2008)}$$

Sample is introduced directly inside a drift tube that might be heated up to 80°C, and a controlled voltage is imposed to change the ionisation conditions and avoid ion-molecule collision in this area (Figure II-20). The combination of a hollow cathode discharge and drift section generates from the humidified air hydronium ions (H_3O^+) to ionise the emissions sample. Charged ions are then separated into a Time of Flight Mass Spectrometer (ToF-MS, Figure II-20).

In the ToF-MS, ions are accelerated by a known electric field. This acceleration procures the same energy to all the ions having the same electrical charge (Boesl, 2017). Their speed is related to their mass-to-charge ratio (m/z). The time taken by a charged particle to reach a detector located at a known distance is measured. The path between the entrance of the flight tube and the detector is increased using a reflectron to obtain a better m/z separation (i.e. a better resolution). This time will depend on the m/z ratio of the particle considered. The heaviest particles are accelerated to the lowest speeds. The determination of the mass-to-charge ratio is based on this time of flight and on the

knowledge of other experimental parameters such as the position of the detector and the acceleration voltage. This gives a mass spectrum measurement up to 510m/z from which it is possible to identify VOCs. This instrument can be equipped to work with different precursor ions such as H_3O^+ or NO^+.

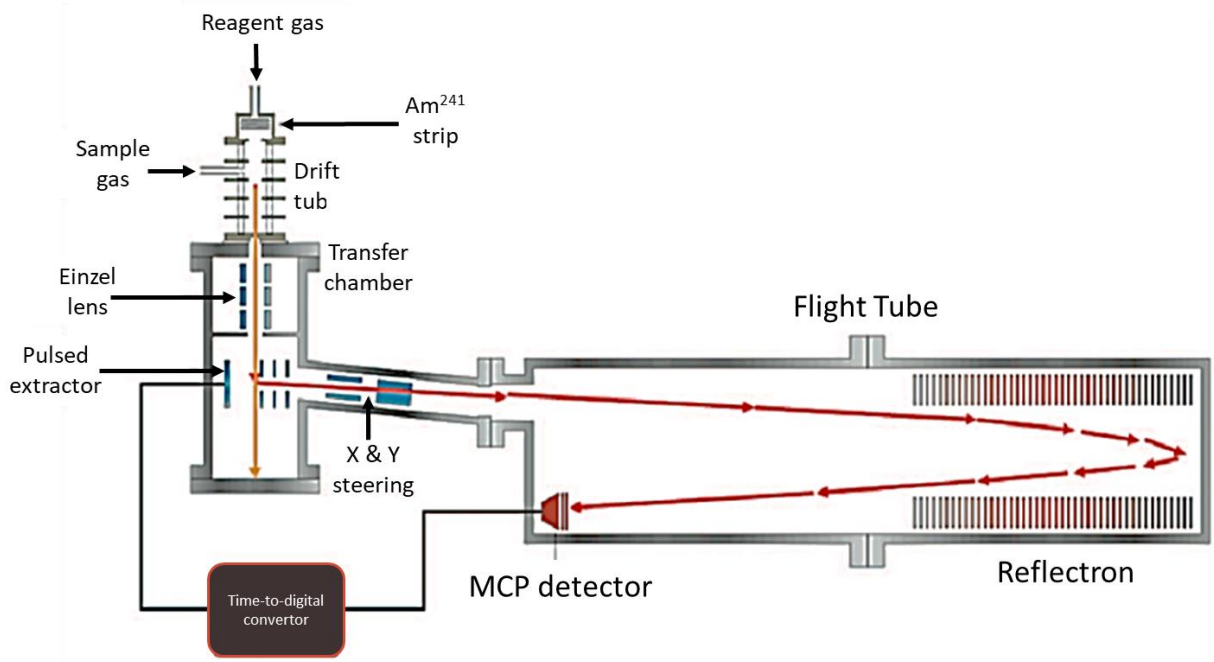

Figure II-20: PTR-MS principle suitable for on-line VOC monitoring with high sensitivity and high resolution: VOCs are ionised in the drift tube using beam of reagent ions (H_3O^+), mass separated by a ToF mass spectrometer (right) and recorded by a detector (Blake et al., 2008; Materić et al., 2015).

However, not all VOCs are detected: the instrument measures only volatile compounds with a higher proton affinity than water (691.7kJ.mol^{-1}) and for example, alkanes are not detected. Nevertheless, it can be also seen as an advantage because N_2 and O_2 having lower proton affinity than water will not react, thus no diluting buffer gas is required.

Furthermore, high molecular weight compounds are difficult to detect due to deposition in the sampling lines and the limitation of the ToF transfer function. This instrument is quantitative, but cannot separate isomers (provides concentration of all molecules of the same weight). The detection limits are close to 1ppbV in less than one minute.

II.2.2.2 On-line particles measurement

After combustion, emissions are conditioned by dilution and cooled down. The next step is the analysis of the particles properties and their composition.

Three distinct values are to be taken into account to characterise the particulate phase: the number concentration, the size distribution and the mass concentration of the particles. Analysis of the chemical composition is also possible using different mass spectrometry techniques. The following part describes these instruments.

II.2.2.2.1 Particle number concentration

A portable high-accuracy counter for nanoparticles Grimm_CPC (Grimm Gmbh) has been used to measure the particle number concentration. It is a Condensation Particle Counter (CPC) Model 5.403 used for various applications: mobile aerosol studies, roadside monitoring, environmental and climatic or health effect studies… (Grimm-Aerosol, 2012; Wright et al., 2007). The CPC is a reference for the nvPM certification measures (ICAO, 2018). Nanoparticles are too small to be detected by optical

techniques. This counter is based on the size increase by condensation using a specific solvent. The CPC is divided in two parts: a first chamber allowing the oversaturation of the particles with butanol at 35°C and a second one to condense these vapours on their surface at 10°C (Figure II-21). The particle diameter increases up to 10µm, before passing by a laser beam. The detection of the resulting light intensity for each particle is recorded at 90°scattering angle by a photodiode (Grimm-Aerosol, 2012). The signal is converted to an electrical pulse and counted.

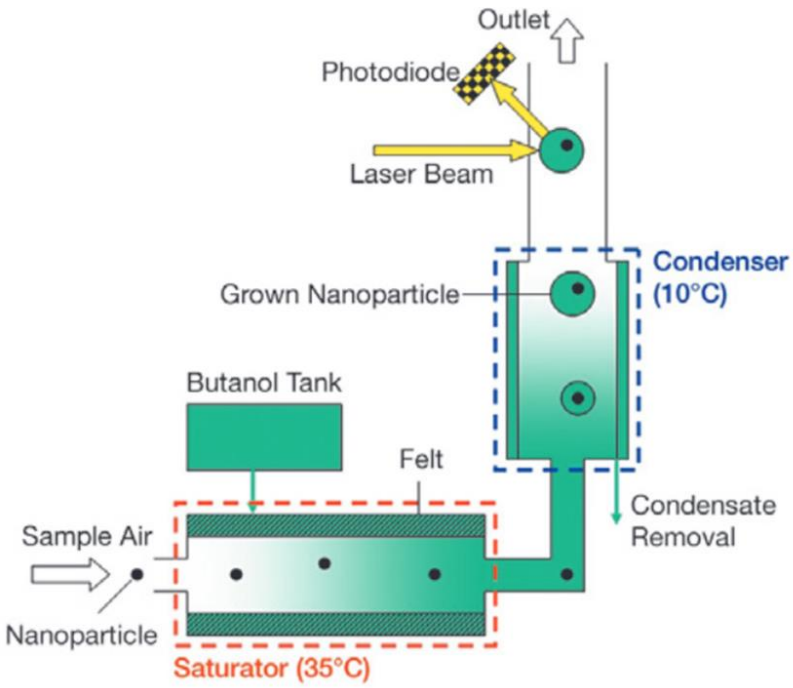

Figure II-21: Operating principle of a CPC (Grimm Aerosol, 2005). Sample enters in the saturation zone and after in the condensation area, before being recorded by the photodiode. The inlet flow is fixed by a pump at 0.3L/min, the frequency of the measurement is 1Hz and the response time is 3.9s.

The temperature difference between saturation and condensation allows the particle detection for diameters greater than 5nm. If the temperature of the saturation zone is too high compared to the one of the condensation area, this can cause an oversaturation in butanol. It will lead to the formation of particles by homogeneous nucleation and to an overestimation of the number of particles. This therefore limits the smallest particle size that can be detected as well as the inlet temperature (lower than 35°C).

This instrument allows the detection of particles for diameters between 4.5 nm and 3 µm and for concentrations between 1 and 10^7 part/cm^3. It should be noted that below 14x10^3 part/cm^3 the device is able to count the particles one by one with a standard deviation of 5% (X. Wang, Caldow, et al., 2010). In this case, the number of particles can be underestimated because some particles will be detected at the same time and will only be counted as one. By crossing the threshold of 10^5 part.cm^{-3}, the CPC switches to photoelectric mode and concentration is calculated from calibrated total scattered light intensity of all particles in the detection area (standard deviation of 10%. - Wang et al., 2010).

II.2.2.2.2 Particle Size Distribution

CPC can be coupled with a classifier to provide the particle size distribution of an emission sample depending on the electric mobility. This system is called a Scanning Mobility Particle Sizer (SMPS, Grimm GmbH) and provides a repartition of the particles in a range of sizes and of the Mean Diameter (Grimm_SMPS+C; Grimm_SMPS+E). The principle is based on the mobility of a charged particle in an electric field and is composed of three devices (Figure II-22).

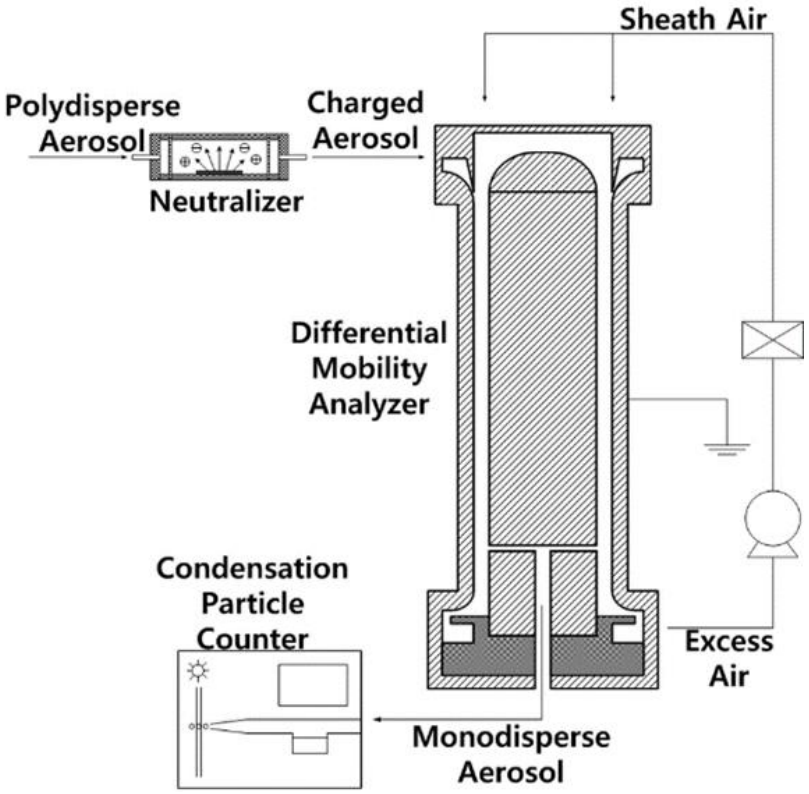

Figure II-22: Schematics of the SMPS: a DMA classifier column coupled with an aDBD neutraliser and a CPC counter (Grimm Aerosol 2009).

- Neutraliser

The first step is to neutralise the charged particle at the entrance of the SMPS. An annular Dielectric Barrier Discharge (aDBD model 5520, Grimm - Figure II-23) is a neutraliser generating a bipolar plasma (B. Y. H. Liu & Pui, 1974). All irregularly charged particles achieve in this bipolar ionic environment a defined stationary so-called Fuchs charge distribution (Fuchs, 1963; Wiedensohler, 1988), regardless of the initial charge of the sample. The phenomena of double charges and bimodal distribution are limited thereafter (i.e. in two distinct modes due to an electrical resonance phenomenon - Lu et al. 2019). This instrument is easy to operate and is a substitute to avoid radioactive sources.

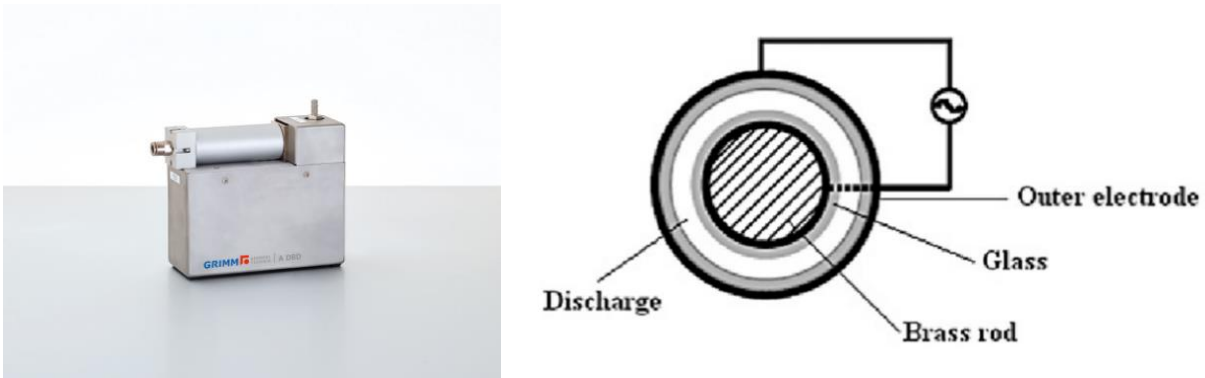

Figure II-23: aDBD model 5520 (left) with a cross-sectional schematic view n(right) of the annular electrode system (Subedi et al., 2009).

- Classifier

The second step is the classification of the neutralised particles. A Differential Mobility Analyser (DMA, Grimm - Figure II-24 - left) classifies nanometric particles between 3nm and 1µm, based on their electrical mobility D_m (Grimm Aerosol, 2009). The charge of each particle being known due to the neutralisation stage and directly dependent on its size, the electrical mobility of each particle can be determined. The voltage value of the DMA has an impact on the classification process. When a voltage is applied, the charged particles are deflected from the straight path in the resulting electric field (Figure II-24 - right) and classified according to their electric mobility. The voltage adjustment allows only particles of a specific electrical mobility to escape from the column through the outlet. The size range can also be selected depending on the length of the vertical electrode. Two different DMAs are used to measure particle sizes between 3 and 150 nm (S- DMA on Figure II-24 - left) or for particles between 5 and 350 nm (M-DMA on Figure II-24 - left).

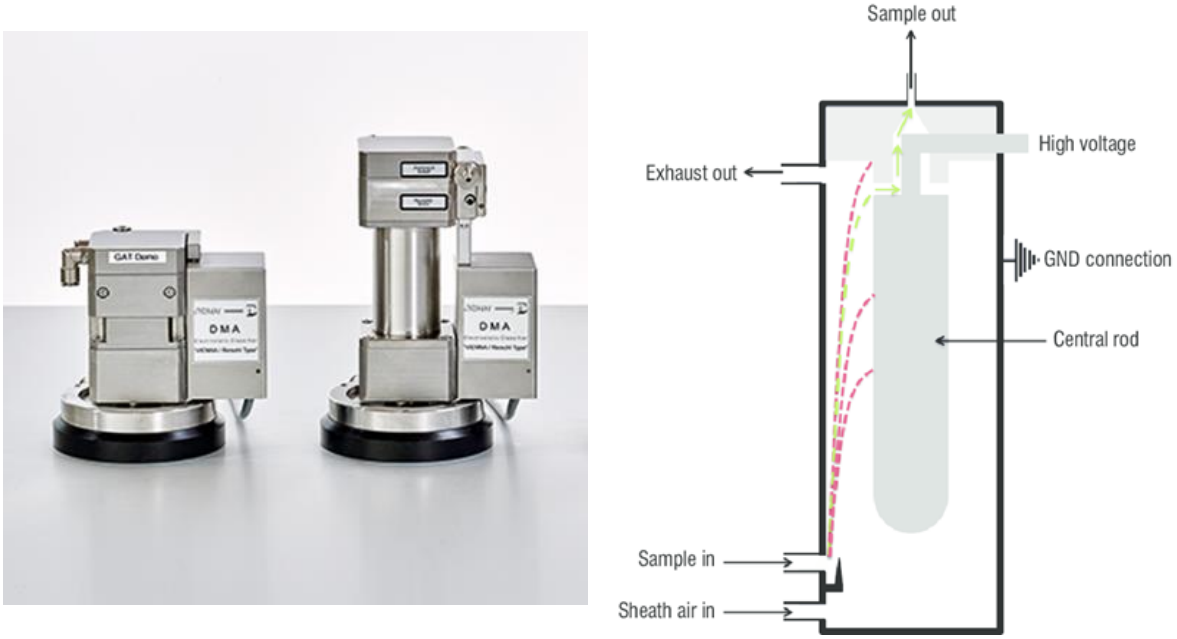

Figure II-24: On the left, two examples of DMA 5706 columns depending on particle size analysis: S-DMA (small one) for particles between 3 and 150 nm and M-DMA (middle size) for particles between 5 and 350 nm. On the right, DMA schematics (I. Ortega, Delhaye, Ouf, et al., 2016): the sheath air protects the central selective electrode and provides a laminar flow.

- Counter and size measurement range selection

The last step is the counting of the particles already classified by the DMA columns. The CPC presented previously (II.2.2.2.1) is used to form an SMPS+C. This system records the number of particles by size classes to provide a size distribution of particles between 5 and 350nm. The acquisition time depends on the number of bins used to record a distribution, i.e. the number of mobility diameter ranges used to count particles (3min40s for 45 bins for example).

There is also the possibility of using a Faraday Cup Electrometer (FCE - Grimm GmbH) to obtain an SMPS+E allowing the detection of positively and negatively charged particles from 2.8 to 150 nm. This instrument is composed of an electrometer and a Faraday cage (Figure II-25). The charged particles are collected inside the well isolated cage on a filter. An electric current is generated by discharge (resistor) and converted into a voltage. This voltage is amplified and measured by a low-noise electrometer to obtain a size distribution over the time. The acquisition time for 45 bins is 55s.

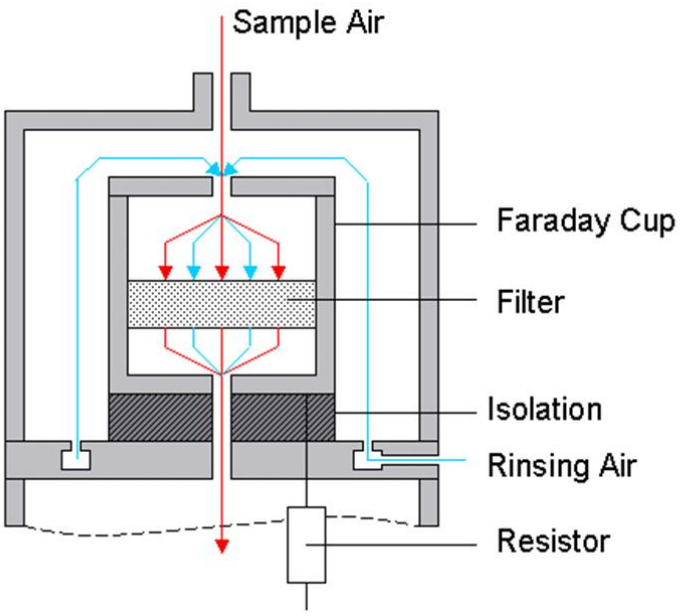

Figure II-25: Schematics of the FCE principal (Keck et al., 2009)

II.2.2.2.3 Particle Mass Concentration

The mass concentration of the particles is provided by an on-line measurement device based on the Laser Induced Incandescence principle (LII-300, Artium Inc., Figure II-26). This technique is one of the most effective to detect soot particle mass and volume fraction in an emission sample (Irimiea, 2017; Lemaire & Mobtil, 2015; Melton, 1984; Yuan et al., 2022) and is used in particular for engine certification.

Soot particles present in the emissions sample are heated by absorption of a pulsed laser radiation in the IR-UV wavelength range (Figure II-26). The excitation source is a double-cavity laser pulsed at 12 Hz of the Nd-YAG type (model PIV400 - Spectra-Physics 2002; Thys and Desmet 2011) which emits in the near infrared at 1064 nm. Submitted to this excitation during a few nanoseconds and having a grey body behaviour, the soot particles absorb the laser energy which results in a rapid increase in their temperature (Michelsen et al., 2015a) until sublimation limit (temperatures between 2500 and 4000K). Particles are cooled by different heat transfers such as conduction, and to a lower extent by thermionic emission and radiation (Figure II-26). These processes generate light/radiative emissions called incandescence, following a law similar to Planck's law (Irimiea, 2017). It is possible, regarding the resulting incandescence signal and the cooling time of these particles, to access the size of the primary particles and the mass concentration of the soot particles (Bouvier, 2006; Michelsen et al., 2015a). The soot particles radiation signal is detected with a fast photo-detector immediately after the heating laser pulse has ceased. Using two emission wavelengths centred respectively in the blue (400 nm) and in the red (800 nm) of the emission spectrum (Bladh et al., 2015), the intensity can be related to the temperature according to Planck's law (principle of pyrometry - Therssen et al. 2007).

The presence of organic compounds adsorbed on the soot particle surfaces affect their optical properties. Indeed, soot particles covered with organic compounds would require more energy to reach the maximum of the incandescence signal and would affect the instrument response as well (Irimiea, 2017; Yon et al., 2018, 2021). To work with the thermal signature of the soot particles, the device should be placed after the CS to measure only the non-volatile phase of the particles without being impacted by the presence of other compounds on the surface of the soot (Irimiea, 2017). The measurement range of mass concentration achieved goes from 0.2 µg/m³ to 2000 mg/m³ with a precision of 2% (Michelsen et al., 2015a).

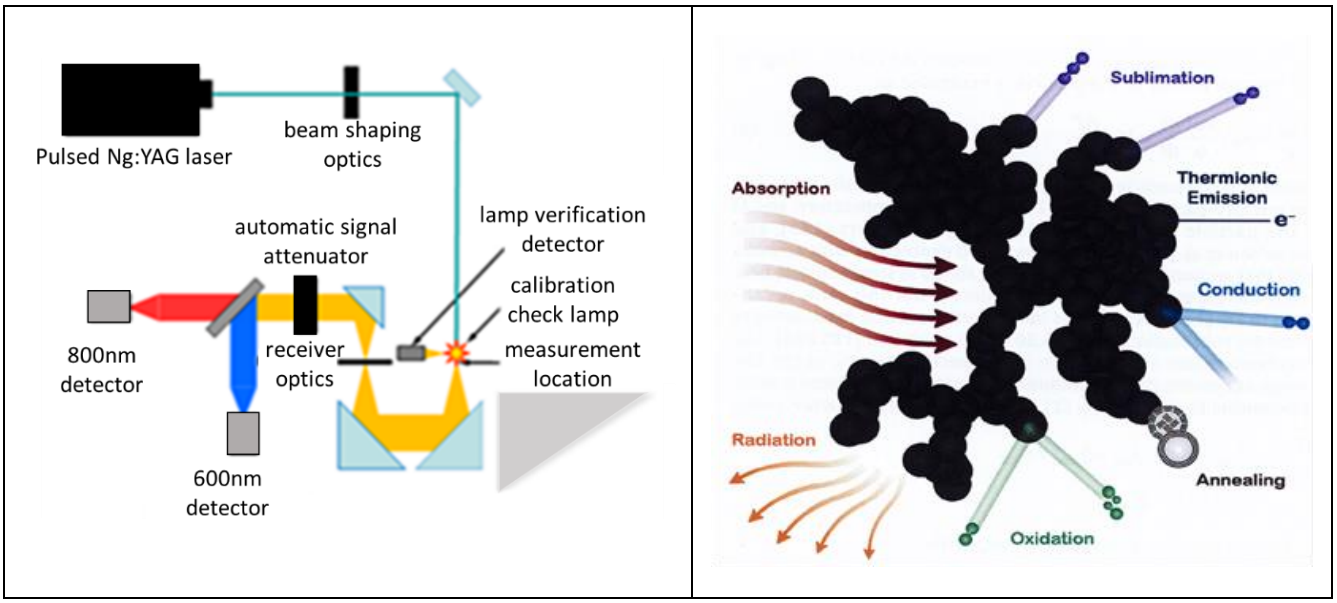

Figure II-26: Schematic figure of LII principle on the left. Illustration of the processes and exchanges influencing the temperature and mass of the particles during the LII signal acquisition (Michelsen et al., 2015a).

II.2.2.2.4 Composition of the particulate phase

Different mass spectrometer techniques (on and off-line) have been employed during this thesis to characterise aerosol chemical composition. The PTR-MS, already presented, was deployed to study the gas phase. Concerning the particulate phase analysis, different options are available.

- High Resolution Aerosol Mass Spectrometry (HR-AMS)

An HR-ToF-AMS provided by IMT Nord Europe Institute (Lille, France - Figure II-27 - left) was deployed to provide quantitative size and chemical mass loading information in real-time for non-refractory sub-micron aerosol particles. This instrument combines size-resolved particle sampling and mass spectrometry techniques into a single measurement system. HR-AMS is used to work on climate change and air quality research (Jayne et al., 2000; Jimenez, 2003). It has already been deployed on aircraft platforms (Bahreini, 2003) and is well adapted to aerosol chamber studies. This instrument gives a direct separation of most ions from inorganic and organic species. It allows an attribution of individual m/z signals to distinct chemical fragments such as C_xH_y, $C_xH_yO_z$, $C_xH_yN_p$, $C_xH_yO_zN_p$ (DeCarlo et al., 2006) and to study the elemental composition regarding the O:C/H:C ratio.

Aerosol particles between 0.04 and 1.0 µm are sampled in a high vacuum system where they are concentrated in a narrow beam (~1 mm) using an aerodynamic lens (Figure II-27 - right). The particle beam arrives at a resistively heated surface where the volatile and semi-volatile chemical components are thermally removed by vaporisation. Particle vaporisation temperature is adjustable from 200°C to 900°C giving a non-refractory fraction including the majority of atmospheric components (for 600°C). Some inorganic components such as sea-salt for example require vaporisation at higher temperature (900°C). Then they are detected by a mass spectrometer based on a standard 70 eV electron impact ionisation quadrupole system. The aerodynamic diameter of the particles is determined from measurements of the time of flight (velocity) of the particles using a beam splitting technique (DeCarlo et al., 2006).

The ToF-MS presents here two ion path modes improving the high-resolution and a large mass range (1-1200m/z). The first mode is called V-mode and is based on a single-reflectron system. The second mode is the W-mode based on a triple-reflection system. Specifically, the main reflectron is opened to accommodate multiple passes, and a small reflectron is inserted between the accelerator and the detector, which were moved further apart from one another. The W-geometry increases twice

the flight length, but reduces the duty cycle (Chernushevich et al., 2017) and provides a better field homogeneity along the ion trajectories.

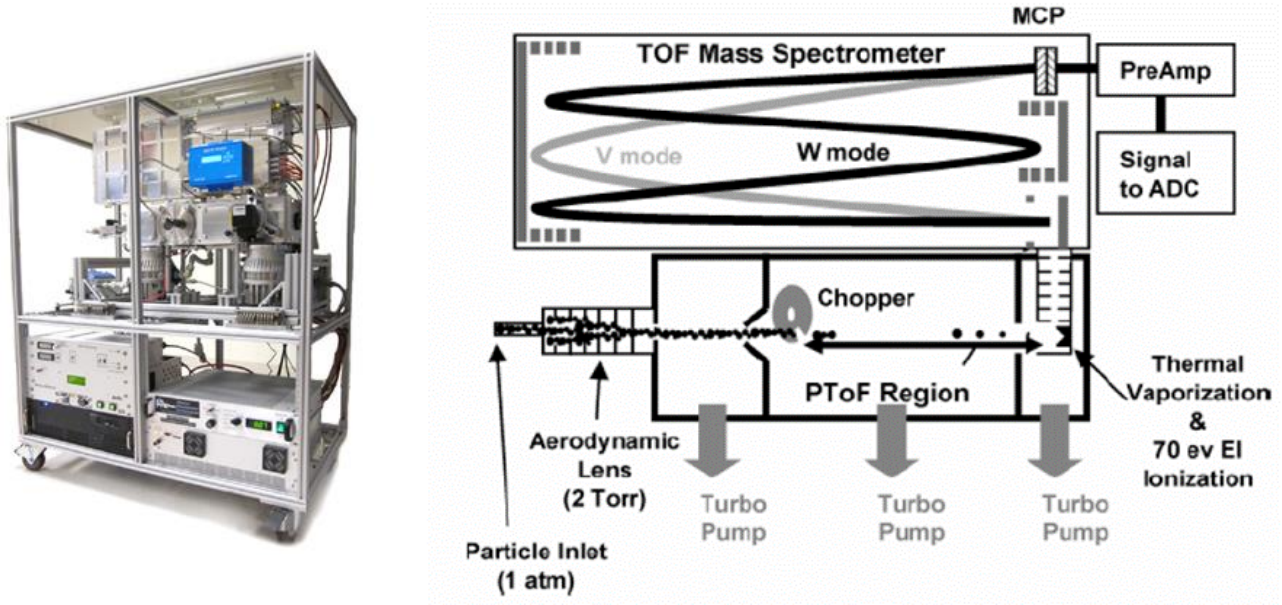

Figure II-27: On the left, Aerodyne HR-AMS instrument. On the right the schematic principle of the HR-ToF-AMS: beam of particles / Vaporisation and Ionisation area/ ToF Mass Spectrometer with two ion path modes: V-mode and W-mode increasing the pathway of the ions and in the same time the resolution (DeCarlo et al., 2006).

The measurement of the aerosol size ranges from 40 nm to 1 µm based on the aerodynamic diameter. The sample flow through the particle lens is 0.1 L/min. Detection limits (for 1 min integration) and mass resolving power depend on the ions path mode: 0.003 $\mu g.m^{-3}$ and 2500 m/Δm for the V-mode; 0.03 $\mu g.m^{-3}$ and 5000 m/Δm for the W-mode. It provides a fast response time for the particle size distribution (1-10s) and for the non-refractory chemical composition (up to 100 Hz mass spectra sampling rate).

- Aerosol Chemical Speciation Monitor (ACSM)

An Aerosol Chemical Speciation Monitor (ACSM-ToF, Aerodyne ltd.) has been also used. This instrument is originally a smaller, lower cost and simpler adaptation of the HR-AMS based on the same measurement principle (Figure II-28). This instrument allows on-line measurements of the particle mass loading and chemical composition for sub-micron aerosol particles (Budisulistiorini et al., 2013; W. Xu et al., 2016). However, it has to be noted that ACSM does not measure the refractory part of aerosols, i.e. any particles vaporised above 600°C, and that the particle sizing is not done by this instrument (unlike the AMS). The ACSM provides the concentrations of Ammonium (NH_4^+), Nitrate (NO_3^-), Sulphates, Chloride and Organic Compounds (total and the proportion of oxidised organic compounds) under ambient conditions.

As for the HR-AMS instrument, the particle sample is transformed into a beam (1 mm diameter) of particles, using a set of aerodynamics lenses, before entering in a vaporisation chamber heated at 600°C (Figure II-28). Inside this thermal area, an electron impactor ionises vaporised particulate matter. Three turbo molecular pumps provide differential pumping to separate efficiently the gas from the particle beam. After that, the ions formed are analysed with the ToF mass spectrometer providing composition information. At the same time as the ion source is operating, background mass spectra

measurements are done (blank) and subtracted from the particle mass spectra. This is done regularly during data acquisition using a 3-way valve and a particle filter (Figure II-28 – left part).

Particle size range (from 40 nm to 1 µm) and inlet flow of the sample through the lens (1 mm) remain the same as for the HR-AMS instrument. However, the accuracy of the ACSM measurements is estimated at ±30% (Ng et al., 2011). The mass range is between 10 and 200 m/z and the limit of detection is under 0.2 $\mu g.m^{-3}$ for 30 min of signal averaging.

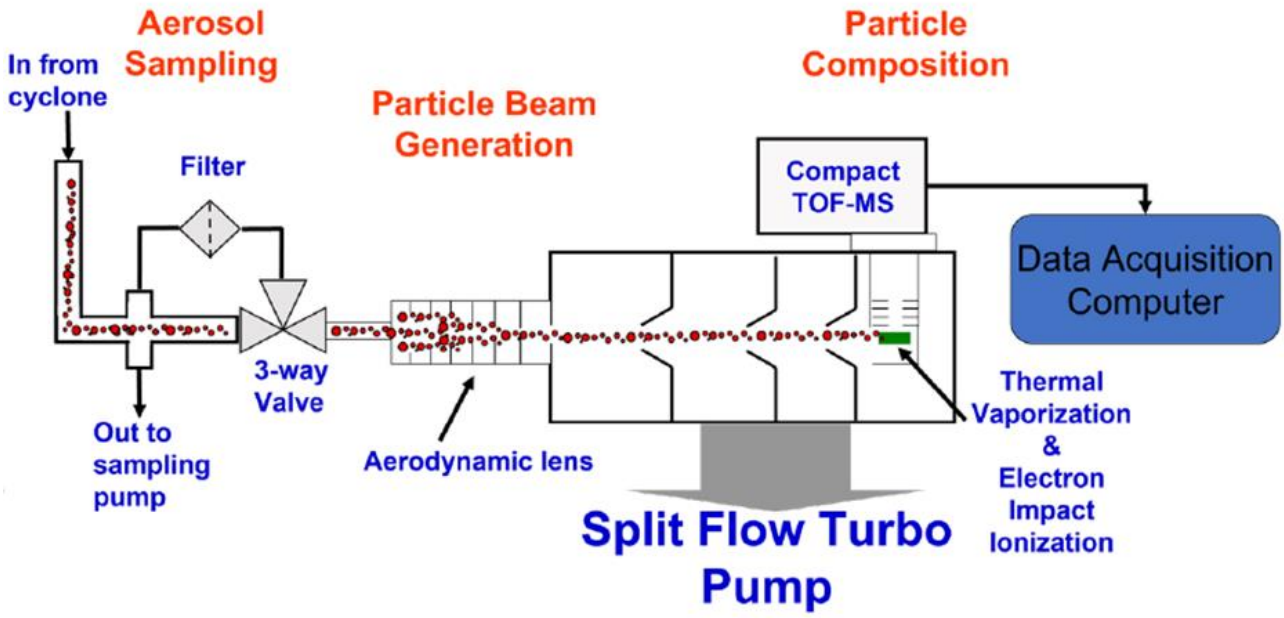

Figure II-28: Schematic principle of ACSM device composed by a vacuum chamber where a particle aerodynamic lens is coupled with a thermal particle vaporisation source and a ToF mass spectrometer (Aerodyne_ACSM).

II.2.2.2.5 Nucleation process insights

One of the main objectives of this thesis is to understand the formation of the vPM in the exhaust of a burner or an engine. To get some insight into the first steps of the nucleation process, i.e. the transition between gaseous precursors and the first smallest solid particles, a Time-of-Flight Mass Spectrometer coupled with an Atmospheric Pressure Interface (API-ToF) is used. This instrument is provided by the Tampere University to determine the chemical composition of nucleation clusters produced in the atmospheric chamber using a unique ion source hardware.

The first part of the instrument corresponds to the chemical ionisation of the sample by nitrate ions (Figure II-29). $NO_3^-(HNO_3)_{m\ (usually\ m\leq 2)}$ primary ions are generated from nitric acid using a corona discharge needle. The sample enters the ion drift tube where it is surrounded concentrically by the sheath gas. The primary nitrate ions are directed towards the centre of the sample flow to interact with the sample using an electrostatic field. These compounds can be ionised through proton-transfer reaction or via clustering with the primary ions. Then a flow of dry nitrogen is added before the entrance of the ToF to remove water molecules from the core ions. The sample passes through three pumped chambers. The first two contain segmented quadrupoles used to guide the ions (Lopez-Hilfiker et al., 2019; Pagonis et al., 2021) in the ToF-MS (scroll pump), and the third one is composed by an ion lens assembly (diaphragm pump). The ion pathway in the ToF corresponds to the V-mode already presented (cf. II.2.2.2.4 and Figure II-27).

The instrument offers the possibility to measure either positive or negative ions and is able to characterise molecular clusters to identify key compounds in atmospheric new particle formation

(Junninen et al., 2010). It can be noted that the ToF is calibrated for gaseous sulphuric acid measurement (Kürten et al., 2012), and a known mass-dependent transmission efficiency can give access to the concentration of other masses (Heinritzi et al., 2016).

The APi-TOF has a very low background noise level, which makes it possible to accumulate signals over long times. The mass accuracy is better than 0.002% and the mass resolving power is 3000 m/Δm (Junninen et al., 2010). The inlet flow is 0.8 L/min and the final pressure in the ToF is around 10^{-6} mbar. The mass range of the instrument corresponds to an estimated mobility diameter of 0.2-2.25 nm and the frequency of the pulsed signal is 12 Hz.

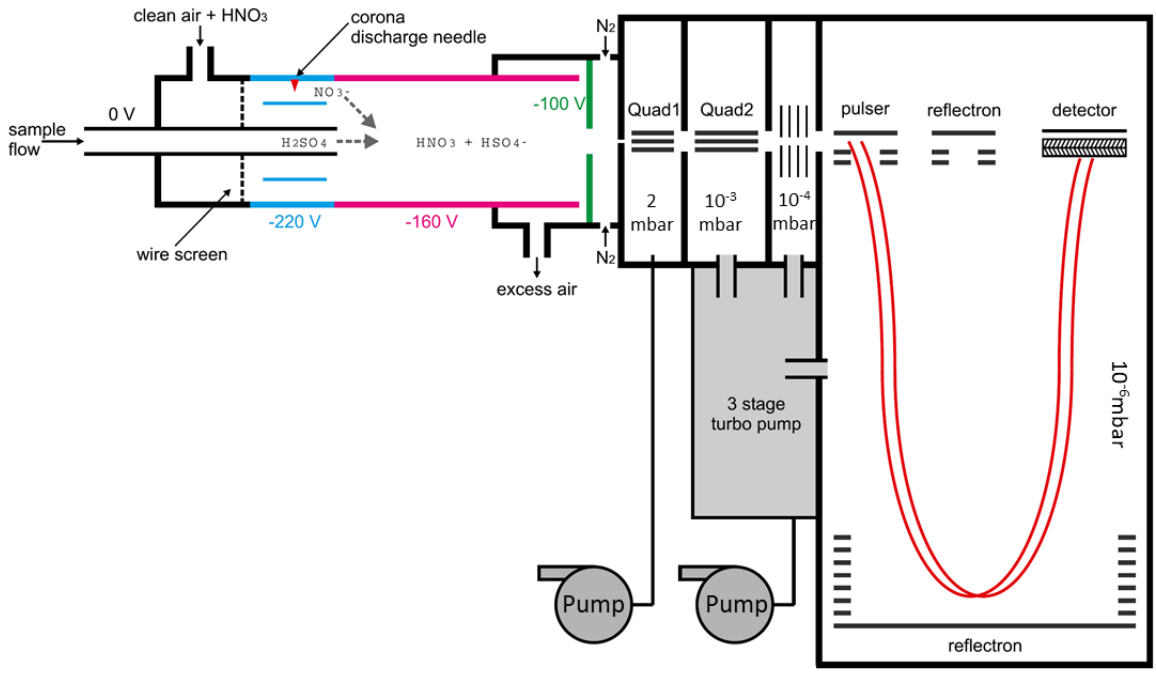

Figure II-29: API-ToF schematic principle. The first part corresponds to the chemical ionisation of the inlet sample using primary nitrate ions NO_3^-. Then the ions pass through 3 pumped chambers equipped with a scroll pump (2 mbar) and a 3-stage turbo pump (from 2 mbar in the first chamber to 10^{-6} mbar in the time-of-flight region). Ions cross two consecutive quadrupole ion guides (Quad1 and Quad2) before reaching an ionic lens stack to guide them grouped to TOF where masses are separated and recorded on a detector (Goethe University).

II.2.2.3 Off-line emissions measurement

Previous studies using on-line mass spectrometry instruments allow a good analysis of the sample. In order to complete this composition investigation, two other off-line mass spectrometry devices are employed using an upstream sampling process to trap particle and gas phases separately. These techniques can propose an alternative to the limited range of detection of the AMS and ACSM (which can handle only particles above ~40 nm) or to identify some specific volatile compounds not recorded by PTR-MS. This section describes the sampling protocol employed, the mass spectrometry instruments used and the analysis method of the mass spectra applied.

II.2.2.3.1 Sampling method

In addition to their characterisation by on-line techniques, samples were collected for off-line analyses. The method used provides samples of aeronautical interest particles by capturing the particulate and gaseous phases of the emissions separately (L. D. Ngo et al., 2020). The collected filters

are then analysed to characterise the chemical composition of their surfaces using the mass spectrometry instruments available at the PhLAM laboratory in Lille.

The sampling system consists of a double filter holder (Figure II-30) held at room temperature. This method has been developed in Lille by the PhLAM laboratory and has already been used and validated by previous studies (Berthier, 2022; Duca, 2020; L. D. Ngo, 2019). The filters contained in the holder are prepared differently (Figure II-30 - right) for the sampling of aeronautical soot (Delhaye et al., 2017). The first one is a quartz fibre filter (Pallflex Tissuquartz, 2500 QTA-UP) to capture the particulate phase, i.e. the soot particles and the compounds present on their surface. The second one is also a quartz fibre filter but with a layer of black carbon applied on the surface to recover the gas phase by adsorption (Faccinetto, 2009; Faccinetto et al., 2015). These fibre filters retain 99.9% of the particles on their surface (Pallflex technical document).

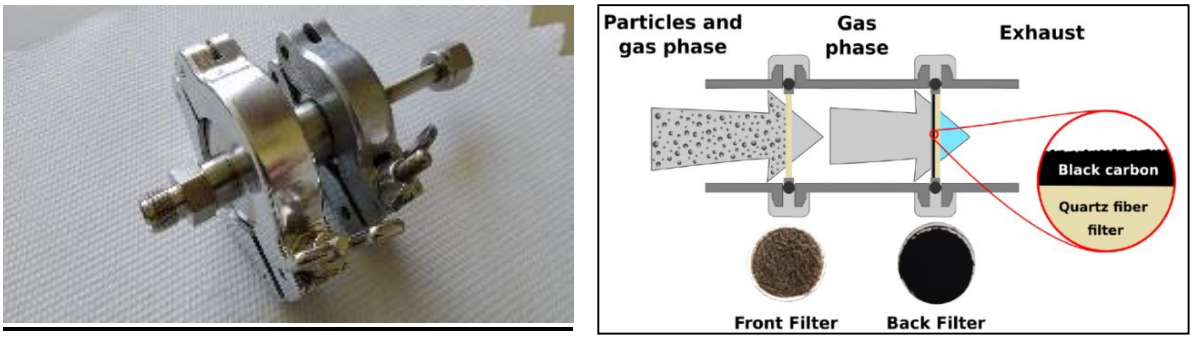

Figure II-30: System of sampling developed in Lille (L. D. Ngo et al., 2020). On the left the experimental sample holder and on the right the schematic principle of the sampling: the particle phase of the emissions is blocked (99.9% efficiency) by a first quartz fibre filter (Front Filter) and the gas phase is collected on a second quartz fibre filter covered by a thin layer of black carbon (Back Filter).

Filters are conditioned before their use by heating at 200°C for 24 hours in an oven to evaporate any adsorbed species that may be present on the surface such as organic compounds (Duca, 2020). Before taking them out, the temperature of the oven is lowered to 60°C to do the transition with the ambient temperature of the laboratory. They are placed in individual boxes and then in a cooler to transport them to the experimental test. During sampling, a pump provides a continuous flow of 2.2 L/min through the filters. The flow rate should allow sufficient particle deposition without damaging the filter surface. The sampling time depends on the mass concentration of the measured particles and must be adapted to get a sufficient deposit on the surface: it can be from a few seconds at the CAST outlet (in the order of 10 mg/m^3), or a few minutes after a CS (less than 1 mg/m^3) to several hours after CESAM chamber. After the sampling, filters are placed in a refrigerator (4°C) to avoid reactions with the external environment and to limit the evaporation of the volatile compounds. The characterisation of the filters obtained is done subsequently using different spectrometry techniques detailed in the following section.

II.2.2.3.2 Mass Spectrometry

During this thesis, two techniques have been used:

- A surface sensitive analytical method called Time-of-Flight Secondary Ion Mass Spectrometry (ToF-SIMS) which uses an ion beam to bombard the surface of the sample, desorb and ionise the compounds in the first layers of the sample surface. One of the drawbacks of this technique is the high fragmentation produced by the energetic (25 keV) primary ion beam.
- High-Resolution Two-Step Laser Mass Spectrometry (HR-L2MS). This technique uses two lasers to desorb and ionise molecular compounds from the sample. The main advantage of

this technique is the low fragmentation achieved in carefully chosen experimental conditions.

Both SIMS and L2MS methods are described in detail in (Duca, 2020). The desorption / ionisation stages are specific to each approach, thus the sensitivity of each instrument to different chemical compounds is different. The combination of both techniques allows a detailed and complete analysis on different species such as PAHs or oxygen- and sulphur-containing compounds. Filters collected during experimental campaigns are large enough to be cut in half to allow the analysis by both techniques.

- Secondary Ion Mass Spectroscopy

A Time of Flight Secondary Ion Mass Spectrometer (ToF-SIMS, Regional Surface Analysis Platform, Chevreul Institute, University of Lille) has been used to study chemical composition of emission samples. This instrument is commonly used in numerous fields such as biosciences, geology or material sciences (Duca, 2020; Greenwalt et al., 2013; Lindgren et al., 2012; Thiel & Sjövall, 2011). It presents a high sensitivity attainable by individual ion detection and a high mass resolution ($\sim 10^4 m/\Delta m$) in particular for low sample surface roughness (Irimiea et al., 2018). The SIMS instrument (Ion-TOF GmbH) is composed (Figure II-31 - left) by an analysis chamber, where the sample is transported, an ion gun, used for the desorption/ionisation step, and a ToF analyser to separate/record the secondary ions. The sample can be placed on a liquid nitrogen cooled sample holder to reduce evaporation of compounds at the surface of the filters.

This machine can be operated in static (surface molecular analysis) or dynamic (depth concentration profile from few nm to few µm) modes. In this thesis, the static mode with a small penetration depth (~1nm) is chosen to allow a sample surface study without chemical information loss of the parent molecules (Vickerman & Briggs, 2013). The first mono-layers analysis is used to obtain fragmented mass spectra of selected Regions Of Interest (ROI) for each sample on a 500 x 500μm^2 surface with 128 x 128 pixels image resolution. These spectra present more signal for compounds with low m/z due to fragmentation.

To analyse a ROI, molecules and atoms are ejected from the sample surface using primary ions bombardment in an ultrahigh vacuum environment at 10^{-9} mbar (Figure II-31). To provide high ionisation efficiency for organic compounds and a lower fragmentation probability of the parent molecule, bismuth ions Bi_3^+ are used as incident particles instead of Cs^+ or O_2^+. The energy of these ions is 25 keV with a current intensity of 0.3pA. Bismuth ions form a focused ion beam of 50 nm on the sample. With desorption, a small part (>10%) of the atoms at the surface are ionised by energy transfer due to collisions (blue ions on Figure II-31 - bottom right). Secondary ions formed are analysed in a ToF-MS (V-mode with an average resolution of 4000-6000 m/Δm). To provide complementary data about the surface analysis, positive or negative ions can be studied independently by changing the polarity of the acceleration plates and of the reflection.

To obtain an m/z mass spectrum (Figure II-32), a calibration that links time of flight of known secondary ions with their mass to charge ratio is needed. To obtain a proper calibration, more than four ions must be used (Irimiea et al., 2018). Having the same initial energy, secondary ions with the same m/z are recorded together to get a Gaussian distribution. The separation and the identification of these accurate masses are related to the mass resolution of the spectrum described by m/Δm with m the mass and Δm the peak width at half maximum.

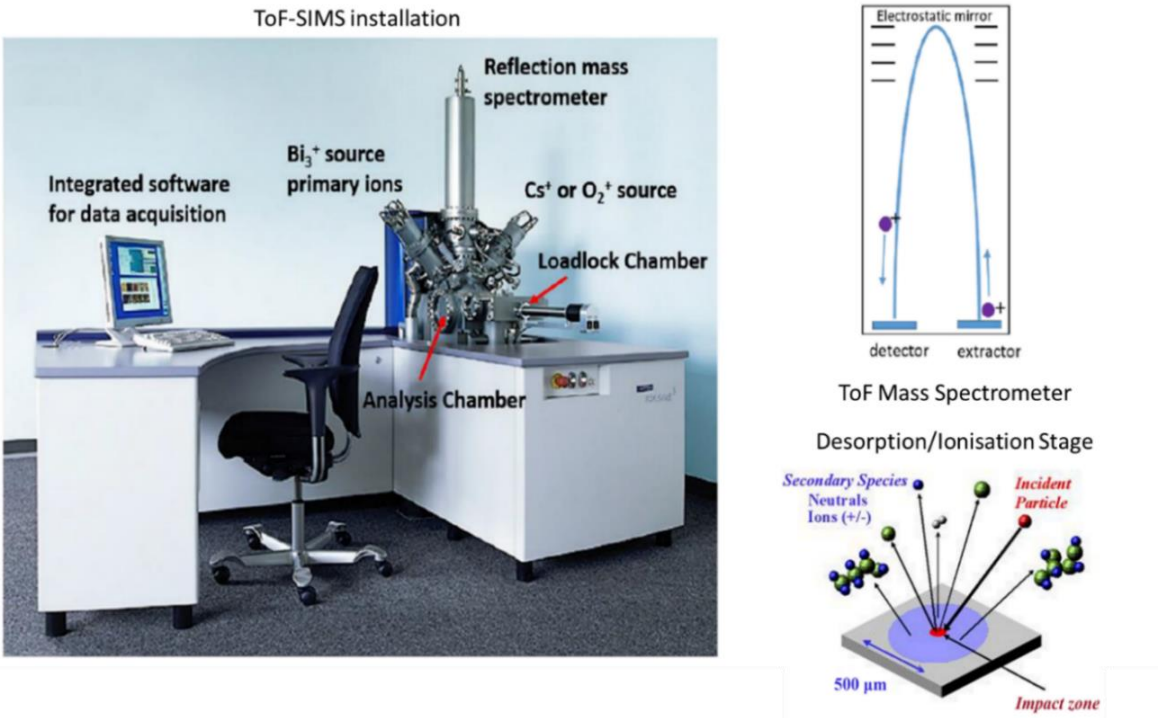

Figure II-31: ToF-SIMS example of installation (Ion-TOF GmbH) on the left: Bi_3^+ gun for the static mode and Cs^+/O_2^+ gun for in-depth distribution analysis. On the top right, a schematic view of the ion path in the ToF Mass Spectrometer: Secondary ions are accelerated in the extraction field using ion optics path before entering in the ToF analyser where an electrostatic mirror repulses them to a detector. On the bottom right, a schematic principle of the desorption step by primary Bi_3^+ ions on the surface of the sample generating neutral molecules and secondary ions (adapted from Wu 2019).

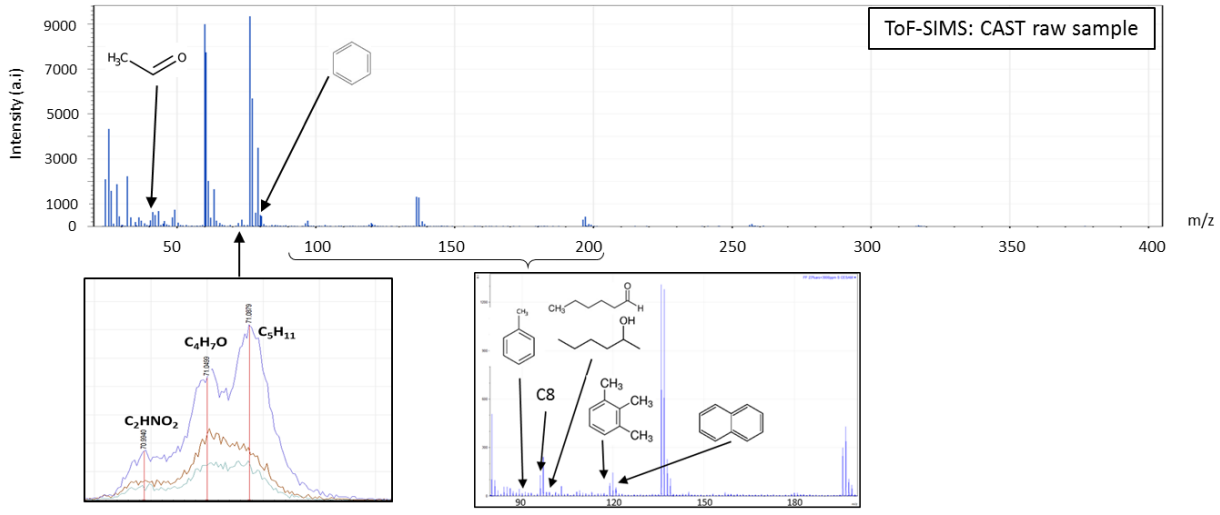

Figure II-32: Example of ToF-SIMS mass spectrum obtained after the analysis of a CAST raw sample (standard Jet –A1 fuel): for each sample, the display spectra are an average of 3 recordings.

- High-Resolution Two-Step Laser Mass Spectrometry

To complement the SIMS measurements and minimise fragmentation, another comprehensive methodology for combustion aerosol analysis called High-Resolution Two-Step Laser Mass Spectrometry (HR-L2MS) has been used. This technique has been developed at PhLAM Laboratory in Lille for almost two decades to characterise emissions samples from different sources for research or

industrial applications (Duca et al., 2019; Faccinetto et al., 2015; Focsa et al., 2006; Mihesan et al., 2007; L. D. Ngo et al., 2020). This instrument is based on a soft laser desorption method and provides a high mass resolution (~1.5x10^4 m/Δm). This machine is a new custom-built instrument (Fasmatech S&T) adapted for the L2MS technique (Duca, 2020). This HR-L2MS device is composed of a desorption laser, an ionisation laser, a new multipolar Radio-Frequency trap coupled to a Time-of-Flight Mass Spectrum (RF/TOF-MS) analyser. The desorption/ ionisation technique used here is different from the one of the SIMS using incident ions: lasers provide a soft desorption of the surface and limit fragmentation during the ionisation process (Faccinetto et al., 2015). In this way, higher m/z signals related to heavier compounds can be recorded compared to SIMS (Figure II-33).

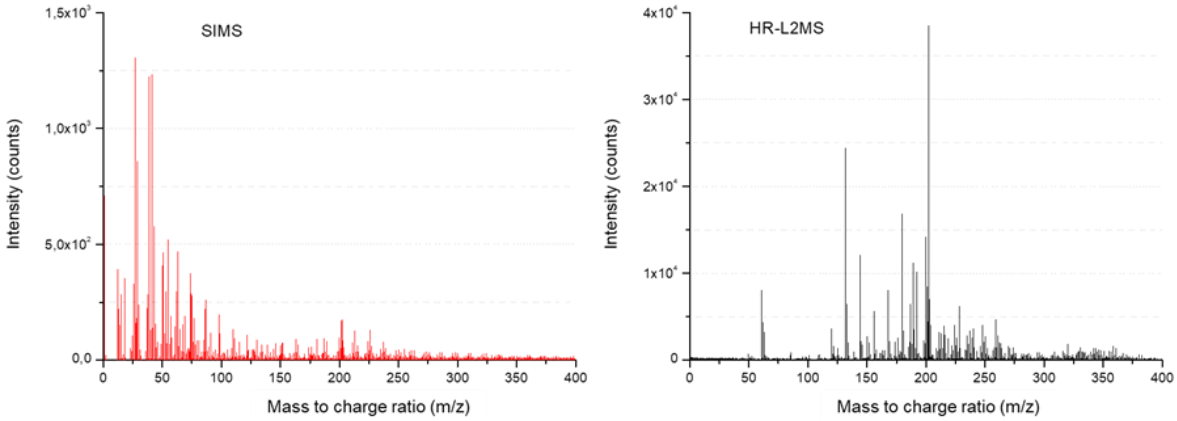

Figure II-33: Comparison between SIMS and HR-L2MS methods for CAST raw sample using Jet A-1 fuel. On the left, SIMS provides a spectrum with a majority of compounds with low m/z (below 100) due to fragmentation; on the right HR-L2MS provides a spectrum with higher m/z compounds.

Inside the analysis chamber (at 10^{-6} mbar), the surface of the sample is desorbed (stage 1 in green on Figure II-34 - Faccinetto 2009) using a nanosecond pulse laser (λ=532 nm - Quantel Brilliant). The fluence (energy delivered per unit area in mJ.cm^{-2}) is controlled to desorb the compounds from the filter surface (laser beam spot ~200 µm) without ablation and to limit the ionisation of the desorbed particles, reducing in this way potential fragmentation of desorbed compounds (Faccinetto et al., 2015). In this study, a low fluence (~10 mJ.cm^{-2}) has been used for the desorption laser. The temperature increases locally with the absorption of the energy provided by a pulse laser and it allows the transfer of the atoms and molecules to the gas phase, affecting only the first monolayers of the sample. In this way, a cloud of neutral molecules (called “plume”) is formed above the sample.

Then, photo-ionisation of desorbed species (stage 2 in purple on Figure II-34) is achieved with a second nanosecond pulse laser (λ=266 nm - Quantel Brilliant). The ionisation laser provides a rectangular laser beam spot ($S_{ionisation}$=5 mm x 10 mm) hitting the plume at 90° of its propagation path in the analysis chamber. The wavelength of the ionisation laser needs to be selected depending on the compounds we want to detect (Bouvier, 2006; Desgroux et al., 2013; Faccinetto et al., 2015; L. D. Ngo et al., 2020). This value is set at 266 nm, with special focus on the analysis of PAH species (Desgroux et al., 2013).

The use of only one laser is also possible, in this case the method is called Laser Desorption Ionisation (LDI), i.e. some ejected species are ionised directly at the desorption step. Both the LDI and L2MS methods were used in this study. For a same desorption fluence, the LDI method presents less ionisation than the L2MS one (as expected). If the desorption fluence is increased in LDI to increase the ion yield, the fragmentation is increased at the same time. Depending on the ion polarity, the use of lasers is adapted: to analyse positive ions, L2MS mode is privileged to target the detection of PAHs; to work on negative ions only the desorption laser (LDI with same desorption fluence) is activated in order to provide the detection of sulphur compounds (Annex A).

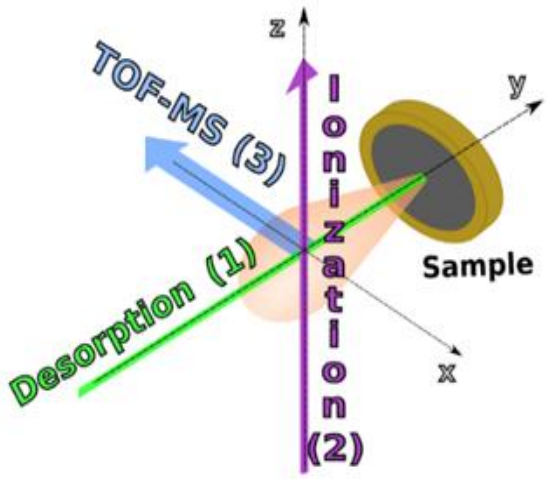

Figure II-34: L2MS technique principle. A desorption laser (1 – using the 2nd harmonic of a nanosecond pulse Nd:YAG laser) hits directly the surface of the sample and a second laser (2 - using the 4th harmonic of a second nanosecond pulse Nd:YAG laser) ionises the cloud of particles formed. Generated ions follow the ion path (3) to the ToF analyser (Duca, 2020).

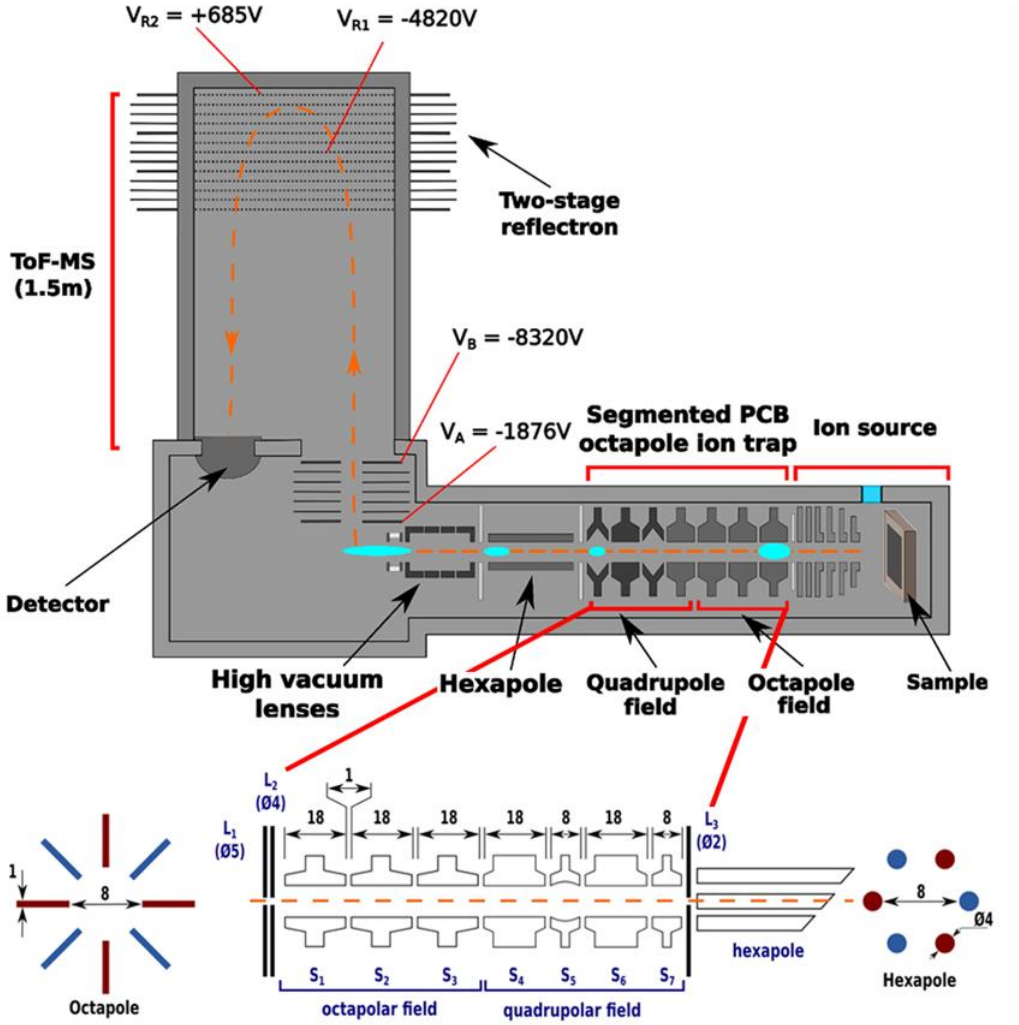

Figure II-35: Schematic representation of the ion path (orange) inside the HR-L2MS instrument with the conditioning of the charged species (blue) through the ion trap (adapted from Duca 2020). A zoom below presents the injection lenses (L_1 and L_2), the segmented Radio-Frequency trap (S_{1-7}), and the transfer lens (L_3) to the hexapole ions guide.

To get a higher resolution, ionised species are extracted from the ionisation area and sent by a set of electrodes to a hybrid multipolar Radio-Frequency trap (Figure II-35), positioned upstream of the ToF analyser tube. This segmented part of the instrument consists of an octapolar field used to capture ions groups at the entrance of the trap, coupled to a quadrupolar field to compress radially these ions packs and to obtain a homogeneous ion cloud. The trapped ions are cooled down by collisions with He atoms injected through a fast solenoid valve and synchronised with the laser pulse. The ions are then sent to the ToF analyser through a hexapole ions guide. This configuration maximises the ion transmissions efficiency for a large m/z range.

II.2.2.3.3 Alignment and calibration of mass spectra

Mass spectrometry techniques have a high interest in many fields and commercial versions are developed. However, there are still different issues and challenges regarding the quantitative management of the measurements. It can be related to the sample analyses and the treatment /interpretation of data. Indeed, the analysis of each spectra from various experiments provides a large amount of data to be processed. After the acquisition of mass spectra, a specific methodology developed in PhLAM and PC2A (Physico-Chimie des Processus de Combustion et de l'Atmosphère) laboratories in Lille is applied to provide a precise identification of the species detected and compare spectra (Duca et al., 2019; Irimiea et al., 2019; L. D. Ngo et al., 2020). The first step is the alignment and the calibration of mass spectra to obtain the signal as a function of the mass over charge ratio (m/z) before working on the molecule assignment a second time. To proceed, it is necessary to separate the particle phase filters (FF), the gas phase filters (BF) and the blanks analysis. Furthermore, for these three categories of filters, negative and positive ions are separated.

- **Alignment**

Electronic jitter in the potentials applied can affect ToF raw data (<1 ns) and generate a misalignment of the spectra (Figure II-36 - right). The objective is to realign these spectra before the calibration. A spectrum of reference is selected and the other spectra are aligned on it using a linear equation:

$$ToF_{old} = a \times ToF_{reference} + \mathrm{b} \qquad (\mathrm{eq.}\,10 - \text{Figure II-36} - \text{left})$$

$$\rightarrow \frac{ToF_{old} - b}{a} = ToF_{new\ aligned} \qquad (\mathrm{eq.}\,11 - \text{Figure II-36} - \text{right})$$

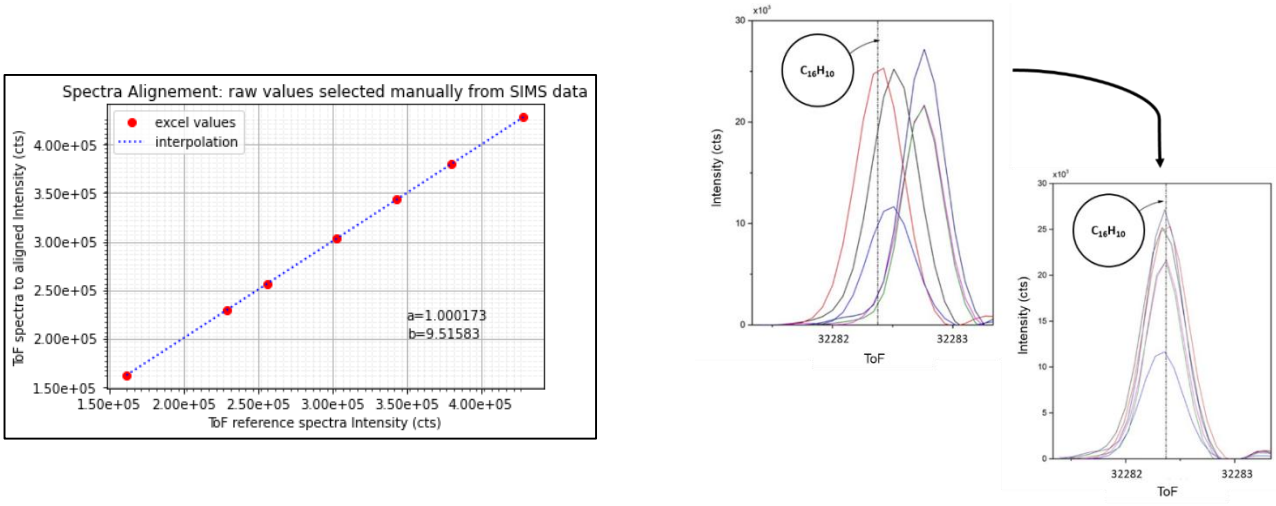

Figure II-36: Alignment process. On the left an example of ToF relation between reference spectrum and spectra to align for a SIMS case. On the right a zoom on pyrene signal before and after the alignment for a HR-L2MS analysis (Berthier, 2022).

- **Calibration**

After the alignment, all spectra are superposed properly at the same ToF scale and calibration step is done using a Python script developed in Lille (PowerShell - Duca et al., 2019). The transition from the ToF scale to the m/z scale is done with a 2nd degree polynomial equation (Duca et al., 2019; L. D. Ngo et al., 2020):

$$m/z = At^2 + Bt + C \qquad \text{(eq. II.12)}$$

(with m/z the mass to charge ratio, t the Time of Flight, A,B and C are fitted parameters)

To solve this equation, a manual signal selection (fit with a Gaussian on PowerShell) is done. A minimum of 6-10 accurate masses all over the range of the spectra is needed to obtain a reasonable calibration. The computer script gives the exact m/z for each molecule selected with the corresponding error (ppm) and the calibration equation. The obtained calibration is validated for an error of less than 10 ppm to be accepted (Thlaijeh, 2021). Once a correct calibration is obtained, the equation can be applied directly to earlier aligned spectra. It is possible using the python script to calibrate each spectrum individually but the cost-efficiency depends on the list of samples to analyse.

- **Assignment of signal detected**

Once all spectra are calibrated, the identification of the species and the comparison between samples are possible. The purpose is to assign a chemical formula to each accurate mass. To facilitate this stage and define a working peak list for the following interpretation, some tools are used, such as mass defect plots. The mass defect (Δm) of a single chemical element or compound is calculated as the difference between the exact mass of the isotope and its nominal integer mass. This nominal mass is the sum of the number of protons and neutrons in a given elemental formula or isotope.

Mass defect plot gives a visual separation and facilitates the assignment of molecular formulas to each accurate mass (Figure II-37). The mass defect plot simplifies the detection of certain species such as hydrocarbons C_nH_m (in green), oxygenated compounds C_nH_mO (in blue) or nitrogenised compounds $C_nH_mNO_p$. For example, two hydrocarbons with the same number of hydrogens but with a variation in the number of carbon atoms have the same mass defect. Otherwise, species with the same amount of carbons but a different hydrogen number have a positive mass defect (in red).

It is also possible to detect atoms such as oxygen or sulphur. Their mass defect is negative and chemical species containing such atoms have lower mass defect values compared to hydrocarbons with the same nominal masses. The efficiency of the assignment of chemical formulas for each accurate mass detected is based on a sufficient mass resolution to separate chemical species with the same nominal mass (Duca, 2020).

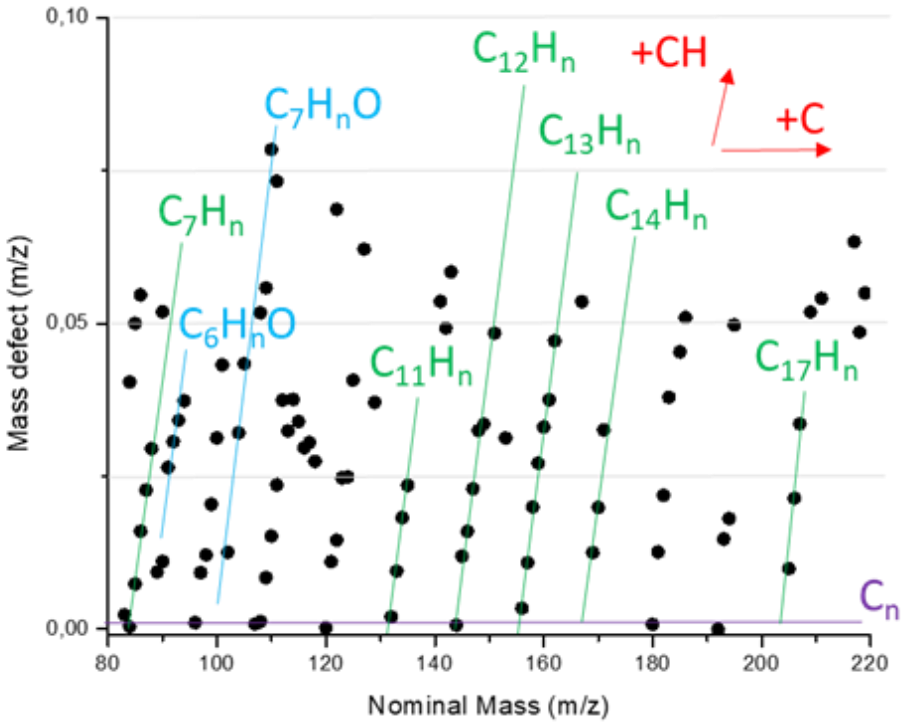

Figure II-37: Example of mass defect plot obtained from the SIMS analysis of soot produced by a miniCAST burner. It corresponds to the analysis of the particulate phase filter. Family species can be regrouped depending on the number of hydrogen or carbon atoms.

II.3 Summary of the materials and methods employed

This chapter was dedicated to the description of the experimental set-up. The experimental measurement line used to quantify the particles (nvPM + vPM) and study their composition is deployed during the UNREAL experimental campaigns (Figure II-38). It is adapted to characterise emissions from the CAST burner, using different liquid fuels, before and after injection in the CESAM chamber. In addition, the instrumentation to be used in this project will go far beyond those used in the standard engine certification characterisation. Indeed, there are very few studies dealing with the properties of vPM and measuring their formation in engine tests is challenging. This is where the use of the CESAM chamber becomes crucial. State-of-the-art characterisation techniques included in the project (HR-ToF-AMS, API-ToF, PTR-ToF-MS, ACSM-ToF, ToF-SIMS and L2MS) provide a unique insight into the chemical composition of particles (both nvPM and vPM) emitted by different aeronautical fuels.

Now, the following chapters will present in detail experimental results. The next one is dedicated to the analysis of CAST parameters (fuel flow, propane/air ratio) and the impact of fuel composition on the set point selection. Then CESAM chamber experiments and results are presented to study the formation of vPM from aeronautical soot particle surrogates at ground level.

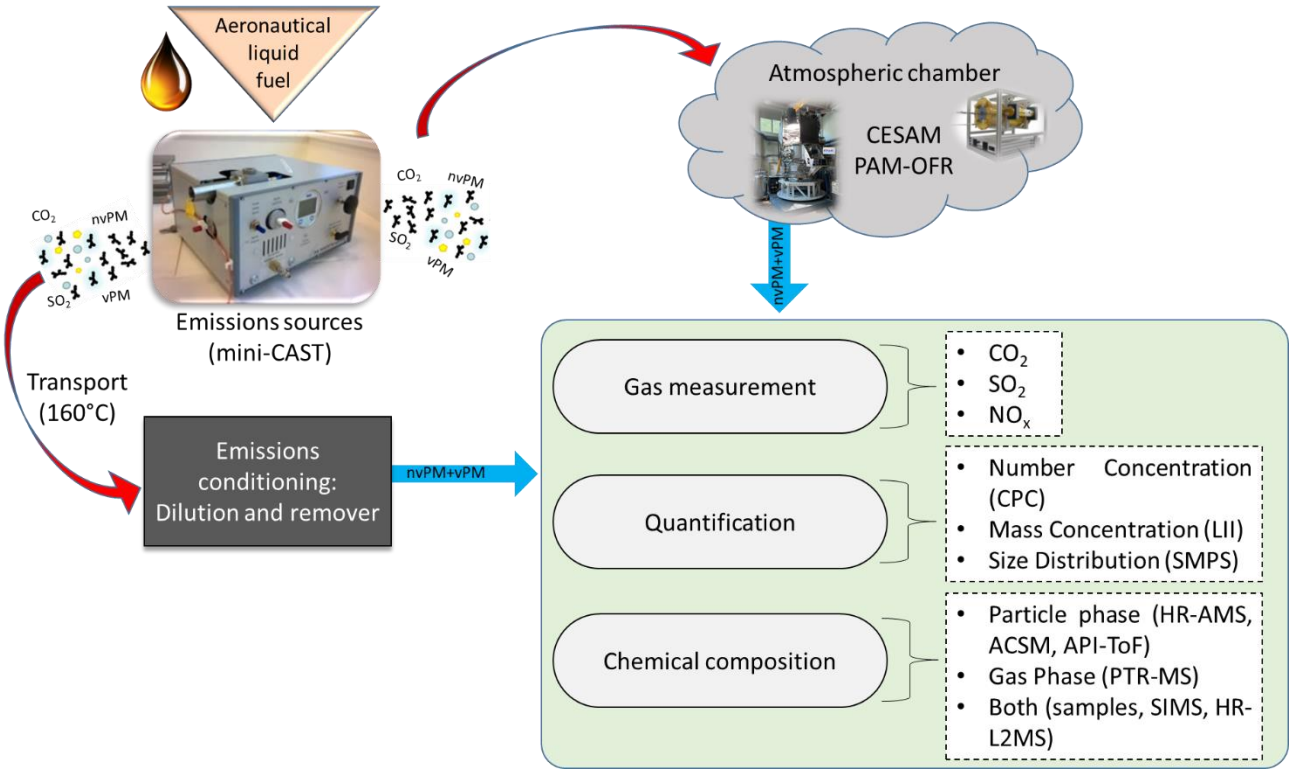

Figure II-38: Summary of the measurement line and facilities used for nvPM and vPM characterisation.

Chapter III. Characterisation of liquid CAST burner emissions with respect to aeronautical fuel composition

The liquid version of the CAST burner (description in II.1.1.1) has been selected to test different aviation fuels and to generate aeronautical soot particle surrogates under atmospheric conditions. This combustion aerosol standard generator has been already used in previous studies on aeronautical emissions (Berthier, 2022; Ortega et al., 2016). It allows a low fuel consumption (on the order of several hundred mL/min) and it is representative in terms of emissions index and particle size compared to emissions from a real engine for a conventional fuel (Jing, 2003; Moore, Shook, et al., 2017). In this chapter, emissions from the combustion of various aeronautical liquid fuels (cf. II.1.1.2) ranging from a standard fuel currently employed in aviation to the use of alternative or modified fuels, have been studied at burner outlet. The objective is to define the operating limits of the CAST soot generator and to evaluate the parameters affecting the selection of a working point according to the matrix fuel.

CAST parameters, such as fuel flow, air oxidation flow, nitrogen flow, propane flow, and dilution flow have been already presented in II.1.1.1. The quenching flow (nitrogen) and the dilution flow are respectively set at 7 L/min and at 20 L/min and remain constant during all experiments. The influencing CAST parameters are thus the fuel, propane and air flows. They have an impact on the mass concentration, number concentration and size distribution of soot particles, as well as the structure of soot aggregates measured at the burner outlet (Richter & Howard, 2000; Xiang et al., 2019). The stability of kerosene flame and therefore the experimental reproducibility depend also on this flow control. For example, the air flow is shared between the kerosene flame at the top and the propane flame at the bottom of the CAST combustion chamber. Depending on the set parameters, propane flame can affect the amount of available oxygen for the main flame and modify the characteristics of the emissions. By controlling these variabilities, it is then possible to generate a wide range of non-volatile particulate matter emissions. Using different aeronautical fuels, it is necessary to determine an operating process common to each fuel to compare and characterise resulting emissions.

This chapter presents in a first part the specifications and the operating limits of the CAST soot generator. Then the selection of a set point allowing to work with different fuels is discussed and a comparison is done with previous studies. A particular attention is given to the stability of the burner and the reproducibility of the emissions over the time. The mass concentration, number concentration, and size distribution of soot particles were also measured as a function of the different input flow rates. After that, nvPM emissions are compared for different fuels by quantification and chemical analysis at CAST outlet to observe the impact of fuel composition on resulting emissions. It also defines the on-line emission analysis methodology that will be used later on the atmospheric chamber measurement campaigns.

III.1 Specificities of the liquid CAST burner

III.1.1 Limits of the burner

The different ranges of flow available limit the use of the burner in terms of flow capacity and flame stability. (Berthier, 2022) already presented details about CAST parameters and determined operating points to work with conventional and synthetic fuels. However, we observed that the head injector of the CAST has been blocked over the time and that the resulting emissions present differences compared to precedent studies (Berthier, 2022). Cleaning the CAST burner also had an impact on emissions. To determine a working point adapted to these changes, a quick overview about some limiting parameters is done here.

III.1.1.1 Flame stability

On Figure III-1, an example of flame obtained with the CAST burner using the reference Jet A-1 fuel is presented. These observations have been done with a fuel flow set at 105 µL/min. The first case (a) corresponds to the observation of the flame when the CAST is closed. The flame is visible at the top of the chamber through the glass window over the burner. In the two other pictures of Figure III-1, the cover of the CAST combustion chamber is removed. In the case (b) a stable flame is visible at the top of the CAST chamber. In the case (c) the principal flame is no longer there but a second flame is formed at the level of the propane flame. It is linked to the combination of high flow of kerosene, a low air flow and the partial block of the injector. It leads to a leak of fuel at the top of the igniter, flowing on the propane flame and starting the ignition of a second kerosene flame at the bottom of the CAST combustion chamber.

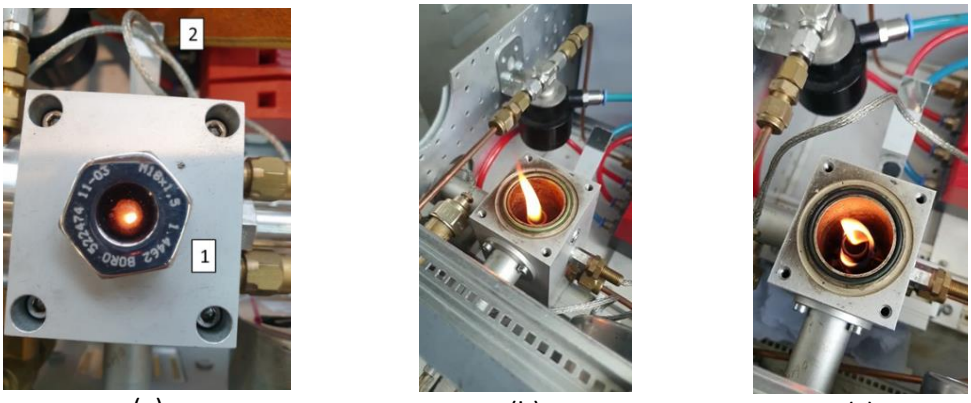

(a) (b) (c)

Figure III-1: CAST flame using reference Jet A-1 fuel. In the case (a), the CAST combustion chamber is closed and the flame is observed through a glass window (number 1) at the top of the burner. Another glass window on the side of the burner associated with a mirror (number 2) gives visual access to the propane flame. In the two other pictures, the CAST combustion chamber is opened. The case (b) presents a stable flame and the case (c) presents the formation of a second flame at the propane flame level due to a leak of fuel (kerosene flame off to emphasise the second flame appearance).

As mentioned in the previous chapter, ordinarily the propane flame will not interfere with the kerosene flame and will not affect the emissions. However, in the case of the formation of a second flame ignited by the propane flame, emissions are impacted. Different parameters can be the source of the formation of this second flame such as an excess of fuel or an insufficient air flow. The presence of two flames is measurable with a SMPS+C. Emissions from CAST burner are diluted (DI-1000) and conditioned using a Catalytic Stripper and a DEED before being recorded by the SMPS.

The Figure III-2 represents the size distribution of particles for a laboratory test done with the reference Jet A-1 fuel on CAST burner. Different air flow values have been tested to observe their impact on the formation of a second kerosene flame. The first distribution (in green – air flow set at 1.7 L/min) is a monomodal centred at 132 nm corresponding to one kerosene flame at the top of the burner. The flow of air is enough to allow a total combustion of the fuel vapours. In both other cases (orange and red – air flow respectively set at 1.6 L/min and 1.54 L/min), the air flow has been decreased and has become insufficient for the combustion of fuel vapours. In these cases, the second resulting flame is characterised by a bi-modal size distribution with the appearance of a second mode at smaller sizes (around 20-25 nm). Data presented in Table III-1 show that the Geometric Mean Diameter (GMD) of soot particles formed at the principal mode decreases and the second mode increases with the air flow reduction: from 132 nm for 1.7 L/min (monomodal) to 122 nm for 1.54 L/min (bimodal). On the other hand, the total particle number increases with the reduction of air flow from 8.9±0.3 x10^4 to 10.2±0.4 x10^4 particles/cm^3 concerning the principal mode. The decrease of the air flow leads to the formation of a second flame that involves a decrease of the GMD and an increase of the total number concentration of particles. In this way, the measurements of CAST emissions can be biased.

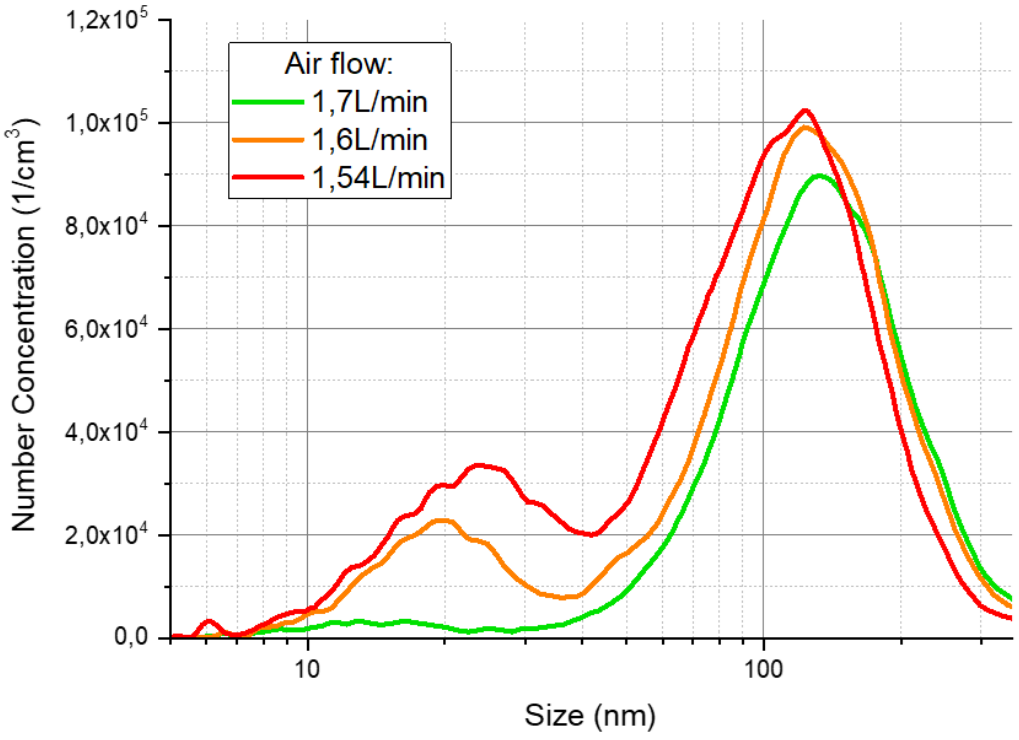

Figure III-2: Example of size distribution with the reference Jet A-1. The mono-modal represents a stable flame of kerosene (Figure III-1-b) and the bimodal flame corresponds to the presence of a second flame at the bottom of the burner (Figure III-1-c). The operating flow values have been set at 105 µL/min for the fuel and 20mL/min for the propane.

Air flow (L/min)	Principal mode		Second mode	
	GMD (nm)	Number Concentration ($1/cm^3$)	GMD (nm)	Number Concentration ($1/cm^3$)
1.7	132	8.9 ± 0.3 x10^4	-	-
1.6	125	9.9 ± 0.3 x10^4	19.86	2.3 ± 0.4 x10^4
1.54	122	10.2 ± 0.4 x10^4	24.37	3.3 ± 0.3 x10^4

Table III-1: Size and number concentration of particles depending on the air flow for a test on CAST burner using the Jet A-1 fuel of reference. The operating flow values have been set at 105 µL/min for the fuel and 20mL/min for the propane.

III.1.1.2 Operating range limits of the CAST burner

To determine a working point for the UNREAL experimental tests, it is necessary to avoid the formation of a second flame of kerosene. This phenomenon has been already observed in (Berthier, 2022) and a representation of the operating range of the CAST has been established as a function of CAST flows parameters to evaluate the different setting possibilities.

Figure III-3 presents the evolution of the CAST flame depending on the propane flow (x-axis) and the air flow (y-axis) for a given fuel flow (105 µL/min). The first representation (case a) is adapted from (Berthier 2022). Depending on propane and air flows, the flame is stable (green area), a second flame can be formed (orange area) or the flame is blown out (white area). For example, when the air flow is too low, it is not sufficient to keep burning the propane flame and the kerosene flame at the same time resulting in the extinction of the flame or the formation of a second flame. However, if the air flow increases for a constant propane flow, the flame becomes more stable and the formation of a second flame is avoided. For example, at 20 mL/min for the propane flow, the air flow value needs to be over 1.4 L/min to avoid the extinction of the flame and over 1.75 L/min to avoid the potential formation of a double flame. It should be noted that these observations do not define a straight limit between the moment where a stable flame is obtained and where a second flame is formed.

When the propane and air flows are set to the maximum (i.e. 50 mL/min and 5 L/min, respectively), the flame will be more stable and the CAST will generate mostly soot particles. If the fuel flow is reduced, the limits of extinction are extended and it is possible to work with lower air and propane flows avoiding a leak of fuel inside the burner combustion chamber. To reduce the air flow, it is necessary beforehand to reduce the propane flame in consequence to avoid an insufficient air flow for the supply of both propane and kerosene flames.

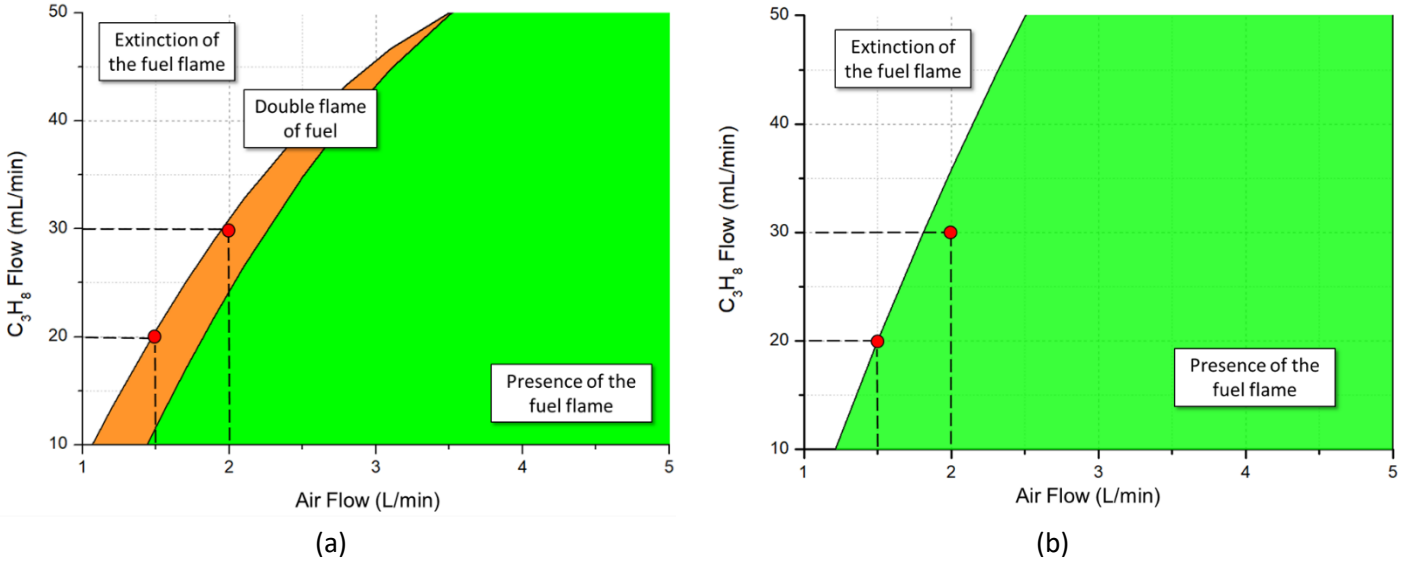

Figure III-3: Operating range of the liquid CAST burner for a fuel flow set at 105µL/min. The first case (a) corresponds to a first test done at the beginning of the thesis (adapted from Berthier, 2022). The second case (b) has been realised at the end of the thesis after CAST burner cleaning. In both tests, the green area corresponds to the stable flame, the orange one indicates the presence of a potential second flame of kerosene on the propane flame, and the white one shows the extinction limits of the CAST. Tests have been done with the reference Jet A-1 fuel at ONERA laboratory.

This first characterisation of the CAST operating range limits was performed at the beginning of the study (2020). During this work, several experimental campaigns have been done using the CAST burner. Some operating points have been repeated to compare tests between them. However, the results obtained present some variations from an experiment to another (cf. details in III.1.2.2). In fact, over the time, the CAST has become more and more clogged and the injection head was almost

completely blocked. This leads to a decrease of the fuel flow compared to the setting value and it can explain the reduction of emissions observed over the time from one repetition to another. The CAST injector head has been cleaned (Figure III-4-a and -b) and a displaced joint possibly responsible for a lack of fuel has been correctly put back (Figure III-4-c). After that, a second study of the CAST operating range limits has been done and we can observe that the formation of a double flame has been avoided due to the absence of fuel leak (Figure III-3-b). For example, the setting of flow rates at (30/2) or at (20/1.5), indicated in red on both figures, gives a second flame in the first representation (Figure III-3-a) but after CAST cleaning (Figure III-3-b), a stable flame is obtained for the same set points.

In the following sections of this study, we need to consider that the CAST evolves over the time explaining that direct quantitative comparisons with previous tests (Berthier, 2022) present some differences. Furthermore, the formation of a second flame needs to be avoided as much as possible in the selection of operating points. A wide range of operating points have been tested to generate soot emissions and results are detailed in III.1.2.

(a) (b) (c)

Figure III-4: CAST burner cleaning. In the first picture (a) the injector head after cleaning. In (b) the cleaning process and in (c) a displaced joint inside the CAST combustion chamber (due to disassembly of the burner).

III.1.2 Selection of CAST working points

After determination of the CAST working limits, the next step was to select a set point to characterise nvPM emissions at burner outlet and to use this point for our experiments on atmospheric chamber with several aeronautical fuels. To measure the soot emissions in CAST exhaust, the experimental set-up described in Figure III-5 is used. After dilution (DI-1000 and DEED) and conditioning (CS and DEED) of the emissions, the number concentration, the mass concentration and the size of soot particles have been measured respectively by a CPC, a LII and a SMPS+C. We consider as source the combination CAST + DI-1000, so only correction for DEED dilution is applied to the data.

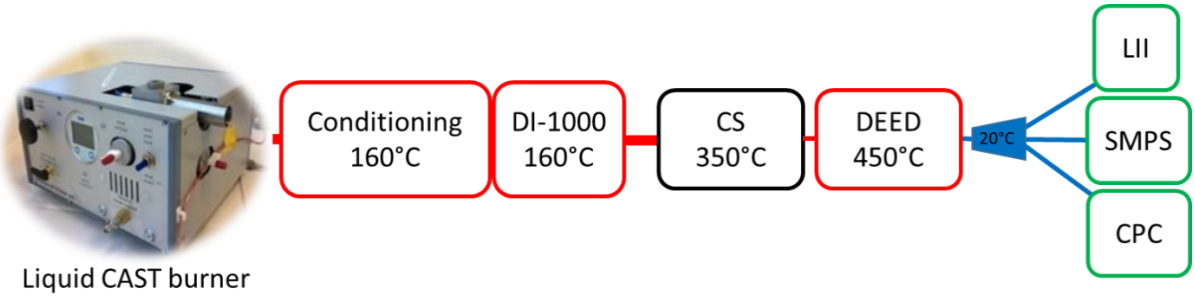

Figure III-5: Experimental set-up to determine CAST stable operating points at ONERA laboratory.

III.1.2.1 Comparison with previous studies using a CAST laboratory burner

The determination of the set point is related to the CAST flow parameters selection. In a previous study based on the same experimental set-up, (Berthier, 2022) already shows that the number and mass concentrations of nvPM increase with the fuel flow (Figure III-6-a and -b), that the particle number increases with propane flow and that air flow affects the size distribution of soot particles (Figure III-6-c). These phenomena are responsible for a reduction in the total particle number and for an increase of the nvPM GMD (Irimiea et al., 2019; Kelesidis et al., 2017; Y. Wang & Chung, 2019). The Figure III-6 presents for each case a comparison of aeronautical soot particle surrogates from the CAST with aircraft emissions from a real engine (SaM146 - Delhaye et al., 2017). The main conclusion is that the airflow and fuel flow of the CAST need to be reduced to obtain comparable characteristics with aircraft emissions (for example GMD from 25 to 50 nm). However, the formation of a second flame can impact the measurements if the air flow is too weak to feed the kerosene flame and the propane flame at the same time (Berthier, 2022). The size distribution becomes bimodal and the intensity of the second mode increases as the air flow decreases (III.1.1.1).

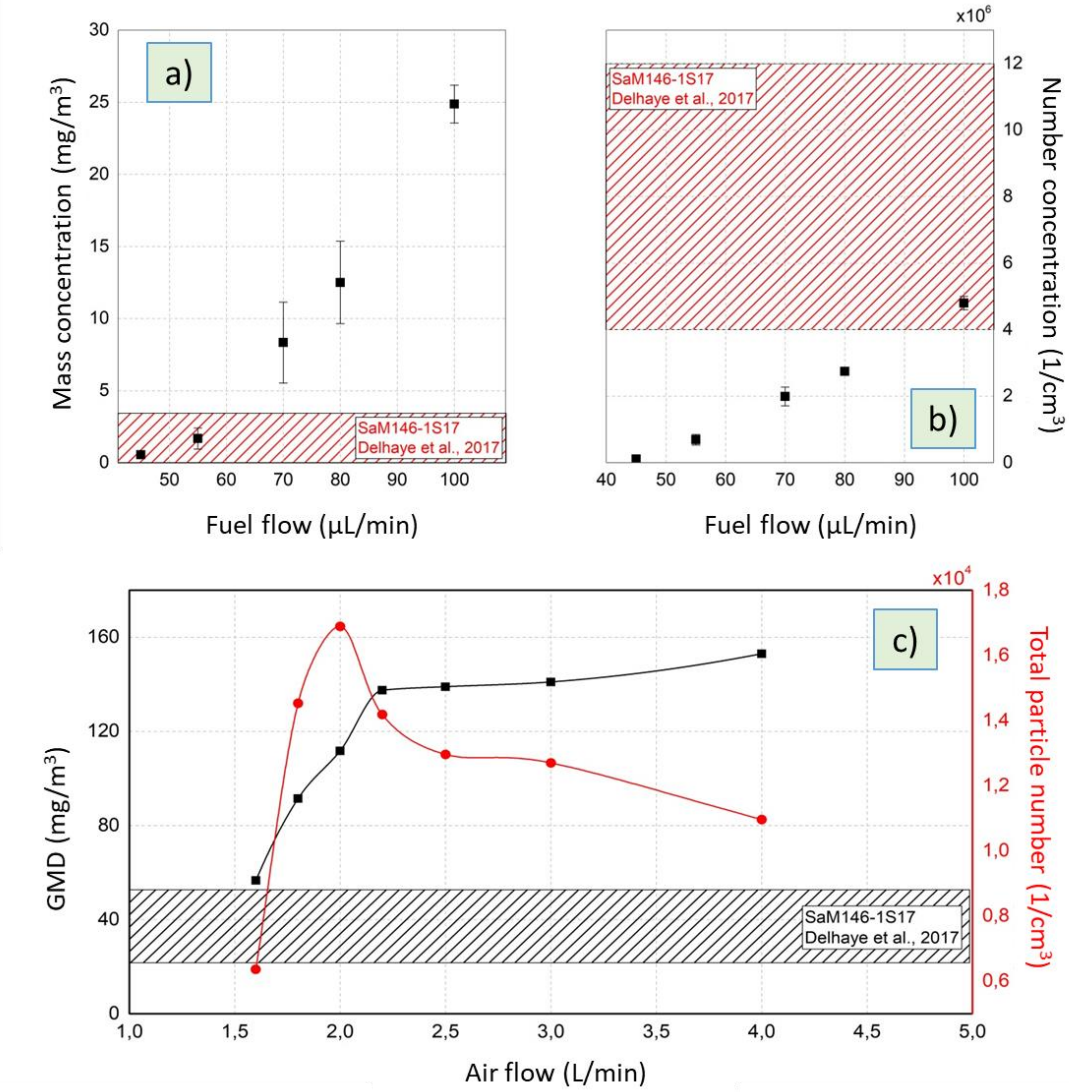

Figure III-6: Mass concentration (a), particle number concentration (b) and Geometric mean diameter (GMD –c) of CAST emissions for Jet A-1 fuel test depending on the fuel flow (with 2 L/min for air flow and 30 mL/min for propane flow in case a and b) and air flow (with 100 µL/min for fuel flow and 30 mL/min for propane flow in case c). Results are from (Berthier, 2022) and have been compared to emissions from SaM146-1S17 engine (Delhaye et al., 2017). No correction by DI-1000 dilution factor.

In (Berthier, 2022), the operating point (105/30/2) set at 105 µL/min for fuel flow, 30 mL/min for propane flow and 2 L/min for air flow has been selected despite the formation of a second flame, to compare results with those from the JETSCREEN project (JETSCREEN Project, 2020). The CAST burner emissions have been evolved over the time (III.1.1.2) and in the case of this study, different fuels than those from (Berthier, 2022) have been tested. Depending on fuel composition, emissions have different properties in terms of number and mass concentrations (Annex B) that can limit the number of stable set points. Taking into account the changes of the CAST, the objective is to verify if the same trends as in (Berthier, 2022) are observable using the (105/30/2) set point and to find another operating point to avoid the formation of a second flame by reducing the air flow or the fuel flow.

III.1.2.2 Stability of the burner and reproducibility of the experiments

To evaluate the stability of the set point (105/30/2) over the time and to estimate the impact of CAST clogging, emissions of the burner have been studied at different moments for the same Jet A-1 fuel, the same operating point and the same set-up. nvPM particles have been measured continuously for 30 min (one acquisition every 4 min) on different days. Figure III-7 presents size distributions obtained to study the stability of the burner over a day (first column) and the reproducibility of the emissions over several days (second column). Three different moments have been selected to follow the evolution of CAST emissions:

- case A corresponding to the previous study done in (Berthier, 2022);
- case B corresponding to the tests done at the beginning of this thesis;
- case C corresponding to the measurements done at the end of the thesis after CAST cleaning.

	Stability of the burner during a day test (<30min)	Reproducibility of the emissions at different days
Case A	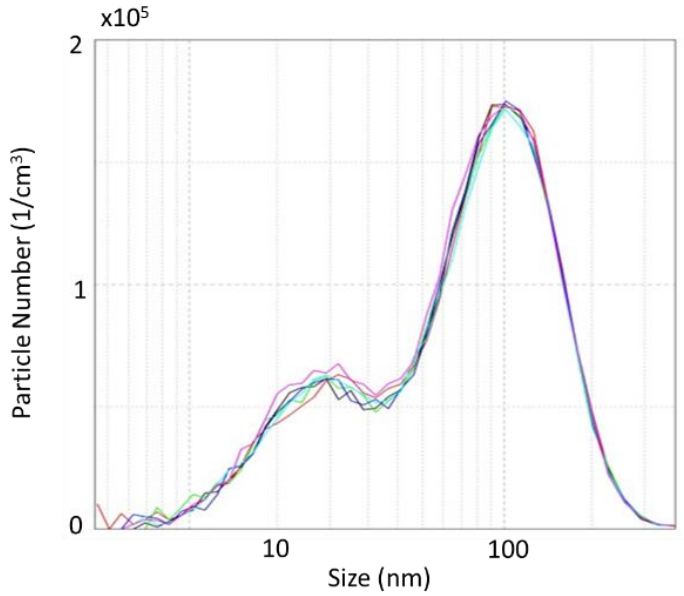 A-1 (Berthier, 2022)	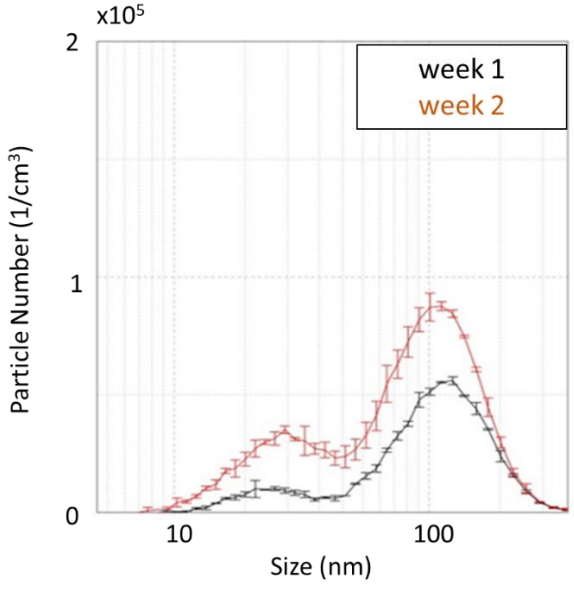 A-2 (Berthier, 2022)

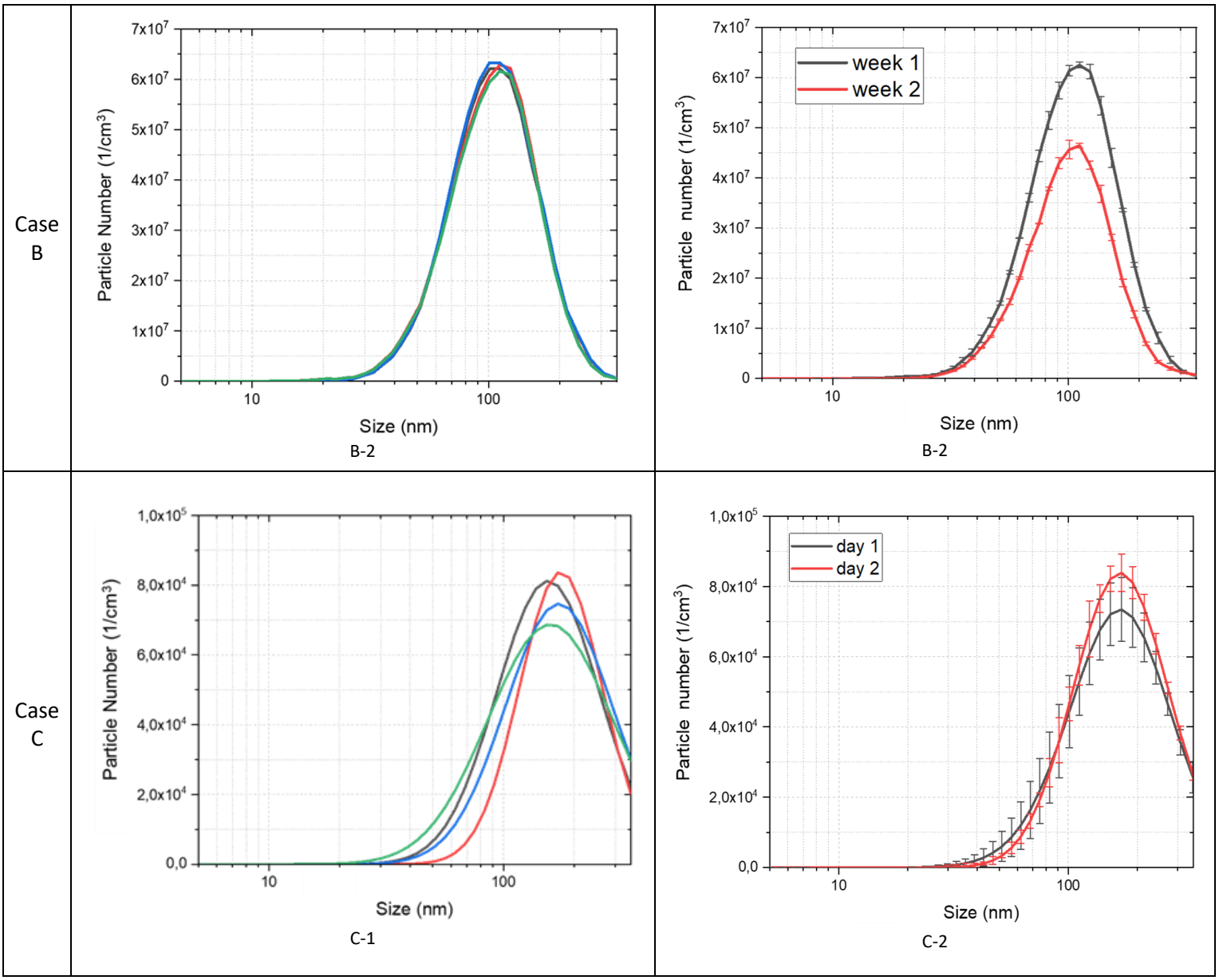

Figure III-7: Comparison of CAST burner stability (first column) and emissions reproducibility (second column) over the time for the (105/30/2) operating point using Jet A-1 fuel. Case A corresponds to results from (Berthier, 2022). Case B represents results obtained during the experimental campaigns in this thesis. Case C shows results obtained after CAST cleaning at the end of the thesis. Only DEED dilution corrections have been applied.

In case A, size distributions present bimodal distributions resulting from the formation of a second flame of kerosene (GMD of the second mode around 20 nm). Nevertheless, the stability of the burner over the time is good with principal modes centred at 110 nm and with comparable particle number concentrations for the different acquisitions (case A-1). Once the flame is stabilised, the emissions can be measured continuously without variations. However, the particle number presents a variation of 30% at two weeks of interval for the repetition test (case A-2). It can be noted that the second flame becomes more pronounced. These differences can come from the fouling of the CAST or the atmospheric conditions (affecting the control of the CAST flows). Therefore, it seems necessary to repeat for each experiment spaced over several days a reference case to justify the reproducibility of the results.

The second test (case B) has been done during UNREAL campaigns to compare emissions to those from previous experiments. Same observations as for case A are done: good stability during test

with a similar GMD (103 nm in case B-1) and total particle number decreases by 26% for the repetition test (case B-2). The principal change concerns the disappearance of the second mode.

At the end of the thesis, the CAST has been disassembled and cleaned. After that, the emissions were different (case C-1): the size distributions present less reproducibility for a daily test and small variations in terms of GMD can be seen (oscillation between 142 and 165nm). These GMD are higher than before due to the cleaning of the CAST. Concerning the repetition tests (case C-2), the GMD remains the same but the particle number changes by 13% (included in the standard deviation measurement).

To get a better overview of the variation of particle emissions over the time for this set point, Table III-2 summarises results obtained for GMD measurements, and for number and BC mass concentrations. It can be noted that the GMD of the particles decreases for successive experiments when the burner becomes more blocked (Case A and B) but after CAST cleaning, particles present a higher GMD (+37% to +46% compared to precedent tests). However, the standard deviation indicates that the repetition of the acquisitions is less stable after the cleaning process (GMD values more dispersed). Regarding the other measurements, the trend is similar with a decrease of the BC mass concentration and the number concentration of particles without CAST cleaning over the tests.

In the case C, the particle number presents lower values even after the cleaning process. It can be explained by the disassembling of the CAST: without clogging, no formation of second flame and no exceeding emissions. Particles obtained are bigger but less numerous compared to precedent studies. BC mass concentration measurement was not available for these last tests.

The study of the CAST emissions for the (105/30/2) operating point at different moments confirms the stability of the burner for daily tests and depending on the clogged state of the burner, the formation of a second flame can be avoided. Cleaning the burner affects mainly particle size.

Tests performed	GMD (nm)	Standard deviation (nm)	Particle Number ($1/cm^3$)	Standard deviation ($1/cm^3$)	BC Mass concentration (mg/m^3)	Standard deviation (mg/m^3)
Case A Previous study (Berthier, 2022)	110	1.2	2.44E+07	4E+05	115.2	13.8
Case B UNREAL campaign	103.3	2.6	5.37E+06	6.71E+05	44.22	1.86
Case C After CAST cleaning	150.95	11.37	4.96E+05	5.28E+04		

Table III-2: Comparison of (105/30/2) CAST set point for three different tests: same fuel (Jet A-1), same set-up, and for each case dilution is corrected. The LII instrument wasn't available during the tests done in case C.

III.1.2.3 Adjustment of the set point to CAST variations

During the different experimental campaigns, the CAST being more blocked, the fuel flow was reduced and the flame became less stable in particular for some fuels such as AtJ. To avoid blowing out the flame or forming a second flame of kerosene on propane flame, the operating point has been modified. Thus during the UNREAL tests, another set point has been defined at 84µL/min to reduce the fuel flow (corresponding to 80% of MFC regulation), 30mL/min for the propane flow and 3L/min for the air flow. This operating point presents a stable flame for all fuels tested (Annex C and Annex D) without the formation of a second flame (Figure III-8-left). After CAST cleaning, the emissions obtained at this set point are on average less numerous and results show more variations in terms of particle number implying that emissions are less reproducible (Figure III-8-right).

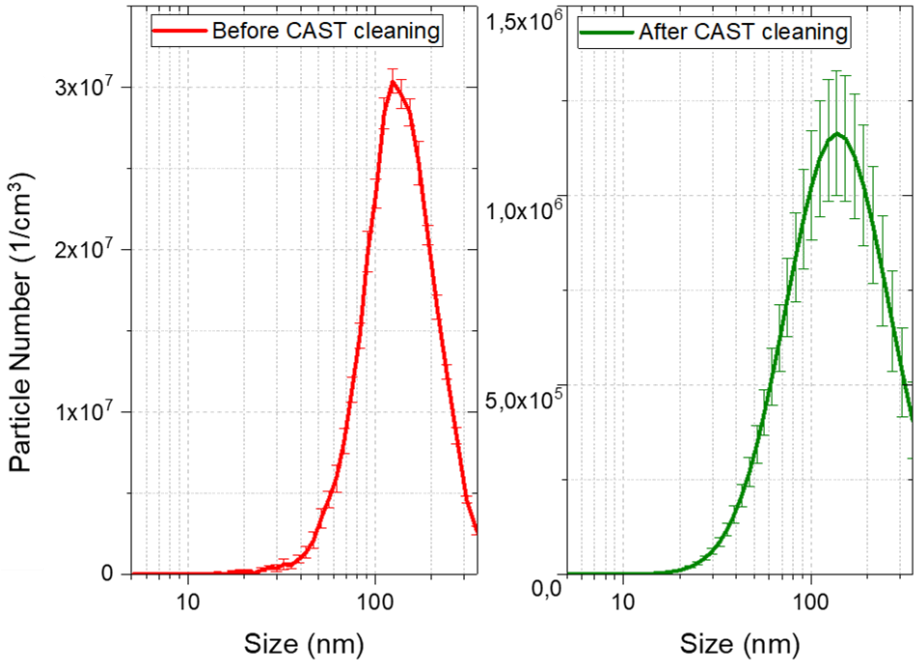

Figure III-8: Comparison of size distributions for (84/30/3) set point before (left) and after (right) CAST cleaning (Jet A-1 fuel).

In addition, the Figure III-9 presents the GMD and GSD for the (84/30/3) operating point compared to results obtained for (105/30/2) set point before and after CAST cleaning. In the case of lower fuel flow (84/30/3), GMD decreases by 7%. The standard deviation becomes higher (4 times more) suggesting that the burner is less stable. In addition, the higher GSD obtained after cleaning process implies that particles are more dispersed around the GMD. On the contrary, the GMD increases by 46% for the Jet A-1 case using (105/30/2) set point after the cleaning process. In comparison, before CAST cleaning particle GMD is higher for the (84/30/3) set point but after CAST cleaning, GMD is higher for the (105/30/2) case.

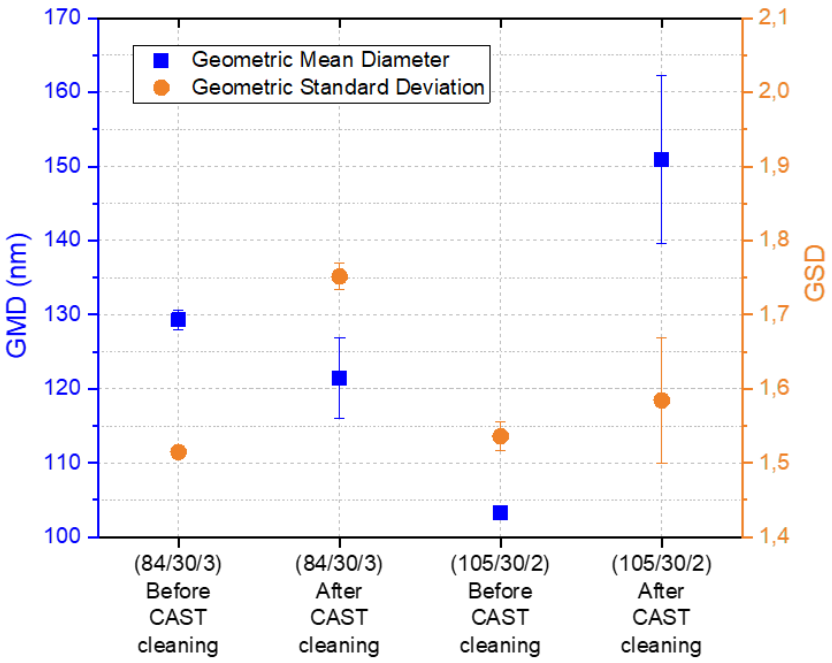

Figure III-9: Comparison of GMD and GSD for the (84/30/3) set point with GMD and GSD for the (105/30/2) set point before and after CAST cleaning. The fuel is Jet A-1 and dilution correction has been applied.

The same decrease trend than for the GMD using the (84/30/3) set point is observed for the mass and number concentrations after the CAST cleaning process. Results are summarised in Table III-3. In comparison, the results obtained for the (105/30/2) set point in Table III-2 regarding the mass and number concentrations are lower. It means that the number of particles is higher for the (84/30/3) case but the particles in CAST exhaust emissions are smaller. So CAST cleaning changes the emissions properties in terms of mass number and size and results show less stability.

(84/30/3) CAST set point	GMD (nm)	Standard deviation (nm)	Particle Number ($1/cm^3$)	Standard deviation ($1/cm^3$)	BC Mass concentration (mg/m^3)	Standard deviation (mg/m^3)
Before CAST cleaning	129.31	1,35	1,56E+07	2,92E+05	222,84	30.71
After CAST cleaning	121,43	5,47	9,87E+05	1,53E+05	Not available	Not available

Table III-3: Comparison of emissions (size, mass and number concentrations) at CAST burner outlet for (84/30/3) set point before and after burner cleaning for Jet A-1 fuel. Dilution corrections have been applied.

III.1.2.4 Summary

This first approach allows a better understanding of the liquid CAST burner parameters impacting the resulting emissions. According to previous observations (Berthier, 2022; I. Ortega, Delhaye, Jing, et al., 2016), the air flow needs to be adapted to the fuel flow and propane flow to avoid the formation of a second flame and/or avoid the extinction of the flame. Furthermore, due to CAST variations, the set parameters need to be modified from one experiment to another. To work in the following sections with the CAST burner, two operating points have been selected:

- The first one is the (105/30/2) set point corresponding to 105 µL/min for fuel flow, 30 mL/min for propane flow and 2 L/min air flow. The flame obtained is stable for all the fuels tested and emissions obtained can be compared to previous studies (Berthier, 2022) despite the potential presence of a second flame;

- The second point corresponds to 84 µL/min for kerosene flow, 30 mL/min for propane flow and 3 L/min oxidation flow and is noted (84/30/3). This fuel flow corresponds to 80% of the flow capacity of the mass flow controller to feed the burner in fuel. This point has been selected during UNREAL experimental campaigns to work on atmospheric experimental chamber taking into account CAST variations and the different fuels tested.

The next section is dedicated to the study of CAST emissions at burner outlet depending on the fuel composition for these operating points. A quantification and a chemical analysis of the emissions composition is proposed.

III.2 Characterisation of CAST emissions depending on fuel

Before moving on atmospheric simulation chamber tests and studying evolution of aeronautical emissions at ground level under ambient conditions, it is important to characterise these emissions at burner exhaust to understand the impact of some parameters such as the choice of the fuel depending on the CAST working point. As mentioned in Chapter I, the certification measurements take into account only the nvPM by conditioning the emissions and by removing the vPM. Thus, to characterise the emissions from different aviation fuels having different compositions, the experiment line is adapted in this part to the nvPM study. The results discussed below correspond to the soot particle mass concentration, number concentration and size distribution measured for the different operating points selected in section (III.1.2.4).

III.2.1 Experimental Set-up

Emissions from CAST have been diluted by the DI-1000 (160°C) and the sample has been driven to a stainless steel splitter through a 1 metre line heated at 160°C. Emissions are then conditioned by combining a CS (350°C) and a DEED to remove the volatile particles that might be present in the sample flow (Figure III-10). At the end of this process, the final sample contains only soot at ambient temperature. After DEED, the sample flow was analysed using a LII to determine the soot mass concentration and by a SMPS to determine particle size distribution (measurement range between 5 nm and 350 nm). The CPC has been alternatively used alone to determine the particle concentration and coupled with a DMA to obtain the size distribution (SMPS device).

In addition to the on-line characterisation techniques, filters have been collected to perform off-line chemical characterisation with mass spectrometry techniques. The sampling has been done with a double filter holder (Ngo et al., 2020) before the sample treatment, thus it corresponds to the raw emissions. This process (detailed in II.2.2.3.1) allows a separation of the particle phase (first filter) from the gas phase (second filter).

The matrix fuel studied here corresponds to the one described in II.1.1.2, containing a standard fuel, a 100% SAF and some modified and blended fuels.

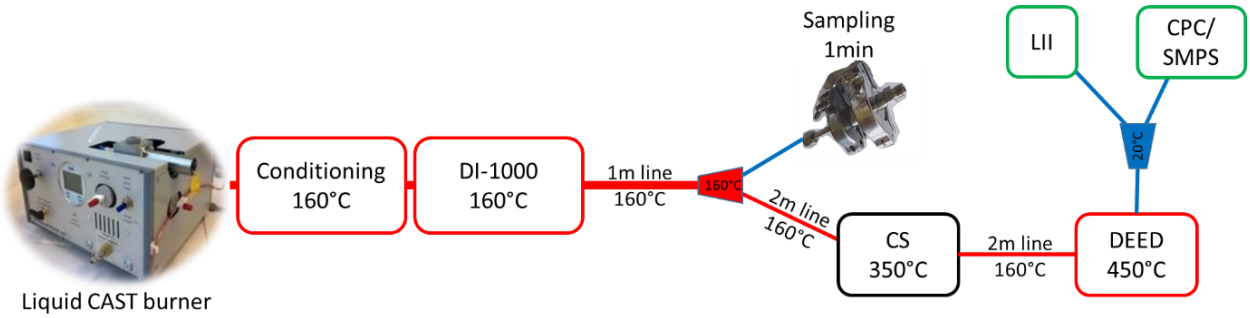

Figure III-10: CAST set-up for emissions comparison depending on the fuels.

III.2.2 Impact of fuel composition on particle emissions

The aim of this first test has been to evaluate the potential impact of sulphur and aromatic contents on emissions and their impact on certification measurements. This part is included in the RAPTOR project (RAPTOR project, 2020) done in parallel with the UNREAL experimental campaign to assess the incidence of ICAO (16 compliant fuel composition specifications in terms of nvPM - ICAO, 2017). The idea was to study how changing composition between different certification tests (in the

accepted limits) can affect results. To observe this, four fuels covering the limits of the American Society for Testing and Materials (ASTM) requirements for certification have been selected:

- the “Low Aromatic and Low Sulphur Jet” fuel with 16% of aromatics content (including 0.5% of naphthalene) and 4 ppm sulphur. From now it will be referred as “Low Jet”;
- the “High Sulphur Jet” fuel with 16% of aromatics content (including 0.5% of naphthalene) and 3000 ppm sulphur;
- the “High Aromatic Jet” fuel with 23% of aromatics content (including 0.5% of naphthalene) and 4 ppm sulphur;
- the “Extreme Jet” fuel with 23% of aromatics content (including 0.5% of naphthalene) and 3000 ppm sulphur.

As the aim of the study was to compare different fuels, the choice of the set point was limited to common stable set points for these four fuels. In regards on the previous study done in (III.1.2), two set points at the same fuel flow with a similar propane/air flows ratio have been selected to compare resulting emissions:

- set point number 1 referred as (105/30/2) → 105 µL/min of kerosene flow, 30 mL/min of propane flow and 2 L/min of air flow;
- set point number 2 referred as (105/20/1.5) → 105 µL/m of kerosene flow, 20 mL/min of propane flow and 1.5 L/min of air flow (to work at a lower air flow).

In this section, the combination of CAST and DI-1000 is considered as the source, so only correction for DEED dilution is applied to the data.

III.2.2.1 Black Carbon Mass Concentration

Figure III-11 depicts the black carbon (BC) mass concentration measured by LII for fuels with different compositions depending on CAST set points (105/30/2) and (105/20/1.5). As it can be seen, measurements have been repeated for each fuel and each operating point. The variability of two measures done during the same test is between 0.1% and 4% for case (105/30/2) and between 0.6% and 5% for case (105/20/1.5). LII was continuously measuring during the tests, while SMPS and CPC have been used alternatively, so we decided to average LII measurements done during SMPS measurements (8 minutes) and during CPC measurements (3 minutes). Table III-4 summarises LII results for CAST set point 1 (105/30/2) and set point 2 (105/20/1.5) with repeated tests.

For the first operating point (in blue - Figure III-11), highest emissions are produced by the Extreme Jet fuel and lowest by the High Sulphur Jet fuel. Results for fuels containing 3000 ppm of sulphur (Extreme Jet and High Sulphur Jet) are expected: there is less black carbon for less aromatic compounds in fuel composition. Indeed, fuels with high amounts of sulphur show a reduction in BC mass concentration of 51% when the aromatic content was reduced from 23% (Extreme Jet) to 16% (High Sulphur Jet). However the results for fuels containing 4 ppm of sulphur are quite surprising. In this case, it is difficult to observe any significant influence from the aromatic content reduction on BC mass concentration. Indeed, for High Aromatic Jet and Low Jet fuels, emissions are quite similar (only 0.3mg/m^3 of difference), being slightly higher for the High Aromatic Jet case. As for the fuels with 3000 ppm of sulphur, BC mass concentration for fuels with 4 ppm of sulphur shows a reduction but a small one (4%) included in the standard deviation measurement. A similar behaviour to that of fuels containing 3000 ppm of sulphur has been expected to be more pronounced: i.e. higher mass concentration for higher aromatic amounts independently to sulphur content.

Concerning the second operating point (in green - Figure III-11), the measures done have a similar behaviour with the one observed for set point 1 and are as expected in particular for fuels with low amounts of sulphur. The highest emissions correspond to fuels with high amounts of aromatics compounds (23% in Extreme Jet and High Aromatic Jet) and lowest emissions to fuels with low

amounts of aromatics compounds (16% in Low Jet and High Sulphur Jet). For fuels with low concentration of aromatic compounds, the emissions from the fuel containing 3000 ppm of sulphur are slightly higher than those from the fuel containing 4 ppm of sulphur. It has to be pointed out that the results for the fuel with 4 ppm of sulphur are more dispersed than those for the fuel with 3000 ppm of sulphur. BC mass concentration is reduced by 26% for the fuel containing 3000 ppm of sulphur and by 42% for the one with 4 ppm of sulphur when the aromatic content is reduced from 23% to 16%. As observed for the first set point, the BC mass concentration decreases if the amount of aromatic compounds is reduced for a given sulphur content.

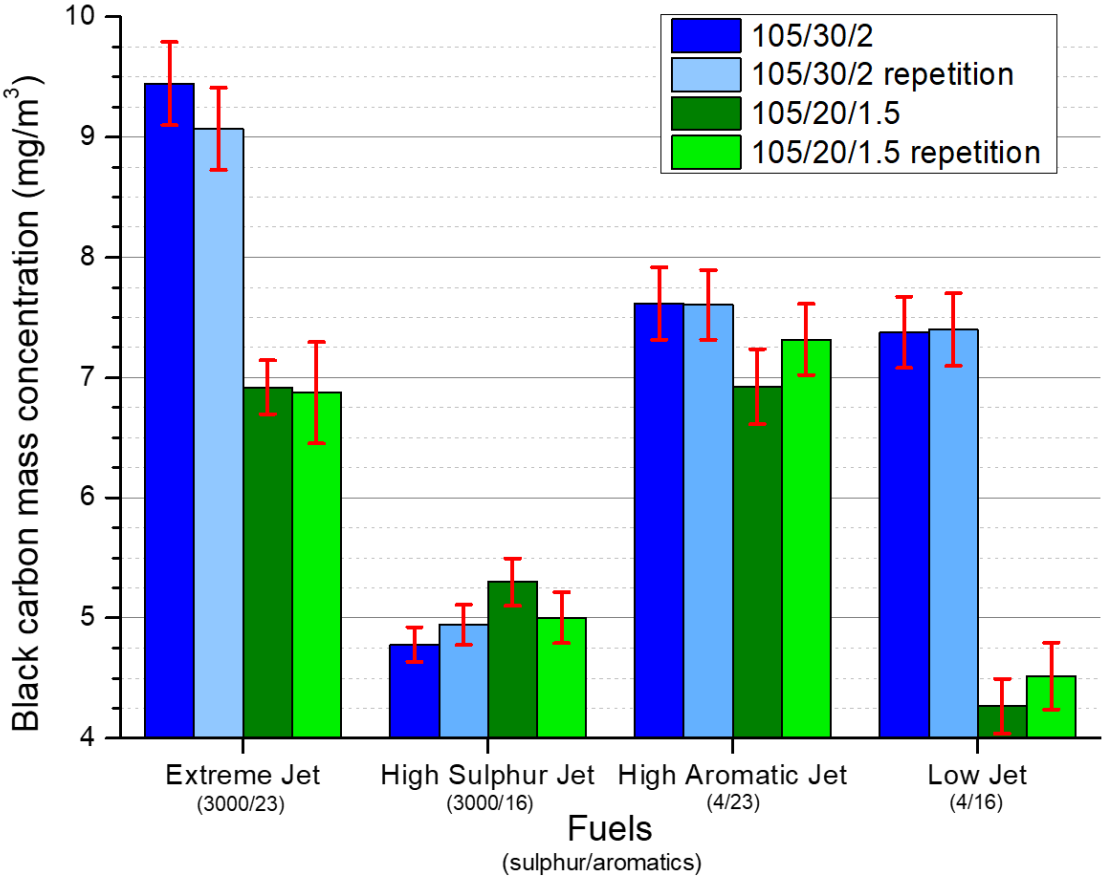

Figure III-11: Black carbon mass concentration comparison for four different fuels and two operating points. The colour shade indicates the repeated test for the same CAST set-up. The sulphur content decreases from the left to the right.

Fuels	Operating point 1: (105/30/2)				Operating point 2: (105/20/1.5)			
	Black carbon mass (mg/m^3) Two repetitions		Standard Deviation (mg/m^3)		Black carbon mass (mg/m^3) Two repetitions		Standard deviation (mg/m^3)	
Extreme Jet	9.4	9.1	0.3	0.3	6.9	6.9	0.2	0.4
High Sulphur Jet	4.8	4.9	0.1	0.2	5.3	5.0	0.2	0.2
High Aromatic Jet	7.6	7.6	0.3	0.3	6.9	7.3	0.3	0.3
Low Jet	7.4	7.4	0.3	0.3	4.3	4.5	0.2	0.3

Table III-4: Black carbon mass concentration measured by LII for different fuels and two operating points.

III.2.2.2 Particle Number Concentration

Figure III-12 depicts the number concentration of particles measured for different fuels and different CAST set points. For both operating points, the trend measured is similar to the one observed for BC mass concentration: reduction of particle number with the reduction of aromatics independently of sulphur content. Table III-5 summarises particle numbers measured by CPC for different fuels and both CAST set points.

In the case of (105/30/2) set point, highest emissions are observed for the Extreme Jet fuel and lowest for the High Sulphur Jet. For fuels with 3000 ppm of sulphur, particle number follows the same trend with a reduction of 29% according to the reduction of aromatics contents. As in the previous Figure III-11, fuels with 4 ppm of sulphur produce similar emissions (6.10^4 particles/cm^3 of difference) and particle number presents as well a negligible reduction (-1.5% included in the standard deviation measurement) with the reduction of aromatic content.

For CAST set point 2, the fuel presenting higher emissions in particle number is also the Extreme Jet and the one presenting lower emissions is the Low Jet. In this case, the difference between the Extreme Jet fuel and the High Sulphur Jet fuel is not as marked as for BC mass concentration. Particle number is reduced by 6% for these fuels, while the ones with 4 ppm of sulphur present a reduction of 33%.

It can be noted that more particles have been detected for set point 2 concerning the three first fuels. It is due to the presence of a second flame for these cases, generating extra amount of particles. More details are given in the following section, by regarding the size distributions of particles.

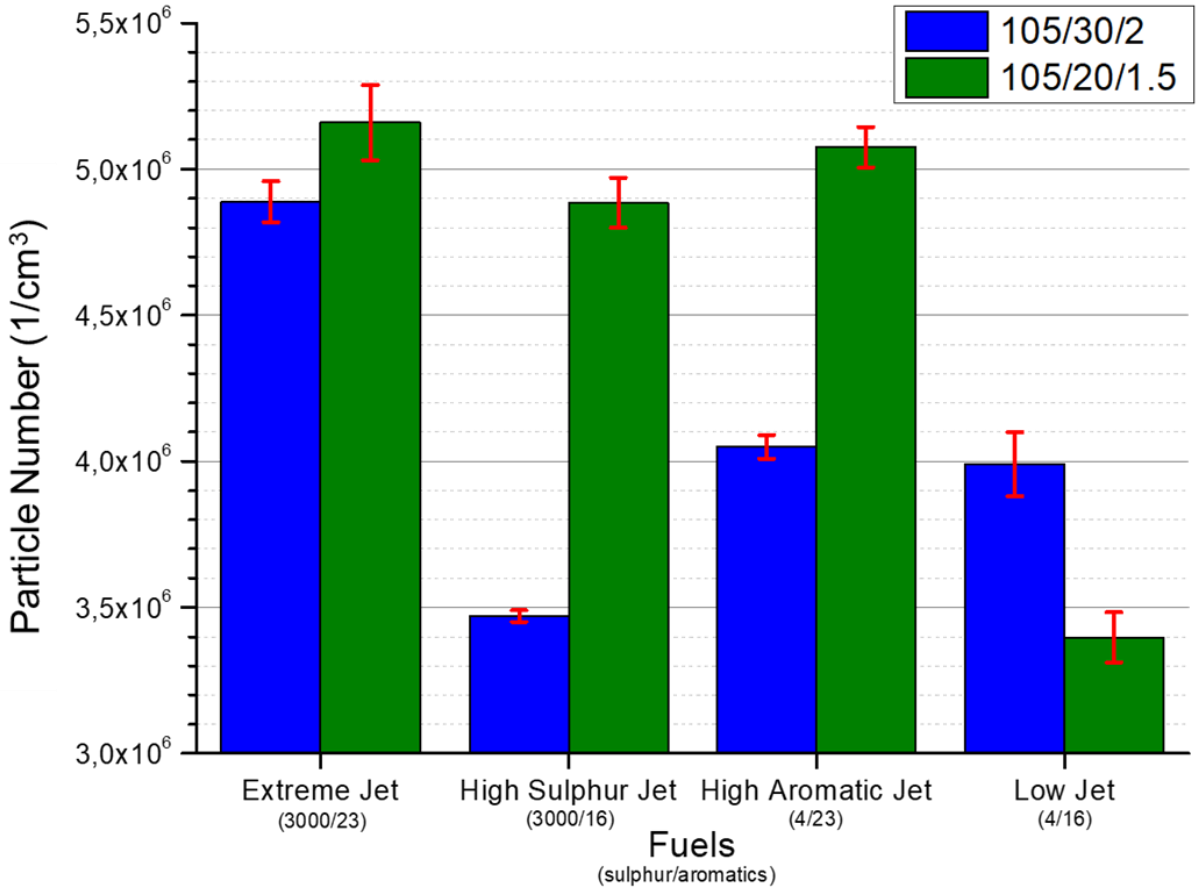

Figure III-12: Particle Number Concentration comparison for four different fuels and two different CAST operating points. The sulphur content decreases from the left to the right.

Fuels	Operating point 1: (105/30/2)		Operating point 2: (105/20/1.5)	
	Particle Number (1/cm^3)	Standard Deviation (1/cm^3)	Particle Number (1/cm^3)	Standard Deviation (1/cm^3)
Extreme Jet	4.88 x10^6	0.07 x10^6	5.16 x10^6	0.13 x10^6
High Sulphur jet	3.47 x10^6	0.02 x10^6	4.89 x10^6	0.09 x10^6
High Aromatic Jet	4.05 x10^6	0.04 x10^6	5.08 x10^6	0.07 x10^6
Low Jet	3.99 x10^6	0.11 x10^6	3.40 x10^6	0.09 x10^6

Table III-5: Particle Number measured by CPC for different fuels and two operating points.

III.2.2.3 Particle Size Distribution

To complete LII and CPC data, SMPS measurements have been done in series with CPC measurements. For both set points, at least two size distributions have been measured. In general, the size distributions were reproducible. Only size distributions taken in different days for same fuel presented some difference (as seen in III.1.2.2) but it is essentially in total particle number, not in terms of diameter (cf. case of Extreme Jet repeated - Figure III-13). Annex E and Annex F depict the raw size distributions obtained for each fuel for both CAST set points.

For the first operating point (105/30/2), Figure III-13 shows a comparison of size distribution obtained for different fuels. Raw size distributions (left plot) have been fitted using a lognormal function (right plot) and average results for the fit for each fuel are given in Table III-6.

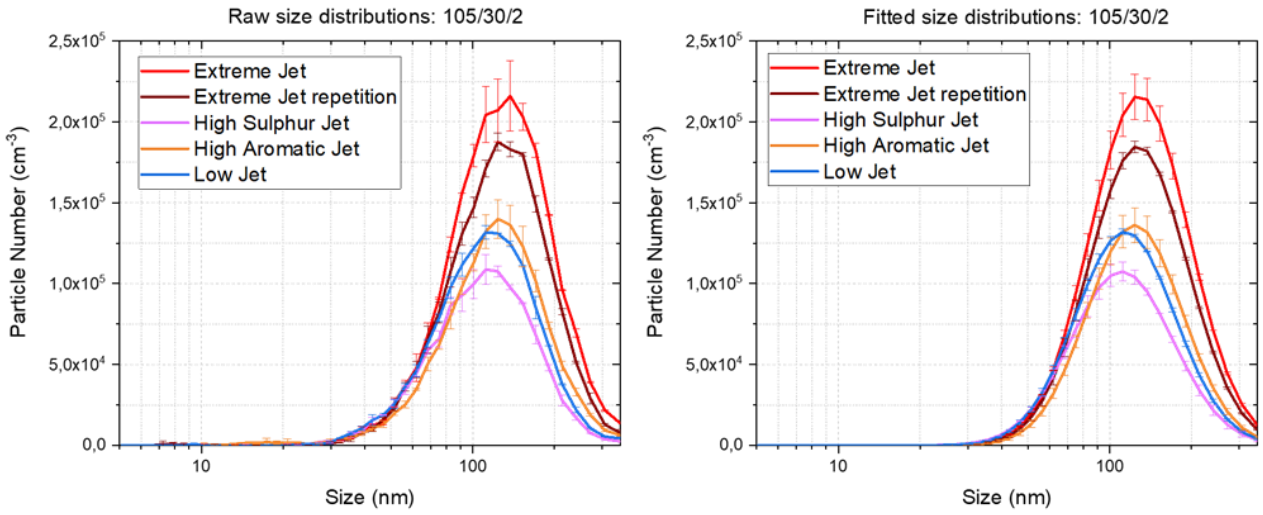

Figure III-13: Size distributions comparison for different fuels measured by SMPS (left panel) and fitted to a lognormal function (right panel). CAST operating point 1.

Fuels	Particle number (1/cm^3)	Standard Deviation (1/cm^3)	GMD (nm)	Standard Deviation (nm)	GSD	Standard Deviation
Extreme Jet	2.15 x10^6	0.09 x10^6	124.4	0.4	1.50	0.01
	1.83 x10^6	0.05 x10^6	123.1	1.8	1.50	0.01
High Sulphur Jet	1.14 x10^6	0.03 x10^6	107.5	2.0	1.53	0.02
High Aromatic Jet	1.32 x10^6	0.05 x10^6	119.9	2.0	1.49	0.02
Low Jet	1.35 x10^6	0.02 x10^6	110.6	0.1	1.51	0.01

Table III-6: Size distribution fit parameters depending on the fuel for CAST set point 1.

As can be seen in Figure III-13, the total number trend observed by SMPS for different fuels is similar to the one observed for particle number measured with CPC. Indeed, for a same amount of sulphur, the concentration number decreases with the reduction of aromatics content in fuel and vice-versa. Regarding the size distributions, particles emitted for all fuels present a mono-modal distribution centred between 105 and 125 nm. The Geometrical Mean Diameter (GMD), based on the repartition of particles along the distribution, is taken into account after fit and is smaller for the fuels with a low amount of aromatic compounds. Figure III-14 represents the different GMD and the Geometric Standard Deviation (GSD) obtained depending on fuel composition. The higher GMDs correspond to fuels with 23% of aromatic contents and the lower to fuels with 16% of aromatic contents. For fuels with 3000 ppm of sulphur, GMD is reduced by 13% and for fuels with 4 ppm of sulphur, GMD presents a modest reduction of 7.7% when aromatic content is reduced from 23% to 16%. With the reduction of aromatics content, soot particles become smaller and less numerous.

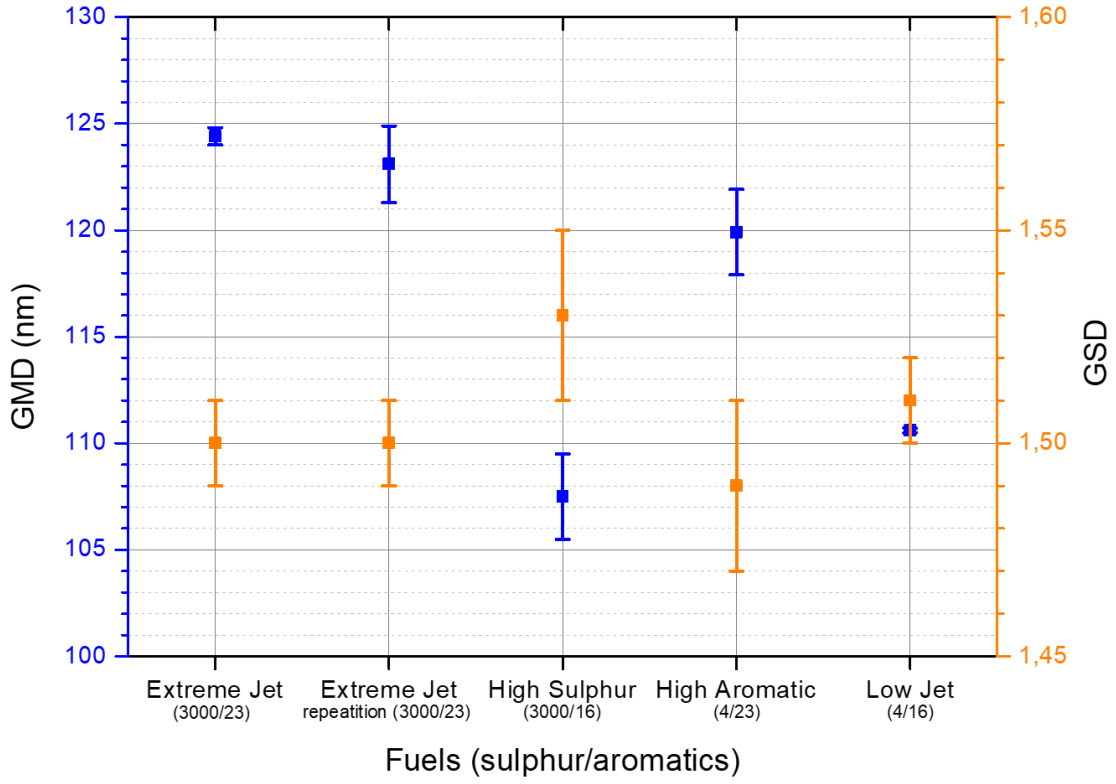

Figure III-14: Geometric Mean Diameter (GMD) and Geometric Standard Deviation (GSD) of fitted size distributions for different fuels.

Concerning the second operating point (105/20/1.5), we can see on Figure III-15 that all fuels except Low Jet fuel (blue) present a bimodal size distribution. The main mode is located at 110 nm and the second mode around 30 nm (due to the formation of a double flame – cf.III.1.1). During the CAST characterisation study, we observed that this CAST set point is sensible to the air flow: a small change in 0.05L/min leads to a shift in the position of the second mode at 30 nm and to a change in its intensity. This is one of the reasons for the discrepancies observed in particular at the second mode.

As for the size distributions obtained for CAST set point 1, we have fitted the size distributions, this time using two lognormal functions to separate both modes (except for the Low Jet fuel). Figure III-15 compares the measured size distributions for the 4 different fuels and Figure III-16 compares the fitted size distributions. Table III-7 summarises the results after fitting processes for the different fuels.

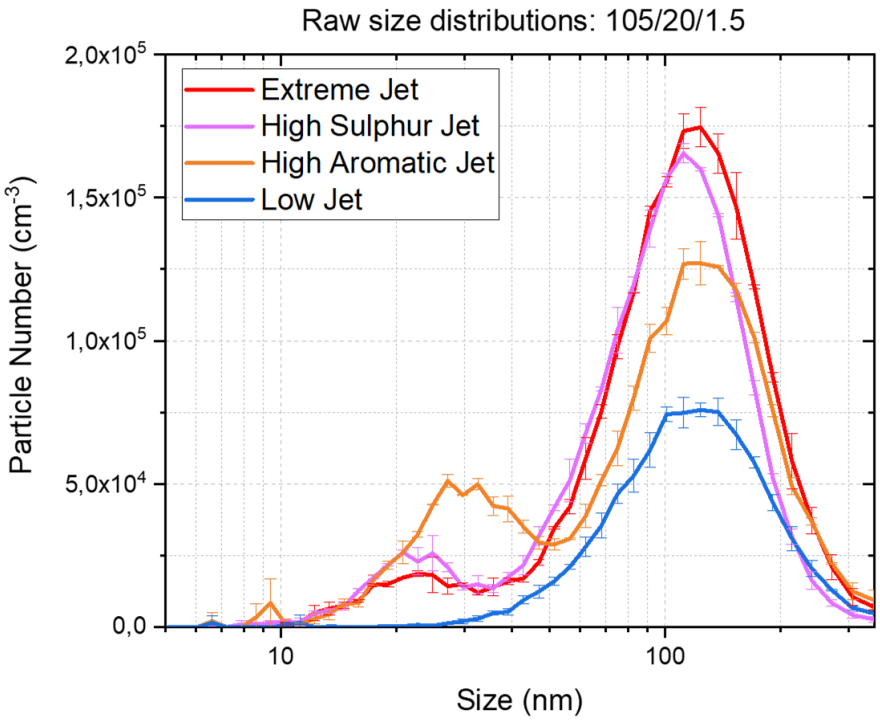

Figure III-15: Raw size distributions comparison for different fuels according to CAST set point 2.

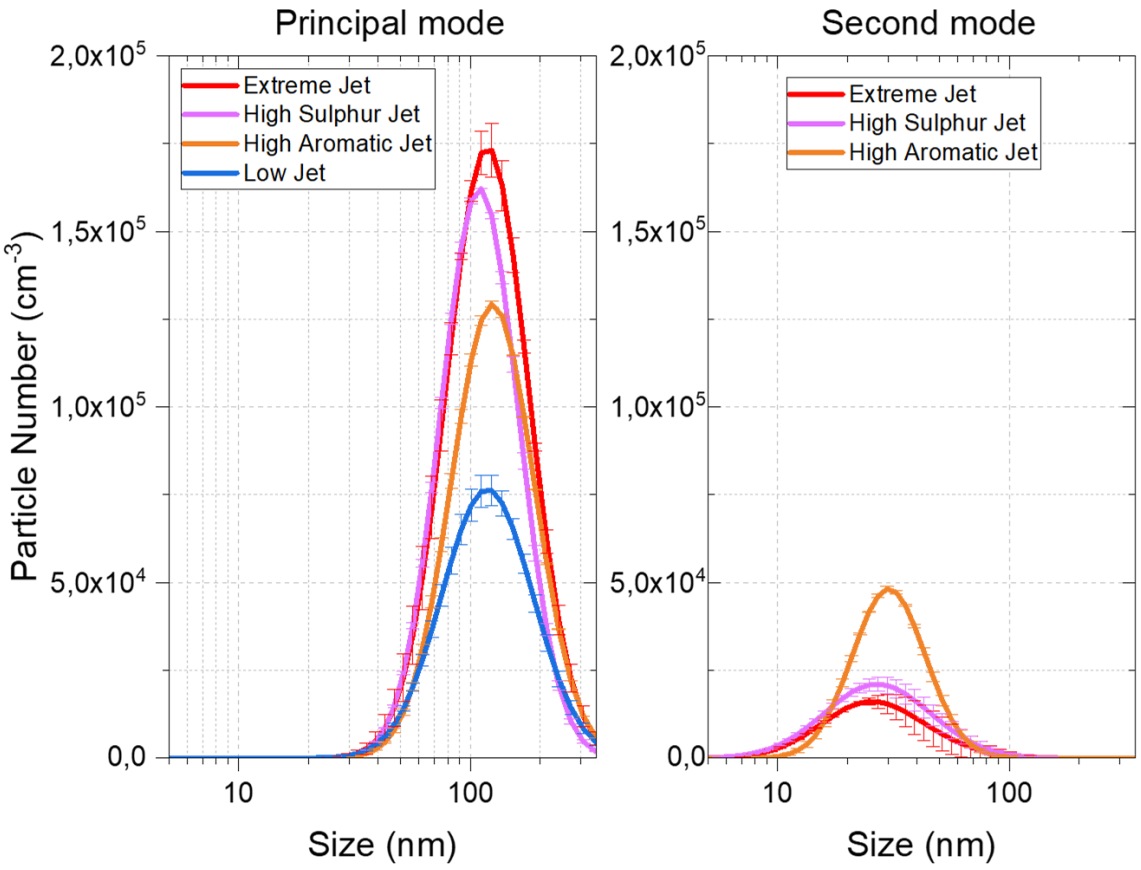

Figure III-16: Fitted size distributions comparison for different fuels and set point 2. On the left the main mode corresponds to the kerosene flame and on the right the second mode due to the second kerosene flame appearance.

Date	Mode 1			Mode 2		
	Particle number ($1/cm^3$)	GMD (nm)	GSD	Particle number ($1/cm^3$)	GMD (nm)	GSD
Extreme Jet	$1.73\pm0.05\cdot10^6$	114.7±2.1	1.50±0.04	$2.33\pm0.54\cdot10^5$	25.8±3.5	1.65±0.12
High Sulphur Jet	$1.54\pm0.01\cdot10^6$	107.0±0.8	1.47±0.01	$3.09\pm0.42\cdot10^5$	26.7±1.3	1.68±0.04
High Aromatic Jet	$1.28\pm0.02\cdot10^6$	120.9±0.7	1.50±0.01	$4.85\pm0.15\cdot10^5$	30.0±0.1	1.44±0.02
Low Jet	$0.83\pm0.04\cdot10^6$	114.0±1.5	1.55±0.01	0	0	0

Table III-7: Size distribution fit parameters for each fuel for CAST set point 2.

The results obtained for the main mode at 110-120 nm (Figure III-16-left) are similar to those obtained for the mono-modal distribution of CAST set point 1 (Figure III-13): the total number of particles decreases with the reduction of aromatics content. Furthermore, for the same amount of sulphur, GMD is smaller for fuels with low aromatic contents (Figure III-17). GMD presents a reduction of 7% when reducing the aromatic contents independently of sulphur contents (3000 and 4ppm). In the case of the second mode (Figure III-16-right), there is no difference in terms of GMD between fuels with 3000 ppm of sulphur. Regarding the fuels with 4 ppm of sulphur, while mode 2 is measured for the High Aromatic Jet fuel, it is not present in Low Jet fuel (no second flame appearance for this test when reducing the aromatic content from 23% to 16%). This fuel with low level of aromatic and sulphur contents generates a smaller flame than for the other fuels. There is no excess of kerosene and it does not leak above the injector head restricting the formation of a second flame at the bottom of the burner combustion chamber. The presence of a second flame can reduce the GMD of the principal mode, explaining that in this CAST set point case, GMD for Extreme Jet and Low Jet are similar.

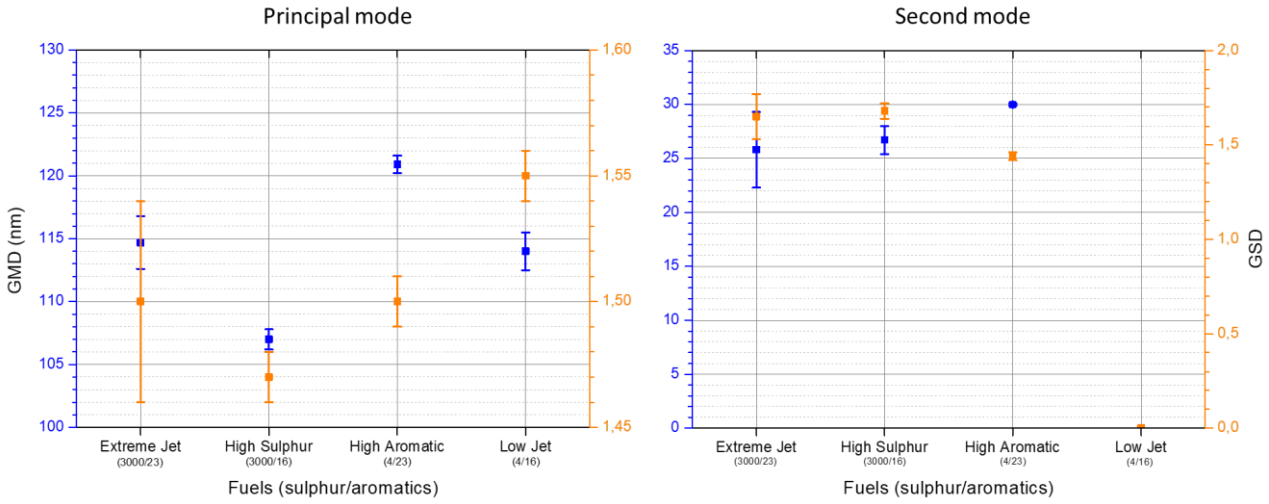

Figure III-17: Geometric Mean Diameter (GMD) and Geometric Standard Deviation (GSD) of fitted size distributions for different fuels for the principal mode (left) and for the second mode (right).

These results confirmed the contradictory trends in terms of mass and particle concentrations observed in previous sections (cf. Figure III-11 and Figure III-12). Indeed the second operating point

(105/20/1.5) presents a second flame for some tests (Figure III-15) and additional particles are formed (second mode observed). The mass concentration is not impacted due to the small sizes of these particles but the particle number concentration is significantly increased. It explains that for some fuels (Extreme Jet, High Aromatic Jet and High Sulphur Jet fuels), the BC mass concentration values are lower for the (105/20/1.5) set point than for the (105/30/2) set point but that particle concentration values are higher for the (105/20/1.5). It is confirmed by the Low Jet fuel case, where no second flame has been formed: no formation of extra-particles and thus mass and particle concentrations are lower for the set point 2 compared to the set point 1. It can also be noted that the set point (105/20/1.5) leads to an unstable flame for some fuels without aromatic contents (such as AtJ). For these reasons, only the first set point at (105/30/2) has been kept.

III.2.3 Comparison with emissions from synthetic fuels

In the previous sub-section, the impact of aromatic and sulphur contents on aeronautical emissions has been estimated in accordance with the ASTM certification limits. To complete this first approach and to consider the development of synthetic fuels to reduce emissions, a comparison between classical fuel and synthetic fuels is proposed, based on a similar experimental set-up and protocol as presented in Figure III-10. The fuels selected in this subsection are the Jet A-1 of reference from JETSCREEN project and the 100% SAF called AtJ, without sulphur and aromatic contents in its composition (cf. II.1.1.2 for details). In addition, a blend of these two fuels mentioned previously and called mix E5 was also added. For this study, the DI-1000 has been replaced by a FPS diluter (II.2.1.1.2) and respective dilution correction values are indicated for each case in following results.

A previous work (Berthier, 2022; JETSCREEN Project, 2020) has already studied differences between the reference Jet A-1 (cf. III.1.2.1) and these fuels (AtJ and mix E5) for the first CAST operating point (105/30/2). The results presented a reduction in terms of BC mass concentration, particle number and size of nvPM with increasing hydrogen content in the fuel, which is linked to a decrease in the level of aromatic compounds. Furthermore, a chemical characterisation by mass spectrometry showed a reduction in PAH concentration for the combustion of alternative fuel compared to the other fuels. This reduction follows the trend previously observed in the reduction of nvPM with an increase in hydrogen content in the fuel.

This subsection takes into account the same three fuels (with the addition of the Extreme Jet to compare with the previous trends observed in III.2.2) but another CAST set point has been selected at (84/30/3) to compare to previous experimental works. This operating point is more adapted for our study regarding the stability of the flame for these fuels: no second flame formation (variation of the flame stability with CAST changes - III.1.2.2).

III.2.3.1 Black Carbon Mass Concentration

Figure III-18 presents the LII measurements for BC mass concentration with the (84/30/3) CAST operating point. The trend is similar compared to the previous operating point (105/30/2) in III.2.2.1 and in (Berthier, 2022): a reduction of the mass concentration is induced by the reduction of aromatics and at the same time by sulphur compounds in fuel composition. Extreme Jet fuel generates the most emissions (21% more than reference Jet A-1) and the sustainable one, i.e. AtJ, generates the least emissions (64.5% less than reference Jet A-1). Being a mix of Jet A-1 and AtJ, the mix E5 fuel presents a BC mass concentration in the middle: 51% less than the Jet A-1 and 40% more than the AtJ. Table III-8 summarises mass concentrations measured by LII for the different fuels with the corresponding dilution factors.

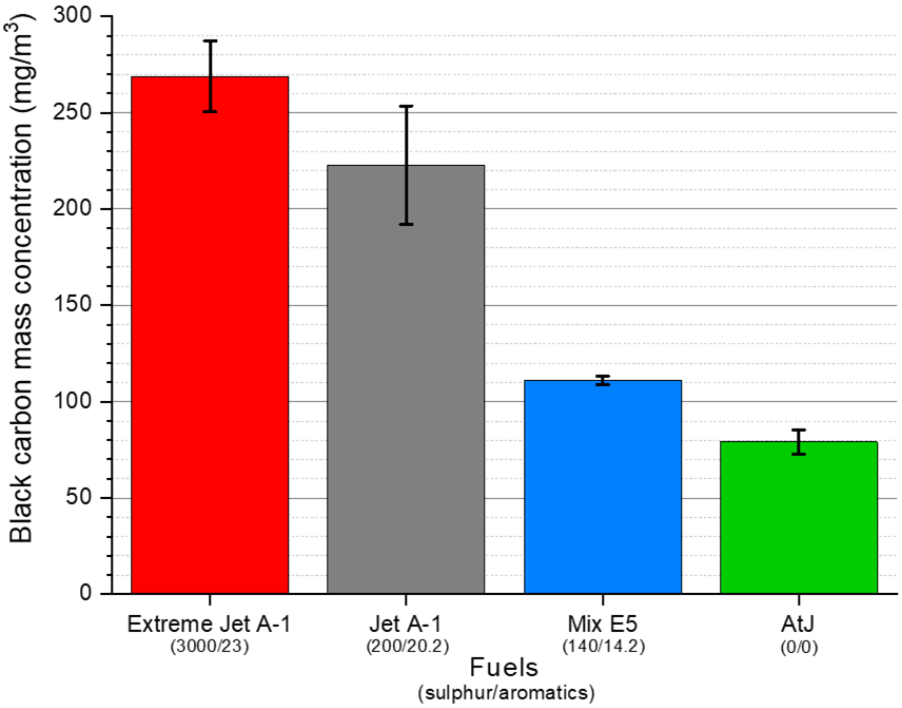

Figure III-18: Black carbon mass concentration comparison for conventional and sustainable fuels. The operating CAST set point is (84/30/3). The aromatics and sulphur contents in fuel composition decrease from left to right.

Fuel	Black carbon mass concentration (mg/m^3) corrected by dilution	Standard deviation (mg/m^3) corrected by dilution	FPS dilution correction	DEED dilution correction
Extreme Jet	268.94	18.42	19	87
Jet A-1	222.84	30.71	15	79
Mix E5	111.08	2.13		87
AtJ	79.04	6.26		91

Table III-8: Black carbon mass concentration measured by LII for conventional and sustainable fuels. The CAST operating point is (84/30/3). BC mass concentration has been already corrected by corresponding dilution factors. FPS diluter has been not used for Mix E5 and AtJ tests and thus only DEED dilution factors are considered for these cases.

As regarding the Extreme Jet case, we can see that (84/30/3) operating point generates more soot particles (Table III-8: 268.94 mg/m^3 taken into account dilution correction) than for the previous (105/30/2) set point (Table III-4: 94.4 mg/m^3, taken into account the correction by 10 for the DI-1000). It is not expected due to the reduction of the fuel flow and oxidation rate impacting the combustion in the present case: for (84/30/3), we should have less particles in terms of mass and number concentrations. To give an idea, Figure III-19 presents an example of the evolution of the BC mass concentration and particle number concentration depending on the CAST set points selected (points numbered from 1 to 14 at the top of the figure – log scales). Over time, both measurements are reduced with the decrease of the fuel flow when the oxidation rate is constant (from point 1 to 7) and it shows that the (105/30/2) set point generates the most particles. Between the point 8 and 14 on the Figure III-19, the oxidation rate was changed and the fuel flow was kept constant. When the oxidation rate is modified from 30/2 to 30/3 (respectively point 7 and point 8), the BC mass concentration as well as the particle number are reduced. It means that with reduction of fuel flow and oxidation rate, the CAST should generate less soot particles.

The explanation about this BC mass concentration difference can come from the delay (8 months) between the two experiments using the (105/30/2) and (84/30/3) set points. Some

differences can affect the emissions such as the burner fouling (III.1.1) or the atmospheric conditions. In addition, the dilution system has been changed. For the (105/30/2) set point, it has been mentioned that results have been expressed taking (CAST-DI-1000) together and applying only DEED correction. The theoretical value of the DI-1000 dilution factor is 10 (cf. II.2.1.1.1) but it has not been measured during the tests to confirm that. Some changes are possible in DI-1000 dilution, especially when it starts to get blocked. Furthermore, for the second (84/30/3) set point, a FPS diluter was combined with the DEED. We already explained (II.2.1.2) that the DEED dilution factor is variable and needs to be controlled frequently. The FPS diluter also presents some variations over the time.

So a quantitative comparison with previous tests is difficult due to the evolution of CAST behaviour over the time and the modification of the set-up. But a qualitative comparison is still possible. In regards to the previous results in (Berthier, 2022) using the (105/30/2) set point, the trend observed for the reduction of BC mass concentration linked to aromatics contents remains the same.

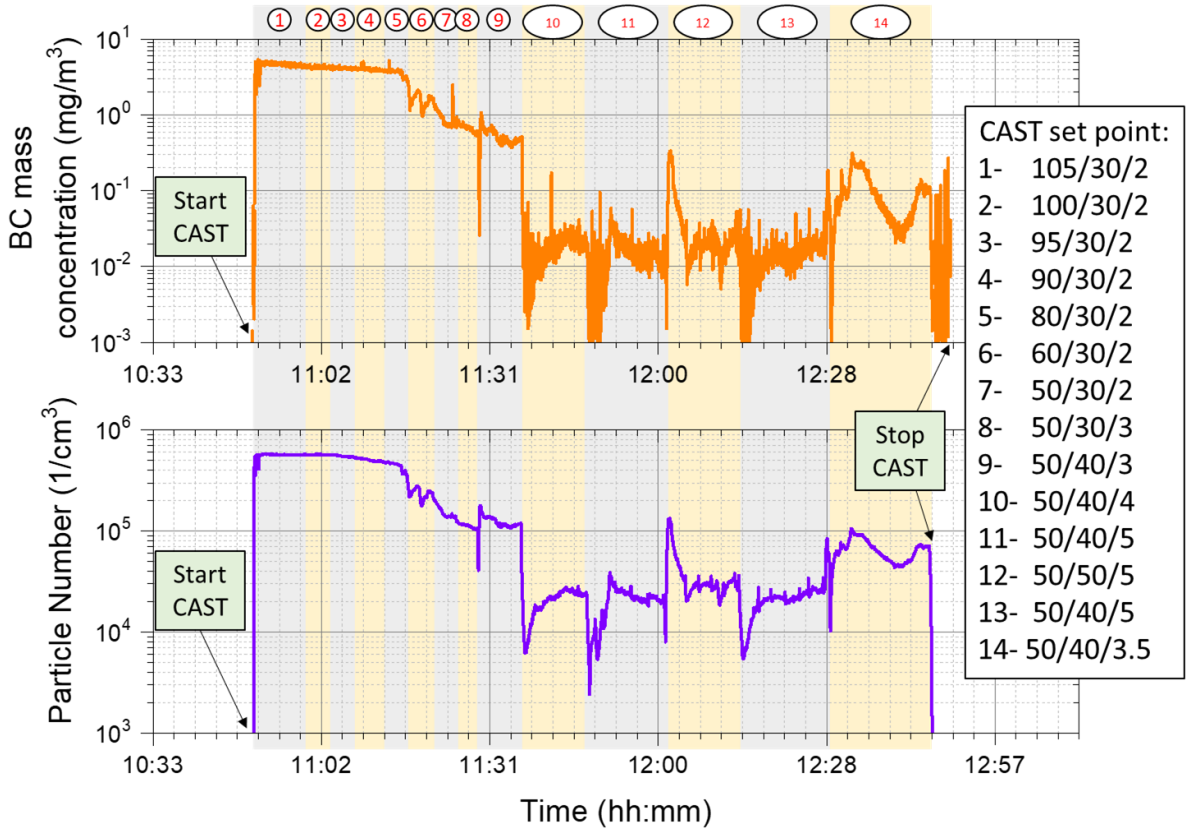

Figure III-19: Example of the impact of fuel flow reduction on the BC mass concentration (top - measured by LII) and on the particle number concentration (bottom - measured by CPC) for a given fuel (High Sulphur Jet) over the time. Log scales.

III.2.3.2 Particle Number Concentration

Similar results as for BC mass concentration are observed on Figure III-20 for the particle number concentration, except for the blend fuel case. Indeed, highest emissions are observed for the Extreme Jet fuel (18% more than Jet A-1) and lowest for the AtJ (27% less than Jet A-1), but the mix E5 generates 7.7% more particles than the Jet A-1. It is non-intuitive, mix E5 being a blend of Jet A-1 and AtJ, and it contradicts the observations in the literature. The same phenomenon has been seen in (Berthier, 2022) with the (105/30/2) set point using the same fuels and same burner. This higher amount of particles formed for Mix E5 case compared to Jet A1 case can be explained by the beginning of the ignition of a second flame of kerosene. It leads to the formation of extra-particles at small sizes. More details are presented in III.2.3.4. It is without impact for mass concentration measurement (following the trend

compared to the other fuel tested) but it affects the particle number concentration measurement. This increase is similar to the ones observed for cases analysed in previous study (cf.III.2.2.3). This warrants further exploration, since other mixed fuels in previous studies have behaved more in line with expectations.

Table III-9 summarises particle number concentrations measured by CPC for the different fuels. The particle number concentration is lower than the one measured for the (105/30/2) operating point in (Berthier, 2022). In relation with the BC mass concentration, we can see that the (84/30/3) operating point generates less particles than the (105/30/2) operating point. It means that particles are bigger in terms of size to explain the higher BC mass concentration values that is confirmed by the study of particle size distributions for the different fuels tested (cf. III.2.3.4).

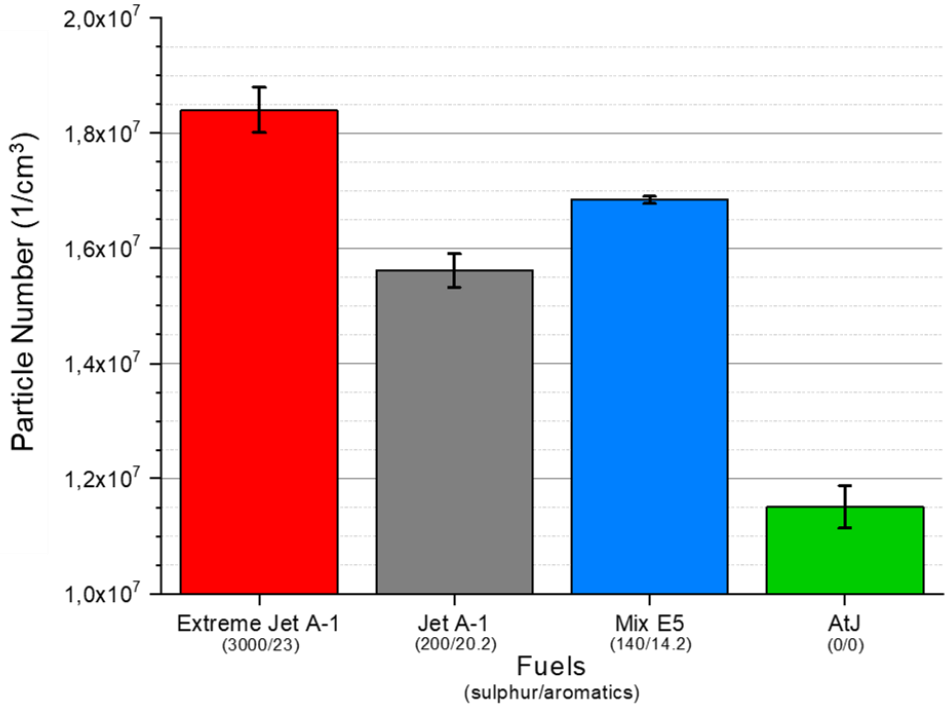

Figure III-20: Particle number concentration comparison for conventional and sustainable fuels (CPC data). The operating CAST set point is (84/30/3). The aromatics and sulphur contents in fuel composition decrease from left to right.

Fuel	Particle number concentration (1/cm^3) corrected by dilution	Standard deviation (1/cm^3) corrected by dilution	FPS dilution factor	DEED dilution factor
Extreme Jet	1.84 x10^7	3.93 x10^5	19	87
Jet A-1	1.56 x10^7	2.92 x10^5	15	79
Mix E5	1.68 x10^7	0.64 x10^5		87
AtJ	1.15 x10^7	3.70 x10^5		91

Table III-9: Particle number concentration for conventional and sustainable fuels for CAST operating point set at (84/30/3).

III.2.3.3 Aromatic and hydrogen contents

To obtain a better overview and to compare operating points, the relation between the percentage reduction of mass and number concentrations with hydrogen content is studied in Figure III-21. In this representation, results of this work for set point (84/30/3) are compared to the ones of (Berthier, 2022) for set point (105/30/2), taking into account three different fuels: the reference Jet A-1, the mix E5 and the AtJ.

The top of Figure III-21 presents the percentage reduction of BC mass concentration (on the left - based on reference Jet A-1 for the reduction) and particle number concentration (on the right - based on mixE5 fuel for the reduction) depending on the aromatics content. We can see that in both cases, the decrease of the aromatics content tends to increase the percentage reduction of BC mass concentration and of particle number concentration. It means that particles generated are less numerous and less heavier for fuels containing less aromatic contents.

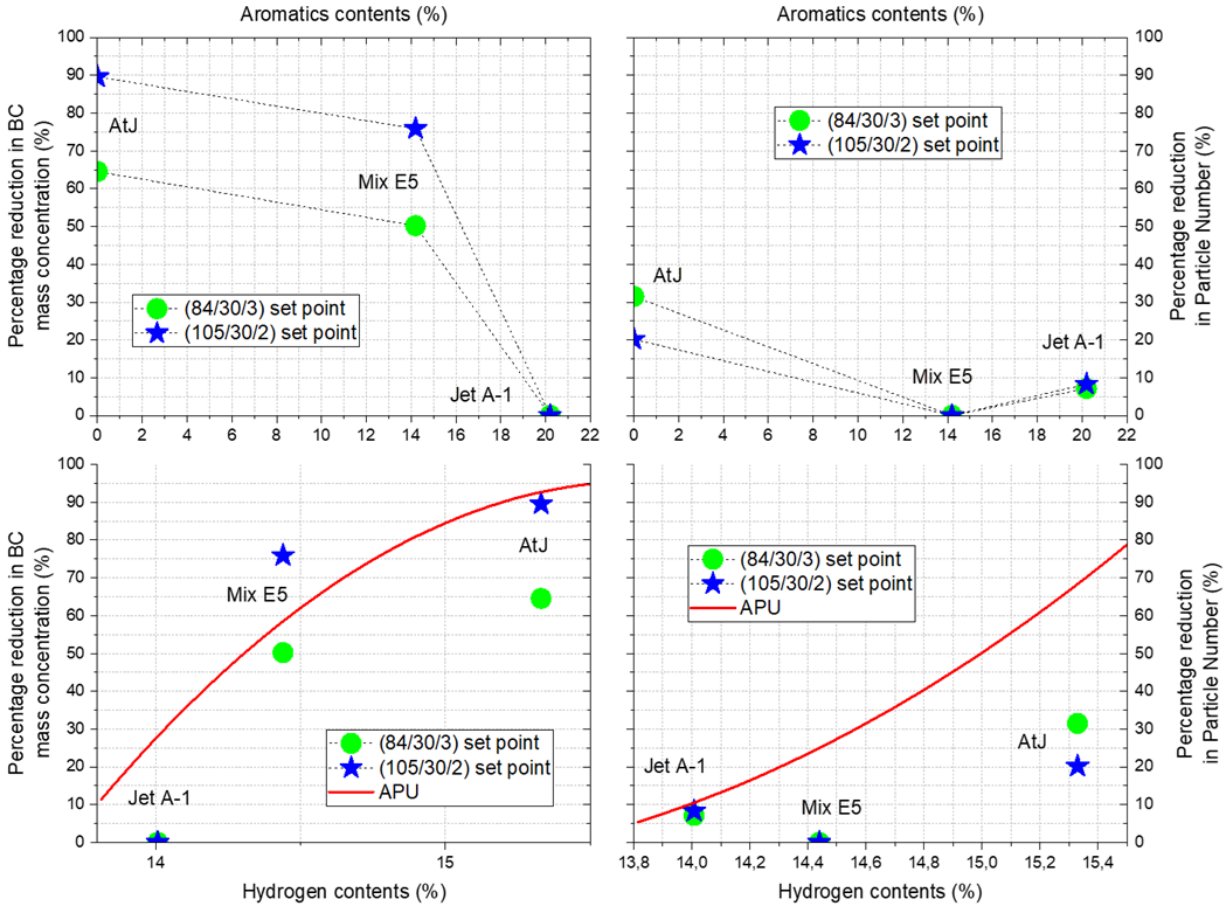

Figure III-21: Percentage reduction of BC mass concentration (left) and Particle number concentration (right) as function of aromatic contents (top) and hydrogen contents (bottom) for the reference fuel Jet A-1, the Mix E5 blend fuel and the AtJ. The (105/30/2) measurements come from a previous study (Berthier, 2022) and the (84/30/3) measurements have been obtained during the UNREAL experimental campaign for this work. On both bottom representations, data are compared to the trend (in red) established on an Auxiliary Power Unit (APU) in unloaded condition (Lobo et al., 2015).

To compare to the literature, a second approach has been done using the link between aromatic and hydrogen contents for each fuel. Hydrogen content (H/C ratio) looks like a better parameter to study the behaviour of nvPM emissions as a function of fuel composition (Lobo et al., 2011). The bottom part of Figure III-21 presents the percentage reduction of BC mass concentration (on the left - based on reference Jet A-1 for the reduction) and particle number (on the right - based on mixE5 fuel for the reduction) depending on these hydrogen contents. This representation is compared to the trend curve (in red) established on an Auxiliary Power Unit (APU) in no-load condition (Lobo et al., 2015). For BC mass concentration, a maximum emission is observed for the lowest hydrogen content and a minimum emission for the highest hydrogen content. It is comparable to the trend obtained by (Lobo et al., 2015) in terms of mass. For the particle number concentration, the APU curve shows a reduction of the number concentration with the increase of H/C ratio. For the tests of this study, the particle number concentration tends also to decrease with the increase of hydrogen content, but the mixE5 fuel presents a small variation as mentioned before compared to the reference curve. Assuming

that the behaviour of the CAST follows the one of the APU concerning the particle number concentration depending on fuel composition, uncertainty of measurement comes from Mix E5 test and not from Jet A-1 test in terms of particle number.

III.2.3.4 Particle Size Distribution

In addition to BC mass concentration and particle number concentration, the size distribution of particles for each fuel has been measured with the SMPS+C (at least two acquisitions). For the set point (84/30/3), all fuels present a mono-modal distribution with a main mode centred at 130 nm (Figure III-22-a). A small amount of the particles is recorded for Mix E5 case between 20-30 nm due to the start of second kerosene flame ignition at the end of the test. As for the particle number concentration, the decrease of aromatic content in fuel composition involves a decrease of the particle number concentration. However in correlation with CPC measurements, it can be noted the same behaviour for mix E5 and Jet A-1: more particles detected for blend fuel.

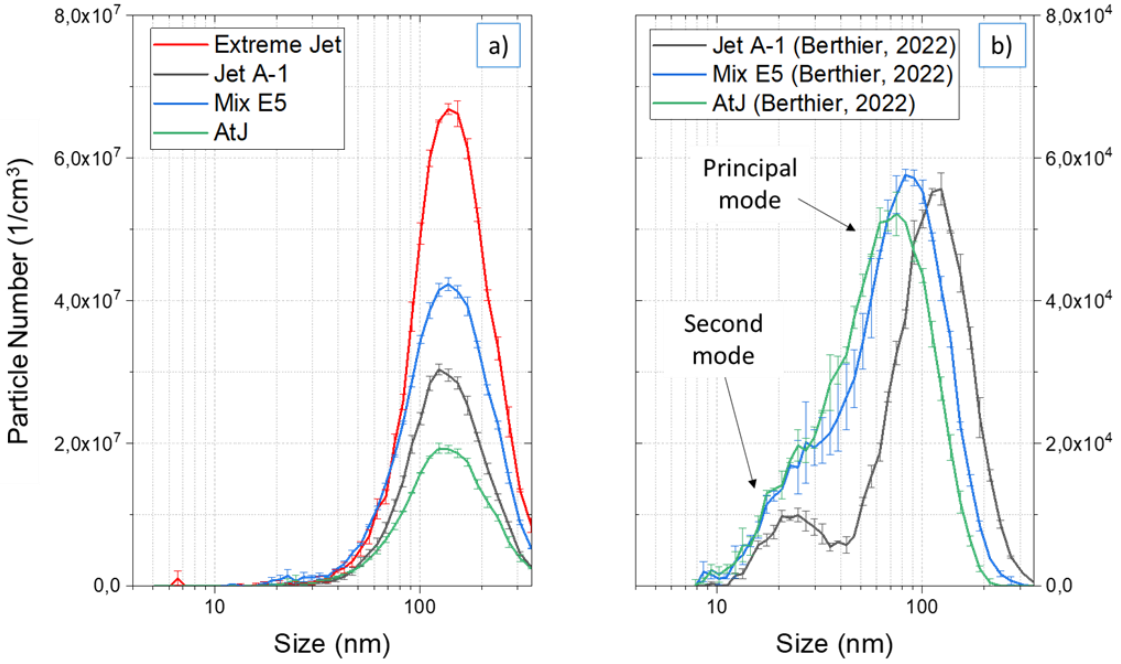

Figure III-22: Size distribution for different fuels at liquid CAST burner exhaust. The figure a) corresponds to the (84/30/3) operating point and the figure b) to the (105/30/2) operating point from (Berthier, 2022). FPS and DEED corrections applied.

The size of the particles for (84/30/3) set point is higher compared to the case of (105/30/2) set point in (Berthier, 2022), where the main mode was centred at 110 nm for the Jet A-1, 83 nm for the Mix E5 and 75 nm for the AtJ (Figure III-22-b). It should be noted that in (Berthier, 2022), the size distribution is completed by a second mode at 25 nm due to the presence of a second flame (propane flame). It explains the decrease of the particle number concentration and also of the particle size compared to set point (84/30/3). Both operating points present a similar trend for the different fuels regarding the reduction of particle number concentration. However, due to the variation of CAST over the time and the difference of set-up, a quantitative comparison is not possible. The (84/30/3) set point is more adapted in this study to synthetic fuels in terms of stability and reproducibility. Indeed, the second kerosene flame inside the burner is not present for this set point compared to the one in (Berthier, 2022).

GMD and GSD are represented on Figure III-23 and summarised in Table III-10 for the set point (84/30/3) depending on the fuels. The higher GMD is obtained for the Extreme Jet case (137 nm) and the lowest for AtJ (128nm), corresponding to the CPC and LII measurements presented above. The

GMD is comparable for Mix E5 and Jet A-1 fuels (1nm of difference). The particle number concentration is higher for the blend fuel, and the BC mass concentration is higher for the reference fuel.

The GMD decreases and the GSD increases with the increase of hydrogen content in the fuel (i.e. the decrease of aromatic content from the left to the right on Figure III-23). The combination of GMD and GSD variations means that the particles become smaller for the combustion of a sustainable fuel and they are less grouped around their principal mode than for the other fuels. The GMD reduction using an alternative fuel is coherent with previous studies (Brem et al., 2015; Durdina et al., 2019; Jonsdottir et al., 2019; Moore et al., 2014; Speth et al., 2015).

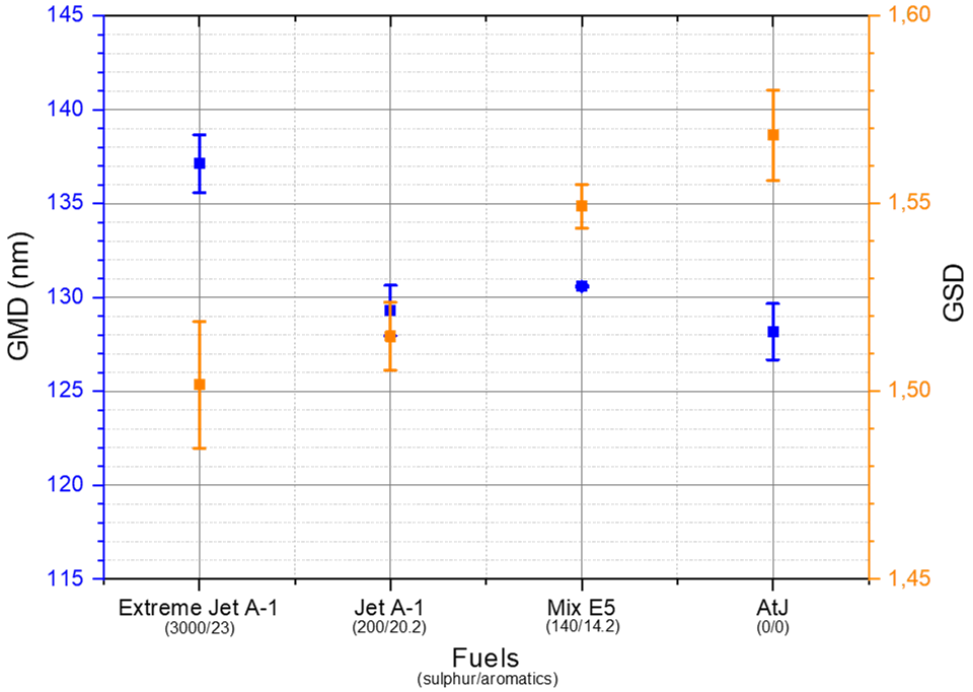

Figure III-23: GMD and GSD for conventional and sustainable fuels. The operating CAST set point is (84/30/3). The aromatics and sulphur contents in fuel composition decrease from left to right.

Fuel	GMD (nm)	Standard Deviation (nm)	GSD	Standard deviation
Extreme Jet	137,1	1,5	1,50	0,02
Jet A-1	129,3	1,3	1,52	0,01
Mix E5	130,6	0,1	1,55	0,01
AtJ	128,2	1,5	1,57	0,01

Table III-10: GMD and GSD measured by SMPS for conventional and sustainable fuels. The operating CAST set point is (84/30/3).

III.2.4 Chemical analysis of emissions depending on fuel composition

To better understand the impact of fuel composition and complete the previous study, some samples have been collected at CAST burner exhaust for different fuels to analyse the chemical composition of these emissions. The system is composed of a sample holder containing 2 quartz fibre filters to dissociate the two phases of the emissions (particles and gas) and has been already described (cf. II.2.2.3.1). The CAST operating point was set at 105 µL/min for kerosene, 30 mL/min for propane and 2 L/min for oxidation flows. A short sampling time of 30s at 2.2 L/min is sufficient at CAST outlet

to ensure enough deposit at the surface of the filter. Thereafter off-line mass spectrometry analysis performed in Lille (PhLAM laboratory – cf. II.2.2.3.2) provides an access to the chemical composition of the emissions.

The Figure III-24 presents the filters collected during the experimental UNREAL campaign. These samples have been obtained at CAST burner outlet and correspond to the particle phase of the emissions (majority of soot). One of the first observations is the difference of deposit on the filter surface depending on the fuel (filter initially white) compared to the blank filter of reference. Sustainable fuels (i.e. AtJ) generate less soot than the other ones, as expected in the literature (Corporan et al., 2005, 2007, 2011; DeWitt et al., 2008; Timko et al., 2011, 2011). The Extreme Jet fuel case presents the most deposit (black layer: 0,125mg of deposit on the surface) and the filter for the blend mixE5 an intermediate deposit (brown layer) as expected due to their compositions and regarding results obtained previously concerning the mass and the number concentration (III.2.3).

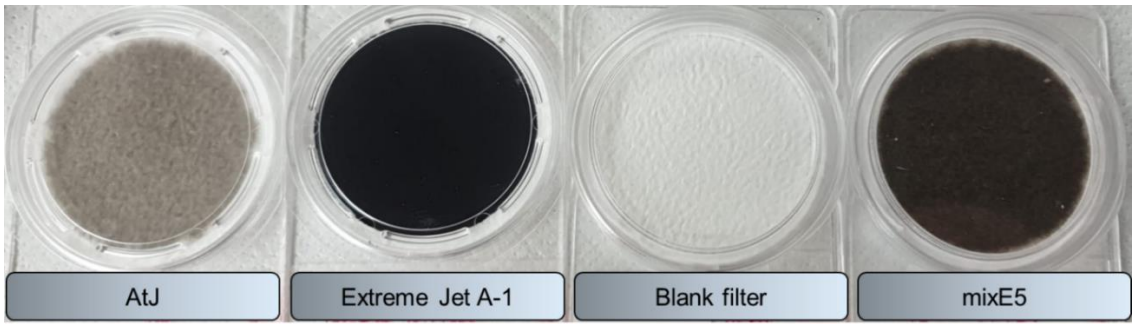

Figure III-24: Example of samples collected at CAST outlet (the front filter) for different fuels to study the particle phase of the emissions. The operating point has been set at (105/30/2) for a sampling time of 30s at 2.2 L/min.

To compare the influence of sulphur and aromatic compounds present in kerosene, an analysis of the chemical composition of emissions from some fuels combustion is studied. Results presented in the following subsections are focused on the Extreme Jet (the doped fuel with 3000 ppm of sulphur and 23% of aromatic contents), the Low Jet (the Jet with few sulphur and aromatic contents) and the AtJ filters.

III.2.4.1 Mass spectra overview

The off-line mass spectrometry instrument used for the analysis of the chemical composition of emissions is a Time of Flight Secondary Ions Mass Spectrometer (ToF-SIMS – cf. II.2.2.3.2). This device presents a high sensitivity and a high mass resolution (~10^4 m/Δm) for low sample roughness (Irimiea et al., 2018). The instrument operates in static mode to analyse the deposit layer on the sample surface in 3 Regions of Interests (ROI) per sample (500 x 500µm^2) using Bismuth ions (25 keV) as primary ions. The analysis of the particulate (front filter) and gaseous (back filter) phases are performed separately with the same protocol using positive and negative ions. Mass spectra obtained present a high fragmentation due to the impact of B_i^{3+} ions on the surface of the filter.

Figure III-25 regroups an example of mass spectra obtained for 3 different fuels: Extreme Jet (b), Low jet (c) and AtJ (d) cases. For each test, the mass spectrum on the left corresponds to the particle phase (front filter – positive ions) and the mass spectrum on the right represents the gas phase (back filter – negative ions) of the emissions. Furthermore, to smooth out the variations linked to the measurements such as the heterogeneity of the filter surface or the variation of the laser fluence, each mass spectrum corresponds to the average of 3 repetitions. Each spectrum has been properly aligned and calibrated before that.

In addition to the samples collected at CAST outlet, a pair of (blank) filters has been exposed to the ambient air in the laboratory during the tests to ensure that in future analyses the species detected by this technique do not come from contamination. In the blank case (Figure III-25-a-2), it should be

noticed the presence of Si compounds (for example Si^+ at 27.977 m/z or Si_2^+ at 55.954 m/z) coming from the filter surface. Indeed, the quartz fibre filter is mainly composed of silicon and as there is no deposit on the surface, incident bismuth ions desorb the first layers at the surface of the blank filter. Furthermore, carbon clusters (C_2^- at 24 m/z) and organic carbon compounds (C_2H^- at 25.008 m/z) are detectable on the blank back filter due to the desorption of the black carbon layer on the surface.

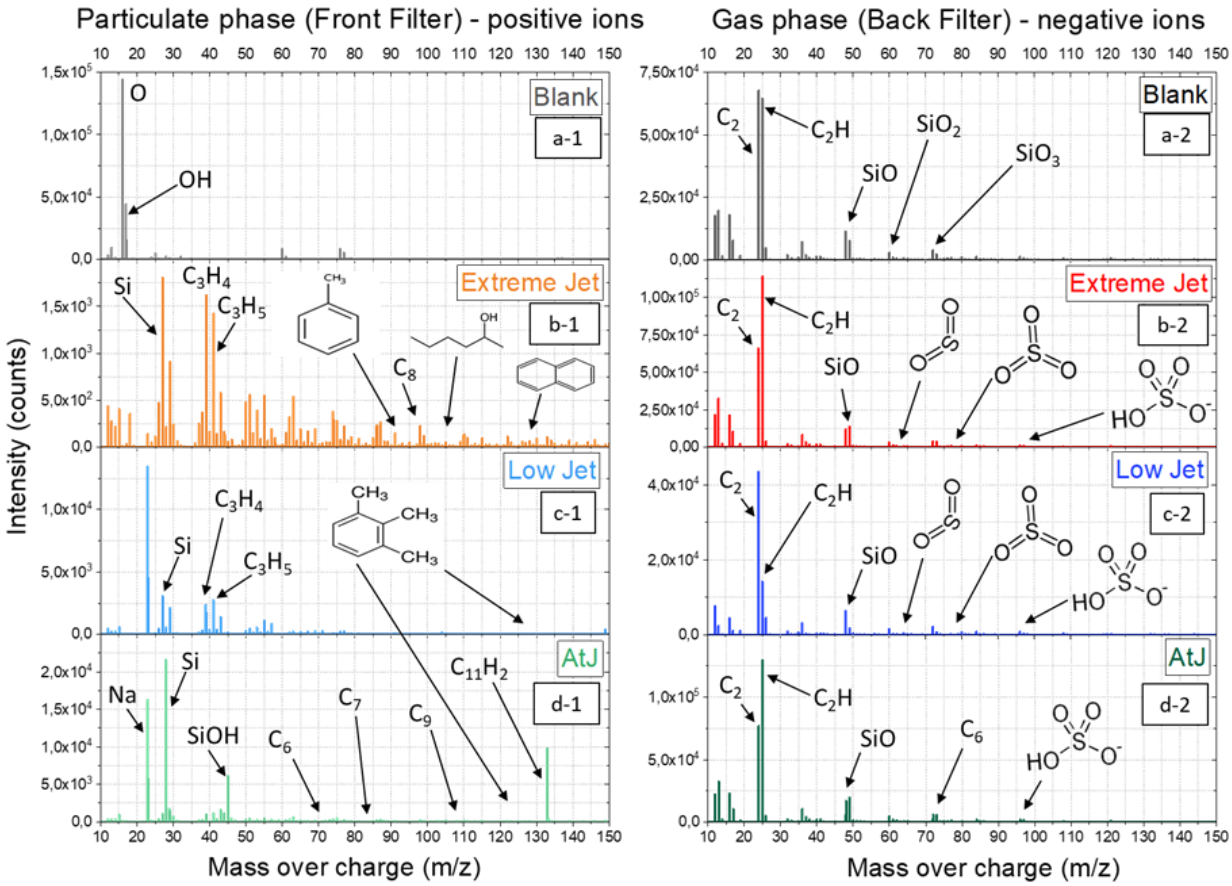

Figure III-25: SIMS mass spectra for CAST tests. The case a) corresponds to the blank filters, the case b) to the Extreme Jet filters, the case c) to the Low Jet filters and the case d) to the AtJ filters. For each case, the particle phase corresponds to the front filter (lighter colour – cases 1) and the gas phase corresponds to the back filter (darker colour – cases 2). Positive ions and negative ions analysis are used respectively for front filter and back filter to bring to light PAH and sulphur compounds.

The other filters collected at CAST outlet for 3 different fuels have been analysed in the same way. Due to high fragmentation, mass spectra obtained (Figure III-25-b, c and d) present accurate masses mainly regrouped between 12 and 120 m/z. Without taking into account Silicon found on blank filters, some other compounds can be identified. For all cases, on the front filter (particle phase) most of the signals recorded are related to carbon clusters (C_6^+ at 72 m/z or C_8^+ at 96 m/z) and hydrocarbons including VOCs and PAHs (benzene at 78.05 m/z, toluene at 92.06 m/z or pyrene at 202.08 m/z). Concerning the back filter (gas phase) some accurate masses are linked to black carbon deposit on filter surface and some other to sulphur compounds (SO_2^- at 63.96 m/z or HSO_4^- at 96.96 m/z). It should be noted that mass spectra cannot be compared directly in terms of intensity in Figure III-25. The intensity of each spectrum is relative to the respective test performed. To study and to identify the chemical composition of the species found at the sample surface, each filter has been analysed separately and normalised respectively by the total account of all accurate masses (cf. III.2.4.3). Thereafter, all mass spectra are expressed as “Intensity/total ion count” to compare fuels.

A particular attention is given to aromatic compounds (Figure III-26-a and -b), known as soot precursors, to VOCs (Figure III-26-c) and sulphur molecules (Figure III-26-d) due to their role in the vPM

formation process. Signals related to PAHs are recorded for the combustion of the three fuels. In the case of the analysis of the particulate phase, the most significant signals are thus related to naphthalene ($C_{10}H_8^+$ at 128.06 m/z, Figure III-26-a), acenaphthylene ($C_{12}H_8^+$ at 152.06 m/z), fluorene ($C_{13}H_{10}^+$ at 166.08 m/z), anthracene ($C_{14}H_{10}^+$ at 178.08 m/z), phenanthrene ($C_{14}H_{10}^+$ at 178.08 m/z) and pyrene ($C_{16}H_{10}^+$ at 202 m/z, Figure III-26-b). An initial visualisation of these spectra suggests a relatively similar chemical composition for the three filters, with a trend toward the formation of less volatile aromatics in the case of the Low Jet fuel and the AtJ (in correlation with preliminary observations in Ngo 2019). The molecules that have been found in the emissions of these fuels are mainly PAHs with 3 and 4 aromatic rings (anthracene or pyrene) as well as hydrocarbon molecules resulting from their fragmentation ($C_{16}H_{11}^+$ at 203.08 m/z, Figure III-26-b). On the surface of the filter collected in the case of Extreme Jet, molecules with a smaller number of carbons ($C_6H_n^+$; $C_8H_n^+$) than in the case of AtJ have also been recorded.

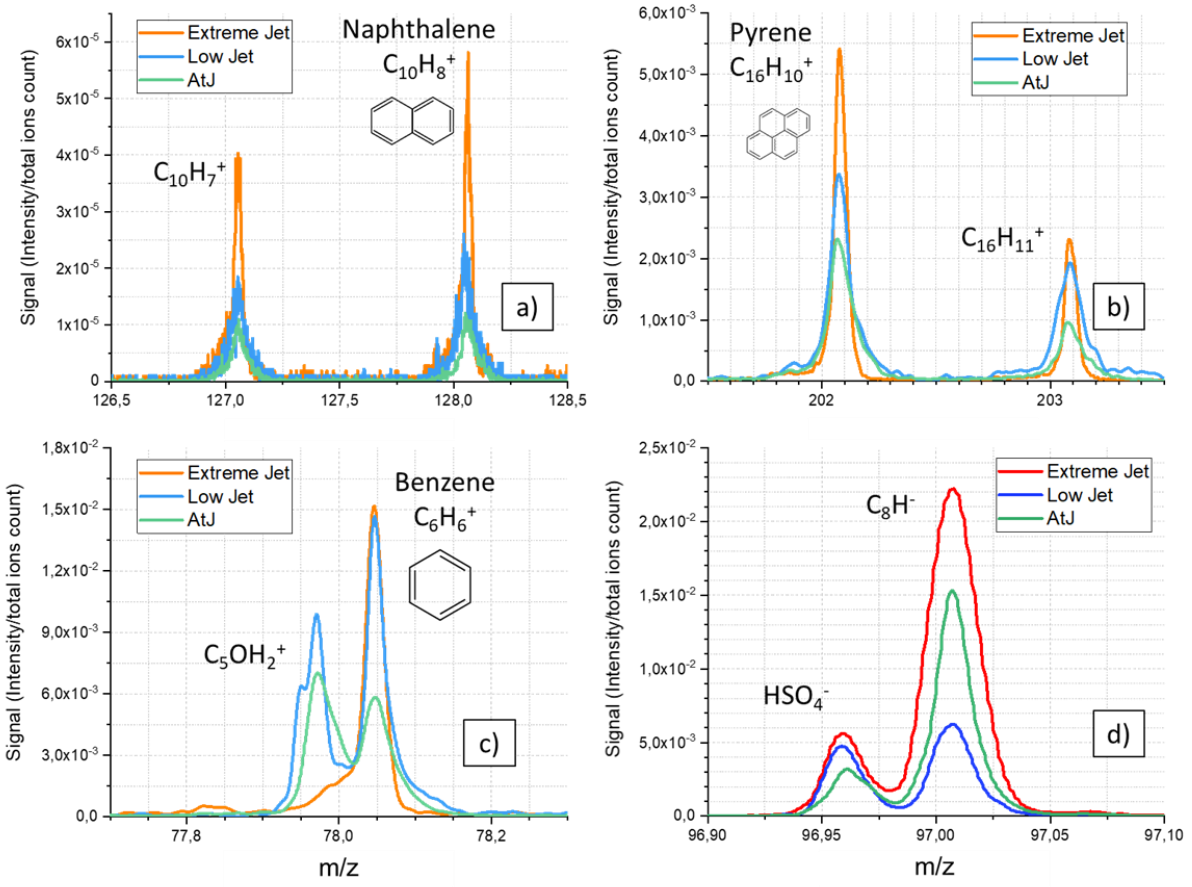

Figure III-26: Example of compounds identified on sample surface for three different fuels after SIMS analysis. The case a) and b) correspond to PAH detection (respectively benzene and pyrene) in the particulate phase (front filter). The case c) and d) correspond to sulphur detection (respectively SO_4^- and HSO_4^-) in the gas phase (back filter). Each spectrum has been normalised by the total ion count to be compared.

Concerning the sulphur compounds, some signals have been recorded as for example the one corresponding to hydrogen sulphate HSO_4^- (Figure III-26-d). The Extreme Jet presents the signal with the higher intensity as expected due to its composition compared to Low Jet and AtJ. However, the difference is not huge between Extreme Jet and Low Jet (15%). Furthermore, sulphur compounds have been found in the emissions resulting from the combustion of the AtJ. The presence of sulphur compounds on this spectrum is related to the CAST burner. Indeed, the contamination is possible by

the use of another fuel on a previous test and there can be some deposit at the CAST outlet and on the line (even after cleaning fuel tank and lines).

After this first overview of the mass spectra, the next step is the identification of all accurate masses before comparing the compounds recorded depending on the fuel used.

III.2.4.2 Identification of chemical species on filters

As explained in II.2.2.3.3, it is possible to use the mass defect (Δm) of a chemical compound to identify the molecules detected on SIMS spectra. Mass defects can be graphically represented depending on the m/z ratio to obtain a visual separation and facilitate the assignment of molecular formulas to each accurate mass. These mass defect plots make it possible to identify the majority of signals, related to PAHs and their fragments (McLafferty & Turecek, 1994). For example, all C_nH_m are on the same lines for a given n with a positive Δm; Si and sulphur compounds have a negative Δm (Duca et al., 2019).

Figure III-27 presents an example of mass defect plot gathering all accurate masses recorded for the 3 fuels (Extreme Jet, Low Jet and AtJ) after the study of the back filter (corresponding to the gas phase) with positive ions (left) and negative ions (right). To identify as many significant accurate masses as possible in the mass spectra, all signals with a signal to noise ratio (S/N) greater than 3 were selected. The previous overview shows that spectra suggest a relatively similar chemical composition for the three filters. In this way, it is easier to identify at first all molecules detected on the three filters without distinction before moving on the comparison. A colour code has been used to regroup different classes of compounds: in black for the hydrocarbons (carbon clusters and organic carbon), in red for the Si compounds, in blue for the sulphur molecules and in green for the unidentified components.

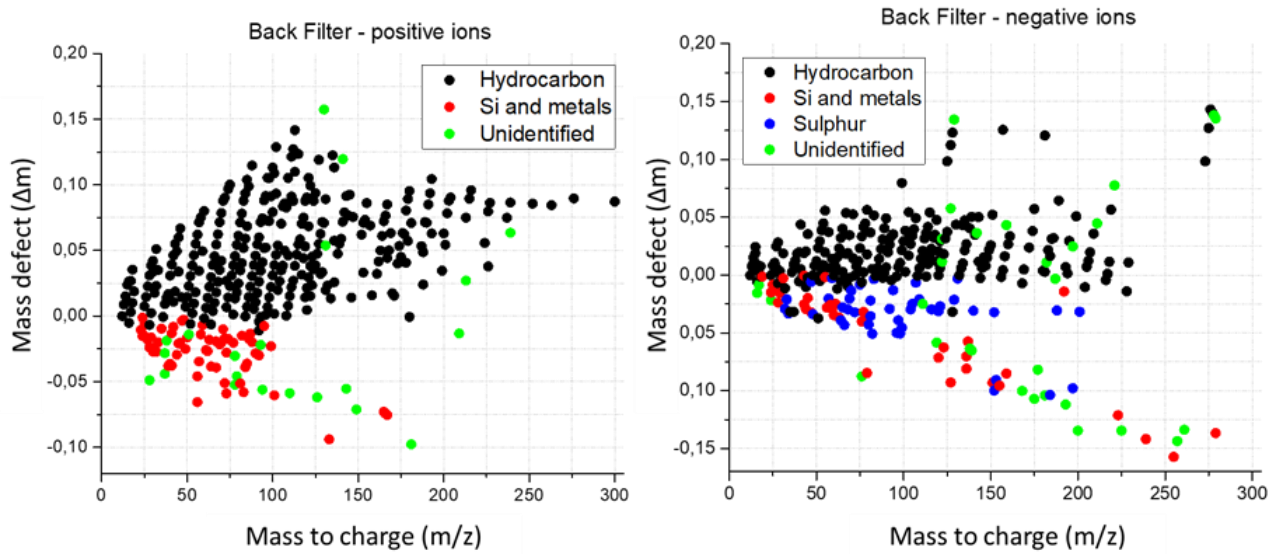

Figure III-27: Mass defect plot study to identify components on UNREAL filter after SIMS analysis. Both graphs correspond to the gas phase of the emissions collected at CAST exhaust (back filter): on the left for positive ions and on the right for the negative ions. Compounds identification is indicated by the colour code: black for hydrocarbon (carbon cluster and organic carbon), red for the Si from the filter matrix, blue for sulphur compounds and green for unidentified molecules. Only mono-charged ions are considered here (z=1).

The first observation is the high amount of hydrocarbon compounds (in black) for a positive mass defect. Beyond the $C_nH_m^+$ molecules, mass defect plots identified silicon components that are the result of the filter surface desorption (blank), i.e. from the matrix of the filter. Sulphur compounds have been also detected in negative mode in the gas phase with the negative mass defect of sulphur (Δm = -0.0292u) shown by a graphical offset compared to hydrocarbon molecules.

The $C_nH_m^+$ hydrocarbon molecules are found in the gas phase or on the surface of soot particles. All the hydrocarbons identified are summarised in Figure III-28 (all fuels regrouped) according to the number of hydrogen (x-axis) and of carbon atoms (y-axis) for the particles phase case on the left and the gas phase case on the right. A colour code has been used to specify if molecules have been detected using the positive ions mode (blue/purple), the negative one (green) or with both (orange/red).

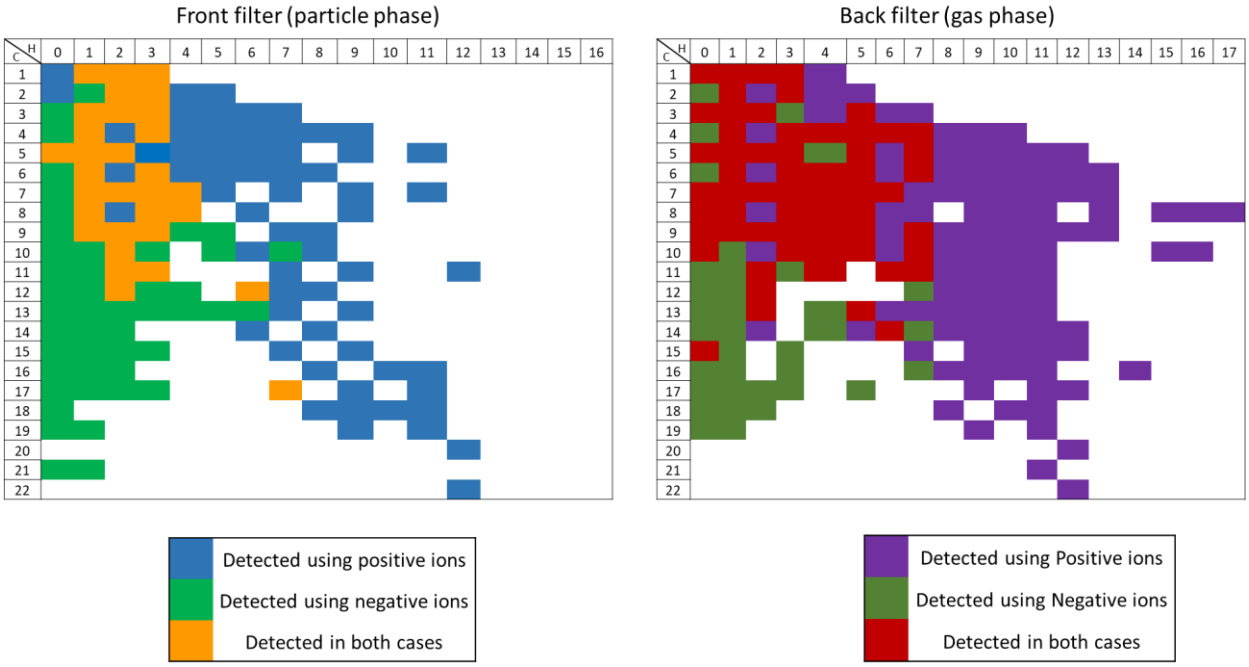

Figure III-28: Identification of hydrocarbons detected in SIMS for the particle phase (left) and gas phase (right) of the emissions from CAST burner. The separation is done between hydrocarbons detected in positive mode (blue/purple), in negative mode (green) or common to the both modes (yellow/red).

There are more molecules identified for the back filter case (Figure III-28- right) but it should be noted that as the SIMS method desorbs the surface of the filter, the ions recorded come from the emissions collected and also from the black carbon layer. We can also see that in the case of the front filter, a majority of hydrocarbons with few hydrogen atoms are detected in negative mode. Hydrocarbons with higher amounts of hydrogen atoms are more visible in the positive mode. The same trend is observable on the back filter. As mentioned before, the objective is to identify the PAHs. The distribution of PAHs on the collected filters depends on their volatility, which is related to the number of C atoms and their number of aromatic rings. Indeed, the compounds formed by one or two aromatic rings being the most volatile are found in the gas phase of the emissions (i.e. on the back filter). Aromatic compounds with more than two aromatic rings are found in the front filter (i.e. particulate phase). PAHs with two aromatic rings are defined as semi-volatile and are found on both filters. This classification has been defined by (Bari et al., 2010) and validated in (L. D. Ngo et al., 2020).

To get a significant evaluation of the impact of fuel composition on emissions, a (semi-) quantitative approach is proposed in the next subsection focused on the sulphur compounds and PAHs.

III.2.4.3 Semi-quantitative comparison of chemical species detected

Once most of the accurate masses on the mass spectra have been identified, the objective has been to perform a semi-quantitative study to better understand and interpret the presence of PAHs and sulphur compounds depending on the fuel composition.

The main part of the molecules identified are carbon clusters and organic carbon (taken into account VOCs and PAHs). Some sulphur compounds have also been recorded. A list (cf. Annex G) of different PAHs, VOCs and sulphur compounds has been used to select some specific compounds and to compare the 3 fuels based on a semi-quantitative approach (I. Ortega, Delhaye, Ouf, et al., 2016). In terms of PAH, it corresponds to the list of 16 PAHs defined in Hussar et al. (2012) and in Samburova et al. (2017). Concerning the sulphur compounds, some molecules can be relevant such as SO_2 (for numerical modelling) or H_2SO_4 (implication in particle formation).

Figure III-29 summarises the results of the quantitative comparison between Extreme Jet, Low jet and AtJ fuels. Three distinct classes are presented: Carbon clusters, Organics Carbon (hydrocarbons) and Sulphur compounds. Based on the list in Annex G, the sum of the different compounds detected and identified is done for each fuel and each category. The separation between front filter FF (particulate phase) and back filter BF (gas phase) is indicated using a colour code to specify the presence of compounds in the emissions. All the values have been normalised by the total ion count of each spectra to compare the relative intensity of each sum.

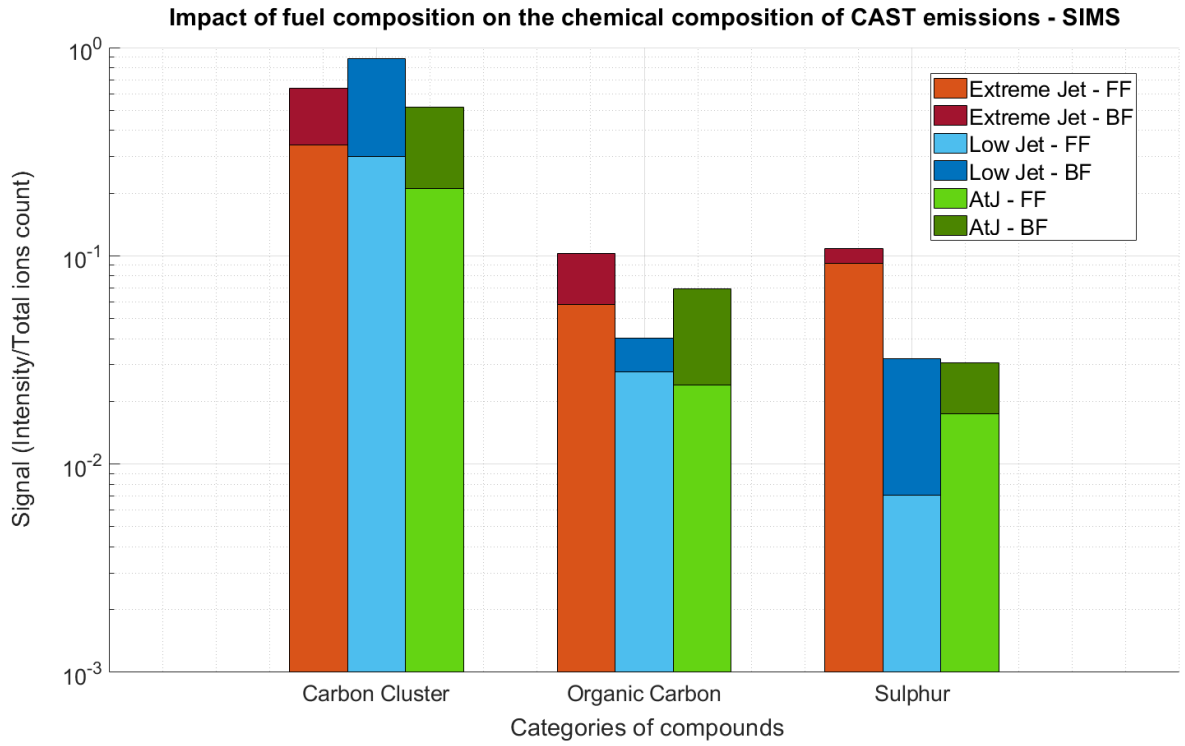

Figure III-29: Semi-quantitative comparison of the impact of fuel composition on the chemical composition of CAST emissions (from SIMS spectra). Carbon Clusters, Organic Carbon (PAHs and VOCs) and Sulphur compounds are studied for 3 different fuels: in orange for the Extreme Jet, in blue for the Low Jet and in green for the AtJ. The particulate phase (FF) and gas phase (BF) are distinguished by the nuance of colour. The signal has been normalised by the total ion count for each spectrum.

The first observation is that the amount of carbon clusters remains equivalent for the three cases but the Extreme Jet generates more organic and sulphur compounds than the other two fuels (log scale). It should be noted that the amount of organic carbon is higher for the AtJ compared to the Low Jet fuel and it is in particular due to the detection of PAHs in the gas phase (BF). It can be explained by the fact that less particles are generated by the AtJ fuel and the adsorption of gas phase is less pronounced for the SAF case. It means that a higher share of the gas phase Organic Carbon is transformed into particles for Low Jet fuel case.

Furthermore, it should be expected the absence of sulphur for the AtJ case but the amount is comparable to the Low Jet case (after normalisation) even if the sum of all sulphur compounds detected for the AtJ is smaller than for the Extreme Jet or Low Jet (less soot generated). As mentioned

before, it may be due to the contamination of the AtJ emissions in the fuel tank of the CAST burner or by residual deposit in the measurement lines, despite the cleaning process between each fuel's use. It has to be noted that there is some internal parts of the burner that cannot be dismounted so they cannot be cleaned. It can be representative of a test bench experiment using an aircraft engine. Indeed, engines usually do not run with 100% SAF fuel and only flights with mixed fuel (30% maximum of AtJ) were possible. Recently pure SAF has been used in a number of aircraft studies (Imperial College London, 2023; UNITED airlines SAF, 2021). In this studies fuel contamination has been an issue in delivering fuel to aircraft (supply line and tanker contamination). For example, some tests have been done using an engine with 100% SAF fuel on the test bench but the engine already worked with Jet A-1 fuel (AIRBUS SAF, 2021). Therefore, there is still some sulphur contamination.

To compare in detail the presence of PAHs, the Figure III-30 gives a repartition of these compounds depending on the fuels (less sulphur and aromatic contents in fuel composition from the left to the right). The Extreme Jet generates the most PAH (high amount of aromatic content in its composition) and the Low Jet the less (low aromatic content in its composition). PAHs are considered as the main precursors of soot particles, so it is possible to link the reduction of their formation during Low Jet combustion to the reduction of nvPM formation (Berthier, 2022). PAHs are mainly detected in the particle phase (front filter - Figure III-30). It means that for classical fuel, the PAHs are principally adsorbed on the soot surface. However, the AtJ presents nearly 3 times more PAH than for the Low Jet fuel. This SAF is supposed to generate less soot than classical fuels but the amount of PAHs is not negligible: PAHs are adsorbed on the soot surface (particulate phase) but are also in the gas phase more than for the other fuels. It is not only an adsorption process, but the soot particles grow from PAHs present in the gas phase, explaining that more particles are formed for Extreme Jet and Low Jet fuels compared to AtJ where PAHs stay in the gas phase.

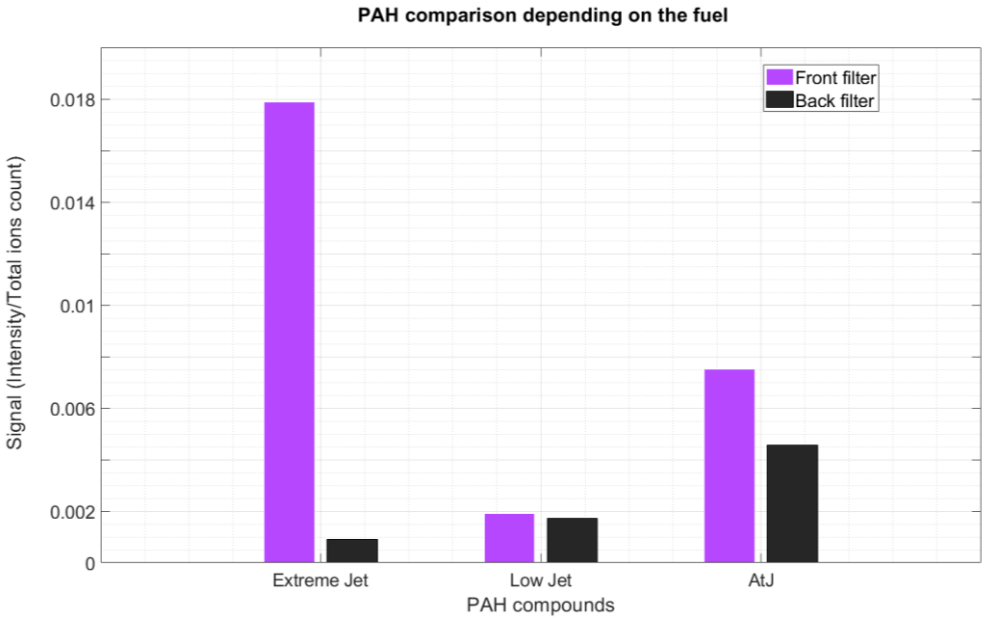

Figure III-30: Semi-quantitative comparison for 3 fuels detailed for PAH detection. The PAHs found in the particle phase correspond to the purple bar plot and in the gas phase to the black bar plot.

III.3 Conclusion

This Chapter has been focused on the use of CAST burner and the characterisation of the resulting emissions using different emission characterisation techniques based on the quantification of the nvPM and the analysis of the chemical composition of emissions by mass spectrometry. The objectives have been to adapt their use on a laboratory scale depending on the fuels and the instruments, to deploy them thereafter for experimental campaigns on a larger scale.

In the first part, the liquid CAST burner adapted for aeronautical fuels under atmospheric conditions has been studied. Its operating limits such as the flow rates parameters, the stability of the flame and the reproducibility of the emissions have been tested. Different CAST operating points have been studied to find a stable working point common for all fuels used. Two set points have been selected for the characterisation of the emissions: (105/30/2) and (84/30/3).

The second part of this chapter has been dedicated to the study of the impact of fuel composition on CAST emissions for the different CAST set points. Conventional aeronautical characterisation methods showed a reduction in the mass concentration, number concentration and size of non-volatile particles for the set points tested, linked to a decrease of the aromatic compounds level in fuel composition (i.e. when the hydrogen content of the fuel increases). Then a second approach has been proposed to study the chemical composition of these emissions. Samples collected at CAST outlet have been analysed by off-line mass spectrometry. The main conclusion is that there is a reduction of PAH concentrations on filters collected for combustion of fuel with low amounts of aromatic content such as SAF. This observation follows the trend previously observed on the reduction of nvPM when hydrogen content in the fuel increases. However, it should be noted that the AtJ fuel (mainly composed of paraffin and no aromatic and no sulphur compounds) generates more PAHs compared to a modified Jet A-1 with low aromatic and sulphur contents. As there are less soot particles from the combustion of a SAF, PAHs are more present in the gas phase and the soot particles grow from PAHs present in the gas phase.

It must be noted that CAST burner do not use the same complex technologies as a real engine and that emissions at burner exhaust are not exactly the same as aircraft exhaust: the combustion is done at atmospheric pressure, the particle sizes are higher than the ones found at engine exhaust... However the CAST is a good surrogate of aircraft engine, allowing the use of different liquid fuels with low fuel consumption and it is representative of fuel complexity (impact of fuel composition on particle emissions well captured).

Then the characterisation of nvPM from the combustion of aeronautical fuels has been done using different complementary methods. These techniques can be adapted to a larger scale such as an experimental atmospheric simulation chamber to study interactions between emissions (nvPM and vPM) of the CAST and atmospheric components at ground level conditions. The next chapter is dedicated to the vPM formation process in a controlled environment.

Chapter IV. Evolution of engine emissions in atmosphere: vPM formation from homogeneous nucleation

Combustion product from aircraft engine released into the atmosphere are composed of various gases and particles (cf. I.4.2). However, these pollutants encounter a decrease of ambient temperature. This variation may lead to some physico-chemical transformation and the formation of volatile Particulate Matter (vPM- cf. I.3.2) in the cooling exhaust gas downstream the engine. As mentioned in Chapter I, the mechanisms behind vPM formation in aircraft engine emissions have not been clearly defined but it is possible to do a parallel with Secondary Aerosols formation (SA), for which the phenomenon is more documented. The SA formation process has been better understood with the development of cutting edge theoretical (McGrath et al., 2012; I. K. Ortega et al., 2012) and experimental techniques (Almeida et al., 2013; Junninen et al., 2010; Kirkby et al., 2011, 2016; Riccobono et al., 2014). A clear example are the experiments done in the CLOUDS atmospheric simulation chamber at CERN (https://home.cern/fr/about/experiments/cloud). Actually, we know that sulphuric acid, ions and ammonia are not the only compounds involved in atmospheric nucleation (Kirkby et al., 2011), but highly oxidised organic compounds (Bianchi et al., 2019; Qi et al., 2018) are also linked to the formation of SA. In the case of aeronautical emissions, vPM come from homogeneous nucleation from gaseous precursors present in engine exhaust emissions. Sulphuric acid (H_2SO_4) is considered as the main compound involved in vPM formation (Kärcher et al., 1995; Kärcher & Fahey, 1997), but the formation mechanism of volatile particles in the exhaust of aircraft engines remains incomplete (Vancassel et al., 2004). Some other components such as organic compounds can play a role and need to be taken into consideration (Kılıç et al., 2018b). In addition, gaseous precursors and vPM formed can interact with pre-existing particles by being adsorbed at their surface (I. Ortega et al., 2016).

The objective of this research is to understand vPM formation processes and their interaction with nvPM within the atmosphere. To study these mechanisms, different experimental campaigns have been done in the framework of the UNREAL project.

This chapter is composed of a description of the preliminary and productive experimental campaigns. Different fuels have been burned to identify potential contributors on new particle formation and an experimental protocol has been defined. Then a reference fuel case emission is documented from a homogeneous nucleation point of view, i.e. experimental results and exploitation of data. The last part is dedicated to a comparison of the emissions for the combustion of different aeronautical fuels to analyse the impact of their compositions on vPM formation process from homogeneous nucleation.

IV.1 Experimental set-up and preparation phase

The measurement campaigns have been divided in two stages: a first stage aiming to optimise the procedure and methods and a second stage with different productive tests. The preparation phase took place the first year of the thesis to adapt the set up to the study of nvPM and vPM for different liquid aeronautical fuels. Then, due to the sanitary crisis, the productive tests have been postponed at the end of the thesis to allow the participation of all project's partners and to finalise the study of vPM formation. All instruments mentioned in the following sections have been already presented in Chapter II.

IV.1.1 General Set-up

To perform the experiment, a CAST burner has been used as a surrogate of an aircraft engine (description in II.1.1.1). This soot generator is made to burn liquid aeronautic fuels at low consumption (a few mL/h). Limits of fuel certification have been already tested to observe the impact of their composition on aeronautical emissions at burner exhaust (cf. III.2.2 and III.2.3).

To study the formation of vPM in detail, the CESAM atmospheric chamber available at LISA laboratory (Créteil University, France) has been set-up to simulate atmospheric processes that can occur behind an aircraft engine at ground level. The CESAM installation is a smog chamber built to investigate multiphase processes (http://cesam.cnrs.fr). The surface/volume ratio (S/V = 4.3 m^{-1}) is low to minimise wall effects and the structure of the chamber allows deep cleaning which permits it to reach very clean experimental conditions even after very "dirty" experiments..

The Figure IV-1 gives a schematic representation of the set-up. Both particulate phases (mass and number concentrations, size distributions – in green Figure IV-1) and gas phases (gas detectors and analysis of the chemical composition – in grey Figure IV-1) are monitored.

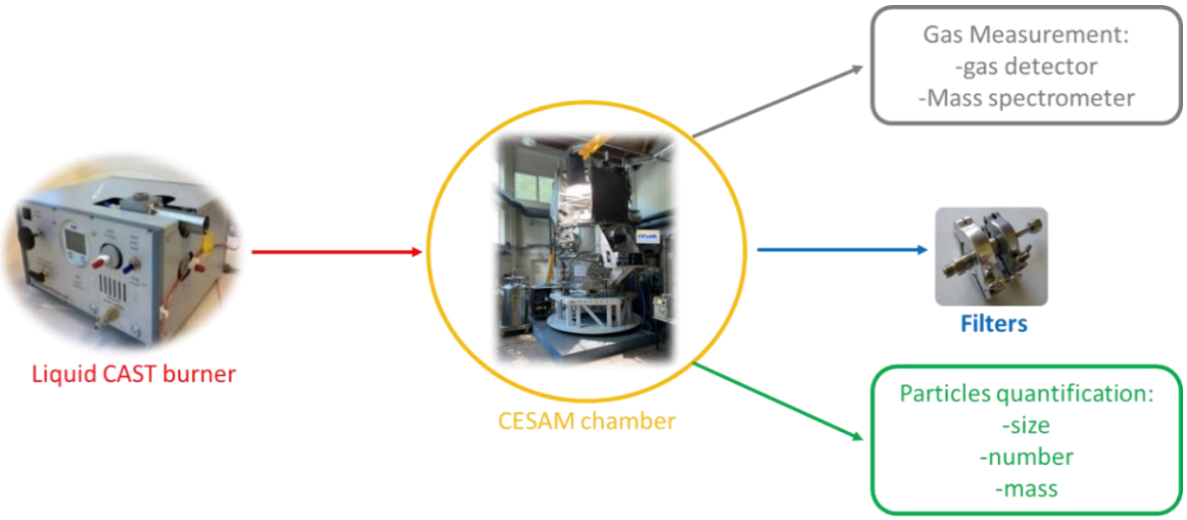

Figure IV-1: General set-up of the UNREAL experimental campaign: emissions from liquid CAST burner (red) are injected inside CESAM atmospheric chamber (orange) to be analysed over the time depending on the chamber parameters (in green the particulate phase; in grey the gas phase). Some filters are collected during the test (in blue) for further off-line analysis.

Different parameters are selected for the experiment to simulate standard ground level conditions. The pressure and the temperature are set respectively at P=1 bar and T=298 K to be representative of the ground level atmospheric conditions. The relative humidity RH is defined at 37% to get comparable conditions to those used in CLOUD experiments, which have studied different atmospheric nucleation mechanisms relative to SA formation (Kirkby et al., 2011, 2016; Lehtipalo et al., 2016b). Sunlight exposure is simulated with three 7 kW Xenon lamps to illuminate the inside of the chamber after emissions introduction. UV filtered below 300 nm are comparable to the solar radiation at noon on the 21st of June at 45° of latitude. North. These parameters correspond to atmospheric conditions encountered in April at Roissy Charles de Gaulle airport (WeatherOnline©, 1999) or Frankfurt airports (Europe).

The experimental protocol is the same for each test. At the beginning, atmosphere is reproduced artificially in the chamber by injection of N_2 and O_2 and during all the experiment, this synthetic air level is maintained constant with a compensation mode. Then, two injections of water of two seconds each are done to obtain the relative humidity level wanted. Chemical reactions in the atmosphere imply radicals such as hydroxyl (Krystynik, 2021; Nosaka & Nosaka, 2016). OH radicals are generated

by using constant slow-flow gaseous nitrous acid injection. This technique can achieve a concentration of OH in the range of 10^6 - 10^7 radicals/cm^3 which is comparable to atmospheric daytime averages ($1.6x10^6$ - $2.5x10^6$ radicals/cm^3) at continental ground level (Hewitt & Harrison, 1985; Li et al., 2018).

As the pressure in the CESAM chamber is the same as the ambient, the introduction of the CAST emissions inside the chamber is done by depression to generate a suction (ΔP=-20 mbar). Due to this intake under pressure, the measuring instruments are disconnected to avoid damages and the emissions injection cannot be monitored in real time. To compare the different experiments depending on fuels tested, the time of injection is related to the amount of CO_2 introduced in the chamber. CO_2 is an inert gas and being directly related to the quantity of fuel burned, its concentration is a function of the carbon content of the fuel. The CO_2 concentration remains unchanged in exhaust gas of aircraft engines and it will be the reference concentration for the tests performed here. Furthermore, the CO_2 emissions normalisation contributes to actual air traffic to calculate the amount of fuel burned (i.e. to get emission index for kg of burned fuel - ICAO, 2017). As all instruments are disconnected from the chamber during this injection time (measuring the ambient air), the amount of CO_2 cannot be followed in real-time implying that this concentration is only measured after the injection. It is used thereafter to normalise the measurements and to compare tests between them for different fuels. For example, an emissions injection of around 10 seconds for a reference fuel such as Jet A-1 introduces in average 60 ppm of CO_2 in the CESAM chamber. A short time of injection is better to not pollute the chamber with soot. The emissions evolution inside the chamber was monitored for 3-4 hours.

IV.1.2 First approach and parameters optimisation

IV.1.2.1 Preliminary tests

The objectives of these preliminary tests were to determine an experimental protocol by validating CAST operating points selected in III.1.2.4 and to define the optimal parameters of the set-up such as the injection time and quantity injected in the chamber or the moment to start the light in the chamber (before or after the injection).

The detailed experimental line deployed to perform two experiments in parallel is presented in Figure IV-2. The first part of the set-up (top) is dedicated to the characterisation of CAST emissions and the second one (bottom) corresponds to the study of vPM formation using the atmospheric CESAM chamber. Mass concentration, number concentration and size distributions of particles have been measured for both cases (in green - Figure IV-2).

In the first part, CAST raw emissions have been diluted and the condensation is avoided by collecting the sample on the CAST outlet with heated sampling lines at 160°C. To remove vPM and measure only nvPM (red path - Figure IV-2), the sample is conditioned by the CS and the DEED before being cooled down to ambient temperature (by the DEED) to perform the measurements. CPC and SMPS data have been recorded alternatively: at least 2 minutes after stabilisation for the concentration number and at least 2 size distributions (8min in total) for particle size. LII measurements have been done continuously. Results have been already detailed in III.2.3: according to the different fuels tested, the mass and number concentrations as well as the size of particles decrease with the increase of Hydrogen content in the fuel.

In the second part of the set-up, the raw emissions of the burner have been introduced directly inside the CESAM chamber using a heated inox tube (1 m line at 160°C). The objective is to analyse the interactions of raw emissions with the atmosphere and also to study vPM formation. Injection times depend on the amount of CO_2 measured after the introduction of emissions in the chamber. The CESAM facility allows a characterisation of the chemical and the physical state of gas (PTR-MS) and particulate (SMPS and ACSM) phases. Gas detectors monitor CO_2, CO, SO_2, O_3 and NO_X evolution over the time. To complete the study of the emissions inside the chamber, some filters have been collected for the different fuels tested and analysed thereafter off-line by mass spectrometry.

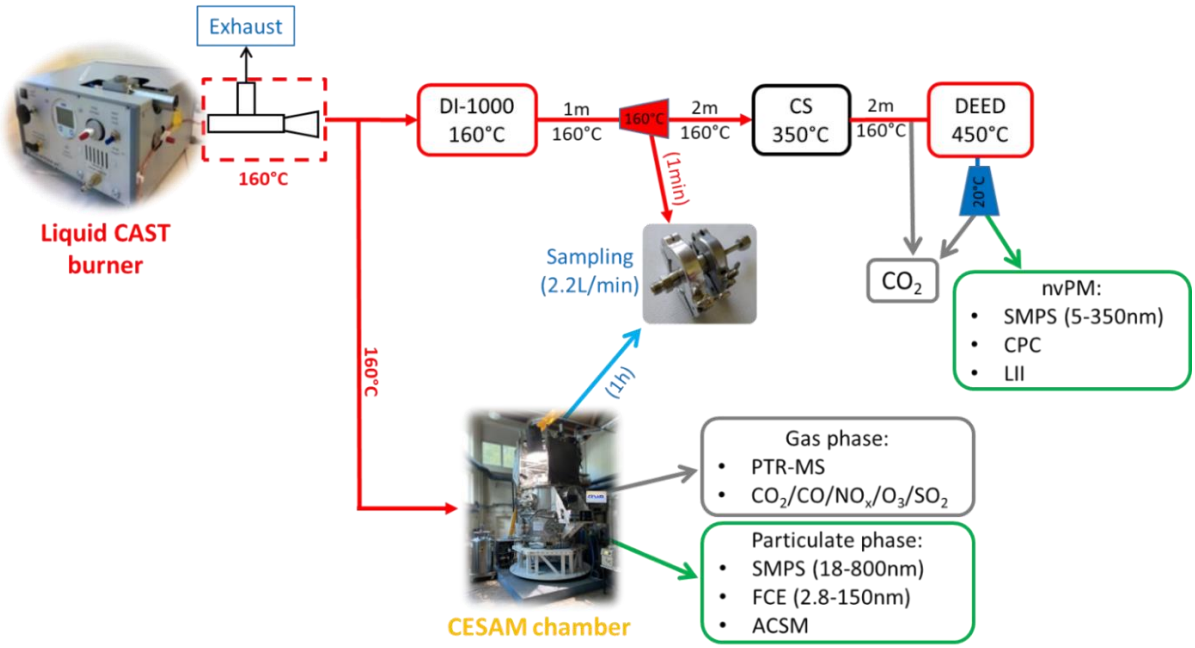

Figure IV-2: Preliminary UNREAL experimental set-up for preliminary tests. Emissions from the CAST are injected in CESAM chamber for a short time and in parallel, the emissions are characterised using the ONERA set-up.

Different CAST operating points (fuel in µL/min, propane in mL/min, air in L/min) have been tested (cf. III.1.2.4) to observe their impact on the flame stability during the experiment. If the proportion of air flow is too low compared to the propane and fuel flows (cf. III.1.1.2), the flame is not stable enough for some fuels in particular during the introduction of emissions in the chamber. Indeed, the suction created for the injection can blow off the flame and thus only kerosene vapour are injected (details of this case in IV.1.2.3). It is notably the case for AtJ fuel (cf. III.1.1.2 and Annex B).

Figure IV-3 presents four tests performed with CESAM chamber for different CAST operating points using the same fuel. It is the first time that such tests are done in such an atmospheric chamber. To ensure that we can form vPM, we tested the Extreme Jet fuel (high amount of sulphur: 3000 ppm) to check if sulphate particles are formed as described by (Ebbinghaus & Wiesen, 2001; Kärcher & Fahey, 1997). The injection time is adapted from the concentration of CO_2 (15 ± 2 ppm) injected with emissions in the chamber to compare the results: from 50s for fuel with high fuel flow to 70s for fuel with low fuel flow. The first case (a) corresponds to the CAST set point (105/20/1.5) and the lights have been activated at the same time as the injection. The second case (b) is a repetition of the precedent case with a modification in the light activation process (+30 min after injection). The third case (c) presents results obtained for the (75/30/2) operating point. The fourth case (d) corresponds to the (105/30/2) set point. For these last two cases, the lights are also activated with a delay of 30 min after injection of CAST emissions. The first line of graphs (a.1 & b.1) presents the evolution of the mass (brown) and number (purple) concentrations of particles in the chamber over the time with wall losses and dilution corrections. The second line of graphs (a.2 & b.2) represents the variation of the size (y-scale) with the evolution of the number concentration of the particles (colour scale) over the time (x-scale). The last line of graphs (a.3 & b.3) gives the monitoring of organic compounds, ammonium NH_4, nitrate NO_3 and sulphate SO_4 concentrations over the experiment (with dilution correction). The emissions injection is indicated by the red dotted line and the light activation is symbolised by the yellow area. Table IV-1 summarises the values measured just after the injection, just after light activation and at the end of the experiment for each case. The Table IV-2 summarises the relative variations compared to the injection value to propose another way to evaluate the number and mass concentrations of the particles in the CESAM chamber.

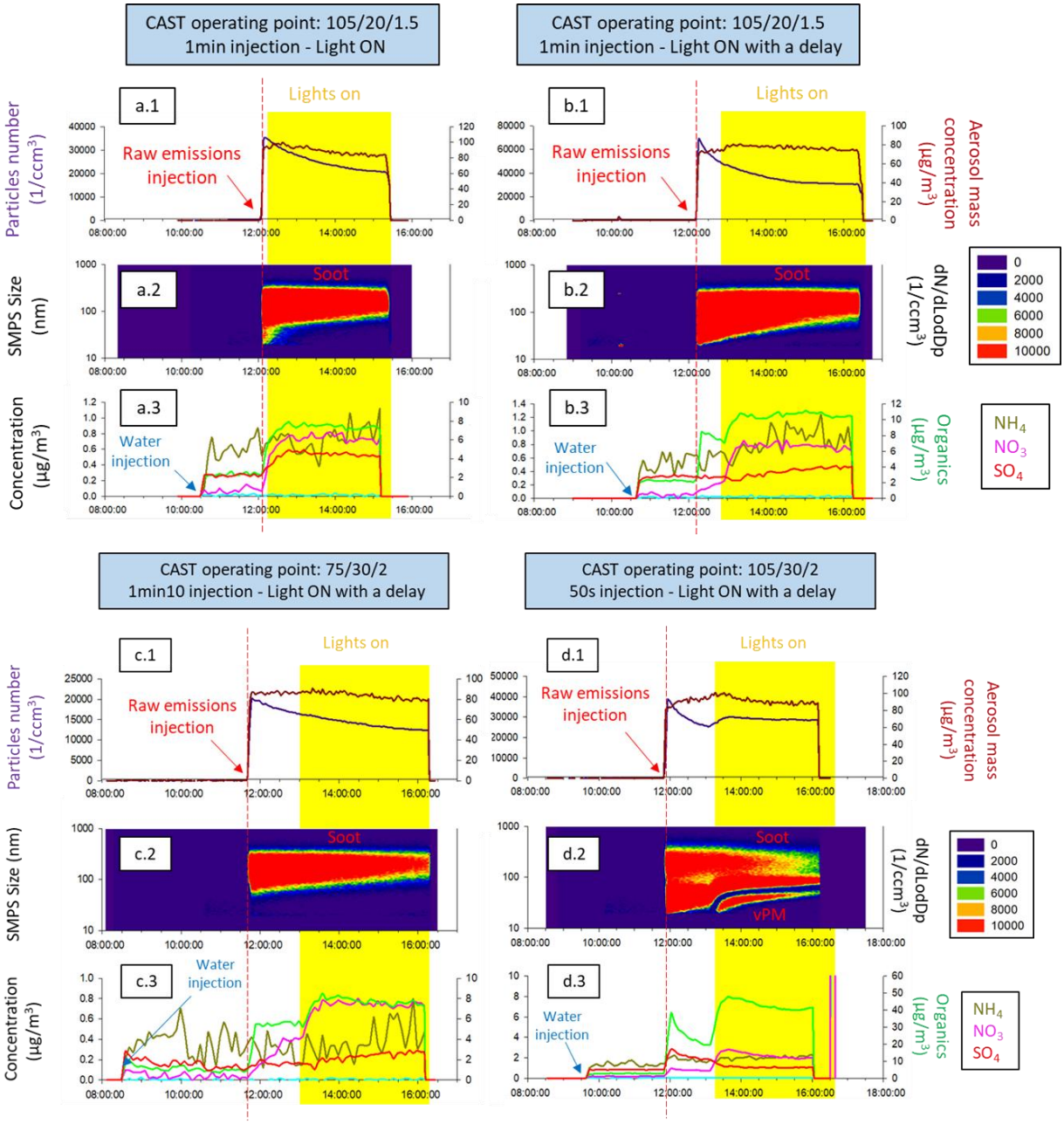

Figure IV-3: Preliminary tests on CESAM chamber using the Extreme Jet fuel for different CAST set points. Lights (yellow area) have been activated during the injection (case a) and with a delay of 30min (case b, c and d). For each case, starting from the top, the first graph presents the evolution of the particle number (left axis) and mass concentration (right axis) over the time inside the chamber after correction of wall loss and dilution. The middle graph represents the evolution of the particle size (left axis in log scale) over the time with the number concentration (colour scale). The bottom graph describes the evolution of some ion concentrations over the time inside the chamber: NH_4^+ (beige), NO_3^+ (pink), and SO_4^+ (red) on the left axis and Organic compounds (green) on the right axis.

Regarding these results (Figure IV-3), it is possible to follow the evolution of emissions inside the chamber depending on the CAST set point used and on the light activation protocol employed. Before the beginning of each test, a water injection is done to recreate ambient atmospheric conditions by having an adequate RH value (37%). Thus for all cases, we can find in the chamber NH_4^+, SO_4^+ and organic compounds (stage 3 on Figure IV-3) at low concentrations (Table IV-1) that can be seen as the background of the experiment. No signals are measured concerning the particles and mass concentrations (stage 1 and 2 on Figure IV-3) assuming that there is no contamination before the beginning of the tests.

Emissions introduced in the chamber are mainly soot particles according to results obtained at CAST burner outlet in III.2.4. After the emissions injection, a first observation can be done on the variations of the number and mass concentrations for the different CAST set points. According to Table IV-1, cases (a.1) and (d.1) with fuel flow set at 105 µL/min induce a higher amount of particles introduced in the chamber at the beginning of the experiment (respectively 1.75 and 1.92 times more) compared to case (c.1) with fuel flow set at 75 µL/min. After the injection and before light activation, the mass concentration remains approximately the same (± 4 µg/m^3) but the number of particles decreases with time due to agglomeration and coagulation of particles (-33% for case b.1, -19% for case c.1 and -35% for case d.1). This trend is confirmed by an increase of the GMD of the soot particles: +6nm for case (b.2) and +4nm for case (d.2). The size of the smallest particles introduced in the chamber is 21.7 nm (case b.2) and the size of the biggest one is 358.7 nm (case c.2). After emissions injection and before light activation, the concentration of organic compounds increases by 3.18 times for case (a.3), by 3.57 times for case (b.3), by 4.81 times for case (c.3) and by 11.76 times for case (d.3) compared to water injection background. In the case where the lights have not been activated directly after injection as for example case d, the concentrations of nitrate and sulphate indicate a slight increase (respectively from 0.1 to 0.93 µg/m^3 and from 0.8 to 2.8 µg/m^3) but ammonium concentration remains unchanged.

Particles	Timeline	Case a (105/20/1.5)	Case b (105/20/1.5)	Case c (75/30/2)	Case d (105/30/2)
Number concentration x10^4 (1/ccm^3)	At emissions injection	3.57 ± 0.52	6.88 ± 0.72	2.03 ± 0.34	3.90 ± 0.86
	At lights on		4.66 ± 0.10	1.66 ± 0.22	3.00 ± 0.36
	At the end of the test	2.08 ± 0.15	3.11 ± 0.23	1.23 ± 0.17	2.87 ± 0.31
Mass concentration (µg/m^3)	At emissions injection	99.13 ± 4.24	74.28 ± 2.27	86.66 ± 2.21	84.32 ± 3.14
	At lights on		81.42 ± 2.64	89.33 ± 2.17	102.16 ± 4.51
	At the end of the test	85.12 ± 3.11	75.71 ± 1.88	78.67 ± 1.94	89.19 ± 3.54
Organic compounds concentration (µg/m^3)	At water injection	2.42 ± 0.45	2.33 ± 0.69	1.61 ± 0.64	3.13 ± 0.31
	At emissions injection	7.71 ± 0.51	8.33 ± 1.02	5.49 ± 0.58	36.84 ± 2.14
	At lights on		10.5 ± 1.10	8.17 ± 0.73	47.85 ± 1.87
	At the end of the test	7.57 ± 0.36	10.3 ± 0.77	7.40 ± 0.38	41.56 ± 1.74

Table IV-1: Comparison of number, mass and organic compounds concentrations in CESAM chamber for different tests depending on the moment of the experiment. Case a and b correspond to set point (105/20/1.5) with a difference in light activation protocol, case c to set point (75/30/2) and case d to set point (105/30/2). Values have been corrected for dilution and wall losses and correspond to an average of 2min measurement. Same amount of CO_2 has been injected for each case.

Particles		Timeline	Case a (105/20/1.5)	Case b (105/20/1.5)	Case c (75/30/2)	Case d (105/30/2)
Number concentration	x10^4 (1/ccm^3)	At emissions injection	3.57 ± 0.52	6.88 ± 0.72	2.03 ± 0.34	3.90 ± 0.86
	Relative variation (%)	At lights on	100%	67.7%	81.8%	76.9%
		At the end of the test	58.3%	45.2%	60.6%	73.6%

Mass concentration	($\mu g/m^3$)	At emissions injection	99.13 ± 4.24	74.28 ± 2.27	86.66 ± 2.21	84.32 ± 3.14
	Relative variation (%)	At lights on	100%	109.6%	103.1%	121.2%
		At the end of the test	85.9%	101.9%	90.8%	105.8%
Organic compounds concentration	Relative variation (%)	At water injection	31.4%	28%	29.3%	8.5%
	($\mu g/m^3$)	At emissions injection	7.71 ± 0.51	8.33 ± 1.02	5.49 ± 0.58	36.84 ± 2.14
	Relative variation (%)	At lights on	100%	126.1%	148.8%	129.9%
		At the end of the test	98.2%	123.6%	134.8%	112.8%

Table IV-2: Relative variations compared to the injection value for number, mass and organic compounds concentrations in CESAM chamber for different tests depending on the moment of the experiment. Case a and b correspond to set point (105/20/1.5) with a difference in light activation protocol, case c to set point (75/30/2) and case d to set point (105/30/2). Values have been corrected for dilution and wall losses and correspond to an average of 2min measurement. Same amount of CO_2 has been injected for each case and values are calculated from Table IV-1 taken as reference to the injection step.

The second observation concerns the impact of light activation during the experiment. It is visible on the emissions by looking at the formation of organic compounds (in green – stage 3 - Figure IV-3). In the first case (a.3), the lights have been activated during the injection. It can be observed that organic compounds have been formed (+5.29 $\mu g/m^3$) although it's not clear whether this formation is related to the injection or the lights. In the case (b.3), the same experiment is repeated but the lights are on 30 minutes after the injection and it confirms that they have a real impact on the organic compounds formation. Indeed, the raw emissions injection step introduced 6 $\mu g/m^3$ of organics in the chamber and after lights on, organics concentration increases to 10.5 $\mu g/m^3$ at a rate of around 0.02%/s. The same phenomenon is observed for the case (c.3) and (d.3) with respectively +2.68 $\mu g/m^3$ and +11.01 $\mu g/m^3$. The case d is accentuated compared to the other ones: when the number concentration presents a small stagnation and the mass concentration presents a small increase with light activation for case b and c, both concentrations increase for case d. It means that new particles have been generated in the chamber besides soot presence and it is confirmed with the graph (d.2). After light activation, the GMD of the soot increases and their number concentration continues to decrease. However, new particle formation is observable under the distribution of soot particles corresponding to vPM. This representation ("banana plot") is currently used to observe the formation of particles from nucleation of atmospheric aerosols particles (Curtius, 2006; Heintzenberg et al., 2007; Monks et al., 2021; Su et al., 2022). The size of these particles increases from 22.5 nm to 49.6 nm in 2 hours and 30 minutes. In case (d.3), the concentration of SO_4 decreases (-35%) and the one of NO_3 increases (3.75 times more than before) when lights are on. Such a formation is not visible for the other cases even if organic compounds concentration increases with light activation indicating that particles are generated. It implies that formation of particles is favoured in the last case where the CAST set point (105/30/2) corresponds to the one selected in Chapter III.

To complete these preliminary observations and to analyse the chemical composition of the emissions, filters have been collected on the CESAM chamber for 1 hour at 2.2 L/min (details in II.2.2.3.1) and thereafter have been studied by mass spectrometry (L2MS at PhLAM laboratory – details in II.2.2.3.2). Figure IV-4 presents spectra obtained for analysis of the particulate phase (blue ones) and the gas phase (red ones) of the emissions using positive ions (top) and negative ions (bottom). The fuel tested is the Extreme Jet and the CAST operating point is set at (105/30/2). In both filters, carbon clusters can be found: related to soot on filters designed for particulate phase and due to the initial

black carbon layer on the filter used for gas phase. PAH have been identified mostly in the particulate phase using the positive mode: naphthalene ($C_{10}H_8^+$ at 128.06 m/z), fluorene ($C_{13}H_{10}^+$ at 166.08 m/z), anthracene ($C_{14}H_{10}^+$ at 178.08 m/z) and pyrene ($C_{16}H_{10}^+$ at 202.08 m/z) for example. Sulphur compounds have been found mostly in the gas phase using the negative mode: sulphur dioxide (SO_2^- at 63.96 m/z), sulphur trioxide (SO_3^- at 79.96 m/z) or hydrogen sulphate (HSO_4^-).

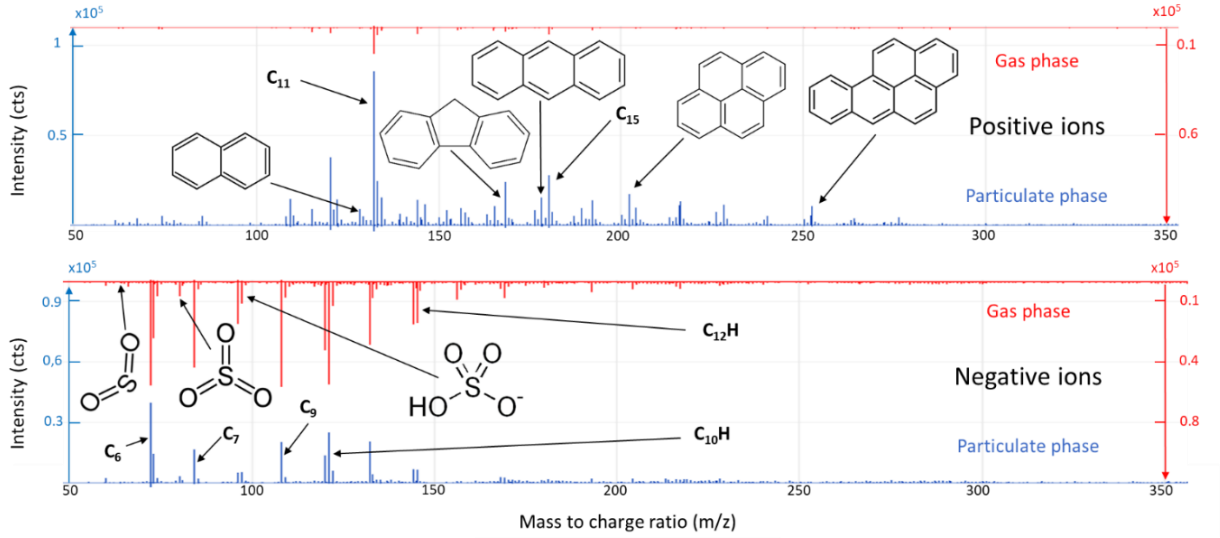

Figure IV-4: L2MS spectra from analysis of filters collected during preliminary tests. The fuel is the Extreme jet and the CAST set point is (105/30/2). The spectra in blue correspond to the filter for the particulate phase and the ones in red correspond to the filter for the gas phase. The top graph displays the positive ions and the bottom one the negative ions. Parameters are set at: $Fluence_{desorption}$=46 mJ/cm² and $Fluence_{ionisation}$=2.9 mJ/cm².

A semi-quantitative comparison between the different compounds identified on the surface of different samples chamber for two CAST set points has been done. The fuel is the same (Extreme Jet) and the set points tested are (105/20/1.5) corresponding to case b in Figure IV-3 and (105/30/2) corresponding to case d in Figure IV-3. The objective was to compare the amount of elemental carbon (i.e. carbon clusters), of organic carbon (mainly PAH and VOC), of sulphur and oxygenated compounds (cf. Annex G for details). Figure IV-5 gives a direct comparison of the particulate phase (left) and the gas phase (right) for these two experiments: in grey for the (105/30/2) set point and in red for the (105/20/1.5) set point. The scale is in log and values have been normalised by the total ions counts for each spectrum to be directly compared. Regarding the particulate phase (Figure IV-5 - left), results confirm that more compounds have been found on soot surface for the (105/30/2) case compared to the (105/20/1.5) one. The amounts of organic, oxygenated and sulphur compounds are respectively 5 times more, 1.7 times more and 25 times more higher for (105/30/2) case. Regarding the gas phase (Figure IV-5 - right), the same trend can be observed but less pronounced. In this case, the high amount of elemental carbon recorded come from the black carbon layer deposit on the filter surface. It can be noted that more sulphur compounds (in particular sulphuric acid) have been found on soot surface than in the gas phase for the case (105/30/2). On the other hand, more sulphur compounds have been found in the gas phase than on soot surface for the second set point. Due to the high amount of sulphuric acid found for the first set point by combining both results (particulate and gas phases) and its role in the nucleation process (Vancassel et al., 2004), these observations contribute to explain the higher amount of vPM formed for (105/30/2) case compared to (105/20/1.5) case. Concerning the oxygenated compounds, few of them have been identified: acetone (C_3H_6O at 58.04 m/z), methyl-vinyl-ketone (C_4H_6O at 70.04 m/z), butanone (C_4H_8O at 72.06 m/z), methylbutanol ($C_5H_{10}O$ at 86.07 m/z) and heptanal ($C_7H_{14}O$ at 114.10 m/z). They are formed in the chamber and can contribute to the formation of vPM. In the further experiments we will pay more attention to them due to the link between HOMs and SA formation (Bianchi et al., 2019).

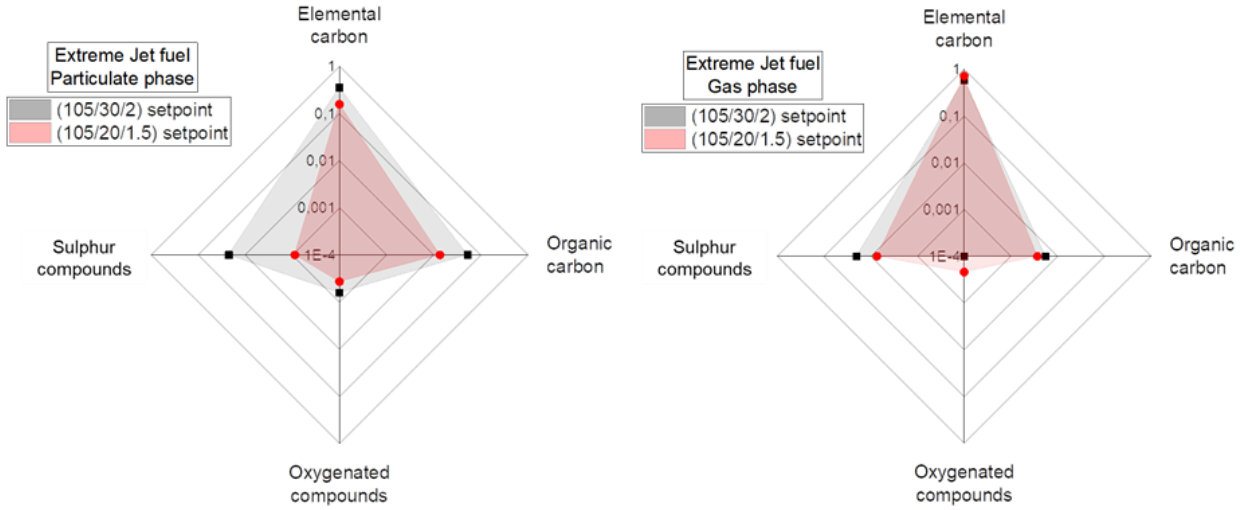

Figure IV-5: Semi-Quantitative comparison between two tests on CESAM chamber for the same fuel (Extreme Jet): on the left for the particulate phase and on the right for the gas phase. The first set point (105/30/2) corresponds to the grey area and the second set point (105/20/1.5) corresponds to the red one. Scale is in log and is the same in each axis. It corresponds to (sum of intensity/total ions counts of the spectra) for each category of compounds.

It appears that CAST set point (105/30/2) is the one that produces the highest amount of vPM precursors (Figure IV-3 case d.2). According to previous studies about the formation of SA in atmospheric environment (Almeida et al., 2013; Kirkby et al., 2011; Kulmala et al., 1996) and about aircraft engine emissions (Kärcher & Fahey, 1997; Vancassel et al., 2004), the vPM come from the nucleation of gaseous precursors found in the emissions. Due to the presence of soot particles in the CESAM chamber, gaseous precursors are adsorbed on soot surface for tests presented on Figure IV-3 (case a, b and c) and the nucleation process is thus limited (Aubagnac-Karkar et al., 2018; Eaves et al., 2015; Zhou et al., 2022). To study the vPM formation avoiding the impact of soot, it is necessary to adapt the set-up before moving on to the productive tests.

IV.1.2.2 Zoom on the homogeneous nucleation case

Formation of particles from nucleation of gaseous precursors is a phenomenon not limited to combustion sources but it has been observed everywhere in the atmosphere (Kulmala et al., 2003). However, the formation mechanism of volatile particles in the exhaust of aircraft engines is less understood compared to the study of atmospheric new particle formation, in particular due to the conditions in which the emissions are produced. The high temperature and high concentration of pre-existing particles in the exhaust of the engine, which act as a condensational sink for vapour and pre-nucleation clusters, hinders the formation of particles. Nucleation can only happen once the exhaust is diluted and cooled down. Measurement represents a big challenge in these conditions. Most of the instruments used in the atmospheric nucleation field cannot deal with such high temperatures and particle concentrations, implying that a pre-treatment of the sample needs to be established and standardised. Then the state-of-the-art techniques used in the atmospheric nucleation field can be used as well to understand the nucleation on engine exhaust. One of the key points is to control the conditions for the formation of particles, using the atmospheric chamber CESAM. However, nvPM and vPM are injected together and it is more difficult to study individually the gas phase nucleation process. vPM are formed in the cooling exhaust gas downstream the combustor when the concentration of pre-existing particles has decreased, favouring homogeneous nucleation versus heterogeneous one (adsorption of gases onto pre-existing particles). To focus on the formation of vPM and to highlight the homogeneous nucleation process by avoiding adsorption of gas precursors on soot surface, it is necessary to separate the particulate phase from the gas phase.

During the preliminary experiments, a test has been done to remove the particulate phase from the CAST emissions using a HEPA filter between the CAST outlet and the CESAM chamber (Figure IV-6). It is the same quartz fibre filter as the ones used for samples collected on CESAM chamber (Pallflex Tissuquartz, 2500 QTA-UP, Figure IV-6 - right). These fibre filters retain 99.9% of the particles on their surface (cf. Pallflex technical document). The set-up included a SMPS sensor that can track efficiency of filtration just after injection. The injection set-up is adapted to work with and without filtration of soot particles from the CAST emissions (Figure IV-6 - left). In the simplified case, only the gas phase is injected inside the chamber and the homogeneous nucleation is the main process in the absence of soot particles.

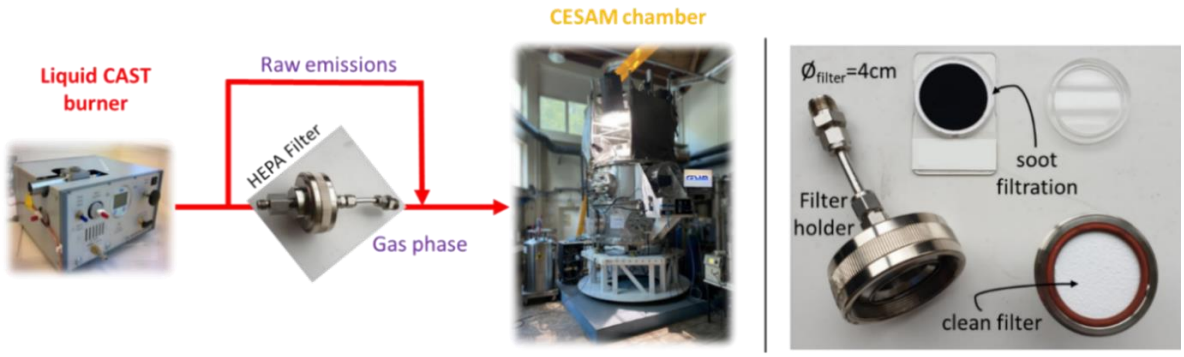

Figure IV-6: Soot filtration with an HEPA filter to separate the gas phase from the particulate phase in CAST emissions. The sample holder is positioned between the CAST exhaust and the CESAM chamber inlet.

To observe the impact of the soot filtration, two complementary experiments have been done with and without HEPA filter. The Extreme Jet fuel is tested for the CAST operating point set at 105 µL/min for the fuel flow, 30 mL/min for the propane flow and 2 L/min for the air flow, noted (105/30/2). The same total amount of CO_2 is introduced with the emissions in the chamber (40 ± 1.6 ppm) for both tests and the lights are activated with a delay of 30 min. Concerning the injection protocol in the CESAM chamber, some differences can be noted. For the first test, an injection of the gas phase (7min) with soot filtration is done (no particles recorded by the SMPS), before a second one of raw emissions to introduce soot particles (10sec) and to observe the interactions between vPM and soot. The second test corresponds to an injection of the gas phase (7min) by filtering the soot to consider only the homogeneous nucleation process from gaseous precursors. Evolutions of the particle number, mass concentration and size of the particles over the time in the CESAM chamber depending on the injection process are presented in Figure IV-7. The first column (case a) corresponds to the injection of raw emissions and the second one (case b) corresponds to the injection of gas phase. The two first graphs (a.1 and b.1) represent the particle number (in blue) and the mass concentration (in red) over the time. The two other plots (a.2 and b.2) correspond to the evolution of the particle size (y-axis range from 20 to 800 nm) and particle number (colour scale) in the chamber over the experiment.

In the first test, no particles are detected in the chamber for gas phase injection. After raw emissions injection, the number and the mass concentrations of particles increase respectively by 1.87×10^4 particles/cm^3 and 51.8 µg/m^3 (case a.1). Soot particles are observable (case a.2) just after the injection and before light activation with a GMD of 128 ± 2 nm. In the second test (b.1), two gas injections have been done to get the same CO_2 concentration in the chamber than for the precedent case. The particle number does not increase but the mass concentration indicates a small change of 2 µg/m^3. The flame has been blown off during the first gas injection, introducing some kerosene vapour in the chamber. This can explain the small variation in mass concentration measurements (more details in IV.1.2.3). No soot particles have been recorded after the injection (no signal over 100 nm before light activation – case b.2), validating the efficiency of the filtration with the HEPA filter.

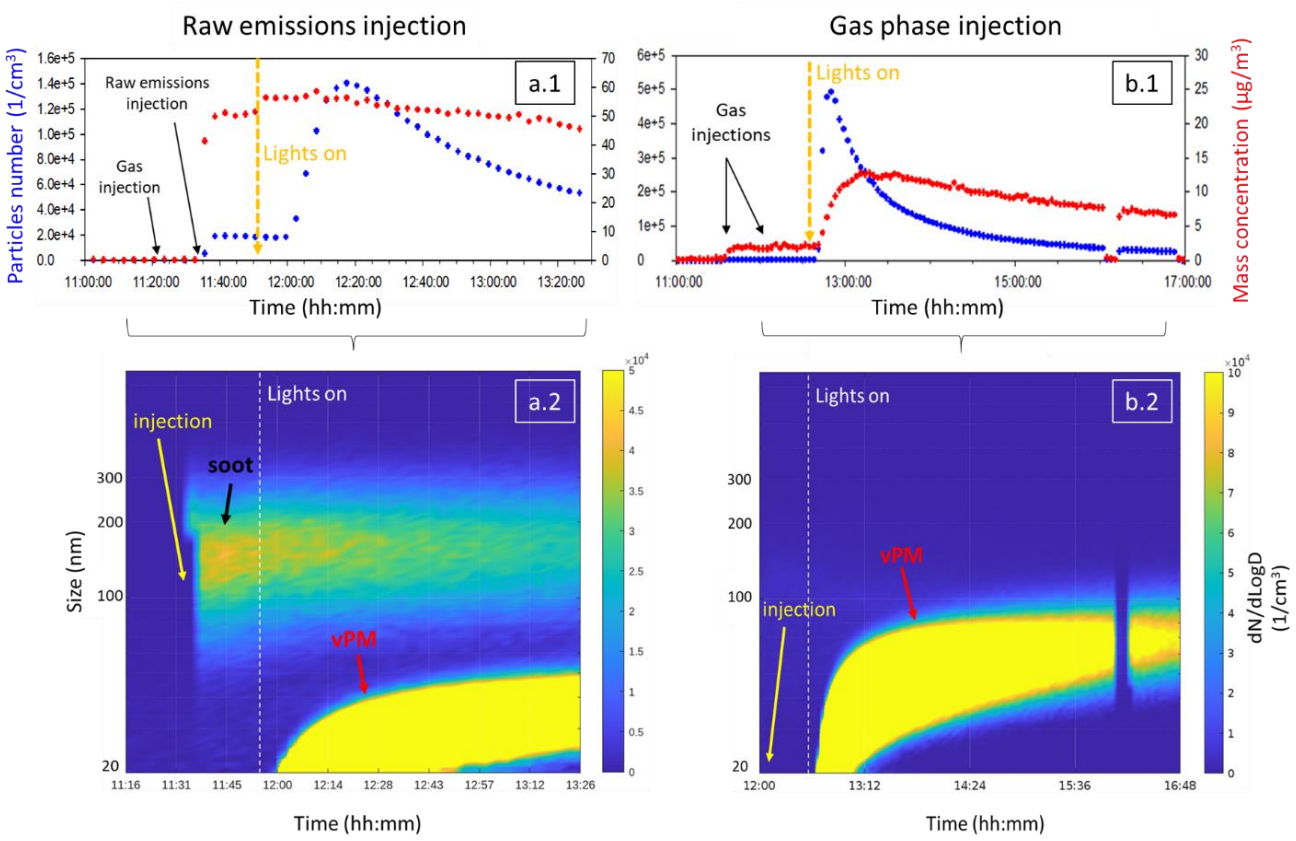

Figure IV-7: Preliminary tests on CESAM chamber without (case a) and with (case b) soot filtration at the injection. The fuel tested is the Extreme Jet for CAST operating point set at (105/30/2). The first line of graphs represents the number and mass concentrations of the particles over the time with dilution correction. The second line corresponds to the evolution of the size (y-axis) and the particle number (colour scale) over the time in the CESAM chamber. Lights on are specified for each case.

After light activation, the number and mass concentrations of particles increase (Figure IV-7 - a.1 and b.1). It can be associated with the formation of new particles for both cases (Figure IV-7 - a.2 and b.2). The main difference concerns the quantity of vPM formed: the particle number is 4 times higher and the mass concentration is 1.5 times higher for the gas injection case than for the raw emissions injection case. Furthermore, a delay after light activation (10min) can be observed before the increase of the particle number for the raw emissions case (Figure IV-7-a.1), but it is immediate for the gas injection case (Figure IV-7-b.1). The presence of soot in this test affects the homogeneous nucleation of gas precursors by adsorbing the gas phase on their surface (GMD increases over the time). It slows down the homogeneous reaction and decreases the formation of vPM. Values are regrouped in Table IV-3.

Particles	Timeline	Case a Raw emissions	Case b Gas phase
Number concentration x10⁴ (1/ccm³)	After gas injection	0	0
	After soot injection	1.87 ± 0.03	
	After light activation	14.2 ± 0.2	49.3 ± 0.1
Mass concentration (µg/m³)	After gas injection	-	2 ± 0.3
	After soot injection	51.8 ± 0.1	
	After light activation	59.1 ± 0.05	12.72 ± 0.1

Table IV-3: Number and Mass concentrations for tests without (case a) and with (case b) soot filtration. The fuel tested is the Extreme Jet for CAST operating point set at (105/30/2). Values correspond to the maximum reached.

After switching on the lamps, the formation of particles has been observed for both cases (Figure IV-7 - a.2 and b.2). The vPM formed for gas phase injection is bigger compared to the raw case. Figure IV-8 presents the evolution of these vPM over the time in the chamber for sizes ranging from 5 to 110 nm. The left graph corresponds to the raw emissions case and the right graph represents the gas phase case. As the Extreme Jet fuel contains a high amount of sulphur in its composition (3000 ppm), the particle formation is observable even with soot presence (left graph). However, some differences can be noted. The size of the vPM formed in the case of gas phase injection reaches 70 nm when the size of vPM formed in the case of raw emissions injection reaches only 45 nm at the end of the experiment. The increase of the new particle sizes is faster for the gas phase injection: 40 nm in 30 min vs 40 nm in 1h for case with soot. Due to the filtration of soot, gas precursors are not adsorbed on their surface and they can be converted by homogeneous nucleation in vPM and contribute to the particle growth. To complete these observations, particles formed are mainly organic compounds (as for the precedent test in IV.1.2.1) and their concentrations are higher for the gas phase injection case (details in Annex H).

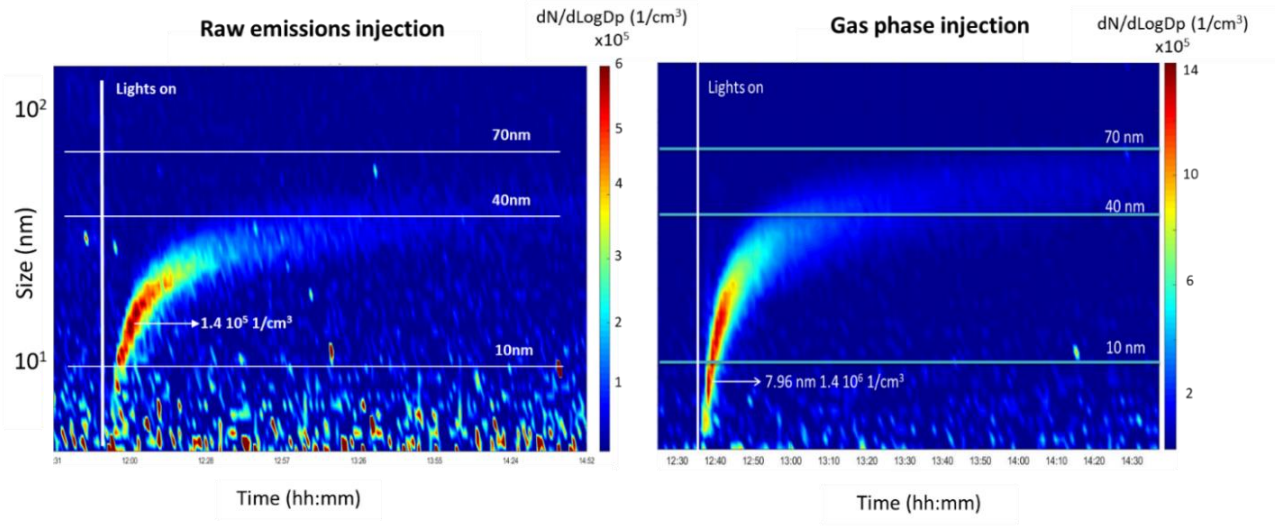

Figure IV-8: Zoom on vPM formation for raw emission injection (left) and for gas phase injection (right). The fuel used is the Extreme Jet and the CAST set point is (105/30/2). Particle number is indicated with the colour scale.

In addition, a link can be done between the variations of number and mass concentrations and the size of particles. Figure IV-9 presents results obtained for the gas phase injection test with particle number and mass concentration on the left and size distribution on the right. The first distribution (in blue Figure IV-9 right) corresponds to the moment when number concentration is maximum (case 1 in Figure IV-9 left) and the second one (in red Figure IV-9 right) corresponds to the moment when mass concentration is maximum (case 2 in Figure IV-9 left). The number and mass concentrations directly increase after light activation. First, small particles are formed (26.9 nm) increasing the number concentration until it reaches its maximum at 4.93×10^5 particles/cm^3. Then due to agglomeration of vPM formed, the particle number decreases but the mass concentration and the GMD of the particles increase. Indeed, when the mass concentration is maximum (13.8 µg/m^3), the size of particles reaches 40 nm.

These observations validated the soot filtration process at the chamber inlet to study the vPM formation from homogeneous nucleation. Different fuels have been tested during preliminary tests in this condition and for all of them, the soot filtration has been successful and new particle formation have been observed (cf. Annex I). Depending on the fuel composition, the vPM formation is more or less pronounced. An exhaustive study is dedicated to fuel comparison in IV.3 for gas phase injection and in 0 for raw emissions injection.

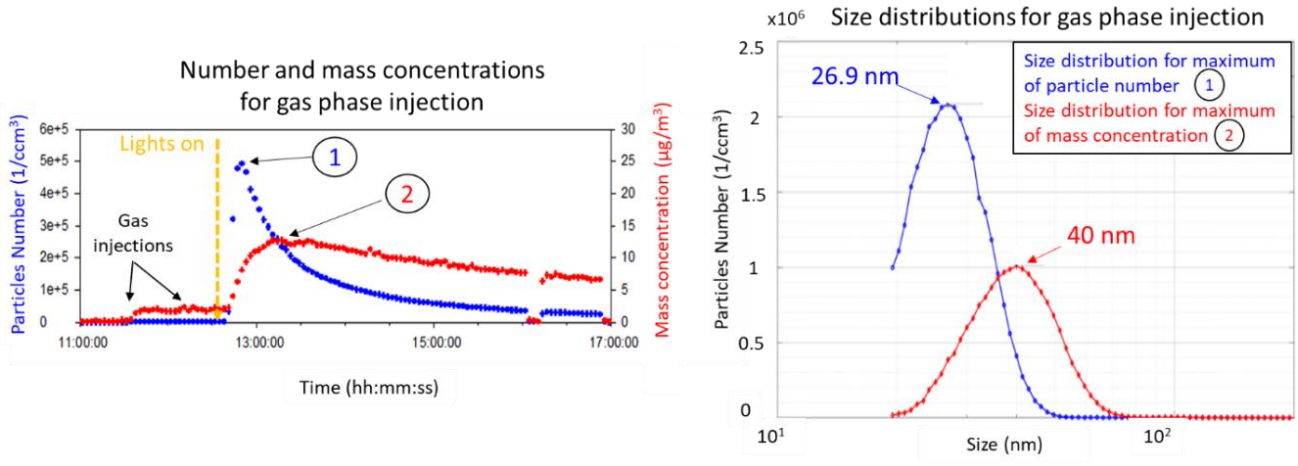

Figure IV-9: Link between Number and Mass concentrations (left) and particle size (right) for test with soot filtration. The fuel tested is the Extreme Jet and the CAST set point is (105/30/2).

IV.1.2.3 Impact of kerosene vapour on vPM formation

At the end of the preliminary experiments, the CAST was more blocked. This can lead to a leak of kerosene on the propane flame generating a second flame (represented thereafter by a bimodal size distribution – III.1.1.1). Or it can blow out the flame when the kerosene flow was too high (105 µL/m) and in this case, kerosene vapour are injected into the chamber instead of raw emissions. To avoid the "contamination" of the sample, the fuel flow has been decreased and the new operating point has been set at (84/30/3) according to Chapter III results. It allows a good stability of the flame for all fuels tested and all optimised parameters discussed in previous sections have been conserved.

To finalise the preliminary experiments by determining the impact of the kerosene vapour on the particle formation inside CESAM chamber, a complementary test has been done using the reference Jet A-1 fuel. The flame was blown off voluntarily and the kerosene vapour have been introduced inside the chamber (1min of injection). Figure IV-10 presents the evolution of the particle size and of the total particle number over the time. First, a blank of the chamber has been done with lights on and no particles have been observed. After water injection and light activation (on the left in Figure IV-10), a high amount of small particles are formed ($7.1 \pm 0.3 \times 10^5$ part/cm^3) increasing from 4.4 nm to 5.7 nm. It confirms the impact of lights in the particle formation process, but these particles condense quickly (in 20min) and their concentration becomes negligible for the following experiment ($<0.5 \times 10^5$ part/cm^3). Indeed, after the introduction of kerosene vapour, the number concentration of particles is 2.4×10^5 part/cm^3 for a GMD of 37.4 ± 0.9 nm. After light activation, total particle number decreases (-75%) to form new particles and their GMD increases to 61.4 ± 0.3 nm. It means that injection of kerosene vapour adds supplementary particles in the chamber leading to the formation of vPM after light activation. It can disturb the homogeneous nucleation process from the gas precursor and thus the measurement. It should be noted that produced particles are bigger for kerosene vapour test (start at 37 nm after light activation - Figure IV-10) compared to the ones obtained for gas phase injection (start at 4 nm after light activation - Figure IV-8). Thus it is possible to notice potential contaminations in the further experiments.

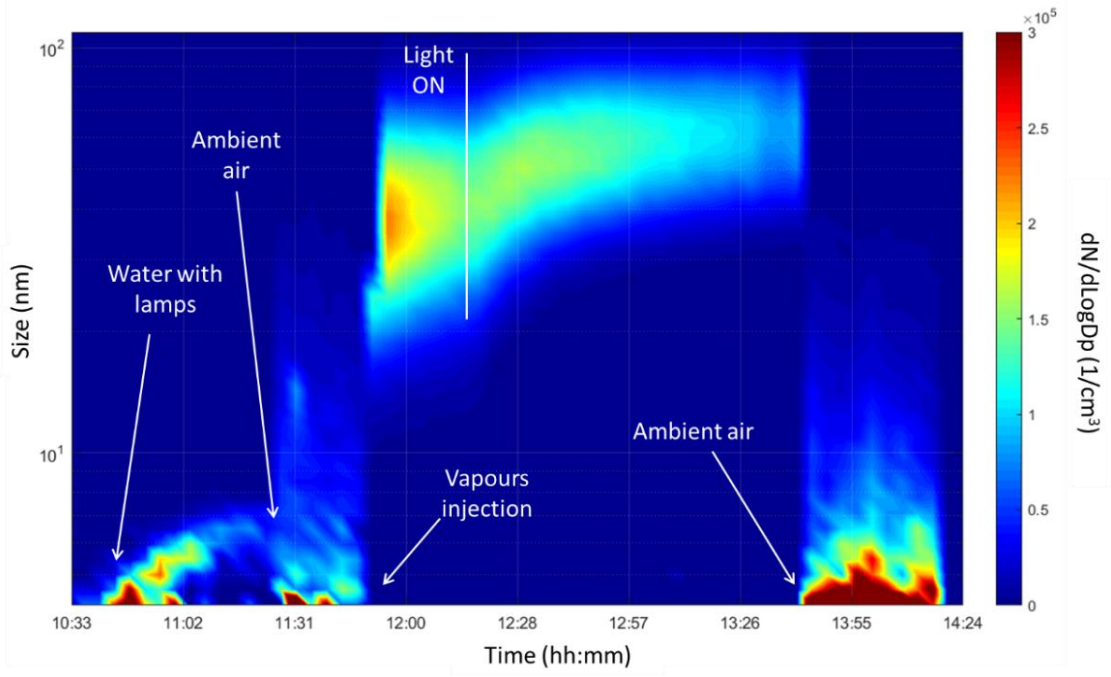

Figure IV-10: Formation of particles in CESAM chamber after injection of kerosene vapour and light activation. The fuel tested is the reference Jet A-1 and the CAST set point is set at (84/30/3). The injection time is 1min corresponding to 14.8 ppm of CO_2 injected. A blank with water and lights on is done at the beginning of the experiment.

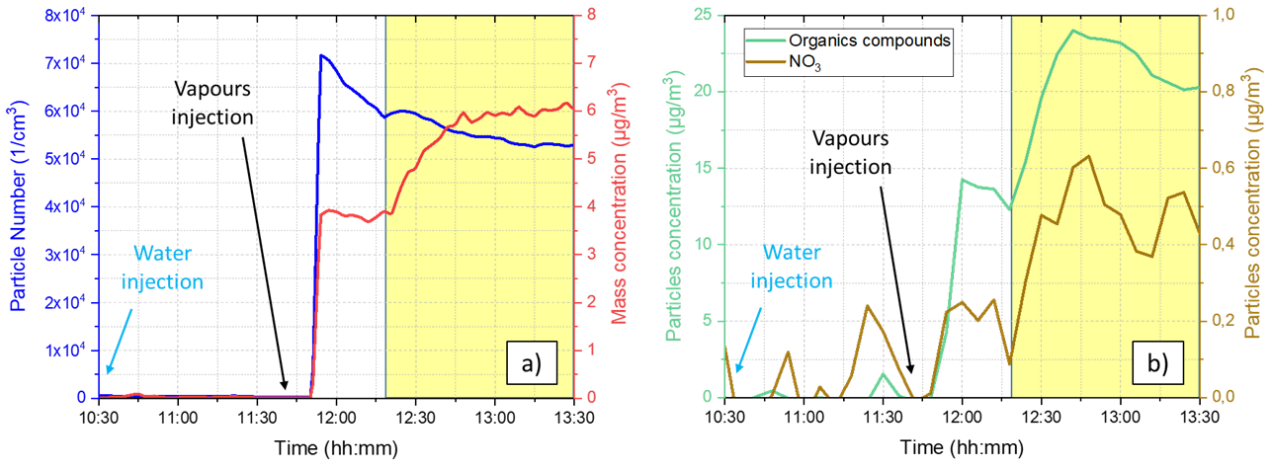

Figure IV-11: Quantification (case a) and chemical analysis (case b) of the particulate phase over the time for kerosene vapour injection in CESAM chamber. The figure a) represents the number (blue) and mass (red) concentrations obtained with an SMPS and corrected for wall loss and dilution rate. The figure b) represents the concentrations of Organic compounds and NO_3^+ monitored with an ACSM corrected for dilution but not for wall losses. The fuel tested is the reference Jet A-1 with (84/30/3) CAST set point. Lights on correspond to yellow areas.

To complete these previous observations, evolution of the number and mass concentrations over the time is presented in Figure IV-11-a. After kerosene vapour injection, number concentration decreases by condensation of vapour from 7.1×10^4 part/cm^3 to 5.9×10^4 part/cm^3 and mass concentration remains constant at 3.8 ± 0.15 µg/m^3. After light activation, formation of vPM observed in Figure IV-10 is characterised in Figure IV-11-a by a small increase of the number concentration (+2% at the bump) and a high increase of the mass concentration (+56% at the end of the test). Particles are formed by nucleation from vapour, and the number of particles decreases due to coagulation.

Particles injected and the ones formed after light activation are mainly composed of organic compounds as represented in Figure IV-11-b. The concentration of organics increases from 13.5 µg/m^3

to 23.4 µg/m^3 after light activation. In addition, a small formation of NO_3^+ can be observed from 0.2 µg/m^3 to 0.6 µg/m^3. No variations concerning NH_4^+ and SO_4^+ concentrations remaining in the background signal (SO_2 concentration introduced in the chamber is similar to the one found in the ambient air and remains constant: 1.3 ppb). It shows that kerosene vapour induce homogeneous nucleation and it explains the small amount of mass concentration observed in Figure IV-7: the flame has been blown off during the test implying that kerosene vapour have been also injected with gas phase in the chamber.

In addition, the composition of the gas phase has been monitored with a PTR-MS. Examples of normalised signals recorded over the time and corrected for the dilution (not for wall losses) for some compounds identified are presented in Figure IV-12. At the injection, the main part of the vapour is composed of hydrocarbons (alkene - case a and b): benzene, naphthalene, fluorene, propene… We can also find organic compounds such as ketene, aldehyde, acid (case c) and nitric compounds (case d). Light activation does not affect the amount of hydrocarbons but forms more oxygenated compounds in the chamber in accordance to precedent results. For example after lights on, the concentration of ketene increases by 44%, the one of acetaldehyde increases by 18%, the one of formic acid increases by 59% and the one of acetone increases by 16% at the end of the test.

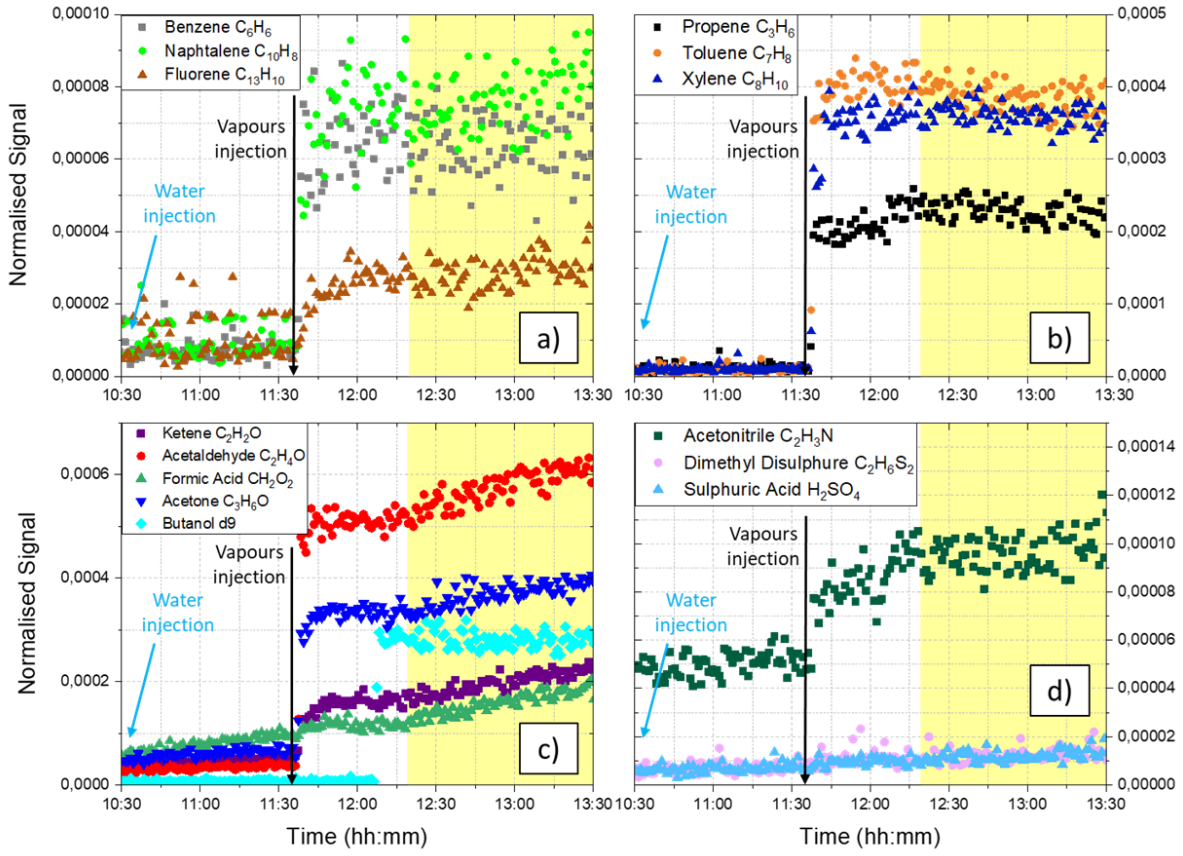

Figure IV-12: Chemical composition of the gas phase for injection of kerosene vapour in CESAM chamber. Fuel tested is the Jet A-1 for (84/30/3) CAST set point. Measurements have been recorded by the PTR-MS and corrected for dilution.

We can conclude that the kerosene vapour contribute to increase the concentration of organic compounds and can lead to the formation of new vPM inside the chamber affecting the homogeneous nucleation process from the gaseous precursors as expected in Figure IV-7.b.1. The same test has been repeated for the same conditions with a second fuel and the same trends have been observed (Annex J). To be sure to inject only gas phase or raw emissions without contamination by vapour, the CAST set point has been changed from (105/30/2) to (84/30/3) for the productive tests.

IV.1.3 Summary of the final set-up toward the first nucleation step

Preparation phase was dedicated to the optimisation of the protocol (light activation, injection monitoring) and to the validation of the CAST operating point discussed in III.1.2. The introduction of the emissions in the chamber is done with and without soot filtration to study homogeneous nucleation independently of soot presence and interactions between nvPM and vPM. The injection is monitored by the concentration of CO_2 and all measurements are normalised by the CO_2 concentration measured at the injection to compare each test. The lights are switched on with a delay of 30min after the injection.

All results presented thereafter in this chapter are based on the set-up presented in Figure IV-13. For the same fuel, gas phase injection is done in the morning (results presented in the following section of this chapter). Then, the chamber is cleaned by pumping and the raw emissions are injected in the afternoon for a second experiment (cf. Chapter V). In this way, uncertainties in the stability of the source when comparing both measurements are reduced.

It should be noted that the physical evolution of emissions in CESAM chamber is different than in aircraft exhaust plume. The initial mixing of the exhaust emissions into the chamber happens at different time and length scales than in an aircraft plume. The initial injection is also different from the initial plume mixing of an aircraft plume, since it is already known that nucleation and initial growth of vPM in aircraft plumes is primarily occurring in the first seconds and minutes of the plume mixing. Furthermore, the chamber then limits further mixing (beyond the roughly few hundred-fold dilution estimated from the CO_2 enhancement) and the exhaust evolves photochemically and microphysically at that fixed dilution factor. This is not the same as the actual evolution in the atmosphere but working with the CESAM chamber allows experiment in a well-controlled environment (ground level).

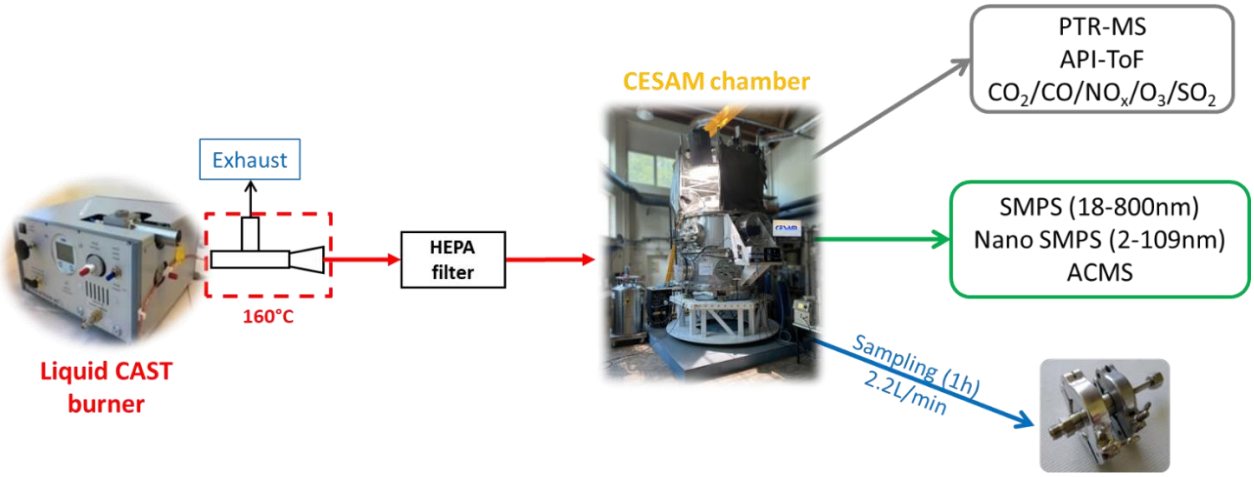

Figure IV-13: Final set-up for productive test on CESAM chamber.

To study the formation of vPM at the nucleation scale and characterise molecular clusters involved in vPM formation process, an Atmospheric Pressure Interface Time of Flight Mass Spectrometer (API-ToF) has been added to the set-up. It allows the analysis of the chemical composition of pre-nucleation clusters produced in the chamber (from 1 molecule to ~2 nm size diameter). The size distribution (Figure IV-14.b) and particle number concentration are obtained using a nano-SMPS (with a range of 2.1 to 109 nm) to capture nucleation mode and a SMPS (19.5 to 800 nm) to capture larger particles as soot. In parallel, an on-line chemical characterisation of the emissions is done using a PTR-MS for the gas phase and using an ACSM for the particulate one. In addition, filters have been collected during 1h on the chamber at 2.2 L/min to be studied thereafter by mass spectrometry techniques. The purpose of this off-line measurement is to compare and complement

the chemical composition analysis of the emission provided by the on-line instruments (ACSM is limited by size of detected particles and compounds detected by PTR-MS are based on proton affinity of water).

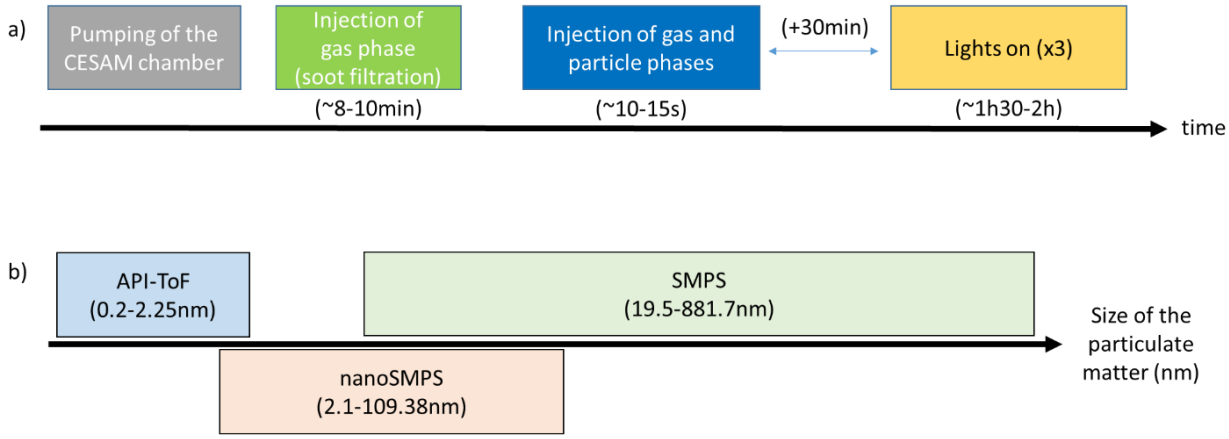

Figure IV-14: Time-chart of the experimental process for injection of CAST emissions in the CESAM chamber (a), and measurement techniques used according to the particle size distribution (b).

IV.2 Homogeneous nucleation in an atmospheric controlled environment: formation of vPM for a reference case

The experimental set-up and the operating process have been described in the previous part of this chapter. The measurements have been done for a CAST set point at (84/30/3); soot particles have been removed from the CAST emissions using an HEPA filter in CAST outlet to study only the gas phase in the CESAM chamber; the lights are switched on 30min after the injection.

To study vPM formation from homogeneous nucleation, a reference case based on the Jet A-1 fuel is presented. This fuel is mainly composed of paraffins (50%) and alkanes (32.3%) and it contains 20.2% of aromatic compounds and 200 ppm of sulphur (more details in II.1.1.2).

IV.2.1 Injection of gas phase in the chamber

Gas phase emissions are introduced without soot particles in the atmospheric chamber for the first productive experiment. In regards to the preliminary tests, an injection of 8min has been done to get a comparable amount of CO_2 and to reach 60 ppm (reference gas remaining constant over the time - cf.IV.1.1). The CAST flame obtained for Jet A-1 fuel combustion was stable and controlled during all the time of injection to prevent extinction and vapour contamination.

After the injection of the emissions in the chamber, the pressure is set to ambient value. After 2min of stabilisation, the concentration of gas introduced have been monitored and values are regrouped in the Table IV-4:

Test	Time	CO_2 (ppm)	CO (ppb)	SO_2 (ppb)	NO_x (ppb)
Gas phase injection	Wait 2min after injection for stabilisation	63.77	383.60	2.36	11.65
		Normalisation by CO_2: ppb per ppm of CO_2 ($x10^{-3}$)	6.02	0.04	0.18

Table IV-4: Gas measurement by LISA gas sensors after gas phase injection inside CESAM chamber. Mass and number concentrations are not quantifiable for this case because no particles have been injected in the chamber with soot filtration. Normalisation is done by CO_2 (division) for each value: ppb per ppm of CO_2.

The evolution of these gases over the time in the atmospheric chamber is presented on Figure IV-15: the concentrations of CO_2, CO, SO_2 and NO_x correspond respectively to case a, case b, case c and case d. The raw data are presented in grey and all of them have been corrected for dilution but not for wall losses (not effective for gas). Light activation is represented by the yellow area.

The first observation is that CO_2 concentration decreases over the time (-2.39 ppb in 2h), even after dilution correction (Figure IV-15.a), despite the fact that CO_2 is not supposed to interact in the reactions. It is due to the losses on the wall that are not corrected in the case of the gas phase. The other observation is that light activation does not affect CO_2 and CO concentrations (Figure IV-15.a and b). The amount of CO_2 injected inside the chamber is 8.5 times higher and the CO concentration is 6 times higher than in the ambient air (observed before gas phase injection).

Concerning the SO_2 (Figure IV-15.c), the injection of gas phase emissions from CAST introduces 2.36ppb of sulphur dioxide in the chamber and this concentration do not change over the time even with light activation (small increase of 0.2ppb at the end is due to dilution correction calculation).

The last representation corresponds to the monitoring of NO_x (Figure IV-15.d). NO and NO_x are recorded and NO_2 is calculated from NO_x-NO=NO_2. After gas phase injection, the concentrations of NO, NO_2 and NO_x increase respectively from 1.52 to 11.03 ppb, from 0.63 to 6.51 ppb and from 1.85 to 17.8 ppb. After light activation, an increase of NO amount (+17%) and a decrease of the NO_2 amount (-23%) are recorded. The photochemistry contributes to generate at first NO. Then, 10min after light activation, the concentration of NO decreases to generate NO_2 inside the chamber. The NO_x concentration decreases continuously (-4.36 ppb in 2h) as NO concentration decreases (-7.27 ppb in 2h) more than NO_2 concentration increases (+2.91 ppb in 2h).

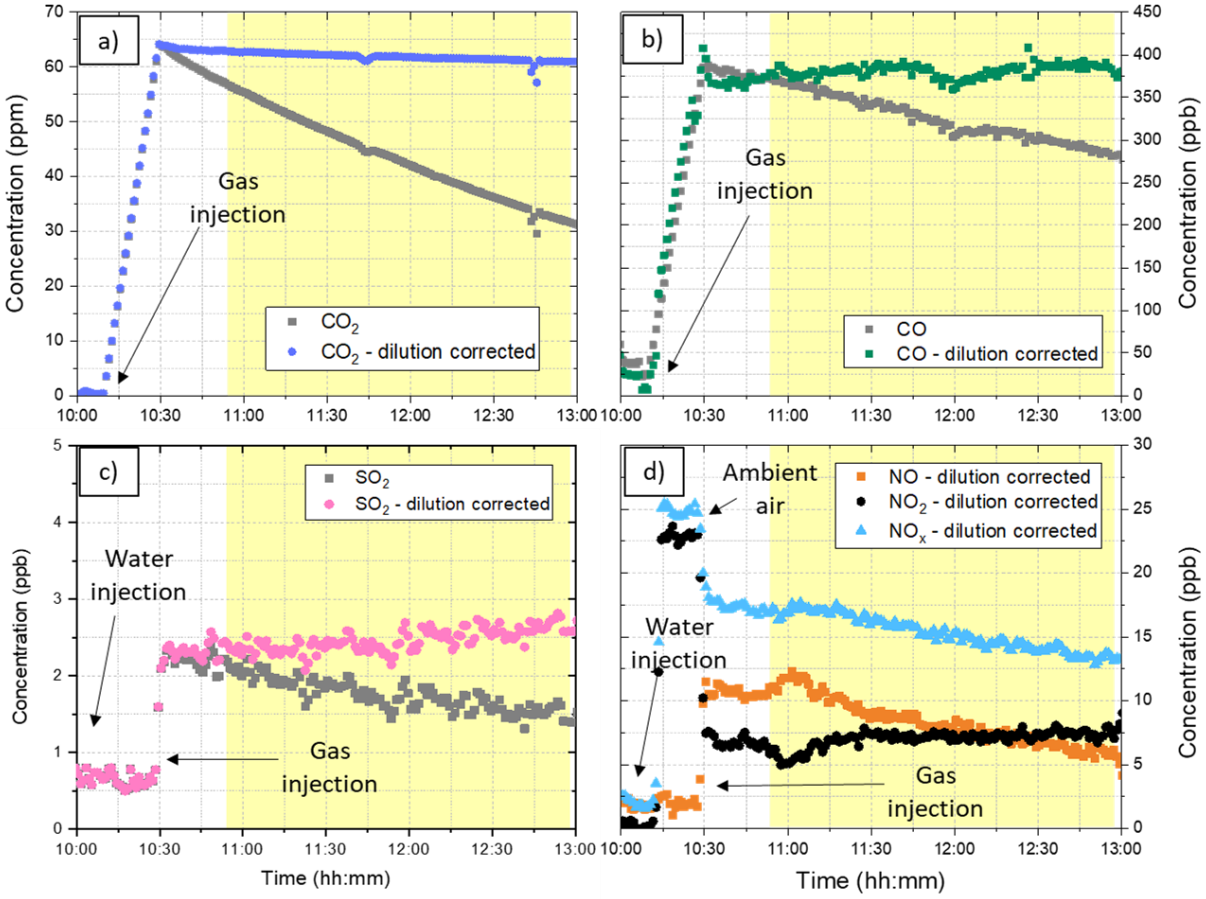

Figure IV-15: Monitoring of gas in CESAM chamber for gas phase injection using Jet A-1 fuel. Cases a and b represent the evolution of CO_2 and the CO concentrations. Case c and d correspond to the concentration of SO_2 and NO_x. The yellow area represents the light activation in the CESAM chamber. Values have been corrected for dilution but not for wall losses.

IV.2.2 New particles formation from homogeneous nucleation

After the injection of gas phase in the chamber, no significant variation of gas concentrations are observed. However, directly after light activation, NO_x have been generated. Due to their implication in SA formation process (cf. I.3.2), the interest is focused on the formation of vPM by homogeneous nucleation from the gas phase. The Figure IV-16 represents the evolution of the particles in the CESAM chamber in terms of size (y-axis) and in terms of particle concentration (colour scale) over the time. The limit of detection of this instrument is 2 nm but the signal is too noisy under 4nm (background). It can be noted also that the instrument has been disconnected from the chamber (3 size distributions have been not recorded corresponding to 15min), but without consequences for the experiment (trend remaining the same).

First observation is that no particles are detected after gas injection but directly after the activation of lights, new vPM are formed. It is represented by a high increase of the particle size conjugated with a high increase of the particle number ("banana plot" shape). The concentration of particles is maximum at the beginning reaching 2.77x10^6 part/cm^3 at 4.2 nm in 7min and decreases with the time due to agglomeration (0.47 x10^6 part/cm^3 at the end of the experiment). The size of particles increases over the time by condensation of gaseous vapour on their surface and agglomeration of small vPM (explaining the decrease of their concentration). At the end of the test, no more significant formation of new particles is observed and the particle size stagnates. The largest size reached by these new vPM formed is 24.39 nm just before switching off the lights. This is confirmed by another SMPS with a cut-off of 20 nm. Results obtained are presented in Annex K.

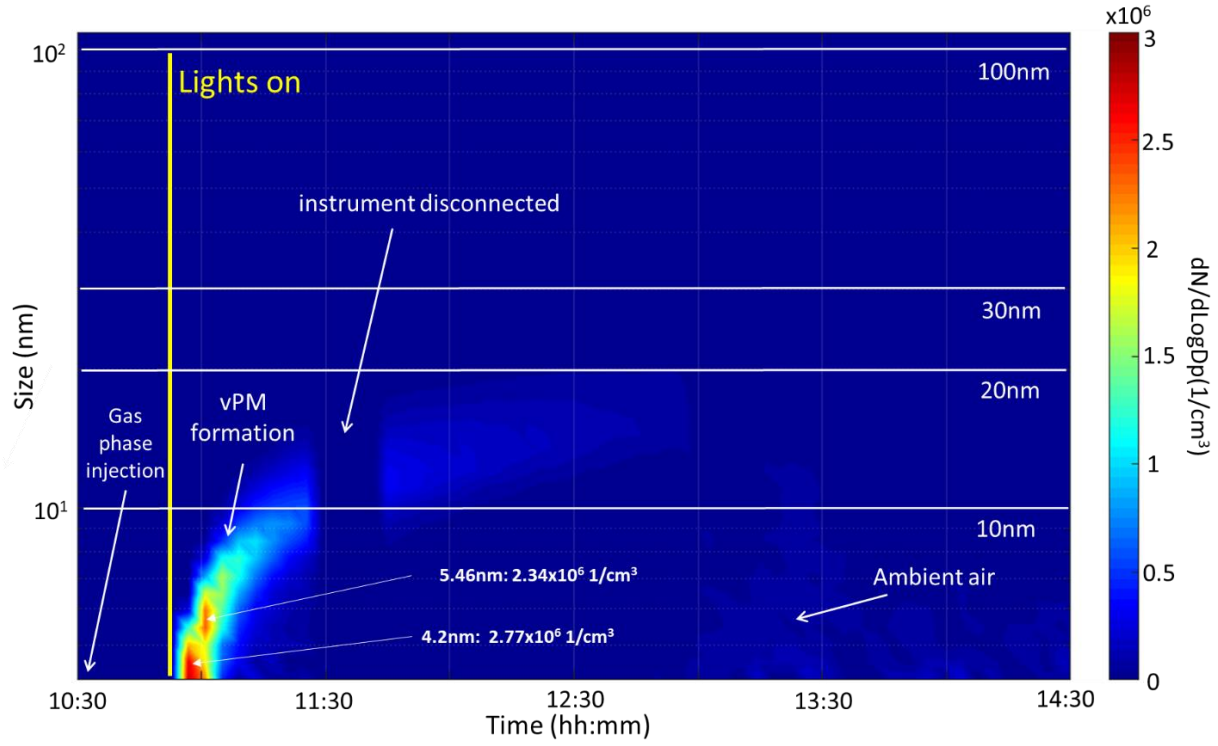

Figure IV-16: Homogeneous nucleation from gas phase leading to vPM formation in CESAM chamber after Jet A-1 fuel combustion. The instrument has been disconnected during the experiment and 3 size distribution recordings have been lost.

Figure IV-17 gives the representation of the number and mass concentrations of particles over the time for two SMPS instruments: on the left to study large particles (20 – 800 nm) and on the right to study vPM formation at smaller size (4 – 109 nm). All data have been corrected for dilution and wall losses. Light activation is indicated by the yellow area.

Due to the limit of detection of the SMPS, the variations of particle concentration are observed with a delay after light activation (Figure IV-17.a) and not all particles have been recorded. It is comparable to the information provided by Annex K. The different times when particles appear in different instruments indirectly give the growth time from 4 to 20 nm. The particle number increases to 4.91×10^3 part/cm^3 (corresponding only to the part of particles bigger than 20nm). In comparison, the nano-SMPS allows the monitoring of particle concentration for smaller sizes. With light activation, the number of particles increases quickly to 2.90×10^5 part/cm^3 corresponding to the high amount of vPM formed at small size and observable on Figure IV-16. Then, the particle number decreases quickly to 1.05×10^5 part/cm^3 (in 30min) due to formation of bigger vPM (increase of the vPM size on Figure IV-16). After that, this decrease is slowing down until the end of the experiment (-15.36% in 50min).

Concerning the mass concentration, the signal recorded by the SMPS is weak (only 0.04 µg/m^3 in Figure IV-17.c), as the main part of the vPM formed has a size under 20 nm. To get a better overview of smaller particles formed, the Figure IV-17.d completes the evolution of mass concentration in the chamber. With light activation, the mass concentration increases to 0.06 µg/m^3 after a small delay (8min). Indeed at first, small particles are generated but too small (4.2 nm) to be recorded by the instrument. After the start of vPM formation (+35min), the mass concentration stabilises at 0.07 µg/m^3. After that, as the number of particles decreases and the particle size increases, the mass concentration stays constant until the end of the experiment. This conservation of mass means that at the beginning of the experiment, particles are numerous, small and light. At the end, there are less particles with larger size thus heavier.

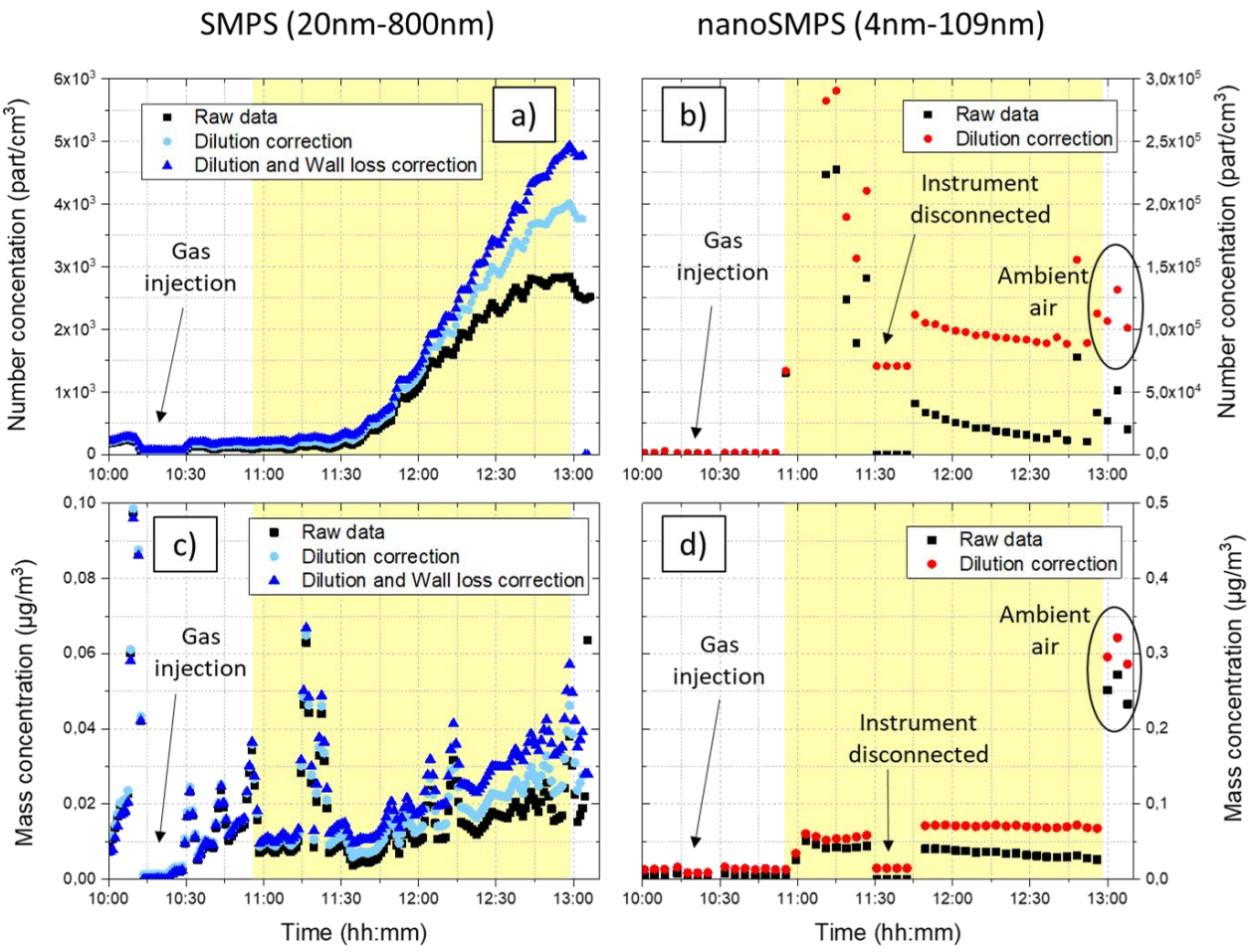

Figure IV-17: Number (left) and mass (right) concentrations of vPM formed inside CESAM chamber for gas phase injection using Jet A-1 fuel. vPM are monitored by SMPS (case a and c) and by nanoSMPS (case b and d). All values have been corrected for dilution and wall losses. The light activation is represented by the yellow area.

IV.2.3 Size of particles and geometric mean diameter

With photochemistry, new particles are formed and their size evolves in the chamber. Figure IV-18 presents the size distributions of particles over the time after light activation. It can be noted that all the distributions are monomodal, confirming that only vPM are present. The first observation is that the particle concentration decreases from $1.17x10^6$ part/cm^3 20min after the light activation to $0.84x10^5$ part/cm^3 120min after light activation (-93%). At the same time, the size of particles increases from 7.10 nm to 17.09 nm. This confirms the previous observations done about formation of bigger vPM but less numerous over the time.

Figure IV-19 represents the Geometric Mean Diameter (GMD) of the particles recorded in the chamber. The geometric mean corresponds to the particle diameter at the 50% probability point. It signifies that half of the particulate matter consists of particles larger than this diameter, while the other half consists of particles with smaller diameters. The standard deviation characterises the variation in particle sizes. It is calculated by dividing the geometric mean by the particle size at the 15.78% probability or by dividing the particle size at the 84.13% probability by the geometric mean. The Figure IV-19.a corresponds to the total GMD mode obtained Jet A-1 test, taken into account all the particles for the calculation: vPM generated by photochemistry and also small particles formed due to contamination after water injection (observable on the left of the Figure IV-19 before gas phase injection and before light activation). The Figure IV-19.b corresponds to the GMD calculated after the fit process (focus only on the vPM formed after light activation). Few differences are observed between both cases: the fitted GMD mode presents less dispersion and becomes higher compared to total GMD mode (presence of some peaks at very small sizes for this case shifting the GMD toward smaller sizes, cf. Figure IV-19-a on the right). After lights on, the vPM GMD increases from 5.22 nm to 16.66 nm. Particles become bigger and the number of small particles decreases with the time: coagulation and agglomeration of pre-existing particles.

These observations confirm that new vPM are formed in a controlled atmosphere by homogeneous nucleation from gaseous precursors and increase in size. The next step is the analysis of the chemical composition of the particles formed.

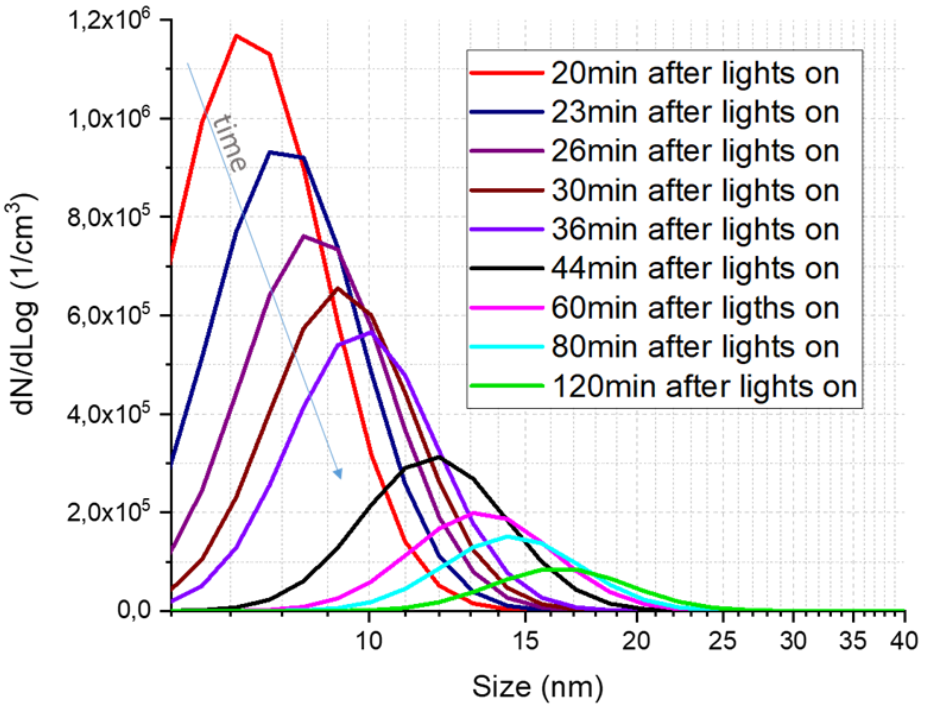

Figure IV-18: Particle size distributions after gas phase injection and light activation in the CESAM chamber.

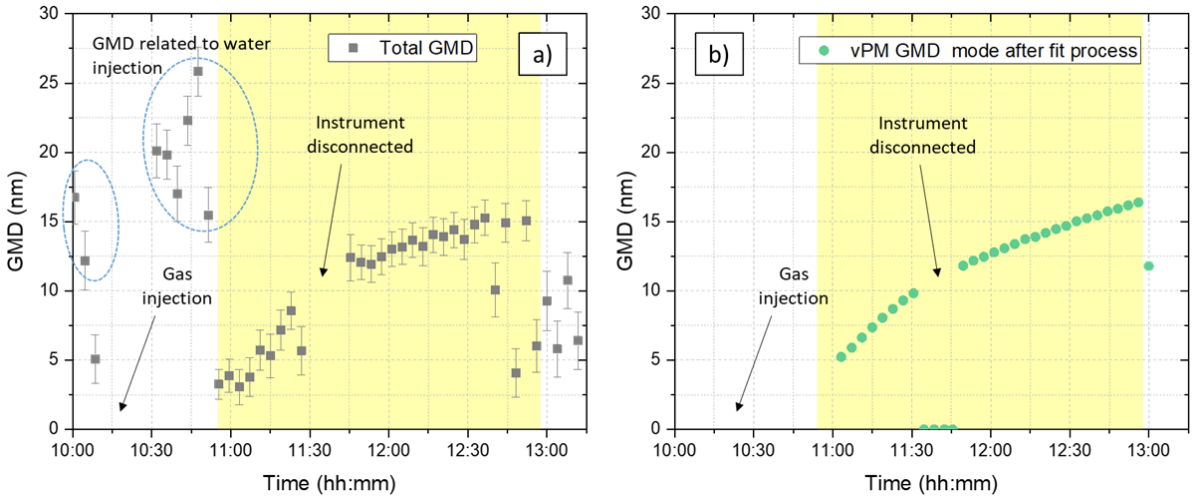

Figure IV-19: GMD of new particles formed in the CESAM chamber for gas phase injection (soot filtration) using jet A-1 fuel. The first representation on the left corresponds to the total GMD calculated by the nanoSMPS. The second representation corresponds to the fitted GMD centred on vPM. Light activation is indicated by the yellow area.

IV.2.4 Towards nucleation step

To study the formation of the first molecular nucleation clusters inside the chamber, an API-ToF (details in II.2.2.2.5) has been used. In regards to SA formation mechanisms, analysis is focused on sulphuric acid and Highly Oxygenated Organic Molecules (HOMs) formation in the chamber after gas phase injection and light activation.

The evolution of H_2SO_4 over the time is represented on Figure IV-20. The raw data (in grey) have been corrected for dilution (in purple) and photochemistry is represented by yellow area. The first observation is that sulphuric acid has been formed directly after the light activation. Its concentration increases quickly to $5.8x10^8$ part/cm^3 and decreases because of nucleation to $1.89x10^8$ part/cm^3 in 30min before stabilisation at $\pm1.87x10^6$ part/cm^3. It is related to the formation of vPM in the chamber: the high formation of sulphuric acid just after light activation leads to the high concentration of small new particles formed and the decrease of H_2SO_4 amount leads to the increase of the new particles size (gas phase molecules are adsorbed on their surface – cf. details in IV.2.5.3).

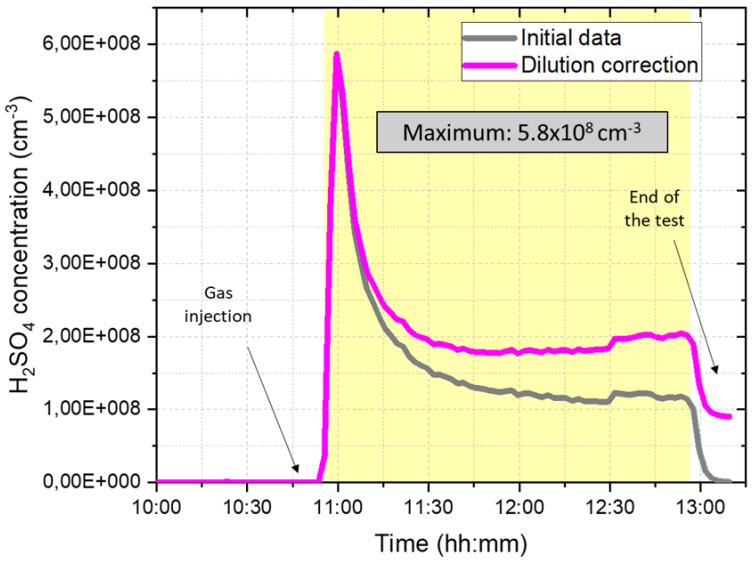

Figure IV-20: Evolution of H_2SO_4 concentration in the CESAM chamber after gas phase injection for Jet A-1 fuel combustion.

To complete the previous observations about sulphuric acid, the impact of highly oxygenated compounds on vPM formation has been also studied. Figure IV-21 presents the evolution of some HOMs derived from toluene (C_7H_8), benzene (C_6H_6) and diphenylmethane ($C_{13}H_{12}$). In this case, it seems that HOMs are lost very fast during the test. Their lifetime is too short to obtain a good signal and not enough spectra are collected to minimise signal to noise ratio. For example, only $C_7H_7O_9$ is generated (Figure IV-21 in orange) after light activation but its concentration decreases quickly. HOMS are only formed when there is a burst of OH at light activation and when there are no particles. When particles start to form, they act as a condensation sink of precursors and HOMs (Figure IV-21 – red dash). In addition, molecular clusters grow and they are not any longer detected by API-ToF. A blank test after water injection and before gas phase injection has been done with lights on. It shows that some HOMs have been already detected in the background. It implies that HOMs are not only generated after gas phase injection but also from the contamination introduced by water injection at the beginning of the test.

The sensitivity of the instrument can be increased for a short moment to try to detect any changes in HOMs concentrations by increasing the NO_3^- primary ions concentration and by saturating the signal. However, no changes were observed (green dash at the end of the experiment on Figure IV-21). It can be noted that the HSO_4^- concentration signal is not affected by sensitivity increase, but the $H_2SO_4^+NO_3^-$ cluster is (cf. Figure IV-20).

In conclusion, sulphuric acid is mainly responsible for vPM formation in this case as no/few HOMs have been detected. To consider the impact of HOMs, some other fuels with less or no sulphur content have been tested (cf. results in IV.3.2).

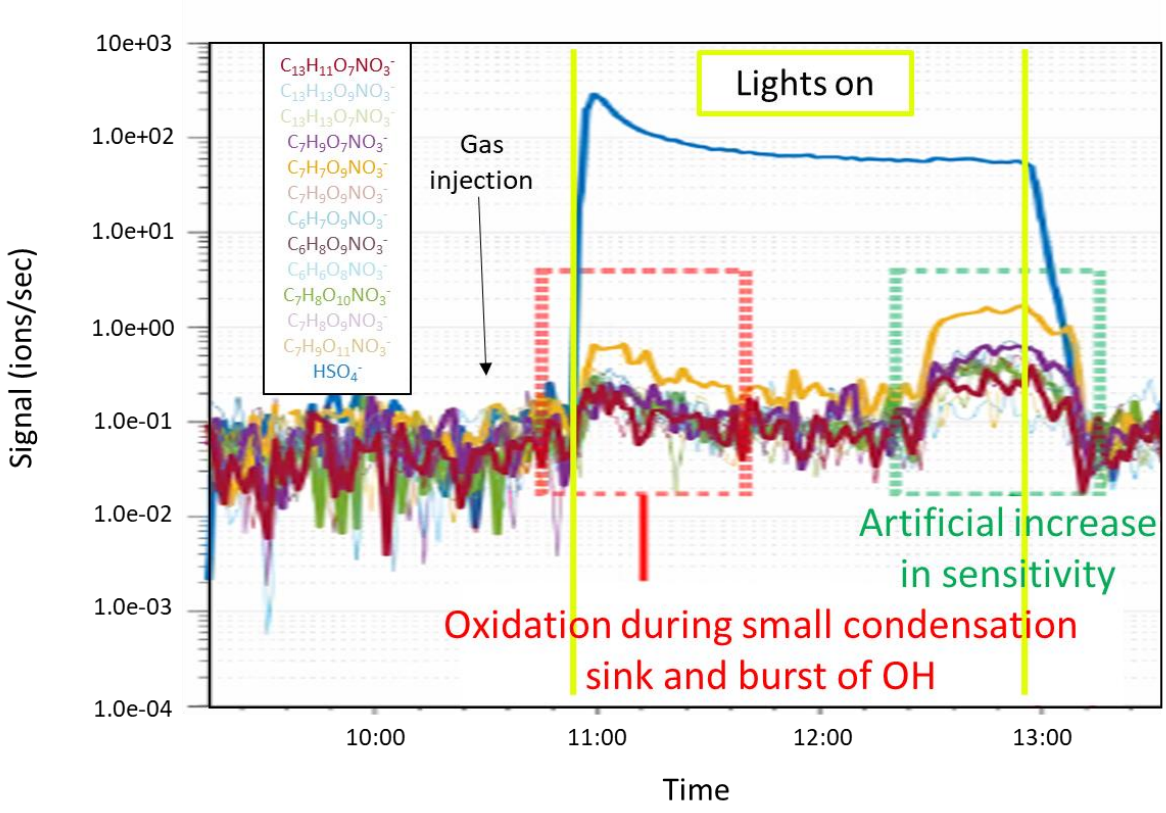

Figure IV-21: Evolution of HOMs concentration in CESAM chamber after gas phase injection for Jet A-1 fuel combustion. Compounds analysed are derived from toluene (C_7H_8), benzene (C_6H_6) and diphenylmethane ($C_{13}H_{12}$).There is a burst of OH at the start leading to a high condensation sink (red dash) for HOMs. The sensitivity has been increased by addition of NO_3^- (green dash).

IV.2.5 Analysis of chemical composition of new particles formed

IV.2.5.1 Analysis of the gas phase

As only gas phase has been introduced in the chamber, the gaseous compounds have been monitored using a PTR-MS (details in II.2.2.1.4). The objective is to observe which compounds are consumed and which ones are formed, to link them and to explain the formation of the vPM.

Figure IV-22 presents the evolution of concentrations for some gaseous compounds depending on photochemistry impact over the time. The cases a) and b) correspond to oxygenated compounds concentrations, the case c) presents the evolution of hydrocarbon concentrations and the case d) regroups nitric and sulphur compounds concentrations. All data have been corrected for dilution.

At the beginning of each test, butanol-d9 ($C_4H_{10}O$, cf. Figure IV-22.b) is introduced in the chamber as an OH radical tracer to determine OH exposure (Barmet et al., 2012).

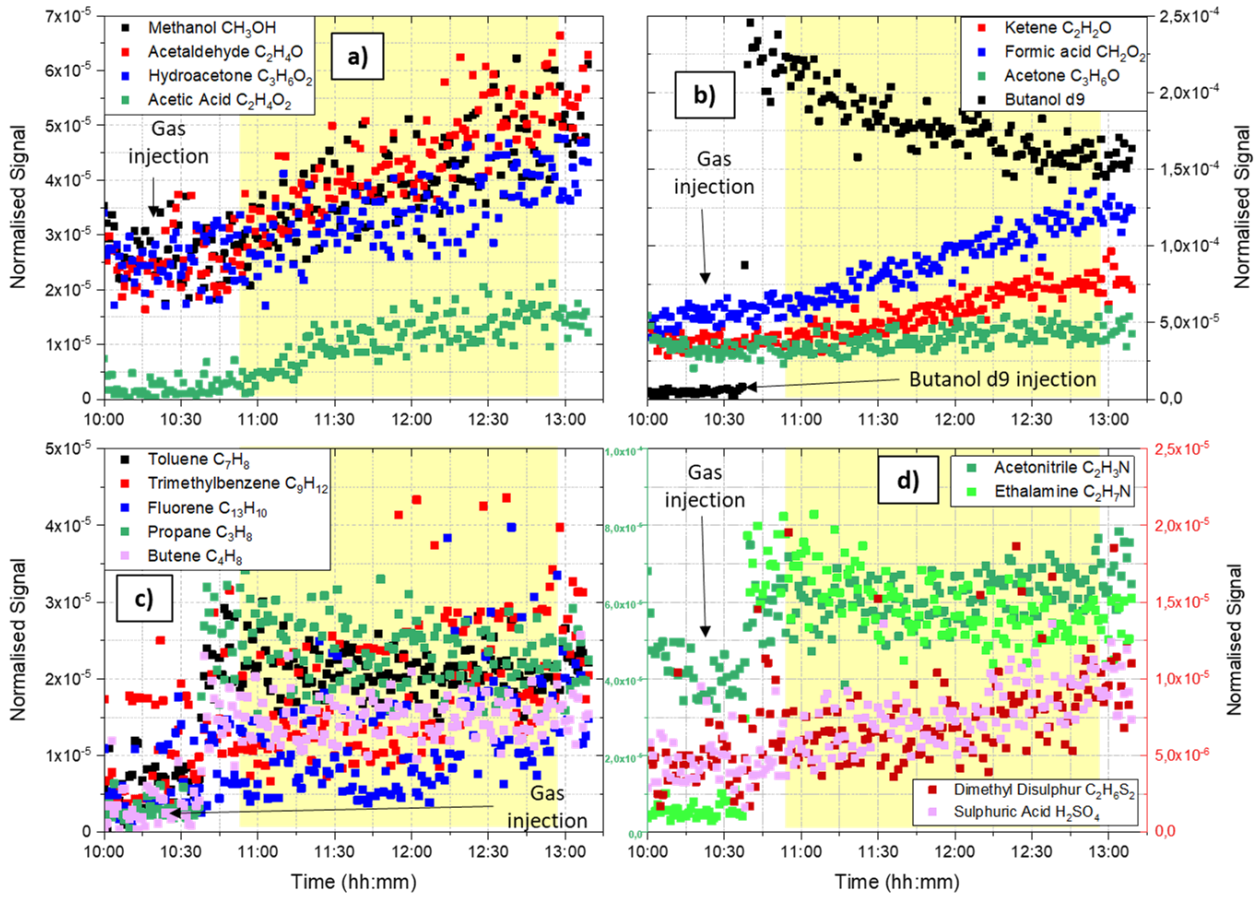

Figure IV-22: Example of gaseous compound concentrations measured with PTR-MS. Figures a) and b) correspond to the Oxygenated compounds with presence of OH tracers (butanol –d9); the case c) corresponds to hydrocarbons compounds and the case d) corresponds to the nitric compounds and sulphur compounds. Light activation is specified by the yellow area. All data have been corrected for dilution.

The first observation is that directly after light activation, the concentration of oxygenated compounds increases in the chamber (Figure IV-22.a and b). It can be noted for example that acetic acid was not present initially in the chamber compared to the other compounds (Figure IV-22.a) and it has been generated after light activation.

Regarding hydrocarbon compounds (Figure IV-22.c), they have been introduced in the chamber with gas phase injection. After light activation, a distinction can be made between heavier compounds

for which the concentration increases slightly (Toluene or Fluorene) and other ones for which concentration remains constant over the test (Propane or Butene). Concerning nitrogen and sulphur containing compounds (Figure IV-22.d), their concentrations tend respectively to decrease and to increase.

The following Table IV-5 regroups all signals detected by the PTR-MS for the Jet A-1 fuel. Only significant variation in the concentration is reported here: before gas injection, after gas injection and after light activation. The colour code indicates if the concentration of a compound decreases (red) or increases (blue), stays unchanged (white) or if the compound is present in the chamber (green). Some VOCs, nitrogenated and oxygenated compounds have been identified. It can be noted that not all the compounds are initially present in the chamber and the light seems to affect them by a reduction or an increase of their concentrations. The concentration of larger aromatics does not change significantly during the experiment. This study will be completed by the analysis of the filters collected and studied with off-line mass spectrometry instruments (cf.IV.2.5.3).

Accurate Mass (with H+) m/z	Identification	Formula ($^+$)	Jet A-1		
			Initially in the chamber	After Gas Injection	After Lights
33,03336	Methanol	CH_3OH			
42,03399	Acetonitrile	C_2H_3N			
43,01625	Ketene	C_2H_2O			
43,05950	Propene	C_3H_6			
44,01396	Cyanic Acid	CHNO			
44,05479	Ethanimine	C_2H_5N			
45,02640	Acetaldehyde	C_2H_4O			
45,06199	Propane	C_3H_8			
46,02783	Formamide	CH_3NO			
46,06886	Ethylamine	C_2H_7N			
47,01262	Formic Acid	CH_2O_2			
49,06511	Ethane Hydrate	C_2H_8O			
51,99057	Sulphane Hydroxide	H_3OS			
57,07040	Butene	C_4H_8			
59,04450	Acetone/ Methyl Vinyl Ether	C_3H_6O			
61,02895	Acetic acid	CH_3COOH			
62,09527	Trimethyloxonium	C_3H_9O			
66,12218	Cyclopentadienyl	C_5H_5			
75,04461	Hydroxyacetone	$C_3H_6O_2$			
75.07919	Butanol d9	$C_4H_{10}O$			
93,05880	Toluene	C_7H_8			
95,00199	Dimethyl Disulphur	$C_2H_6S_2$			
96,98858	Sulfate	SO_4			
98,98110	Sulphuric Acid	H_2SO_4			
121,10173	Trimethylbenzene	C_9H_{12}			

Table IV-5: Compounds detected by PTR-MS for gas phase injection in the CESAM chamber after Jet A-1 fuel combustion. The name of the compounds and the related [M+1] detected mass are indicated. Presence of compounds in the sample is indicated in green; the decrease of the concentration of the compound in red; the increase of the concentration of the compound in blue and in white no trend are recorded.

IV.2.5.2 Study of the particulate phase

To analyse the composition of the vPM formed in the chamber, the particulate phase is monitored by an ACSM (cf. II.2.2.2.4). This instrument provides the concentrations of the organic compounds, sulphate, nitrate, and ammonium. The organic compounds are composed mostly by the Oxygenated Organic Aerosols OOA ($C_nH_mO_y$ as CO_2^+, $H_3C_2O^+$, …) and by the Hydrocarbon Organic Aerosols HOA ($C_nH_m^+$). Some specific fragments are used as for example at m/z 43 (noted f43, ratio of the signal m/z 43 respect to the total signal of the spectra) corresponding to $C_2H_3O^+$, at m/z 44 (f44) corresponding to CO_2^+, at m/z 57 (f57) corresponding to $C_4H_9^+$+$C_3H_5O^+$ and at m/z 60 (f60) corresponding to $C_2H_4O_2^+$. The sulphate family regroups fragments of $H_2SO_4^+$, HSO_3^+, SO_3^+, SO_2^+, SO^+. The ammonium family contains some fragments such as NH_3^+, NH_2^+, NH^+. The nitrate family corresponds to HNO_3^+, NO_2^+, NO^+ fragments.

Figure IV-23 represents the evolution of these families over the time inside the chamber after gas phase injection. The observations are that no signal is detected after injection and after light activation. Indeed, particles are below the detection limit of the instrument (40 nm), as the GMD of the vPM formed reaches 16.66 nm at the end of the experiment (maximum 25 nm). It means that the new vPM formed in the chamber are too small to be studied with an ACSM. Only OOA fragments concentration presents some variations. However, it corresponds to contamination after water injection as seen previously. Another way to analyse the chemical composition of the particulate phase is the study of samples collected during the test and analysed off-line by mass spectrometry. Results are presented in the following section (IV.2.5.3).

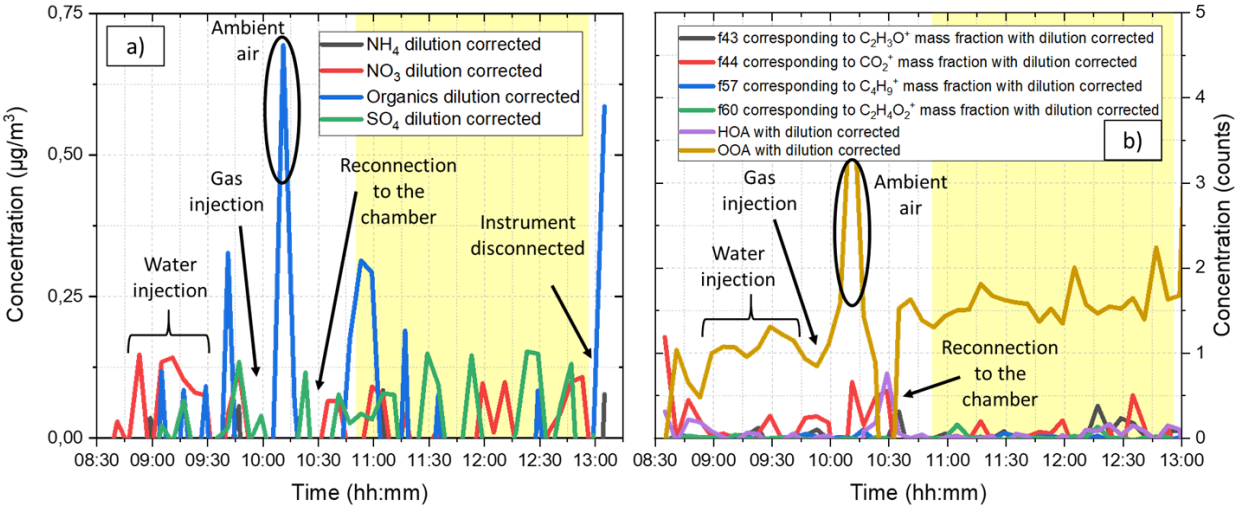

Figure IV-23: Analysis of the particulate phase in CESAM chamber for gas phase injection after Jet A-1 fuel combustion. The case a) corresponds to nitrate, sulphate, ammonium and total organics concentrations. The case b) presents in detail the evolution of organics fragments. All data have been corrected for dilution. Lights on correspond to yellow areas.

IV.2.5.3 Chemical composition of vPM by off-line emissions measurement

To complete the previous observations, some filters have been collected on the chamber using the double-filter sampling system described in II.2.2.3. The sampling took 1h at 2.2L/min. It has been done when the formation of particles inside the chamber has slowed down (1h after gas phase injection to avoid the impact of sampling on vPM formation). The filters have been analysed at PhLAM laboratory in Lille using the high-resolution mass spectrometry L2MS instrument (cf. II.2.2.3.2). These results complete the previous chemical analysis of the particulate phase (limited by ACSM particles detection) and of the gas phase (PTR-MS).

- Mass spectra for Jet A-1 fuel test after gas phase injection

To analyse the surface of the sample collected on CESAM chamber, the fluence of the desorption laser was set at 34.5 ± 0.4 µJ/cm² and the fluence of the ionisation laser was set at 6.3 ± 0.3 mJ/cm². The parameters of detection are optimised for PAH detection (wavelength of the ionisation laser). The Front Filter (noted FF) corresponds to the particulate phase sampling and the Back Filter (noted BF) corresponds to the gas phase sampling. Each filter is analysed for positive and negative ions detection and each measurement is repeated 3 times to obtain an average signal.

No signal has been recorded after the analysis of the FF for the positive mode and few signals have been recorded for the FF in negative mode. It is related to the fact that there is not enough deposit on the sample surface due to the short time of sampling (1h) and the low sampling flow (2.2 L/min). Indeed, the deposit on the FF for particle phase is 0.23 µg for the gas injection case in the CESAM chamber. It is spread on a 4.5 cm² area (sample surface), which means 0.5 ng/mm². The PM available for analysis in the 0.057 mm² spot of the desorption laser is 0.03 ng, at the detection limit of the instrument. In comparison, the deposit on a sample collected at CAST burner exhaust is 0.125 mg corresponding to 16 ng per spot of desorption laser (cf. III.2.4).

Mass spectra obtained from gas phase analysis are regrouped on Figure IV-24 presenting the intensity of each signal depending on the mass over charge ratio. More species have been detected on the BF. It is mainly due to the presence of a black carbon layer on the filter's surface (carbon clusters). In addition, some hydrocarbons and some sulphur compounds such as SO_3^- and HSO_4^- have been detected.

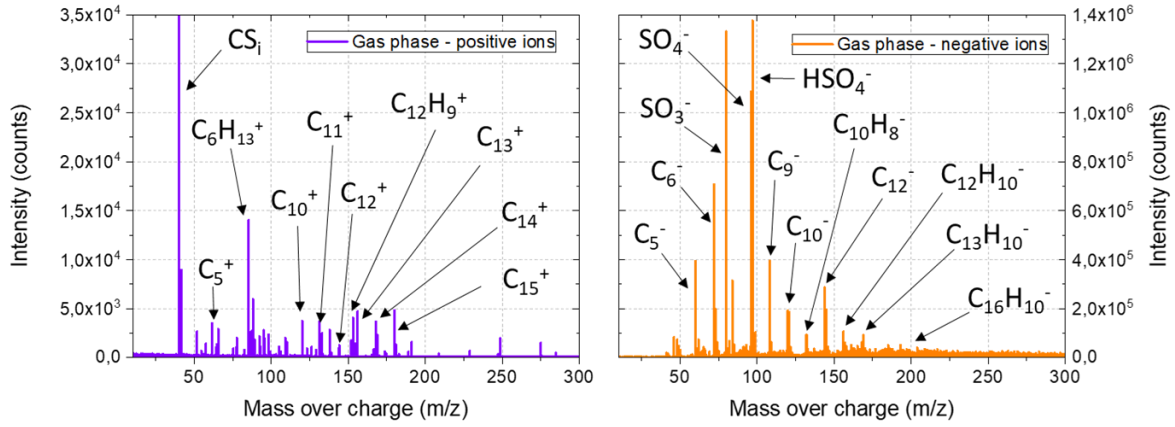

Figure IV-24: Mass Spectra obtained from the analysis of filters by HR-L2MS. Samples correspond to tests done for gas phase injection (soot filtration) after Jet A-1 fuel combustion. The two bottom spectra correspond to the back filter for gas phase study in positive (left) and negative (right) ions mode. Few signals have been detected on the front filter.

- Identification

Due to the low quantity of matter deposited on the sample surface during the experiment, few species have been detected and identified. Most of them correspond to carbons clusters and hydrocarbons. However some sulphur and PAH compounds have been found and they are regrouped in Table IV-6. It can be observed the presence of sulphuric acid that has been generated in high quantities just after light activation (IV.2.4).

PAH			Sulphur compounds	
Name	Formula	Mass (m/z)	Formula	Mass (m/z)
Naphthalene	$C_{10}H_8$	128,06	SO_2	63,96
Acenaphthylene	$C_{12}H_8$	152,06	HSO_2	64,97

Acenaphthene	$C_{12}H_{10}$	154,08	H_2SO_2	65,977
Fluorene	$C_{13}H_{10}$	166,08	SO_3	79,95
Anthracene	$C_{14}H_{10}$	178,08	HSO_3	80,96
Pyrene	$C_{16}H_{10}$	202,08	H_2SO_3	81,97
Benzo(a)anthracene	$C_{18}H_{12}$	228,09	SO_4	95,95
Benzo(a)pyrene	$C_{20}H_{12}$	252,09	HSO_4	96,96
Indeno(1,2,3-cd)pyrene	$C_{22}H_{12}$	276,09	H_2SO_4	97,967
Dibenzoanthracene	$C_{22}H_{14}$	278,11		

Table IV-6: Identification of compounds recorded after analysis with the L2MS instrument for samples collected in the case of gas phase injection from Jet A-1 combustion.

IV.2.6 Summary of first results

The set-up deployed allows the study of the evolution of the gas phase without soot presence at ground level under atmospheric conditions for the combustion of a reference fuel. Directly after photochemistry activation, new vPM are formed by homogeneous nucleation from gaseous precursors. The maximum size of the new particles formed reaches 24.39 nm at the end of the experiment and the GMD increases to 16.66 nm. At the same time, particle number increases with vPM formation and then decreases over the time due to agglomeration of new particles. The mass concentration increases before becoming constant. This conservation of the mass corresponds to the conversion of numerous small particles into fewer and larger particles.

The formation of vPM is mainly due to sulphuric acid (H_2SO_4) that comes from SO_2 oxidation. HOMs and nitric acid are less relevant in this case. The presence of sulphur in fuel composition has an impact on new particle formation. Other fuels have been tested to check the impact of composition of different fuels and complete these previous observations. Results are presented in the next section to discuss in particular about aromatics and sulphur impact on vPM formation.

Furthermore, the different chemical analyses show that vPM formation is linked to sulphuric acid, but growth is linked to organics. It was too difficult to detect oxygenated compounds with the off-line techniques due to the small amount of deposit on samples collected and due to the volatility of these compounds. In addition, the off-line mass spectrometry analysis allows the detection of different sulphur compounds such as SO_2, HSO_4^-, or sulphuric acid. Such information is relevant for numerical simulation models.

IV.3 Impact of aeronautical fuel composition on vPM formation from homogeneous nucleation in atmosphere

In the precedent section, the formation of new vPM after injection of gas phase in a controlled atmospheric chamber has been studied for a common fuel case. To analyse the impact of the fuel composition on particle formation, the previous observations are compared in this section to the results obtained for tests performed with three other fuels. Fuel composition have been selected to represent a big range of different composition in the point of view of Sulphur and Aromatic contents (details in II.1.1.2):

- The reference Jet A-1 fuel contains 20.2% of aromatics compounds and 200 ppm of sulphur (Europe certification);
- The AtJ is a Sustainable Aviation Fuel (SAF) without aromatic and sulphur content. It is used to see if particles can be generated in absence of sulphur;
- The Mix E5 is a blend of the two previous fuels (70% of Jet A-1 + 30% of AtJ) and its composition respects the limit allowed (% of SAF in a fuel) to be used on a real engine test;
- The Extreme Jet fuel is a modified fuel and does not correspond to a real fuel. This fuel is employed to test the higher limit of the ASTM certification in sulphur (3000 ppm) and aromatic compounds content (23%).

All these experiments using the different fuels have been done with the same conditions as described previously for the reference case. CAST set point was fixed at (84/30/3), gas phase injection and soot filtration during 8 min to get a similar amount of CO_2 inside the CESAM chamber and with a delay of 30min before light activation.

To compare results of the different tests, all data have been normalised by the CO_2 concentrations measured in the chamber. A comparison of the vPM formed in terms of size, number and mass concentrations, and chemical composition for the different tests is proposed in the following subsections.

IV.3.1 Gas monitoring for different fuels

The injection process being the same, the gas phase of CAST emissions is introduced in the CESAM chamber and the CO_2 concentration is monitored to get a similar amount between tests. The Table IV-7 regroups the gas data measured by the LISA detectors just after the injection (2min of stabilisation).

Fuel test	Injection case	CO_2 (ppm)	Corresponding injection time	CO (ppb)	CO (ppb per ppm of CO_2)	SO_2 (ppb)	SO_2 (ppb per ppm of CO_2)	NO_x (ppb)	NO_x (ppb per ppm of CO_2)
Jet A-1	After gas injection	63.77	8min	383.60	6.02	2.36	0.04	11.65	0.18
Extreme Jet	After gas injection	55.57	8min	418.55	7.53	23.63	0.43	7.90	0.14
Mix E5	After gas injection	85.64	8min+5min	532.80	6.22	4.77	0.06	14.69	0.17
AtJ	After gas injection	82.28	10min	421.84	5.12	1.64	0.02	16.73	0.20

Table IV-7: Gas monitoring inside CESAM chamber after gas phase injection for different fuels. Values have been normalised by respective CO_2 concentrations for each fuel test.

The first observation is that CO_2 concentrations are different for each fuel test: 63.77 ppm for Jet A-1, 55.57 ppm for Extreme Jet (-13%), 85.64 ppm for Mix E5 (+34%) and 82.28 ppm for AtJ (+29%). A representation of these concentrations over the time with dilution correction is proposed on Figure IV-25. As for the Jet A-1 case (cf. IV.2.1), the CO_2 concentration decreases during the experiment due to wall losses (no correction available for gas measurements) and the amount of carbon dioxide is not affected by light activation. It can be noted also that two gas injections have been done for the Mix E5 case. After the first injection, the CO_2 concentration was too low (48.58 ppm) compared to the one of the Jet A-1 case (63.77 ppm). To increase this amount, a second injection (shorter: 5min) has been done. As all instruments have been disconnected during this process, gas concentration was not controlled and the CO_2 amount exceeds the expectation (85.64 ppm). To compare data obtained for each fuel test, all following results have been normalised by CO_2 concentrations indicated in Table IV-7.

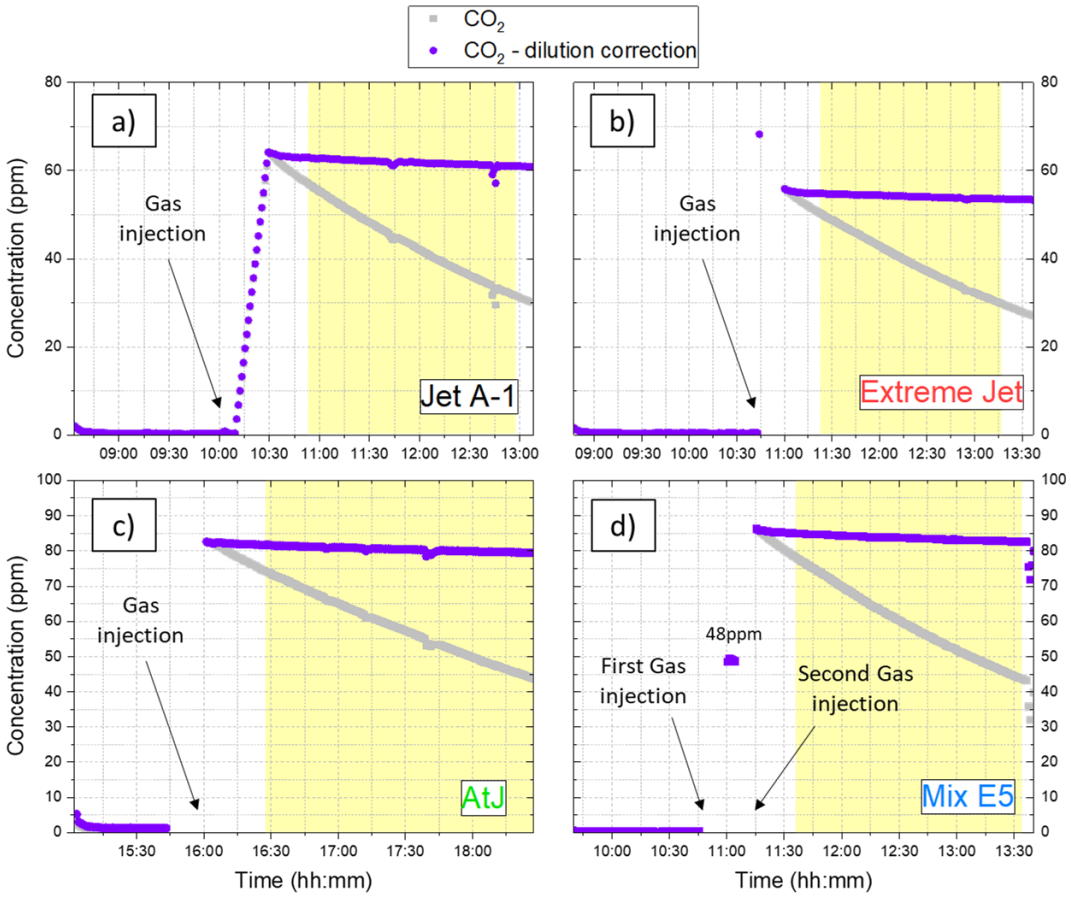

Figure IV-25: Monitoring of CO_2 concentration in CESAM chamber over the time after gas phase injection for tests with four different fuels: Jet A-1 (case a), Extreme Jet (case b), AtJ (case c) and Mix E5 (case d). Raw data (grey) have been corrected for dilution (purple). Lights on are represented by the yellow area.

Figure IV-26 presents the evolution of CO (case a) and SO_2 (case b) concentrations in the chamber for the four experiments: in black the Jet A-1 fuel test, in red the Extreme Jet one, in blue the Mix E5 one and in green the AtJ one. The data have been corrected for dilution and expressed in ppb par ppm of CO_2. The time axis is centred on the moment when lights have been activated in the chamber.

CO concentration does not change over the time after the injection, even with light activation (Figure IV-26.a). It can be noted that a higher amount of CO has been introduced in the chamber for the fuel with the highest concentration of aromatic compounds (7.53 ppb per ppm of CO_2 for the Extreme Jet). On the other hand, the AtJ fuel test generates less CO than the other ones (5.12 ppb per ppm of CO_2). Mix E5 and Jet A-1 fuels present a similar CO concentration (respectively 6.22 and 6.02 ppb per ppm of CO_2) over the time, despite the fact that Jet A-1 fuel contains more aromatics than Mix

E5 (20.2% vs 14.2%). This can be explained by the background after water injection at the beginning of the experiment. The background CO concentration is higher for the Mix E5 test (1.34 ppb per ppm of CO_2) than for the jet A-1 test (0.76 ppb per ppm of CO_2). If we subtract the background CO concentration, we can see how less CO was injected for Mix E5 (+4.79 ppb per ppm of CO_2) than for Jet A-1 fuel case (+4.98 ppb per ppm of CO_2) although the values are indeed close.

Concerning the amount of SO_2 introduced into the chamber (Figure IV-26.b), the same trends as for CO concentrations can be observed: the higher SO_2 concentration corresponds to the Extreme Jet case (0.43 ppb per ppm of CO_2) as it is the fuel with the higher amount of sulphur in its composition compared to the other ones. It can be noted that the same trend as in III.2.3.2 can be observed between the Mix E5 and Jet A-1 fuels: higher amount of SO_2 for Mix E5 (0.06 ppb per ppm of CO_2 after two gas injections) than for the Jet A1 (0.04 ppb per ppm of CO_2 after one gas injection) despite Jet A-1 has 60 ppm of sulphur more than Mix E5. The AtJ case presents a small amount of SO_2 after the injection of gas phase (0.02 ppb per ppm of CO_2) that is not expected due to its composition (0 ppm of sulphur). It can be explained by a small contamination of the sample during the injection process. Even while AtJ is the first fuel tested to avoid such contamination, the connection between CAST exhaust and CESAM chamber is used for all tests. More details will be presented in section IV.3.6.

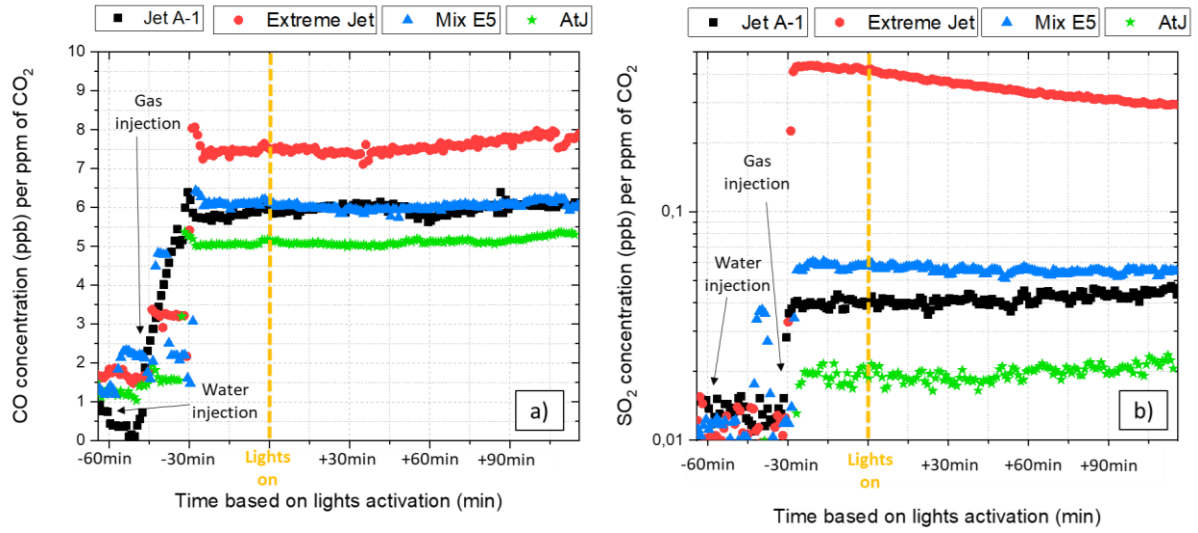

Figure IV-26: Concentrations of CO (case a) and SO_2 (case b with log scale representation) over the time in the atmospheric chamber after gas phase injection for four different fuels (Jet A-1 in black, Extreme Jet in red, AtJ in green and Mix E5 in blue). All data have been corrected for dilution and normalised by CO_2 concentration to be compared on the same graph.

Figure IV-27 regroups the concentrations of NO, NO_2 and NO_x after gas phase injection in the CESAM chamber for the Jet A-1 (case a), the Extreme Jet (case b), the AtJ (case c) and the Mix E5 (case d) cases. NO_2 has been obtained by subtraction between NO_x and NO and all data have been corrected for dilution and normalised by CO_2 concentration.

After water injection, a residual amount of NO_x is recorded (background of the experiment). Then, the same trend as observed for Jet A-1 case (IV.2.1) is repeated for all cases. After gas phase injection, the concentration of NO_x decreases slightly for all cases (in the order of -0.01 ppb per ppm of CO_2). Directly after light activation, the NO concentration increases quickly (+0.02 ppb per ppm of CO_2) as the NO_2 concentration decreases (0.01 ppb per ppm of CO_2). At the same time, NO_x concentration presents a small increase. After 5min, the NO concentration starts to decrease and the NO gas particles are converted into NO_2. The NO_x concentration decreases until the end of the test as more NO have been consumed than NO_2 has been formed.

It can be noted that Jet A-1 and Extreme Jet generate more NO_x than the other fuels after the injection of the gas phase in the chamber. Furthermore, after lamps have been switched off, the NO_2

concentration increases and the NO concentration decreases quickly. It is due to the conversion of NO to NO_2 by O_3 + NO, HO_2 + NO and RO_2 + NO (details in V.2.1).

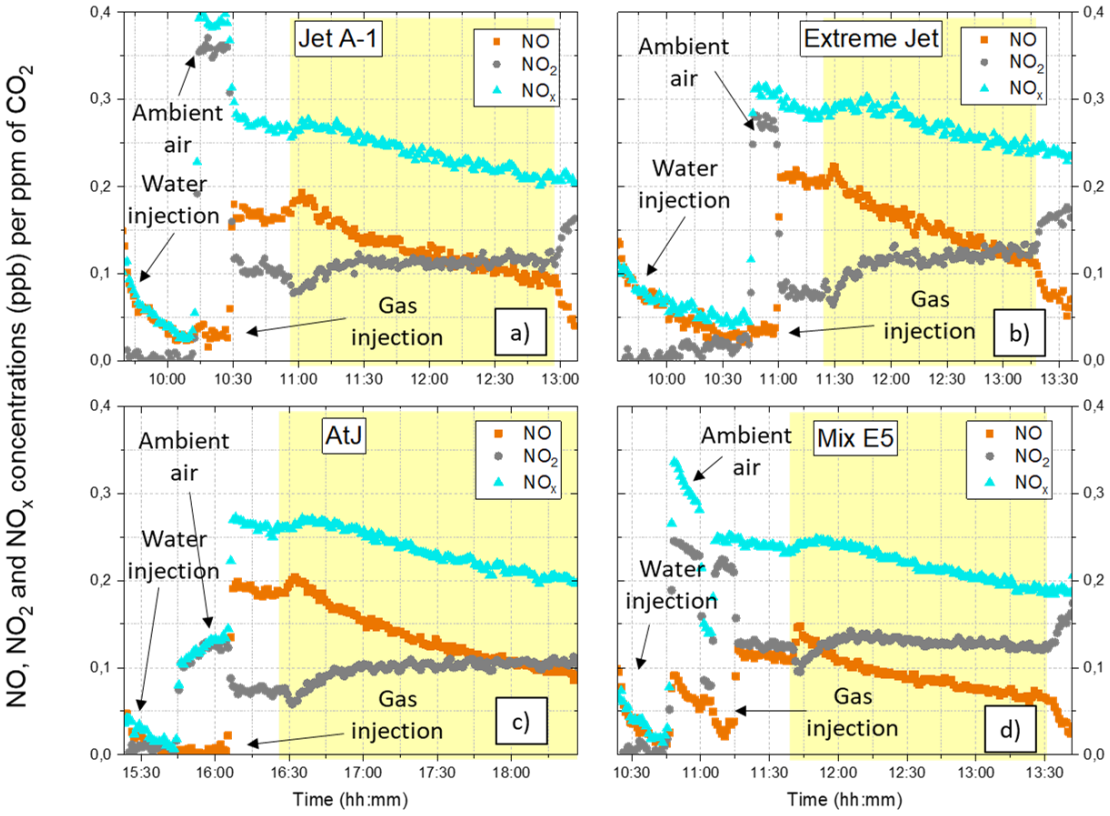

Figure IV-27: Monitoring of NO_x, NO and NO_2 concentrations after gas phase injection for four different fuels: Jet A-1 (case a), Extreme Jet (case b), AtJ (case c) and Mix E5 (case d). Lights are represented by yellow areas. Data have been corrected for dilution and normalised by CO_2 concentrations.

IV.3.2 Formation of particles linked to aromatic and sulphur fuel contents

After injection of gas phase in the chamber, no vPM formation is observed. However, directly after the start of the photochemistry, new particles are generated for all fuel cases, even for AtJ fuel without sulphur and aromatics contents in its composition. Figure IV-28 presents the vPM formation obtained for each test: case a) for Jet A-1, case b) for Extreme Jet, case c) for Mix E5 and case d) for AtJ. The evolution of particle size (y-axis) and particle concentration (colour scale) is represented over the time (x-axis). It should be noted that particle concentrations presented on graphs have not been normalised by CO_2 concentration.

The first observation is that for all fuels tested, vPM formation can be observed. However, the vPM formed and the rate of formation are different. For the Extreme Jet fuel, the mixE5 fuel and the Jet A-1 fuel, the formation is instantaneous after light activation. For the AtJ case, a short delay of 3 min can be observed before vPM formation (Figure IV-28.d). It is linked to the fact that only 2 lamps have been activated for this test (one light of the CESAM chamber was out of use), affecting the result in terms of vPM formed (number concentration and size) and reducing the photochemistry (2 lamps over 3 available means 1/3 less OH exposure). Then, for the Extreme Jet and the Mix E5 cases, the size of particles increases faster than for the other cases (from 10 nm to 20 nm respectively in 5min and in 10min). In these experiments, particles reach a maximum at 66.95 nm for the Extreme Jet fuel and at 34.97 nm for the Mix E5 fuel before the end of the experiment (Figure IV-28.a and b). Concerning the Jet A-1 test, the vPM formation process is slower (from 10 nm to 20 nm in 1h) and the size of particles reaches only 24.39 nm at the end. The particle size for the AtJ case tends to increase slowly to 17 nm

in 1h45. It should be noted that maximum sizes reached are linked with the amount of condensable species that have been injected in the chamber (or generated by oxidation when lights on). Regarding the amount of CO_2 and SO_2 injected initially (respectively 85.64 ppm vs 63.77 ppm and 4.77 ppb vs 2.36 ppb), it explains the fact that more vPM are formed and that particles are taller for the Mix E5 test than for the Jet A-1 test. Indeed, the concentrations of vPM formed after light activation are higher for Extreme Jet and Mix E5 cases (respectively $3.23x10^5$ part/cm^3 per ppm of CO_2 and $2.1x10^5$ part/cm^3 per ppm of CO_2) compared to the Jet A-1 ($0.43x10^5$ part/cm^3 per ppm of CO_2) and the AtJ ($0.35x10^5$ part/cm^3 per ppm of CO_2) tests. It confirms that higher amounts of SO_2 in the chamber generate more particles and these particles can grow to higher size.

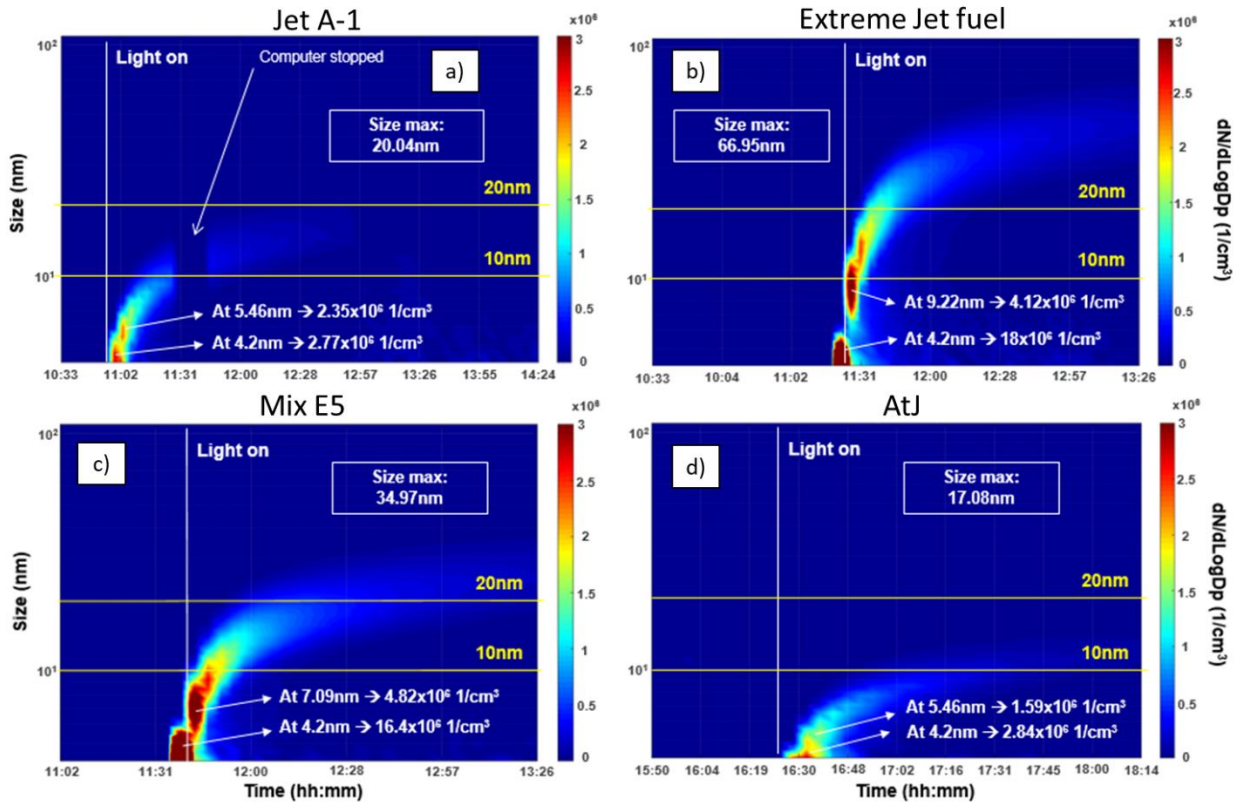

Figure IV-28: Evolution of the particle size and particle concentration over the time in the CESAM chamber for gas phase injection. Four fuels have been tested: Jet A-1 (case a), Extreme Jet (case b), Mix E5 (case c) and AtJ (case d).

Figure IV-29 presents the evolution of the number (blue) and mass (red) concentrations in the CESAM chamber for the Extreme Jet (left) and Mix E5 (right) fuels, as the particles formed in these both cases exceed 20 nm in size. Data have been corrected for dilution and wall losses, and normalised by CO_2 concentration. The delay between light activation and particle detection corresponds to the time that new particles formed need to reach 20 nm (limit of the instrument). Results will be compared thereafter to the case of Jet A-1 (cf. IV.2.2).

In both cases, number and mass concentrations increase after light activation. In the case of the Extreme Jet, the particle number reaches $2.07x10^3$ part/cm^3 (per ppm of CO_2) before it decreases and stabilises at $1.40x10^3$ part/cm^3 (per ppm of CO_2). The mass concentration increases during all the tests to reach 0.047 µg/m^3 (per ppm of CO_2) at the end and stops to increase after light extinction. Concerning the Mix E5 case, less particles have been generated: the number concentration increases to $0.58x10^3$ part/cm^3 (per ppm of CO_2) and the mass reaches 0.0057 µg/m^3 (per ppm of CO_2) at the end of the test. Fuel with high amounts of sulphur in its composition generates more vPM in terms of number and mass concentrations. Regarding mass concentrations, the vPM formation is still in progress and stopped only when lamps are switched off.

These representations are a good illustration on how a huge amount of sulphur (Extreme Jet case) produced a lot of particles at the beginning that act as condensation sink, implying that particle number goes down, while for mixE5 test there is no such peak and particle number keep growing all the time.

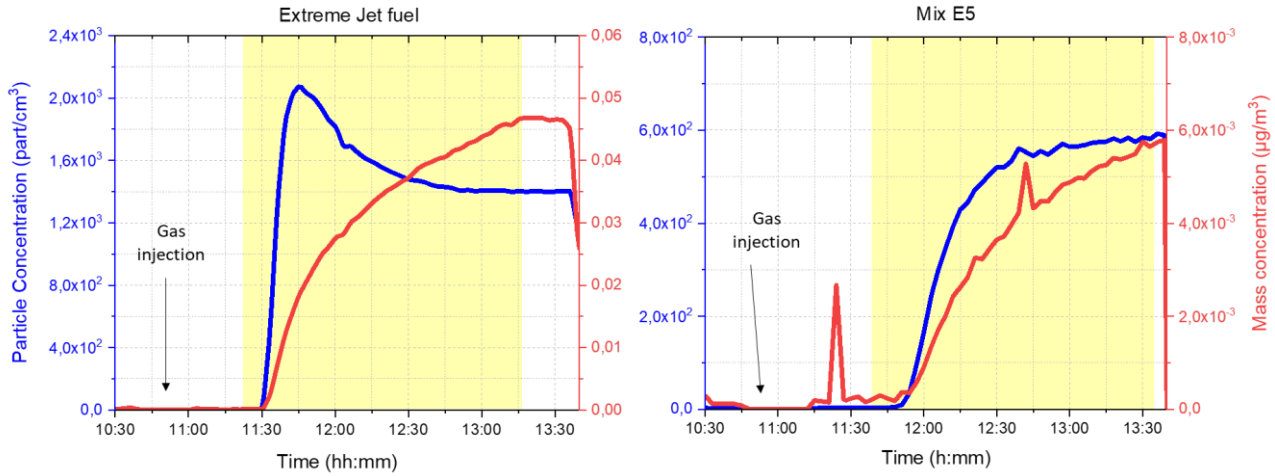

Figure IV-29: Particle and mass concentrations over the time for Extreme Jet with the LISA SMPS in the case of gas injection. Data have been corrected for dilution and wall losses and normalised by CO_2 concentration.

To compare the particle (on the left) and mass (on the right) concentrations for the four fuels tested, Figure IV-30 summarises results obtained depending on the time of the test (log scale). Different mean values have been calculated for each fuel case: before lights on (grey), after lights on (orange) and at the end of the experiment (purple). Data have been corrected for dilution and wall losses and normalised by CO_2 concentration.

The number (left) and the mass (right) concentrations increase until the end of the experiment for all fuels except for particles concentration of the Extreme Jet case (high agglomeration of vPM formed decreasing the particle concentration, but increasing the mass concentration at the end). AtJ does not present values before lights on due to the limit of detection of the instrument. It appears clearly that Extreme Jet and Mix E5 generate more particles due to the higher amount of SO_2 injected in the chamber despite Mix E5 has less sulphur content than Jet A-1 (even after normalisation by CO_2 concentration).

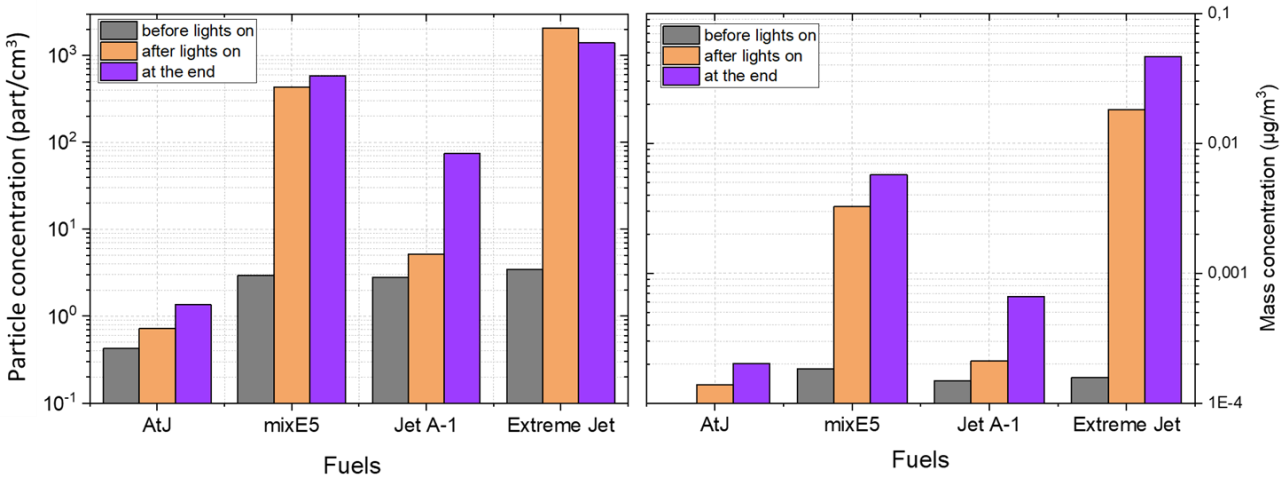

Figure IV-30: Evolution of particle number and mass concentration (SMPS) for different fuels depending on the light in the chamber. Data have been corrected for dilution and normalised by CO_2 concentration.

To study the evolution of the vPM size in the chamber over the time for the different tests, a comparison with the vPM GMD for Jet A-1 case studied in the previous section (IV.2.3) is done. Figure IV-31 presents the fitted GMD mode (same process as for Jet A-1 fuel case) obtained for Jet A-1 (case a), Extreme Jet (case b), Mix E5 (case c) and AtJ (case d). All size distributions have been fitted by monomodal to get these GMD modes.

The highest GMD calculated corresponds to the case of the Extreme Jet fuel (Figure IV-31.b) with 45.47 nm at the end of the experiment. It can be noted that GMD continues to increase slightly (+1.08 nm) even after the lights are off due to condensation of gas phase on vPM surface and agglomeration of particles formed. For the other fuels, the GMD increases respectively to 12.27 nm for AtJ, to 16.39 nm for Jet A-1 and to 25.98 nm for Mix E5. Furthermore, the GSD of particles formed are higher for Extreme Jet (1.284±0.008) and Mix E5 (1.251±0.003) compared to Jet A-1 and AtJ cases (respectively 1.192±0.008 and 1.164±0.014). It means that particle sizes are more dispersed around their GMD for fuels generating more particles. It confirms that fuel with high amounts of sulphur generates numerous bigger new particles in the atmosphere at ground level.

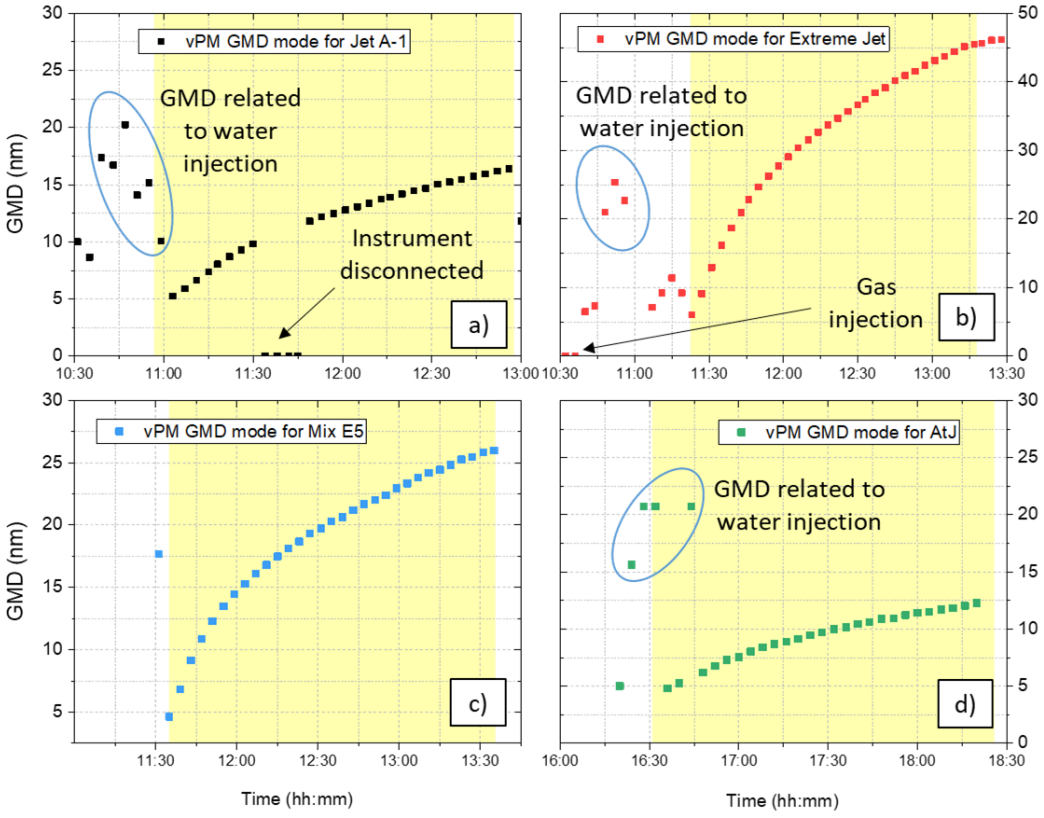

Figure IV-31: Fitted GMD modes after gas phase injection in the CESAM chamber for different fuels tested: Jet A-1 (case a), Extreme Jet (case b), blend Mix E5 (case c) and AtJ (case d) fuels.

IV.3.3 Contribution of sulphuric acid in particle formation process

To study the impact of sulphur on the vPM formation process, an API-ToF instrument has been used to monitor the concentration of the H_2SO_4 molecules in the chamber. Figure IV-32 regroups the different concentrations of sulphuric acid obtained (log scale) for the four fuels tested (in blue for Jet A-1, in purple for Extreme Jet, in dark green for the Mix E5 and in green for AtJ). Data have been corrected for dilution and normalised by CO_2 concentration. Results are compared depending on the moment of the experiment: before and after water injection, after gas phase injection and after light activation. The spider plot represents the maximum of H_2SO_4 formed in the chamber just after light activation depending on the fuel used.

The first observation is that after injection of the gas phase, H_2SO_4 molecules are only present for the Extreme Jet case (concentration constant at 2.2 ± 0.1 x10^4 part/cm^3 per ppm of CO_2). In the other cases, the background did not change before light activation. With the start of the photochemistry, the formation of H_2SO_4 is observable for all fuels even for AtJ. It contributes to the hypothesis of sulphur contamination during the injection process or maybe in the CAST internal circuit that cannot be cleaned between different fuel tests, even if AtJ was the first fuel tested in this campaign, other fuels containing sulphur were tested before the campaign. The maximum formation of sulphuric acid is obtained for the Extreme Jet fuel: 2.7x10^7 part/cm^3.

After the high formation peak of H_2SO_4, the concentration decreases for all cases and the concentration stabilises over the time until the lamps are switched off (visible on another representation proposed in Annex L). It means that with photochemistry, SO_2 oxidation leads to the formation of H_2SO_4 leading to the formation of vPM. This process is accentuated for fuels with high amounts of sulphur in their concentration such as Extreme Jet fuel.

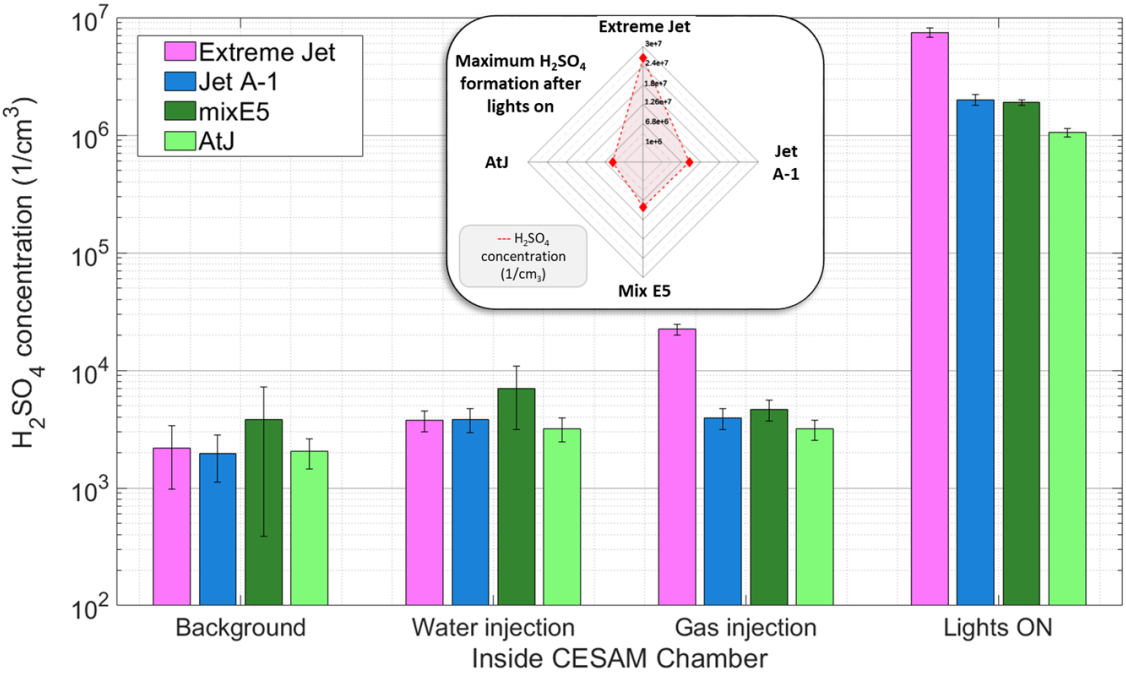

Figure IV-32: Evolution of H_2SO_4 concentration inside the chamber for gas phase injection depending on the fuels tested and on the moment of the experiment (before and after light activation). All data have been corrected for dilution and normalised by CO_2 concentration. The supplementary graph represents as a spider plot a comparison between maximum concentrations of H_2SO_4 molecules formed in the chamber for each test.

Concerning the HOMs, some of them have been recorded after gas phase injection and light activation in the chamber. However, they are also already present for the test performed after water injection with lights on (background of the chamber). Results are comparable to the ones obtained for Jet A-1 case (cf.IV.2.4). Formation of vPM is mainly due to sulphuric acid formed from SO_2 oxidation.

IV.3.4 Growth rate of new particles formed in the chamber

Based on the GMD values calculated in IV.3.2 and the H_2SO_4 concentration determined in IV.3.3, it is possible to estimate the growth rate of the particles formed during the experiment (increase of the size in nm per minute then converted in hours). After the high increase of H_2SO_4 concentration due to light activation, the concentration of sulphuric acid decreases (nucleation) and becomes stable after some minutes (details in Annex L). At this stabilised period, a mean value of the sulphuric acid

concentration has been calculated. Then the growth is estimated at the same period of time by fitting the GMD with a linear equation. Details of the calculation are presented in Annex R.

Growth rates (nm per hour) have been plotted as function of the H_2SO_4 concentration (for a stable period) and compared to the literature. The Figure IV-33 is taken from Lehtipalo et al. (2016) and results obtained in this study were added for each test: in black for Jet A-1 case, in dark-red for Extreme Jet case, in purple for Mix E5 case and in orange for AtJ. The other points come from CLOUD chamber experiments and correspond to growth rates as a function of the measured sulphuric acid (H_2SO_4) concentration with different amounts of ammonia (NH_3) and dimethylamine (DMA) in the chamber. The literature data were already presented and explained in more details in I.3.2.5.

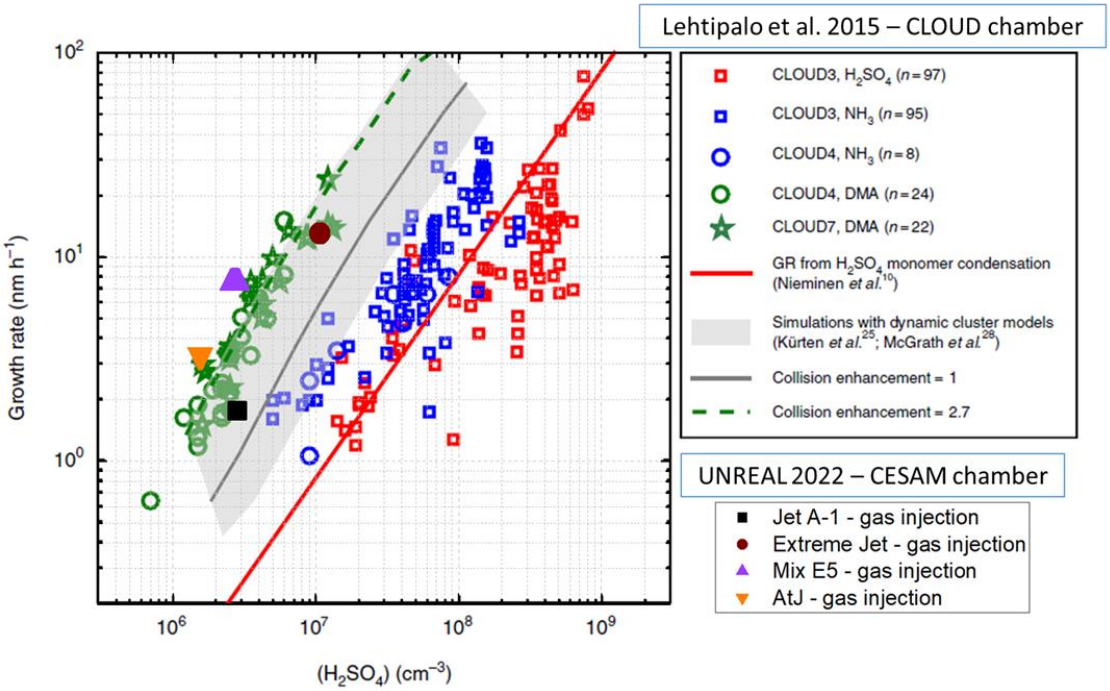

Figure IV-33: Comparison of the growth rate for homogeneous nucleation cases using different aeronautical fuels with growth rates calculated in different systems by (Lehtipalo et al., 2016a). The data corresponding to the UNREAL project performed with the CESAM chamber (ambient temperature and pressure, RH=38%) are indicated in black for Jet A-1, in dark-red for Extreme Jet, in purple for Mix E5 and in orange for AtJ. Data related to (Lehtipalo et al., 2016a) correspond to experiments done in the CLOUD chamber. Growth rates of 2 nm particles are determined with the appearance time method between 1.5 and 2.5 nm as a function of the measured sulphuric acid (H_2SO_4) concentration with different amounts of ammonia (NH_3) and dimethylamine (DMA) in the chamber. More details in I.3.2.5 and Figure I-22.

It can be noted that the growth observed for the different cases cannot be due only to sulphuric acid: results obtained are far from the red line corresponding to GR from H_2SO_4 monomer condensation. While sulphuric acid plays a key role in the particle formation, the growth is primarily driven by organic compounds originated from combustion (cf. IV.3.5). It is also interesting to notice that fuel cases can be regrouped in 2 lines: one for pure jets and other for SAF and blend. The growth rates of Extreme Jet and Jet A-1 (corresponding to the fuels with higher amounts of sulphur in their composition) are in a range between collision enhancement of 1 to 2.7. Concerning Mix E5 and AtJ cases, growth rates are over the collision enhancement limit at 2.7. As Mix E5 fuel contains 30% of AtJ, we can think that there is something in the composition of this fuel that leads to organic compounds that are better growing the particles than those emitted by Jet fuels. For example, in the case of the Mix E5 fuel, the growth is higher than for Jet A-1 fuel, even though the amount of H_2SO_4 for both is similar (cf. IV.3.3). This suggests that there is a higher concentration of condensable vapour for Mix E5 fuel. It's important to note that this does not necessarily mean that there are more organic compounds present, but also, that the existing organic compounds might have lower vapour pressure, indicating a higher degree of oxidation.

While growth rates observed for AtJ and Mix E5 fuels are higher than those corresponding to Jet fuels, it can be noted as well that Mix E5 generates more vPM than AtJ and Jet A-1 (IV.3.2), even if the amount of sulphuric acid for Mix E5 and Jet A-1 was similar (Figure IV-32). It seems that in the case of pure AtJ some compounds able to grow the particles are generated, but that cannot form new particles while when AtJ is blended with Jet A-1 the compounds emitted can both generate particles and grow them. Furthermore, as growth and vPM formation is smaller for the pure Jet A-1, it can be observed that these compounds are specifically formed when mixing both fuels. Further studies will be needed to understand this phenomenon specifically and to determine the exact nature of these compounds.

IV.3.5 On-line analysis of the chemical composition of vPM formed

- On-line study of the particulate phase

As observed for Jet A-1 fuel test, particles formed are mainly organic compounds, but the detection using an ACSM is limited by their size. The Extreme Jet fuel is the only test where GMD of particles exceeds 40 nm (no monitoring of the particulate phase possible for Mix E5 and AtJ). Figure IV-34 presents the evolution of NH_4 (case a), total organics (case b), SO_4 (case c) and organic fragments (case d) for the Extreme Jet case. All data have been corrected for dilution.

Before light activation, only some organics (OOA fragments) are recorded in the chamber. After light activation, vPM formation started and the size of particles increased. The concentration of NH_4^+ reaches 1.26 µg/m^3 and the concentration of SO_4^+ increases to 5.06 µg/m^3 before the end of the experiment. Concerning the organics, the main variations are related to the OOA concentration. HOA concentration starts to decrease just after light activation and is entirely converted to OOA, contributing to explain the increase of total organics during the test.

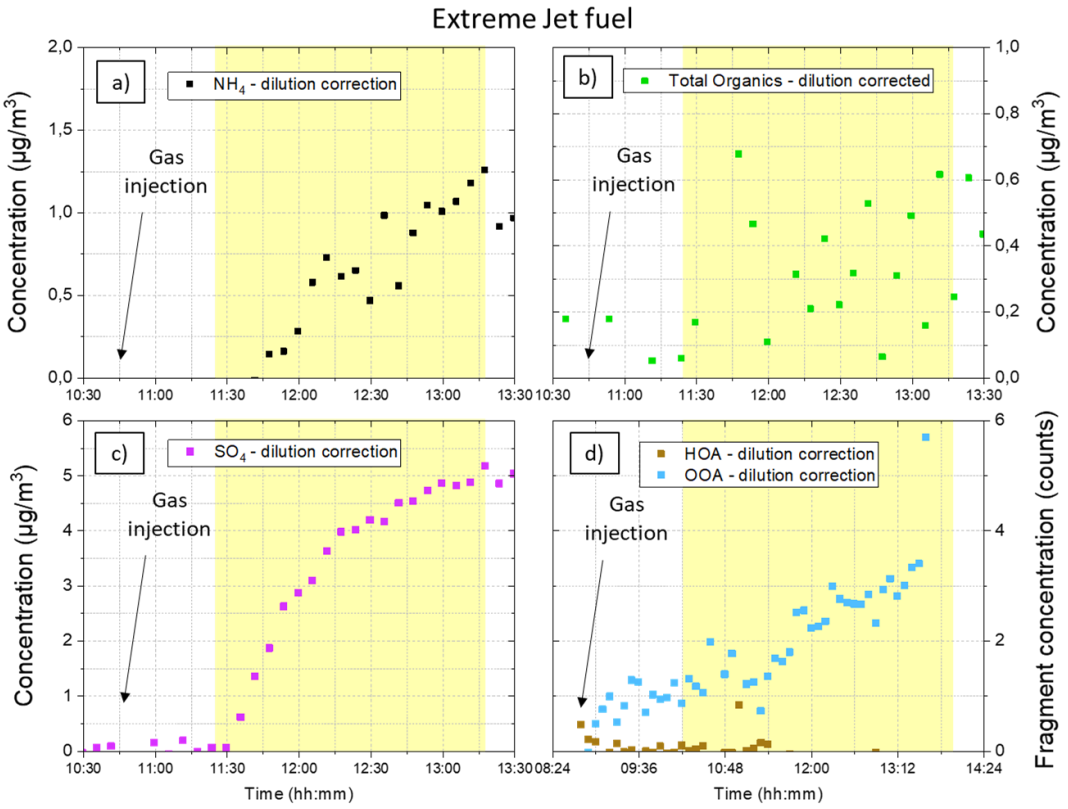

Figure IV-34: Monitoring of NH_4^+ (case a), total organics (case b), SO_4^+ (case c) and organic fragments (case d) recorded by ACSM on particles generated after gas phase injection in the CESAM chamber for Extreme Jet case. Light activation corresponds to the yellow area. All data have been corrected for dilution.

- On-line analysis of the gas phase

To monitor the gas phase injected and follow the evolution of the gases in the CESAM chamber, their concentrations have been monitored using a PTR-MS and compared to the compounds already identified for the Jet A-1 case (IV.2.5.1). However, PTR-MS data did not provide any insight on the vPM formation/growth. The principal compounds detected by the PTR-MS are reported in Annex M. The majority of them are organics and their concentration increases over time.

IV.3.6 Off-line mass spectrometry analysis

To go furthermore, different filters have been collected and thereafter analysed in Lille with HR-L2MS. A first approach has been done concerning the sulphur compounds at the surface of the filters. Previously (IV.2.5.3), it has been already seen that there are few deposits on sample surfaces, that most of the compounds identified are carbons clusters and hydrocarbons and finally that organic compounds are not detectable on the filters. It can be also noted that no PAH compounds (naphthalene, fluorene, pyrene…) have been found at the surface of the filter (signal obtained corresponds to the one obtained for the analysis of the blank filter). For more details about the compounds researched, refer to the Annex G.

For each sample, three mass spectra have been obtained and averaged. The sum of all these intensities for the same compounds has been normalised by the respective entire spectra signal and normalised by the CO_2 concentration (corresponding to its injection case). In this way, it is possible to do a semi-quantitative comparison between the different fuels tested. The Figure IV-35 corresponds to the sulphur compounds comparison. The analysis is focused on the gas phase using negative ions (more relevant to study sulphur compounds) and a particular interest is given to SO_3, SO_4, HSO_4 and H_2SO_4.

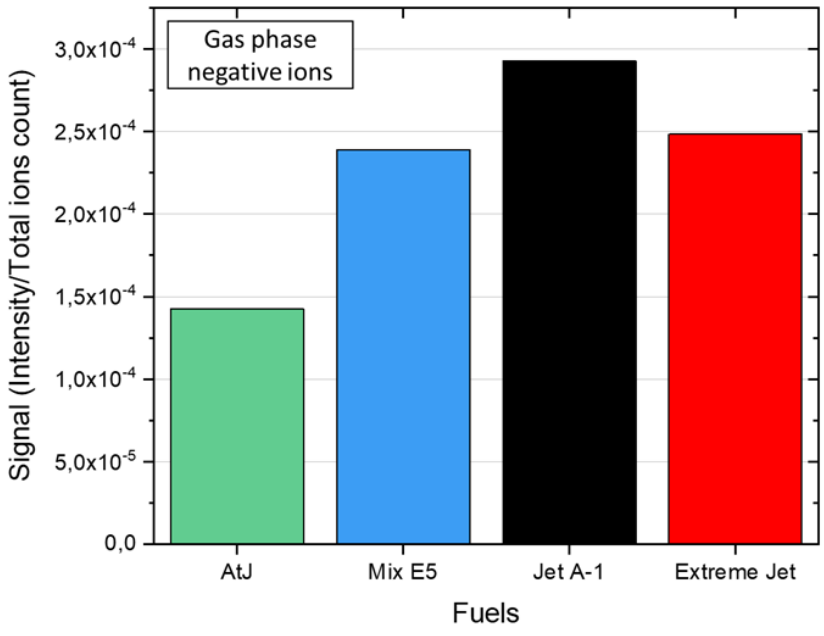

Figure IV-35: Semi-quantitative comparison for different fuels after gas phase injection in the atmospheric chamber. The sulphur content in fuel composition increases from the left to the right. The results correspond to the sulphur compounds found in the gas phase (Back Filter). Data have been normalised by total ions count and by CO_2 concentration.

It can be noted that fuels with high amounts of sulphur in their composition (Jet A-1 and Extreme Jet) generate more sulphur compounds than the other fuels. But the amount of sulphur is smaller for Extreme Jet than for Jet A-1 due to the normalisation by total ions count (more signals for Extreme Jet

on the mass spectrum so higher total ions count compared to the reference fuel). Furthermore, it should be noticed that only gas phase analysis is shown here. Concerning the particulate phase of the emissions, the vPM formed were too small and not enough particles have been collected on the filter to get a good signal in mass spectrometry. In the case of Extreme Jet, more particles have been formed due to the presence of more condensable gases. It may be that more sulphur compounds can be found on the particulate phase for this fuel compared to Jet A-1 and this trend is confirmed by the results presented at the end of this study (cf. V.2.4.3).

It can be observed the presence of sulphur for the AtJ case. It confirms the contamination of the sample during the injection process. The chamber is cleaned before each experiment and according to the gas detector there is no SO_2 inside the chamber at the beginning of each experiment before emissions injection. But it is possible to observe a small amount of SO_2 (Figure IV-26) at the injection of gas in the chamber for the AtJ case. It is a small amount (almost in the background) but it indicates that a contamination of the emissions is possible by a residue of sulphur particles stocked in the CAST or in the line. Nowadays it is not possible to use SAF directly on a new engine. Preliminary tests are done using classical fuel (as Jet A-1) and these fuels contain sulphur. Thus, this contamination can be a representation of the real case for us in this study.

IV.4 Summary

To conclude about this homogeneous nucleation process from gaseous precursors after soot filtration at the entrance of the CESAM chamber, it is possible to see that vPM have been formed for all fuels tested. Depending on the fuel composition, the number and mass concentrations of particles are different. Furthermore, depending on the amount of vapours introduced in the chamber at the beginning of the test and how condensable they are, the maximum size of vPM formed is impacted: for example higher GMD for blend fuel case than for reference fuel case because more combustion gases (1.3 times more CO_2) has been injected in the chamber. After light activation, fuels with high sulphur amounts generate more promptly new particles, which reach higher GMD. It can be noted that chamber studies are suppressing initial nucleation and then allowing photochemical processing to occur as the shifted nucleation occurs. This is different from the situation in an actual aircraft plume, but such study gives a good overview to understand the basic mechanisms.

The analysis of the particulate and gas phase shows that oxygenated compounds (PTR-MS and API-ToF), organics (ACSM), sulphur and PAH compounds (L2MS) have been formed. Sulphuric acid is the main contributor to the formation of vPM in the case of fuel with high amounts of sulphur, though in the case of Mix E5 fuel, higher vPM formation than expected is observed. Finally, regarding the growth rate of the particles, there is a higher concentration of condensable vapour for SAF and blend fuels. The growth is not only due to sulphuric acid, most likely in this case is linked to organics in the combustion gases. The higher growth rate found for SAF-containing fuels and the unexpected formation of vPM observed for Mix E5 fuel suggest that the blend of SAF and standard Jet lead to the emission of some specific compound that is not present in the emissions from any of the pure fuels.

Figure IV-36 presents a summary of the main results depending on the conditions of the experiment. It gives a significant advancement of the work done previously by Miracolo et al. (2011), also using a chamber approach to understanding organic contributions to vPM. The next step is the study of the real case where vPM and nvPM are both injected into the chamber. In this case, there will still be homogeneous nucleation but it will be limited compared to the case exposed in this chapter. Indeed other reactions such as the condensation on pre-existing soot particles or heterogeneous nucleation need to be taken into account. This will be the topic of the next Chapter.

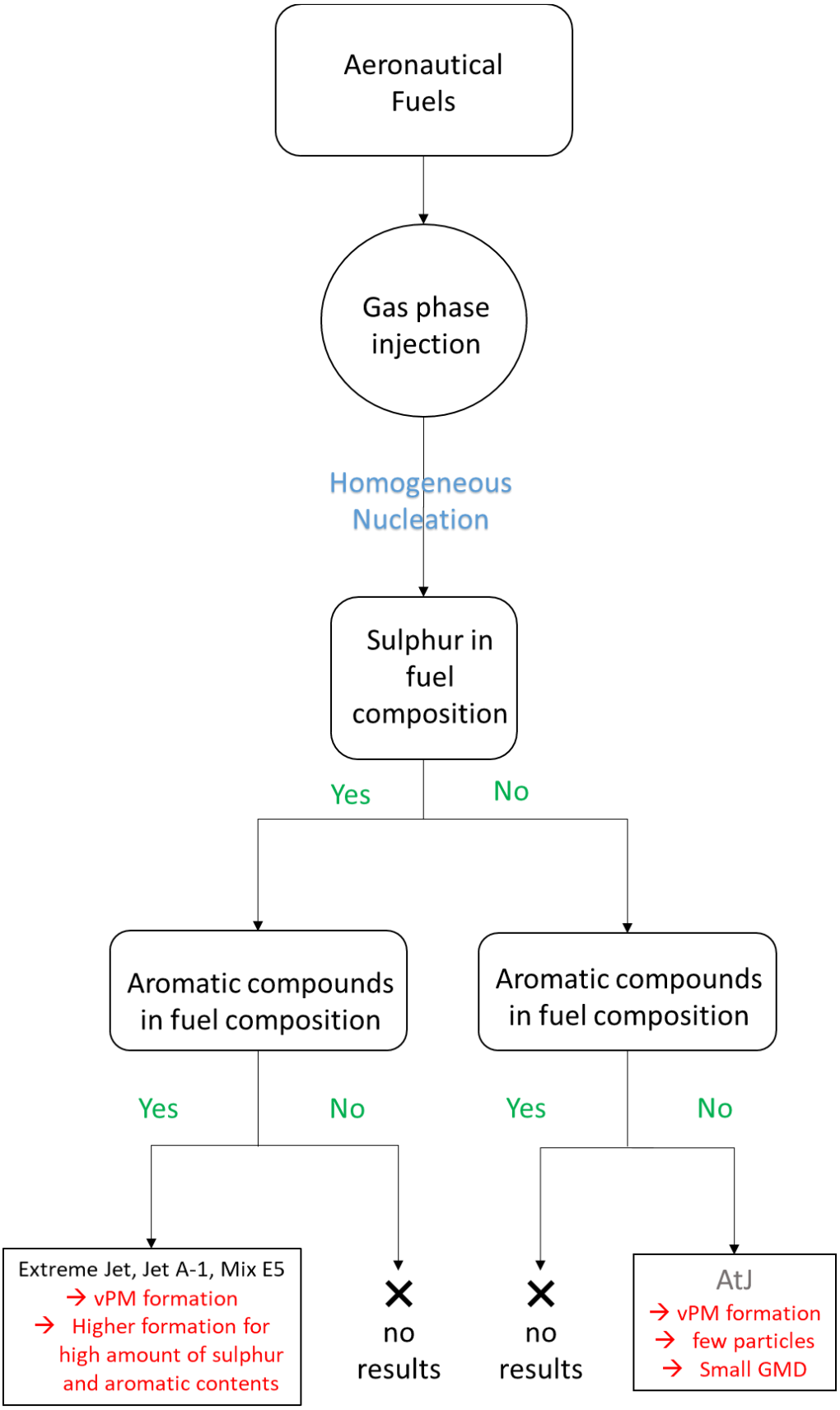

Figure IV-36: Summary of vPM formation after injection of gas phase in CESAM chamber depending on the fuel composition in terms of sulphur and aromatics contents.

Chapter V. Evolution of engine emissions in atmosphere: vPM formation in the presence of soot particles

In the previous chapter, a first approach has been done to study specifically the formation of volatile particulate Matter (vPM) from gaseous precursors by removing soot particles (nvPM) from CAST emissions before injection inside the CESAM chamber. The next step is to consider the raw emissions, to study the interactions between gas phase and soot particles (heterogeneous process) and how these interactions affect vPM formation. In that respect, the objective of this chapter is to understand the formation of new vPM based on a realistic case.

The experimental set-up (Figure V-1) and the fuels used remain the same as those described in the previous chapter. CAST set point is still set at 84µL/min for the kerosene flow, 30mL/min for the propane flow and 3L/min for air flow (noted 84/30/3). This time, the protocol of injection is divided in two steps. In first place, a gas phase injection is done where nvPM are filtered using an HEPA filter as in previous experiments (cf. IV.1.2.2). Then a second one is done where the raw emissions are introduced in the chamber. Gas precursors continue to form particles based on the homogeneous nucleation process but also interact with soot by heterogeneous nucleation (Tuovinen et al., 2020). These interactions such as adsorption and condensation cannot be neglected (Kulmala et al., 2003; Starik, 2007).

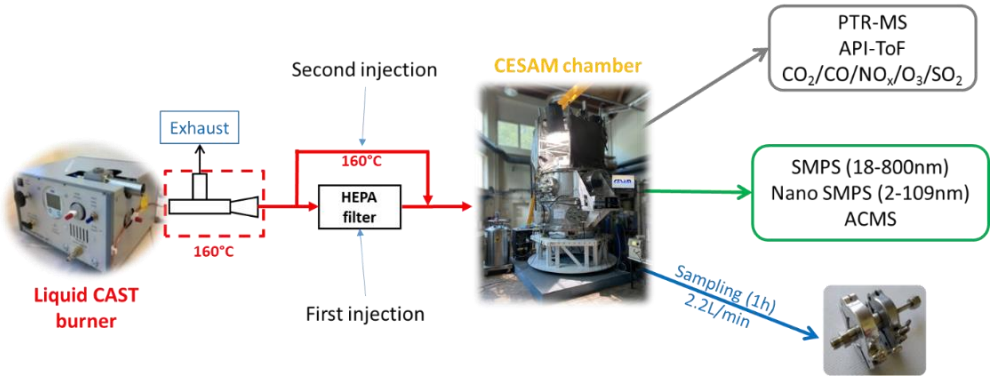

Figure V-1: Experimental set-up used to study interaction between vPM and soot particles inside CESAM chamber. The injection is done in two steps: a first one for the gas phase with soot filtration and a second one for the raw CAST emissions. Particulate phase is analysed by instruments (description in II.2.2.2) regrouped in the green box and gas phase by those in the grey box. Filters have been collected in parallel for 1h at 2.2L/min.

In the case of raw emission injection, the amount of gas phase introduced in the chamber can be too small to observe significantly a formation of vPM (cf. IV.1.2.1). The separation of both injections in this experiment allows the introduction of a sufficient amount of gas precursors and the formation of vPM is highlighted despite the presence of soot. Furthermore, soot injection is limited compared to gas injection to avoid contamination of the chamber by a large amount of soot and thus the adsorption of all gaseous precursors on their surface (Cazorla et al., 2013; Kalbermatter et al., 2022). Both injections are monitored to introduce a comparable amount of CO_2 in accordance with previous tests for homogeneous nucleation case (cf. Chapter IV). The first injection of gas emissions from CAST burner with soot filtration is done for some minutes: 8min to get 60 ppm of CO_2. After a delay (6 to 8min) to verify the concentrations of gas introduced in the chamber, the second injection of the raw emissions (nvPM and gas phase) is done for 15s. In the same way as for the first injection, the CO_2 concentration and also the soot amount are monitored to compare experiments for different fuels. Lights are activated 30min after the end of the second injection.

V.1 Formation of vPM at ground atmospheric conditions for a realistic case with a reference fuel

V.1.1 Injection of gas and particulate phases in the chamber

In this section, the reference Jet A-1 fuel is used to study both homogeneous and heterogeneous nucleation processes inside the CESAM chamber. The objective is to see if vPM can be formed in presence of soot and to compare the results with the ones obtained for the gas phase injection test presented in IV.3.

For all injections, gas sensors monitored CO_2, NO_x, CO and SO_2 introduced in the chamber and these values are presented in Table V-1. "Gas sample" case represents the homogeneous nucleation test for gas phase injection (cf. Chapter IV) and the "Raw sample" case corresponds to the test done with raw emissions injection (Chapter V).

Test	Injection	CO_2 (ppm)	CO (ppb)	CO (per ppm/CO_2)	SO_2 (ppb)	SO_2 (per ppm/CO_2)	NO_x (ppb)	NO_x (per ppm/CO_2)
Gas sample (Chapter IV)	After gas injection	63.77	383.60	6.02	2.36	0.04	11.65	0.18
Raw sample (Chapter V)	After gas injection	53.67	389.06	7.25	2.23	0.04	11.81	0.22
	After soot injection	59.36	413.74	6.97	2.55	0.04	14.30	0.24

Table V-1: Gas measurement by LISA gas sensors after raw emissions injection inside CESAM chamber ("Raw sample" case) compared to the study of the homogeneous nucleation test ("Gas sample" case). Mass and Number concentrations are not quantifiable for "gas sample" cases because no particles have been injected in the chamber with soot filtration. Normalisation is done by CO_2 (division) for each value to compare data between cases.

For both gas injection cases, the injection time is the same (8min) to get a comparable CO_2 concentration. The objective is to reproduce the experiment done in IV.2 and check if amounts of gas inside the chamber are similar before adding soot emissions. The first observation concerning this gas phase injection is that concentrations of CO_2 are different from 10 ppm but amounts of NO_x (0.16 ppb of difference), of SO_2 (0.13 ppb of difference) and CO (1.4% of difference) are close. It is difficult to control the amount of gas injected inside the chamber due to the under depression injection process (cf. details in IV.1.1). Therefore, it is complicated to reproduce exactly the same test by injecting the same amount of gas in the chamber. To compare both tests, results are normalised by the CO_2 concentration as mentioned in the precedent chapter (cf. IV.1.1). After that, it is possible to see that SO_2 amounts are identical, but more CO and NO_x have been injected during the second test. No number and mass concentrations have been recorded for gas injection.

For the "raw sample" case, the delay between the two injections (with and without HEPA filter) has been minimised (8min) corresponding to stabilisation of CO_2 amount, connection/disconnection of instruments and pumping of the chamber to generate the suction. During this time, as nucleation in dark is negligible, no changes are observable concerning vPM formation (cf. IV.1.2.1). After soot injection, the concentration of CO_2 has increased by 10% (+5.7 ppb) compared to the gas injection. Other concentrations have also increased: +24 ppb of CO (-4% per ppm of CO_2), +0.3% of NO_x (unchanged per ppm of CO_2) and +2.5 ppb of SO_2 (unchanged per ppm of CO_2). The number and the mass concentrations related to soot particles injected in the chamber are respectively 7.55×10^3 part/cm^3 (127.2 part/cm^3 per ppm of CO_2) and 18.55 µg/m^3 (0.31 µg/m^3 per ppm of CO_2).

The gas evolution in the chamber is presented in Figure V-2 for the CO_2 (case a) and CO (case b) concentrations over the time for the "raw sample" case. The raw data (in grey) has been corrected for dilution (in purple and green) and light activation is represented by the yellow area. Over the test, the

CO_2 concentration decreases by 2 ppm (Figure V-2.a). This is due to wall losses that are not considered for gases in value correction. The CO_2 amount has been set after 2min of stabilisation (post injection) at 59.36 ppm as reference concentration for normalisation before the losses become more relevant. The CO amount introduced in the chamber also presents a decrease over the time of ±5 ppb due to wall losses (zoom out on scale in Figure V-2.b). CO is not interacting with particles already present or newly formed.

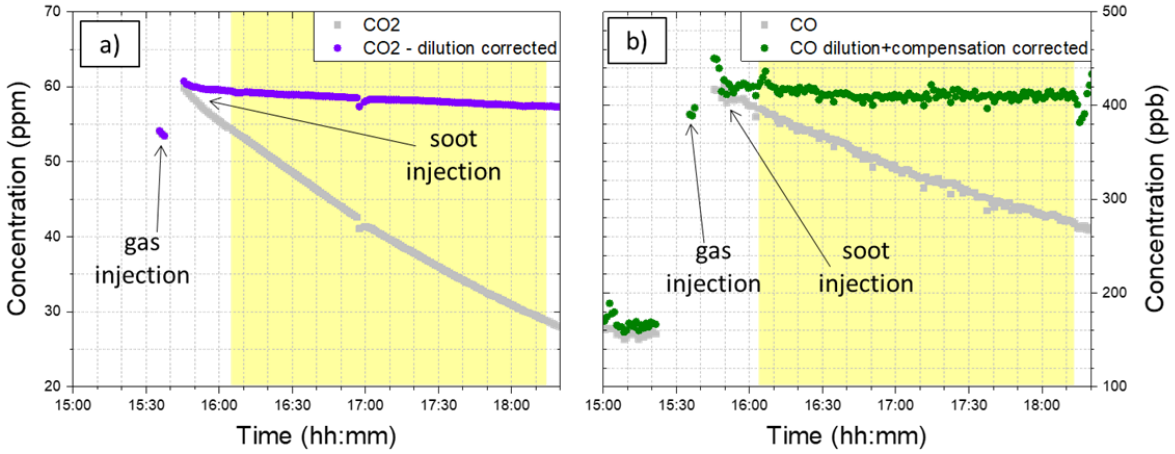

Figure V-2: Monitoring using gas sensors of CO_2 (case a) and CO (case b) concentrations over the time after soot injection (Jet A-1 fuel) in CESAM chamber. Values have been corrected for dilution and the yellow area corresponds to the light activation period.

In addition, the concentrations of SO_2 and NO_X have been also monitored and their evolution over the time in the chamber is presented in Figure V-3 (respectively case a and case b). After water and raw emissions injections, an additional injection of SO_2 has been done to observe its impact on vPM formation. Thus, 60 µL of SO_2 have been added in the chamber using a syringe, taking into account the volume of the chamber this corresponds to 14.2 ppb. The SO_2 concentration increased by 12.45 ppb, what is coherent with the volume injected. The amount of SO_2 tends to decrease with time implying that SO_2 interacts with atmosphere components to form H_2SO_4 and generate volatile particles as in the SOA formation process (Donahue et al., 2013; Kulmala & Wagner, 1996). It can be noted that CO and CO_2 concentrations are not impacted by the SO_2 injection.

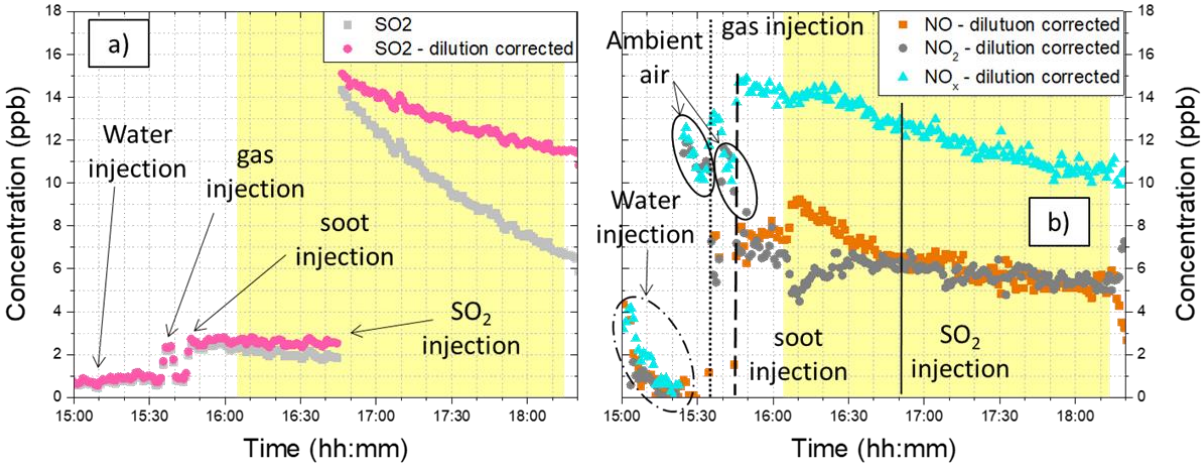

Figure V-3: Monitoring of SO_2 (case a) and NO_x (case b) concentrations after raw emissions injection in CESAM chamber over the time for Jet A-1 fuel. A water injection is done at the beginning of the test before introduction of gas and soot emissions (in 2 steps). An additional SO_2 injection is done at 16:44 using a syringe (+60 µL). The concentration of SO_2 increases from 2.55 ppb (obtained after gas and soot injection) to 15 ppb. All values have been corrected for dilution and yellow areas correspond to light activation period.

The evolution of NO_x in the chamber has been also monitored (Figure V-3-b). NO and NO_x have been measured and NO_2 values have been obtained from the difference between NO_x-NO. Times of gas and soot injections are represented on the graph by dotted and dashed lines, respectively. The disconnection of the SMPS from the chamber is represented by a circle. Data have been also corrected for dilution and yellow area corresponds to light activation. The first observation is that NO_x comes with water as contaminant and its concentration decreases quickly (from 4.17 ppb to 0.53 ppb in 20min). After gas and soot injections, concentrations of NO_x, NO and NO_2 remain constant and equal respectively to 14.3±0.3 ppb, 7.5±0.3 ppb and 6.8±0.4 ppb. With light activation, NO is generated (peak at 9 ppb) and is directly converted into NO_2 (+1.5 ppb). NO_x concentration increases slightly (+0.5 ppb in 15min) corresponding to the increase of NO_2, and then its concentration decreases continuously (-3.4 ppb at the end of the experiment). NO_2 concentration presents small variations (-1 ppb) until the end of the test. After SO_2 injection, the decrease of the NO_x and NO concentrations slows down. It means that formation of sulphuric acid is dominant (cf. V.1.4.1) compared to nitric acid formation.

V.1.2 New vPM formation under atmospheric conditions

After the injection of raw emissions inside the CESAM chamber, the interest is focused on their evolution and on the interactions between gas precursors and particles.

Figure V-4 gives two representations of a new vPM formation event for the injection of CAST emissions (gas phase and raw emissions) in the chamber after Jet A-1 fuel combustion. These two representations of the particle size (y-axis) and concentration number (colour scale) over the time are complementary: the soot particles are monitored using the LISA SMPS (Figure V-4.a - range from 20 to 800 nm) and the vPM are recorded using the nanoSMPS (Figure V-4.b - range from 4 to 120 nm). It is possible to adjust the colour scale corresponding to the concentration number to get a better representation of the particle formation event (cf. example in Annex N).

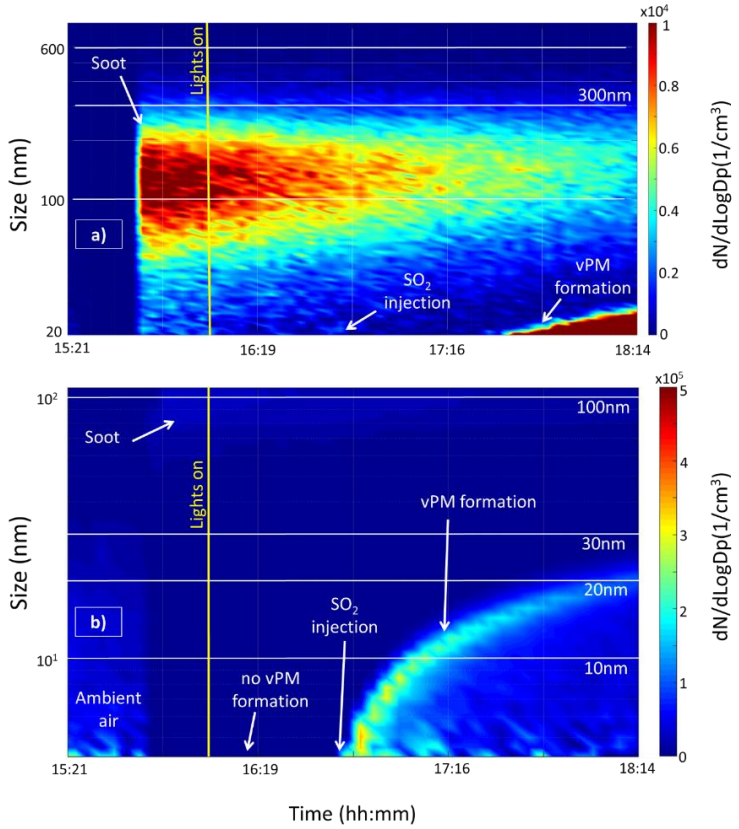

Figure V-4: vPM formation for raw emissions injection inside the CESAM chamber using Jet A-1 fuel. The figure a) represents soot particles (in the middle) and vPM formation (bottom right) over the time using the LISA SMPS (20-800 nm but no signal

over 600 nm). The second figure b) represents the evolution of the size (y-axis) and of the particle concentration (colour scale) using the nanoSMPS (4-120 nm). Both instruments have been disconnected during injection and a blank of the "ambient air" outside the chamber has been done at this moment. Lights have been activated 30min after the injection and are represented by the yellow line. SO_2 has been added at 16:46 to induce the appearance of vPM inside the chamber.

During the injection of gas and raw emissions inside the chamber, all instruments have been disconnected and a blank of the ambient air around the chamber has been done (Figure V-4.b). After that, the complete size distribution signal for soot particles has been monitored between 73 and 187 nm (Figure V-4.a) and the number concentration decreases from 10^4 to $0.6x10^4$ part/cm^3 over the experiment. Soot particles are also observed on Figure V-4.b at 100 nm directly after the second injection (at the limit of detection of the instrument). However, no vPM is formed, even with light activation (on both representations). This is due to the presence of soot particles: gaseous precursors are adsorbed on their surface and the homogeneous nucleation is limited compared to the heterogeneous reaction. The adsorption of precursors at soot surface is confirmed by the increase of their Geometric Mean Diameter (GMD – cf. details in V.1.3) over the time.

As there is no vPM formed, the experiment has been modified to study the contribution of sulphur to the emission formation process. As mentioned before, a sulphur dioxide injection has been done inside the CESAM chamber (at 16h46 - Figure V-4) and the concentration of SO_2 has increased by 5.88 times. Lights have been kept on and just after this complementary injection, vPM formation has been observed. Only particles above 4 nm are considered with the nanoSMPS to avoid the noisy signal and the background (detailed in Annex O). At the same time that SO_2 concentration decreases (Figure V-3.a), number concentration and size of new particles generated increase, reaching sizes up to 20 nm (Figure V-4.b). The Jet A-1 contains 200 ppm of sulphur but due to the presence of soot in the chamber, it is not enough to form vPM. It confirms the predominance of heterogeneous processes over homogeneous ones when raw emissions are introduced in the chamber. However, with this test modification, it shows that if sulphur concentration is sufficiently high, the particle formation is possible.

It can be noted that vPM are observed on Figure V-4.a with a delay (45min after SO_2 injection) due to the limit of detection of the instrument for particles under 20 nm. When the new particles formed after SO_2 injection are recorded by the instrument (right bottom - Figure V-4.a), the soot concentration number has been halved due to coagulation and wall loss (around $0.4x10^4$ part/cm^3).

To complete the previous observations, Figure V-5 gives a representation of the total number (in blue) and total mass (in red) concentrations of particles (vPM and soot) in the CESAM chamber over the time. Mass concentration is calculated from the particle number assuming a constant unit density for the particles. All the values have been corrected for wall losses and dilution.

Until detection of the new vPM formed after SO_2 injection (i.e. at 17h30), the mass concentration corresponds to soot particles and it remains constant over the time (17.5 ± 1 µg/m^3). The number concentration of soot is decreasing slightly from $7.5x10^3$ to $6.9x10^3$ part/cm^3. It means that the number of soot particles is reduced but the mass is kept: the result is an increase of the soot size (cf. details in V.1.3.1) to conserve this mass.

The detection of the new particles formed is represented by an increase of the total number concentration (+116%) but also by an increase of the total mass concentration (very slightly from 17.5 ± 1 to 18.3 ± 0.2 µg/m^3). It confirms that a large amount of small vPM have been formed in the chamber after the injection of SO_2 concentration (i.e. implicitly formation of H_2SO_4 – cf. V.1.4.1).

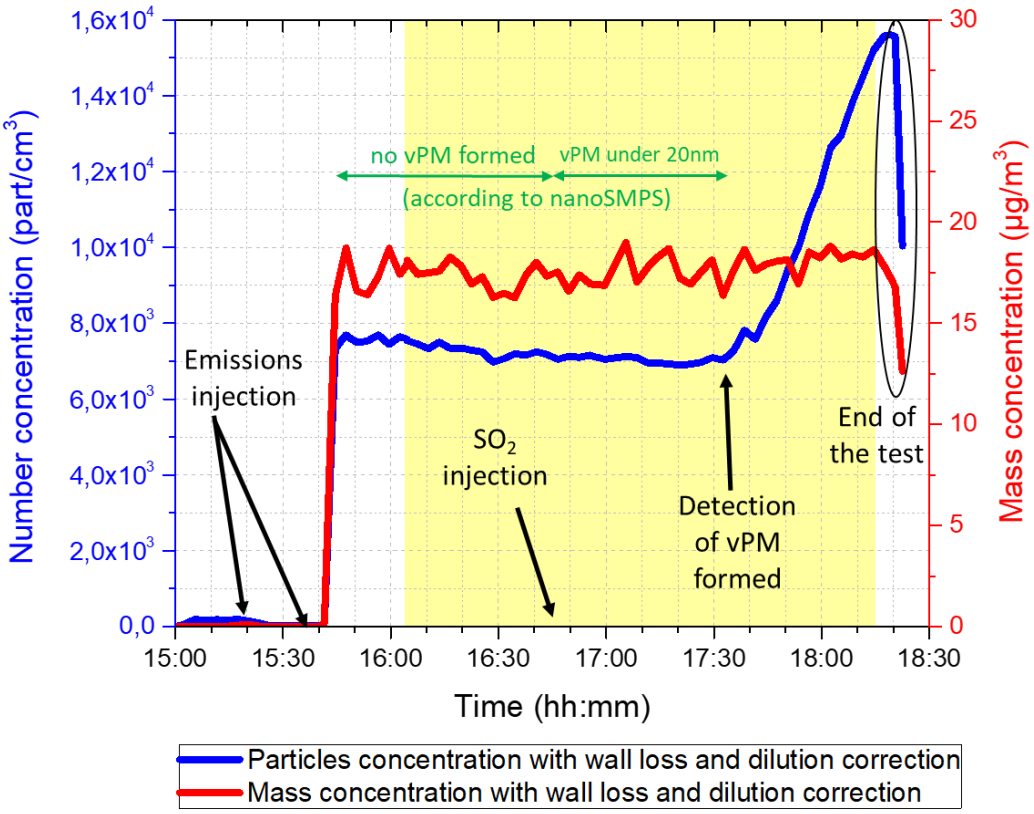

Figure V-5: Particle and mass concentrations inside the CESAM chamber after injection of CAST raw emissions from Jet A-1 combustion (LISA SMPS). Particles recorded have a diameter higher than 20nm. Switching lamps on and off are delimited by the yellow area. SO_2 injection is specified at 16:46 and vPM are detected at 17:30. Values have been corrected for dilution and wall losses.

To understand what are the new particles formed in the chamber after SO_2 injection, the chemical composition of the particulate phase is studied (based on ACMS data). Figure V-6 represents the evolution of Organic compounds (case a) and of NH_4^+ and NO_3^+ concentrations (case b) in CESAM chamber after emissions injection. The data have been corrected for dilution and light activation period is indicated by the yellow area.

Regarding the evolution of compounds concentration after the CAST emissions injection (Figure V-6.a), it is possible to see that organics present in the chamber get transformed by oxidation. Then the saturation vapour pressure of these compounds decreases and they condense easier on soot particles. An increase of their concentration from 2.78 µg/m^3 to 3.4±0.5 µg/m^3 is observed. However, SO_2 injection do not has an influence on organic concentration. It should be noted that ACMS recorded signals for particles over 40 nm. It means that only soot particles have been monitored due to the absence of vPM before SO_2 injection and that these organic compounds detected are only on soot particles. After light activation, oxidised organic compounds have condensed on soot explaining the increase of their concentration and contributing to increase the size of nvPM (cf. V.1.3.1).

In the case of Figure V-6.b, the light activation does not affect NO_3^+ or NH_4^+ concentrations but the SO_2 injection contributed to increase the NH_4^+ amount. With the doping process, the ammonium present in the chamber is combined with sulphuric acid to form clusters of ammonium sulphate, as ammonia/ammonium cannot be transformed into particles (Erupe et al., 2011; Lehtipalo et al., 2018; M. Wang et al., 2022; L. Xu, Yang, et al., 2021). Then these clusters either grow large enough to be detected by the ACSM or are absorbed onto the soot surface. Its concentration increases up to 1 µg/m^3. However, concerning the nitrate, the signal detected is too low (at the limit of detection of the instrument) and no conclusion can be made.

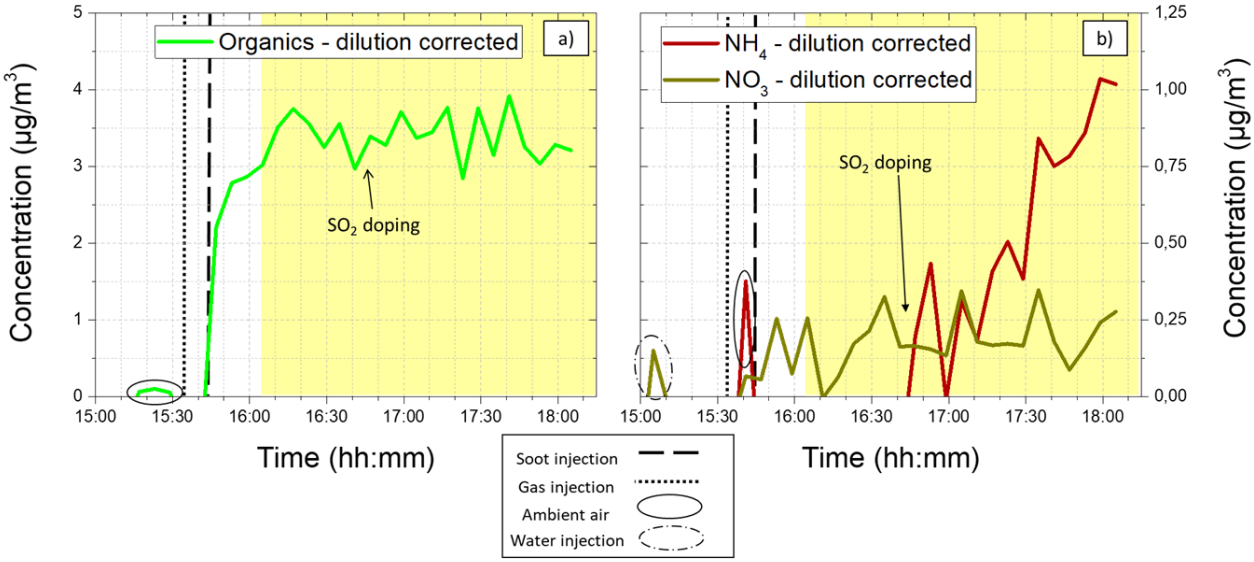

Figure V-6: Monitoring with ACSM of organic compounds (case a) and NH_4, NO_3 (case b) concentrations for raw emissions injection test using Jet A-1 fuel. Data have been corrected for dilution and yellow area indicates light activation period.

V.1.3 Particle size evolution

Previous observations show that the vPM formation is limited by the presence of soot. By studying the GMD of nvPM, it is possible to confirm that gaseous precursors and new particles formed are adsorbed on the soot surface.

V.1.3.1 Geometric Mean Diameter of soot particles

The Figure V-7.a) represents total size distributions at different periods of the test (LISA SMPS). After the injection of raw emissions and before the injection of SO_2 inside the chamber, the size distributions are monomodal and centred at 105 nm, corresponding to soot particles in accordance with the observations already done on Figure V-4.a. After the addition of sulphur dioxide, the size distributions become bimodal: the presence of soot particles is recorded around 105 nm and the one of vPM around 20 nm. However, the part of the bimodal size distribution corresponding to the vPM mode is incomplete due to the limit of detection of the instrument and cannot be used to calculate the vPM GMD (no maximum of the distribution detected). Thus, LISA SMPS is used to obtain soot GMD and nanoSMPS for vPM GMD calculation due to their respective size limitations.

For the study of the soot particles present in the chamber, only the mode at 104 nm has been selected (Figure V-7.b) and then fitted (Figure V-7.c) to estimate the soot GMD over the experiment. It should be noted that the number concentration decreases with time. Indeed, 10 min before light activation, the concentration number of particles is 10.2×10^3 part/cm^3. When the lights were on, this value decreased to 9.6×10^3 part/cm^3 and 10min after light activation to 9.3×10^3 part/cm^3. Finally 2h after light activation, the concentration of soot particles was $4.x10^3$ part/cm^3 (decrease of 59% compared to the initial value). In the same time, the mean diameter of soot particles increased from 109 nm (10min before lights) to 136 nm (2h after light activation).

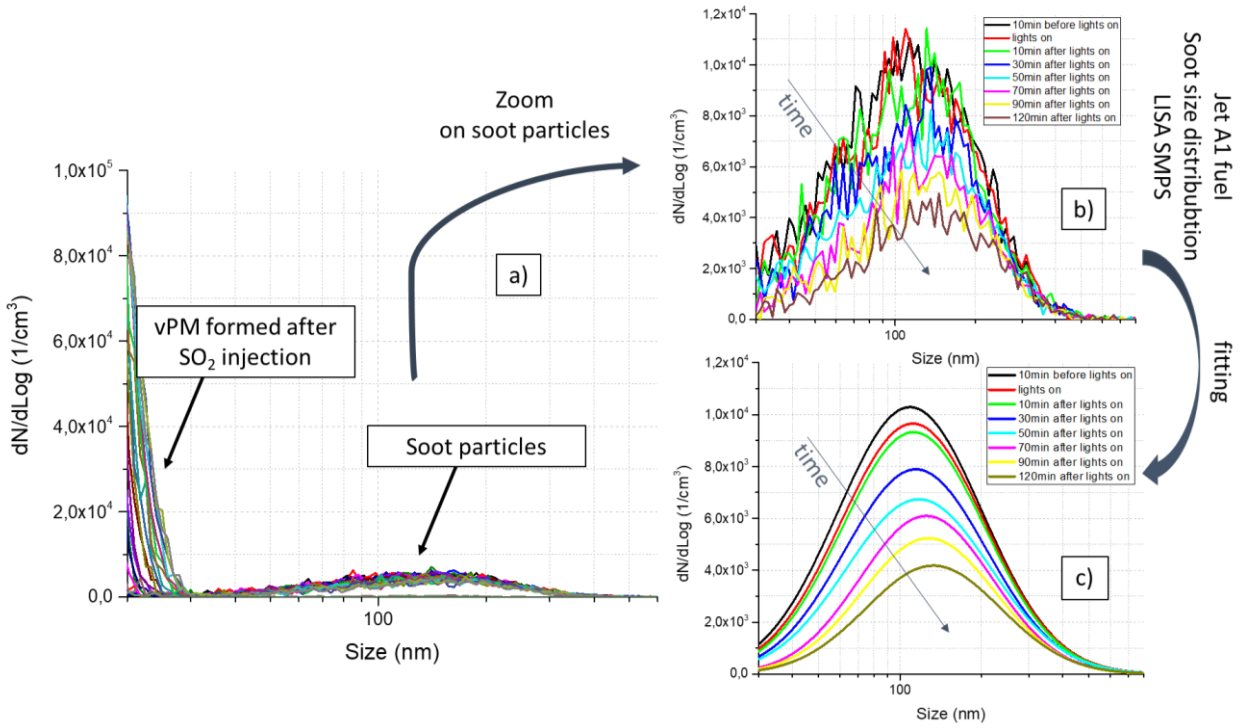

Figure V-7: Size Distributions for raw emissions injection in the chamber (LISA SMPS). The figure a) presents the entire size distribution with soot particles above 100 nm and vPM formed after SO_2 injection at 20 nm. The figure b) is a zoom of the raw signal on soot particles and the figure c) corresponds to a fit of this zoom to get the corresponding GMD (MATLAB).

The soot GMD is represented over the time on Figure V-8.a (in red). The total GMD (in black - taken into account all particles detected in the chamber) is added to show the difference before and after fit process. After light activation, the size of soot particles increases due to adsorption of gaseous precursors and organic compounds (cf. Figure V-6) on their surface. After the injection of SO_2, the difference between the soot GMD and total GMD calculations is highlighted when the vPM formed become detectable by the instrument (i.e. vPM size > 20 nm). Taking into account all these new particles, the total GMD decreases and becomes more representative of the vPM size. Otherwise, the fitted soot GMD continues to increase from 109 nm to 136 nm by condensation of vPM on the soot surface.

It is possible to see that soot interacts with other particles:

- by agglomeration with soot (cf. reduction of number concentration – Figure V-7.c);
- by absorption of organics and vPM formed (cf. GMD increase - Figure V-8.b).

The trend of increasing GMD for soot particles is not linear during the entire experiment. Figure V-8.b represents a zoom on the fitted soot GMD with linear equations related to variation of size over the time: before lights, between lights and SO_2 addition, and after SO_2 injection. Indeed, before the light activation, the GMD is constant (114±0.4 nm). However with photochemistry, the GMD increases from 114 to 118 nm with a slope of 8.5° (linear fitting) and the soot size increases more after SO_2 injection from 118 nm to 136 nm with a twice steep slope (18.7°).

The nature of the deposit on the soot surface evolves over time. At the beginning, without lights, nothing is formed in the chamber. After light activation, organic compounds present in the chamber have been oxidised, thus reducing their volatility and making them to condense (with gas precursors) on soot contributing to increase the soot GMD.

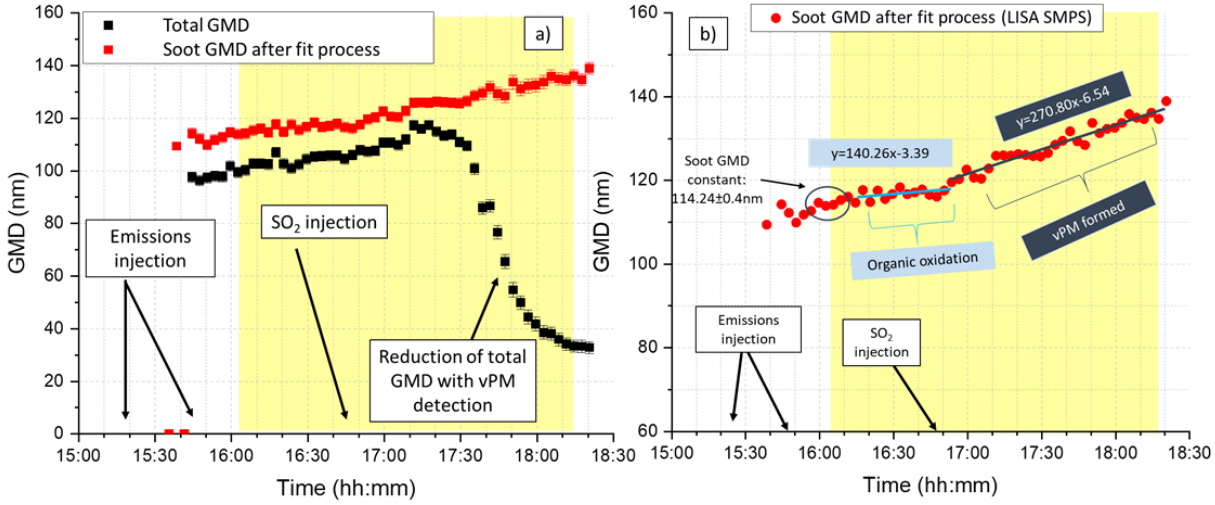

Figure V-8: Total GMD (in black) and fitted soot GMD (in red) for raw emissions injection in the atmospheric chamber. First Representation (a) corresponds to a comparison of the two GMDs and the second representation (b) is a zoom on fitted soot GMD representing highlighting the difference part of soot evolution. Light activation is represented by the yellow area.

Then after SO_2 injection, H_2SO_4 is formed in the chamber (cf. V.1.4.1 for details). These vapours condense onto soot particles and contribute to the formation of vPM. Thus the deposited layer on the soot surface is different from the previous one and this second increase is due to adsorption of vPM newly formed onto the soot surface. It is difficult to estimate this quantity over the time because no instrument was dedicated to the measure of the mass in the chamber. The mass concentration cannot be obtained with a SMPS because the density of particles was hypothetically set at a constant value (density=1 for soot particles, cf. Annex P). However in this case, density of particles is not the same for organics, vPM and soot, making it difficult to distinguish between vPM absorption and soot agglomeration after SO_2 injection.

V.1.3.2 Geometric Mean Diameter of vPM formed

To complete the study of soot GMD, the size of new vPM formed is also analysed. The size distributions (nanoSMPS) related to the vPM formation can be observed after the introduction of SO_2 in the chamber on Figure V-9. Bimodal distributions have been obtained. It is explained by the detection of a first mode related to the first small vPM formed (persisting despite the agglomeration on pre-existing vPM or soot particles) and by the detection of a second mode due to the formation and evolution in size of vPM after injection of sulphur dioxide in the chamber. It can be noted the presence of the background signal measured at the limit of detection of the instrument. The same procedure as for soot particles has been used to get a better estimation of their GMD over the time (selection of a mode and fitting process).

GMD obtained after the fit process are presented on Figure V-10. To avoid soot in this calculation, only particles below 40 nm have been selected and the particles at the limit of detection (noise/background) have not been considered.

To calculate the vPM GMD, different tests have been done. The first one (in purple - Figure V-10) corresponds to the fitted vPM GMD focused only on the vPM increasing in size over the time (i.e. monomodal of vPM formed after SO_2 injection at 20 nm) without taken into account small vPM formed between 7 nm and 10 nm. A second test is done considering a bi-modal distribution composed by the small vPM mode around 7 nm (in blue - Figure V-10) and by the vPM mode around 25 nm (in green - Figure V-10). Each of these modes is fitted individually to get the respective GMD independently from the other one. The total GMD of vPM is represented in black. Some complementary details of this procedure are explained in Annex O.

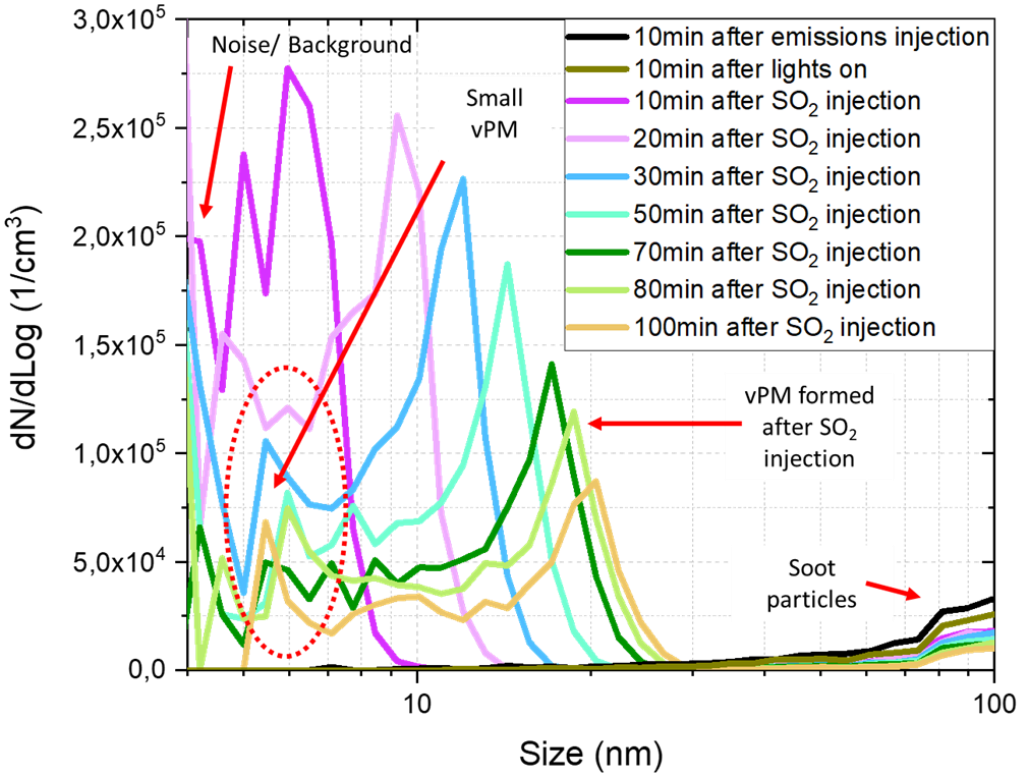

Figure V-9: Size distributions over the time obtained with a nanoSMPS for new vPM formed inside the chamber after injection of raw emissions and SO_2 addition using Jet A-1 fuel. Bimodal distributions are related to the small vPM detected at the limit of detection and the vPM formed after SO_2 injection.

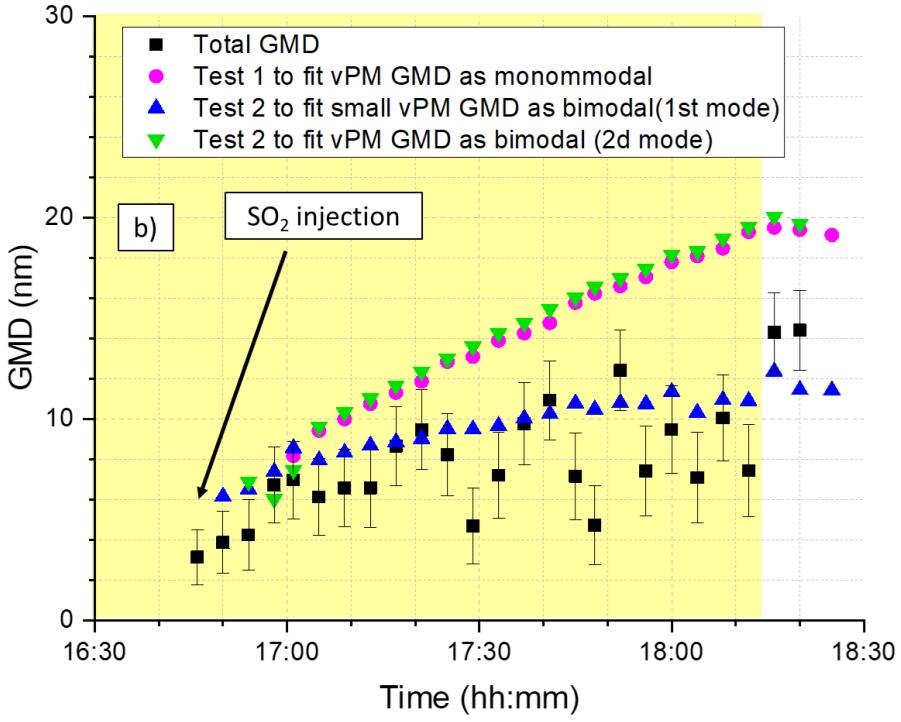

Figure V-10: Measurement of the vPM GMD after raw emissions injection in the chamber (nanoSMPS). It represents the total GMD (black) in comparison to 3 different fitted GMD: in magenta for the vPM with a one-fit-mode, in green for the vPM with a 2-fit-mode and in blue for the small vPM with a 2-fit-mode. Light activation is represented by the yellow area.

The first observation is that for all cases, the GMD of vPM increases once SO_2 is injected in the chamber with lights on (Figure V-10). Concerning the vPM GMD (in purple and in green), the size of these new particles reaches 20 nm before the end of the test. Both methods (fit of the vPM mode with a monomodal and fit of the vPM mode with a bimodal) present a similar result, indicating that both modes are independent. It is interesting to see that also the small mode grows (in blue). When the lights are turned off, the formation of vPM is stopped too: no more homogeneous nucleation.

Figure V-11 summarises the fitted GMD calculated for soot particles (in red) using the LISA SMPS and the fitted GMD obtained for vPM formed (in green) after SO_2 injection using the nanoSMPS. The light activation is indicated by the yellow area and details of soot GMD variations are specified.

The GMD increases in both cases until the end of the experiment. For the vPM it is due to the injection of SO_2 starting the nucleation between gas precursors and SO_2, leading to the formation of new particles. For the soot, the increase of the size comes from the absorption of different compounds at their surface: firstly from the condensation of gaseous precursors and organics (oxidation and diminution of vapour pressure), then from agglomeration of newly formed vPM. Eventually surface oxidation of soot can also help. After the injection of SO_2, the size of the vPM increases by 10.42 nm in 1h at the same time the soot particle size increases by 15.48 nm in 1h. The experiment has been stopped 1.5 hours after sulphur injection because the vPM formation being forced by SO_2 injection was just a test concerning sulphur impact and the variation of organics amount and vPM size started to stagnate.

In conclusion, the formation of particles inside CESAM chamber is affected by the presence of soot, adsorbing on their surface vPM precursors. With SO_2 injection, the formation of new particles can be observed despite the presence of soot. To understand the formation of vPM in the chamber, some compounds such as sulphuric acid (Kulmala et al., 2013) and oxygenated compounds (Kirkby et al., 2016), known to be involved in particle formation, are studied.

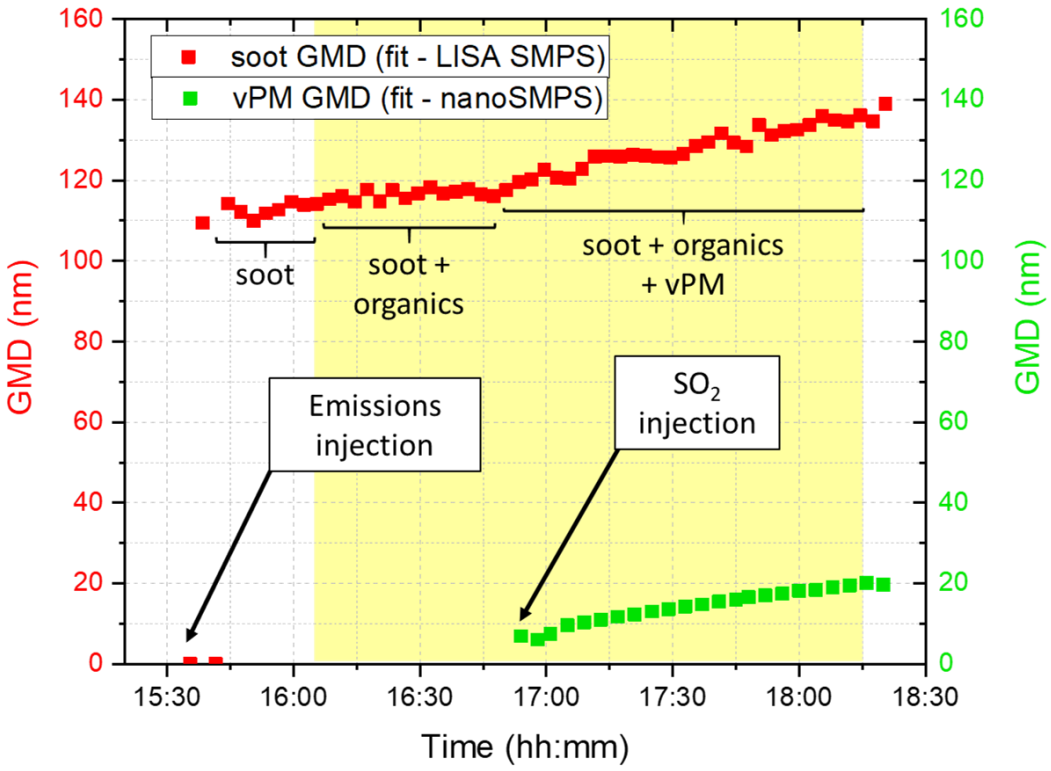

Figure V-11: GMD of soot particles (LISA SMPS - in red) and GMD of vPM formed (nanoSMPS - in green) after fitting process for raw emissions injection in the CESAM chamber (Jet A-1 combustion). Light activation corresponds to the yellow area.

V.1.4 Pathway for vPM formation at ground atmospheric conditions

V.1.4.1 Impact of sulphuric acid on vPM formation

To complete the previous observations by studying the impact of SO_2 on vPM formation, an on-line mass spectrometer instrument (API-ToF) has been employed. The first step was to focus on the presence of sulphuric acid H_2SO_4 due to its role in the particle formation process (Kirkby et al., 2011; Riipinen et al., 2007).

The evolution of sulphuric acid in the CESAM chamber over the time is represented in Figure V-12.a for the raw emissions injection case using Jet A-1 fuel. The concentration is recorded in molecules per cm^{-3}. Figure V-12.b and Figure V-12.c give respectively a representation of SO_2 concentration (gas phase - in ppb) and of SO_4 concentration (particulate phase – in $\mu g/m^3$) in the CESAM chamber. The ACSM sulphate denomination regroups fragments of $H_2SO_4^+$, HSO_3^+, SO_3^+, SO_2^+, SO^+. The photochemistry applied in the chamber using lamps corresponds to the yellow areas and all values have been corrected for dilution.

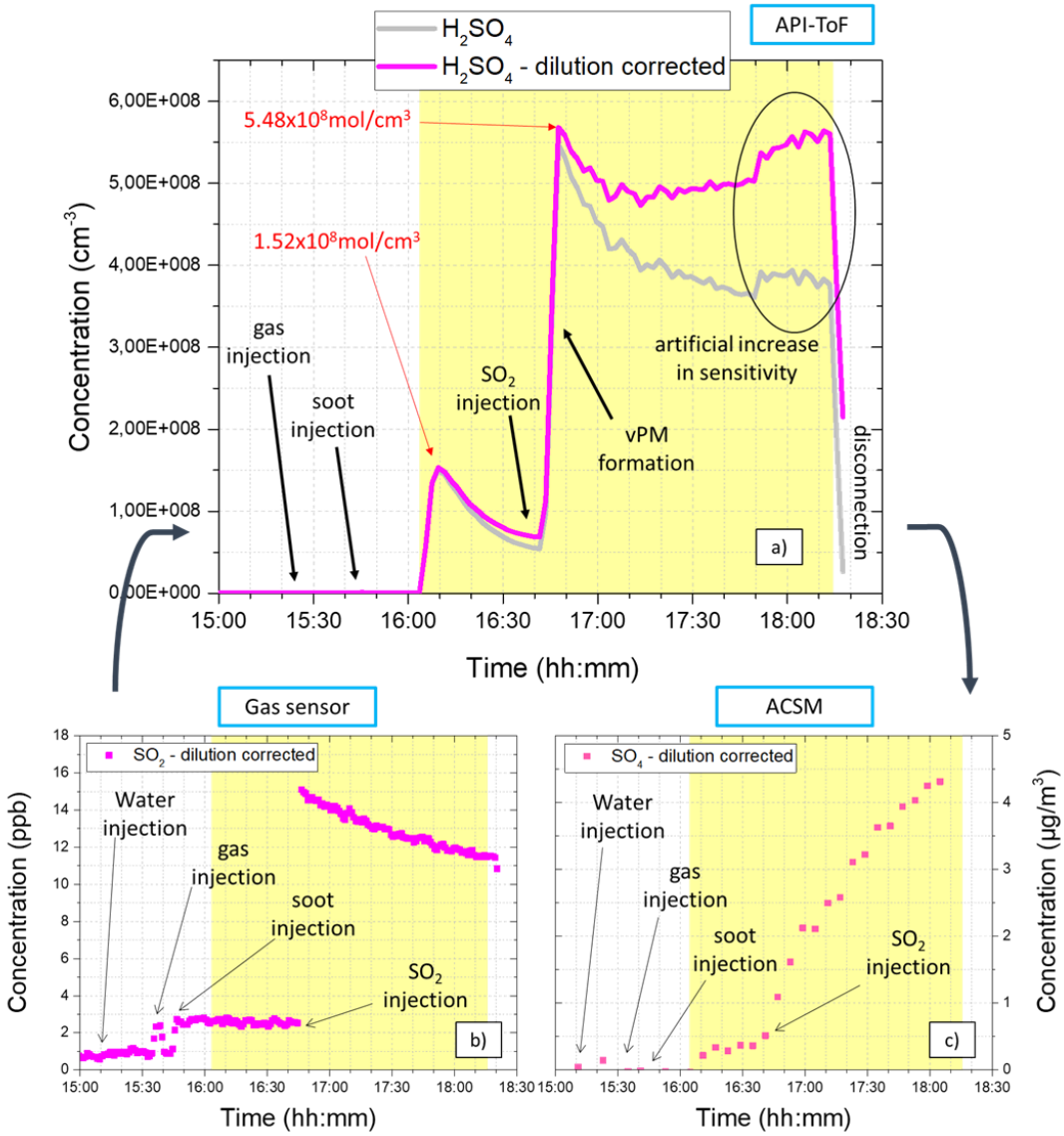

Figure V-12: Monitoring of sulphuric acid H_2SO_4 (case a – recorded with an API-ToF in molecule per cm^{-3}), of SO_2 (case b – recorded with a gas sensor in ppb) and of SO_4 (case c - recorded by the ACSM in $\mu g/m^3$) concentrations in CESAM chamber for raw emissions injection (Jet A-1 fuel combustion). Data have been corrected for dilution (plot in purple) and yellow areas

indicate light activation periods. Concerning the case a), the sensitivity of the instrument has been increased at the end of the test, implying an increase of the signal but it is not due to increase of H_2SO_4 concentration on the signal.

The first observation is that H_2SO_4 concentration presents a first peak after light activation (Figure V-12.a) due to the oxidation of sulphur dioxide introduced with raw emissions ($1.52x10^8$ mol/cm^3) and then a second one due to the addition of SO_2 in the chamber ($5.48x10^8$ mol/cm^3). The concentration of H_2SO_4 increases more after SO_2 injection: 3.6 times more than for the previous H_2SO_4 peak linked to light activation.

Indeed, after soot injection and before light activation, SO_2 concentration introduced in the chamber remains constant at 2.75 ppb (only 0.1 ppb of change - Figure V-12.b) and neither H_2SO_4 nor SO_4 are present. Then, directly after light activation, SO_2 concentration decreases from 2.66 ppb to 2.45 ppb (i.e. -210 ppt), being oxidised in H_2SO_4 (first peak of H_2SO_4 at $1.52x10^8$ mol/cm^3, i.e. 6.14 ppt). Sulphuric acid concentration decreases by half directly after the peak of formation. It corresponds to the adsorption of sulphuric acid on soot particles. Indeed, the heterogeneous nucleation process was dominant and the formation of vPM is limited by the absorption of gaseous precursors on soot surface (cf. soot GMD in V.1.3.1). It can be noted that absorption of SO4 is observed also in ACSM, this kind of confirmation of the condensation on soot (Figure V-12.c), its concentration reaching 0.36 µg/m^3. As no vPM have been observed in the chamber (Figure V-4) and as no more organic compounds have been formed (Figure V-6.a), the injection of SO_2 has been done before the entire stabilisation of the first H_2SO_4 concentration step.

After the injection of SO_2 with lights kept on, a significant increase of H_2SO_4 concentration is observed (second peak at $5.48x10^8$ mol/cm^3, i.e. 23.08 ppt - Figure V-12.a). Quickly, the SO_2 amount decreases over the time (-24%) to generate H_2SO_4. Then sulphuric acid concentration decreases also (from $5.48x10^8$ mol/cm^3 to $4.83x10^8$ mol/cm^3), that is linked to the formation vPM (confirmed by the increase of the vPM number concentration). It implies that formation of vPM is related to the amount of SO_2 present in the chamber at the beginning of the test: more SO_2 boosts the formation of vPM despites the presence of soot.

Then a stabilisation of the sulphuric acid concentration (at $4.8x10^8 \pm 1$ mol/cm^3) is observed 15-20min after the maximum peak value for the second step. Finally, a slight increase of the concentration is recorded (+0.69 mol/cm^3, i.e. +0.86 ppt). At the end of the test, the sensitivity of the instrument has been increased artificially to observe any change. As the sulphuric acid concentration presents low variations, the experiment has been stopped. In parallel, the amount of SO_4 particles increased continually until it reached 4.31 µg/m^3 at the end of the experiment (concentration is multiplied by 12).

To summarise, at the beginning of the test, sulphuric acid is adsorbed on soot particles and it contributes to increase their size. After SO_2 injection (+12.44 ppb) and oxidation into H_2SO_4 (+20.29 ppt, i.e. 0.02 ppb), vPM have been formed (lights already on). Regarding the evolution of H_2SO_4 and vPM concentration, sulphur acid nucleation is the main mechanism leading to the formation of new particles in this case. The next step is to check if when the sulphur concentration is low (i.e. before SO_2 injection), other mechanisms take over such as Highly Oxygenated Organic molecules (Kruza et al., 2020; Pytel et al., 2022).

V.1.4.2 Oxygenated molecules and organic compounds

Highly Oxygenated Organic molecules (HOMs) are formed in the atmosphere by autoxidation (cf. details in I.3.2.3) involving peroxy radicals from volatile organic compounds (VOCs). HOMs condense on pre-existing particles such as soot in the case of this study and contribute to the formation of new particles such as Secondary Organic Aerosols (Bianchi et al. 2019; Pospisilova et al. 2020; Tan et al. 2022).

During these experiments, HOMs have been observed on-line using an API-ToF instrument. Figure V-13 presents different oxygenated molecules monitored for the gas phase injection case (left)

and for the raw emissions injection case (right) using Jet A-1 fuel. Values have been compared to the sulphuric acid signal. This Figure presents the evolution of different HOM molecules derived for example from toluene (C_7H_8), benzene (C_6H_6) and associated to NO_3^- ion (related to their detection with a nitrate chemical ionisation API-ToF – cf. II.2.2.2.5).

The first observation is that there is no HOM formation for the raw emissions injection case. It seems that they are lost very fast during the experiment (cf. gas phase injection case) and their lifetime is too short to obtain a good signal. In Figure V-13.a, only the molecule $C_7H_7O_9$ presents a signal after activation of the lights for the gas phase injection case. There is a burst of OH when lights are on (red dash), leading to the formation of HOMs, but as particle formation goes so fast, they quickly disappear from the clusters phase (API-ToF just sees molecules and clusters up to ~2 nm). Thus, no formation is detected other than that of H_2SO_4 in the raw emissions injection case.

If the sensitivity is increased for a short moment (increase of the NO_3^- concentration for detection represented by green dash - Figure V-13) no additional HOMs are recorded. Only the artificial increase of sensitivity allows a higher sensitivity detection for HOM compounds, but it is also related to the increase of the background. Indeed, a blank of the chamber after water injection and light activation has been done before emissions injections and some HOMs are already present in the background. The HSO_4^- molecule is not affected by the increase of sensitivity but the $H_2SO_4{}^+NO_3^-$ cluster is (not shown here but presented on Figure V-12.a).

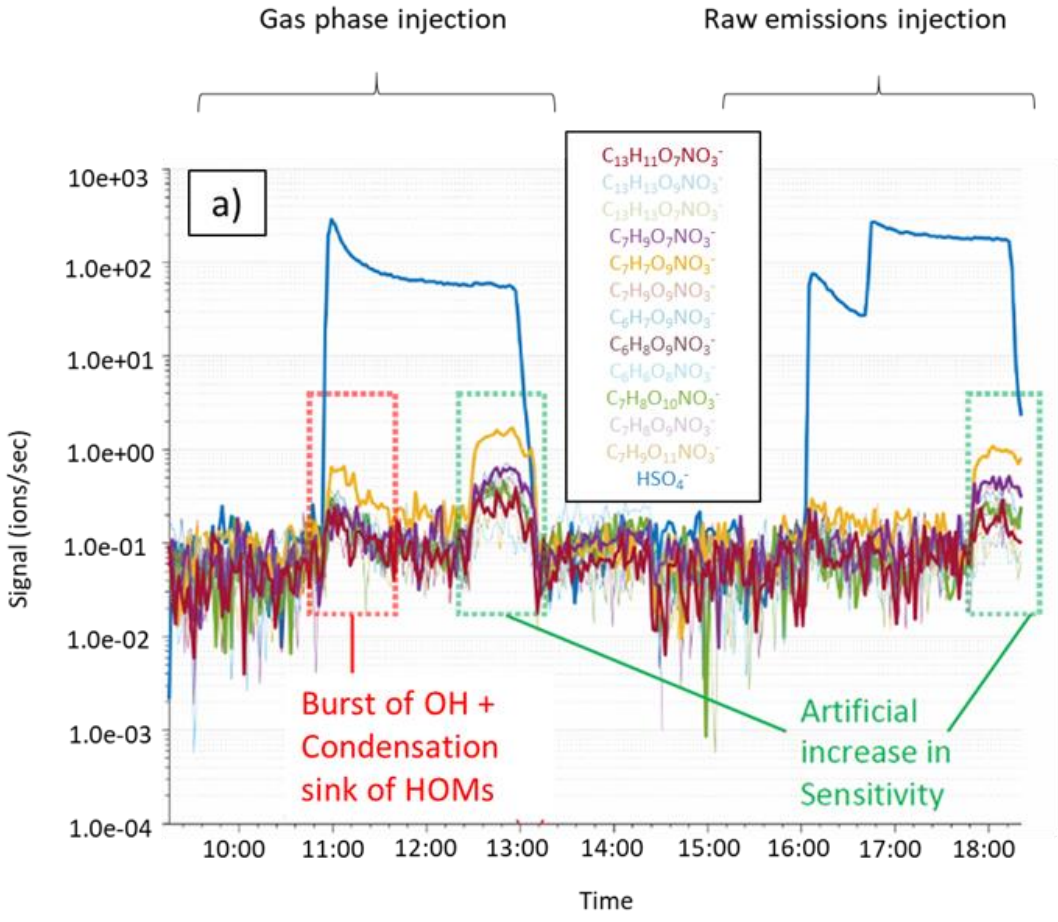

Figure V-13: HOMs detection using an API-ToF for gas phase injection (morning) and raw emissions injection (afternoon) cases after Jet A-1 fuel combustion. HOMs derived from toluene (C_7H_8), benzene (C_6H_6) and diphenylmethane ($C_{13}H_{12}$) compared to the H_2SO_4 signal. OH burst corresponds to oxidation processes to form HOMs and then vPM formed act as a condensation sink of precursors and HOMs (red dash). NO_3^- concentration is increased (green dash) to increase sensitivity.

To complete this approach, the analysis of the chemical composition of the particulate phase is done in parallel using an ACSM (cf. II.2.2.2.4). The organic concentration has already been monitored (V.1.2) and this denomination regroups various molecules and fragments. The main part of them are the Oxygenated Organics Aerosols OOA ($C_nH_mO_y^+$ as CO_2^+, $H_3C_2O^+$, …) and the Hydrocarbon Organics Aerosols HOA ($C_nH_m^+$). Other fragments can be assimilated to different notations such as f43, f44, f57 and f60 corresponding respectively to ($C_2H_3O^+$ + $C_3H_7^+$), (CO_2^+), ($C_4H_9^+$ + $C_3H_5O^+$) and ($C_2H_4O_2^+$) mass fractions.

Figure V-14 represents the evolution of organic compounds (case a) and of different organic fragments over the time for raw emissions injection. Case b) corresponds to f43 and f44 and case c) to OOA and HOA. All values have been corrected for dilution. In Figure V-14.a, the concentration of total organic compounds increases after light activation (+0.89 µg/m^3 compared to the initial amount injected with soot), but it is not affected by SO_2 injection.

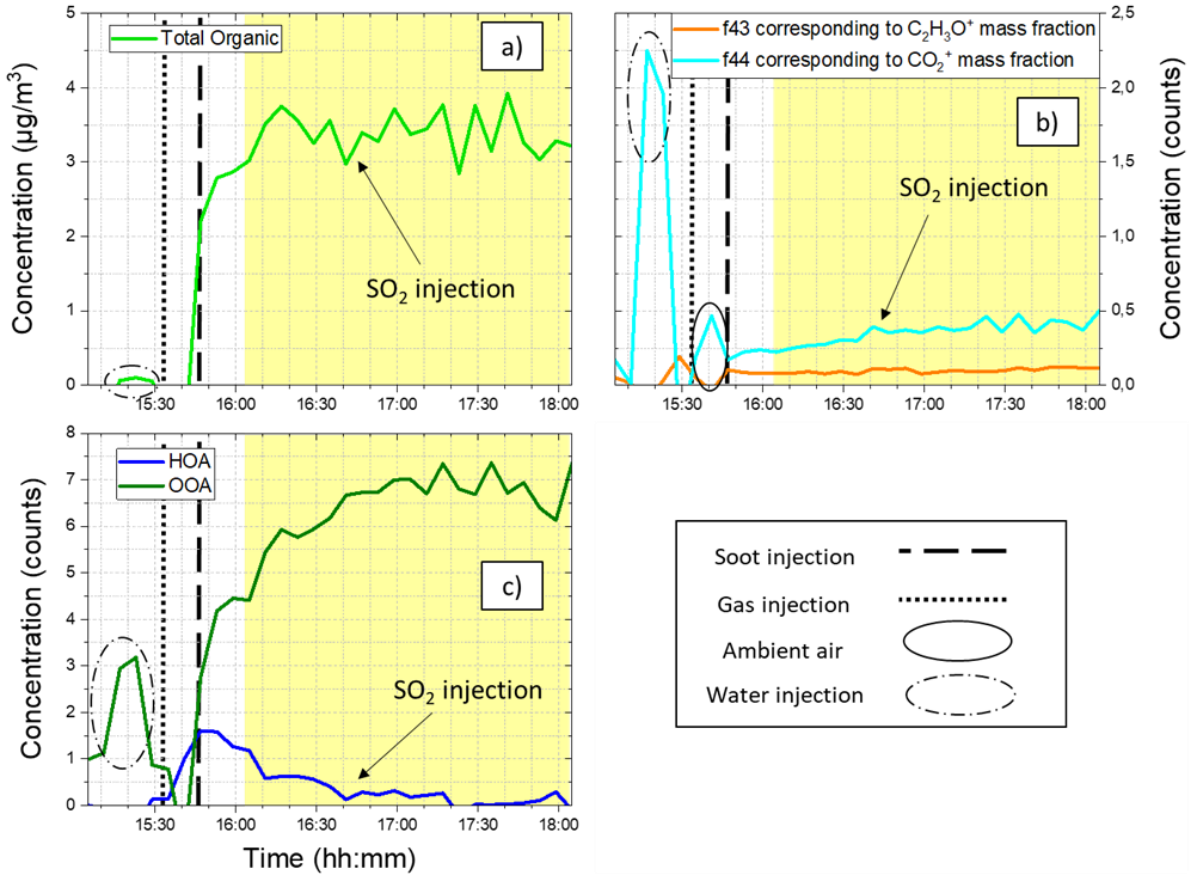

Figure V-14: Measure of the particle phase chemical composition using an ACSM for raw emissions injection (Jet A-1 fuel). The light activation is represented by the yellow area. The figure a) represents the evolution of organic compounds, the figure b) the evolution of fragment f43 and f44, figure c) the evolution of OOA for Oxygenated Organics Aerosols and HOA for Hydrocarbon Organics Aerosols. It should be noted that the ACSM instrument cannot detect particles under 40nm.

Concerning the OOA and HOA concentrations after soot injection (Figure V-14.c), HOA introduced in the chamber represents 1.58 counts and OOA represents 4.08 counts. First particles detected by the instrument are the HOA. It is explained by the presence of unburned compounds in emissions. In comparison, OOA compounds are not present in a significant amount in CAST emissions. Some of them are formed after water injection (not keep) and thereafter they are absorbed on soot surface. After light activation, concentrations of OOA and total organics increase respectively by +30% and by +25% in 20min. Concerning the OOA, their concentration reaches a maximum value at 7 ± 0.3

counts. However, at the same time, HOA concentration decreases relatively quickly (-69% in 30min) after lights are turned on. This is explained by the conversion of HOA in OOA. Then, organics can be found on soot particles due to adsorption, explaining the increase of their GMD (cf. V.1.3). HOA and Organics are not affected by the SO_2 injection (HOA already consumed, Organics already decreasing).

Regarding the other fragments, complementary information is provided. The concentration of fragment f44 (CO_2^+ - Figure V-14.b in blue) increases after light activation (+0.038 counts in 30min) and also after sulphur injection (+0.03 counts). It makes sense as f44 is linked with oxidation: when lights are switched on, its concentration starts to increase and when SO_2 is introduced in the chamber, a competitor is added for OH. No change over the time for fragment f43 ($CH_3CO^+ + C_3H_7^+$ - Figure V-14.b in orange).

In conclusion, OOA concentration increases when HOA concentration decreases. It means that oxygenated compounds have been formed with light activation and then have been adsorbed on soot particles, leading to their GMD increase (V.1.3.1).

V.1.5 Evolution of the gas phase composition

To complete the particle phase analysis, the gas phase of the emissions is characterised with a PTR-MS (cf. presentation in II.2.2.1.4) to monitor online Volatile Organic Compounds (VOCs). The objective is to study the evolution of different compounds such as oxygenated or sulphuric containing molecules depending on the light activation and SO_2 injection. With the appearance or the disappearance of some compounds, it is possible to link them to the formation of the vPM and understand the mechanism involved in this process.

Figure V-15 regroups concentrations of different compounds over the time for the raw emissions injection test based on Jet A-1 fuel combustion:

- Oxygenated molecules such as ketene and acetaldehyde (case a), formic acid and formaldehyde monohydrate (case b), acetone and hydroxyethanolate (case c);
- Hydrocarbons such as toluene, propane and cyclopentadienide (respectively case d, e, f);
- Nitrogenated molecules such as ethylamine and ethanimine (case g);
- Sulphur compounds such as sulphuric acid, dimethyl sulphide and butanethiol (case h)
- and OH tracer butanol d9 (case i).

Water injection and light activation are represented respectively by grey and yellow areas. Soot and SO_2 injections are specified also on each graphic by dotted lines (respectively black and blue).

First observations are that some contaminants are introduced in the chamber with water injections: such as ketene (case a) and formic acid (case b). After emissions injection and light activation, concentration of oxygenated compounds increases (case a, b and c) while concentration of hydrocarbons (case d, e and f) and nitrogenated (case g) compounds decreases. At the beginning of each test, Butanol-d9 is introduced inside the chamber. It is used as an OH radical tracer in atmospheric chemistry studies to determine OH exposure. In this test, the reduction of OH tracers (case i) is in accordance with the formation of oxygenated compounds after light activation. Even if it is difficult to quantify the variation of concentration due to a low signal, it should be noted that light activation has a higher impact on oxygenated compounds with a higher number of atoms (case c). After SO_2 injection, the formation of oxygenated compounds is slowed down, but the consumptions of hydrocarbons and nitrogenated molecules follow the same trend (slight break in slope). Concerning the different sulphur compounds observed in the gas phase of the emissions, no significant changes can be observed. With light activation, their concentrations continue to decrease slightly before being stabilised by SO_2 injection. Sulphuric acid H_2SO_4 formed from oxidation of SO_2 are converted in vPM or goes directly on the soot volume surface.

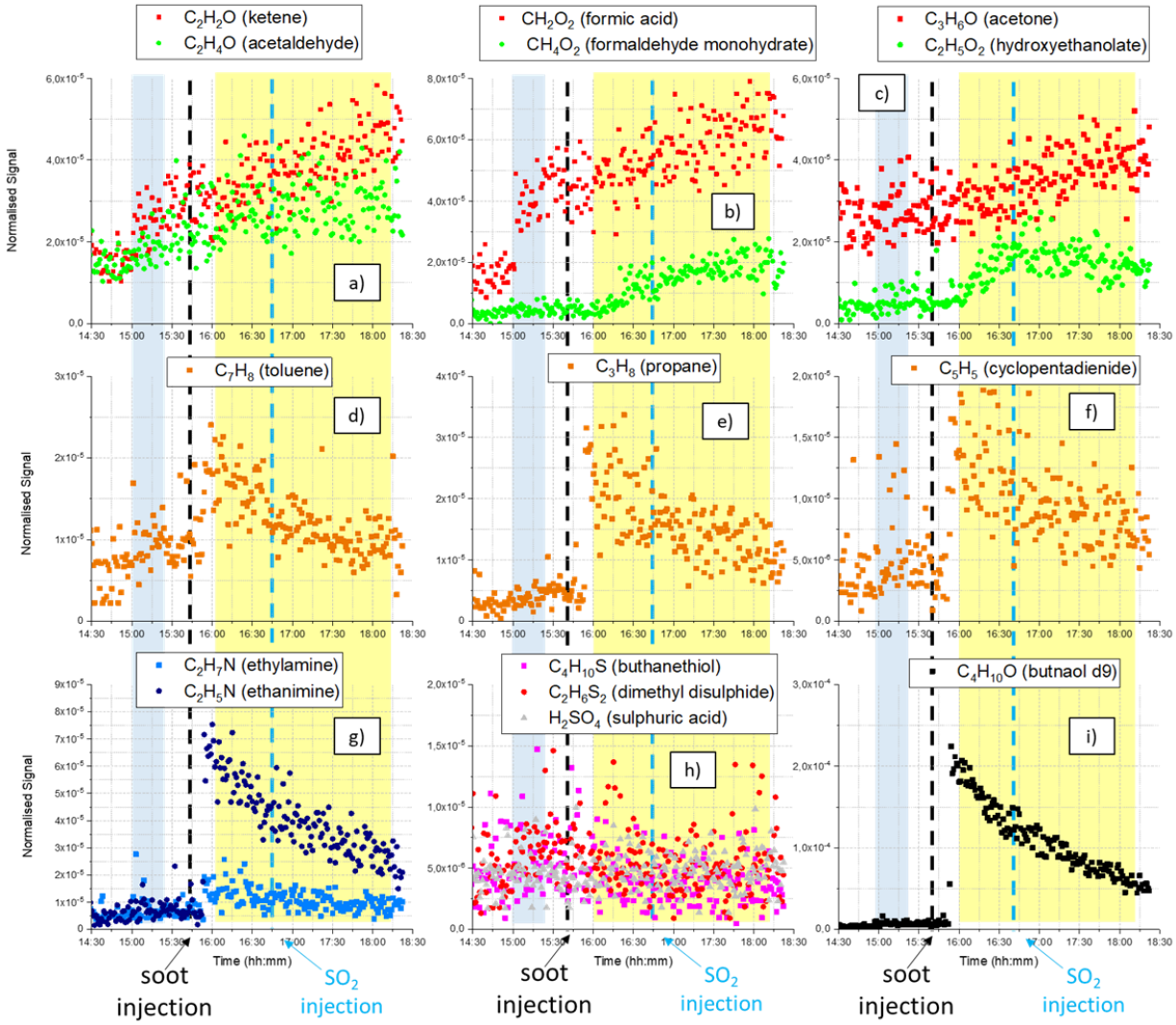

Figure V-15: Compound concentrations measured with PTR-MS for raw emissions injection (Jet A-1 fuel). The top line (a, b, c) corresponds to oxygenated compounds; the middle one to hydrocarbons (d, e, f); the bottom one to nitrogenated compounds (g), sulphur compounds (h) and OH tracers (i). Water injections and lights on correspond respectively to grey and yellow areas. The soot injection is represented by black dotted lines and SO_2 injection by blue dotted lines.

V.1.6 Comparison of injection processes for the reference case

V.1.6.1 vPM formation depending on soot presence

In Chapter IV, the same investigation has been done to study vPM formation for gas phase injection inside the CESAM chamber. To have a better overview of the impact of soot presence on vPM formation, a comparison with these previous results is presented here.

Figure V-16 presents the size (y-axis) and particle number (colour scale) evolutions over the time for the homogeneous nucleation process from gaseous precursors without soot particles (case a – gas phase injection – cf. IV.2.2) and with soot particles (case b – raw emissions injection). These experiments have been done the same day using the Jet A-1 fuel. Both plots have been set at the same particle concentration scale to get a better visual comparison (from 0 to $3x10^3$ part/cm^3). It can be noted that soot particles at 100 nm are not observable using this representation for the raw emission injection case (Figure V-16.b) due to their low concentration. Furthermore, as there is no vPM

formation detectable from gaseous precursors nucleation after light activation for the case b), the comparison is done with particles generated after SO_2 injection (even if it is not the same vPM formation due to the doped injection, but it gives an idea of the sulphur impact on this process).

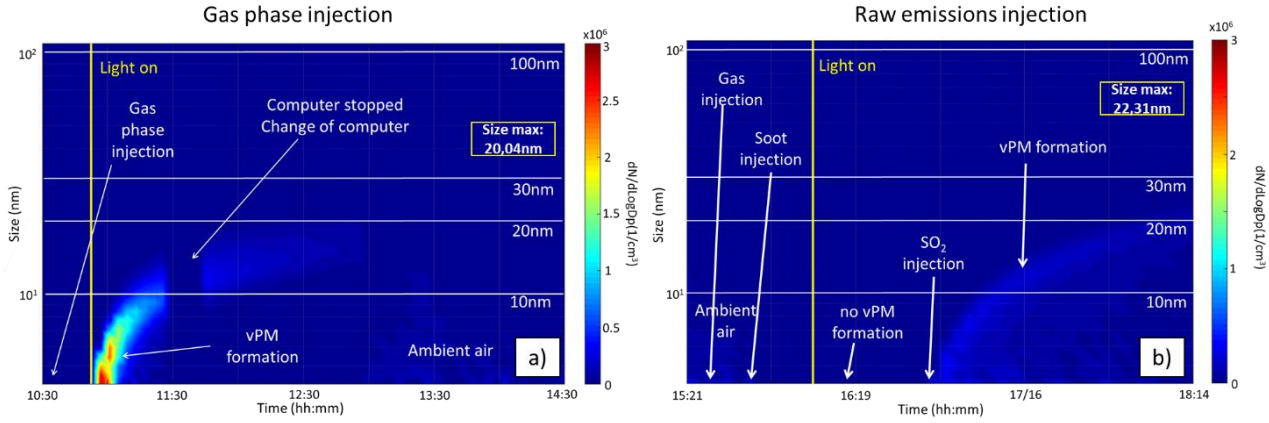

Figure V-16: New vPM formation for gas phase injection (case a - morning) and for raw emissions injection (case b - afternoon) using Jet A-1 fuel. Same particle number and size scales for both figures.

Once emissions have been injected (or SO_2 added) in the chamber, vPM are formed directly after light activation in both cases (in the second case the SO_2 injection has been done with lights on). The consequence is an increase of the particle concentration at the beginning of the process related to the formation of vPM and then an increase of the size of these particles by condensation of vapours on them and by agglomeration of particles formed. In comparison, the concentration number of new particles formed at smaller size is higher for the gas phase injection case: in the order of 10^4 part/cm^3 per ppm of CO_2 (Figure V-16.a) versus 10^3 part/cm^3 per ppm of CO_2 (Figure V-16.b) at the very beginning of the vPM formation process. On the contrary, the size of the new particles formed is larger for the raw emissions case (22.31 nm at the end of the test) compared to the gas phase injection case (20.04 nm). Whether the lamps were on or not, the oxidation will depend on irradiation. If larger particles are obtained for raw emissions, it is due to the fact that more vapour are condensing. One option is that in the gas injection case, much more particles are formed, and there are more particles to distribute the gas. If there are much less particles, it is possible to grow them larger by having a similar amount of gas. As lot of SO_2 has been injected, there are vapours to grow the particles.

Size range (nm)	Gas phase injection		Raw emissions injection (after SO_2 injection)	
	Particles concentration x10^5 (1/cm^3)	Correction by CO_2 x10^5 (1/cm^3)	Particles concentration x10^5 (1/cm^3)	Correction by CO_2 x10^5 (1/cm^3)
4.2	27.7	0.434	2.63	0.044
4.59	26.7	0.419	3.36	0.057
5.0	20.9	0.328	3.45	0.058
5.46	23.5	0.369	3.17	0.053
5.96	22.8	0.358	2.77	0.067

Table V-2: Number concentration of vPM formed for both nucleation cases: gas phase injection on the left and raw emissions injection on the right. The fuel is the Jet A-1 of reference and the values are normalised by CO_2 concentrations monitored during the injection (63.77 ppm for the gas phase injection and 59.36 ppm for the raw emissions injection).

The maximum values of particle concentrations for both nucleation cases at small sizes are reported in Table V-2 (without on the left and with on the right CO_2 normalisation). The gas injection

case presents 9 to 10 times more particles than for the raw emission injection case (taken into account the first 20min of the experiment). Without soot particles, the homogeneous nucleation process is dominant and the conversion of gaseous precursors in vPM is more important. With soot addition, the homogeneous process is limited by the heterogeneous one and no vPM formation is observable. Even after SO_2 injection, the formation of vPM is less important for the raw emission injection test (Figure V-16.b) than for the gas phase injection case (Figure V-16.a).

The next step is the study of vPM from a chemical point of view to observe the main differences between the two cases. Figure V-17 proposes a comparison between the two tests: on the left gas phase injection case and on the right raw emissions injection case. The comparison is focused on the evolution of SO_2 concentration (figures a and b), H_2SO_4 concentration (figures c and d). All data have been corrected for dilution and normalised by the respective CO_2 initial amounts (63.77 ppm for gas phase injection test and 59.36 ppm for raw emissions injection case). The light activation is represented on all figures by the yellow area.

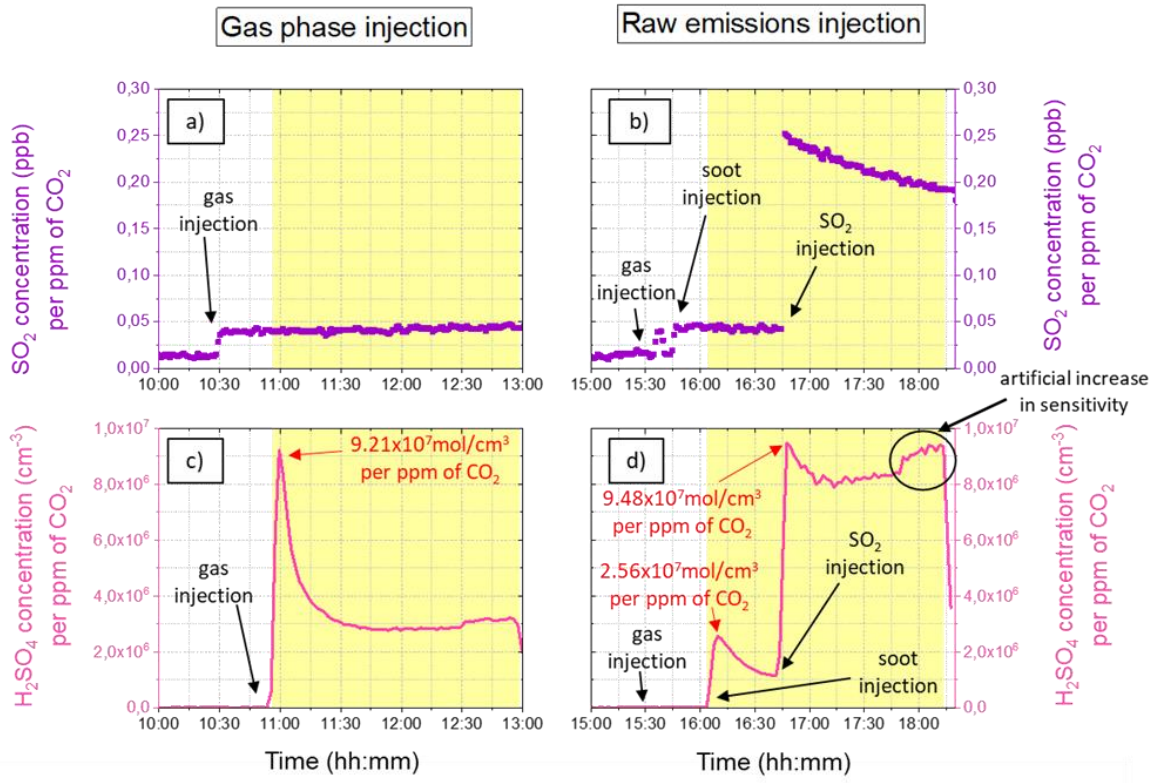

Figure V-17: Comparison between homogeneous nucleation cases for gas phase injection (left) and raw emissions injection (right) using Jet A-1 fuel. The top line of figures (a, b) represents the monitoring of SO_2 concentrations (in ppb) and the bottom line (c, d) represents the evolution of H_2SO_4 concentrations (in mol/cm³) in the chamber. Light activation is represented by the yellow area. All values have been corrected for dilution and normalised by the respective CO_2 amount: 63.77ppm for gas injection case and 59.36ppm for raw emissions injection.

The first observation is that after emissions injections, SO_2 concentrations are comparable and remain constant over the time: 0.041±0.002 ppb per ppm of CO_2 for gas phase injection (Figure V-17.a) and 0.043±0.002 ppb per ppm of CO_2 for raw emissions injection (Figure V-17.b). These concentrations are not affected by light activation. But after injection of sulphur dioxide in the chamber in the second test, the concentration of SO_2 becomes 6 times higher than for the gas phase injection case and decreases thereafter over time. This high amount of SO_2 introduced is related to the formation peak of H_2SO_4 in the chamber (Figure V-17.d).

After light activation, the concentration of sulphuric acid presents a higher formation peak for the case without soot particles ($9.21x10^7$ mol/cm^3 per ppm of CO_2 on Figure V-17.c) than for the case with soot particles ($2.56x10^7$ mol/cm^3 per ppm of CO_2 on Figure V-17.d). With similar Concentrations of SO_2 for both tests, this difference is explained by the presence of soot absorbing gaseous precursors and limiting the formation of H_2SO_4. Or/and H_2SO_4 itself is adsorbed or even starts to nucleate small molecular clusters that then are absorbed in soot. The small formation of H_2SO_4 for the raw emissions injection case explains that no vPM have been generated in the chamber. In comparison, for the same initial amount of SO_2, the concentration of sulphuric acid is 3.6 times higher and vPM are formed (increase of particle concentration) for the gas phase injection due to the absence of soot particles.

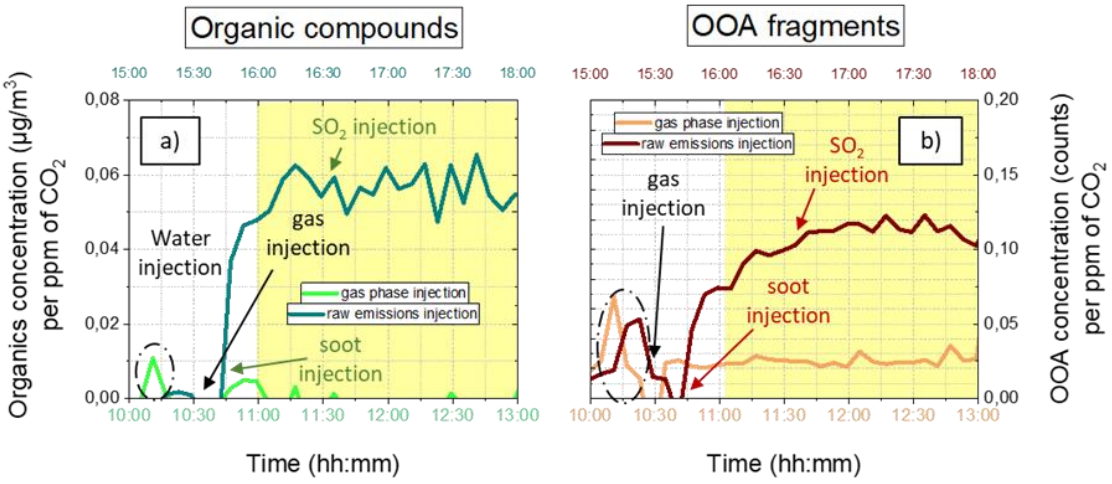

Figure V-18: Comparison between homogeneous nucleation cases for gas phase injection (green and brown) and raw emissions injection (dark-green and dark-brown) using Jet A-1 fuel. The case a) compares organic concentrations (in green - µg/m3) and case b) represents the monitoring of OOA fragment (in brown - in counts) concentrations in the chamber. Light activation is represented by the yellow area. All values have been corrected for dilution and normalised by the respective CO2 amount: 63.77ppm for gas injection case and 59.36ppm for raw emissions injection.

Figure V-18 presents the monitoring of organic compound and OOA fragment concentrations (respectively figures a and b) for the both tests. No formation of organic compounds is observed for the gas phase injection case (cf. organics in green Figure V-18.a). As ACMS instrument recorded only particles above 40 nm and as the size of vPM formed are around 20 nm, no organics have been detected for the test without soot, on the contrary to the test with soot (in dark-green Figure V-18.a) where organics are present on soot surface. Indeed, organics have been injected with gas phase at the beginning of the experiment (0.047 µg/m^3 per ppm of CO_2 before light activation – dark-green on Figure V-18.a). Then with light activation, they have been more oxidised and they condensed more on soot (to reach 0.059 µg/m^3 per ppm of CO_2). Indeed, the concentration of OOA oxygenated organics increases by 29.4% (+0.045 counts per ppm of CO_2 – dark-brown on Figure V-18.b) due to the oxidation of HOA hydrocarbons organics (cf. V.1.4.2 for more details). OOA fragments concentration reaches +57.4% at the moment of SO_2 injection compared to the initial amount introduced in the chamber (growth function that reaches an asymptotic limit). For the gas phase injection (brown - Figure V-18.b), no variation of the OOA concentration is recorded (particles formed are under limit of detection) and the initial amount of OOA detected comes from the water injection.

After SO_2 injection, the concentration of H_2SO_4 increases for raw emissions injection case until $9.48x10^7$mol/cm^3 per ppm of CO_2 (Figure V-17.d) that is comparable to the value obtained for gas phase injection case at the beginning of the test (3% of difference). However, to get this H_2SO_4 concentration, the amount of SO_2 is 6 times higher (Figure V-17.b) than the one of the first test (Figure V-17.a). It means that with the presence of soot, the concentration of SO_2 necessary to generate a comparable

sulphuric acid amount to form thereafter vPM, needs to be higher than the one of the case without soot. Some extra details are presented in Annex Q.

To complete this study, a comparison of the gas phase analysis for both tests using the PTR-MS instrument has been done: consider Figure IV-22 for gas phase injection and Figure V-15 for raw emissions injection. The number of molecules presenting variation over the time is low for both cases. Some differences can be noted, for example the detection of methanol (CH_3OH) only after the gas phase injection case or of butadiene (C_4H_6) only for raw emissions injection. Overall, for both cases, the VOCs and nitrogenated compounds concentrations decrease when oxygenated ones increase. The main difference is that concentration of these compounds is higher for the gas phase injection case (cf. IV.2.5.1 and V.1.4 for details).

V.1.6.2 GMD of newly formed vPM and growth rate depending on the soot presence

In the case of raw emissions injection, organic compounds and vPM formed can be absorbed on the soot surface. This is confirmed by the increase of the soot GMD over the time after light activation and after SO_2 injection (cf. V.1.2).

Concerning the size of vPM formed in the chamber, the maximum reached is comparable for both cases: 20.04 nm for gas phase injection (cf. IV.2.3) and 22.31 nm for raw emissions injection (cf. V.1.3.2). The vPM size is higher in the second test after SO_2 injection (more vapours available). Indeed, it can be noted that the particle size increases faster for the raw emissions injection case: only 1h30 to reach 22.31 nm compared to 2h for 20.04 nm for the gas phase injection case (Figure V-16). However this comparison between the two tests needs to be considered with caution. It has been already shown that more H_2SO_4 molecules have been formed after SO_2 injection than for the gas phase injection case.

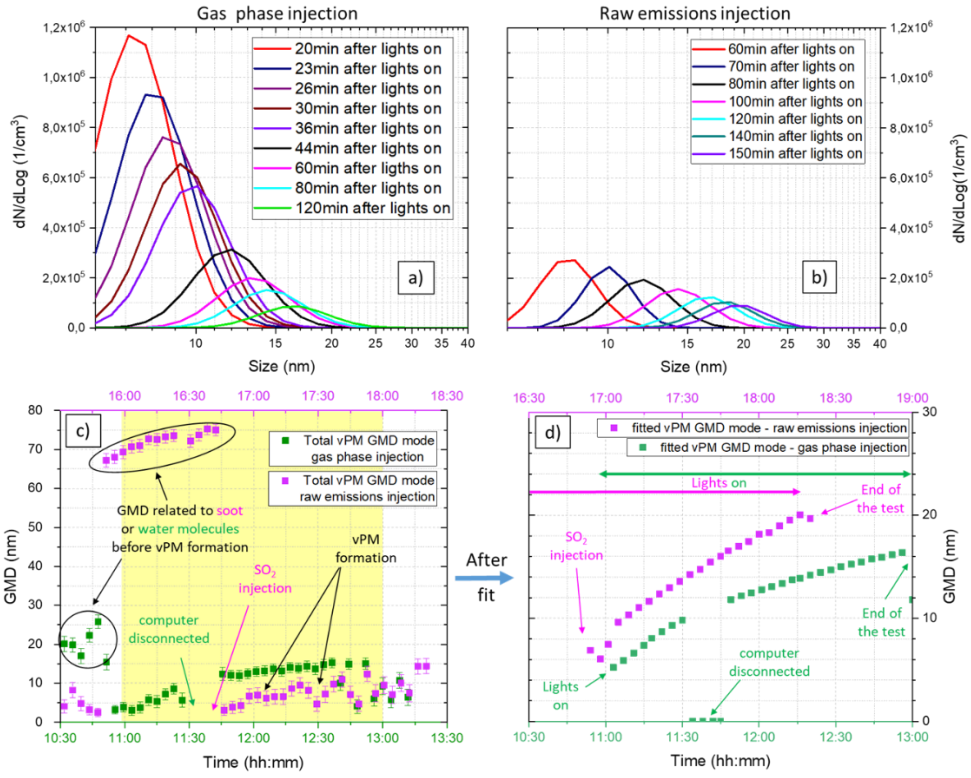

Figure V-19: Comparison of size distributions (a and b) and vPM GMDs (c and d) for gas phase injection and for raw emissions injection cases using Jet A-1 fuel. The yellow area indicates the light activation. Particle concentrations have been normalised by the respective CO_2 concentration.

Fitted size distributions of the particles formed inside the chamber are represented on Figure V-19.a) for the gas phase injection test and on Figure V-19.b) for the raw emissions injection test. The number of particles decreases in both cases, while the GMD of the particles increases at the same time after light activation. To compare the two experiments, it should be noted that there is a delay of 40min for the raw emissions injection case because the SO_2 injection have been done 40min after light activation (i.e. "60min after lights on" in Figure V-19.a is compared to "100min after lights on" in Figure V-19.b). The Figure V-19.c represents the total GMD obtained for both cases and the Figure V-19.d corresponds to the vPM GMD calculated after the fitting procedure for both cases: initialised at the start of vPM formation, i.e. light activation for gas phase injection case (in green) and SO_2 injection for raw emissions injection case (in purple).

The study of the size distributions over the time contributes to confirm the previous observations done about the concentration of particles: more particles formed for the gas phase injection case. Data are summarised in Table V-3 to compare the vPM formation in terms of number and size for both nucleation cases. For the same reference time, the concentration number of particles is higher for the gas phase injection, but the size increases faster for the raw emissions injection case (Figure V-19.d). This is due to the larger amount of sulphur dioxide introduced in the atmospheric chamber leading to a higher formation of H_2SO_4 and thereafter contributing to the vPM formation process. With time, for a similar size (for example at 14 nm), the particle concentrations become comparable between both cases (around 0.25 ± 0.01 x10^4 part/cm^3 per ppm of CO_2).

Time after the start of vPM formation (colour referred to Figure V-19.a and .b)	Gas phase injection - Figure V-19.a		Raw emissions injection case Figure V-19.b) (SO_2 injection)	
	Particles concentration (part/cm^3) – CO_2 correction	Size (nm)	Particles concentration (part/cm^3) – CO_2 correction	Size (nm)
+20min (in red)	1.83x10^4	7.1	0.45x10^4	8
+40min (in black)	0.49x10^4	12	0.33x10^4	12
+60min (in purple)	0.31x10^4	13.11	0.26x10^4	14.23
+80min (in cyan)	0.24x10^4	14.32	0.21x10^4	17.09

Table V-3: Particle concentrations and size comparison depending on the nucleation case for Jet A-1 combustion. Values have been corrected by their respective CO_2 amount at the injection. N.B. vPM formation started 40min late for the raw emissions injection case after light activation.

The calculation of the growth rate (GR) for the vPM formed in the chamber (increase of the size in nm per minute then converted in hours) depending on the emissions injection cases is done based on the procedure already described in IV.3.4 (cf. details in Annex R). Then growth rates are plotted as function of the H_2SO_4 concentration (for a stable period) and compared to the literature (details in section I.3.2.5). The Figure V-20 comes from Lehtipalo et al. (2016) and data obtained in this study are added on it : black diamond for the vPM formation in gas phase injection case and black circle for vPM formed in raw emissions injection case. It gives an idea of how many condensable vapours are available for each case, and for example for the raw case, amount of soot and size will play an important role.

The red line corresponds to the growth rate with only sulphuric acid. Regarding the results obtained for the Jet A-1 case, GR cannot be explained only with sulphuric acid and it means that other compounds contribute to the growth of the clusters (cluster-cluster collisions), and in our case most likely organic compounds coming from combustion. The two points (for gas injection and for raw emissions injection) are in a different "collision enhancement" line, being the gas injection in a higher enhancement line. This is expected since soot will act as a condensation sink, reducing the amount of vapours available for growing the particles and thus reducing the growth rate.

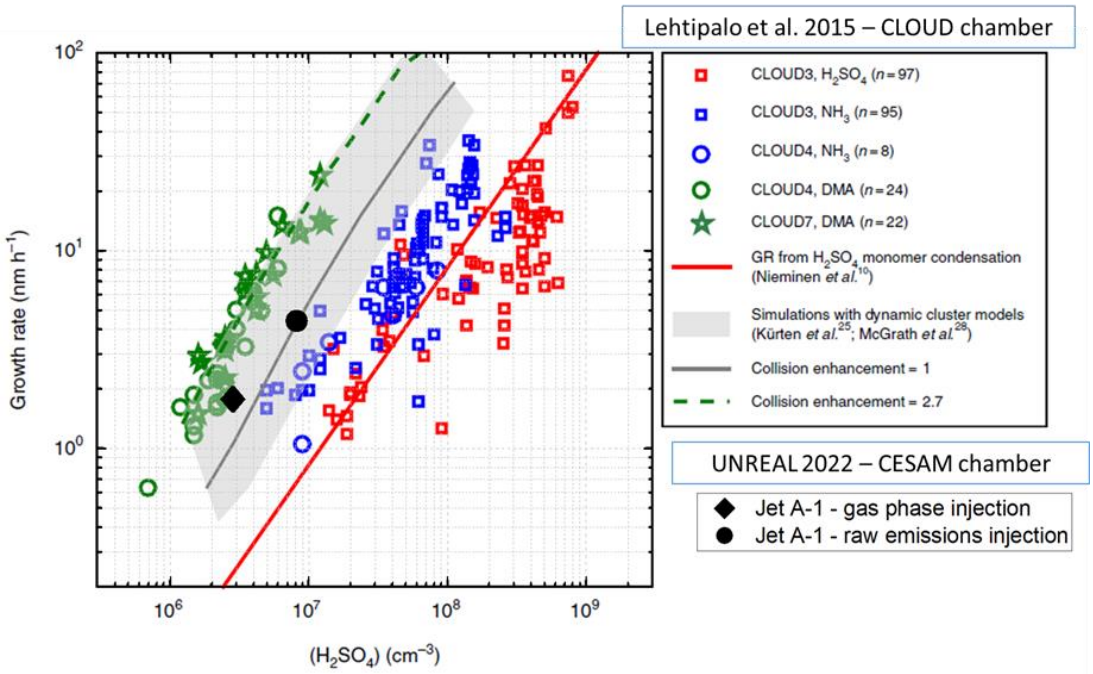

Figure V-20: Comparison of the growth rate calculated for gas phase injection and raw emissions injection cases using jet A-1 fuel with growth rates calculated in different systems by Lehtipalo et al. (2016). The data corresponding to the UNREAL project with the CESAM chamber (ambient temperature and pressure, RH=38%) are indicated in black concerning the vPM formation. Data related to Lehtipalo et al. (2016) corresponds to experiments done in the CLOUD chamber. Growth rates of 2 nm particles are determined by the appearance time method between 1.5 and 2.5 nm as a function of the sulphuric acid (H_2SO_4) concentration measured with different amounts of ammonia (NH_3) and dimethylamine (DMA) in the chamber.

V.1.7 Summary of results for raw emissions injection case

Based on the study of particle concentrations and GMD of soot, the homogeneous process is limited when it is in competition with the heterogeneous one due to the presence of soot particles. Sulphuric acid and organic compounds are adsorbed on the nvPM surface, limiting the formation of vPM.

In the case of raw emissions injection, the vPM formation is not observable using the reference Jet A-1 fuel. Not enough H_2SO_4 is generated in the raw emissions injection case: a big portion is adsorbed on soot, and homogeneous nucleation cannot overcome heterogeneous processes. It might have nucleation for small particles, but then those get into soot. An injection of SO_2 is done to generate enough H_2SO_4 for new particle formation despite the presence of soot. However, it implies a higher sulphur dioxide concentration than for a regular test to generate new particles by photochemistry.

To compare the vPM formation depending on the injection case (with and without soot), the same analysis needs to be repeated with a fuel where vPM formation can be observed for gas phase injection and for raw emissions injection without addition of sulphur in the chamber (cf. V.2.3).

V.2 Impact of fuel composition on vPM formation for raw emissions injection at ground level atmospheric conditions

In the previous part of this chapter, the formation of vPM and their interactions with soot particles after raw emissions injection in the CESAM chamber using the Jet A-1 fuel have been studied. A comparison of these previous results with the ones obtained for different fuels is proposed in the following sections. The objective is to understand the formation of vPM in the atmospheric chamber with the presence of soot (heterogeneous processes) depending on the fuel composition. A particular attention is given to the impact of sulphuric and aromatic contents. This part of the chapter presents in the same way as for section V.1 a comparison of the vPM formation in terms of size, mass and number concentrations and a comparative analysis of the chemical composition of the emissions. The fuels tested here are the Jet A-1 (reference fuel used in V.1), the Extreme Jet (23% of aromatic content and 3000 ppm of sulphur), the blend fuel called mix E5 (70% of Jet A-1 and 30% of AtJ) and the sustainable AtJ fuel (no aromatic and no sulphuric compounds). More details are available in II.1.1.2 concerning their composition. The experimental set-up, the CAST operating point (84/30/3) and the injection process (without soot filtration) remain identical to the ones presented at the beginning of this chapter (Figure V-1). Furthermore, the data representation is the same as before: photochemistry is indicated by yellow areas, data have been corrected for dilution and normalised by the respective CO_2 concentrations.

V.2.1 Emissions injection in the CESAM chamber for different fuels

For each test (4 fuels in 4 days), gases have been monitored after emissions injection and reported in Table V-4. The mass and number concentrations of particles for raw emissions injection (limit of detection of the instrument, i.e. no signal after gas injection) have been also indicated in Table V-5. A first injection of gas phase has been done (2 times for Extreme Jet case to get a comparable amount of CO_2 with Jet A-1 case) and then a second injection of raw emissions has been done (2 times for AtJ case to obtain enough soot particles compared to Jet A-1 case, at least 1 µg/m^3 of soot). To compare the different tests, a normalisation by CO_2 concentration is necessary as tests are not perfectly reproducible (some ppm of difference for CO_2 concentration).

Fuel test	Injection case	CO_2 (ppm)	Corresponding injection time	CO (ppb)	CO (per ppm/CO_2)	SO_2 (ppb)	SO_2 (per ppm/CO_2)	NO_x (ppb)	NO_x (per ppm/CO_2)
Jet A-1	After gas injection	53.67	8min	389.06	7.25	2.23	0.04	11.81	0.22
	After soot injection	59.36	15s	413.74	6.97	2.55	0.04	14.30	0.24
Extreme Jet	After gas injection	58.68	8min + 3min	431.71	7.36	27.7	0.47	12.91	0.22
	After soot injection	61.88	10s	449.59	7.27	28.96	0.47	14.85	0.24
Mix E5	After gas injection	56.32	8min	357.42	6.35	4.05	0.07	12.95	0.23
	After soot injection	61.66	15s	369.63	5.99	4.49	0.07	15.42	0.25
AtJ	After gas injection	47.24	8min	277.39	5.87	0.96	0.02	9.92	0.21
	After soot injection	77.55	10s + 2min	373.6	4.82	1.38	0.02	25.59	0.33

Table V-4: Comparison of gas concentrations injected in the CESAM chamber for 4 different fuels. For each case, the first injection corresponds to the gas phase with soot filtration and the second one to the raw emissions.

Fuel test	Injection case	CO_2 (ppm)	Injection time	Mass concentration		dN/dLog		GMD (nm)
				($\mu g/m^3$)	(per ppm of CO_2)	($1/cm^3$)	(per ppm of CO_2)	
Jet A-1	After soot injection	59.36	15s	18.55	0.31	$7.55x10^3$	127.19	110
Extreme Jet	After soot injection	61.88	10s	19.31	0.31	$6.36x10^3$	102.78	144
Mix E5	After soot injection	61.66	15s	3.10	0.05	$4.96x10^3$	80.44	65.1
AtJ	After soot injection	77.55	10s + 2min	4.42	0.06	$10.02x10^3$	129.21	59.9

Table V-5: Comparison of gas concentrations injected in the CESAM chamber for 4 different fuels. For each case, the gas and particle mass and number concentrations with soot GMD have been measured just after injection without lights (2min of stabilisation).

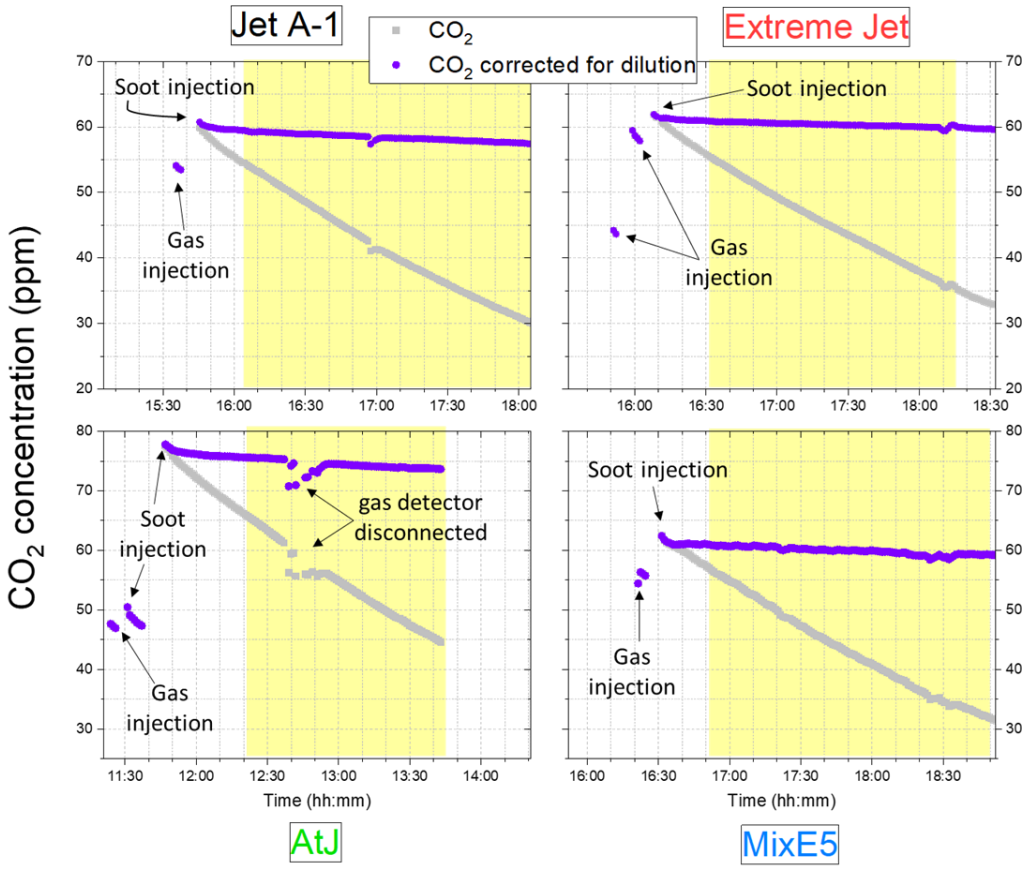

Figure V-21: CO_2 concentrations in CESAM chamber depending on the fuel used after raw emissions injection. Light activation is indicated by yellow areas. Raw CO_2 data are presented in grey and correction for dilution in purple.

CO_2 amounts introduced in the chamber are different depending on the tests (Figure V-21). Small variations for Jet A-1, Extreme Jet and MixE5 fuels (60.9 ± 1.4 ppm after second injection) can be explained by the absence of direct control of gas injection due to the under-pressure process. Furthermore, it can be noted a small decrease of the CO_2 concentration over time (from 1.5 to 3 ppm) due to wall losses not corrected for gas phase. For the AtJ case, the amount of CO_2 is 27% higher than for the other cases because two soot injections have been done to get enough of soot inside the CESAM

chamber. Indeed, CAST emissions have been injected for 10 sec (arbitrary time for the other fuel tests to get 60 ppm of CO_2). However, after this first soot injection, the CO_2 concentration (47.24 ppm) and the amount of soot (0.069 µg/m^3) were too small compared to the other tests. To obtain a comparable concentration in the chamber, a second injection of 2min has been done to obtain at least 1 µg/m^3 of soot. After this additional step, the mass concentration increases (4.42 µg/m^3) and more small particles are introduced in the chamber than for the other fuels. The AtJ case generates 129.21 part/cm^3 per ppm of CO_2 representing 25.7% more particles than for the Extreme Jet case, but the particle concentration remains comparable to the one of the Jet A-1 case (+1.6% after CO_2 normalisation).

Figure V-22 presents the variation of CO concentrations, centred on light activation, for the 4 fuels tested. Injections of gas and soot particles are specified on the graph for each case by dotted lines. A small decrease of the concentration can be noted over the time due to wall losses. Furthermore, fuels with higher amounts of sulphur and aromatic contents in their compositions generate higher amounts of CO (+4.3% for Extreme Jet case compared to Jet A-1 test).

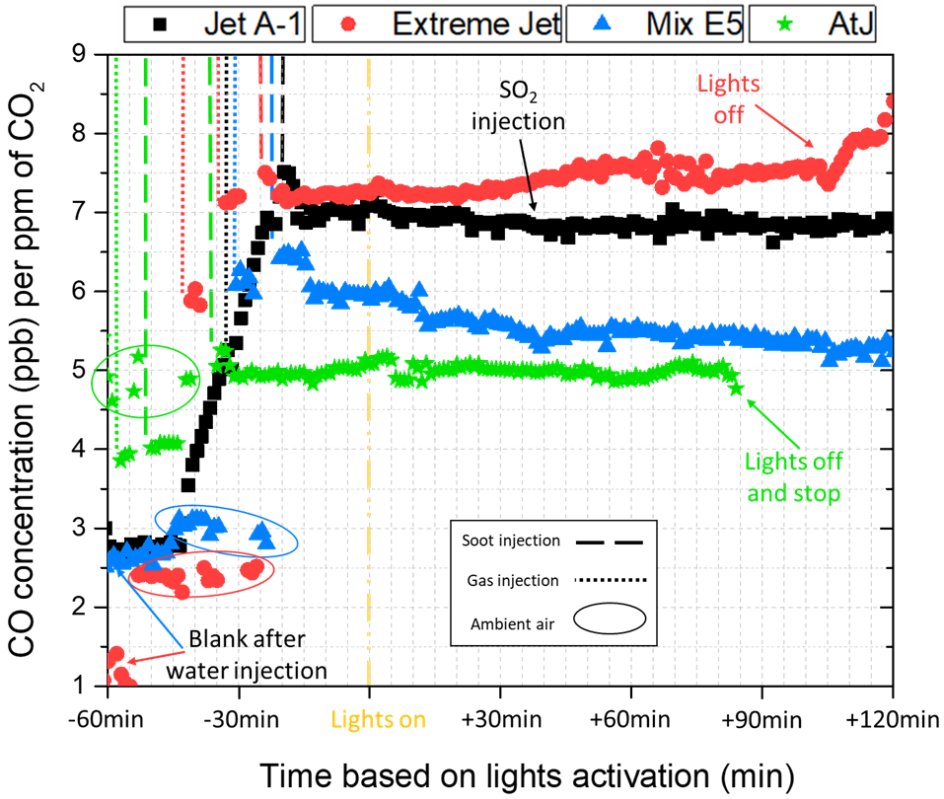

Figure V-22: CO concentrations in CESAM chamber for 4 fuels after raw emissions injection. Extreme Jet is represented in red, Jet A-1 in black, Mix E5 in blue and AtJ in green. Values have been corrected for dilution and normalised by CO_2. The representation is centred on light activation indicated in yellow and times of injection are specified by dotted lines.

The evolution of SO_2 concentration depending on fuel tested is represented on Figure V-23 (log scale and centred on light activation). It seems in general that fuels with higher amounts of sulphur in their compositions give higher SO_2 concentration after injection (10 times more for Extreme Jet than for the other fuels) except for the Jet A-1 case. As seen before, the reference fuel generates less CO than the blend fuel (Mix E5 = 70% Jet-A1 + 30% AtJ). After additional SO_2 injection, the trend is respected. After light activation, the concentration of SO_2 decreases over the time due to formation of sulphuric acid (cf. Figure V-27) and condensation on soot surface. It can be noted the presence of SO_2 after emissions injection in the case of AtJ fuel (0.02 ppb per ppm of CO_2 after injection and no variation of the concentration after light activation). This is due to a small contamination by sulphur coming from the injection line or the internal tubes in the CAST burner.

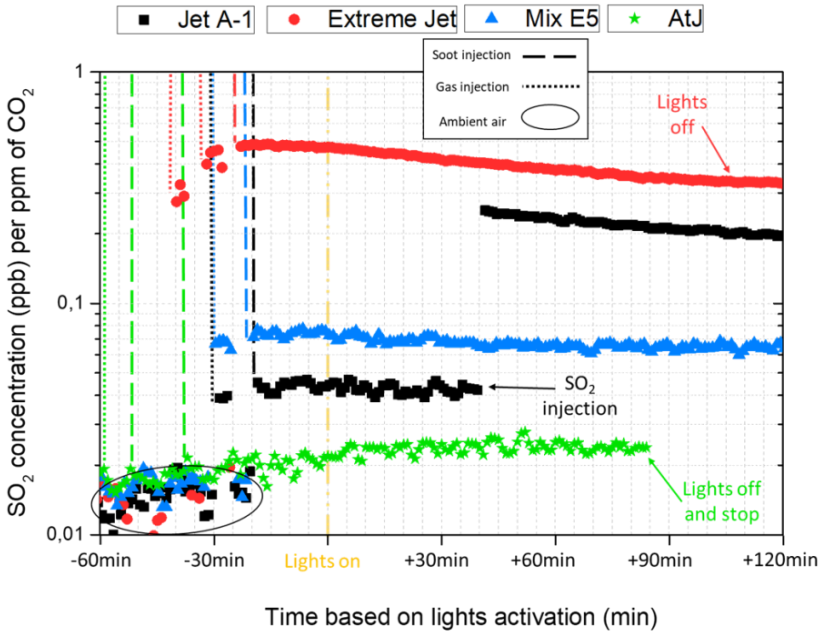

Figure V-23: SO_2 concentrations in CESAM chamber depending on the fuel used after raw emissions injection. Extreme Jet is represented in red, Jet A-1 in black, Mix E5 in blue and AtJ in green. Values have been corrected for dilution and normalised by CO_2. Light activation is indicated in yellow and times of injection are specified by dotted lines.

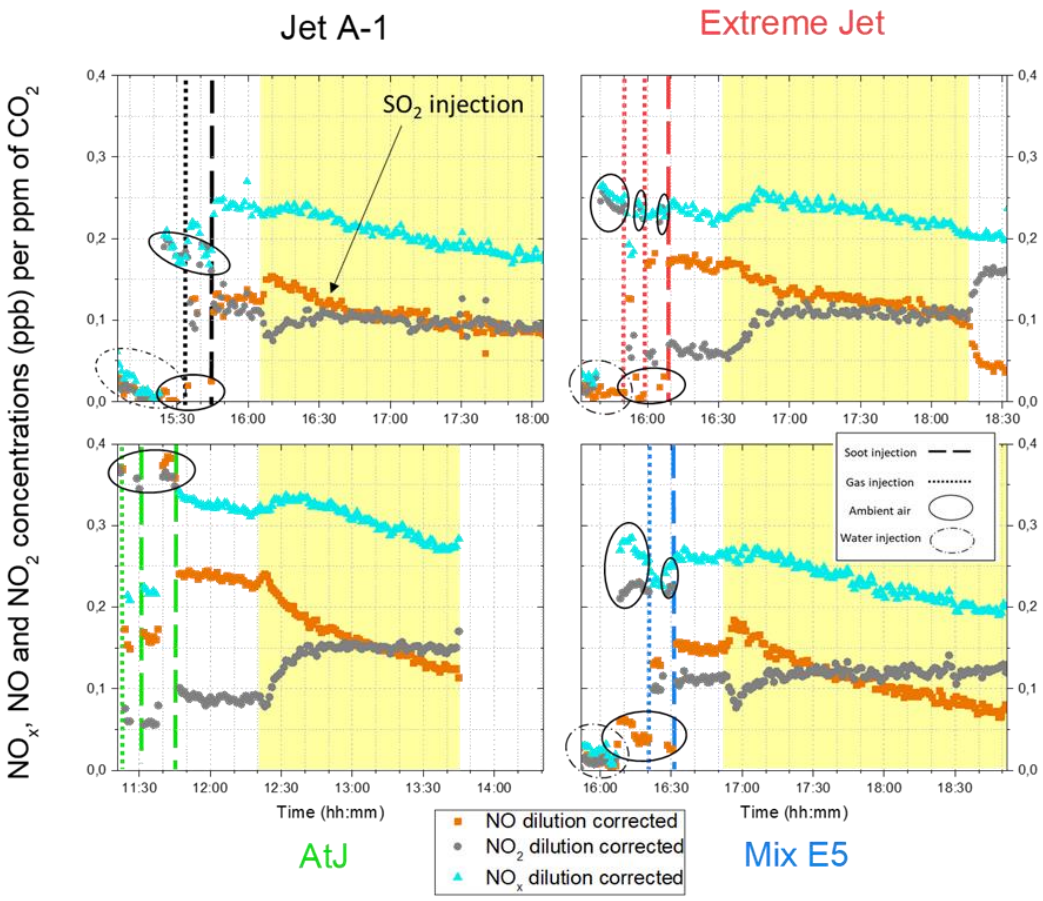

Figure V-24: NO_x concentrations in the CESAM chamber depending on the fuel used for raw emissions injection case. Values have been corrected for dilution and normalised by respective CO_2 concentrations (cf. values in Table V-4). Light activation is indicated in yellow. Injections of emissions are indicated by dotted lines.

Figure V-24 describes the evolution of NO, NO_2 and NO_x concentrations in the chamber over the time for all fuels tested. For all cases, the NO_x concentration is increasing right after light activation (conversion of NO in NO_2) : +0.012 ppb per ppm of CO_2 for Jet A-1, +0.034 ppb per ppm of CO_2 for Extreme, +0.026 ppb per ppm of CO_2 for AtJ and +0.014 ppb per ppm of CO_2 for Mix E5. Then with the decrease of NO concentration to form NO_2, the concentration of total NO_x is also decreasing (-0.06 ppb per ppm of CO_2). AtJ case presents a higher concentration of NO_x compared to the other fuels (more soot injected at the beginning of the experiment).

One can notice a change in the NO_2 and NO concentrations after light extinction in the chamber in particular for the Extreme Jet fuel case. Figure V-25 presents the evolution of NO, NO_2 and O_3 concentrations over the time (values have been corrected for dilution and normalised by CO_2 concentration). Just after the lights were switched off, the concentration of NO_2 increases remarkably (+0.053 ppb per ppm of CO_2) and the one of NO decreases fast (0.064 ppb per ppm of CO_2). The conversion of NO into NO_2 is the main reaction after light extinction. NO_2 is photolabile and is continuously dissociated to NO + O when the light is on, which makes ozone by subsequent O + O_2. When the lights are turned off, the steady state in the NO_2 (and O_3) photolysis system shuts down and the available NO is quickly converted to NO_2 by [O_3 + NO], [HO_2 + NO] and [RO_2 + NO] reactions. NO_2 also keeps converting to NO_3 with O_3. In the absence of light there are not many pathways to NO from NO_2 and NO_3.

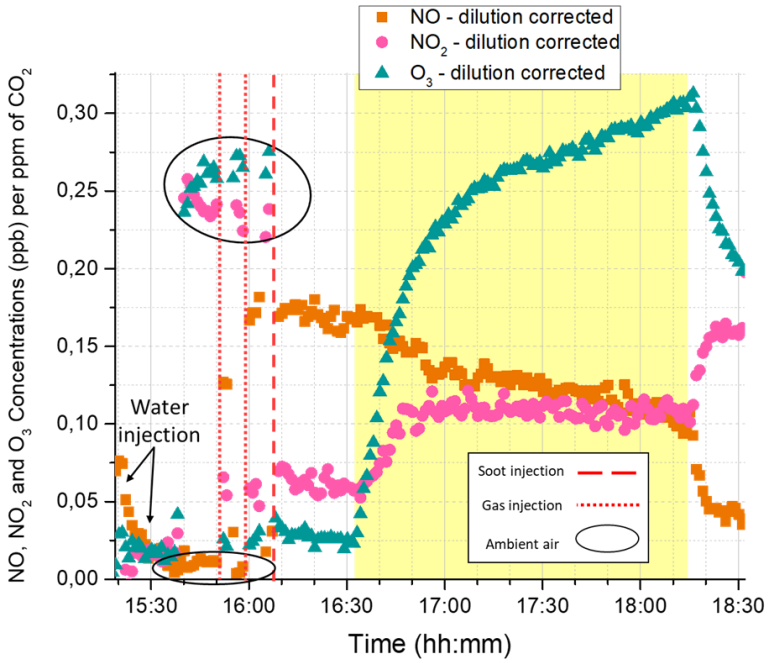

Figure V-25: Evolution of NO, NO_2 and O_3 concentrations inside the CESAM chamber after light extinction (end of yellow area) for Extreme Jet fuel after raw emissions injection. Values have been normalised by CO_2 concentration (59.36 ppm).

V.2.2 New particles formation for different fuels

V.2.2.1 vPM formation depending on fuel composition

After raw emissions injection, all instruments are reconnected to the chamber to monitor gas and to study nvPM evolution and vPM formation over the time. The lights are switched on 30min after the soot injection.

The evolution of the size and the particle concentration inside the CESAM chamber is represented on Figure V-26. For each fuel case, two representations are given: a first one focused on soot particles introduced in the chamber (from 20 to 800 nm using the LISA SMPS) and a second one focused on vPM formed in the chamber (from 4 to 109 nm using the nanoSMPS). The Jet A-1 fuel

experiment (case a.1 for soot and case a.2 for vPM) is compared to tests performed with Extreme Jet (case b.1 for soot and case b.2 for vPM), mix E5 (case c.1 for soot and case c.2 for vPM) and AtJ (case d.1 for soot and case d.2 for vPM). The particle concentration in the chamber is represented by the colour scale and is adapted for each representation to compare directly the results: from 0 to 10^4 part/cm^3 for soot particle graphs and from 0 to 5x10^5 part/cm^3 for vPM graphs. A one-by-one adapted scale representation can be found in Annex S to highlight the vPM particles recorded for each experiment.

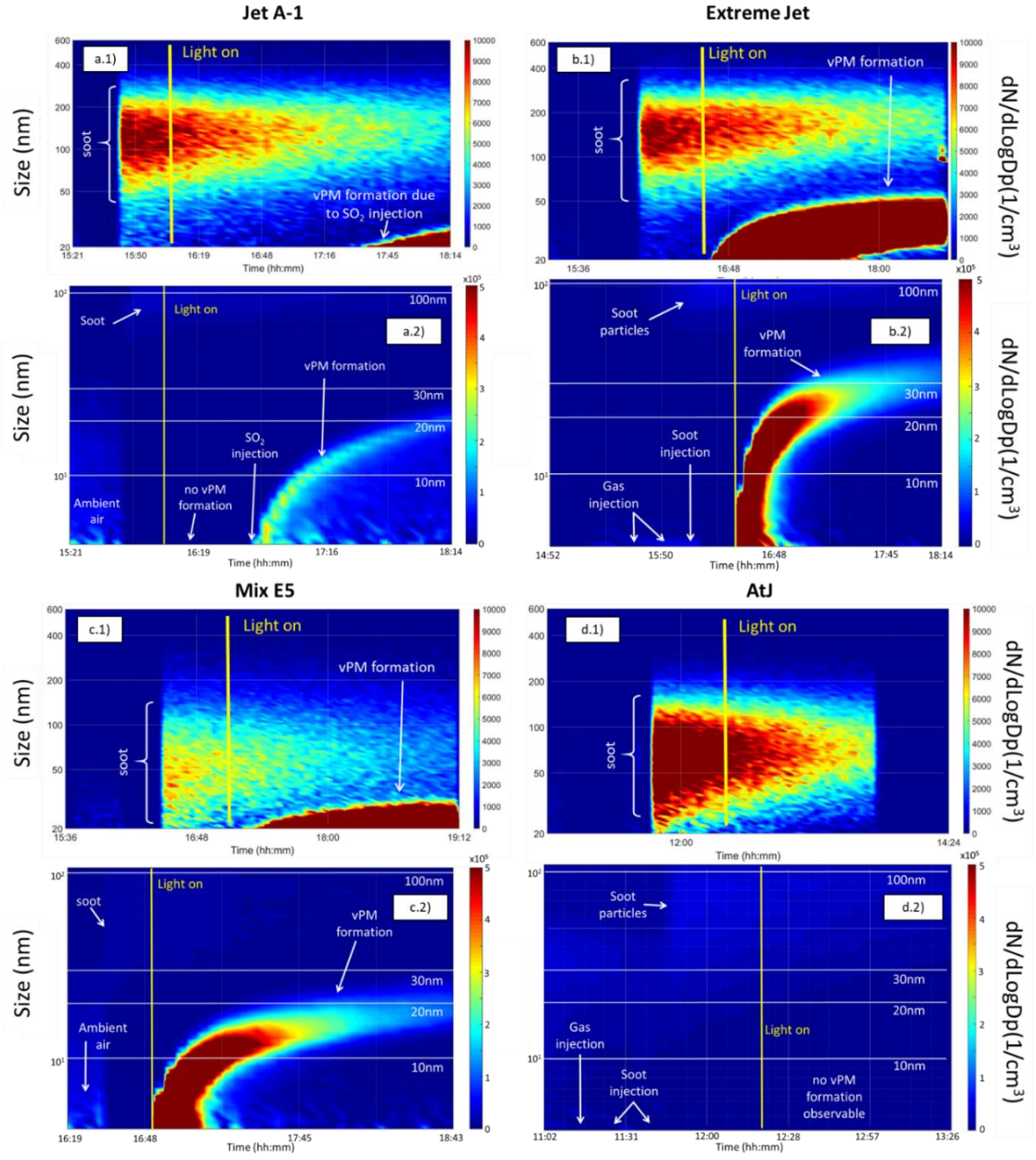

Figure V-26: Size and particle concentration comparison between 4 different fuels after raw emissions injections in CESAM chamber. The reference case is the Jet A-1 (case a.1 for vPM and case a.2 for soot particles). The other fuels are the Extreme Jet (case b.1 for vPM and case b.2 for soot particles), the mix E5 (case c.1 for vPM and case c.2 for soot particles) and the AtJ (case d.1 for vPM and case d.2 for soot particles). The concentration of particles (represented by the colour scale) has been set at 5x10^6 part/cm^3 for vPM representations and at 10^4 part/cm^3 to compare each case more simply.

On these graphs, only soot particles are visible at the beginning of the experiment (before light activation). The GMD of soot particles is 110.0 nm for the Jet A-1 case (Figure V-26.a.1), is 144.0 nm for the Extreme Jet (Figure V-26.b.1), is 65.1 nm for the Mix E5 (Figure V-26.c.1) and is 59.9 nm for the AtJ (Figure V-26.d.1). The first observation is that the Extreme Jet and Jet A-1 fuels generate larger soot particles compared to the blend and SAF fuels. This is in line with mass and number concentrations reported in Table V-4 and with results obtained in III.2.3. For Extreme Jet and Jet A-1 fuels, mass concentrations of soot particles injected are higher than for the two other cases by a factor of 6 and the smallest number concentration of soot particles recorded after injection corresponds to the Mix E5 case (less particles and smaller size). It can be noted that in the case of number concentration of soot particles this is the highest for the AtJ. It confirms that for this test many small particles have been injected, compared to Extreme Jet or Jet A-1 cases where soot particles were bigger but less numerous.

Directly after light activation, new particles are formed for 2 cases: the Extreme Jet (Figure V-26.b.2) and the Mix E5 (Figure V-26.c.2) fuels. For the Extreme Jet case, vPM are generated by homogeneous nucleation from the gaseous precursors despites the high amount of soot introduced. It can be explained by the presence of sulphur in its composition (3000 ppm). Concerning the Mix E5, with less sulphur in its composition, the explanation might be that less soot have been injected in the chamber (Table V-5), implying that homogeneous nucleation can overcome heterogeneous processes. Nevertheless it has to be noted that in the only gas injection case, Mix E5 fuel was found to form more particles than jet A-1 even having less sulphur content. The first observation is that vPM formation and growth is faster for Extreme Jet reaching 30 nm in 20min, compared to Mix E5 reaching 20 nm in 1h. At the end of the experiment, the maximum vPM size is 25.53nm for the Mix E5 and 45.06nm for the Extreme Jet. Furthermore, the number concentration of newly formed particles are significantly higher for these two fuels compared to Jet A-1 (case with SO_2 injection): 3 times more for Extreme Jet and 1.5 times more for Mix E5 after CO_2 normalisation.

For the AtJ case, no vPM formation has been observed either before or after light activation (cf. Annex T). It is exactly the same trend as for the Jet A-1 case before SO_2 injection. Indeed, a higher quantity of soot has been injected inside the chamber at the beginning of the test for these fuels compared to the Extreme Jet and the Mix E5 cases (cf. Table V-4). The homogeneous nucleation will be more affected by a higher soot amount (adsorption of gaseous precursors) and heterogeneous processes will be dominant, limiting the vPM formation in the AtJ case.

To explain the high amount of vPM formed in the chamber for Extreme Jet and Mix E5 fuels, concentrations of H_2SO_4 monitored for the four fuels are represented on Figure V-27. The graph is centred on the light activation step and data have been corrected for dilution and normalised by CO_2 concentration.

No sulphuric acid is present in the chamber before light activation but, directly after turning on the lamps, peaks of H_2SO_4 formation are observed for all cases. Then their concentrations decrease over the experiment corresponding to the conversion of H_2SO_4 into vPM and adsorption on soot, before being stabilised (stabilisation of the vPM size on Figure V-26). However, the amount of sulphuric acid formed is different depending on the test. It is linked to the fuel composition and the amount of sulphur content initially introduced in the chamber. Thus, higher amounts of H_2SO_4 are obtained for Extreme Jet fuel (1.94 mol/cm^3 per ppm of CO_2) and for Mix E5 fuel (0.93 mol/cm^3 per ppm of CO_2). For Jet A-1 (before SO_2 injection), few sulphuric acid molecules have been formed due to adsorption of gaseous precursors on soot particles (0.25 mol/cm^3 per ppm of CO_2). Concerning the AtJ, there is no sulphur in the fuel composition so value obtained is expected (0.07 mol/cm^3 per ppm of CO_2). The concentration of SO_2 is too low/not existent in these both cases to lead to the formation of H_2SO_4 and then to the formation of vPM. The addition of sulphur dioxide in the chamber for the Jet A-1 contributes to the formation of more sulphuric acid, enough to allow homogeneous nucleation even in the presence of soot. The peak of sulphuric acid obtained for Jet A-1 after SO_2 doping is comparable to the one obtained for Mix E5. After stabilisation, new amount of sulphuric acid obtained for Jet A-1 is comparable to the one of Extreme Jet case (a difference of 0.07 mol/cm^3 per ppm of CO_2).

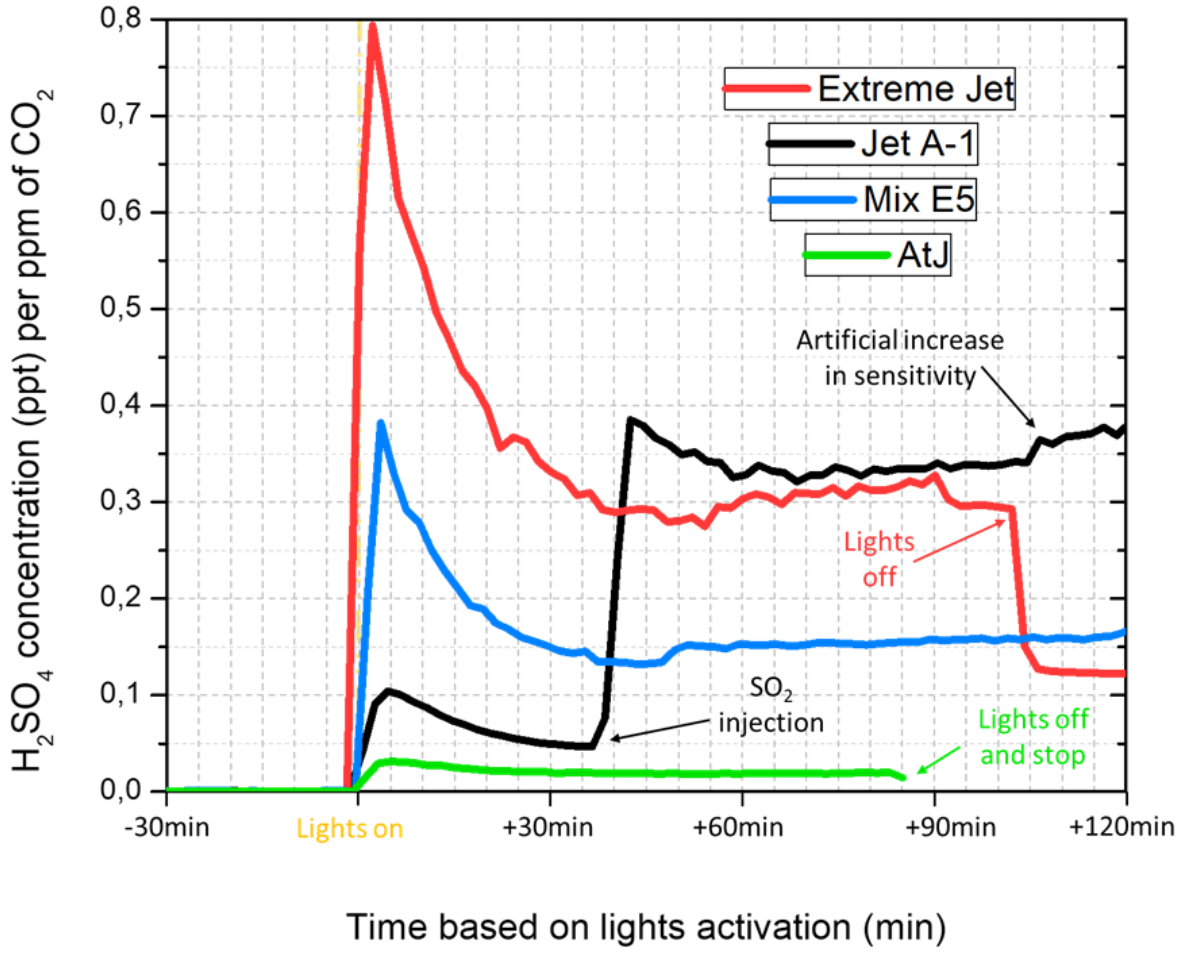

Figure V-27: H_2SO_4 concentrations in CESAM chamber depending on the fuel used after raw emissions injection. The representation is centred on light activation indicated in yellow. Data have been corrected for dilution and normalised by respective CO_2 concentration. Conversion: data in ppt x 2.46.10^7 gives data in mol/cm^3.

The concentrations of total organic compounds for the four cases studied after raw emissions injection are presented on Figure V-28. Organics recorded correspond to the ones adsorbed on soot surface (it is reminded the limit of detection of the instrument at 40 nm). Data were corrected for dilution and normalised by respective CO_2 concentration.

Organic compounds are introduced in the chamber with soot injection and then for all cases they are oxidised by light activation, making it easier to condense them on soot particles (increase of soot GMD – cf. V.2.2.2). The same conclusion as before can be made: fuels with higher aromatic contents in their compositions generate more organics. It is the case for the Extreme Jet fuel: 0.09 µg/m^3 per ppm of CO_2 for organics injected (2 times more than Jet A-1 case) and +0.04 µg/m^3 per ppm of CO_2 for organics formed (2.5 times more than for Jet A-1 test). Less organics have been obtained for AtJ (0.01 µg/m^3 per ppm of CO_2 for organics injected and +0.002 µg/m^3 per ppm of CO_2 for organics formed) and for Mix E5 (0.018 µg/m^3 per ppm of CO_2 for organics injected and +0.006 µg/m^3 per ppm of CO_2 for organics formed). Extra details about organic fragments concentration are presented in Annex U.

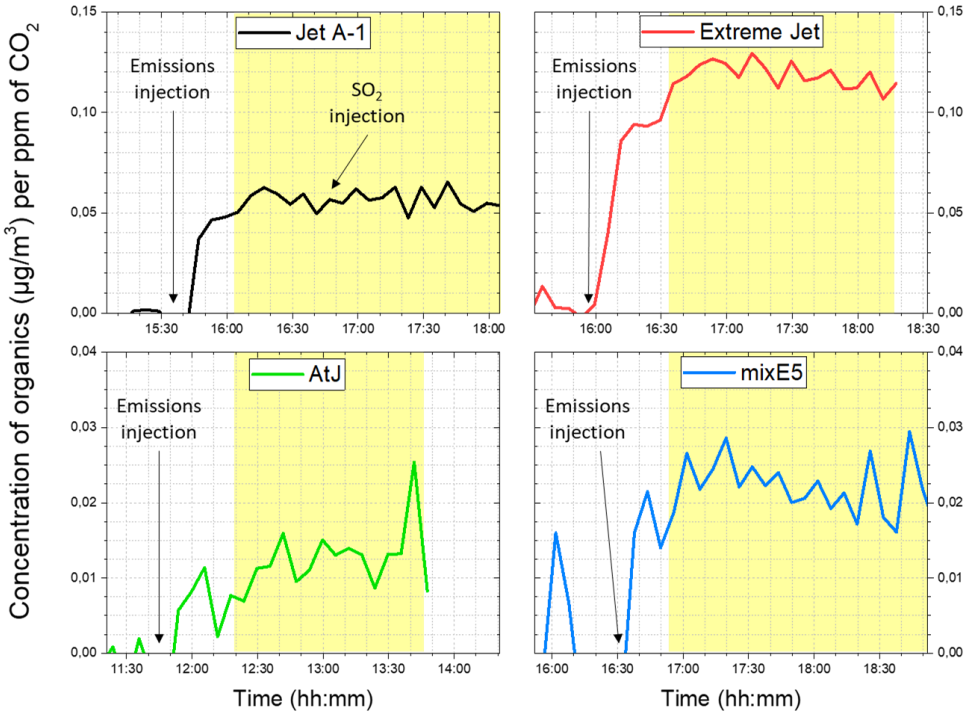

Figure V-28: Organic concentrations in CESAM chamber depending on the fuel used after raw emissions injection. Values have been corrected for dilution and normalised by CO_2 concentrations. Light activation is indicated by yellow areas.

To complete these previous observations, the evolution over the time of the particle number and mass concentrations in the CESAM chamber is presented on Figure V-29 for the different fuels tested. Values have been corrected for dilution and wall losses and have been normalised by their respective CO_2 concentrations.

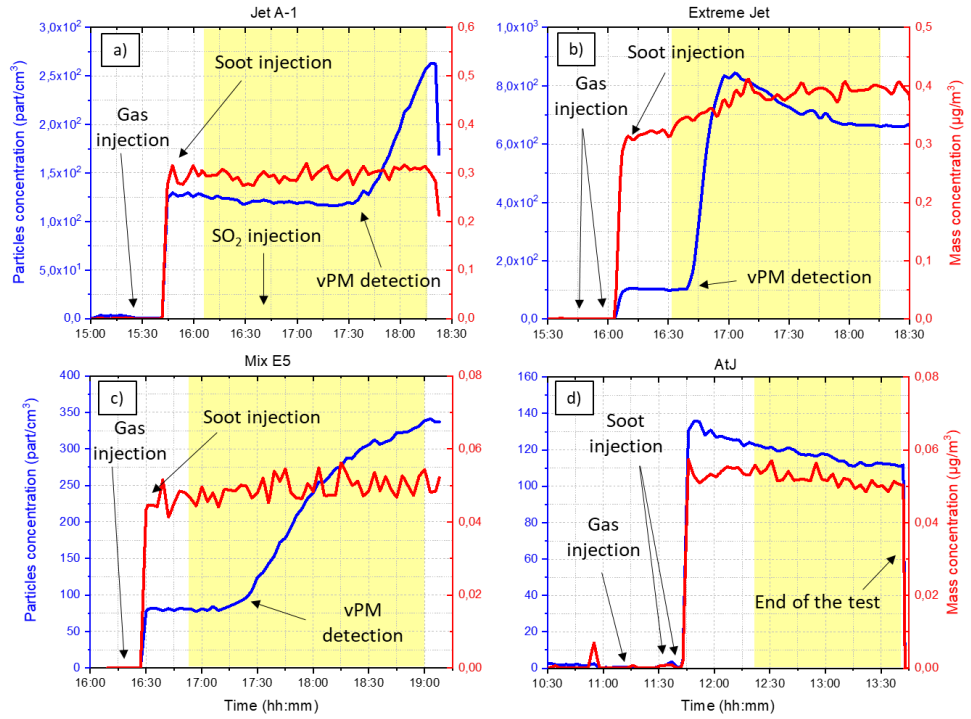

Figure V-29: Number (in blue) and mass (in red) concentrations of particles for different fuels after raw emissions injection in the CESAM chamber (LISA SMPS – limit of detection at 20nm). Light activation corresponds to the yellow area. All values

have been corrected for dilution and wall losses and have been normalised by the respective CO_2 concentrations. It should be noted that there is a delay between light activation and the increase of particle concentration corresponding to vPM formation due to the limit of detection of the instrument (only particles above 20nm).

Number and mass concentrations measured before light activation correspond to the amount of soot particles introduced in the chamber. For all cases, the number concentration decreases due to agglomeration of soot particles but the mass remains constant: for example -2 part/cm^3 per ppm of CO_2 for Extreme Jet and Mix E5 fuels and -8 part/cm^3 per ppm of CO_2 for Jet A-1 and AtJ cases 20min after raw emissions injection.

After light activation, the mass concentration increases due to the formation of new particles for Extreme Jet (from 0.315 ± 0.003 µg/m^3 to 0.396 ± 0.01 µg/m^3 per ppm of CO_2) and for Mix E5 (Figure V-29.b and Figure V-29.c, respectively). This trend is similar to the one observed for Jet A-1 (Figure V-29.a and V.1.2 for details) after SO_2 injection. It can be noticed that more particles are generated for Extreme Jet than for the other cases for a given time: the particle concentration increases from 103.59 part/cm^3 per ppm of CO_2 to 841.95 part/cm^3 per ppm of CO_2 in 30min (8 fold increase). For Mix E5, the number of particles increases from 81.58 part/cm^3 per ppm of CO_2 to 338.96 part/cm^3 per ppm of CO_2 in 2h (4 fold increase). It means that for raw emissions injection and after light activation, the Extreme Jet case generates twice more particles in 4x less time than for the Mix E5 case and 4x more particles in 2x less time than for the Jet A-1 case. Concerning the AtJ case, the concentration number of particles decreases (due to agglomeration and coagulation) with time and no vPM formation has been detected even after light activation. Homogeneous nucleation process is minimised by adsorption of gas phase and new vPM formed on soot surface (more nvPM introduced for this test at the beginning of the experiment than for the other fuels).

After the peak of number concentration obtained due to detection of particles formed, the number concentration decreases over time by agglomeration (-182 part/cm^3 per ppm of CO_2 for the Extreme Jet case) and the mass concentration remains constant. vPM formation is slowed down and heterogeneous processes take the lead. A similar trend is observed for Mix E5 fuel but less pronounced (increases of mass concentration from 0.045 ± 0.003 µg/m^3 to 0.05 ± 0.003 µg/m^3 before stagnation). The experiment was stopped for Mix E5 once the concentration of particles had reached a maximum at 341 part/cm^3 per ppm of CO_2.

A study of the soot and vPM sizes is proposed in the next section to estimate the impact of vPM adsorption on soot surface for raw emissions injection tests.

V.2.2.2 Size of soot and vPM particles in the CESAM chamber

To complete previous observations, GMDs of vPM and soot particles are calculated for the different fuels tested. The objective is to verify that soot size increases for all cases due to adsorption of vPM and gas precursors on the particle surface (in particular for AtJ case).

The total GMD obtained for each case takes into account all particles present in the chamber (soot and vPM). As seen before, it can be a problem to estimate correctly the size of the vPM. Based on the same process as described in V.1.3, size distributions (bimodal) have been fitted for each fuel by separating the soot GMD (LISA SMPS) from the vPM GMD (nanoSMPS) in calculations. The Jet A-1 case has been already studied in the previous part of this chapter (cf. V.1.3). For Extreme Jet and Mix E5, the vPM GMD and the soot GMD have been obtained after a fit of the corresponding size distributions. Concerning the AtJ, as there is no vPM formed, only one fitted mode for soot GMD is needed (no size distribution corresponding to vPM formation). Results are summarised in Figure V-30 for the four tests. The soot GMD are represented in red and the vPM GMDs are represented in green. Concerning the Jet A-1 case, vPM mode corresponds to the new particles formed after SO_2 injection.

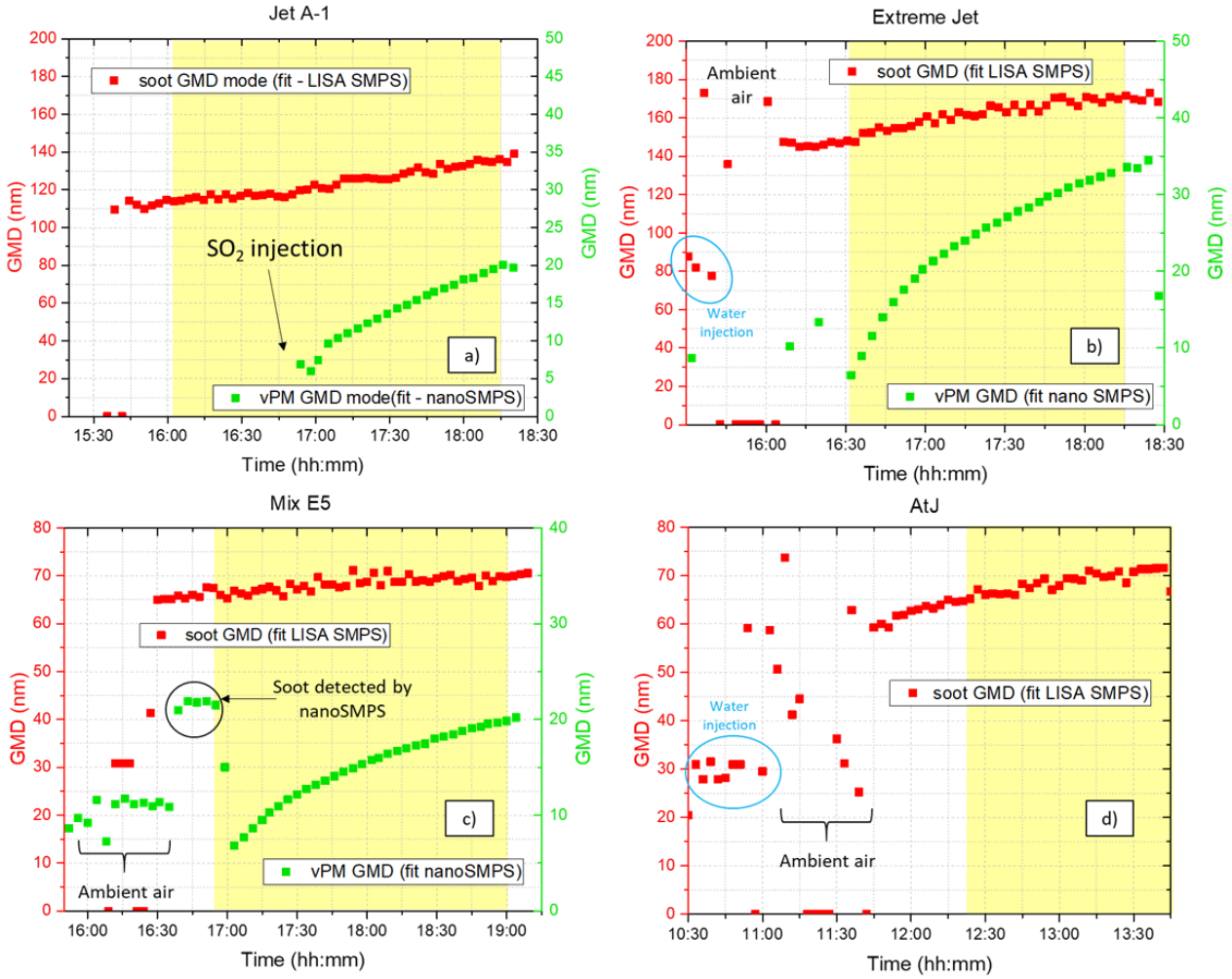

Figure V-30: Comparison of soot GMD and vPM GMD for different fuels after raw emissions injection in the CESAM chamber. Soot particle GMDs are fitted using LISA SMPS data and vPM GMDs are fitted using nanoSMPS data. The yellow area corresponds to the light activation.

The first observation is that the GMD of soot particles increases for all cases. Values of GMD at the beginning and at the end of the experiment have been summarised in Table V-6. For Jet A-1 (with sulphur doping) and Extreme Jet, larger particles have been injected at the beginning of the test compared to the other fuels. At the end, soot particles for Extreme Jet present a much larger diameter compared to Jet A-1 (+27%). The soot particle size increases by 23.6% for the Jet A-1 case, by 20.1% for the Extreme Jet, by 19.3% for the AtJ and only by 8.3% for the Mix E5 from the start (injection) to the end.

Concerning the GMD of vPM formed, the Extreme Jet case gives larger new particles with a final GMD at 34.47nm, which is 1.7 times more than for the Jet A-1 or the Mix E5 cases (respectively 20 and 20.02nm). The formation of vPM can be linked to the variation of the soot GMD. Indeed, for the Extreme Jet and the Mix E5, the soot size increases more after light activation. It corresponds to the onset of the vPM formation process meaning that new particles are adsorbed on soot surface:

- +5.5% increase in soot size before lights on and +13.8% after lights on for the Extreme Jet;
- +2.9% increase in soot size before lights on and +5.2% after lights on for the Mix E5;
- +10.9% increase in soot size before lights on and +11.5% after lights on for the Jet A-1.

For the Jet A-1 case, no vPM are formed because gaseous precursors are adsorbed on soot surface. In this case, the increase of the soot GMD before lights on (+10.9%) is comparable to the AtJ case (+11.8% increase in soot size). It is linked to the high amount of soot particles injected at the beginning (Table V-4) compared to the Extreme Jet and Mix E5 cases. However, as there is no vPM for the AtJ fuel, the growth rate of soot size decreases with time (+6.7% after lights). This means that there are no more organics or vPM formed in the chamber, contributing to the growth of soot.

It should be also noted that the GMD increases faster for the Extreme Jet than for the two other fuels presenting vPM formation.

Fuels	GMD of soot particles (nm)			GMD of vPM formed (nm)	
	At the start	Lights on	At the end	Lights on	At the end
Jet A-1	110	122 (SO_2 injection)	136	7.4 (SO_2 injection)	20
Extreme Jet	144	152	173	6.4	34.47
Mix E5	65.1	67	70.5	6.8	20.2
AtJ	59.9	67	71.5		

Table V-6: GMD of soot particles and vPM formed inside the CESAM chamber for four different fuels after raw emissions injection. For the Jet A-1 case, the reference is the SO_2 injection and not the light activation.

The growth rate (GR) of the vPM formed (in nm/h) for the different fuels tested have been calculated from vPM GMD and expressed as a function of the sulphuric acid concentration. Figure V-31 regroups the GR obtained for the different raw emissions injection tests performed: with a black square for Jet A-1 case, with a dark-red circle for Extreme Jet case and with a purple triangle for Mix E5 case (no signal for AtJ as there is no vPM formed).

First of all, Jet A-1 point is in a lower enhancement factor line and its GR is small. It mainly means that the amount of condensable compounds in this case is smaller compared to the other tests. Among the three fuels, this case was the one with the highest number of soot particles, so this can be at least one part of the explanation. What is key here is that Extreme Jet, with a similar concentration of sulphuric acid, reaches GR much larger. This means that more condensable vapours are available other than H_2SO_4. Soot concentrations are not too different, so it cannot explain the difference and it probably comes from condensable vapours generated by Extreme Jet. Mix E5 is in a similar enhancement line (with a collision enhancement factor of 2.7) to the Extreme Jet, or even slightly higher, but here the soot amount is lower so this might explain the small difference. Since all of the results obtained for the different fuels tested are out of the red points, that means that the growth is not only sulphuric acid, most likely in this case is linked to organics in the combustion gases.

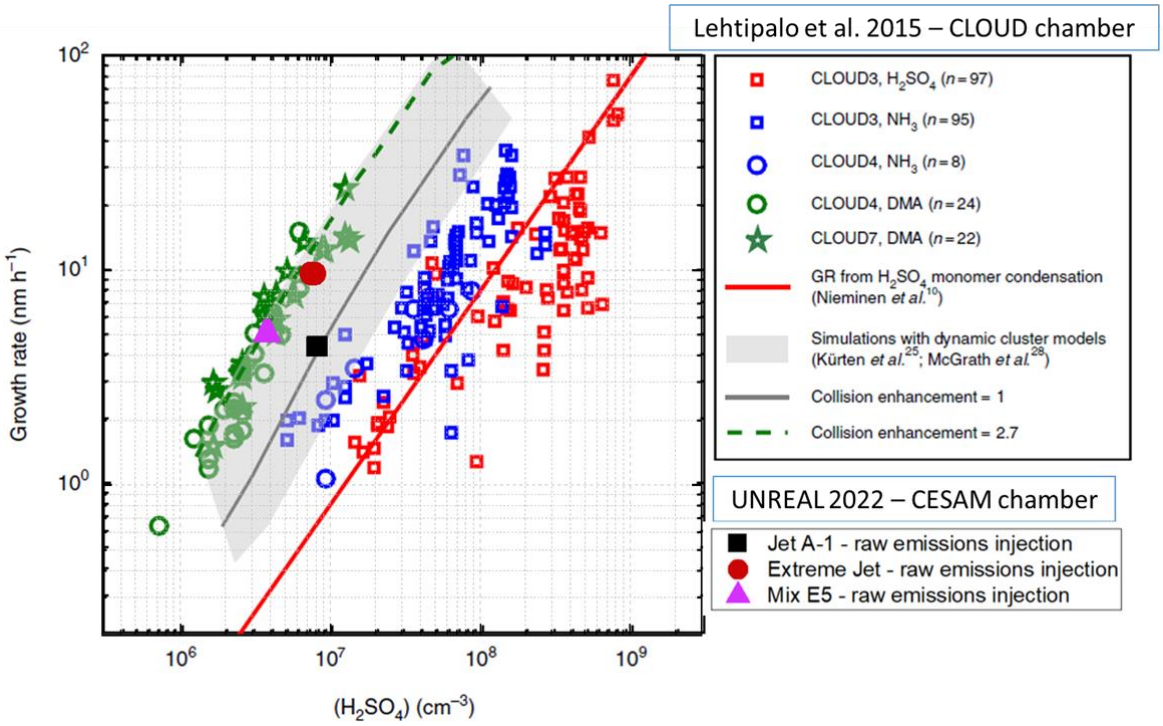

Figure V-31: Comparison of the growth rate calculated for vPM formed after raw emissions injection using four fuels with growth rates calculated in different systems by Lehtipalo et al. (2016). The data corresponding to the UNREAL project for vPM formation within the CESAM chamber (ambient temperature and pressure, RH=38%) are indicated in black for Jet A-1, in dark- red for Extreme Jet and in purple for Mix E5. Data related to Lehtipalo et al. (2016) corresponds to experiments done in the CLOUD chamber. Growth rates of 2 nm particles are determined with the appearance time method between 1.5 and 2.5 nm as a function of the measured sulphuric acid (H_2SO_4) concentration with different amounts of ammonia (NH_3) and dimethylamine (DMA) in the chamber. More details in I.3.2.5.

V.2.3 Comparison of homogeneous nucleation process depending on emissions injection for an extreme case

V.2.3.1 vPM formation for Extreme Jet fuel with and without soot particles

A comparison between tests performed with and without soot injection for the Extreme Jet fuel is proposed in this section. A first approach has already been done for the reference Jet A-1 fuel (V.1.6) but in this case, sulphur dioxide doping initiated the vPM formation. As seen in the previous section, Extreme Jet fuel leads to the formation of new particles inside the CESAM chamber even with the presence of soot particles and without additional injection of SO_2 (cf. V.2.2.1). This fuel is a good candidate with the higher amount of aromatics (23%) and higher amount of sulphur content (3000 ppm) allowed by certification, to compare the formation of vPM from gaseous precursors by homogeneous nucleation depending on the emissions introduced in the atmospheric chamber: only gas phase or raw emissions injection.

Figure V-32 presents the evolution of particle sizes (x-axis) and their number concentrations (y-axis) in the CESAM chamber depending on the injection case for the Extreme Jet fuel. The gas phase injection test is done in the morning and the raw emission injection test is done in the afternoon. The case a) corresponds to the particles detected between 4 and 109 nm, i.e. for vPM detection (nanoSMPS), and the case b) corresponds to the particles detected between 20 and 800 nm, i.e. for soot monitoring (LISA SMPS). The particle concentration scale is set from 0 to $5x10^5$ part/cm^3.

The first observation (Figure V-32.a) concerns the size of particles formed after light activation in the chamber. The gas phase injection case leads to formation of bigger vPM (reaching at the end of the test 66.95 nm) compared to the raw emissions injection case (limitation on growth: 46.02 nm). It is explained by the presence of soot particles in the second test (Figure V-32.b) and by the adsorption of gaseous precursors and H_2SO_4 molecules on their surface (cf.V.2.2.1).

Concerning the particle concentration, the gas phase injection case generates more vPM (Figure V-32.b). To get a better comparison, maximum concentration values for each size under 10 nm are reported in Table V-7 for both injection cases. Results have been normalised by CO_2 concentrations. It confirms that the case without soot leads to the formation of more particles directly after light activation at small sizes than for the case with soot (3 times more at 4.2 nm). The difference of vPM amount formed is halved for higher sizes (only 1.6 times more at 10.07 nm).

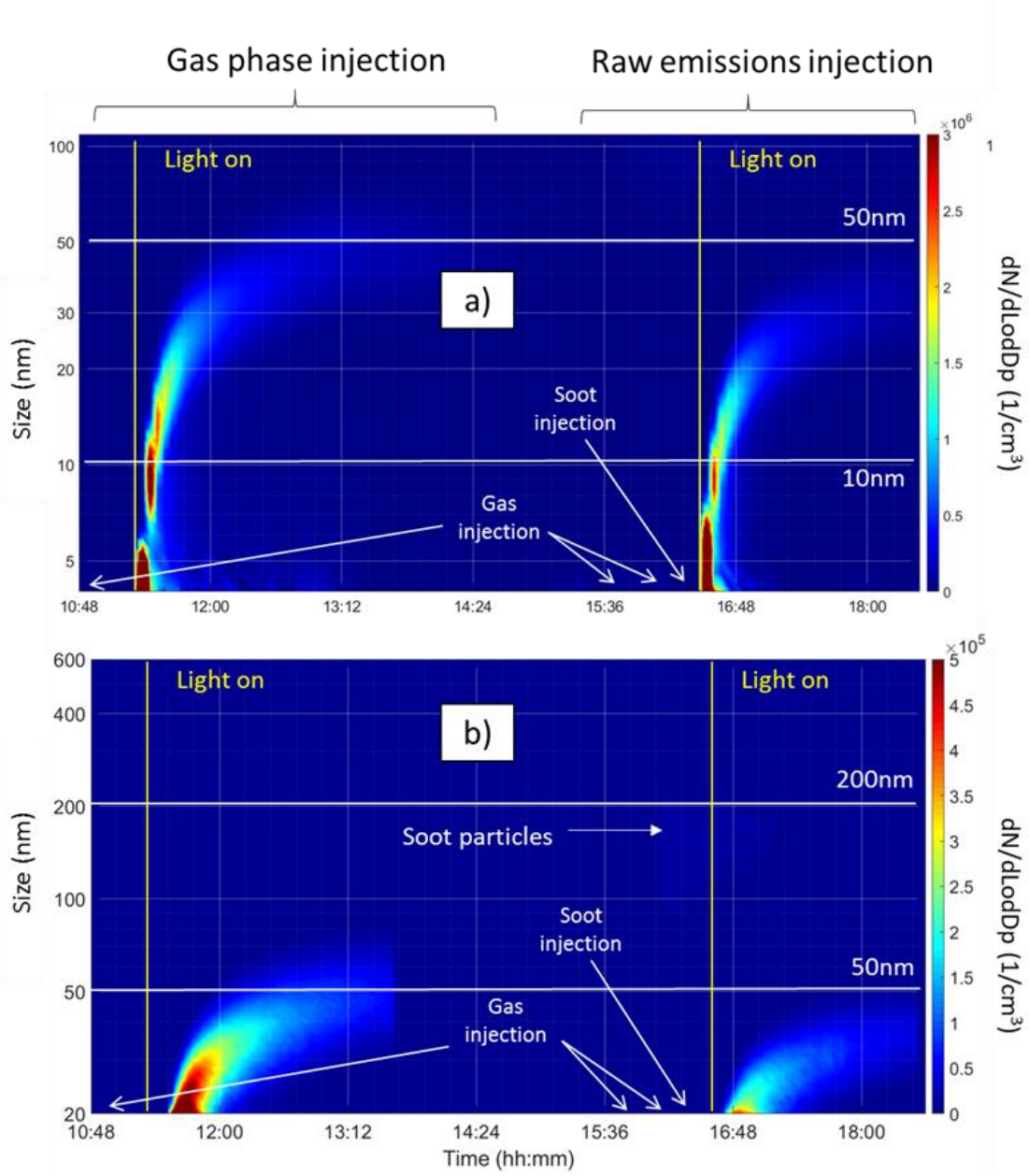

Figure V-32: Comparison of vPM size and particle concentrations for two injection tests: gas phase injection (morning) and raw emissions injection (afternoon) for Extreme Jet case. a) Particles detected between 4 and 109 nm (nanoSMPS); b) particles detected between 20 and 800 nm (LISA SMPS). The colour scale representing the particle concentration is set at maximum 5x10⁵ part/cm³.

Size (nm)	Homogeneous nucleation		Homogeneous and heterogeneous nucleation	
	Particles concentration x10^6 (1/cm^3)	Correction by CO_2 x10^4 (1/cm^3)	Particles concentration x10^6 (1/cm^3)	Correction by CO_2 x10^4 (1/cm^3)
4.2	18	32.39	6.72	10.86
4.59	12.7	22.85	6.18	9.99
5.0	6.54	11.77	5.93	9.58
5.46	2.57	4.62	6.09	9.84
5.96	1.01	1.82	4.92	7.95
6.5	1.29	2.32	3.37	5.45
7.09	2.28	4.10	1.72	2.78
7.74	3.24	5.83	2.15	3.47
8.45	3.9	7.02	2.77	4.48
9.22	4.12	7.41	2.82	4.56
10.07	3.73	6.71	2.55	4.12

Table V-7: Number concentration of vPM formed for both nucleation cases as function of size. The fuel is Extreme Jet and the values are normalised by CO2 monitored during the injection (respectively 55.57ppm and 61.88ppm).

To complete this analysis, a representation of the number (in blue) and mass (in red) concentrations is given on Figure V-33 depending on the injection process: gas phase case on the left and raw emissions case on the right.

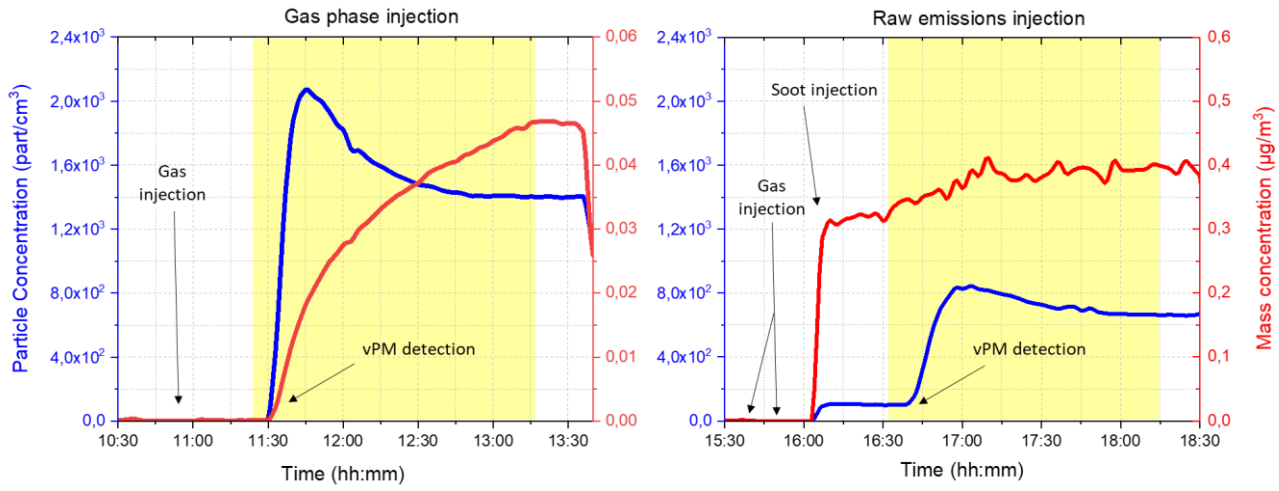

Figure V-33: Comparison of the particle number (in blue) and mass (in red) concentrations for Extreme Jet fuel after gas phase injection (left) and raw emissions injection (right). The delay between light activation and vPM formation is due to the limit of detection of the instrument (20 nm). Light activation is represented by yellow areas. Data have been corrected from dilution and wall losses and normalised by CO_2 concentration.

Before light activation, no particles are detected for the gas phase injection. For the raw emissions case, 104.71 part/cm^3 (0.31 µg/m^3 per ppm of CO_2) of soot is introduced in the chamber . Then, for both cases, the formation of vPM starts with the activation of the lights. For raw emissions injection, the mass concentration of particles introduced in the chamber increases to 0.40 µg/m^3 with light activation and the number concentration increases to 843.56 part/cm^3 in 22min. For the gas phase injection case, the particle concentration increases from 0 to 2.07x10^3 part/cm^3 in 16min and the mass concentration increases from 0 to 0.047 µg/m^3. It confirms that homogeneous case is favoured with the absence of soot particles and more vPM are generated in a faster way.

With time, particle concentration decreases (due to agglomeration) but mass concentration is still increasing. For the case without soot, particle concentration is reduced by 33% but the mass concentration is nearly duplicated (from 0.024 µg/m^3 to 0.046 µg/m^3). For the case with soot particles, as seen previously (V.2.2.1), the particle concentration has decreased by 12% and the mass concentration has barely changed (+1µg/m^3).

To complete the previous observations, Figure V-34 presents a study of the chemical composition of the particulate phase (ACSM – centred on light activation). Organic compounds, OOA fragments, ammonium and SO_4 concentrations have been corrected for dilution and normalised by CO_2 concentration to be compared. Gas phase injection case is represented in orange and the raw emissions injection case is represented in blue. As the limit of detection of the instrument is 40nm, the signal monitored for the case without soot is low compared to the signal obtained for the case with soot particles.

Before light activation, only organics (oxygenated OOA and hydrogenated HOA) have been detected in the chamber for raw emissions injection. But after light activation, the concentrations of organics, SO_4 and NH_4 increase for both cases. For the test with soot injection, the concentration of organics is quickly stabilised at 0.12 µg/m^3 per ppm of CO_2 in 10min and at 0.20 counts in 40min for OOA fragments. For SO_4 and NH_4, the concentrations increase until the end of the experiment. Due to the adsorption of organics, sulphate and ammonium on soot particles, it is possible to record them but it is not comparable directly to the gas phase injection case, where particles are not detected by the ACSM. At least sulphate concentration is 2.77 times higher for the raw emissions case at the end of the tests compared to the gas phase injection case.

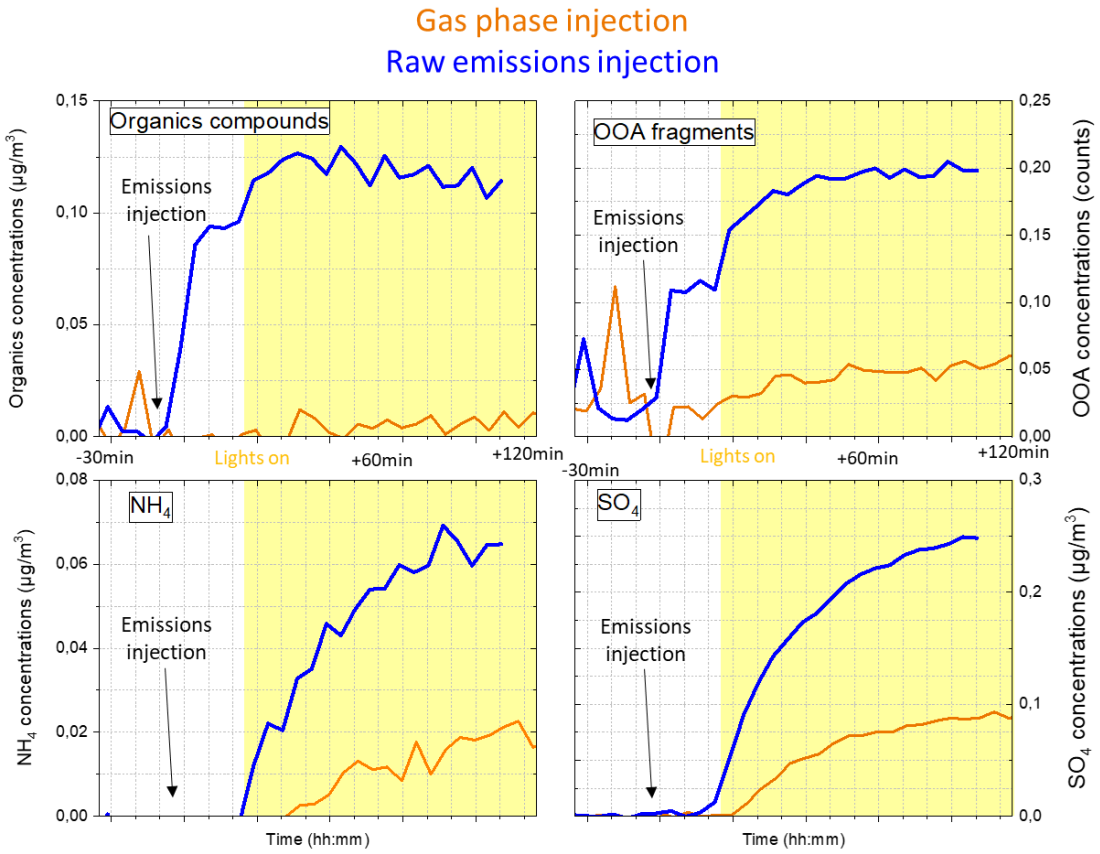

Figure V-34: Comparison of Organics, sulphate and nitrate concentrations (ACSM) for gas phase (orange) and raw emissions (blue) injection in the case of Extreme Jet fuel. Light activation is indicated by yellow areas. Data were corrected for dilution and normalised by CO_2 concentration.

V.2.3.2 GMD and growth rate for Extreme Jet fuel depending on injection case

Figure V-35 summarises the fitted GMDs for soot (in red), for vPM corresponding to the raw emissions injection (in green) and for vPM corresponding to the gas phase injection (in blue). Details of the GMD calculation are presented in Annex W.

To compare the two injection cases, the synchronisation of the vPM formation start has been adjusted on the time of light activation. Size of soot particles increases before light activation due to condensation of gaseous precursors and organics and thereafter due to agglomeration of newly vPM formed on their surface. For vPM, the GMD is larger for the gas phase injection case (45.47 nm) compared to the raw emissions injection case (34.42 nm) at the end of the experiment. The GMD analysis confirms that soot presence impacts vPM formation by limiting the increase of vPM GMD.

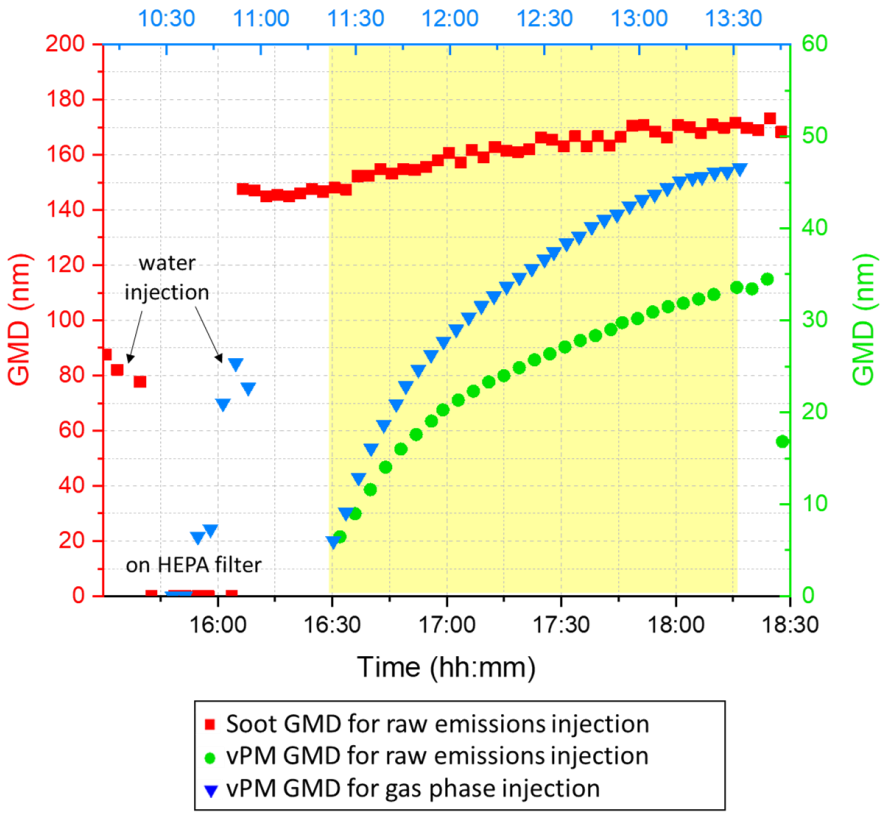

Figure V-35: GMD comparison depending on the nucleation process for the Extreme jet fuel. Lamps activation corresponds to the yellow area.

In addition, the growth rate (GR in nm/h) of the formed vPM for the both tests has been calculated using the same procedure as presented in IV.3.4 (more details in I.6.2.5). Results obtained show that GR for both points seems to be in the same or really similar lines in terms of growth enhancement (with factor of 2.7), implying that the amount of condensable vapours should be similar. It can be expected that the GR for the raw emissions test has a lower enhancement factor. One potential explanation can be found on Figure V-33. In the gas phase injection case, as there was no soot particles present that can act as condensation sinks, there was a large amount of sulphuric acid present, leading to a burst of particles. These particles act as a condensation sink for precursors. So finally the fact that there is no soot is compensated with this burst of vPM.

V.2.4 Generalisation of vPM formation process by homogeneous nucleation depending on experimental conditions

V.2.4.1 Particle concentration

Figure V-36 presents the particle concentration (same scale) for gas phase injection (left) and for raw emissions injection (right) depending on the fuel tested. Comparison is done before and after light activation, and at the end of the test.

For raw emissions injection, soot was introduced in the chamber at the beginning of the test explaining the higher particle concentration measured compared to the gas phase injection case. After the light activation, the particle number increases more for the gas phase case due to the higher amount of vPM formed in the chamber. At the end of the test, the particle concentration is 2.8 times higher for Extreme Jet gas phase injection and 1.6 times more for Mix E5 gas phase injection.

It can be noted also that Mix E5 case generates more particles than Jet A-1 for gas phase injection (after lights and at the end of the test) and for raw emissions injection (only at the end due to limit of detection of the instrument). For the first case, more SO_2 has been injected in the chamber (IV.3.1) for the Mix E5 fuel. For the second case, in addition of higher amount of SO_2 introduced in the chamber, there is as well a higher amount of soot introduced for Jet A-1 case compared to the blend fuel test, implying that more gas precursors have condensed on soot surface and less vPM have been formed.

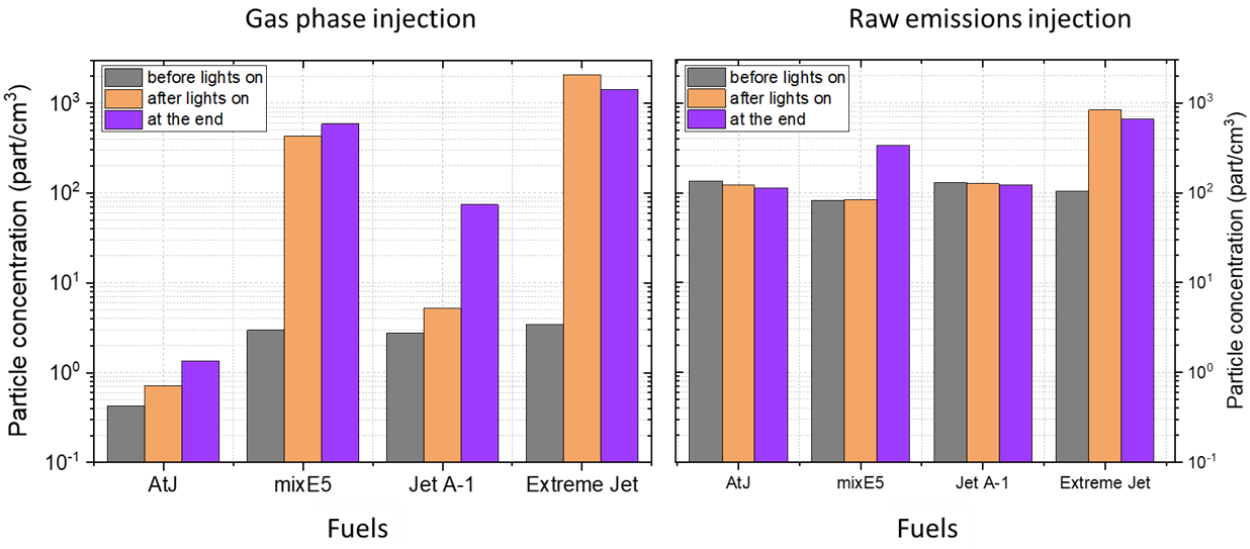

Figure V-36: Comparison of particle concentration in the CESAM chamber for four fuels tested depending on the injection process: gas phase on the left and raw emissions on the right.

V.2.4.2 Particle sizes and growth rate

GMDs calculated for vPM formed in the chamber are regrouped in Table V-8 for both injection cases. The size of vPM formed is higher for gas phase injection than for raw emissions injection case for a same fuel tested except for Jet A-1 fuel due to SO_2 injection: +32% for Extreme jet case, +28.6% for Mix E5 case and -18% for Jet A-1 case (not really representative for this test).

Furthermore, the maximum vPM size reached at the end of the experiment (presented on Figure V-37) is higher for gas phase injection and in particular for fuel with high amounts of sulphur in their composition: +44% for Extreme Jet, +40% for Mix E5. For the Jet A-1 case, the vPM formed after SO_2 injection for raw emissions injection are bigger than for the other test (+10%).

This is explained by the amount of vapours available for condensation, that depends on injection and on soot present (both number and size, larger soot will condensate easier).

Fuels	vPM GMD for gas phase injection (nm)	vPM GMD for raw emissions injection (nm)
Jet A-1	16.39	20
Extreme Jet	45.47	34.47
Mix E5	25.98	20.2
AtJ	12.27	

Table V-8: GMD of soot particles and vPM formed inside CESAM chamber for four different fuels after gas phase and raw emissions injection. For the Jet A-1 case, the reference is the SO_2 injection and not light activation.

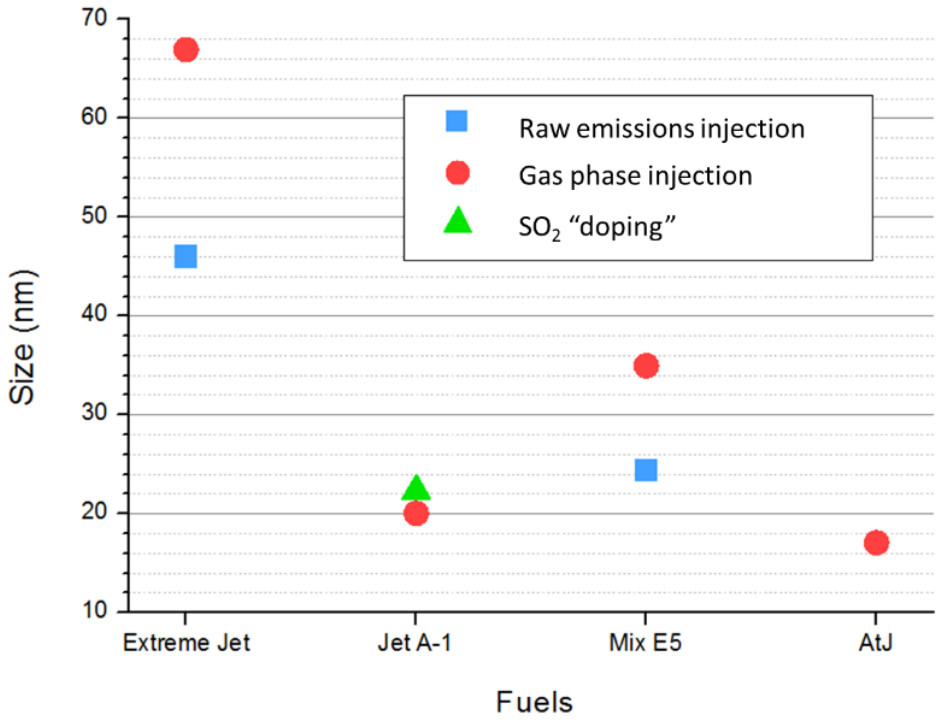

Figure V-37: Maximum size of particles formed in the CESAM chamber depending on the injection case. Raw emissions case is represented in blue, gas phase case corresponds to red data and SO_2 injection for Jet A-1 case is indicated in green.

As in previous results (V.1.6.2), the growth rate of the vPM formed (in nm/h) calculated for the different fuels tested have been regrouped on Figure V-38 (cf. details of the reference graph in section I.6.2.5). Gas phase injection tests are indicated by diamond and raw emissions injection case by circle. Their respective growth rates are located close to the limit between DMA and Sulphur/NH_3 areas.

For raw injections, Jet A-1 growth rate is lower compared to other fuels. It means that less condensable vapours are available, implying that less condensable compounds have been formed, and/or there is more soot introduced in the chamber at the beginning of the experiment. Indeed, Table V-5 shows that for Jet-A1 test, more soot have been introduced compared to other fuels in terms of particle number. Thus, the main difference in growth rate between gas and raw injection cases is explained by soot presence.

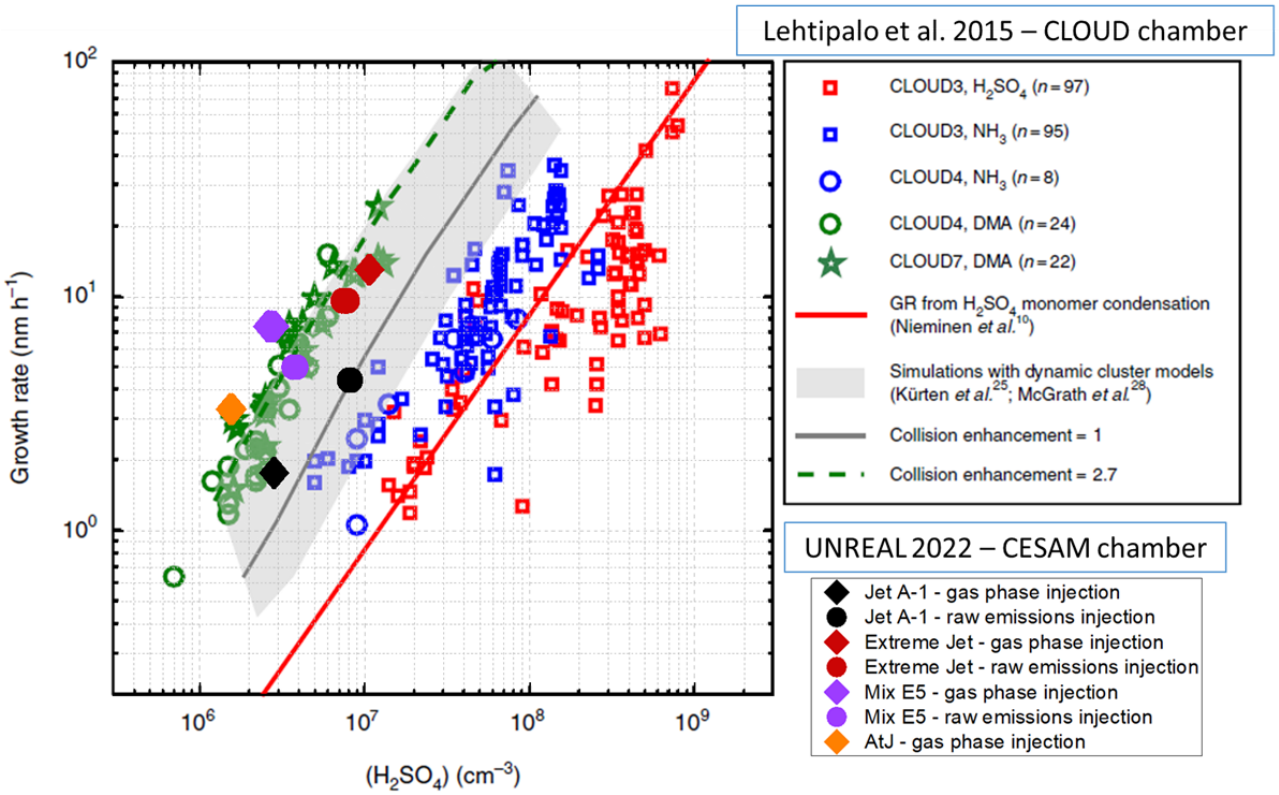

Figure V-38: Comparison of the growth rate calculated for vPM formed after gas phase and raw emissions injection using four fuels with growth rates calculated in different systems by Lehtipalo et al. (2016). The data corresponding to the UNREAL project for vPM formation within the CESAM chamber (ambient temperature and pressure, RH=38%) are indicated in black for Jet A-1, in dark- red for Extreme Jet, in purple for Mix E5 and in orange for AtJ. Diamonds are for gas phase injection cases and circles for raw emissions injection cases. Data related to Lehtipalo et al. (2016) corresponds to experiments done in the CLOUD chamber. Growth rates of 2 nm particles are determined with the appearance time method between 1.5 and 2.5 nm as a function of the measured sulphuric acid (H_2SO_4) concentration with different amounts of ammonia (NH_3) and dimethylamine (DMA) in the chamber. More details in I.6.2.5.

V.2.4.3 Semi-quantitative comparison of chemical species detected:

Samples have been collected during experimental tests for each fuel and each injection case. They have been thereafter analysed off-line at PhLAM laboratory by mass spectrometry (cf. II.2.2.3). Despite the low amount of matter collected on the filters, some species have been detected and identified in the recorded mass spectra. The main part of the molecules identified are carbon clusters and organic carbon (taken into account VOCs and PAHs). Some specific compounds has been selected (cf. Annexe III-6) to compare the four fuels for both injection cases on a semi-quantitative approach.

Figure V-39 and Figure V-40 summarise the results of the semi-quantitative comparison between Extreme Jet, Jet A-1, Mix E5 and AtJ fuels for two categories: sulphur compounds and PAH. Based on the list in Annexe III-6, the sum of the signals (integrated areas) of different compounds detected and identified is done for each fuel and each category. The separation between the particulate phase and the gas phase is indicated using a colour code to specify the presence of compounds in the samples. All signals have been normalised by the total ions count of each spectra to compare the relative intensity of each sum. Furthermore, values obtained have been normalised by respective CO_2 concentrations.

The first observation (Figure V-39) is that depending on the fuel tested for the raw emission injection, the amount of sulphur species detected decreases in accordance with the amount of sulphur in fuel concentration (more signal for Extreme Jet and less signal for AtJ). It can be noted that fuels having the most sulphur compounds in the particulate phase (i.e. more condensation vapour)

correspond to fuels generating the most vPM after light activation (Mix E5 and Extreme Jet). For the gas phase injection case, sulphur species are only found on the gas phase (too few deposits on the filter dedicated to the sampling of the particulate phase). Then, it can be noted that more sulphur species have been recorded for raw emissions injection case and they can be found mainly in the particulate phase in particular due to the adsorption of H_2SO_4 compounds (higher signal for particulate phase except for Jet A-1 case where SO_2 has been introduced in the chamber). For the gas phase, the same trend is observed except for the Jet A-1, presenting more sulphur species than the Extreme Jet case. These results also confirm the contamination of the AtJ test by sulphur for both injection cases.

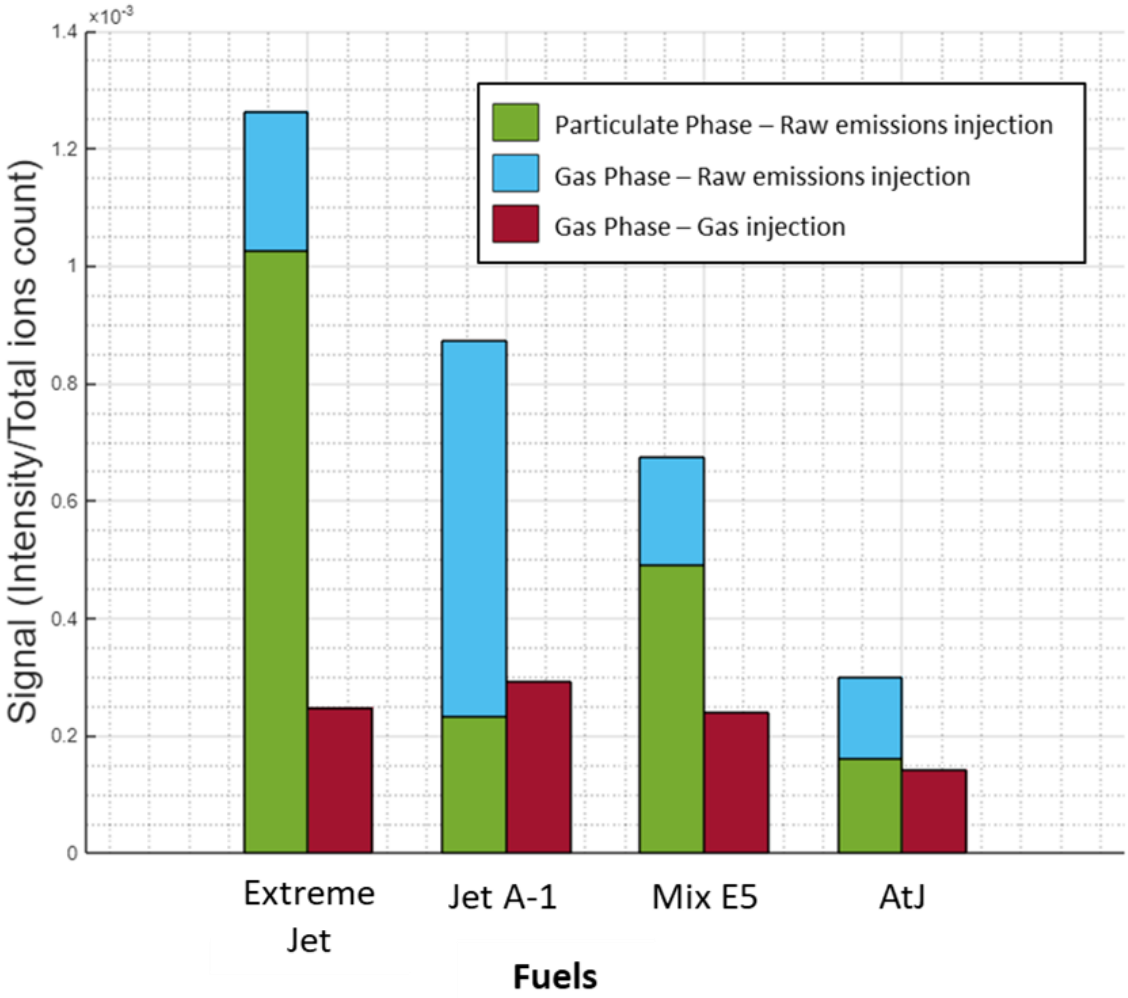

Figure V-39: Semi-quantitative comparison of the impact of fuel composition on the chemical composition of emissions in the CESAM chamber after light activation and ageing (L2MS spectra). Sulphur compounds comparison for 4 different fuels: Extreme jet, Jet A-1, Mix E5 and AtJ. Gas phase injection case is represented in dark-red gas phase. Raw emissions injection case is represented in green for particulate phase and in cyan for gas phase. The signal has been normalised by the total ions count for each spectrum and corrected by CO_2 concentration.

Concerning the PAHs present in the chamber after emissions ageing for raw emissions injection (Figure V-40), the higher amount formed corresponds to the Extreme Jet test and the lower amounts formed correspond to AtJ and Jet A-1 tests. Extreme Jet is kind of an isolated case, and it has a lot of aromatics, so it is not too surprising that there is rather high PAH. Most of the PAH found are present in the gas phase. The test generating the most vPM corresponds to the Mix E5 and the Extreme Jet, presenting here the most amount of PAH compounds. This is not expected for the Mix E5, since the aromatic content is lower than extreme and jet A-1 fuels. Further investigations are needed to

understand this point. For gas phase injection, the detection was not possible due to low deposit on sample surface (signal in the blank).

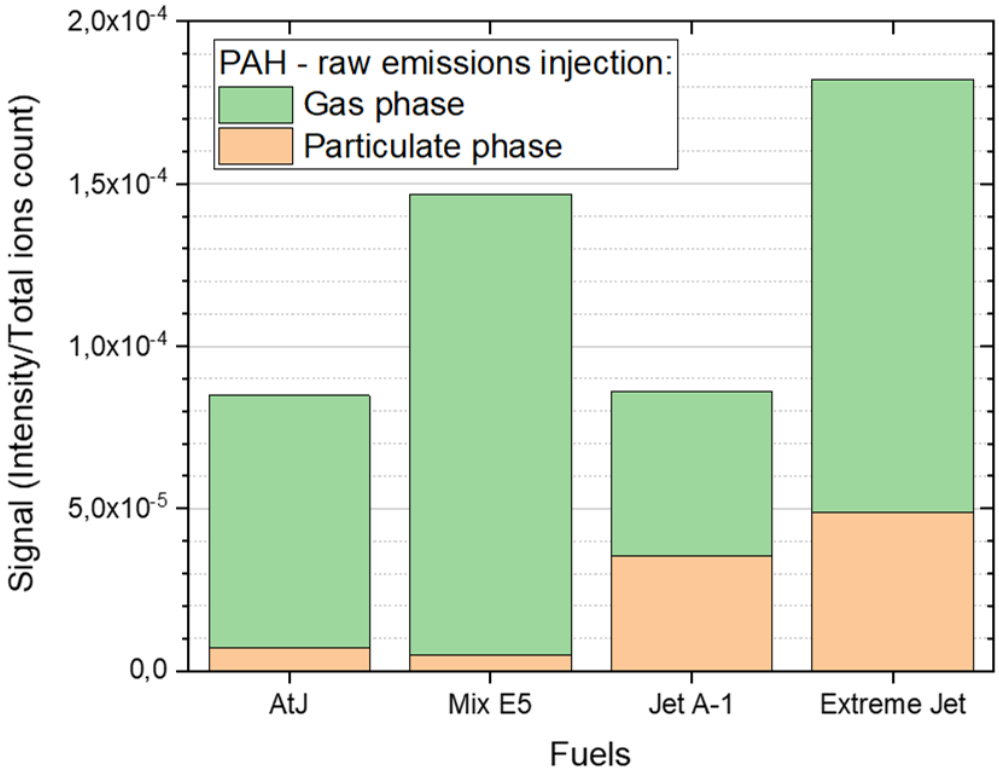

Figure V-40: Semi-quantitative comparison of the impact of fuel composition on the chemical composition of emissions in CESAM chamber after light activation and ageing (L2MS spectra). PAH compounds comparison for 4 different fuels: Extreme jet, Jet A-1, Mix E5 and AtJ. Raw emissions injection case is represented in blue for particulate phase (FF) and in red for gas phase (BF). The signal has been normalised by the total ions count for each spectrum and values have been corrected by CO_2 concentrations.

V.3 Conclusions

New particle formation is possible at ground atmospheric conditions by homogeneous nucleation from aeronautical emissions depending on the composition of the fuel and on the soot presence. A high amount of sulphur content in the fuel composition favours the formation of vPM in the chamber in terms of size and number concentration. Principal results are summarised on Figure V-41 depending on the fuel composition. Results obtained in Chapter IV for gas phase injection and in Chapter V for raw emissions injection case are represented in red on the Figure. To complete all the paths of this representation, some results obtained during preliminary tests (with CAST operating point set at 105/30/2) have been added to get an idea of all cases possible. Details of these tests are presented in Annex I.

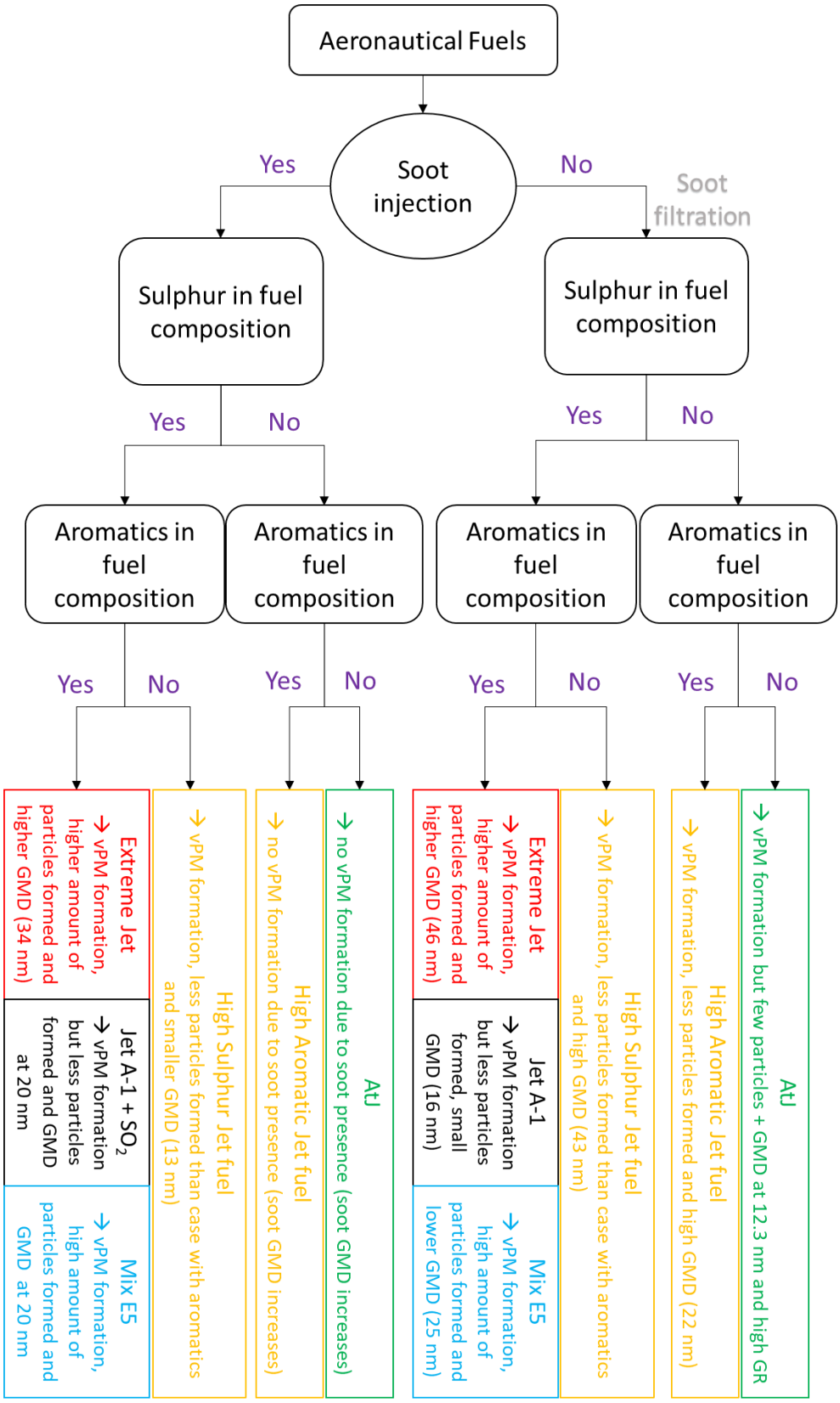

Figure V-41: Summary of vPM formation results depending on the fuel composition and of the injection process (cf. Annex I for High Aromatic and High Sulphur Jet fuels).

Chapter VI. Conclusion and Perspectives

Aviation emissions adversely affect air quality in and around airports, contributing to public health concerns for airport workers and within neighbouring communities (Hudda et al., 2020; Neu, 2020). At aircraft engine exhaust, different effluents are rejected in the atmosphere (Lee et al., 2021; Schripp et al., 2022): greenhouse gases like CO_2 (2% of these anthropic emissions are related to air transport worldwide), particulate matter (PM), volatile organic compounds (VOCs), sulphur dioxide (SO_2), carbon monoxide (CO) and unburnt hydrocarbons (HC). This work is focused on the study of volatile and non-volatile Particulate Matter (vPM and nvPM, respectively – IATA, 2023) and their interactions under atmospheric conditions at ground level.

nvPM is defined as particles present in the engine exhaust that can withstand temperatures exceeding 350°C (ICAO, 2017, 2018) and it mainly consists of soot particles coming from incomplete fuel combustion. Numerous compounds are adsorbed on their surface, such as sulphates or Polycyclic Aromatic Hydrocarbons (PAHs). Soot particles are in particular involved in the formation of contrails in the atmosphere by condensation of H_2O molecules on their surface, impacting the Radiative Forcing of the Earth. The mechanisms of formation of soot particles are better known nowadays (Johansson et al., 2018; T. L. D. Ngo, 2019; Thomson, 2023). On the other hand, vPM are formed by nucleation from gaseous precursors in the cooling exhaust gas downstream of the engine. While sulphuric acid is a major contributor to vPM formation (Kılıç et al., 2018a; Kulmala et al., 2003), it doesn't explain all observed vPM, suggesting the involvement of other sources (organic compounds, DMA,…). The molecular mechanisms behind this phenomenon remain unknown. nvPM can be also referred to as primary aerosol particles and vPM as secondary aerosol particles. Our knowledge about the mechanisms of formation of secondary aerosols has been well improved these recent years (Almeida et al., 2013; Kirkby et al., 2016; M. Wang et al., 2022), and different mechanisms have been discovered to explain new particle formation observed in the atmosphere.

As part of the UNREAL project (Unveiling Nucleation mechanism in aiRcraft Engine exhAust and its Link with fuel composition), the main objective of this work was to understand the formation of vPM in downstream of the aircraft engine depending on the composition of the fuel. Understanding the mechanisms of formation of these particles and their reaction with atmospheric components is key (Lee et al., 2021) to propose a solution to reduce their impact on air quality over the coming years.

Indeed, one of the actual objectives of the aviation industry is to reduce fuel consumption and environmental footprint. Numerous efforts to reduce these emissions and fuel consumption have been done in recent decades in accordance with the standards set by international regulation with improvements in aerodynamics and combustion. In this study, a particular attention is paid to the deployment of sustainable aviation fuels (SAF - Koumelis, 2023; Staples et al., 2018) and their impact on emissions at engine exhaust. The aim of SAF is to decrease the net CO_2 and nvPM emissions. However, combustion of these fuels may lead to new pollutants that can react with atmosphere by formation of secondary aerosols (Corbin et al., 2022; Kılıç et al., 2018a). The impact of fuel composition on emissions is one of the main focuses of this study. To consider a large spectrum of fuel composition (with high/low amount of sulphur and high/low content of aromatic compounds), different fuels from standard Jet A-1 to 100% SAF have been tested in this work.

The evaluation of the physicochemical characteristics of the particulate emissions from aeronautical fuels combustion from aircraft engines (nvPM + vPM) in real conditions is difficult to achieve from the technical and economical point of view. Measuring vPM presents challenges due to the conditions under which these are formed. Collecting emissions at airports or during flight can be done using specific methods that fit with nvPM measurements (AVIATOR, 2020; Voigt et al., 2021), but

these are not ideally suited for vPM analysis. Ambient conditions can influence vPM formation, making it difficult to establish certification standards. The distances required behind the engine for vPM formation are also a constraint on test benches, where the sampling is done in the exit plane of the engine. Alternative experiments have been conducted to study particle formation.

Atmospheric processes under well controlled conditions can be simulated at ground level using experimental chambers in different laboratories. Aircraft emissions can be injected into these chambers to analyse their atmospheric evolution over time. vPM formation and interaction with nvPM have been studied in this work with the Multiphase Atmospheric Experimental Simulation Chamber (CESAM - LISA). This chamber is able to reproduce atmospheric conditions at ground level to allow a good understanding of basic mechanisms: temperature, Relative Humidity (RH), solar irradiance, background etc. Different studies have been already carried out on CESAM dealing with atmospheric interaction of different aerosol particles (Grimonprez et al., 2021; Lamkaddam et al., 2017). However it is necessary to remember that the physical evolution of emissions in such chamber is different than the one observed in an aircraft exhaust plume in the atmosphere (dilution and cool down are different from a real case and emissions are not injected in continuous). Furthermore, connecting an aircraft engine to such installation is not possible. One option is to adapt the scale of the study, starting with generating emissions in a laboratory using burners. To obtain soot surrogate comparable to some extent to emissions from real aircraft engines, a liquid Combustion Aerosol Standard (CAST) generator has been employed (Jing, 2009; I. Ortega, Delhaye, Jing, et al., 2016). The combustion is done at atmospheric pressure and the particles have higher sizes than the ones found at engine exhaust but this burner allows the use of liquid fuel at small flow (from 0 to 105 µL/min) and the study of aeronautical emissions in the laboratory. The design of the CAST is based on the use of a propane flame to vaporise the liquid fuel in the combustion chamber to generate a flame. A part of this work was dedicated to characterise CAST emissions for aircraft fuels of different chemical compositions and to study the stability and reproducibility of the emissions.

Raw emissions of the CAST burner have been characterised using various techniques, developed following SAE E-31 recommendations (ICAO, 2017), to quantify non-volatile particulate matter (nvPM) and to analyse the chemical composition of the emissions. The objective was to compare emissions from the combustion of different fuels before moving on the study of the impact of soot presence on vPM formation. Emissions are conditioned (dilution and temperature) and before analysis, a catalytic stripper heated to 350°C is deployed to oxidise organic compounds and indirectly capture sulphur species in the gas phase and on particle surfaces, isolating nvPM. This temperature was selected to align with the definition of aeronautical industry that distinguishes particles between volatile and non-volatile with a reference temperature of 350°C (ICAO, 2018). Then, particle mass and total particle number concentrations were monitored by Laser Induced Incandescence (LII, Artium Inc.) and Condensation Particle Counter (CPC, Grimm GmbH), while particle size distribution was measured using a Scanning Mobility Particle Sizer (SMPS, Grimm). Furthermore, some filters have been collected at CAST raw exhaust to analyse thereafter the chemical composition of the emissions by mass spectrometry (L2MS and SIMS, Lille University).

Key parameters, such as flow rates and flame stability have been evaluated: the air flow needs to be adapted to the fuel flow and propane flow to avoid the formation of a second flame and/or avoid the extinction of the flame and to get a stable flame for all fuels tested. In respect to these constraints and after preliminary tests, two set points, noted (105/30/2) and (84/30/3), were chosen for emissions characterisation. The reproducibility of the tests is possible for a short period and some variations can be observed due to CAST clogging over the different experimental campaigns. An investigation about how fuel composition influenced CAST emissions for the different set points has been done. A decrease in nvPM emissions (number concentration, mass concentration and size distribution) can be observed in correlation with the quantity of aromatic compounds in the fuel for the set points tested. Moreover, the analysis by mass spectrometry based on a semi-quantitative approach (Delhaye et al., 2017), revealed a decrease in the relative intensity of PAHs when alternative fuels were employed. These

observations are aligned with the trend reported in literature of reduction of non-volatile particulate matter mass and number concentration when the hydrogen content in the fuel increases (Lobo et al., 2015). It can be noted that the AtJ, primarily composed of paraffin with no aromatic or no sulphur compounds, generates less soot than classical fuels but generates more PAH than for a fuel with low amount of sulphur and aromatic contents. This can be explained by the low cetane index of the AtJ compared to the other fuels (3 to 4 times lower), which can lead to bad combustion and then to the formation of some PAH in combustion despite the fact that no aromatics are present in this fuel composition. On the other hand, a higher share of the gas phase for organic carbon is transformed into particles for classical fuel cases. It seems that emissions of CAST burner for AtJ are less representative compared to the other fuels. It can be noted that in engine emissions, the low cetane index is compensated by high pressure inside the combustion chamber. Finally, results obtained show a good stability and a good reproducibility of the emissions over experimental campaign: Geometric Mean Diameter (GMD) and particle concentration number were similar. This suggests that the use of the CAST is suitable to evaluate and compare the emissions from various aircraft fuels.

The next step has been focused on vPM formation in atmospheric conditions, after combustion of different aeronautical liquid fuels. The CAST burner emissions have been injected into CESAM atmospheric chamber. This chamber allows to reproduce ground level conditions similar to the ones encountered in Spring at European airports (WeatherOnline©, 1999). Then the evolution of the number concentration, of the mass concentration (calculated from the particle number assuming a constant density for soot particles) and of the size of the particles has been monitored on-line. In addition, the chemical composition of the emissions has been measured both on-line (HR-ACSM, HR-AMS, API-ToF, PTR-ToF-MS) and off-line (filters and mass spectrometry). This study is innovator in many aspects. The instrumentation used in this project goes far beyond those used in the standard engine certification. Indeed, there are very few studies dealing with formation and characterisation of vPM in engine tests (Kılıç et al., 2018a). This is where the use of the CESAM chamber and state-of-the-art characterisation techniques provides a unique insight on the process of vPM formation and its interactions with nvPM.

To study the formation of vPM from gaseous precursors in first place, we have performed a series of measurements removing particulate phase from combustion emissions (using an HEPA filter between the CAST burner and the CESAM chamber) to avoid the condensation sink of soot. For all fuels tested formation of vPM by homogeneous nucleation has been observed in the atmospheric chamber in absence of nvPM. This phenomenon is particularly highlighted for fuels with high amounts of sulphur in their compositions. Fuels with high sulphur amounts generate new particles faster, in addition these particles reach higher GMD. The analysis of the particulate and gas phase chemical composition shows that oxygenated organic compounds (PTR-MS and API-ToF), organic compounds (ACSM), sulphur and PAH compounds (L2MS) have been formed. Sulphuric acid is the main contributor to the formation of vPM in the case of fuel with high amounts of sulphur. Furthermore, the growth rate (GR) of the particles is higher for SAF (more PAH at CAST exhaust given more condensable gases) and blend fuel than for classical fuel or fuel with high amounts of sulphur. It can be expected that blended fuel follows a trend between the one of alternative and the one of classical fuels (0.7 GR of Jet A-1 + 0.3 GR of AtJ). However it seems that the combination of AtJ and Jet A-1 in the blend fuel contributes to increase the growth of particles (higher concentration of condensable vapour), but contributes also to form particles since higher particle formation was observed in the case of blended fuel compared to pure ones. On-line characterisation techniques were completed by filter sampling and off-line mass spectrometry analysis, highlighting the presence of oxygenated hydrocarbons, sulphur and nitrogen compounds. By employing semi-quantitative methods, it was possible to link the relative chemical composition (sulphur relative intensity) with vPM formation and their repartitions in particulate and gaseous phases, showing that fuels with higher amount of sulphur generates more sulphuric acid and then form more vPM for a comparable amount of CO_2 injected in the chamber.

The final phase of the study involved investigating the real scenario where both vPM and non-volatile particulate matter (nvPM) were introduced into the chamber. In this case the formation of vPM is only observed for the fuels containing high amounts of sulphur (confirmed by a SO_2 doped test). Indeed, for SAF and classical fuels respectively without and with regulatory content of sulphur (200 ppm), not enough H_2SO_4 is generated after raw emissions injection and photochemistry activation. The main part of the precursors and sulphuric acid is adsorbed on soot particles, and homogeneous nucleation cannot overcome heterogeneous processes. However, vPM are formed for test with the blended fuel. Higher growth is also observed (similar to the one obtained for gas phase injection) compared to other fuels and this growth cannot be explained only by sulphuric acid, implying that other compounds should be playing a role and that more investigations are needed. The sulphur present in this fuel combined to the low cetane index leading to less efficient combustion (more PAH and condensable gases) can explain this trend. In the case of raw emissions injection, the chemical characterisation shows that a small amount of organic compounds have been formed in presence of soot. A semi-quantitative comparison of the filters collected presented an expected trend: more sulphur compounds in accordance with fuel composition but more PAH for high sulphur fuel (higher cetane index) and blend fuel (low cetane index). In the case of fuels with high amounts of sulphur (3000 ppm), vPM formation can be observed and number concentration and GMD of particles are higher compared to the other fuels. However, particles formed are less numerous and their sizes are smaller than for the previous case of injection (i.e. without soot particles in the chamber). Furthermore, comparing both injection cases, the growth rate of the particles do not change significantly for fuel with high amounts of sulphur, since high amounts of vPM are formed, acting as condensation sink for gaseous precursors, as in the case where soot particles are present.

The CESAM chamber is a good alternative to study in a laboratory the formation of secondary aerosols from multiphase atmospheric processes representative of those occurring in natural atmosphere even if the initial mixing of the exhaust emissions into the chamber happens at different time and length scales than in an aircraft plume. Experiments using this simulation chamber provide a first approach of the impact of aeronautical fuels composition on emissions obtained with an aircraft engine substitute. The perspectives for the next step are to study the same processes of particle formation with a real aircraft engine on a test bench or on tarmac. However, it is not possible to bring this installation on a test bench or to connect an aircraft engine to the chamber. An alternative to the use of an atmospheric chamber has been deployed in preliminary experiments done during this work.

A Potential Aerosol Mass Oxidation Flow Reactor (PAM-OFR) has been tested in parallel with the CESAM chamber experiment to study ageing of emissions from the CAST burner (some details are provided in Annex X). This portative reactor provides a highly oxidising environment to simulate atmospheric oxidation processes from one to several days in just a few minutes in real time (Cao et al., 2020; Kılıç et al., 2018a). The amount of soot injected in CESAM chamber is limited to avoid contamination of the chamber so the gas to soot ratio is not representative of real emissions (more gaseous precursors are injected compared to soot particles), while emissions are injected without separation between gas and particulate phases inside the PAM-OFR so this ratio corresponds to the real ratio obtained from the combustion of the fuel tested (heterogeneous processes are dominant).

Thus, the PAM-OFR can be a substitute for an atmospheric chamber to simulate atmospheric oxidation of several hours in just a few minutes on the field. Other experimental projects allowed the deployment of PAM-OFR to study the aircraft engine emissions on the tarmac. For example for the AVIATOR campaign with an A340 (Ciudad Real, Spain) or for the VOLCAN campaign with 100% SAF and an A321neo (Toulouse, France). In this last case, the PAM has been combined with an ice nucleation chamber to work on contrails formation under low temperature conditions (cruise level). Results are still under process but it is a good illustration of the use of the PAM on the field to work on volatile particles at engine exhaust.

To conclude this work, the study of vPM formation at ground level in atmospheric conditions is possible using a liquid burner and an atmospheric chamber. The nucleation process of gaseous precursors is predominant in absence of soot. The vPM formation process depends on the fuel composition, especially on sulphur content. Fuels with higher sulphur content produce higher particle number concentrations and also lead to the formation of larger particles. The combination of different complementary techniques allows a good characterisation of the emissions generated from the combustion of various aeronautical fuels. To go further, studies should be done to understand this process: why blend fuel produced more particles than Jet fuel and pure AtJ. This includes a more precise chemical characterisation and examining different blend ratios to determine if this effect is specific to this particular blend ratio (70% Jet and 30% AtJ) or if a trend emerges with varying ratios. Additionally, exploring blends with other fuels could provide insights into whether this is a specific issue with AtJ or if other SAF with compositions closer to Jet fuels exhibit similar issues. Ideally, an interesting follow-up would be to compare these results for the same fuel with combustion on a test bench with a real engine to confirm that the observations are not specific to the CAST burner.

Furthermore, ONERA emissions team has also invested in the purchase of a PAM-OFR to analyse particle oxidation and vPM formation directly at the engine exhaust. Finally to continue this work, results obtained in this study can be used for microphysics modelling to develop nucleation models and to understand the molecular mechanism behind atmospheric particle formation (Kirkby et al., 2016; Riccobono et al., 2014).

Annexes

Annex A: Impact of laser fluence for L2MS analysis.

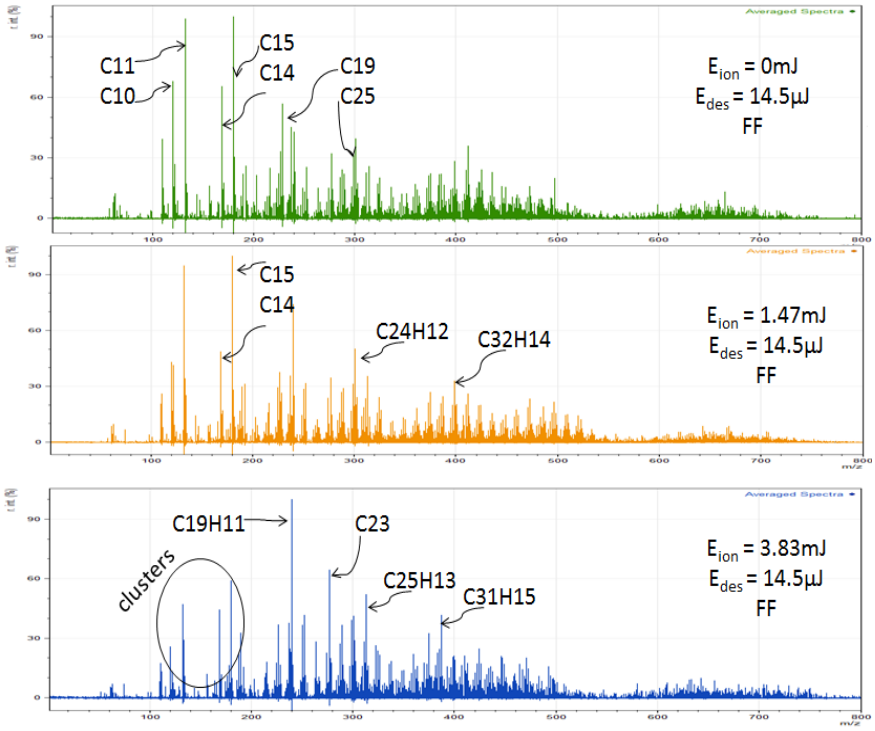

Example of mass spectrometry analysis by HR-L2MS (normalised by the maximum accurate mass for each spectrum) for the same filter (FF=particle phase – reference CAST raw sample) and different ionisation energies for a given desorption energy. The presence of PAH compounds and carbon clusters can be observed: with a low energy of ionisation, carbon clusters are predominant and with a too high energy, fragmentation is observed.

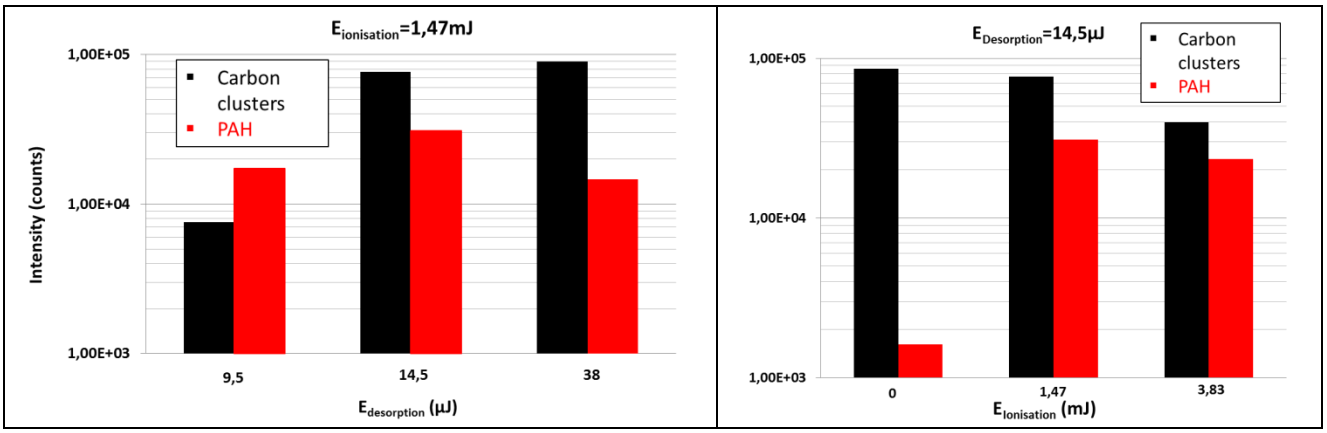

Determination of desorption (left) and ionisation (right) energies for a reference CAST raw sample based on a brief semi-quantitative comparison of the carbon clusters and PAH identified at the surface of the filter. A good compromise is a laser energy of desorption around 14µJ and a laser ionisation energy around 1.5mJ to get relevant detection of PAH.

Annex B: Impact of fuel composition on CAST emissions

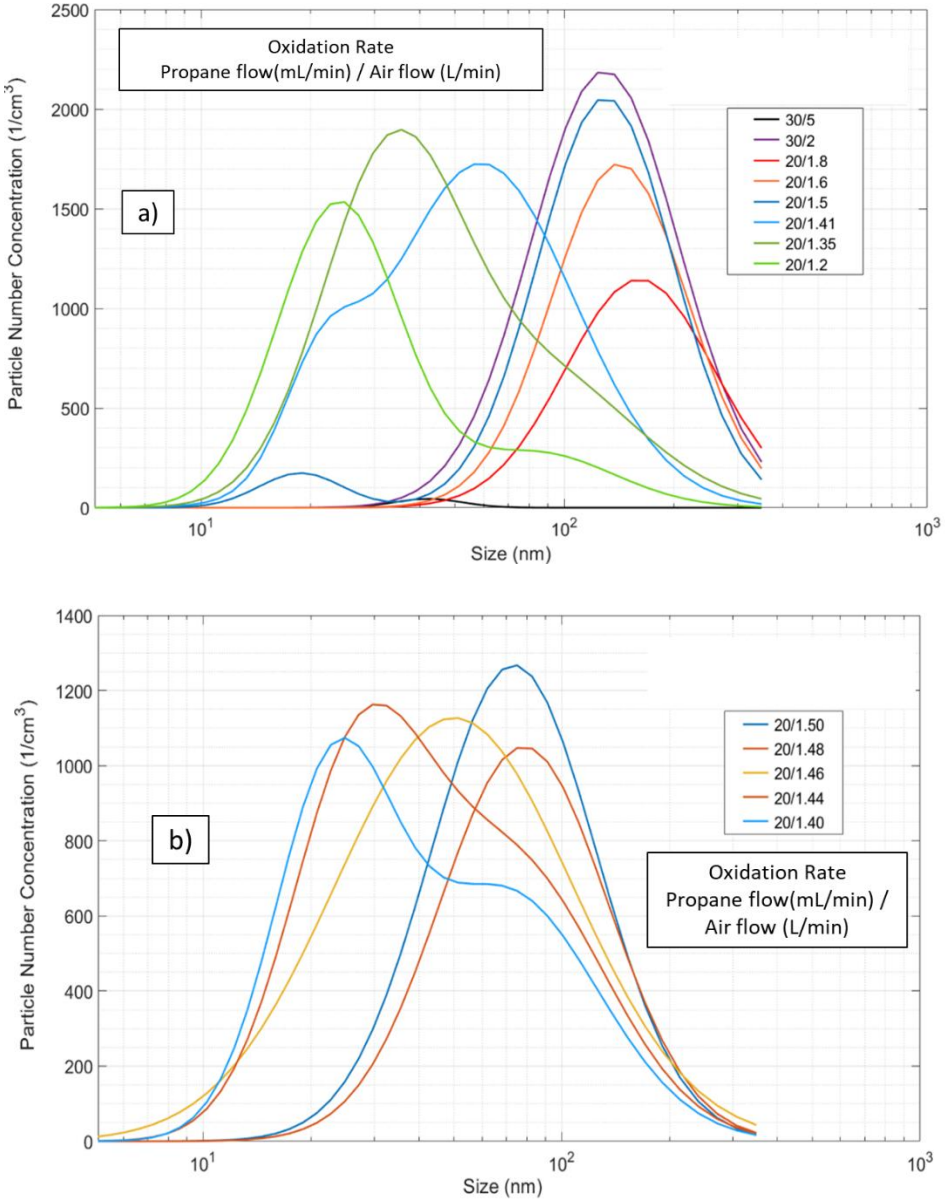

Influence of Fuels selection on size distributions of CAST emissions at burner exhaust depending on propane/ air flows ratio for two different fuels at 105 µL/min. In the first case (a), the fuel tested is the High Aromatic Jet and two propane flows have been set at 30 and 20 mL/min. In the second case (b) the fuel is the AtJ and the test has been done for one propane fuel set at 20 mL/min.

A second mode appears for low air flow. If the oxidation becomes too low, the second flame takes precedence over the principal kerosene flame in terms of particle size and particle concentration. In the case of the AtJ, the flame is less stable and the range of air flow is limited at 1.4 L/min with the appearance of a second flame affecting in the same way the principal mode. Fuels with low amounts of aromatics compounds in their composition limit the selection of the operating point due to the limitation of the air flow selection to get a stable flame without a second flame. For example the set point (105/20/1.4) does not correspond to our requirement but the operating point set at (105/20/1.5) limits the second flame formation and is stable.

Annex C: Impact of fuel flow on CAST emissions in terms of particle mass concentration for different air flows.

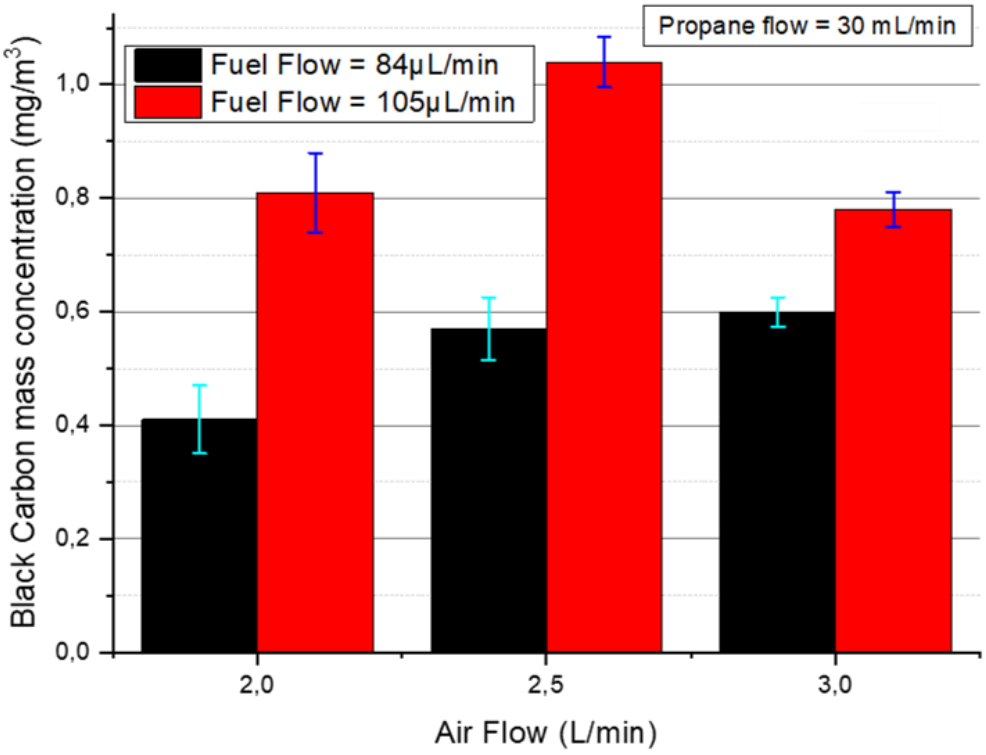

This graph presents the impact of fuel flow at 84 µL/min and at 105 µL/min on the black carbon mass concentration depending on the air flow for a given propane flow set at 30 mL/min. The propane flow has been set at 30mL/min and the fuel tested is the Extreme Jet. This test has been done with the Extreme Jet fuel to determine another operating point. For every air flow, the 105 µL/min case generates more BC mass concentration than the 84µL/min case. At 2 L/min of air flow, the difference is about a factor 2 but it decreases with the increase of the air flow (factor 1.3 at 3 L/min). Furthermore, it seems that the air flow can be optimised in terms of particle formation. Indeed for the case 105µL/min, the mass concentration of soot particles is maximal for a propane/air flow ratio of 30/2.5 but is still not maximised for the 84µL/min case.

The following table resumes the black carbon mass concentration, particle number and GMD measurements for the Extreme Jet fuel at CAST burner exhaust depending on the fuel flow and air flow for a propane flow set at 30mL/min.

Air flow (L/min)	Fuel flow: 84µL/min			Fuel flow: 105µL/min		
	Mass concentration (mg/m^3)	Total particle number $x10^3$ ($1/cm^3$)	GMD (nm)	Mass concentration (mg/m^3)	Total particle number $x10^3$ ($1/cm^3$)	GMD (nm)
2.00	0.41 ± 0.06	2.01	143.6 ± 1.7	0.81 ± 0.07	3.01	123.8 ± 1.7
2.50	0.57 ± 0.06	2.01	141.4 ± 1.7	1.04 ± 0.04	2.85	133.3 ± 1.8
3.00	0.60 ± 0.03	1.76	148.0 ± 1.5	0.78 ± 0.03	2.58	140.6 ± 1.5

Annex D: Impact of CAST oxidation parameters on black carbon mass concentration for a fuel flow set at 105µL/min.

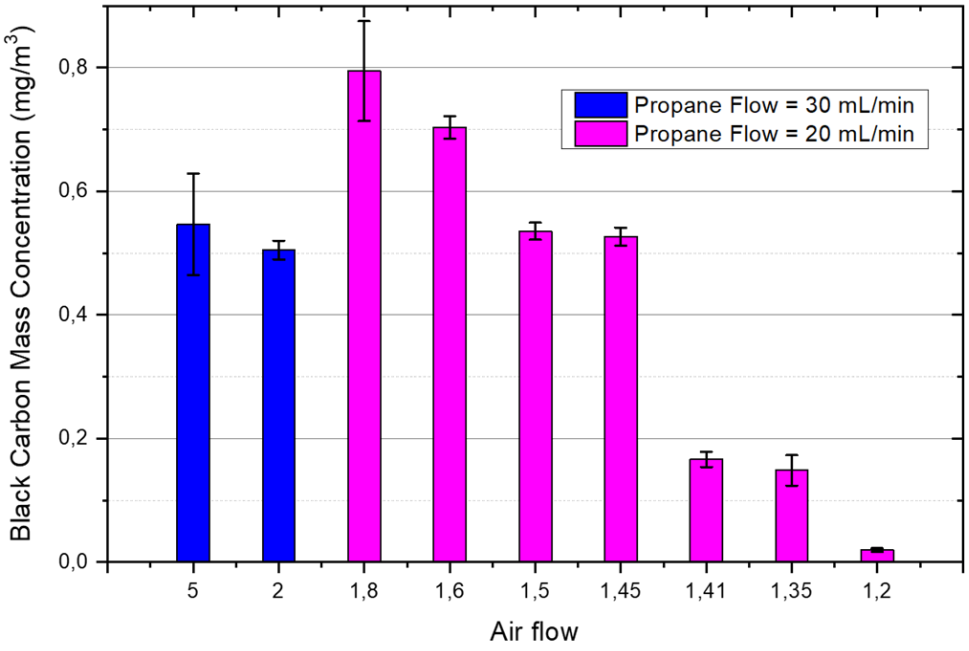

Different air flows have been tested for the High Aromatic Jet fuel. The propane flow has been set at 30 and then at 20mL/min for an air flow varying from 1.2 to 3L/min. For a propane flow at 30mL/min, two operating points are compared at (30/5) and at (30/2) and both size distributions are mono-modal (Annex C).

For both propane flows, the mass concentration decreases with the augmentation of the air flow. Furthermore, for the same propane/air ratio, the mass concentration is 3.4 times higher for 30mL/min (0.505mg/m^3 for the case 30/2) than for 20mL/min (0.148mg/m^3 case 20/1.35) of propane flow. The operating point 105/30/2 is stable for all fuels tested and avoids the formation of a second flame. To compare this point to another one with a lower air flow and a comparable propane/ air ratio, the 105/20/1.5 point (limiting the appearance of a second flame) have been selected.

The following table presents a comparison of black carbon mass concentration and size of particles measured for the High Aromatics Jet A-1 fuel depending on the propane/ air flows ratio for a fuel flow set at 105µL/min.

Propane/air flows		30/5	30/2	20/1.8	20/1.6	20/1.5	20/1.45	20/1.41	20/1.35	20/1.2
Mass concentration (mg/m^3)		0.55	0.50	0.79	0.70	0.54	0.53	0.17	0.15	0.02
Standard deviation		0.08	0.02	0.08	0.02	0.01	0.01	0.01	0.02	0.002
GMD (nm)	Kerosene Flame	41.3	128.2	161.2	140.7	129.4	62.1	58.9	89.4	82.5
	Second Flame	-	-	-	-	19.1	28.7	24.8	35.5	24.0

Annex E: Size distributions measured for first CAST set point (105/30/2) depending on the fuel composition (III.2.2.3).

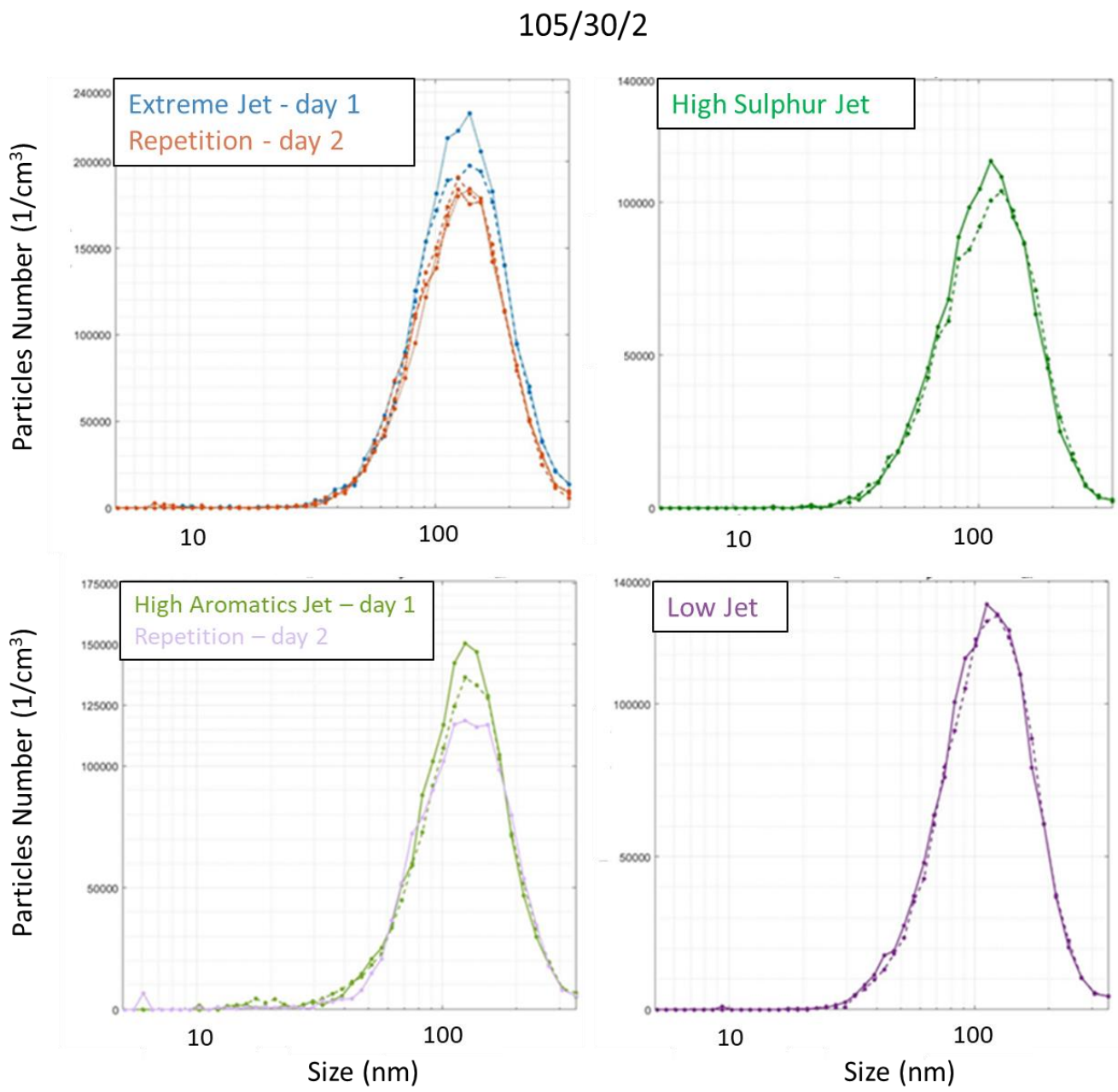

The four fuels tested at (105/30/2) are:

- the Extreme Jet (23% of aromatics contents + 3000 ppm of sulphur),
- the High Sulphur Jet (16% of aromatics contents + 3000 ppm of sulphur),
- the High Aromatic Jet (23% of aromatics contents + 4 ppm of sulphur),
- and the Low Jet (16% of aromatics contents + 4 ppm of sulphur).

Some repetitions have been done for some of them over 2 days.

Annex F: Size distributions measured for second CAST set point (105/20/1.5) depending on the fuel composition (III.2.2.3).

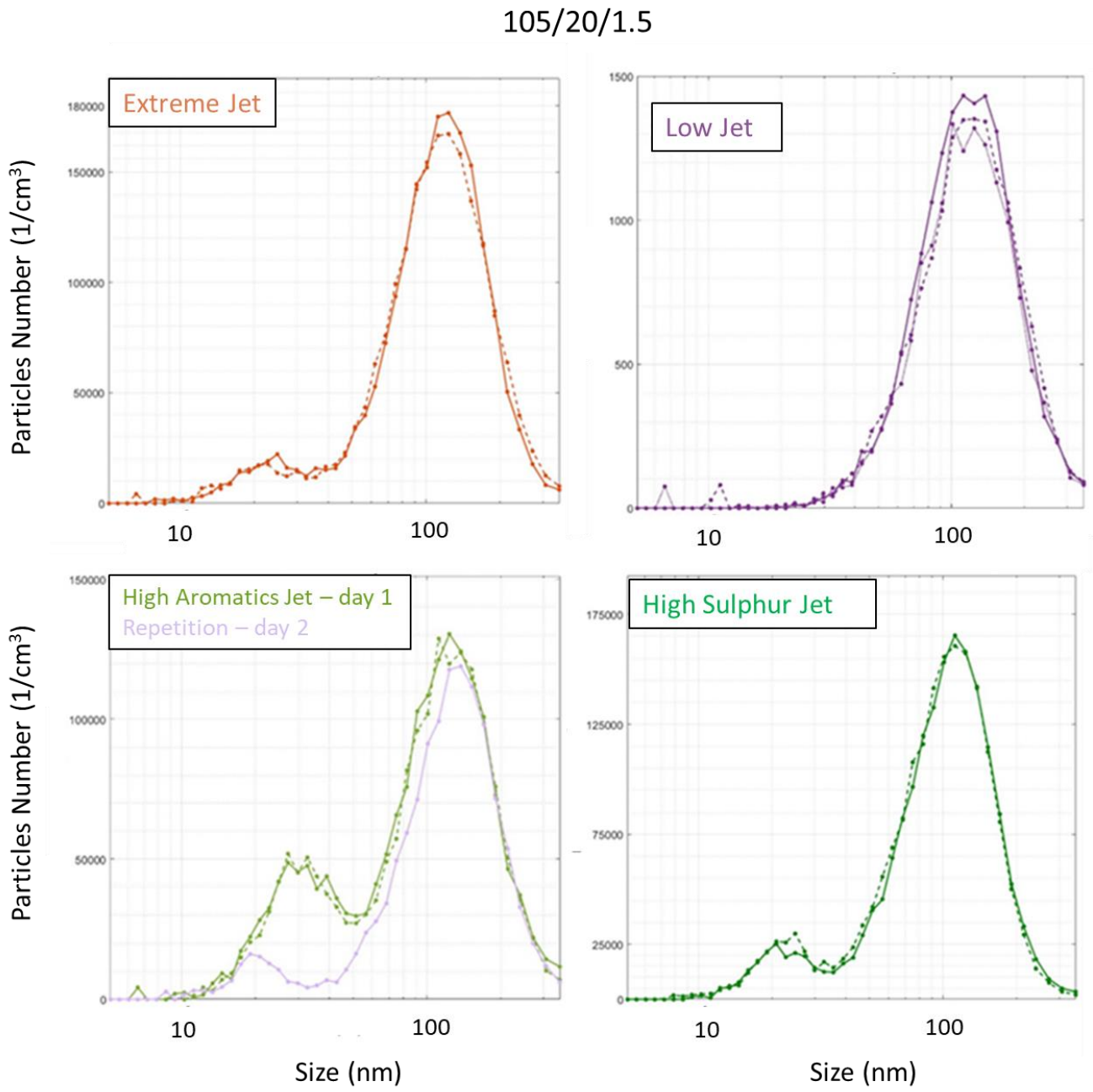

The four fuels tested at (105/20/1.5) are:

- the Extreme Jet (23% of aromatics contents + 3000 ppm of sulphur),
- the High Sulphur Jet (16% of aromatics contents + 3000 ppm of sulphur),
- the High Aromatic Jet (23% of aromatics contents + 4 ppm of sulphur),
- and the Low Jet (16% of aromatics contents + 4 ppm of sulphur).

One of them has been repeated over 2 days.

Annex G: List of chemical compounds researched for the semi-quantitative approach using mass spectrometry off-line instruments.

Name	Formula	m/z
HAP		
Naphthalene	$C_{10}H_8$	128,06
Acenaphthylene	$C_{12}H_8$	152,06
Acenaphthene	$C_{12}H_{10}$	154,08
Fluorene	$C_{13}H_{10}$	166,08
Antracene/Phenanthrene	$C_{14}H_{10}$	178,08
Fluoranthene/ Pyrene	$C_{16}H_{10}$	202,08
Benzo(a)anthracene/ Chrysene	$C_{18}H_{12}$	228,09
Benzo(a)Pyrene Benzo(b)fluoranthene Benzo(k)fluoranthene Benzo(ghi)perylene	$C_{20}H_{12}$	252,09
Indeno(1,2,3-cd)Pyrene	$C_{22}H_{12}$	276,09
Dibenzoanthracene	$C_{22}H_{14}$	278,11
Sulphur Content		
Sulphur	S	31,97
Sulphur dioxide	SO_2	63,96
Hydrogen sulphate	HSO_2	64,97
Sulphur trioxide	SO_3	79,95
Hydrogen sulphate	HSO_3	80,96
Sulphate	SO_4	95,95
Hydrogen sulphate	HSO_4	96,96
Sulphuric acid	H_2SO_4	97,97

Name	Formula	m/z
COV		
Acetylene	C_2H_2	26,01
Ethylene	C_2H_4	28,03
Propene	C_3H_6	42,05
Benzene	C_6H_6	78,05
Toluene	C_7H_8	92,06
Ethylbenzene/ Xylene	C_8H_{10}	106,078
Oxygenated Compounds		
Formaldehyde	CH_2O	30,01
Carbon dioxide	CO_2	44,01
Acetaldehyde	C_2H_4O	44,03
Formic Acid	CH_2O_2	46,01
Acetone	C_3H_6O	58,04
Acetic acid	CH_3COOH	60,02
Methyl Vinyl Ketone	C_4H_6O	70,04
Butanone	C_4H_8O	72,06
2-methyl-3-buten-2-ol	$C_5H_{10}O$	86,07
3-Hydroxybutanone	$C_4H_8O_2$	88,05
Hexanal	$C_6H_{12}O$	100,09
Heptanal	$C_7H_{14}O$	114,1
Hexanol	$C_7H_{16}O$	116,12

Annex H: Composition of emissions in CESAM chamber for tests with (first graph) and without (second graph) soot filtration using Extreme Jet fuel and CAST operating point set at (105/30/2).

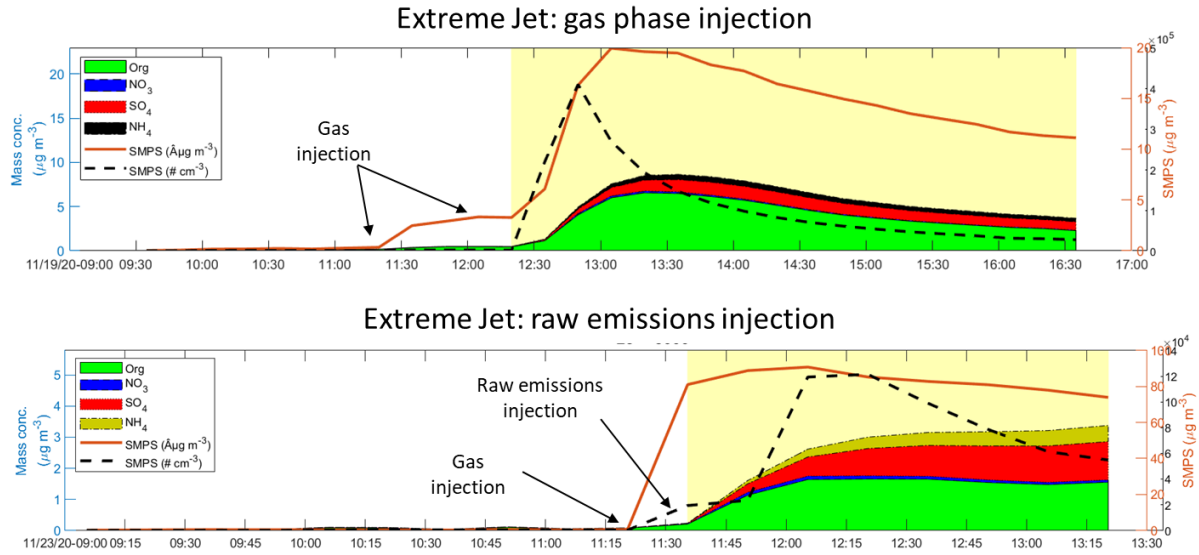

The both graphs represent the concentration of organic compounds (green), NO_3 (blue), SO_4 (red), NH_4 (black/brown) on the y-left-axis and the number and mass concentrations on the y-right-axis measured with an Aerosol Mass Spectrometer (cf. II.2.2.2.4) for more details about the instrument).

After emissions injection, only a residual amount of organic molecules is recorded in both cases (less than 0.35 µg/m^3). After light activation, the main compounds formed in the chamber are organics and SO_4: respectively 6.5 µg/m^3 and 1.5 µg/m^3 for gas phase injection and 1.6 µg/m^3 and 1 µg/m^3 for raw emissions injection. The formation of SO_4 involves that sulphuric acid has been generated and then has been consumed to form new particles. More compounds are generated for the gas injection case.

To complete these results, PTR-MS (details II.2.2.1.4) provides the chemical composition of the gas emissions in the chamber. For both cases, different compounds have been found in common (more signal for gas phase injection case). The majority corresponds to aromatics compounds (Benzene, Toluene, Xylene, TMB, Naphthalene, Anthracene) and oxygenated compounds (Formaldehyde, Acetaldehyde, Formic Acid, Acetone, Butanone, 3-OH-Butanone, Hexanal, Hexanol). Some examples are given on the following graphs representing the evolution of some species over the time for gas phase injection. The fuel tested is the Extreme Jet for (105/30/2) CAST set point. Lights are represented by the yellow section. Organic compounds and oxygenated compounds constitute the main part of the emissions at the end of the experiment. The principal conclusion is that fuel with high amounts of sulphur compounds promotes the formation of vPM, in particular in the case where soot has been removed.

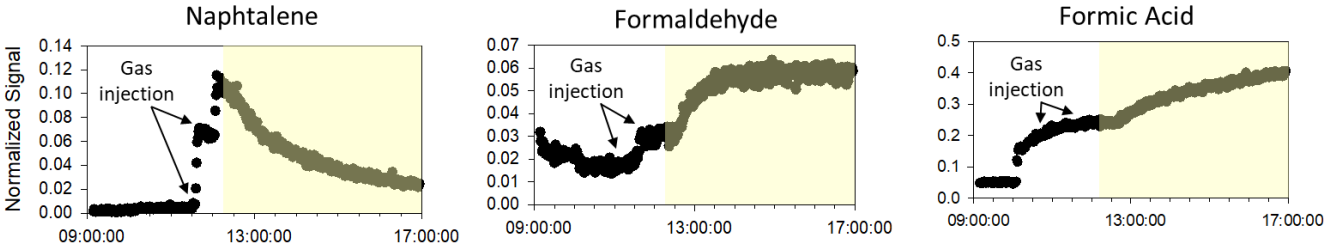

Annex I: vPM formation for different fuels after injection of gas phase with soot filtration in CESAM chamber during preparation tests.

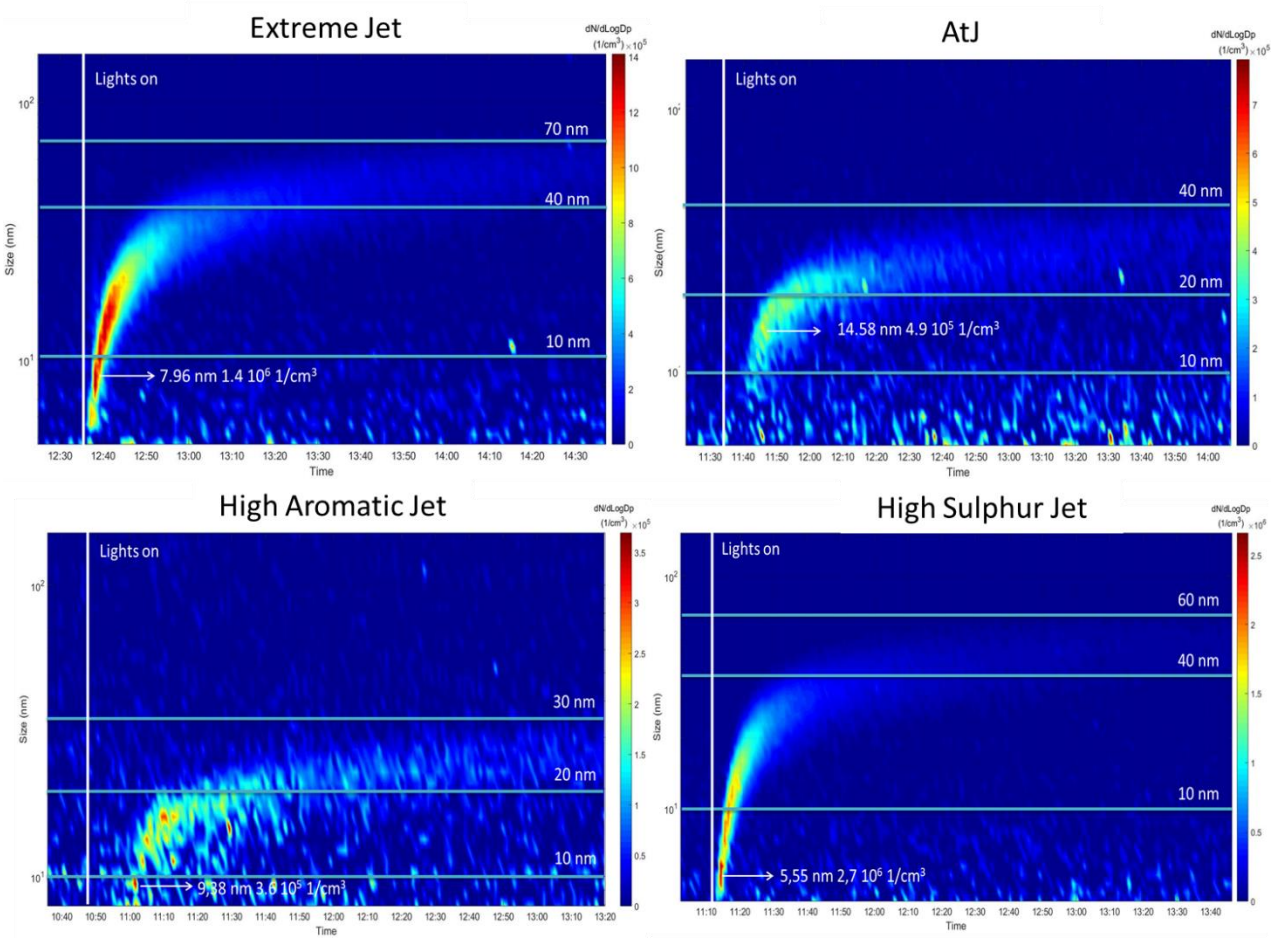

Four fuels have been tested: Extreme Jet, AtJ, High Aromatic and High Sulphur Jet. CAST operating point is set at (105/30/2). The injection protocol is the same for all tests: introduction of gas phase with soot filtration, same CO_2 concentration at the end of the injection, lights on with a delay of 30min. Each graph represents the size of the particles (y-axis in log scale) and particle number (colour scale) over the time. The maximum particle number measured is indicated according to the corresponding size.

vPM formation can be observed for all cases after light activation in the CESAM chamber. Fuels with higher amounts of sulphur in their composition (Extreme Jet and High Sulphur Jet with 3000 ppm) generate more vPM and the size of these new particles increases faster and reaches a higher value compared to the other fuels. However, it can be noted that vPM are formed even without sulphur for the case of the AtJ. It confirms that sulphur is not the only agent involved in the formation of volatile particles at engine exhaust. More details in section IV.3.3.

In comparison, the graphs below represent the formation of vPM after raw emissions injection in the chamber for the same four fuels and same CAST set point (105/30/2). The main observation is that vPM formation has been only recorded for tests with fuels having a high amount of sulphur in their composition (3000 ppm). In the case of High Aromatic Jet (4 ppm of sulphur) and AtJ (0 ppm of sulphur), no particles have been formed. All gas precursors are condensed on the soot surface and homogeneous nucleation cannot occur. Only soot particles are present in the chamber for these both cases.

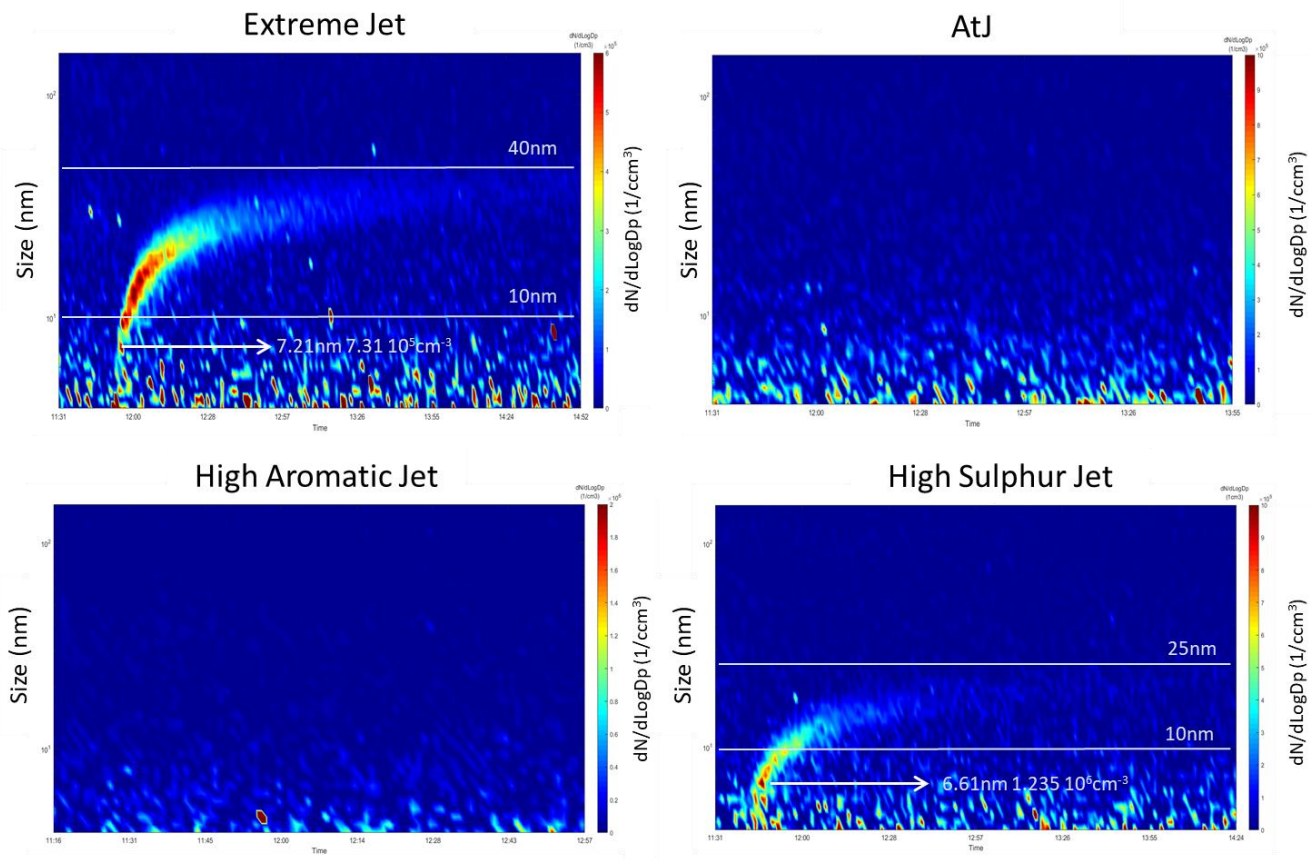
Extreme Jet
40nm
10nm
7.21nm 7.31 10⁵cm⁻³
Size (nm)
dN/dLogDp (1/ccm³)
Time
AtJ
High Aromatic Jet
High Sulphur Jet
25nm
10nm
6.61nm 1.235 10⁶cm⁻³

Annex J: Kerosene vapour injection in CESAM chamber for two different fuels: reference Jet A-1 and Jet VOLCAN.

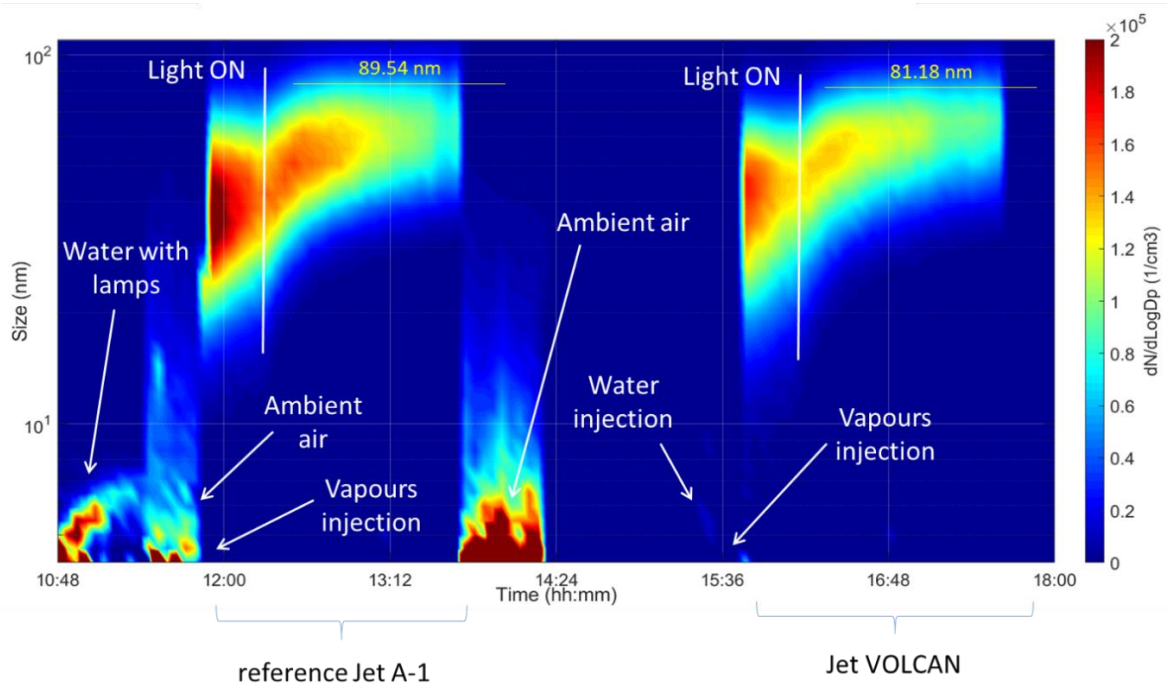

Two fuels have been tested the same day: the reference Jet A-1 and the Jet VOLCAN (cf. details in section II.1.1.2 for the fuel composition). The CAST set point is set at (84/30/3) to avoid the formation of a second flame due to fuel leak in the burner. The kerosene flame has been blown off voluntarily and kerosene vapour have been introduced in the chamber. The injection protocol is the same for both tests: 1min of injection to obtain 14.5 ± 0.3 ppm of CO_2 and lights are on with a delay of 30min. First graph (above) corresponds to the evolution of the size (y-axis) and particle number (colour scale) over the time for both fuel tests. The second one (below) represents the evolution of organic and nitrate concentrations over the experiment. OOA and HOA are respectively Oxidised Organic Aerosol (H_2O^+, CO^+, $C_2H_3O^+$…) and Hydrocarbon-like Organic Aerosol ($C_2H_4^+$, $C_3H_7^+$, $C_4H_9^+$…). They correspond to some organic fragments (the more relevant here), thus included in organic concentration measurement.

Regarding the first graph, particles are detected after the injection of kerosene vapour in the chamber for both tests. The number concentration of particles is more important for the Jet A-1 case ($0.4x10^5$ particles/cm^3 of difference) and particles GMD is slightly higher: 36 nm for Jet A-1 vs 32 nm for Jet VOLCAN. After light activation, vPM are formed in both cases. The growth rate is similar (7.6 nm for Jet A-1 and 6 nm every 10 min) and the size of particles reaches 89.54 nm for Jet A-1 case and 81 nm for Jet VOLCAN case. Considering fuel compositions, it seems that fuel with less amount of aromatic and sulphur contents generates more particles from the kerosene vapour. Furthermore, it can be observed that before vapour injection, particles can be formed from nucleation from the water phase in both cases. Indeed, after water injection, lights have been activated and a small amount of particles has been generated.

Regarding the graph below presenting the composition of emissions particulate phase in CESAM chamber before and after light activation, the main part of kerosene vapour is composed of organic compounds at the injection. After light activation, their concentrations increase: +68% in Jet A-1 case and +48% in Jet VOLCAN case. There are more particles injected and formed in the case of the reference Jet A-1. Furthermore, regarding the fragments OOA and HOA, we can see that HOA has been consumed to form OOA.

It shows that kerosene vapour can affect the homogeneous nucleation for the different fuels tested.

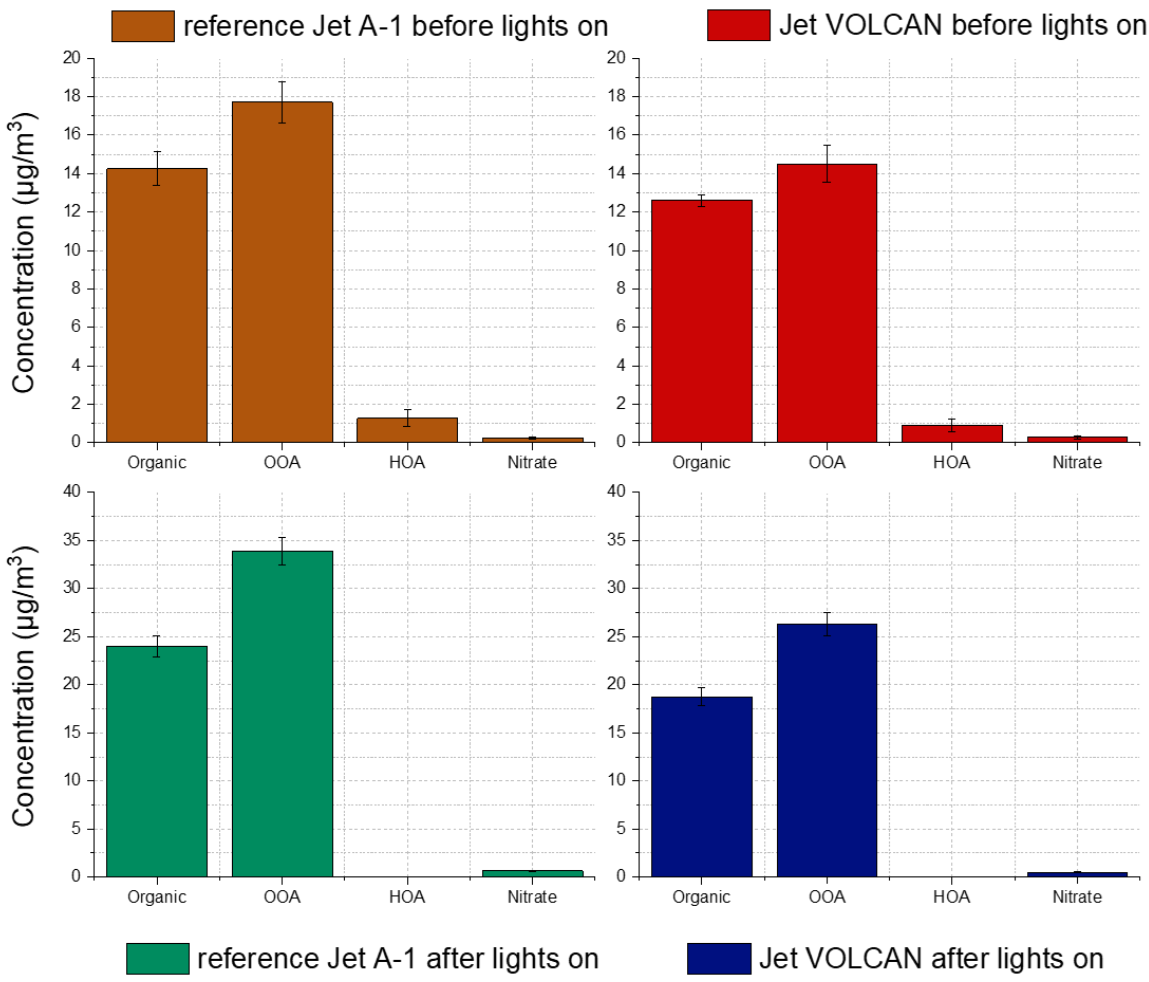
reference Jet A-1 before lights on
Jet VOLCAN before lights on
Concentration (µg/m3)
Organic
OOA
HOA
Nitrate
reference Jet A-1 after lights on
Jet VOLCAN after lights on

Annex K: Evolution of vPM inside the CESAM chamber for gas phase injection from the Jet A-1 fuel combustion.

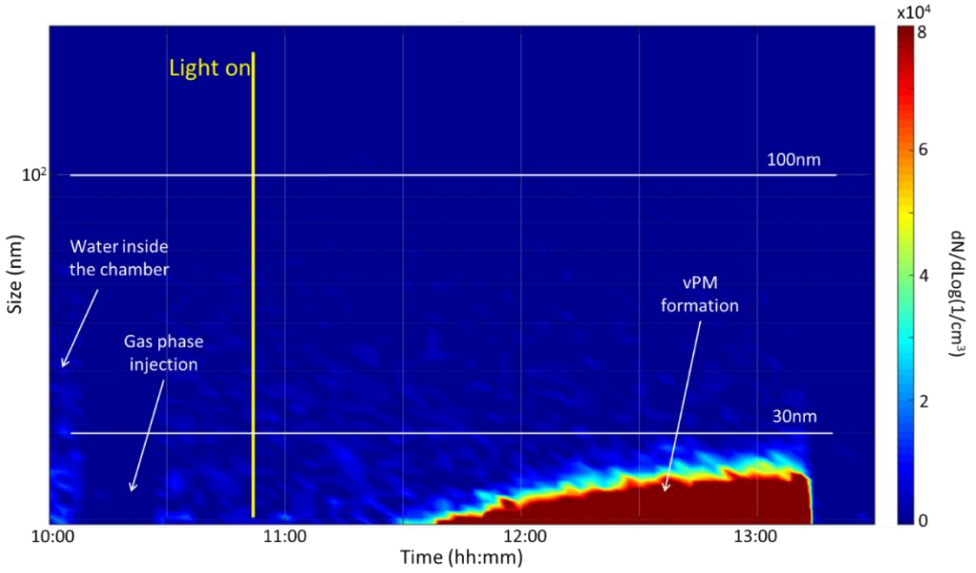

The first Figure represents the size (y-axis) and number concentration (colour scale) of particles over the time. Some particles have been generated after the water injection. The SMPS is disconnected from the chamber for the injection of gas phase (chamber under depression). The first vPM formation phenomenon observed is 1h10 after the injection (40min after lights on). It is the time for new particles formed to reach the limit of detection of this instrument (smaller particles are not recorded by the instrument). The size of the particles increases with the time ("banana plot") but do not exceed 24.39nm. The concentration of particles inside the chamber is low and the corresponding colour scale is saturated to get a better point of view of the particles formed. The second Figure presents the number concentration (C_n on the left) and the mass concentration (C_m on the right) of particles in the chamber after injection of gas phase and detection of vPM. All data have been corrected by wall losses and dilution. Particles Number increases but with a delay after light activation, comparable to the one observed for the banana plot. The signal of the mass concentration is really weak, even after the detection of particles. It means that particles observed are just a small part of the vPM formed inside the chamber. To get a better overview of the smaller particles and complete this approach, a nanoSMPS has been set with a range from 4 nm to 109 nm.

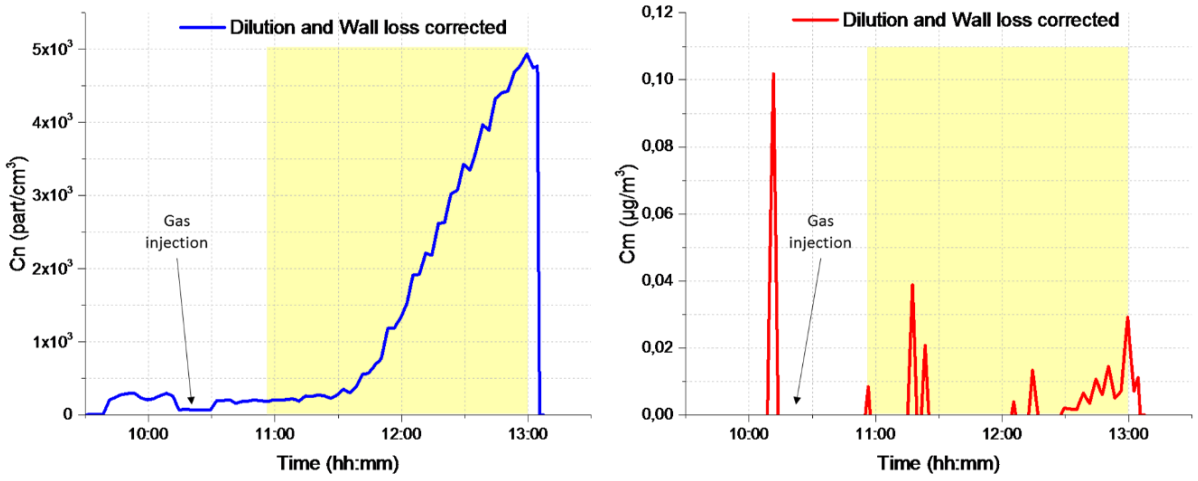

Annex L: Monitoring H_2SO_4 concentration in the CESAM chamber with an API-ToF.

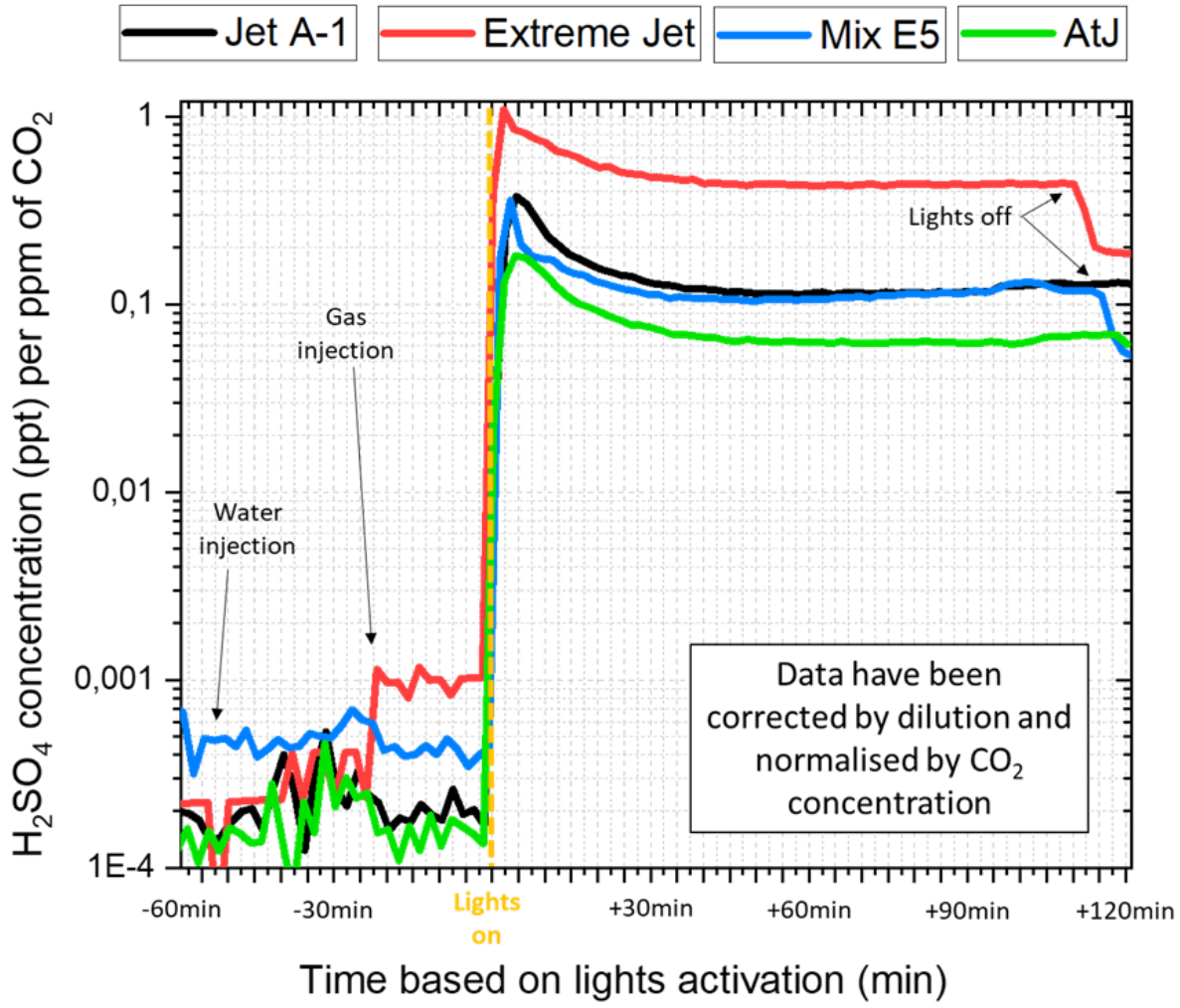

It combines the different concentrations of sulphuric acid obtained (log scale) for the four fuels tested. Data have been corrected for dilution ratio and normalised by CO_2 concentration. The graph is centred on the light activation (x-scale).

Annex M: PTR-MS data comparison for gas phase injection depending on the fuel used.

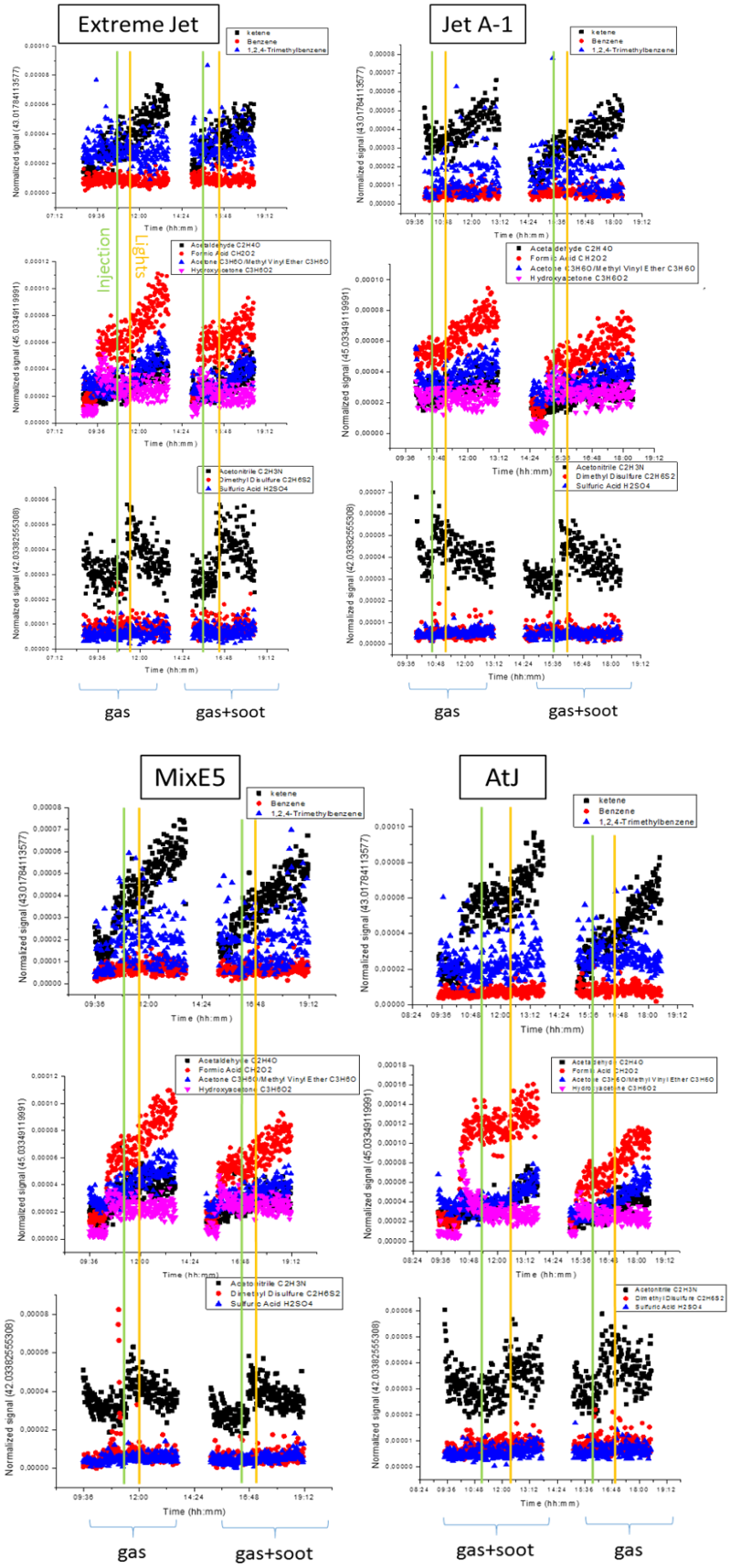

Annex N: Formation of new volatile particles in CESAM chamber after injection of raw emissions.

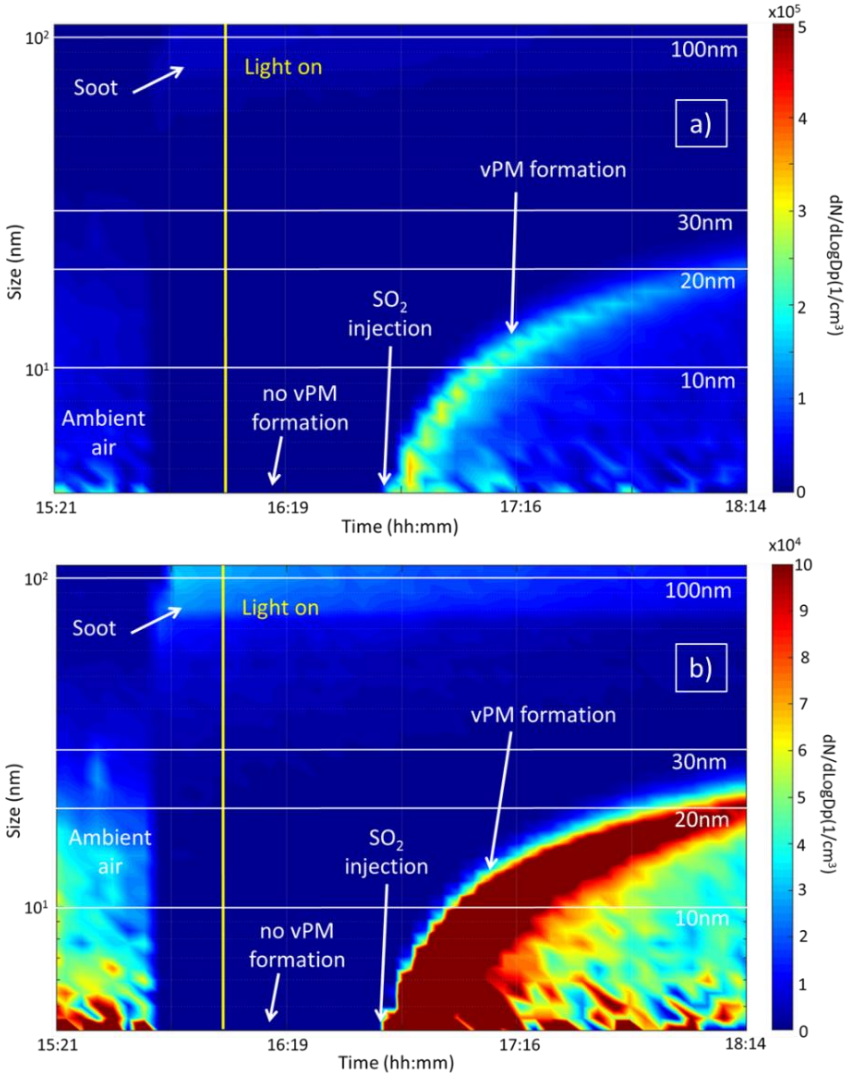

Two tracking plots of size particle distribution along time in the CESAM chamber for the injection of CAST emissions (gas phase and raw emissions) after Jet A-1 fuel combustion are presented. It can be associated with the vPM formation. These Figures are obtained with the nanoSMPS (range from 5 to 109 nm). It should be noted that both figures correspond to the same result but the colour scale representing the particles concentration is different: 0 to $5x10^5$part/cm^3 for the case a) and 0 to $10x10^4$part/cm^3 for the case b). It gives two visualisations of this phenomenon and on the second representation, soot particles are more visible (case b - at the top of the graph but the instrument cannot record all signals. Details are presented in V.1.2.

Annex O: Size distributions obtained after raw emissions injection, lights activation and SO_2 injection in the CESAM chamber.

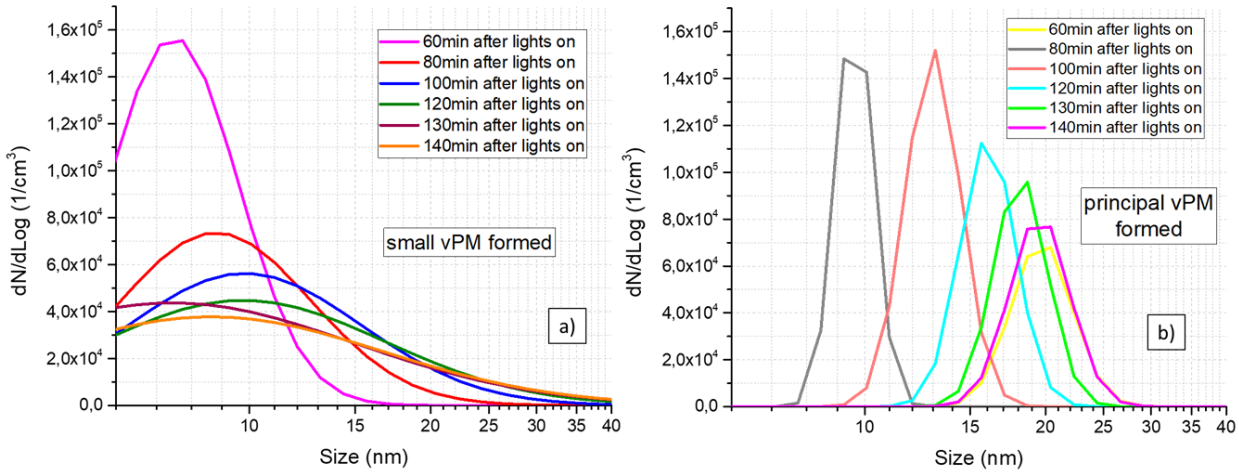

The fuel used is the Jet A-1 and the CAST operating point is set at (84/30/3). For the small particles (a), the GMD remains the same around 10nm but the concentration decreases with time of almost 3. For the vPM (b), the GMD increases due to agglomeration of vPM and condensation of gases. To obtain the GMD for these size distributions, a one fit mode has been applied only on particles above 10nm and also a two-fit-mode has been applied on both vPM (small and principal) modes.

The total GMD for vPM obtained is presented on the following Figure. The GMD calculated is affected by soot presence at the beginning of the experiment, and after SO_2 injection by the new vPM formed. Light activation is indicated by the yellow area. SO_2 injection was done at 16h46.

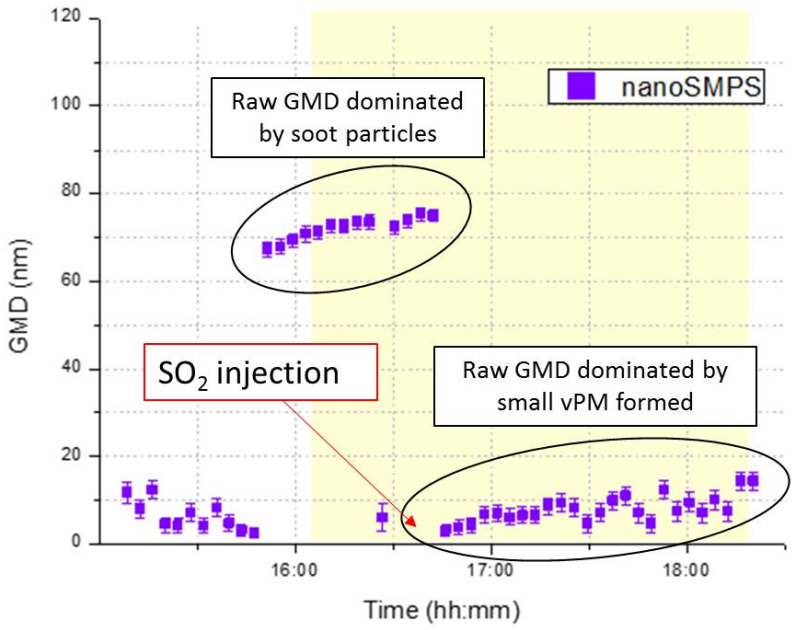

Annex P: Calculation of the soot volume and estimation of their density in the chamber for raw emission injection using Jet A-1 fuel.

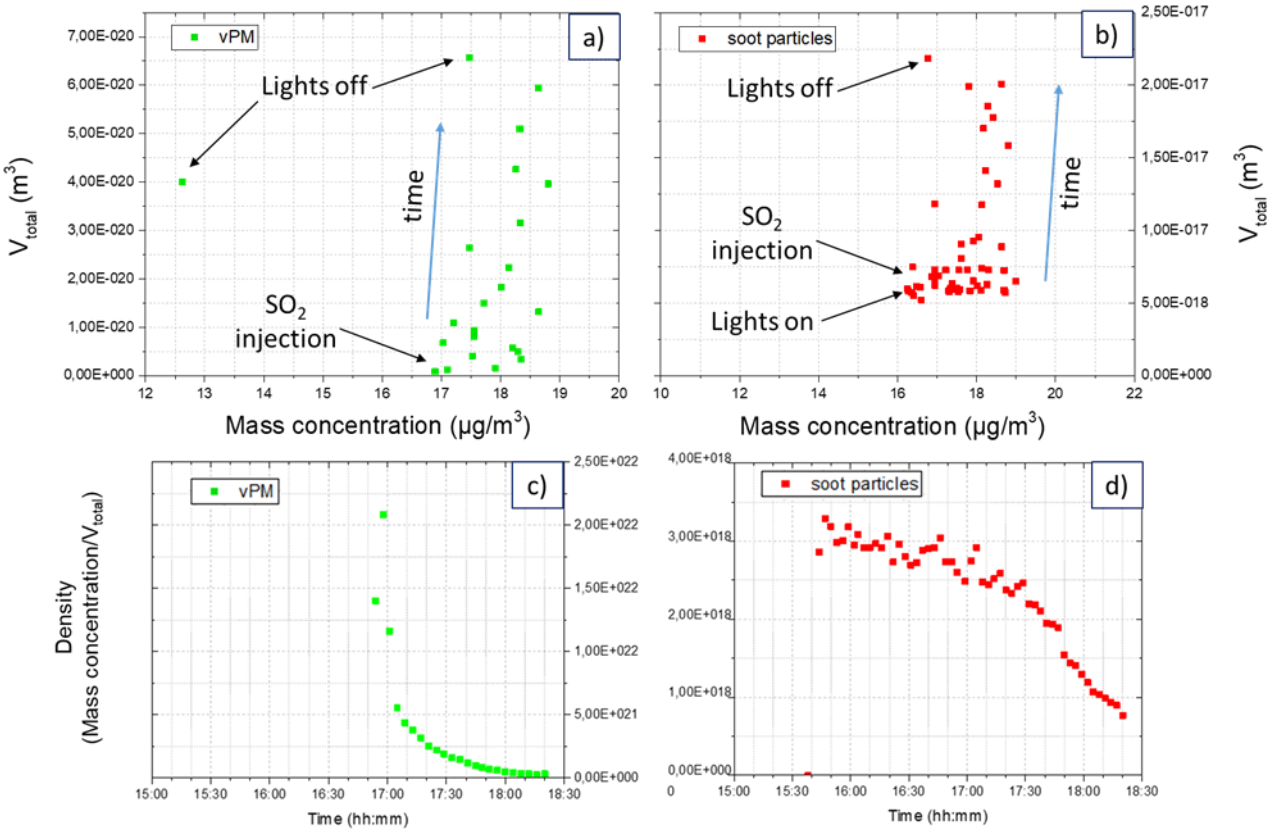

Based on the hypothesis of a density equal to 1 for soot particles over the time, the volume of particles has been estimated. Using the GMD, the volume of a single particle is determined (assuming a spherical shape) and then is multiplied by the number of particles recorded by the SMPS to get the total Volume in the chamber. Then this volume is represented on figure a) for vPM and figure b) for soot depending on the mass concentration. The main observation is that for vPM case, the repartition of the particle volume increases with time for comparable mass concentration ($\pm 2 \mu g/m^3$) in accordance with vPM GMD and number concentration increases. For soot particles, before SO_2 injection, as there is no vPM formed and few changes in terms of GMD, the volume concentration of particles remains regrouped. But with vPM formation, the GMD increases more and the volume of soot increases also.

For the two last figures, the density is evaluated, dividing the mass concentration by the volume of particles. In both cases (vPM in c and soot in d), the density decreases with time. It is related to the increase of respective GMD. The volume increases but the density decreases.

Annex Q: Chemical comparison of particle and gas phase after injection of CAST emissions without soot and after injection of raw emissions using Jet A-1 fuel.

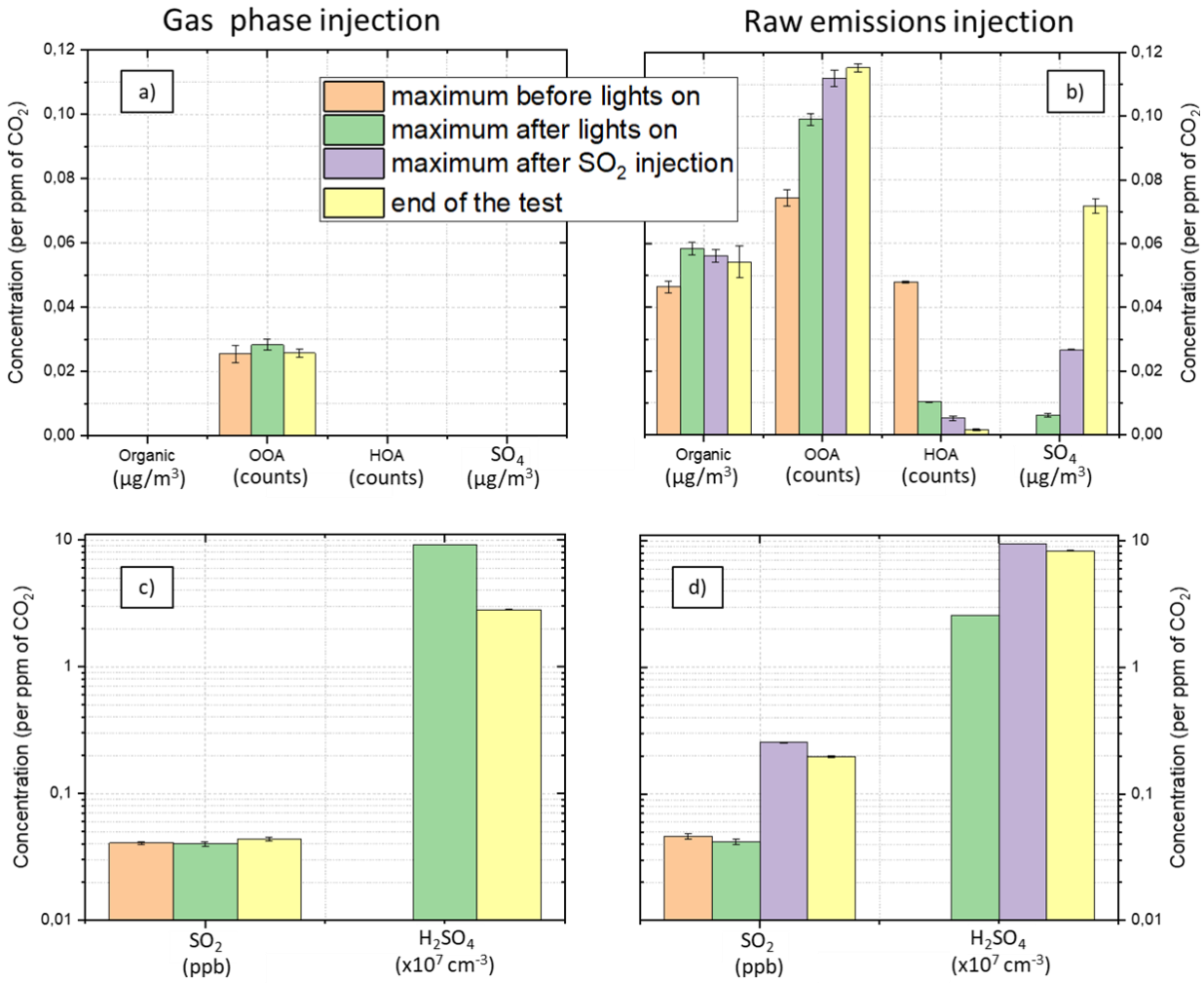

Chemical comparison of particle and gas phase after injection of CAST emissions without soot (left cases a and c) and after injection of raw emissions (right cases b and d) using Jet A-1 fuel. Organics and SO_4 concentrations (in µg/m^3) are represented in cases a and b depending on the presence of soot. OOA and HOA are organics fragments and correspond respectively to Oxygenated Organics Aerosols and Hydrocarbon Organics Aerosols (expressed in counts). The figures c and d present the evolution of SO_2 and H_2SO_4 concentrations at different moments of the test: before (orange) and after (green) light activation, after SO_2 injection (purple) and at the end of the experiment (yellow). All values have been corrected for dilution and normalised by their respective CO_2 concentration.

For the test with soot particles, the HOA concentration decreases when OOA concentration increases over the time. After light activation, the HOA concentration decreases (-0.037 counts) more than OOA concentration increases (+0.025 counts) due to absorption of HOA on the soot surface in addition to the oxidation process. Then after SO_2 injection, the increase of OOA concentration is higher (+0.013 counts) than the decrease of HOA concentration (-0.005 counts) due to formation of new particles.

Annex R: Growth rate calculation depending on the sulphuric acid concentration for gas phase injection and raw emissions injection cases (Jet A-1 fuel).

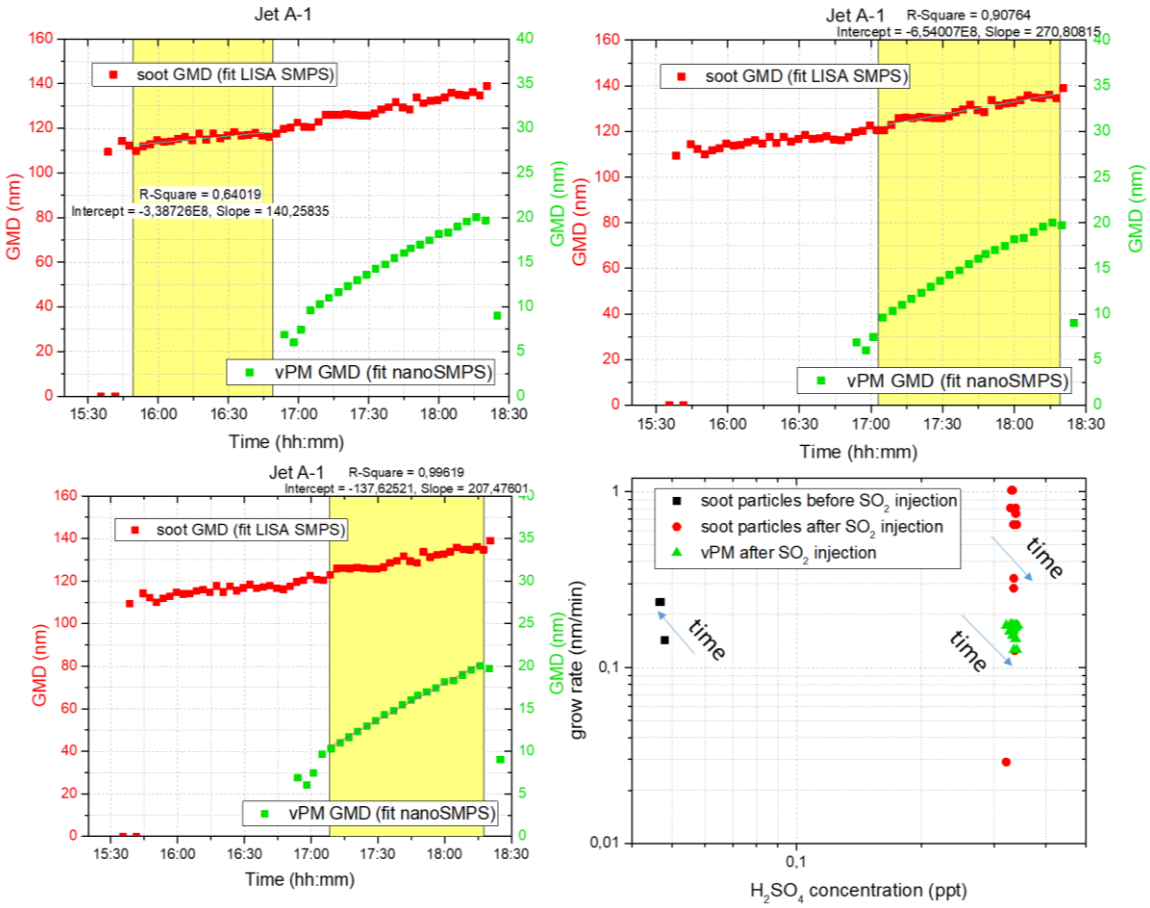

Based on the GMD obtained and fitted for both cases (with Jet A-1 fuel), it is possible to express the growth rate of particles formed in the chamber as a function of the H_2SO_4 concentration.

A first test has been done for the raw emission injection case to observe the impact of lights and SO_2 injection on vPM formation. GMD values have been interpolated by linear fit to get all the GMD values over the time (per minutes): for soot before SO_2 injection, for soot after SO_2 injection and for vPM after SO_2 injection. Then the growth rate is calculated (in nm/min) and plotted depending on the H_2SO_4 concentration (in ppt here) for a stable period during the test (i.e. stabilisation after the peak of sulphuric acid for light activation and after the peak of sulphuric acid for SO_2 injection). The first observation is that the growth rate of the soot before and after SO_2 injection is different. The soot particles at the end of the test present a higher growth rate (increase of the GMD) for higher H_2SO_4 concentration. It can be noted that the growth rate for soot particles makes no real sense. The vPM formed after sulphur injection have a smaller growth rate than the soot for the same case. The values are scattered due to the interpolation.

To get a better representation, a second test has been done to fit by a linear equation the GMD according to the stable sulphuric acid concentration period (Figure below). The first part of the figure presents the fitted curves. For the case “soot injection stable before SO_2 (soot)”, the period of stability of sulphuric acid was short due to the injection of SO_2 just after. Moreover, for the case “soot injection stable after SO_2 (soot)”, the GMD increases per step, given a bad coefficient R^2 for a linear fit. After that, the growth rate is estimated per hour and the bottom part of the following Figure presents the comparison of growth rate calculated by interpolation and by fitted mode depending on sulphuric acid concentration. The main difference is that values of growth rate are less dispersed using the fitted mode. It is better to compare these data to the literature (Lehtipalo et al., 2016a).

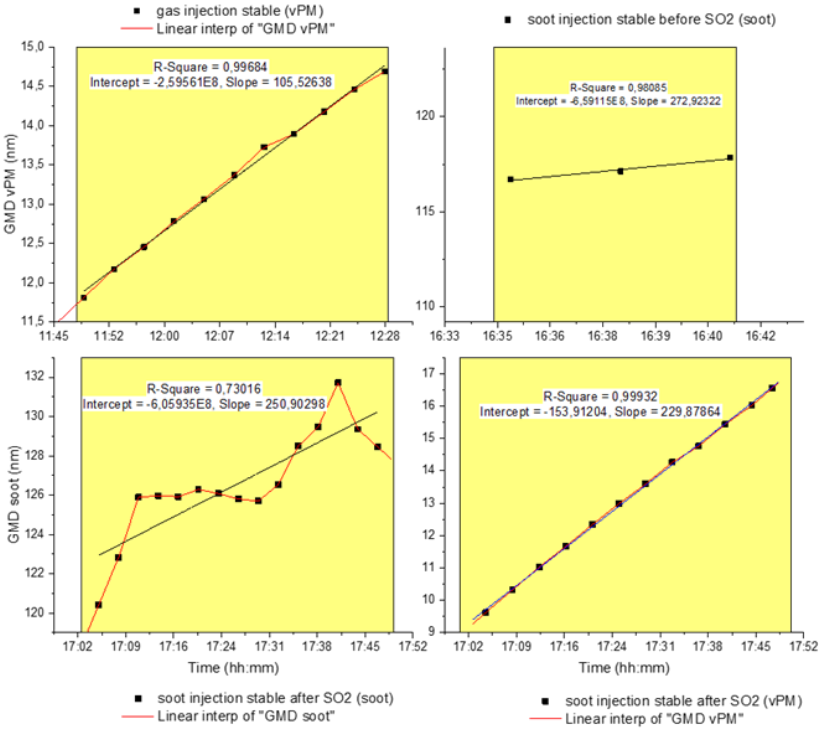
gas injection stable (vPM)
Linear interp of "GMD vPM"
R-Square = 0,99684
Intercept = -2,59561E8, Slope = 105,52638
GMD vPM (nm)
soot injection stable before SO2 (soot)
R-Square = 0,98085
Intercept = -6,59115E8, Slope = 272,92322
R-Square = 0,73016
Intercept = -6,05935E8, Slope = 250,90298
GMD soot (nm)
R-Square = 0,99932
Intercept = -153,91204, Slope = 229,87864
Time (hh:mm)
soot injection stable after SO2 (soot)
Linear interp of "GMD soot"
soot injection stable after SO2 (vPM)
Linear interp of "GMD vPM"

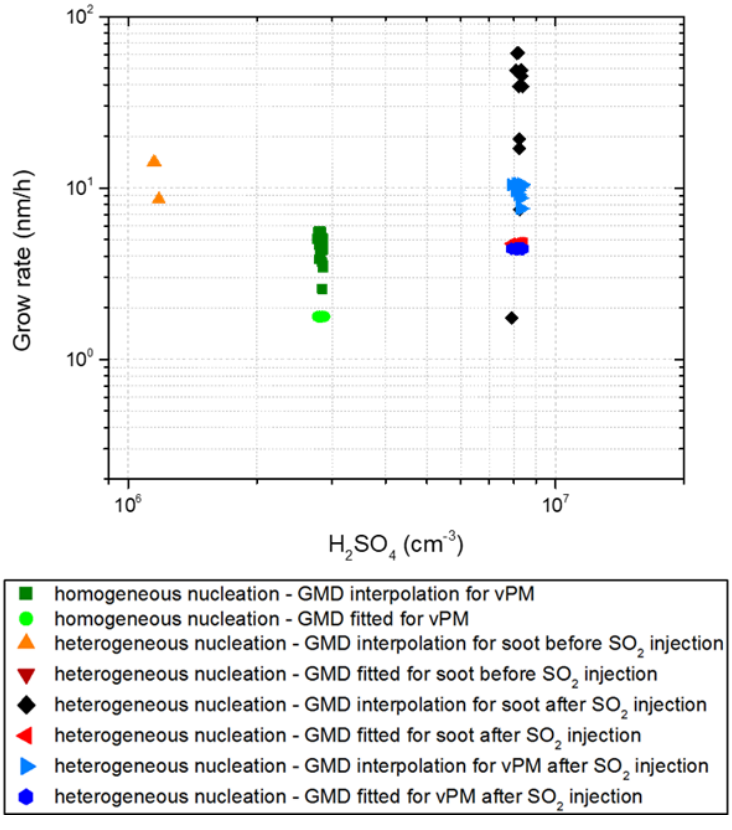
Grow rate (nm/h)
H_2SO_4 (cm^{-3})
homogeneous nucleation - GMD interpolation for vPM
homogeneous nucleation - GMD fitted for vPM
heterogeneous nucleation - GMD interpolation for soot before SO_2 injection
heterogeneous nucleation - GMD fitted for soot before SO_2 injection
heterogeneous nucleation - GMD interpolation for soot after SO_2 injection
heterogeneous nucleation - GMD fitted for soot after SO_2 injection
heterogeneous nucleation - GMD interpolation for vPM after SO_2 injection
heterogeneous nucleation - GMD fitted for vPM after SO_2 injection

Annex S: Comparison of vPM formation depending on the fuel tested with an adapted concentration scale for each case.

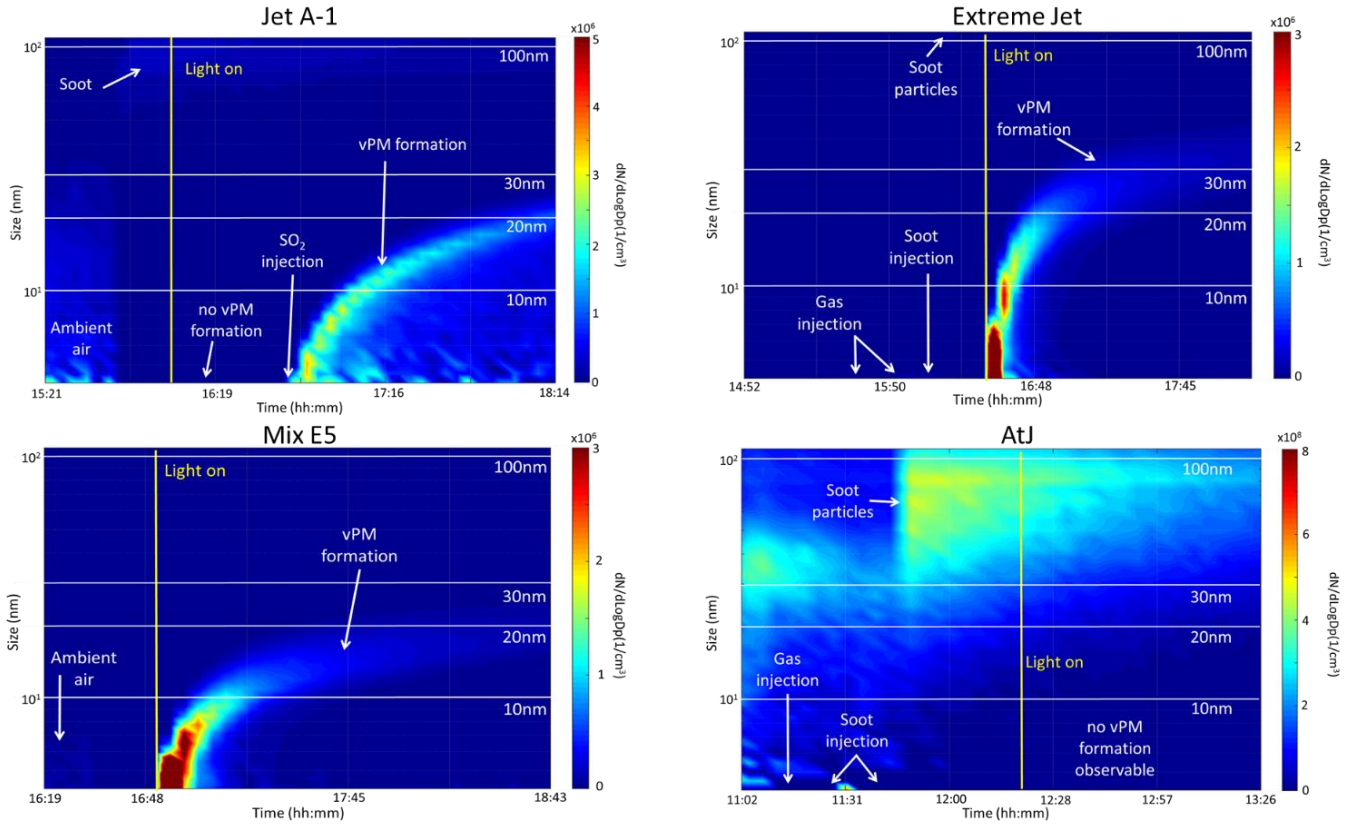

These figures present variations of new particles formed in terms of size and number concentrations for 4 different fuels. Particle concentration scale is adapted for each representations to visualise the vPM formation without image saturation:

- From 0 to $5x10^6$ part/cm^3 for the Jet A-1;
- From 0 to $3x10^6$ part/cm^3 for the Extreme Jet;
- From 0 to $3x10^6$ part/cm^3 for the mix E5;
- From 0 to $8x10^8$ part/cm^3 for the AtJ.

Annex T: Comparison of vPM formation depending on the fuel tested with a low concentration scale for each case.

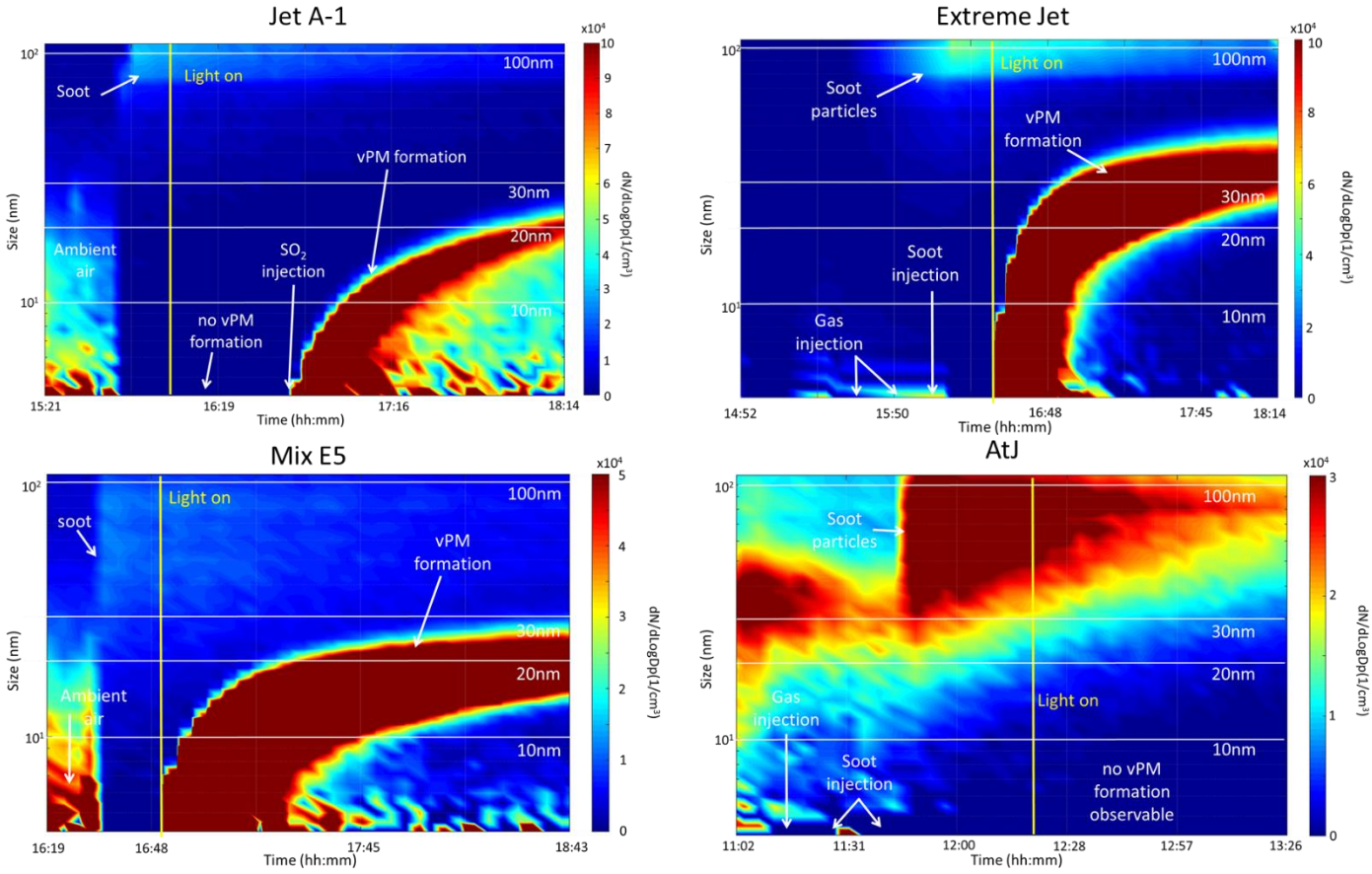

These figures present variations of new particles formed in terms of size and number concentrations for 4 different fuels. Particle concentration scale is adapted for each representation to visualise any signal related to vPM formation (saturation of the images):

- From 0 to 10x10^4 part/cm^3 for the Jet A-1;
- From 0 to 10x10^4 part/cm^3 for the Extreme Jet;
- From 0 to 5x10^4 part/cm^3 for the mix E5;
- From 0 to 3x10^4 part/cm^3 for the AtJ.

Annex U: Organic, sulphate and nitrate concentrations comparison in the CESAM chamber depending on the fuel tested for raw emissions injection case.

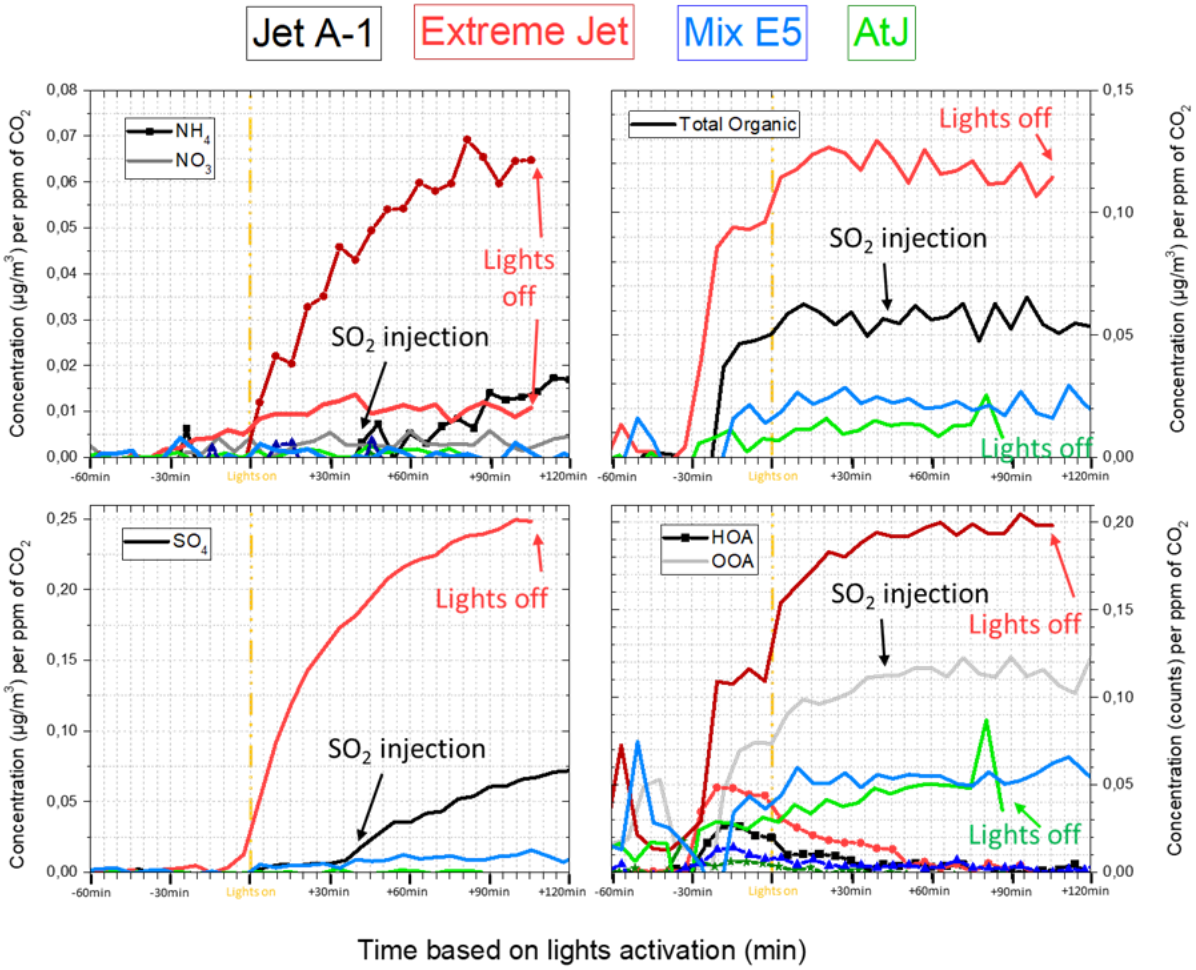

The representation is centred on light activation indicated in yellow. Data have been corrected for dilution and normalised by respective CO_2 concentration.

Organics concentration increases after light activation in the CESAM chamber for all cases using different fuel compositions. This Figure gives some details about sulphate, nitrate and organic concentrations over the time for the different tests done. The Jet A-1 data are represented in black, the Extreme Jet data are represented in red, the Mix E5 data are represented in blue and the AtJ data are represented in green. All values have been corrected for dilution and normalised by respective CO_2 concentrations. Each case has been centred on the light activation to compare the particle phase chemical composition over the experiment.

Concerning nitrate and ammonia, a signal is recorded only for the Extreme Jet case and their concentrations increase after light activation (high amount of NH_3 formed by photochemistry). After SO_2 injection, NH_4 molecules are also formed in the chamber for the Jet A-1 case.

Concerning the SO_4 in the chamber, signal is detected right after light activation for Extreme Jet (high increase of the concentration) and for Jet A-1 just after SO_2 injection. Really small signal is observed for the Mix E5 test.

Concerning total organic compounds, they are injected at the beginning of the test with soot emissions and their concentration increases in all cases after light activation. Details of oxygenated organics OOA and hydrogenated organics HOA concentration variations are also presented. In accordance with total organic concentration increase OOA concentration increases with the decrease

of HOA concentration (oxidation of organic compounds). The Extreme Jet and the Jet A-1 cases generate more OOA fragments than the other tests.

Organic fragments (second Figure) corresponding to (CO_2^+), ($C_2H_3^+$), ($C_4H_9^+$+$C_3H_5O^+$) and ($C_2H_4O_2^+$) mass fractions can be assimilated to different notations respectively: f43, f44, f57 and f60.

There are few variations over the time: f57 and f60 concentrations decrease after light activations according to the decrease of hydrogenated organics concentrations and then remain constant. The concentrations of f43 and f44 organic fragments increase over the time (higher slope for f44) after light activation, according to the increase of oxygenated organic concentrations.

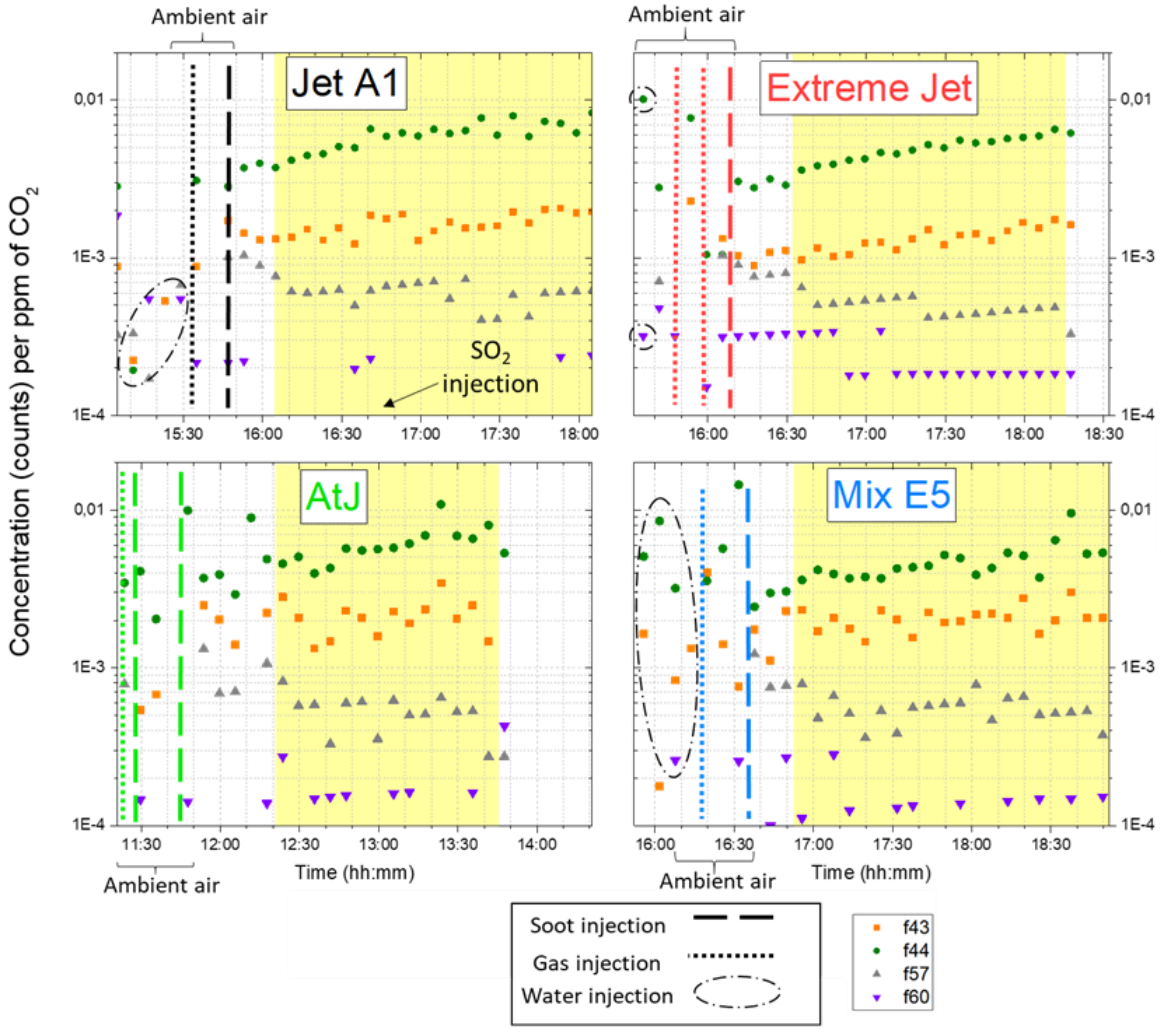

Annex V: Comparison of gas compounds evolution in the CESAM chamber for different fuels tested depending on the light activation.

Extracted Mass average (with H+)	Identification		Raw emissions injection							
			Before Lights ON				After Lights ON			
m/z	Name	Formula	Extreme Jet	JetA-1	MixE5	AtJ	Extreme Jet	JetA-1	MixE5	AtJ
29,04	Ethylene	C_2H_4								
31,02	Formaldehyde	CH_2O								
33,03	Methanol	CH_3OH								
42,03	Acetonitrile	C_2H_3N								
43,02	Ketene	C_2H_2O								
43,06	Propene	C_3H_6								
44,01	Cyanic acid	CHNO								
44,05	Ethanimine	C_2H_5N								
45,03	Acetaldehyde	C_2H_4O								
45,06	Propane	C_3H_8								
45,99	Formate	CHO_2								
46,03	Formamide	CH_3NO								
46,07	Ethylamine	C_2H_7N								
47,01	Formic Acid	CH_2O_2								
47,04	Ethanol	C_2H_5OH								
49,06	Ethane Hydrate	C_2H_8O								
51,99	Sulphane Hydroxide	H_3OS								
59,04	Acetone C3H6O/ Methyl Vinyl Ether	C_3H_6O								
61,2	Acetic acid	CH_3COOH								
62,1	Trimethyloxonium	C_3H_9O								
63	Nitrate	NO_3								
65,06	Pyramidane	C_5H_4								
66,12	Butanol d9	$C_4H_{10}O$								
71,02	Methyl Vinyl Ketone	C_4H_6O								
75,02	Hydroxyacetone	$C_3H_6O_2$								
93,06	Toluene	C_7H_8								
177,1	Cyclopent-acenaphthylene	$C_{14}H_8$								

Few gaseous compounds have been recorded and identified during the experiment. This table summarises the compounds identified in the gas phase with significant variations (increase/decrease) in the CESAM chamber for the four fuels tested. Gas analysis using a PTR-MS in CESAM chamber depending on the fuel used after raw emissions injection. The mass average takes into account the additional hydrogen ion. The green colour indicates the presence of compounds; in red the concentration of the compound is decreasing; in blue the concentration is increasing and in white there is no change.

Annex W: Details about Size distributions and GMD of particles for Extreme Jet fuel to compare gas phase injection and raw emissions injection cases.

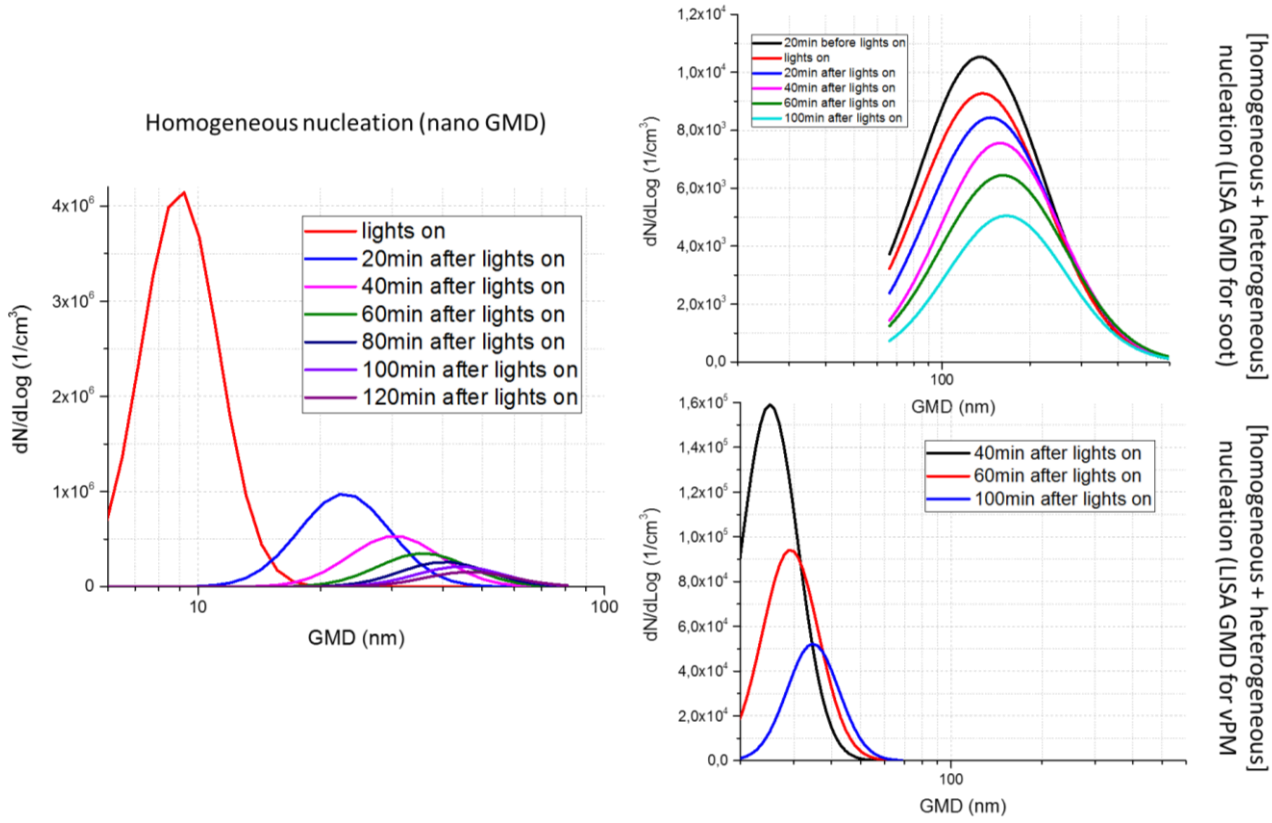

On the first Figure, size distribution of new vPM formed for comparison of nucleation cases with Extreme Jet fuel. On the left, homogeneous nucleation case for gas phase injection and on the right raw emissions injection case (for soot and for vPM). Concerning the vPM, their size increases with time (for both SMPS) and the particle concentration decreases. The same trend is observable for soot particles.

Gas injection case (second Figure) and raw emissions case (third Figure) correspond respectively to the GMD calculated for the both nucleation cases. For each representation, fitted GMD (green for vPM and red for soot) are compared to total GMD estimated by instruments (nano and LISA SMPS).

For the gas phase injection case, the fitted and total GMD for vPM are similar in the case of LISA SMPS but differences are presented in the nanoSMPS case. Indeed, in the LISA SMPS case, particles have a size over 20 nm to be recorded so the total GMD does not take into account small particles at the limit of detection or in the noise/ background signal contrary to nanoSMPS. The fitted process avoids the parasite signal and gives the GMD for principal vPM formed and observable on the “banana plot”.

For the raw emissions injection case, the fit allows the separation between soot and vPM formed in the LISA SMPS case compared to the total GMD. Concerning the nanoSMPS, the fit and raw GMDs are more similar than for the other nucleation case. vPM formed are smaller than for homogeneous nucleation cases.

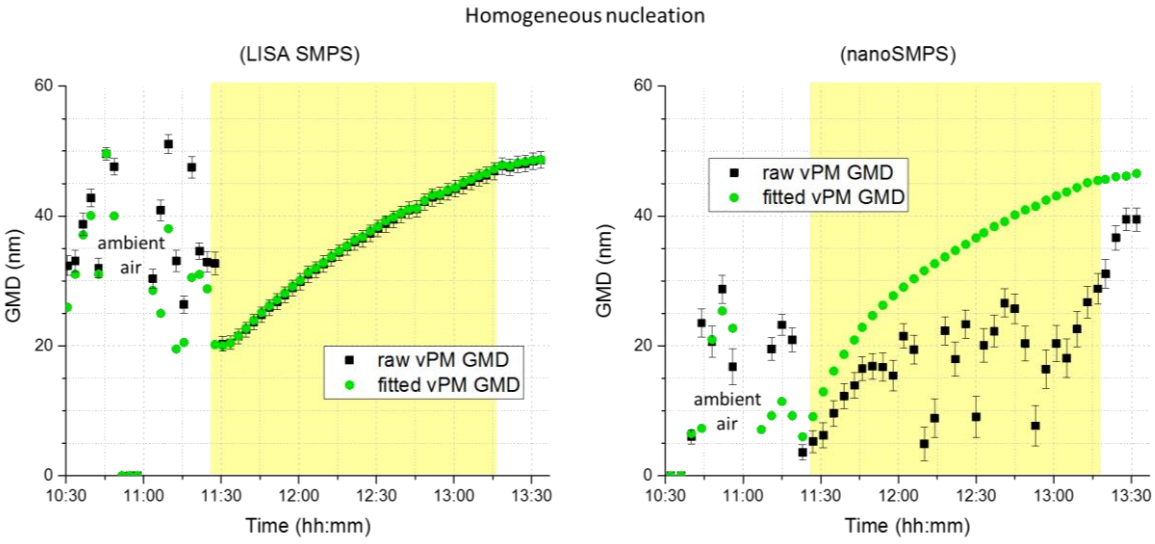

Comparison of fitted GMD (green) with total GMD (black) for vPM obtained after gas phase injection for Extreme Jet fuel. On the left, the LISA SMPS data and on the right the nanoSMPS data.

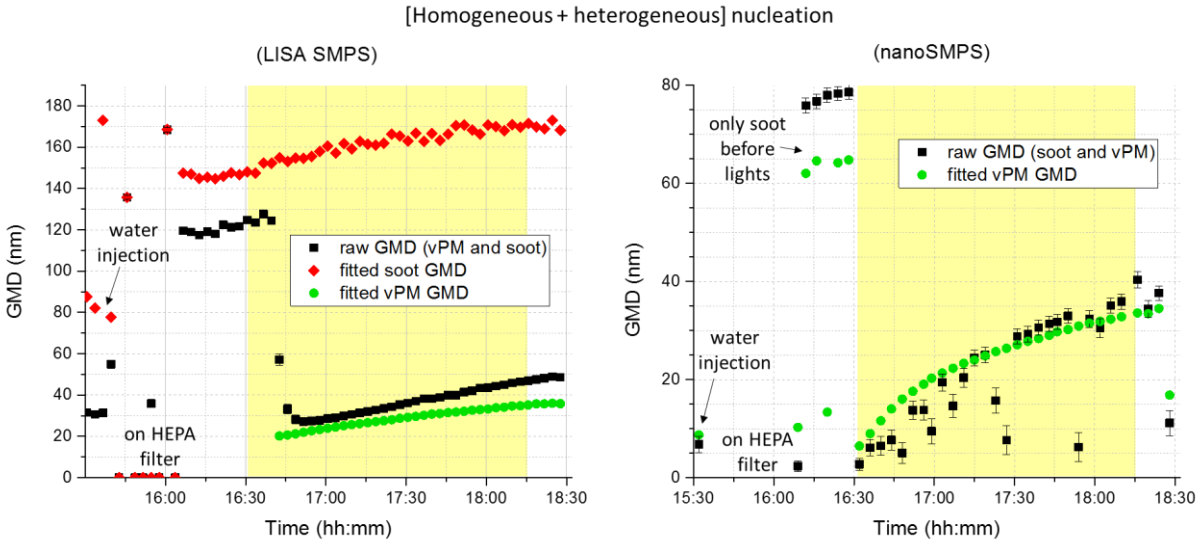

Comparison of fitted soot (red) and fitted vPM GMDs (green) with total GMD (black) after raw emissions injection for Extreme Jet fuel. On the left, the LISA SMPS data and on the right the nanoSMPS data.

Annex X: Comparison of vPM formation event using CESAM chamber and PAM-OFR.

A test has been done with gas phase injection (3h in CESAM chamber and simulation of 12 days of atmospheric oxidation with the PAM-OFR). The main difference between the two devices is that for CESAM chamber test emissions are injected punctually and then are exposed to light (OH concentration from $2x10^6$ to $2x10^7$ molecules.cm^{-3}) to follow their evolution. In the case of PAM, the OH exposure is fixed (in the range 10^{10}-10^{12} molecules.cm^{-3} to simulate 0.5 to 15 days of atmospheric oxidation) and emissions are introduced continuously.

Emissions after oxidation in CESAM atmospheric chamber are compared with emissions after oxidation through PAM-OFR and preliminary results show that in both cases vPM formation is observed (without dilution correction). The OH exposure and the injection process are different between CESAM chamber and PAM-OFR, so some differences can be noted concerning the particle concentration that is constant for PAM due to continuous injection and decreases for CESAM test due to agglomeration of particles. Despite these differences, it has been observed that for comparison tests using different fuels with variations in terms of aromatics and sulphur contents, the trends remain the same: more particles and higher GMD for fuels with higher sulphur and aromatic contents in their composition compared to fuels with low aromatic and sulphur contents.

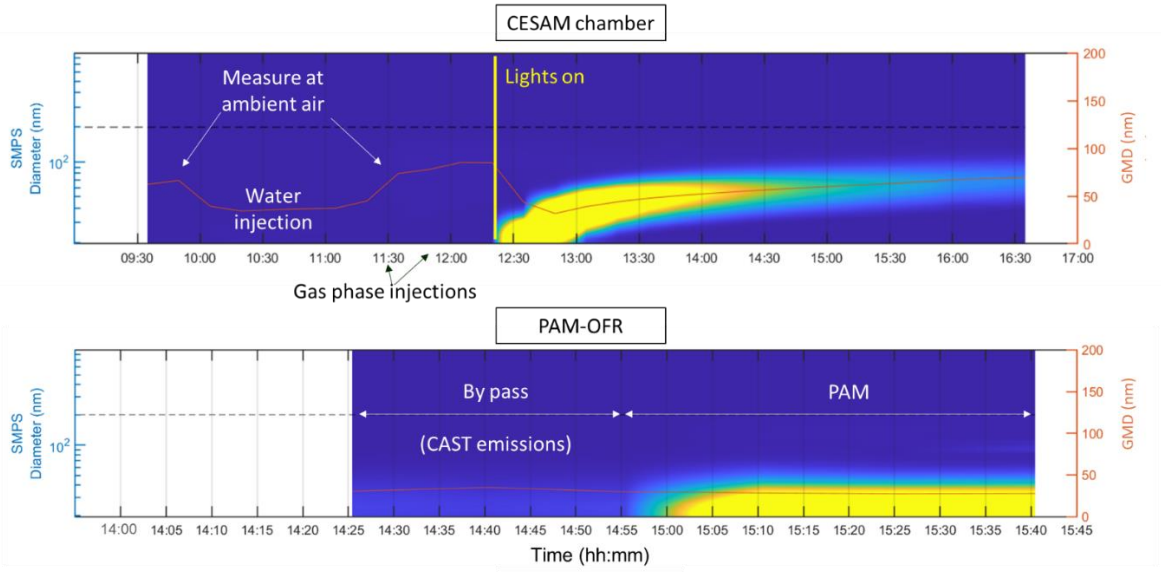

This graph represents the particle formation after oxidation of the emissions for CESAM chamber (with Xenon lamps – top figure) and for PAM-OFR (UV lamps – bottom figure) experiments after gas phase injection (HR-AMS). The fuel tested is the same: Extreme Jet fuel (best candidate for vPM formation process). Two gas phase injections have been done for the CESAM chamber test and light activation is specified by yellow line. As the particles evolved in the atmospheric chamber, the CAST is connected to the FPS diluter and to the installation bypass/PAM-OFR. The switch between bypass and PAM-OFR is indicated on the bottom graph. The OH exposure in the PAM-OFR is $4.01x10^{12}$ molecules/cm^3.s corresponding to 14.6 days of atmospheric oxidation.

The main difference is that the size of new particles formed increases and that particle concentration decreases for CESAM chamber case compared to PAM case. At the end of the test, the particle size reaches 64 nm for CESAM chamber test but remains constant at 27 nm for PAM-OFR test. It is explained by the fact that experiment in CESAM chamber evolves over the time (coagulation and agglomeration of vPM) while in PAM the OH exposure is fixed and emissions are introduced continuously.

BIBLIOGRAPHY

Abis, L., Loubet, B., Ciuraru, R., Lafouge, F., Dequiedt, S., Houot, S., Maron, P. A., & Bourgeteau-Sadet, S. (2018). Profiles of volatile organic compound emissions from soils amended with organic waste products. *Science of The Total Environment*, *636*, 1333–1343. https://doi.org/10.1016/j.scitotenv.2018.04.232

Aerodyne_ACSM. (n.d.). Aerosol Chemical Speciation Monitor. *Aerodyne*. Retrieved 7 August 2022, from https://www.aerodyne.com/product/aerosol-chemical-speciation-monitor/

Agarwal, A., Speth, R. L., Fritz, T. M., Jacob, S. D., Rindlisbacher, T., Iovinelli, R., Owen, B., Miake-Lye, R. C., Sabnis, J. S., & Barrett, S. R. H. (2019). SCOPE11 Method for Estimating Aircraft Black Carbon Mass and Particle Number Emissions. *Environmental Science & Technology*, *53*(3), 1364–1373. https://doi.org/10.1021/acs.est.8b04060

AIRBUS SAF. (2021, September 1). *An A350 fuelled by 100% SAF just took off | Airbus*. https://www.airbus.com/en/newsroom/stories/2021-03-an-a350-fuelled-by-100-saf-just-took-off

Airbus ZEROe project. (2022). *ZEROe—Zero emission—Airbus*. https://www.airbus.com/en/innovation/zero-emission/hydrogen/zeroe

Albrecht, S. R., Novelli, A., Hofzumahaus, A., Kang, S., Baker, Y., Mentel, T., Wahner, A., & Fuchs, H. (2019). Measurements of hydroperoxy radicals (HO_2) at atmospheric concentrations using bromide chemical ionisation mass spectrometry. *Atmospheric Measurement Techniques*, *12*(2), 891–902. https://doi.org/10.5194/amt-12-891-2019

Almeida, J., Schobesberger, S., Kürten, A., Ortega, I. K., Kupiainen-Määttä, O., Praplan, A. P., Adamov, A., Amorim, A., Bianchi, F., Breitenlechner, M., David, A., Dommen, J., Donahue, N. M., Downard, A., Dunne, E., Duplissy, J., Ehrhart, S., Flagan, R. C., Franchin, A., … Kirkby, J. (2013). Molecular understanding of sulphuric acid–amine particle nucleation in the atmosphere. *Nature*, *502*(7471), Article 7471. https://doi.org/10.1038/nature12663

Alvarez-Láinez, M., Lasprilla, J., & Noreña-Caro, D. (2014, March 20). *Virtual Concept International Workshop 2014 Innovation on Product design and manufacture, Medellin, Colombia SMART FILTERS MADE FROM POLYMER NANOFIBERS*. https://doi.org/10.13140/2.1.4971.8080

Amanatidis, S., Ntziachristos, L., Giechaskiel, B., Katsaounis, D., Samaras, Z., & Bergmann, A. (2013). Evaluation of an oxidation catalyst ("catalytic stripper") in eliminating volatile material from combustion aerosol. *Journal of Aerosol Science*, *57*, 144–155. https://doi.org/10.1016/j.jaerosci.2012.12.001

Arnold, F., Kiendler, A., Wiedemer, V., Aberle, S., Stilp, T., & Busen, R. (2000). Chemiion concentration measurements in jet engine exhaust at the ground: Implications for ion chemistry and aerosol formation in the wake of a jet aircraft. *Geophysical Research Letters*, *27*(12), 1723–1726. https://doi.org/10.1029/1999GL011096

ASTM D1655. (2022). *Standard Specification for Aviation Turbine Fuels*. https://www.astm.org/d1655-22a.html

ASTM D6379. (2021). *Standard Test Method for Determination of Aromatic Hydrocarbon Types in Aviation Fuels and Petroleum Distillates—High Performance Liquid Chromatography Method with Refractive Index Detection*. https://www.astm.org/d6379-21e01.html

ASTM D7042. (2021). *Standard Test Method for Dynamic Viscosity and Density of Liquids by Stabinger Viscometer (and the Calculation of Kinematic Viscosity)*. https://www.astm.org/d7042-21a.html

ASTM D7566. (2009). *ASTM D 7566: 2009 Standard Specification for Aviation Turbine Fu*. https://infostore.saiglobal.com/en-us/standards/astm-d-7566-2009-158110_saig_astm_astm_386596/

Atkinson, R. (2000). Atmospheric chemistry of VOCs and NO(x). *Atmospheric Environment*, *34*(12–14), 2063–2101. Scopus. https://doi.org/10.1016/S1352-2310(99)00460-4

ATMO-ACCESS. (2020). *Atmospheric simulation chambers*. Facilities. https://www.atmo-access.eu/atmospheric-simulation-chambers/

Aubagnac-Karkar, D., El Bakali, A., & Desgroux, P. (2018). Soot particles inception and PAH condensation modelling applied in a soot model utilizing a sectional method. *Combustion and Flame*, *189*, 190–206. https://doi.org/10.1016/j.combustflame.2017.10.027

Aviation Fuel Quality Requirements for Jointly Operated Systems. (2020). *CERTIFICATE OF ANALYSIS*.

AVIATOR. (2020). *AVIATOR Project: Assessing aViation emission Impact on local Air quality at airports: TOwards Regulation – Grant Agreement No. 814801*. https://aviatorproject.eu/

Babayi, F., Pakravan, M., Maassoumi, A. A., & Tavasoli, A. (2012). PALYNOLOGICAL STUDY OF SALIX L. (SALICACEAE) IN IRAN. *Iran. J. Bot.*, *18*, 118-126.

Bahreini, R. (2003). Aircraft-based aerosol size and composition measurements during ACE-Asia using an Aerodyne aerosol mass spectrometer. *Journal of Geophysical Research*, *108*(D23), 8645. https://doi.org/10.1029/2002JD003226

Balthasar, M. (2000). Detailed Soot Modelling in Laminar and Turbulent Reacting Flows. [Thesis/doccomp, Lund University]. In *Lund Reports on Combustion Physics* (Vol. 59). http://lup.lub.lu.se/record/40688

Bari, Md. A., Baumbach, G., Kuch, B., & Scheffknecht, G. (2010). Particle-phase concentrations of polycyclic aromatic hydrocarbons in ambient air of rural residential areas in southern Germany. *Air Quality, Atmosphere, & Health*, *3*(2), 103–116. https://doi.org/10.1007/s11869-009-0057-8

Barmet, P., Dommen, J., DeCarlo, P. F., Tritscher, T., Praplan, A. P., Platt, S. M., Prévôt, A. S. H., Donahue, N. M., & Baltensperger, U. (2012). OH clock determination by proton transfer reaction mass spectrometry at an environmental chamber. *Atmospheric Measurement Techniques*, *5*(3), 647–656. https://doi.org/10.5194/amt-5-647-2012

Baron, P. A., & Klaus, W. (2002). Aerosol Measurement: Principles, Techniques, and Applications. Second Edition Edited by Paul A. Baron (National Institute for Occupational Safety and Health) and Klaus Willeke (University of Cincinnati). Wiley-Interscience: New York. 2001. xxiv + 1132

pp. $195.00. ISBN: 0-471-35636-0. *Journal of the American Chemical Society*, *124*(18), 5251–5251. https://doi.org/10.1021/ja015375e

Ben Amara, A., Kaoubi, S., & Starck, L. (2016). Toward an optimal formulation of alternative jet fuels: Enhanced Oxidation and Thermal Stability by the addition of cyclic molecules. *Fuel*, *173*, 98–105. https://doi.org/10.1016/j.fuel.2016.01.040

Berruyer, O. (2017, January 24). *2. La Pollution aux particules fines*. Les-Crises.fr. https://www.les-crises.fr/la-pollution-aux-particules-fines/

Berthier, A. (2022). *Impact de la composition du carburant sur les émissions aéronautiques, une approche multi-échelles* [Thèse]. https://www.theses.fr/2022ULILR019

Betrancourt, C., Liu, F., Desgroux, P., Mercier, X., Faccinetto, A., Salamanca, M., Ruwe, L., Kohse-Höinghaus, K., Emmrich, D., Beyer, A., Gölzhäuser, A., & Tritscher, T. (2017). Investigation of the Size of the Incandescent Incipient Soot Particles in Premixed Sooting and Nucleation Flames of n -Butane Using LII, HIM, and 1nm-SMPS. *Aerosol Science and Technology*, *51*. https://doi.org/10.1080/02786826.2017.1325440

Beyersdorf, A. J., Timko, M. T., Ziemba, L. D., Bulzan, D., Corporan, E., Herndon, S. C., Howard, R., Miake-Lye, R., Thornhill, K. L., Winstead, E., Wey, C., Yu, Z., & Anderson, B. E. (2014). Reductions in aircraft particulate emissions due to the use of Fischer–Tropsch fuels. *Atmospheric Chemistry and Physics*, *14*(1), 11–23. https://doi.org/10.5194/acp-14-11-2014

Bianchi, F., Kurtén, T., Riva, M., Mohr, C., Rissanen, M. P., Roldin, P., Berndt, T., Crounse, J. D., Wennberg, P. O., Mentel, T. F., Wildt, J., Junninen, H., Jokinen, T., Kulmala, M., Worsnop, D. R., Thornton, J. A., Donahue, N., Kjaergaard, H. G., & Ehn, M. (2019). Highly Oxygenated Organic Molecules (HOM) from Gas-Phase Autoxidation Involving Peroxy Radicals: A Key Contributor to Atmospheric Aerosol. *Chemical Reviews*, *119*(6), 3472–3509. https://doi.org/10.1021/acs.chemrev.8b00395

Bladh, H., Olofsson, N.-E., Mouton, T., Simonsson, J., Mercier, X., Faccinetto, A., Bengtsson, P.-E., & Desgroux, P. (2015). Probing the smallest soot particles in low-sooting premixed flames using

laser-induced incandescence. *Proceedings of the Combustion Institute*, *35*(2), 1843–1850. https://doi.org/10.1016/j.proci.2014.06.001

Blake, R., Monks, P., & Ellis, A. M. (2008). Proton transfer reaction mass spectrometry. *Spectroscopy Europe*, *24*, 17–20.

Bockhorn, H., & Schäfer, T. (1994). Growth of Soot Particles in Premixed Flames by Surface Reactions. In H. Bockhorn (Ed.), *Soot Formation in Combustion: Mechanisms and Models* (pp. 253–274). Springer. https://doi.org/10.1007/978-3-642-85167-4_14

Boesl, U. (2017). Time-of-flight mass spectrometry: Introduction to the basics. *Mass Spectrometry Reviews*, *36*(1), 86–109. https://doi.org/10.1002/mas.21520

Borghi, R., & Destriau, M. (1995). *La combustion et les flammes*. https://www.decitre.fr/livres/la-combustion-et-les-flammes-9782710806844.html

Boucher, O., & Randall, D. (2013). *Clouds and Aerosols* (CLimate Change 2013: The Physical Science Basis). Cambridge University Press, Cambridge, UK, and NY, USA; eds. Stocker, T. F. et al. https://www.ipcc.ch/report/ar5/wg1/

Boulon, J., Sellegri, K., Katrib, Y., Wang, J., Miet, K., Langmann, B., Laj, P., & Doussin, J.-F. (2013). Sub-3 nm Particles Detection in a Large Photoreactor Background: Possible Implications for New Particles Formation Studies in a Smog Chamber. *Aerosol Science and Technology*, *47*(2), 153–157. https://doi.org/10.1080/02786826.2012.733040

Bouvier, Y. (2006). *Caractérisation de suies et de précurseurs de suies dans des flammes par incandescence induite par laser* [Thèse de doctorat, Université Lille 1 - Sciences et technologies]. https://www.sudoc.abes.fr/cbs/xslt/DB=2.1//SRCH?IKT=12&TRM=103268960

Brem, B. T., Durdina, L., Siegerist, F., Beyerle, P., Bruderer, K., Rindlisbacher, T., Rocci-Denis, S., Andac, M. G., Zelina, J., Penanhoat, O., & Wang, J. (2015). Effects of Fuel Aromatic Content on Nonvolatile Particulate Emissions of an In-Production Aircraft Gas Turbine. *Environmental Science & Technology*, *49*(22), 13149–13157. https://doi.org/10.1021/acs.est.5b04167

Brown, R. C., Miake-Lye, R. C., Anderson, M. R., Kolb, C. E., & Resch, T. J. (1996). Aerosol dynamics in near-field aircraft plumes. *Journal of Geophysical Research: Atmospheres*, *101*(D17), 22939–22953. https://doi.org/10.1029/96JD01918

Budisulistiorini, S., Canagaratna, M., Croteau, P., Marth, W., Baumann, K., Edgerton, E., Shaw, S., Knipping, E., Worsnop, D., Jayne, J., Gold, A., & Surratt, J. (2013). Real-time Continuous Characterization of Secondary Organic Aerosol Derived from Isoprene Epoxydiols (IEPOX) in Downtown Atlanta, Georgia, using the Aerodyne Aerosol Chemical Speciation Monitor (ACSM). *Environmental Science & Technology*, *47*. https://doi.org/10.1021/es400023n

Burg. (2014). *Airparif Actualité n°42—Décembre 2014—Le carbone suie: Enjeu présent et futur | Airparif*. https://www.airparif.asso.fr/dossiers-fiches-thematiques/2014/airparif-actus-le-carbone-suie-enjeu-present-et-futur

Cao, J., Wang, Q., Li, L., Zhang, Y., Tian, J., Chen, L. W. A., Ho, S. S. H., Wang, X., Chow, J. C., & Watson, J. G. (2020). Evaluation of the Oxidation Flow Reactor for particulate matter emission limit certification. *Atmospheric Environment*, *224*, 117086. https://doi.org/10.1016/j.atmosenv.2019.117086

Carbone, F., Attoui, M., & Gomez, A. (2016). Challenges of measuring nascent soot in flames as evidenced by high-resolution differential mobility analysis. *Aerosol Science and Technology*, *50*(7), 740–757. https://doi.org/10.1080/02786826.2016.1179715

Cazorla, A., Bahadur, R., Suski, K., Cahill, J., Chand, D., Schmid, B., Ramanathan, V., & Prather, K. (2013). Relating aerosol absorption due to soot, organic carbon, and dust to emission sources determined from in-situ chemical measurements. *Atmospheric Chemistry & Physics Discussions*, *13*, 3451–3483. https://doi.org/10.5194/acpd-13-3451-2013

CESAM_EUROCHAMP. (2020). *CESAM | Eurochamp*. https://www.eurochamp.org/simulation-chambers/CESAM

Chen, M., Titcombe, M., Jiang, J., Jen, C., Kuang, C., Fischer, M. L., Eisele, F. L., Siepmann, J. I., Hanson, D. R., Zhao, J., & McMurry, P. H. (2012). Acid–base chemical reaction model for nucleation

rates in the polluted atmospheric boundary layer. *Proceedings of the National Academy of Sciences*, *109*(46), 18713–18718. https://doi.org/10.1073/pnas.1210285109

Cheng, X., Chen, Q., Jie Li, Y., Zheng, Y., Liao, K., & Huang, G. (2021). Highly oxygenated organic molecules produced by the oxidation of benzene and toluene in a wide range of OH exposure and NO_x conditions. *Atmospheric Chemistry and Physics*, *21*(15), 12005–12019. https://doi.org/10.5194/acp-21-12005-2021

Chernushevich, I. V., Merenbloom, S. I., Liu, S., & Bloomfield, N. (2017). A W-Geometry Ortho-TOF MS with High Resolution and Up to 100% Duty Cycle for MS/MS. *Journal of The American Society for Mass Spectrometry*, *28*(10), 2143–2150. https://doi.org/10.1007/s13361-017-1742-8

Cochet, A., Bodoc, V., Brossard, C., Dessornes, O., Guin, C., Lecourt, R., Orain, M., & Vincent-Randonnier, A. (2016). *ONERA Test Facilities for Combustion in Aero Gas Turbine Engines, and Associated Optical Diagnostics*. https://doi.org/10.12762/2016.AL11-01

Corbin, J. C., Schripp, T., Anderson, B. E., Smallwood, G. J., LeClercq, P., Crosbie, E. C., Achterberg, S., Whitefield, P. D., Miake-Lye, R. C., Yu, Z., Freedman, A., Trueblood, M., Satterfield, D., Liu, W., Oßwald, P., Robinson, C., Shook, M. A., Moore, R. H., & Lobo, P. (2022). Aircraft-engine particulate matter emissions from conventional and sustainable aviation fuel combustion: Comparison of measurement techniques for mass, number, and size. *Atmospheric Measurement Techniques*, *15*(10), 3223–3242. https://doi.org/10.5194/amt-15-3223-2022

Corporan, E., DeWitt, M. J., Belovich, V., Pawlik, R., Lynch, A. C., Gord, J. R., & Meyer, T. R. (2007). Emissions Characteristics of a Turbine Engine and Research Combustor Burning a Fischer−Tropsch Jet Fuel. *Energy & Fuels*, *21*(5), 2615–2626. https://doi.org/10.1021/ef070015j

Corporan, E., Edwards, T., Shafer, L., DeWitt, M. J., Klingshirn, C., Zabarnick, S., West, Z., Striebich, R., Graham, J., & Klein, J. (2011). Chemical, Thermal Stability, Seal Swell, and Emissions Studies of Alternative Jet Fuels. *Energy & Fuels*, *25*(3), 955–966. https://doi.org/10.1021/ef101520v

Corporan, E., Reich, R., Monroig, O., DeWitt, M., Larson, V., Aulich, T., Mann, M., & Seames, W. (2005). Impacts of Biodiesel on Pollutant Emissions of a JP-8–Fueled Turbine Engine. *Journal of the Air & Waste Management Association (1995)*, *55*, 940–949. https://doi.org/10.1080/10473289.2005.10464680

CORSIA. (2022). *Carbon Offsetting and Reduction Scheme for International Aviation (CORSIA)*. https://www.icao.int/environmental-protection/CORSIA/Pages/default.aspx

Crayford, A., Johnson, M., Marsh, R., Sevcenco, Y., Walters, D., Williams, P., Christie, S., Chung, W., Petzold, A., Ibrahim, A., Delhaye, D., Quincey, P., Bowen, P., Coe, H., Raper, D., & Wilson, C. (2011). *SAMPLE III: Contribution to aircraft engine PM certification requirement and standard. Final Report*. https://www.researchgate.net/publication/263651454_SAMPLE_III_Contribution_to_aircraft_engine_PM_certification_requirement_and_standard_Final_Report

Crounse, J. D., Nielsen, L. B., Jørgensen, S., Kjaergaard, H. G., & Wennberg, P. O. (2013). Autoxidation of Organic Compounds in the Atmosphere. *The Journal of Physical Chemistry Letters*, *4*(20), 3513–3520. https://doi.org/10.1021/jz4019207

Crump, J. G., & Seinfeld, J. H. (1981). Turbulent deposition and gravitational sedimentation of an aerosol in a vessel of arbitrary shape. *Journal of Aerosol Science*, *12*(5), 405–415. https://doi.org/10.1016/0021-8502(81)90036-7

Curtius, J. (2006). Nucleation of atmospheric aerosol particles. *Comptes Rendus Physique*, *7*(9), 1027–1045. https://doi.org/10.1016/j.crhy.2006.10.018

Dahl, J. (2008). *Jet engine*. https://de.wikipedia.org/wiki/Datei:Jet_engine.svg

Daoudi, M., Schiffmann, P., Faccinetto, A., Frobert, A., & Desgroux, P. (2023). Comprehensive characterization of particulate matter emissions produced by a liquid-fueled miniCAST burner. *Aerosol Science and Technology*, *57*(9), 872–889. https://doi.org/10.1080/02786826.2023.2228372

DeCarlo, P. F., Kimmel, J. R., Trimborn, A., Northway, M. J., Jayne, J. T., Aiken, A. C., Gonin, M., Fuhrer, K., Horvath, T., Docherty, K. S., Worsnop, D. R., & Jimenez, J. L. (2006). Field-deployable, high-resolution, time-of-flight aerosol mass spectrometer. *Analytical Chemistry*, *78*(24), 8281–8289. https://doi.org/10.1021/ac061249n

Defence Standard 91-091. (2019). *Turbine Fuel , Kerosene Type, Jet A 1; NATO Code: F35; Joint Service Designation: AVTUR*. chrome-extension://efaidnbmnnnibpcajpcglclefindmkaj/http://inaca.or.id/wp-content/uploads/2019/11/Def-Stan-91-091-Issue-11-Oct-2019-Turbine-Fuel-Kerosene-Type-Jet-A-1-NATO-CodeF-35-Joint-Service-Designation-AVTUR.pdf

Dekati_dilution. (n.d.). *Dekati Ltd. - Leading provider of fine particle measurement solutions*. Dekati Ltd. Retrieved 1 August 2022, from https://www.dekati.com/

Delhaye, D., Ouf, F.-X., Ferry, D., Ortega, I. K., Penanhoat, O., Peillon, S., Salm, F., Vancassel, X., Focsa, C., Irimiea, C., Harivel, N., Perez, B., Quinton, E., Yon, J., & Gaffie, D. (2017). The MERMOSE project: Characterization of particulate matter emissions of a commercial aircraft engine. *Journal of Aerosol Science*, *105*, 48–63. https://doi.org/10.1016/j.jaerosci.2016.11.018

Desgroux, P., Faccinetto, A., Mercier, X., Mouton, T., Aubagnac Karkar, D., & El Bakali, A. (2017). Comparative study of the soot formation process in a “nucleation” and a “sooting” low pressure premixed methane flame. *Combustion and Flame*, *184*, 153–166. https://doi.org/10.1016/j.combustflame.2017.05.034

Desgroux, P., Mercier, X., & Thomson, K. A. (2013). Study of the formation of soot and its precursors in flames using optical diagnostics. *Proceedings of the Combustion Institute*, *34*(1), 1713–1738. https://doi.org/10.1016/j.proci.2012.09.004

Deutscher Wetterdienst. (2015). *Wetter und Klima—Deutscher Wetterdienst—Particle Size-Distribution*. https://www.dwd.de/EN/research/observing_atmosphere/composition_atmosphere/aerosol/cont_nav/particle_size_distribution_node.html

DeWitt, M., Corporan, E., Graham, J. L., & Minus, D. (2008). Effects of Aromatic Type and Concentration in Fischer− Tropsch Fuel on Emissions Production and Material Compatibility. *Energy & Fuels*, *22*. https://doi.org/10.1021/ef8001179

Di Biagio, C., Formenti, P., Balkanski, Y., Caponi, L., Cazaunau, M., Pangui, E., Journet, E., Nowak, S., Caquineau, S., Andreae, M., Kandler, K., Saeed, T., Piketh, S., Seibert, D., Williams, E., & Doussin, J.-F. (2017). Global scale variability of the mineral dust long-wave refractive index: A new dataset of in situ measurements for climate modeling and remote sensing. *Atmospheric Chemistry and Physics*, *17*, 1901–1929. https://doi.org/10.5194/acp-17-1901-2017

Di Biagio, C., Formenti, P., Styler, S. A., Pangui, E., & Doussin, J.-F. (2014). Laboratory chamber measurements of the longwave extinction spectra and complex refractive indices of African and Asian mineral dusts: IN SITU MINERAL DUST LONGWAVE EXTINCTION. *Geophysical Research Letters*, *41*(17), 6289–6297. https://doi.org/10.1002/2014GL060213

Donahue, N., Ortega, I., Chuang, W., Riipinen, I., Riccobono, F., Schobesberger, S., Dommen, J., Baltensperger, U., Kulmala, M., Worsnop, D., & Vehkamaki, H. (2013). How do organic vapors contribute to new-particle formation? *Faraday Discussions*, *165*, 91–104. https://doi.org/10.1039/C3FD00046J

Duca, D. (2020). *Physico-chemical characterization of size-selected internal combustion engine nanoparticles and original method for measuring adsorption energies on carbonaceous surfaces by laser mass spectrometry* [These de doctorat, Université de Lille (2018-2021)]. http://www.theses.fr/2020LILUR019

Duca, D., Irimiea, C., Faccinetto, A., Noble, J., Vojković, M., Carpentier, Y., Ortega, I., Pirim, C., & Focsa, C. (2019). On the benefits of using multivariate analysis in mass spectrometric studies of combustion-generated aerosols. *Faraday Discussions*, *218*. https://doi.org/10.1039/C8FD00238J

Duca, D., Rahman, M., Carpentier, Y., Pirim, C., Boies, A., & Focsa, C. (2021). Chemical characterization of size-selected nanoparticles emitted by a gasoline direct injection engine: Impact of a catalytic stripper. *Fuel*, *294*, 120317. https://doi.org/10.1016/j.fuel.2021.120317

Duporté, G., Flaud, P.-M., Geneste, E., Augagneur, S., Pangui, E., Lamkaddam, H., Gratien, A., Doussin, J.-F., Budzinski, H., Villenave, E., & Perraudin, E. (2016). Experimental Study of the Formation of Organosulfates from α-Pinene Oxidation. Part I: Product Identification, Formation Mechanisms and Effect of Relative Humidity. *The Journal of Physical Chemistry A*, *120*(40), 7909–7923. https://doi.org/10.1021/acs.jpca.6b08504

Durdina, L., Brem, B. T., Schönenberger, D., Siegerist, F., Anet, J. G., & Rindlisbacher, T. (2019). Nonvolatile Particulate Matter Emissions of a Business Jet Measured at Ground Level and Estimated for Cruising Altitudes. *Environmental Science & Technology*, *53*(21), 12865–12872. https://doi.org/10.1021/acs.est.9b02513

EASA. (2022). *European Aviation Environmental Report 2022: Sustainability crucial for long-term viability of the sector*. EASA Eco. https://www.easa.europa.eu/eco/eaer

Eaves, N. A., Dworkin, S. B., & Thomson, M. J. (2015). The importance of reversibility in modeling soot nucleation and condensation processes. *Proceedings of the Combustion Institute*, *35*(2), 1787–1794. https://doi.org/10.1016/j.proci.2014.05.036

Ebbinghaus, A., & Wiesen, P. (2001). Aircraft fuels and their effect upon engine emissions. *Air & Space Europe*, *3*(1), 101–103. https://doi.org/10.1016/S1290-0958(01)90026-7

EEA. (2021). *Air quality in Europe 2021—European Environment Agency* [Briefing]. https://www.eea.europa.eu/publications/air-quality-in-europe-2021/

Environment S.A. (2010). *AF22 Module Technical Manuel: UV fluorescent, sulfur dioxide analyzer.* http://www.environnement-sa.com

Erupe, M. E., Viggiano, A. A., & Lee, S.-H. (2011). The effect of trimethylamine on atmospheric nucleation involving H_2SO_4. *Atmospheric Chemistry and Physics*, *11*(10), 4767–4775. https://doi.org/10.5194/acp-11-4767-2011

Ess, M. N., Bertò, M., Irwin, M., Modini, R. L., Gysel-Beer, M., & Vasilatou, K. (2021). Optical and morphological properties of soot particles generated by the miniCAST 5201 BC generator. *Aerosol Science and Technology*, *55*(7), 828–847. https://doi.org/10.1080/02786826.2021.1901847

Ess, M. N., & Vasilatou, K. (2019). Characterization of a new miniCAST with diffusion flame and premixed flame options: Generation of particles with high EC content in the size range 30 nm to 200 nm. *Aerosol Science and Technology*, *53*(1), 29–44. https://doi.org/10.1080/02786826.2018.1536818

European Commission. (2020, April 21). *European Commission* [Text]. European Commission - Have your say. https://ec.europa.eu/info/law/better-regulation/have-your-say/initiatives/12303-Carburants-durables-pour-laviation-ReFuelEU-Aviation_fr

European Commission. (2021). *COMMUNICATION FROM THE COMMISSION TO THE EUROPEAN PARLIAMENT, THE COUNCIL, THE EUROPEAN ECONOMIC AND SOCIAL COMMITTEE AND THE COMMITTEE OF THE REGIONS EMPTY Pathway to a Healthy Planet for All*. https://eur-lex.europa.eu/legal-content/EN/TXT/?uri=CELEX%3A52021DC0400&qid=1623311742827

Faccinetto, A. (2009). *High sensitivity detection of polycyclic aromatic hydrocarbons desorbed from soot particles using laser desorption/laser ionisation/time-of-flight mass spectrometry. An approach for studying the soot growth process in flames.* https://www.researchgate.net/publication/281292611_High_sensitivity_detection_of_polycyclic_aromatic_hydrocarbons_desorbed_from_soot_particles_using_laser_desorptionlaser_ionisationtime-of-flight_mass_spectrometry_An_approach_for_studying_the_soot_gro

Faccinetto, A., Focsa, C., Desgroux, P., & Ziskind, M. (2015). Progress toward the Quantitative Analysis of PAHs Adsorbed on Soot by Laser Desorption/Laser Ionization/Time-of-Flight Mass Spectrometry. *Environmental Science & Technology*. https://doi.org/10.1021/acs.est.5b02703

Focsa, C., Mihesan, C., Ziskind, M., Chazallon, B., Therssen, E., Desgroux, P., & Destombes, J. (2006). Wavelength-selective vibrationally excited photodesorption with tunable IR sources. *Journal of Physics: Condensed Matter*, *18*, S1357. https://doi.org/10.1088/0953-8984/18/30/S02

Frenklach, M. (2002). Reaction mechanism of soot formation in flames. *Physical Chemistry Chemical Physics*, *4*(11), 2028–2037. https://doi.org/10.1039/b110045a

Frenklach, M., & Wang, H. (1991). Detailed modeling of soot particle nucleation and growth. *Symposium (International) on Combustion*, *23*(1), 1559–1566. https://doi.org/10.1016/S0082-0784(06)80426-1

Fuchs, N. A. (1963). On the stationary charge distribution on aerosol particles in a bipolar ionic atmosphere. *Geofisica Pura e Applicata*, *56*(1), 185–193. https://doi.org/10.1007/BF01993343

Garmash, O., Rissanen, M. P., Pullinen, I., Schmitt, S., Kausiala, O., Tillmann, R., Zhao, D., Percival, C., Bannan, T. J., Priestley, M., Hallquist, Å. M., Kleist, E., Kiendler-Scharr, A., Hallquist, M., Berndt, T., McFiggans, G., Wildt, J., Mentel, T. F., & Ehn, M. (2020). Multi-generation OH oxidation as a source for highly oxygenated organic molecules from aromatics. *Atmospheric Chemistry and Physics*, *20*(1), 515–537. https://doi.org/10.5194/acp-20-515-2020

Giechaskiel, B., Melas, A., Lähde, T., & Martini, G. (2020). Non-Volatile Particle Number Emission Measurements with Catalytic Strippers: A Review. *Vehicles*, *2*, 342–364. https://doi.org/10.3390/vehicles2020019

GIFAS. (2023). *Publication de la feuille de route « Article 301 » de décarbonation de l'aérien*. GIFAS. https://www.gifas.fr/news/publication-de-la-feuille-de-route-article-301-de-decarbonation-de-l-aerien

Goethe University. (n.d.). *Goethe-Universität—Nitrate CI-APi-TOF*. Retrieved 21 February 2023, from https://www.goethe-university-frankfurt.de/65565008/nitrate_CI_APi_TOF

Graham, J., Rahmes, T., & Vannice, W. (2013). *Impact of Alternative Jet Fuel and Fuel Blends on Non-Metallic Materials Used in Commercial Aircraft Fuel Systems*.

Green Car Congress. (2018). *PNNL technology, LanzaTech delivering on alcohol-to-jet synthetic paraffinic kerosene*. Green Car Congress. https://www.greencarcongress.com/2018/06/20180612-pnnl.html

Greenwalt, D. E., Goreva, Y. S., Siljeström, S. M., Rose, T., & Harbach, R. E. (2013). Hemoglobin-derived porphyrins preserved in a Middle Eocene blood-engorged mosquito. *Proceedings of the National Academy of Sciences of the United States of America*, *110*(46), 18496–18500. https://doi.org/10.1073/pnas.1310885110

Grimm-Aerosol. (2012). *Condensation Particle Counter Model 5.403*. https://www.bodc.ac.uk/data/documents/nodb/pdf/grimm_5403_cpc.pdf

Grimm_CPC. (n.d.). *CPC*. Retrieved 6 August 2022, from https://www.grimm-aerosol.com/products-en/nanoparticle-counters/cpc/

Grimm_SMPS+C. (n.d.). *SMPS+C*. Retrieved 6 August 2022, from https://www.grimm-aerosol.com/products-en/nanoparticle-sizers/smps-c/

Grimm_SMPS+E. (n.d.). *SMPS+E*. Retrieved 6 August 2022, from https://www.grimm-aerosol.com/products-en/nanoparticle-sizers/smps-e/57055706/

Grimonprez, S., Wu, J., Faccinetto, A., Gosselin, S., Riber, E., Cuenot, B., Cazaunau, M., Pangui, E., Formenti, P., Doussin, J.-F., Petitprez, D., & Desgroux, P. (2021). Hydrophilic properties of soot particles exposed to OH radicals: A possible new mechanism involved in the contrail formation. *Proceedings of the Combustion Institute*, *38*(4), 6441–6450. https://doi.org/10.1016/j.proci.2020.06.306

Grobler, C., Wolfe, P. J., Dasadhikari, K., Dedoussi, I. C., Allroggen, F., Speth, R. L., Eastham, S. D., Agarwal, A., Staples, M. D., Sabnis, J., & Barrett, S. R. H. (2019). Marginal climate and air quality costs of aviation emissions. *Environmental Research Letters*, *14*(11), 114031. https://doi.org/10.1088/1748-9326/ab4942

Guo, H., Wei, J., Li, X., Ho, H. C., Song, Y., Wu, J., & Li, W. (2021). Do socioeconomic factors modify the effects of PM1 and SO2 on lung cancer incidence in China? *Science of The Total Environment*, *756*, 143998. https://doi.org/10.1016/j.scitotenv.2020.143998

Gutiérrez-Antonio, C., Gómez-Castro, F. I., de Lira-Flores, J. A., & Hernández, S. (2017). A review on the production processes of renewable jet fuel. *Renewable and Sustainable Energy Reviews*, *79*, 709–729. https://doi.org/10.1016/j.rser.2017.05.108

Gysel, M., Nyeki, S., Weingartner, E., Baltensperger, U., Giebl, H., Hitzenberger, R., Petzold, A., & Wilson, C. W. (2003). Properties of jet engine combustion particles during the PartEmis experiment: Hygroscopicity at subsaturated conditions. *Geophysical Research Letters*, *30*(11). https://doi.org/10.1029/2003GL016896

Haider, K., Lafouge, F., Carpentier, Y., HOUOT, S., Petitprez, D., Loubet, B., Focsa, C., & Ciuraru, R. (2022). Chemical identification and quantification of volatile organic compounds emitted by sewage sludge. *Science of The Total Environment*, *838*, 155948. https://doi.org/10.1016/j.scitotenv.2022.155948

Hatfield, J. L., Sauer, T. J., & Prueger, J. H. (2005). RADIATION BALANCE. In D. Hillel (Ed.), *Encyclopedia of Soils in the Environment* (pp. 355–359). Elsevier. https://doi.org/10.1016/B0-12-348530-4/00407-0

He, Q. F. (2015). *Characterization of Organosulfates and Organonitrates in the Pearl River Delta (PRD) Region, South China*. Guangzhou Institute of Geochemistry, Chinese Academy of Sciences.

Heinritzi, M., Simon, M., Steiner, G., Wagner, A. C., Kürten, A., Hansel, A., & Curtius, J. (2016). Characterization of the mass-dependent transmission efficiency of a CIMS. *Atmospheric Measurement Techniques*, *9*(4), 1449–1460. https://doi.org/10.5194/amt-9-1449-2016

Heintzenberg, J., Wehner, B., & Birmili, W. (2007). 'How to find bananas in the atmospheric aerosol': New approach for analyzing atmospheric nucleation and growth events. *Tellus B*, *59*(2), 273–282. https://doi.org/10.1111/j.1600-0889.2007.00249.x

Hewitt, C. N., & Harrison, R. M. (1985). Tropospheric concentrations of the hydroxyl radical—A review. *Atmospheric Environment (1967)*, *19*(4), 545–554. https://doi.org/10.1016/0004-6981(85)90033-2

Heyder, J. (2004). Deposition of Inhaled Particles in the Human Respiratory Tract and Consequences for Regional Targeting in Respiratory Drug Delivery. *Proceedings of the American Thoracic Society*, *1*(4), 315–320. https://doi.org/10.1513/pats.200409-046TA

Heyne, J., Rauch, B., Le Clercq, P., & Colket, M. (2021). Sustainable aviation fuel prescreening tools and procedures. *Fuel*, *290*, 120004. https://doi.org/10.1016/j.fuel.2020.120004

Hileman, J. I., & Stratton, R. W. (2014). Alternative jet fuel feasibility. *Transport Policy*, *34*, 52–62. https://doi.org/10.1016/j.tranpol.2014.02.018

Hinds, W. C., & Zhu, Y. (1982). *Aerosol Technology: Properties, Behavior, and Measurement of Airborne Particles, 3rd Edition | Wiley*. Wiley.Com. https://www.wiley.com/en-us/Aerosol+Technology%3A+Properties%2C+Behavior%2C+and+Measurement+of+Airborne+Particles%2C+3rd+Edition-p-9781119494041

Homann, K.-H., & Wagner, H. G. (1996). *Dynamics of Exothermicity*. CRC Press.

Hoyle, C. R., Boy, M., Donahue, N. M., Fry, J. L., Glasius, M., Guenther, A., Hallar, A. G., Huff Hartz, K., Petters, M. D., Petäjä, T., Rosenoern, T., & Sullivan, A. P. (2011). A review of the anthropogenic influence on biogenic secondary organic aerosol. *Atmospheric Chemistry and Physics*, *11*(1), 321–343. Scopus. https://doi.org/10.5194/acp-11-321-2011

Huang, M., Xu, J., Cai, S., Liu, X., Hu, C., Gu, X., Zhao, W., Fang, L., & Zhang, W. (2018). Chemical analysis of particulate products of aged 1,3,5-trimethylbenzene secondary organic aerosol in the presence of ammonia. *Atmospheric Pollution Research*, *9*(1), 146–155. Scopus. https://doi.org/10.1016/j.apr.2017.08.003

Hudda, N., Durant, L. W., Fruin, S. A., & Durant, J. L. (2020). Impacts of Aviation Emissions on Near-Airport Residential Air Quality. *Environmental Science & Technology*, *54*(14), 8580–8588. https://doi.org/10.1021/acs.est.0c01859

Hudda, N., & Fruin, S. A. (2016). International Airport Impacts to Air Quality: Size and Related Properties of Large Increases in Ultrafine Particle Number Concentrations. *Environmental Science & Technology*, *50*(7), 3362–3370. https://doi.org/10.1021/acs.est.5b05313

Hudda, N., Gould, T., Hartin, K., Larson, T. V., & Fruin, S. A. (2014). Emissions from an International Airport Increase Particle Number Concentrations 4-fold at 10 km Downwind. *Environmental Science & Technology*, *48*(12), 6628–6635. https://doi.org/10.1021/es5001566

Hussar, E., Richards, S., Lin, Z.-Q., Dixon, R. P., & Johnson, K. A. (2012). Human Health Risk Assessment of 16 Priority Polycyclic Aromatic Hydrocarbons in Soils of Chattanooga, Tennessee, USA. *Water, Air, and Soil Pollution*, *223*(9), 5535–5548. https://doi.org/10.1007/s11270-012-1265-7

IATA. (2023). *Airline Profitability Outlook Strengthens*. https://www.iata.org/en/pressroom/2023-releases/2023-06-05-01/

ICAO. (2016). *New particulate matter standard for aircraft gas turbine engines* [Environnemental Report ICAO]. chrome-extension://efaidnbmnnnibpcajpcglclefindmkaj/https://www.icao.int/environmental-protection/Documents/EnvironmentalReports/2016/ENVReport2016_pg85-88.pdf

ICAO. (2017). *Annex 16—Environmental Protection—Volume II - Aircraft Engine Emissions*. ICAO. https://store.icao.int/en/annex-16-environmental-protection-volume-ii-aircraft-engine-emissions

ICAO. (2018). *ICAO Sustainable aviation Fuel Guide*. https://icao.int/environmental-protection/Documents/Sustainable%20Aviation%20Fuels%20Guide_100519.pdf.

ICAO. (2022). *ICAO Environmental Report 2022*. https://www.icao.int/environmental-protection/Pages/envrep2022.aspx

ICAO. (2023). *Assembly—All Documents*. https://www.icao.int/environmental-protection/Documents/Forms/AllItems.aspx?RootFolder=%2fenvironmental%2dprotection%2fDocuments%2fAssembly&FolderCTID=0x01200048E70A3021A9504D98DF706482A68A4C

ICAO: CORSIA. (2022). *Carbon Offsetting and Reduction Scheme for International Aviation (CORSIA)*. https://www.icao.int/environmental-protection/CORSIA/Pages/default.aspx

ICAO: E-HAPI. (2022). *Electric and Hybrid Aircraft Platform for Innovation (E-HAPI)*. https://www.icao.int/environmental-protection/Pages/electric-aircraft.aspx

Ikhenazene, R., Pirim, C., Noble, J. A., Irimiea, C., Carpentier, Y., Ortega, I. K., Ouf, F.-X., Focsa, C., & Chazallon, B. (2020). Ice Nucleation Activities of Carbon-Bearing Materials in Deposition Mode: From Graphite to Airplane Soot Surrogates. *The Journal of Physical Chemistry C*, *124*(1), 489–503. https://doi.org/10.1021/acs.jpcc.9b08715

Imperial College London. (2023, November 28). *World's first transatlantic flight on 100% sustainable aviation fuel takes off | Imperial News | Imperial College London*. Imperial News. https://www.imperial.ac.uk/news/249753/worlds-first-transatlantic-flight-100-sustainable/

IPCC. (1999). *Aviation and the Global Atmosphere* (Penner, J.E., Lister, D.H., Griggs, D. J., Dokken, D.J., McFarland, M. (Eds.)). Intergovernmental Panel on Climate Change Special Report. Cambridge University Press, Cambridge, UK. https://www.ipcc.ch/report/aviation-and-the-global-atmosphere-2/

IPCC. (2013). *Working Group I*. ClimateChange.

Irimiea, C. (2017). *Characterization of soot particles and their precursors by coupling laser-based techniques* [These de doctorat, Lille 1]. http://www.theses.fr/2017LIL10066

Irimiea, C., Faccinetto, A., Carpentier, Y., Ortega, I.-K., Nuns, N., Therssen, E., Desgroux, P., & Focsa, C. (2018). A comprehensive protocol for chemical analysis of flame combustion emissions by secondary ion mass spectrometry. *Rapid Communications in Mass Spectrometry*, *32*(13), 1015–1025. https://doi.org/10.1002/rcm.8133

Irimiea, C., Faccinetto, A., Mercier, X., Ortega, I.-K., Nuns, N., Therssen, E., Desgroux, P., & Focsa, C. (2019). Unveiling trends in soot nucleation and growth: When secondary ion mass spectrometry meets statistical analysis. *Carbon*, *144*, 815–830. https://doi.org/10.1016/j.carbon.2018.12.015

Jayne, J. T., Leard, D. C., Zhang, X., Davidovits, P., Smith, K. A., Kolb, C. E., & Worsnop, D. R. (2000). Development of an Aerosol Mass Spectrometer for Size and Composition Analysis of Submicron Particles. *Aerosol Science and Technology*, *33*(1–2), 49–70. https://doi.org/10.1080/027868200410840

JETSCREEN Project. (2020). *JET Fuel SCREENing and Optimization | JETSCREEN Project | Fact Sheet | H2020 | CORDIS | European Commission*. https://cordis.europa.eu/project/id/723525/fr

Jimenez, J. L. (2003). Ambient aerosol sampling using the Aerodyne Aerosol Mass Spectrometer. *Journal of Geophysical Research*, *108*(D7), 8425. https://doi.org/10.1029/2001JD001213

Jing. (2009). *CAST Combustion Aerosol Standard*. http://www.sootgenerator.com/

Jing, L. (2003). CAST SOOT GENERATOR FOR LIQUID FUEL. . . *August*, 2.

Johansson, K. O., Dillstrom, T., Elvati, P., Campbell, M. F., Schrader, P. E., Popolan-Vaida, D. M., Richards-Henderson, N. K., Wilson, K. R., Violi, A., & Michelsen, H. A. (2017). Radical–radical reactions, pyrene nucleation, and incipient soot formation in combustion. *Proceedings of the Combustion Institute*, *36*(1), 799–806. https://doi.org/10.1016/j.proci.2016.07.130

Johansson, K. O., Dillstrom, T., Monti, M., El Gabaly, F., Campbell, M. F., Schrader, P. E., Popolan-Vaida, D. M., Richards-Henderson, N. K., Wilson, K. R., Violi, A., & Michelsen, H. A. (2016). Formation and emission of large furans and oxygenated hydrocarbons from flames. *Proceedings of the National Academy of Sciences*, *113*(30), 8374–8379. https://doi.org/10.1073/pnas.1604772113

Johansson, K. O., Head-Gordon, M. P., Schrader, P. E., Wilson, K. R., & Michelsen, H. A. (2018). Resonance-stabilized hydrocarbon-radical chain reactions may explain soot inception and growth. *Science (New York, N.Y.)*, *361*(6406), 997–1000. https://doi.org/10.1126/science.aat3417

Jonsdottir, H., Delaval, M., Leni, Z., Keller, A., Brem, B., Siegerist, F., Schönenberger, D., Durdina, L., Elser, M., Burtscher, H., Liati, A., & Geiser, M. (2019). Non-volatile particle emissions from

aircraft turbine engines at ground-idle induce oxidative stress in bronchial cells. *Communications Biology*, *2*, 90. https://doi.org/10.1038/s42003-019-0332-7

Junninen, H., Ehn, M., Petäjä, T., Luosujärvi, L., Kotiaho, T., Kostiainen, R., Rohner, U., Gonin, M., Fuhrer, K., Kulmala, M., & Worsnop, D. (2010). A high-resolution mass spectrometer to measure atmospheric ion composition. *Atmospheric Measurement Techniques*, *3*. https://doi.org/10.5194/amt-3-1039-2010

Kalbermatter, D. M., Močnik, G., Drinovec, L., Visser, B., Röhrbein, J., Oscity, M., Weingartner, E., Hyvärinen, A.-P., & Vasilatou, K. (2022). Comparing black-carbon- and aerosol-absorption-measuring instruments – a new system using lab-generated soot coated with controlled amounts of secondary organic matter. *Atmospheric Measurement Techniques*, *15*(2), 561–572. https://doi.org/10.5194/amt-15-561-2022

Kandaramath Hari, T., Yaakob, Z., & Binitha, N. N. (2015). Aviation biofuel from renewable resources: Routes, opportunities and challenges. *Renewable and Sustainable Energy Reviews*, *42*, 1234–1244. https://doi.org/10.1016/j.rser.2014.10.095

Kärcher, B. (2018). Formation and Radiative Forcing of Contrail Cirrus. *Nature Communications*, *9*. https://doi.org/10.1038/s41467-018-04068-0

Kärcher, B., & Fahey, D. W. (1997). The role of sulfur emission in volatile particle formation in jet aircraft exhaust plumes. *Geophysical Research Letters*, *24*(4), 389–392. https://doi.org/10.1029/97GL00119

Kärcher, B., Peter, Th., & Ottmann, R. (1995). Contrail formation: Homogeneous nucleation of H2SO4/H2O droplets. *Geophysical Research Letters*, *22*(12), 1501–1504. https://doi.org/10.1029/95GL01337

Keck, L., Spielvogel, J., & Grimm, H. (2009). From nanoparticles to large aerosols: Ultrafast measurement methods for size and concentration. *Journal of Physics: Conference Series*, *170*, 012007. https://doi.org/10.1088/1742-6596/170/1/012007

Kelesidis, G. A., Goudeli, E., & Pratsinis, S. E. (2017). Morphology and mobility diameter of carbonaceous aerosols during agglomeration and surface growth. *Carbon*, *121*, 527–535. https://doi.org/10.1016/j.carbon.2017.06.004

Kelesidis, G. A., & Pratsinis, S. E. (2019). Estimating the internal and surface oxidation of soot agglomerates. *Combustion and Flame*, *209*, 493–499. https://doi.org/10.1016/j.combustflame.2019.08.001

Kim, K.-H., Jahan, S. A., Kabir, E., & Brown, R. J. C. (2013). A review of airborne polycyclic aromatic hydrocarbons (PAHs) and their human health effects. *Environment International*, *60*, 71–80. https://doi.org/10.1016/j.envint.2013.07.019

Kinsey, J., Dong, Y., Williams, D., & Logan, R. (2010). Physical characterization of the fine particle emissions from commercial aircraft engines during the Aircraft Particle Emissions eXperiment (APEX) 1–3. *Atmospheric Environment*, *44*, 2147–2156. https://doi.org/10.1016/j.atmosenv.2010.02.010

Kirkby, J., Curtius, J., Almeida, J., Dunne, E., Duplissy, J., Ehrhart, S., Franchin, A., Gagné, S., Ickes, L., Kürten, A., Kupc, A., Metzger, A., Riccobono, F., Rondo, L., Schobesberger, S., Tsagkogeorgas, G., Wimmer, D., Amorim, A., Bianchi, F., … Kulmala, M. (2011). Role of sulphuric acid, ammonia and galactic cosmic rays in atmospheric aerosol nucleation. *Nature*, *476*(7361), Article 7361. https://doi.org/10.1038/nature10343

Kirkby, J., Duplissy, J., Sengupta, K., Frege, C., Gordon, H., Williamson, C., Heinritzi, M., Simon, M., Yan, C., Almeida, J., Tröstl, J., Nieminen, T., Ortega, I., Wagner, R., Adamov, A., Amorim, A., Bernhammer, A.-K., Bianchi, F., Breitenlechner, M., & Curtius, J. (2016). Ion-induced nucleation of pure biogenic particles. *Nature*, *533*, 521–526. https://doi.org/10.1038/nature17953

Kılıç, D., El Haddad, I., Brem, B. T., Bruns, E., Bozetti, C., Corbin, J., Durdina, L., Huang, R.-J., Jiang, J., Klein, F., Lavi, A., Pieber, S. M., Rindlisbacher, T., Rudich, Y., Slowik, J. G., Wang, J., Baltensperger, U., & Prévôt, A. S. H. (2018a). Identification of secondary aerosol precursors

emitted by an aircraft turbofan. *Atmospheric Chemistry and Physics*, *18*(10), 7379–7391. https://doi.org/10.5194/acp-18-7379-2018

Kılıç, D., El Haddad, I., Brem, B. T., Bruns, E., Bozetti, C., Corbin, J., Durdina, L., Huang, R.-J., Jiang, J., Klein, F., Lavi, A., Pieber, S. M., Rindlisbacher, T., Rudich, Y., Slowik, J. G., Wang, J., Baltensperger, U., & Prévôt, A. S. H. (2018b). Identification of secondary aerosol precursors emitted by an aircraft turbofan. *Atmospheric Chemistry and Physics*, *18*(10), 7379–7391. https://doi.org/10.5194/acp-18-7379-2018

Kohse-Höinghaus, K. (2019). A new era for combustion research. *Pure and Applied Chemistry*, *91*. https://doi.org/10.1515/pac-2018-0608

Koumelis, T. (2023, April 27). European aviation industry welcomes EU trilogue agreement on ReFuelEU Aviation Regulation. *TravelDailyNews International*. https://www.traveldailynews.com/aviation/european-aviation-industry-welcomes-eu-trilogue-agreement-on-refueleu-aviation-regulation/

Kroll, J. H., & Seinfeld, J. H. (2008). Chemistry of secondary organic aerosol: Formation and evolution of low-volatility organics in the atmosphere. *Atmospheric Environment*, *42*(16), 3593–3624. Scopus. https://doi.org/10.1016/j.atmosenv.2008.01.003

Kruza, M., McFiggans, G., Waring, M. S., Wells, J. R., & Carslaw, N. (2020). Indoor secondary organic aerosols: Towards an improved representation of their formation and composition in models. *Atmospheric Environment: X*, *240*, 10.1016/j.atmosenv.2020.117784. https://doi.org/10.1016/j.atmosenv.2020.117784

Krystynik, P. (2021). *Advanced Oxidation Processes (AOPs) – Utilization of Hydroxyl Radical and Singlet Oxygen*. https://doi.org/10.5772/intechopen.98189

Kuang, C., Chen, M., Zhao, J., Smith, J., McMurry, P. H., & Wang, J. (2012). Size and time-resolved growth rate measurements of 1 to 5 nm freshly formed atmospheric nuclei. *Atmospheric Chemistry and Physics*, *12*(7), 3573–3589. https://doi.org/10.5194/acp-12-3573-2012

Kulmala, M., Dal Maso, M., Mäkelä, J., Pirjola, L., Väkevä, M., Aalto, P., MIIKKULAINEN, P., HÄMERI, K., & O'Dowd, C. (2003). On the formation, growth and composition of nucleation mode particles. *Tellus B*, *53*, 479–490. https://doi.org/10.1034/j.1600-0889.2001.530411.x

Kulmala, M., Kontkanen, J., Junninen, H., Lehtipalo, K., Manninen, H. E., Nieminen, T., Petäjä, T., Sipilä, M., Schobesberger, S., Rantala, P., Franchin, A., Jokinen, T., Järvinen, E., Äijälä, M., Kangasluoma, J., Hakala, J., Aalto, P. P., Paasonen, P., Mikkilä, J., … Worsnop, D. R. (2013). Direct observations of atmospheric aerosol nucleation. *Science (New York, N.Y.)*, *339*(6122), 943–946. https://doi.org/10.1126/science.1227385

Kulmala, M., Laaksonen, A., Aalto, P., Vesala, T., Pirjola, L., Kerminen, V.-M., Korhonen, P., Hillamo, R., Virkkula, A., & Aurela, M. (1996). Formation, growth, and properties of atmospheric aerosol particles and cloud droplets. *Geophysica*, *32*, 217–233.

Kulmala, M., & Wagner, P. E. (1996). *Nucleation and Atmospheric Aerosols 1996*. Elsevier.

Kürten, A., Jokinen, T., Simon, M., Sipilä, M., Sarnela, N., Junninen, H., Adamov, A., Almeida, J., Amorim, A., Bianchi, F., Breitenlechner, M., Dommen, J., Donahue, N., Duplissy, J., Ehrhart, S., Flagan, R., Franchin, A., Hakala, J., Hansel, A., & Curtius, J. (2014). Neutral molecular cluster formation of sulfuric acid–dimethylamine observed in real time under atmospheric conditions. *Proceedings of the National Academy of Sciences*, *111*, 15019–15024. https://doi.org/10.1073/pnas.1404853111

Kürten, A., Rondo, L., Ehrhart, S., & Curtius, J. (2012). Calibration of a Chemical Ionization Mass Spectrometer for the Measurement of Gaseous Sulfuric Acid. *The Journal of Physical Chemistry A*, *116*(24), 6375–6386. https://doi.org/10.1021/jp212123n

Kurtén, T., Loukonen, V., Vehkamäki, H., & Kulmala, M. (2008). Amines are likely to enhance neutral and ion-induced sulfuric acid-water nucleation in the atmosphere more effectively than ammonia. *Atmospheric Chemistry and Physics*, *8*(14), 4095–4103. https://doi.org/10.5194/acp-8-4095-2008

Kuwata, M., & Martin, S. T. (2012). Phase of atmospheric secondary organic material affects its reactivity. *Proceedings of the National Academy of Sciences of the United States of America*, *109*(43), 17354–17359. Scopus. https://doi.org/10.1073/pnas.1209071109

Lai, A. C., & Nazaroff, W. W. (2000). MODELING INDOOR PARTICLE DEPOSITION FROM TURBULENT FLOW ONTO SMOOTH SURFACES. *Journal of Aerosol Science*, *31*(4), 463–476. https://doi.org/10.1016/S0021-8502(99)00536-4

Lakey, P. S. J., Won, Y., Shaw, D., Østerstrøm, F. F., Mattila, J., Reidy, E., Bottorff, B., Rosales, C., Wang, C., Ampollini, L., Zhou, S., Novoselac, A., Kahan, T. F., DeCarlo, P. F., Abbatt, J. P. D., Stevens, P. S., Farmer, D. K., Carslaw, N., Rim, D., & Shiraiwa, M. (2021). Spatial and temporal scales of variability for indoor air constituents. *Communications Chemistry*, *4*(1), Article 1. https://doi.org/10.1038/s42004-021-00548-5

Lamkaddam, H. (2017). *Etude en atmosphère simulée de la formation d'Aérosol Organique Secondaire issue de la photooxydation du n-dodécane: Impact des paramètres environnementaux* [These de doctorat, Paris Est]. http://www.theses.fr/2017PESC1128

Lamkaddam, H., Gratien, A., Pangui, E., Cazaunau, M., Picquet-Varrault, B., & Doussin, J.-F. (2017). High-NO $_x$ Photooxidation of *n* -Dodecane: Temperature Dependence of SOA Formation. *Environmental Science & Technology*, *51*(1), 192–201. https://doi.org/10.1021/acs.est.6b03821

Lee, D. S., Fahey, D. W., Forster, P. M., Newton, P. J., Wit, R. C. N., Lim, L. L., Owen, B., & Sausen, R. (2009). Aviation and global climate change in the 21st century. *Atmospheric Environment*, *43*(22), 3520–3537. https://doi.org/10.1016/j.atmosenv.2009.04.024

Lee, D. S., Fahey, D. W., Skowron, A., Allen, M. R., Burkhardt, U., Chen, Q., Doherty, S. J., Freeman, S., Forster, P. M., Fuglestvedt, J., Gettelman, A., De León, R. R., Lim, L. L., Lund, M. T., Millar, R. J., Owen, B., Penner, J. E., Pitari, G., Prather, M. J., … Wilcox, L. J. (2021). The contribution of global aviation to anthropogenic climate forcing for 2000 to 2018. *Atmospheric Environment*, *244*, 117834. https://doi.org/10.1016/j.atmosenv.2020.117834

Lehtipalo, K., Rondo, L., Kontkanen, J., Schobesberger, S., Jokinen, T., Sarnela, N., Kürten, A., Ehrhart, S., Franchin, A., Nieminen, T., Riccobono, F., Sipilä, M., Yli-Juuti, T., Duplissy, J., Adamov, A., Ahlm, L., Almeida, J., Amorim, A., Bianchi, F., … Kulmala, M. (2016a). The effect of acid–base clustering and ions on the growth of atmospheric nano-particles. *Nature Communications*, *7*(1), Article 1. https://doi.org/10.1038/ncomms11594

Lehtipalo, K., Rondo, L., Kontkanen, J., Schobesberger, S., Jokinen, T., Sarnela, N., Kürten, A., Ehrhart, S., Franchin, A., Nieminen, T., Riccobono, F., Sipilä, M., Yli-Juuti, T., Duplissy, J., Adamov, A., Ahlm, L., Almeida, J., Amorim, A., Bianchi, F., … Kulmala, M. (2016b). The effect of acid–base clustering and ions on the growth of atmospheric nano-particles. *Nature Communications*, *7*(1), Article 1. https://doi.org/10.1038/ncomms11594

Lehtipalo, K., Yan, C., Dada, L., Bianchi, F., Xiao, M., Wagner, R., Stolzenburg, D., Ahonen, L. R., Amorim, A., Baccarini, A., Bauer, P. S., Baumgartner, B., Bergen, A., Bernhammer, A.-K., Breitenlechner, M., Brilke, S., Buchholz, A., Mazon, S. B., Chen, D., … Worsnop, D. R. (2018). Multicomponent new particle formation from sulfuric acid, ammonia, and biogenic vapors. *Science Advances*, *4*(12), eaau5363. https://doi.org/10.1126/sciadv.aau5363

Lemaire, R., & Mobtil, M. (2015). Modeling laser-induced incandescence of soot ñ A new approach based on the use of inverse techniques. *Applied Physics B*, *119*. https://doi.org/10.1007/s00340-015-6032-1

Lentini, D. (2018). *IMPATTO AMBIENTALE DEI MOTORI AERONAUTICI∗ (ENVIRONMENTAL IMPACT OF AIRCRAFT ENGINES)*.

Leppä, J., Anttila, T., Kerminen, V.-M., Kulmala, M., & Lehtinen, K. E. J. (2011). Atmospheric new particle formation: Real and apparent growth of neutral and charged particles. *Atmospheric Chemistry and Physics*, *11*(10), 4939–4955. https://doi.org/10.5194/acp-11-4939-2011

Li, M., Karu, E., Brenninkmeijer, C., Fischer, H., Lelieveld, J., & Williams, J. (2018). Tropospheric OH and stratospheric OH and Cl concentrations determined from CH4, CH3Cl, and SF6 measurements.

Npj Climate and Atmospheric Science, *1*(1), Article 1. https://doi.org/10.1038/s41612-018-0041-9

Liggio, J., & Li, S.-M. (2006). Organosulfate formation during the uptake of pinonaldehyde on acidic sulfate aerosols. *Geophysical Research Letters - GEOPHYS RES LETT*, *331*. https://doi.org/10.1029/2006GL026079

Lin, S., Munsie, J. P., Herdt-Losavio, M., Hwang, S. A., Civerolo, K., McGarry, K., & Gentile, T. (2008). Residential proximity to large airports and potential health impacts in New York State. *International Archives of Occupational and Environmental Health*, *81*(7), 797–804. https://doi.org/10.1007/s00420-007-0265-1

Lindgren, J., Uvdal, P., Sjövall, P., Nilsson, D. E., Engdahl, A., Schultz, B. P., & Thiel, V. (2012). Molecular preservation of the pigment melanin in fossil melanosomes. *Nature Communications*, *3*(1), Article 1. https://doi.org/10.1038/ncomms1819

Liu, B. Y. H., & Pui, D. Y. H. (1974). Equilibrium bipolar charge distribution of aerosols. *Journal of Colloid and Interface Science*, *49*(2), 305–312. https://doi.org/10.1016/0021-9797(74)90366-X

Liu, G., Yan, B., & Chen, G. (2013). Technical review on jet fuel production. *Renewable and Sustainable Energy Reviews*, *25*, 59–70. https://doi.org/10.1016/j.rser.2013.03.025

Lobo, P., Christie, S., Khandelwal, B., Blakey, S. G., & Raper, D. W. (2015). Evaluation of Non-volatile Particulate Matter Emission Characteristics of an Aircraft Auxiliary Power Unit with Varying Alternative Jet Fuel Blend Ratios. *Energy & Fuels*, *29*(11), 7705–7711. https://doi.org/10.1021/acs.energyfuels.5b01758

Lobo, P., Hagen, D. E., & Whitefield, P. D. (2011). Comparison of PM Emissions from a Commercial Jet Engine Burning Conventional, Biomass, and Fischer–Tropsch Fuels. *Environmental Science & Technology*, *45*(24), 10744–10749. https://doi.org/10.1021/es201902e

Lobo, P., Rye, L., Williams, P. I., Christie, S., Uryga-Bugajska, I., Wilson, C. W., Hagen, D. E., Whitefield, P. D., Blakey, S., Coe, H., Raper, D., & Pourkashanian, M. (2012). Impact of Alternative Fuels on Emissions Characteristics of a Gas Turbine Engine – Part 1: Gaseous and Particulate Matter

Emissions. *Environmental Science & Technology*, *46*(19), 10805–10811. https://doi.org/10.1021/es301898u

Lopez-Hilfiker, F. D., Pospisilova, V., Huang, W., Kalberer, M., Mohr, C., Stefenelli, G., Thornton, J. A., Baltensperger, U., Prevot, A. S. H., & Slowik, J. G. (2019). An extractive electrospray ionization time-of-flight mass spectrometer (EESI-TOF) for online measurement of atmospheric aerosol particles. *Atmospheric Measurement Techniques*, *12*(9), 4867–4886. https://doi.org/10.5194/amt-12-4867-2019

Loukonen, V., Kurtén, T., Ortega, I. K., Vehkamäki, H., Pádua, A. a. H., Sellegri, K., & Kulmala, M. (2010). Enhancing effect of dimethylamine in sulfuric acid nucleation in the presence of water – a computational study. *Atmospheric Chemistry and Physics*, *10*(10), 4961–4974. https://doi.org/10.5194/acp-10-4961-2010

Lu, W., Abbas, Y., Mustafa, M. F., Pan, C., & Wang, H. (2019). A review on application of dielectric barrier discharge plasma technology on the abatement of volatile organic compounds. *Frontiers of Environmental Science & Engineering*, *13*(2), Article 2. https://doi.org/10.1007/s11783-019-1108-5

Luning Prak, D., Cooke, J., Dickerson, T., McDaniel, A., & Cowart, J. (2021). Cetane number, derived cetane number, and cetane index: When correlations fail to predict combustibility. *Fuel*, *289*, 119963. https://doi.org/10.1016/j.fuel.2020.119963

Luning Prak, D. J., Jones, M. H., Trulove, P., McDaniel, A. M., Dickerson, T., & Cowart, J. S. (2015). Physical and Chemical Analysis of Alcohol-to-Jet (ATJ) Fuel and Development of Surrogate Fuel Mixtures. *Energy & Fuels*, *29*(6), 3760–3769. https://doi.org/10.1021/acs.energyfuels.5b00668

Mamakos, A., Khalek, I., Giannelli, R., & Spears, M. (2013). Characterization of Combustion Aerosol Produced by a Mini-CAST and Treated in a Catalytic Stripper. *Aerosol Science and Technology*, *47*(8), 927–936. https://doi.org/10.1080/02786826.2013.802762

Massabò, D., Danelli, S. G., Brotto, P., Comite, A., Costa, C., Di Cesare, A., Doussin, J. F., Ferraro, F., Formenti, P., Gatta, E., Negretti, L., Oliva, M., Parodi, F., Vezzulli, L., & Prati, P. (2018). ChAMBRe: A new atmospheric simulation chamber for aerosol modelling and bio-aerosol research. *Atmospheric Measurement Techniques*, *11*(10), 5885–5900. https://doi.org/10.5194/amt-11-5885-2018

Materić, D., Bruhn, D., Turner, C., Morgan, G., Mason, N., & Gauci, V. (2015). Methods in plant foliar volatile organic compounds research1. *Applications in Plant Sciences*, *3*(12), apps.1500044. https://doi.org/10.3732/apps.1500044

Maugendre, M. (2009). *Etude des particules de suie dans les flammes de kérosène et de diester* [These de doctorat, Rouen, INSA]. https://www.theses.fr/2009ISAM0016

Mawhood, B., Gazis, E., de Jong, S., Hoefnagels, R., & Slade, R. (2016). Production pathways for renewable jet fuel: A review of commercialization status and future prospects. *Biofuels Bioproducts and Biorefining*, *Advance online publication*. https://doi.org/10.1002/bbb.1644

McGann, B., Kim, K., Lee, T., Temme, J., & Kweon, C.-B. (2020). Effect of the Cetane Number on Jet Fuel Spray Ignition at High-Temperature and -Pressure Conditions. *Energy & Fuels*, *34*(2), 1337–1346. https://doi.org/10.1021/acs.energyfuels.9b03170

McGrath, M. J., Olenius, T., Ortega, I. K., Loukonen, V., Paasonen, P., Kurtén, T., Kulmala, M., & Vehkamäki, H. (2012). Atmospheric Cluster Dynamics Code: A flexible method for solution of the birth-death equations. *Atmospheric Chemistry and Physics*, *12*(5), 2345–2355. https://doi.org/10.5194/acp-12-2345-2012

McLafferty, F. W., & Turecek, F. (1994). Interpretation of Mass Spectra, 4th ed. *Journal of Chemical Education*, *71*(2), A54. https://doi.org/10.1021/ed071pA54.5

Melas, A. D., Koidi, V., Deloglou, D., Daskalos, E., Zarvalis, D., Papaioannou, E., & Konstandopoulos, A. G. (2020). Development and evaluation of a catalytic stripper for the measurement of solid ultrafine particle emissions from internal combustion engines. *Aerosol Science and Technology*, *54*(6), 704–717. https://doi.org/10.1080/02786826.2020.1718061

Melton, L. A. (1984). Soot diagnostics based on laser heating. *Applied Optics*, *23*(13), 2201–2208. https://doi.org/10.1364/AO.23.002201

Merikanto, J., Spracklen, D. V., Mann, G. W., Pickering, S. J., & Carslaw, K. S. (2009). Impact of nucleation on global CCN. *Atmospheric Chemistry and Physics*, *9*(21), 8601–8616. https://doi.org/10.5194/acp-9-8601-2009

Metzger, A., Verheggen, B., Dommen, J., Duplissy, J., Prevot, A., Weingartner, E., Riipinen, I., Kulmala, M., Spracklen, D., Carslaw, K., & Baltensperger, U. (2010). Evidence for the role of organics in aerosol particle formation under atmospheric conditions. *Proceedings of the National Academy of Sciences of the United States of America*, *107*, 6646–6651. https://doi.org/10.1073/pnas.0911330107

Miake-Lye, R. C., Brown, R. C., Anderson, M. R., & Kolb, C. E. (1994). Calculations of condensation and chemistry in an aircraft contrail. *DLR, Impact of Emissions From Aircraft and Spacecraft Upon the Atmosphere*, *DLR-Mitteilung*(94–06), 274–279. Legacy CDMS.

Michelsen, H. A., Schulz, C., Smallwood, G. J., & Will, S. (2015a). Laser-induced incandescence: Particulate diagnostics for combustion, atmospheric, and industrial applications. *Progress in Energy and Combustion Science*, *51*, 2–48. https://doi.org/10.1016/j.pecs.2015.07.001

Michelsen, H. A., Schulz, C., Smallwood, G. J., & Will, S. (2015b). Laser-induced incandescence: Particulate diagnostics for combustion, atmospheric, and industrial applications. *Progress in Energy and Combustion Science*, *51*, 2–48. https://doi.org/10.1016/j.pecs.2015.07.001

Mihesan, C., Ziskind, M., Therssen, E., Desgroux, P., & Focsa, C. (2007). Parametric study of polycyclic aromatic hydrocarbon laser desorption. *Journal of Physics: Condensed Matter*, *20*, 025221. https://doi.org/10.1088/0953-8984/20/02/025221

Miracolo, M. A., Hennigan, C. J., Ranjan, M., Nguyen, N. T., Gordon, T. D., Lipsky, E. M., Presto, A. A., Donahue, N. M., & Robinson, A. L. (2011). Secondary aerosol formation from photochemical aging of aircraft exhaust in a smog chamber. *Atmospheric Chemistry and Physics*, *11*(9), 4135–4147. https://doi.org/10.5194/acp-11-4135-2011

Monks, P., Ravishankara, A. R., von Schneidemesser, E., & Sommariva, R. (2021). Opinion: Papers that shaped tropospheric chemistry. *Atmospheric Chemistry and Physics*, *21*, 12909–12948. https://doi.org/10.5194/acp-21-12909-2021

Moore, R. H., Shook, M. A., Ziemba, L. D., DiGangi, J. P., Winstead, E. L., Rauch, B., Jurkat, T., Thornhill, K. L., Crosbie, E. C., Robinson, C., Shingler, T. J., & Anderson, B. E. (2017). Take-off engine particle emission indices for in-service aircraft at Los Angeles International Airport. *Scientific Data*, *4*(1), 170198. https://doi.org/10.1038/sdata.2017.198

Moore, R. H., Shook, M., Beyersdorf, A., Corr, C., Herndon, S., Knighton, W. B., Miake-Lye, R., Thornhill, K. L., Winstead, E. L., Yu, Z., Ziemba, L. D., & Anderson, B. E. (2015). Influence of Jet Fuel Composition on Aircraft Engine Emissions: A Synthesis of Aerosol Emissions Data from the NASA APEX, AAFEX, and ACCESS Missions. *Energy & Fuels*, *29*(4), 2591–2600. https://doi.org/10.1021/ef502618w

Moore, R. H., Thornhill, K. L., Weinzierl, B., Sauer, D., D'Ascoli, E., Kim, J., Lichtenstern, M., Scheibe, M., Beaton, B., Beyersdorf, A. J., Barrick, J., Bulzan, D., Corr, C. A., Crosbie, E., Jurkat, T., Martin, R., Riddick, D., Shook, M., Slover, G., … Anderson, B. E. (2017). Biofuel blending reduces particle emissions from aircraft engines at cruise conditions. *Nature*, *543*(7645), Article 7645. https://doi.org/10.1038/nature21420

Moore, R. H., Ziemba, L. D., Dutcher, D., Beyersdorf, A. J., Chan, K., Crumeyrolle, S., Raymond, T. M., Thornhill, K. L., Winstead, E. L., & Anderson, B. E. (2014). Mapping the Operation of the Miniature Combustion Aerosol Standard (Mini-CAST) Soot Generator. *Aerosol Science and Technology*, *48*(5), 467–479. https://doi.org/10.1080/02786826.2014.890694

Mueller, L., Jakobi, G., Orasche, J., Karg, E., Sklorz, M., Abbaszade, G., Weggler, B., Jing, L., Schnelle-Kreis, J., & Zimmermann, R. (2015). Online determination of polycyclic aromatic hydrocarbon formation from a flame soot generator. *Analytical and Bioanalytical Chemistry*, *407*(20), 5911–5922. https://doi.org/10.1007/s00216-015-8549-x

Nadykto, A., & Yu, F. (2003). Uptake of neutral polar vapor molecules by charged clusters/particles: Enhancement due to dipole-charge interaction. *Journal of Geophysical Research (Atmospheres)*, *108*, 4717. https://doi.org/10.1029/2003JD003664

National Academies of Sciences. (1998). *The Atmospheric Sciences: Entering the Twenty-First Century: Vol. Chapter 2 p137* (Earth's radiative balance). https://doi.org/10.17226/6021

Nault, B. A., Campuzano-Jost, P., Day, D. A., Jo, D. S., Schroder, J. C., Allen, H. M., Bahreini, R., Bian, H., Blake, D. R., Chin, M., Clegg, S. L., Colarco, P. R., Crounse, J. D., Cubison, M. J., DeCarlo, P. F., Dibb, J. E., Diskin, G. S., Hodzic, A., Hu, W., … Jimenez, J. L. (2021). Chemical transport models often underestimate inorganic aerosol acidity in remote regions of the atmosphere. *Communications Earth & Environment*, *2*(1), Article 1. https://doi.org/10.1038/s43247-021-00164-0

Neu. (2020). *Emissions des transports aériens et leur impact sur le climat*. https://scnat.ch/fr/id/cSx4y

Ng, N. L., Herndon, S. C., Trimborn, A., Canagaratna, M. R., Croteau, P. L., Onasch, T. B., Sueper, D., Worsnop, D. R., Zhang, Q., Sun, Y. L., & Jayne, J. T. (2011). An Aerosol Chemical Speciation Monitor (ACSM) for Routine Monitoring of the Composition and Mass Concentrations of Ambient Aerosol. *Aerosol Science and Technology*, *45*(7), 780–794. https://doi.org/10.1080/02786826.2011.560211

Ngo, L. D., Duca, D., Carpentier, Y., Noble, J. A., Ikhenazene, R., Vojkovic, M., Irimiea, C., Ortega, I. K., Lefevre, G., Yon, J., Faccinetto, A., Therssen, E., Ziskind, M., Chazallon, B., Pirim, C., & Focsa, C. (2020). Chemical discrimination of the particulate and gas phases of miniCAST exhausts using a two-filter collection method. *Atmospheric Measurement Techniques*, *13*(2), 951–967. https://doi.org/10.5194/amt-13-951-2020

Ngo, T. L. D. (2019). *Characterization of soot particles and their precursors produced during the combustion of conventional and alternative fuels: An in-situ laser diagnostics and ex-situ mass spectrometry investigation* [These de doctorat, Université de Lille (2018-2021)]. http://www.theses.fr/2019LILUR040

Nguyen, T. B., Laskin, A., Laskin, J., & Nizkorodov, S. A. (2012). Direct aqueous photochemistry of isoprene high-NO x secondary organic aerosol. *Physical Chemistry Chemical Physics*, *14*(27), 9702–9714. Scopus. https://doi.org/10.1039/c2cp40944e

Nieminen, T., Lehtinen, K. E. J., & Kulmala, M. (2010). Sub-10 nm particle growth by vapor condensation – effects of vapor molecule size and particle thermal speed. *Atmospheric Chemistry and Physics*, *10*(20), 9773–9779. https://doi.org/10.5194/acp-10-9773-2010

NOAA. (2021). *Global Monitoring Laboratory—Carbon Cycle Greenhouse Gases*. https://gml.noaa.gov/ccgg/trends/global.html

Nosaka, Y., & Nosaka, A. (2016). Understanding Hydroxyl Radical (•OH) Generation Processes in Photocatalysis. *ACS Energy Letters*, *1*(2), 356–359. https://doi.org/10.1021/acsenergylett.6b00174

Odabasi, M., Ongan, O., & Cetin, E. (2005). Quantitative analysis of volatile organic compounds (VOCs) in atmospheric particles. *Atmospheric Environment*, *39*(20), 3763–3770. Scopus. https://doi.org/10.1016/j.atmosenv.2005.02.048

Ono, K., Matsukawa, Y., Dewa, K., Watanabe, A., Takahashi, K., Saito, Y., Matsushita, Y., Aoki, H., Era, K., Aoki, T., & Yamaguchi, T. (2015). Formation mechanisms of soot from high-molecular-weight polycyclic aromatic hydrocarbons. *Combustion and Flame*, *162*(6), 2670–2678. https://doi.org/10.1016/j.combustflame.2015.03.022

Ortega, I., Delhaye, D., Jing, L., Ledur, D., Ferry, D., Irimiea, C., Pirim, C., Chazallon, B., Focsa, C., Ouf, F.-X., Salm, F., & Vancassel, X. (2016). *Combustion aerosol standard generator for aeronautic fuel* [Poster]. 22th EAC conference.

Ortega, I., Delhaye, D., Ouf, F.-X., Ferry, D., Focsa, C., Irimiea, C., Carpentier, Y., Chazallon, B., Parent, P., Laffon, C., Penanhoat, O., Harivel, N., Gaffie, D., & Vancassel, X. (2016). Measuring Non-Volatile Particle Properties in the Exhaust of an Aircraft Engine [PDF]. *AerospaceLab Journal*, *Issue 11*, 14 pages. https://doi.org/10.12762/2016.AL11-08

Ortega, I. K., Kupiainen, O., Kurtén, T., Olenius, T., Wilkman, O., McGrath, M. J., Loukonen, V., & Vehkamäki, H. (2012). From quantum chemical formation free energies to evaporation rates. *Atmospheric Chemistry and Physics*, *12*(1), 225–235. https://doi.org/10.5194/acp-12-225-2012

Ouf, F.-X. (2006). *Caractérisation des aérosols émis lors d'un incendie* [These de doctorat, Rouen]. https://www.theses.fr/2006ROUES003

Ouf, F.-X., Parent, P., Laffon, C., Marhaba, I., Ferry, D., Marcillaud, B., Antonsson, E., Benkoula, S., Liu, X.-J., Nicolas, C., Robert, E., Patanen, M., Barreda, F.-A., Sublemontier, O., Coppalle, A., Yon, J., Miserque, F., Mostefaoui, T., Regier, T. Z., … Miron, C. (2016). First in-flight synchrotron X-ray absorption and photoemission study of carbon soot nanoparticles. *Scientific Reports*, *6*(1), 36495. https://doi.org/10.1038/srep36495

Pagonis, D., Campuzano-Jost, P., Guo, H., Day, D. A., Schueneman, M. K., Brown, W. L., Nault, B. A., Stark, H., Siemens, K., Laskin, A., Piel, F., Tomsche, L., Wisthaler, A., Coggon, M. M., Gkatzelis, G. I., Halliday, H. S., Krechmer, J. E., Moore, R. H., Thomson, D. S., … Jimenez, J. L. (2021). Airborne extractive electrospray mass spectrometry measurements of the chemical composition of organic aerosol. *Atmospheric Measurement Techniques*, *14*(2), 1545–1559. https://doi.org/10.5194/amt-14-1545-2021

Pallflex technical document. (n.d.). *Pallflex 2500 qat up 47 mm x 25*. UGAP.FR. Retrieved 21 February 2023, from http://www.ugap.fr/achat-public/pallflex-2500-qat-up-47-mm-x-25_2570146.html

Pan, X. (2011). Sulfur Oxides: Sources, Exposures and Health Effects. In J. O. Nriagu (Ed.), *Encyclopedia of Environmental Health* (pp. 290–296). Elsevier. https://doi.org/10.1016/B978-0-444-52272-6.00069-6

Pandey, S. K., Kim, K.-H., & Brown, R. J. C. (2011). A review of techniques for the determination of polycyclic aromatic hydrocarbons in air. *TRAC Trends Anal. Chem.*, *30*(11), Article 11.

Pankow, J. F., & Asher, W. E. (2008). SIMPOL.1: A simple group contribution method for predicting vapor pressures and enthalpies of vaporization of multifunctional organic compounds. *Atmospheric Chemistry and Physics*, *8*(10), 2773–2796. Scopus. https://doi.org/10.5194/acp-8-2773-2008

Pascal, M. (2013). Assessing the public health impacts of urban air pollution in 25 European cities: Results of the Aphekom project [Review of *Assessing the public health impacts of urban air pollution in 25 European cities: Results of the Aphekom project*, by M. Corso, O. Chanel, C. Declercq, C. Badaloni, G. Cesaroni, S. Henschel, K. Meister, D. Haluza, P. Martin-Olmedo, & S. Medina]. *Science of The Total Environment*, *449*, 390–400. https://doi.org/10.1016/j.scitotenv.2013.01.077

Pascal, M., Corso, M., Chanel, O., Declercq, C., Badaloni, C., Cesaroni, G., Henschel, S., Meister, K., Haluza, D., Martin-Olmedo, P., Medina, S., & Aphekom group. (2013). Assessing the public health impacts of urban air pollution in 25 European cities: Results of the Aphekom project. *The Science of the Total Environment*, *449*, 390–400. https://doi.org/10.1016/j.scitotenv.2013.01.077

Paulot, F., & Jacob, D. J. (2014). Hidden cost of U.S. agricultural exports: Particulate matter from ammonia emissions. *Environmental Science and Technology*, *48*(2), 903–908. Scopus. https://doi.org/10.1021/es4034793

Peng, W., McCaffery, C., Kuittinen, N., Rönkkö, T., Cocker, D. R., & Karavalakis, G. (2022). Secondary Organic and Inorganic Aerosol Formation from a GDI Vehicle under Different Driving Conditions. *Atmosphere*, *13*(3), Article 3. https://doi.org/10.3390/atmos13030433

Penner, J. E., Lister, D., Griggs, D., Docken, D., & MacFarland, M. (1999). *Aviation and the Global Atmosphere: A Special Report of the Intergovernmental Panel on Climate Change*. https://archive.ipcc.ch/ipccreports/sres/aviation/index.php?idp=0

Penner, J. E., Zhou, C., Garnier, A., & Mitchell, D. L. (2018). Anthropogenic Aerosol Indirect Effects in Cirrus Clouds. *Journal of Geophysical Research. Atmospheres*, *123*(20), 11652–11677. https://doi.org/10.1029/2018JD029204

Pomerol, C., Lagabrielle, Y., Renard, M., & Guillot, S. (2011). *Éléments de géologie*. Dunod.

Popa, D., & Udrea, F. (2019). Towards Integrated Mid-Infrared Gas Sensors. *Sensors*, *19*(9), Article 9. https://doi.org/10.3390/s19092076

Pope, C. A., Burnett, R. T., Turner, M. C., Cohen, A., Krewski, D., Jerrett, M., Gapstur, S. M., & Thun, M. J. (2011). Lung cancer and cardiovascular disease mortality associated with ambient air pollution and cigarette smoke: Shape of the exposure-response relationships. *Environmental Health Perspectives*, *119*(11), 1616–1621. https://doi.org/10.1289/ehp.1103639

Pospisilova, V., Lopez-Hilfiker, F. D., Bell, D. M., El Haddad, I., Mohr, C., Huang, W., Heikkinen, L., Xiao, M., Dommen, J., Prevot, A. S. H., Baltensperger, U., & Slowik, J. G. (2020). On the fate of oxygenated organic molecules in atmospheric aerosol particles. *Science Advances*, *6*(11), eaax8922. https://doi.org/10.1126/sciadv.aax8922

Pye, H. O. T., Nenes, A., Alexander, B., Ault, A. P., Barth, M. C., Clegg, S. L., Collett Jr., J. L., Fahey, K. M., Hennigan, C. J., Herrmann, H., Kanakidou, M., Kelly, J. T., Ku, I.-T., McNeill, V. F., Riemer, N., Schaefer, T., Shi, G., Tilgner, A., Walker, J. T., … Zuend, A. (2020). The acidity of atmospheric particles and clouds. *Atmospheric Chemistry and Physics*, *20*(8), 4809–4888. https://doi.org/10.5194/acp-20-4809-2020

Pytel, K., Marcinkowska, R., Rutkowska, M., & Zabiegała, B. (2022). Recent advances on SOA formation in indoor air, fate and strategies for SOA characterization in indoor air—A review. *Science of The Total Environment*, *843*, 156948. https://doi.org/10.1016/j.scitotenv.2022.156948

Qi, X., Ding, A., Roldin, P., Xu, Z., Zhou, P., Sarnela, N., Nie, W., Huang, X., Rusanen, A., Ehn, M., Rissanen, M. P., Petäjä, T., Kulmala, M., & Boy, M. (2018). Modelling studies of HOMs and their contributions to new particle formation and growth: Comparison of boreal forest in Finland

and a polluted environment in China. *Atmospheric Chemistry and Physics*, *18*(16), 11779–11791. https://doi.org/10.5194/acp-18-11779-2018

RAPTOR project. (2020). *Home*. RAPTOR. https://aviation-pm.eu/

Riccobono, F., Schobesberger, S., Scott, C. E., Dommen, J., Ortega, I. K., Rondo, L., Almeida, J., Amorim, A., Bianchi, F., Breitenlechner, M., David, A., Downard, A., Dunne, E. M., Duplissy, J., Ehrhart, S., Flagan, R. C., Franchin, A., Hansel, A., Junninen, H., … Baltensperger, U. (2014). Oxidation products of biogenic emissions contribute to nucleation of atmospheric particles. *Science (New York, N.Y.)*, *344*(6185), 717–721. https://doi.org/10.1126/science.1243527

Richter, H., & Howard, J. B. (2000). Formation of polycyclic aromatic hydrocarbons and their growth to soot—A review of chemical reaction pathways. *Progress in Energy and Combustion Science*, *26*(4–6), 565–608. https://doi.org/10.1016/S0360-1285(00)00009-5

Riipinen, I., Sihto, S.-L., Kulmala, M., Arnold, F., Dal Maso, M., Birmili, W., Saarnio, K., Teinilä, K., Kerminen, V.-M., Laaksonen, A., & Lehtinen, K. E. J. (2007). Connections between atmospheric sulphuric acid and new particle formation during QUEST III–IV campaigns in Heidelberg and Hyytiälä. *Atmospheric Chemistry and Physics*, *7*(8), 1899–1914. https://doi.org/10.5194/acp-7-1899-2007

Riipinen, I., Yli-Juuti, T., Pierce, J. R., Petäjä, T., Worsnop, D. R., Kulmala, M., & Donahue, N. M. (2012). The contribution of organics to atmospheric nanoparticle growth. *Nature Geoscience*, *5*(7), Article 7. https://doi.org/10.1038/ngeo1499

Riley, K., Cook, R., Carr, E., & Manning, B. (2021). A Systematic Review of The Impact of Commercial Aircraft Activity on Air Quality Near Airports. *City and Environment Interactions*, *11*, 10.1016/j.cacint.2021.100066. https://doi.org/10.1016/j.cacint.2021.100066

Robinson, A. L., Donahue, N. M., Shrivastava, M. K., Weitkamp, E. A., Sage, A. M., Grieshop, A. P., Lane, T. E., Pierce, J. R., & Pandis, S. N. (2007). Rethinking organic aerosols: Semivolatile emissions and photochemical aging. *Science*, *315*(5816), 1259–1262. Scopus. https://doi.org/10.1126/science.1133061

Rogak, S. N., & Flagan, R. C. (1990). Stokes drag on self-similar clusters of spheres. *Journal of Colloid and Interface Science*, *134*(1), 206–218. https://doi.org/10.1016/0021-9797(90)90268-S

SAFRAN. (2022). *M88—Performances et fiabilité en opération*. Safran. https://www.safran-group.com/fr/produits-services/m88-performances-fiabilite-operation

Samburova, V., Zielinska, B., & Khlystov, A. (2017). Do 16 Polycyclic Aromatic Hydrocarbons Represent PAH Air Toxicity? *Toxics*, *5*(3), 17. https://doi.org/10.3390/toxics5030017

SAPHIR_EUROCHAMP. (2020). *SAPHIR | Eurochamp*. https://www.eurochamp.org/simulation-chambers/SAPHIR

Schripp, T., Anderson, B. E., Bauder, U., Rauch, B., Corbin, J. C., Smallwood, G. J., Lobo, P., Crosbie, E. C., Shook, M. A., Miake-Lye, R. C., Yu, Z., Freedman, A., Whitefield, P. D., Robinson, C. E., Achterberg, S. L., Köhler, M., Oßwald, P., Grein, T., Sauer, D., … LeClercq, P. (2022). Aircraft engine particulate matter emissions from sustainable aviation fuels: Results from ground-based measurements during the NASA/DLR campaign ECLIF2/ND-MAX. *Fuel*, *325*, 124764. https://doi.org/10.1016/j.fuel.2022.124764

Schumann, U. (2005). Formation, properties and climatic effects of contrails. *Comptes Rendus Physique*, *6*(4), 549–565. https://doi.org/10.1016/j.crhy.2005.05.002

Schumann, U., Arnold, F., Busen, R., Curtius, J., Kärcher, B., Kiendler, A., Petzold, A., Schlager, H., Schröder, F., & Wohlfrom, K.-H. (2002). Influence of fuel sulfur on the composition of aircraft exhaust plumes: The experiments SULFUR 1–7. *Journal of Geophysical Research: Atmospheres*, *107*(D15), AAC 2-1-AAC 2-27. https://doi.org/10.1029/2001JD000813

Schumann, U., Baumann, R., Baumgardner, D., Bedka, S., Duda, D., Freudenthaler, V., Gayet, J.-F., Heymsfield, A., Minnis, P., Quante, M., Raschke, E., Schlager, H., Vázquez-Navarro, M., Voigt, C., & Wang, Z. (2016). Properties of individual contrails: A compilation of observations and some comparisons. *Atmospheric Chemistry and Physics Discussions*, 1–62. https://doi.org/10.5194/acp-2016-773

Seinfeld, J. H., & Pandis, S. N. (2006). *Atmospheric Chemistry and Physics: From Air Pollution to Climate Change, 3rd Edition | Wiley*. Wiley.Com. https://www.wiley.com/en-us/Atmospheric+Chemistry+and+Physics%3A+From+Air+Pollution+to+Climate+Change%2C+3rd+Edition-p-9781118947401

Shine, K. P. (2015). Radiative Forcing and Climate Change. In *Encyclopedia of Aerospace Engineering* (pp. 1–11). John Wiley & Sons, Ltd. https://doi.org/10.1002/9780470686652.eae526.pub2

Shirmohammadi, F., Sowlat, M. H., Hasheminassab, S., Saffari, A., Ban-Weiss, G., & Sioutas, C. (2017). Emission rates of particle number, mass and black carbon by the Los Angeles International Airport (LAX) and its impact on air quality in Los Angeles. *Atmospheric Environment*, *151*, 82–93. https://doi.org/10.1016/j.atmosenv.2016.12.005

Sipila, M., Berndt, T., Petaja, T., Brus, D., Vanhanen, J., Stratmann, F., Patokoski, J., Mauldin III, R. L., Hyvärinen, A.-P., Lihavainen, H., & Kulmala, M. (2010). The role of sulfuric acid in atmospheric nucleation. *Science*, *327*(5970), 1243–1246. Scopus. https://doi.org/10.1126/science.1180315

Smallwood, G. J., Snelling, D. R., Liu, F., & Gu¨lder, O. L. (2000). Clouds Over Soot Evaporation: Errors in Modeling Laser-Induced Incandescence of Soot. *Journal of Heat Transfer*, *123*(4), 814–818. https://doi.org/10.1115/1.1370507

Smith, J., Barsanti, K., Friedli, H., Ehn, M., Kulmala, M., Collins, D., Scheckman, J., Williams, B., & McMurry, P. (2010). Observations of aminium salts in atmospheric nanoparticles and possible climatic implications. *Proceedings of the National Academy of Sciences of the United States of America*, *107*, 6634–6639. https://doi.org/10.1073/pnas.0912127107

Smith, J. N., DUNN, M. J., VANREKEN, T. M., IIDA, K., STOLZENBURG, M. R., MCMURRY, P. H., & HUEY, L. G. (2008). Chemical composition of atmospheric nanoparticles formed from nucleation in Tecamac, Mexico: Evidence for an important role for organic species in nanoparticle growth. *Chemical Composition of Atmospheric Nanoparticles Formed from Nucleation in Tecamac, Mexico : Evidence for an Important Role for Organic Species in Nanoparticle Growth*, *35*(4), L04808.1-L04808.5.

Sokan-Adeaga, A., Ana, G., Sokan-Adeaga, M., Sokan-Adeaga, E., & Ejike, O. (2019). *Secondary inorganic aerosols: Impacts on the global climate system and human health*. *3*, 249–259. https://doi.org/10.15406/bij.2019.03.00152

Song, K., Gong, Y., Guo, S., Lv, D., Wang, H., Wan, Z., Yu, Y., Tang, R., Li, T., Tan, R., Zhu, W., Shen, R., & Lu, S. (2022). Investigation of partition coefficients and fingerprints of atmospheric gas- and particle-phase intermediate volatility and semi-volatile organic compounds using pixel-based approaches. *Journal of Chromatography A*, *1665*, 462808. https://doi.org/10.1016/j.chroma.2022.462808

Spectra-Physics. (2002). *Quanta-Ray PRO-Series Pulsed Nd: YAG Lasers User's Manual*. chrome-extension://efaidnbmnnnibpcajpcglclefindmkaj/http://publish.illinois.edu/ae-lambros/files/2017/07/Lab-Series-Users-Manual_Nd_YAG.pdf

Speth, R. L., Rojo, C., Malina, R., & Barrett, S. R. H. (2015). Black carbon emissions reductions from combustion of alternative jet fuels. *Atmospheric Environment*, *105*, 37–42. https://doi.org/10.1016/j.atmosenv.2015.01.040

Staples, M. D., Malina, R., Suresh, P., Hileman, J. I., & Barrett, S. R. H. (2018). Aviation CO2 emissions reductions from the use of alternative jet fuels. *Energy Policy*, *114*, 342–354. https://doi.org/10.1016/j.enpol.2017.12.007

Starik, A. (2007). Gaseous and Particulate Emissions with Jet Engine Exhaust and Atmospheric Pollution. In *Adv Propuls Technol High Speed Aircr* (Vol. 15, pp. 15-1–15).

Stone, D., Whalley, L. K., & Heard, D. E. (2012). Tropospheric OH and HO2 radicals: Field measurements and model comparisons. *Chemical Society Reviews*, *41*(19), 6348–6404. https://doi.org/10.1039/C2CS35140D

Stuhlmann, R. (1995). The impact of clouds on the radiative heating of the earth surface-atmosphere system determined from satellite data. *Advances in Space Research*, *16*(10), 37–49. https://doi.org/10.1016/0273-1177(95)00378-R

Su, P., Joutsensaari, J., Dada, L., Zaidan, M. A., Nieminen, T., Li, X., Wu, Y., Decesari, S., Tarkoma, S., Petäjä, T., Kulmala, M., & Pellikka, P. (2022). New particle formation event detection with Mask R-CNN. *Atmospheric Chemistry and Physics*, *22*(2), 1293–1309. https://doi.org/10.5194/acp-22-1293-2022

Subedi, D., Tyata, R., Khadgi, A., & Wong, C. (2009). Treatment of water by dielectric barrier discharge. *Journal of Science and Technology in the Tropics*, *5*, 117–123.

Surratt, J. D., Kroll, J. H., Kleindienst, T. E., Edney, E. O., Claeys, M., Sorooshian, A., Ng, N. L., Offenberg, J. H., Lewandowski, M., Jaoui, M., Flagan, R. C., & Seinfeld, J. H. (2007). Evidence for Organosulfates in Secondary Organic Aerosol. *Environmental Science & Technology*, *41*(2), 517–527. https://doi.org/10.1021/es062081q

Tammet, H. (2012). The Function-Updated Millikan Model: A Tool for Nanometer Particle Size-Mobility Conversions. *Aerosol Science and Technology - AEROSOL SCI TECH*, *46*. https://doi.org/10.1080/02786826.2012.700740

Tammet, H. (2017). *The concept of the mobility diameter: A terminological remark by H. Tammet*.

Tan, S., Chen, X., & Yin, S. (2022). Comparison results of eight oxygenated organic molecules: Unexpected contribution to new particle formation in the atmosphere. *Atmospheric Environment*, *268*, 118817. https://doi.org/10.1016/j.atmosenv.2021.118817

Therssen, E., Bouvier, y., Schoemaecker-Moreau, C., Mercier, X., Desgroux, P., Ziskind, M., & Focsa, C. (2007). Determination of the ratio of soot refractive index function E(m) at the two wavelengths 532 and 1064 nm by laser induced incandescence. *Applied Physics B - Laser and Optics*, *89*(2–3), 417–427. https://doi.org/10.1007/s00340-007-2759-7

Thiel, V., & Sjövall, P. (2011). Using Time-of-Flight Secondary Ion Mass Spectrometry to Study Biomarkers. *Annual Review of Earth and Planetary Sciences*, *39*, 125–156. https://doi.org/10.1146/annurev-earth-040610-133525

Thlaijeh, S. (2021). *Characterization of organic matter by laser desorption-mass spectrometry (LDMS): Application to primitive life and the search for life on Mars.* [Lille]. https://phlam.univ-

lille.fr/en/summaries-of-the-thesis/archives/thlaijeh-siveen-characterization-of-organic-matter-by-laser-desorption-mass-spectrometry-ldms-application-to-primitive-life-and-the-search-for-life-on-mars/

Thomson, M. J. (2023). Modeling soot formation in flames and reactors: Recent progress and current challenges. *Proceedings of the Combustion Institute*, *39*(1), 805–823. https://doi.org/10.1016/j.proci.2022.07.263

Thys, M., & Desmet, E. (Eds.). (2011). *Laser beams: Theory, properties, and applications*. Nova Science Publishers. 978-1-60876-266-8

Timko, M. T., Herndon, S. C., de la Rosa Blanco, E., Wood, E. C., Yu, Z., Miake-Lye, R. C., Knighton, W. B., Shafer, L., DeWitt, M. J., & Corporan, E. (2011). Combustion Products of Petroleum Jet Fuel, a Fischer–Tropsch Synthetic Fuel, and a Biomass Fatty Acid Methyl Ester Fuel for a Gas Turbine Engine. *Combustion Science and Technology*, *183*(10), 1039–1068. https://doi.org/10.1080/00102202.2011.581717

Tolbert, M. A., Rossi, M. J., & Golden, D. M. (2013). Heterogeneous interactions of chlorine nitrate, hydrogen chloride, and nitric acid with sulfuric acid surfaces at stratospheric temperatures. *Geophys. Res. Lett.*, *75*(8), 847–850. Scopus.

Tsigaridis, K., & Kanakidou, M. (2007). Secondary organic aerosol importance in the future atmosphere. *Atmospheric Environment*, *41*(22), 4682–4692. Scopus. https://doi.org/10.1016/j.atmosenv.2007.03.045

Tuovinen, S., Kontkanen, J., Jiang, J., & Kulmala, M. (2020). Investigating the effectiveness of condensation sink based on heterogeneous nucleation theory. *Journal of Aerosol Science*, *149*, 105613. https://doi.org/10.1016/j.jaerosci.2020.105613

UCAR. (n.d.). *Layers of Earth's Atmosphere | Center for Science Education*. Retrieved 21 March 2023, from https://scied.ucar.edu/learning-zone/atmosphere/layers-earths-atmosphere

Unal, A., Hu, Y., Chang, M., Odman, M., & Russell, A. (2005). Airport related emissions and impacts on air quality: Application to the Atlanta International Airport. *Atmospheric Environment*, *39*, 5787–5798. https://doi.org/10.1016/j.atmosenv.2005.05.051

UNITED airlines SAF. (2021). *United Flies World's First Passenger Flight On 100% Sustainable Aviation Fuel Supplying One Of Its Engines | GE News*. https://www.ge.com/news/reports/united-flies-worlds-first-passenger-flight-on-100-sustainable-aviation-fuel-supplying-one

UNREAL project. (2019). *Dévoilement du mécanisme de nucléation dans les gaz d'échappement des moteurs d'avion et de son lien avec la composition du carburant*. Agence nationale de la recherche. https://anr.fr/Projet-ANR-18-CE22-0019

Updyke, K. M., Nguyen, T. B., & Nizkorodov, S. A. (2012). Formation of brown carbon via reactions of ammonia with secondary organic aerosols from biogenic and anthropogenic precursors. *Atmospheric Environment*, *63*, 22–31. Scopus. https://doi.org/10.1016/j.atmosenv.2012.09.012

Vancassel, X., Sorokin, A., Mirabel, P., Petzold, A., & Wilson, C. (2004). Volatile particles formation during PartEmis: A modelling study. *Atmospheric Chemistry and Physics*, *4*(2), 439–447. https://doi.org/10.5194/acp-4-439-2004

Vázquez-Navarro, M., Mannstein, H., & Kox, S. (2015). Contrail life cycle and properties from 1 year of MSG/SEVIRI rapid-scan images. *Atmospheric Chemistry and Physics*, *15*(15), 8739–8749. https://doi.org/10.5194/acp-15-8739-2015

Veshkini, A., Dworkin, S., & Thomson, M. (2016). Understanding soot particle size evolution in laminar ethylene/air diffusion flames using novel soot coalescence models. *Combustion Theory and Modelling*, *20*, 1–28. https://doi.org/10.1080/13647830.2016.1169319

Vickerman, J. C., & Briggs, D. (2013). *ToF-SIMS: Materials Analysis by Mass Spectrometry*. IM Publications. 978-1-906715-17-5

Voigt, C., Kleine, J., Sauer, D., Moore, R. H., Bräuer, T., Le Clercq, P., Kaufmann, S., Scheibe, M., Jurkat-Witschas, T., Aigner, M., Bauder, U., Boose, Y., Borrmann, S., Crosbie, E., Diskin, G. S., DiGangi,

J., Hahn, V., Heckl, C., Huber, F., … Anderson, B. E. (2021). Cleaner burning aviation fuels can reduce contrail cloudiness. *Communications Earth & Environment*, *2*(1), Article 1. https://doi.org/10.1038/s43247-021-00174-y

Vorster, S., Ungerer, M., & Volschenk, J. (2013). 2050 Scenarios for Long-Haul Tourism in the Evolving Global Climate Change Regime. *Sustainability*, *5*(1), Article 1. https://doi.org/10.3390/su5010001

Vozka, P., Vrtiška, D., Šimáček, P., & Kilaz, G. (2019). Impact of Alternative Fuel Blending Components on Fuel Composition and Properties in Blends with Jet A. *Energy & Fuels*, *33*(4), 3275–3289. https://doi.org/10.1021/acs.energyfuels.9b00105

Wang, J., Doussin, J. F., Perrier, S., Perraudin, E., Katrib, Y., Pangui, E., & Picquet-Varrault, B. (2011). Design of a new multi-phase experimental simulation chamber for atmospheric photosmog, aerosol and cloud chemistry research. *Atmospheric Measurement Techniques*, *4*(11), 2465–2494. https://doi.org/10.5194/amt-4-2465-2011

Wang, M., Xiao, M., Bertozzi, B., Marie, G., Rörup, B., Schulze, B., Bardakov, R., He, X.-C., Shen, J., Scholz, W., Marten, R., Dada, L., Baalbaki, R., Lopez, B., Lamkaddam, H., Manninen, H. E., Amorim, A., Ataei, F., Bogert, P., … Donahue, N. M. (2022). Synergistic HNO3–H2SO4–NH3 upper tropospheric particle formation. *Nature*, *605*(7910), Article 7910. https://doi.org/10.1038/s41586-022-04605-4

Wang, W.-C., & Tao, L. (2016). Bio-jet fuel conversion technologies. *Renewable and Sustainable Energy Reviews*, *53*, 801–822. https://doi.org/10.1016/j.rser.2015.09.016

Wang, X., Caldow, R., Sem, G. J., Hama, N., & Sakurai, H. (2010). Evaluation of a condensation particle counter for vehicle emission measurement: Experimental procedure and effects of calibration aerosol material. *Journal of Aerosol Science*, *41*(3), 306–318. https://doi.org/10.1016/j.jaerosci.2010.01.001

Wang, X., Chen, J., Zhuang, G., Surratt, J. D., Chan, M. N., & Seinfeld, J. H. (2010). Evidence for high molecular weight nitrogen-containing organic salts in urban aerosols [Review of *Evidence for*

high molecular weight nitrogen-containing organic salts in urban aerosols, by X. Yang & H. Chen]. *Environmental Science and Technology*, *44*(12), 4441–4446. Scopus. https://doi.org/10.1021/es1001117

Wang, Y., & Chung, S. H. (2019). Soot formation in laminar counterflow flames. *Progress in Energy and Combustion Science*, *74*, 152–238. https://doi.org/10.1016/j.pecs.2019.05.003

Wang, Y., Liu, P., Li, Y. J., Bateman, A. P., Martin, S. T., & Hung, H.-M. (2018). The Reactivity of Toluene-Derived Secondary Organic Material with Ammonia and the Influence of Water Vapor. *Journal of Physical Chemistry A*, *122*(38), 7739–7747. Scopus. https://doi.org/10.1021/acs.jpca.8b06685

WeatherOnline©. (1999, 2021). *Overview France—Forecast maps—Weather forecast*. https://www.weatheronline.co.uk/France.htm

Westerdahl, D., Fruin, S., & Fine, P. (2008). The Los Angeles International Airport as a source of ultrafine particles and other pollutants to nearby communities. *Atmospheric Environment*, *42*, 3143–3155. https://doi.org/10.1016/j.atmosenv.2007.09.006

WHO. (2018). *Neuf personnes sur 10 respirent un air pollué dans le monde*. https://www.who.int/fr/news/item/02-05-2018-9-out-of-10-people-worldwide-breathe-polluted-air-but-more-countries-are-taking-action

WHO. (2021). *Global Air Quality Guidelines*. https://www.who.int/news-room/questions-and-answers/item/who-global-air-quality-guidelines

Wiedensohler, A. (1988). An approximation of the bipolar charge distribution for particles in the submicron size range. *Journal of Aerosol Science*, *19*(3), 387–389. https://doi.org/10.1016/0021-8502(88)90278-9

Williams, B. J., Goldstein, A. H., Kreisberg, N. M., & Hering, S. V. (2010). In situ measurements of gas/particle-phase transitions for atmospheric semivolatile organic compounds. *Proceedings of the National Academy of Sciences*, *107*(15), 6676–6681. https://doi.org/10.1073/pnas.0911858107

Wong, H.-W., Beyersdorf, A. J., Heath, C. M., Ziemba, L. D., Winstead, E. L., Thornhill, K. L., Tacina, K. M., Ross, R. C., Albo, S. E., Bulzan, D. L., Anderson, B. E., & Miake-Lye, R. C. (2013). Laboratory and modeling studies on the effects of water and soot emissions and ambient conditions on the properties of contrail ice particles in the jet regime. *Atmospheric Chemistry and Physics*, *13*(19), 10049–10060. https://doi.org/10.5194/acp-13-10049-2013

Wong, H.-W., Jun, M., Peck, J., Waitz, I. A., & Miake-Lye, R. C. (2014). Detailed Microphysical Modeling of the Formation of Organic and Sulfuric Acid Coatings on Aircraft Emitted Soot Particles in the Near Field. *Aerosol Science and Technology*, *48*(9), 981–995. https://doi.org/10.1080/02786826.2014.953243

Wong, H.-W., Jun, M., Peck, J., Waitz, I. A., & Miake-Lye, R. C. (2015). Roles of Organic Emissions in the Formation of Near Field Aircraft-Emitted Volatile Particulate Matter: A Kinetic Microphysical Modeling Study. *ASME*. https://dspace.mit.edu/handle/1721.1/106275

Wong, H.-W., & Miake-Lye, R. C. (2010). Parametric studies of contrail ice particle formation in jet regime using microphysical parcel modeling. *Atmospheric Chemistry and Physics*, *10*(7), 3261–3272. https://doi.org/10.5194/acp-10-3261-2010

Wong, H.-W., Yelvington, P. E., Timko, M. T., Onasch, T. B., Miake-Lye, R. C., Zhang, J., & Waitz, I. A. (2008). Microphysical Modeling of Ground-Level Aircraft-Emitted Aerosol Formation: Roles of Sulfur-Containing Species. *Journal of Propulsion and Power*, *24*(3), 590–602. https://doi.org/10.2514/1.32293

Wright, M. D., Keitch, P. A., & Henshaw, D. L. (2007). *SMALL-ION AND NANO-AEROSOL SIZE DISTRIBUTION AND CONCENTRATION PROFILE FROM CANDLE BURNING*. 4.

Wu, J. (2019). *Theoretical and experimental studies on the hygroscopic properties of soot particles sampled from a kerosene diffusion flame: Impact of the aging processes by O3 and SO2* [These de doctorat, Université de Lille (2018-2021)]. http://www.theses.fr/2019LILUR035

Xiang, Y., Yuan, Z., Wang, S., & Fan, A. (2019). Effects of flow rate and fuel/air ratio on propagation behaviors of diffusion H2/air flames in a micro-combustor. *Energy*, *179*, 315–322. https://doi.org/10.1016/j.energy.2019.05.052

Xu, L., Du, L., Tsona, N. T., & Ge, M. (2021). Anthropogenic Effects on Biogenic Secondary Organic Aerosol Formation. *Advances in Atmospheric Sciences*, *38*(7), 1053–1084. https://doi.org/10.1007/s00376-020-0284-3

Xu, L., Yang, Z., Tsona, N. T., Wang, X., George, C., & Du, L. (2021). Anthropogenic–Biogenic Interactions at Night: Enhanced Formation of Secondary Aerosols and Particulate Nitrogen- and Sulfur-Containing Organics from β-Pinene Oxidation. *Environmental Science & Technology*, *55*(12), 7794–7807. https://doi.org/10.1021/acs.est.0c07879

Xu, W., Croteau, P., Williams, L., Onasch, T., Cross, E., Zhang, X., Robinson, W., Worsnop, D., & Jayne, J. (2016). Laboratory characterization of an Aerosol Chemical Speciation Monitor with PM2.5 measurement capability. *Aerosol Science and Technology*, *51*, 00. https://doi.org/10.1080/02786826.2016.1241859

Yim, S. H. L., Lee, G., Lee, I., Allroggen, F., Ashok, A., Caiazzo, F., Eastham, S., Malina, R., & Barrett, S. (2015). Global, regional and local health impacts of civil aviation emissions. *Environmental Research Letters*, *10*. https://doi.org/10.1088/1748-9326/10/3/034001

Yon, J. (2014). *Caractérisation physique et chimique des nanoparticules*. https://hal.science/cel-01682720/file/Cours%20CORIA-IRSN%20Partie%201.pdf

Yon, J., Morán, J., Lespinasse, F., Escudero, F., Godard, G., Mazur, M., Liu, F., & Fuentes, A. (2021). Horizontal Planar Angular Light Scattering (HPALS) characterization of soot produced in a laminar axisymmetric coflow ethylene diffusion flame. *Combustion and Flame*, *232*, 111539. https://doi.org/10.1016/j.combustflame.2021.111539

Yon, J., Ouf, F.-X., Hebert, D., Mitchell, J. B., Teuscher, N., Garrec, J.-L. L., Bescond, A., Baumann, W., Ourdani, D., Bizien, T., & Perez, J. (2018). Investigation of soot oxidation by coupling LII, SAXS

and scattering measurements. *Combustion and Flame*, *190*, 441–453. https://doi.org/10.1016/j.combustflame.2017.12.014

Yu, F., & Turco, R. P. (1997). The role of ions in the formation and evolution of particles in aircraft plumes. *Geophysical Research Letters*, *24*(15), 1927–1930. https://doi.org/10.1029/97GL01822

Yu, F., Turco, R. P., & Kärcher, B. (1999). The possible role of organics in the formation and evolution of ultrafine aircraft particles. *Journal of Geophysical Research: Atmospheres*, *104*(D4), 4079–4087. https://doi.org/10.1029/1998JD200062

Yu, H., McGraw, R., & Lee, S.-H. (2012). Effects of amines on formation of sub-3 nm particles and their subsequent growth. *Geophysical Research Letters - GEOPHYS RES LETT*, *39*. https://doi.org/10.1029/2011GL050099

Yu, Z., Timko, M. T., Herndon, S. C., Miake-Lye, R., C., Beyersdorf, A. J., Ziemba, L. D., Winstead, E. L., & Anderson, B. E. (2019). Mode-specific, semi-volatile chemical composition of particulate matter emissions from a commercial gas turbine aircraft engine. *Atmospheric Environment*, *218*, 116974. https://doi.org/10.1016/j.atmosenv.2019.116974

Yuan, R., Lobo, P., Smallwood, G. J., Johnson, M. P., Parker, M. C., Butcher, D., & Spencer, A. (2022). Measurement of black carbon emissions from multiple engine and source types using laser-induced incandescence: Sensitivity to laser fluence. *Atmospheric Measurement Techniques*, *15*(2), 241–259. https://doi.org/10.5194/amt-15-241-2022

Zaporozhets, O., & Synylo, K. (2019). *Modeling of Air Pollution at Airports*. https://doi.org/10.5772/intechopen.84172

Zhang, B. (2020). The Effect of Aerosols to Climate Change and Society. *Journal of Geoscience and Environment Protection*, *08*, 55–78. https://doi.org/10.4236/gep.2020.88006

Zhang, Y., Cheng, M., Gao, J., & Li, J. (2023). Review of the influencing factors of secondary organic aerosol formation and aging mechanism based on photochemical smog chamber simulation

methods. *Journal of Environmental Sciences*, *123*, 545–559. https://doi.org/10.1016/j.jes.2022.10.033

Zhang, Y., Tian, R., Meng, S., Kook, S., Kim, K. S., & Kweon, C.-B. (2021). Effect of the jet fuel cetane number on combustion in a small-bore compression-ignition engine. *Fuel*, *292*, 120301. https://doi.org/10.1016/j.fuel.2021.120301

Zhao, D., Pullinen, I., Fuchs, H., Schrade, S., Wu, R., Acir, I.-H., Tillmann, R., Rohrer, F., Wildt, J., Guo, Y., Kiendler-Scharr, A., Wahner, A., Kang, S., Vereecken, L., & Mentel, T. F. (2021). Highly oxygenated organic molecule (HOM) formation in the isoprene oxidation by NO_3 radical. *Atmospheric Chemistry and Physics*, *21*(12), 9681–9704. https://doi.org/10.5194/acp-21-9681-2021

Zheng, L., Cronly, J., Ubogu, E., Ahmed, I., Zhang, Y., & Khandelwal, B. (2019). Experimental investigation on alternative fuel combustion performance using a gas turbine combustor. *Applied Energy*, *238*, 1530–1542. https://doi.org/10.1016/j.apenergy.2019.01.175

Zhou, Y., Chu, Q., Hou, D., Chen, D., & You, X. (2022). Molecular Dynamics Study on the Condensation of PAH Molecules on Quasi Soot Surfaces. *The Journal of Physical Chemistry A*, *126*(4), 630–639. https://doi.org/10.1021/acs.jpca.1c09366

This page is intentionally left blank

MECANISMES DE NUCLEATION DES PARTICULES VOLATILES DANS LES EMISSIONS DES MOTEURS D'AVIONS ET LEURS LIENS AVEC LA COMPOSITION DU CARBURANT

RESUME

L'une des préoccupations actuelles de l'industrie aéronautique est la diminution de la consommation de carburant et de l'empreinte environnementale. En effet, les émissions aéronautiques ont un impact sur la qualité de l'air et notamment au niveau des zones aéroportuaires. Comme d'autres secteurs du transport, le trafic aérien génère des gaz à effet de serre (2 % du total dans le monde), des traînées de condensation ainsi que des particules volatiles et non volatiles (vPM et nvPM).

Pour réduire ces émissions, différentes approches ont été pensées avec en particulier l'usage de carburants aéronautiques durables (SAF - Sustainable Aviation Fuels). L'objectif des SAF est de réduire les émissions nettes de CO_2 et de nvPM. Cependant, la combustion de ces carburants peut entraîner la formation de nouveaux polluants qui réagissent avec l'atmosphère en formant des aérosols secondaires (SA). Dans le cadre du projet UNREAL (Unveiling Nucleation mechanism in aiRcraft Engine exhAust and its Link with fuel composition), l'objectif de ce travail était d'étudier les différents mécanismes au niveau moléculaire à l'origine de la formation de nouvelles particules à partir des rejets moteurs alimentés par des carburants de compositions différentes, allant du Jet A-1 standard à du carburant 100 % SAF.

La caractérisation physico-chimique des émissions en conditions réelles en sortie moteur est un défi à la fois d'un point de vue technique et économique. Pour pallier à cela un brûleur mini-CAST, adapté à la combustion de carburants liquides aéronautiques, a été utilisé comme alternative pour obtenir des émissions comparables, dans une certaine mesure, à celles des moteurs aéronautiques. Une diminution des émissions de nvPM (concentration en nombre, concentration en masse et distribution de tailles) peut être observée en corrélation avec la quantité de composés aromatiques présents dans le carburant. De plus, l'analyse par spectrométrie de masse a révélé une diminution de l'intensité relative des HAP lors de l'emploi de carburants alternatifs. Les émissions du brûleur ont été injectées, avec ou sans filtration des suies, dans une chambre atmosphérique de vieillissement (chambre CESAM reproduisant les conditions atmosphériques au niveau du sol - LISA). Pour tous les carburants testés, la formation de vPM par nucléation homogène a été observée dans la chambre atmosphérique en l'absence de nvPM. Ce phénomène est particulièrement prononcé pour les carburants comprenant de grandes quantités de soufre dans leur composition. Cependant, dans les cas réels (présence de suies), la formation de vPM n'est observée que pour les carburants contenant de fortes quantités de soufre. La concentration de précurseurs gazeux formés pour les autres carburants n'est pas suffisante pour produire des vPM, notamment avec l'adsorption des gaz à la surface des particules de suies (nucléation hétérogène). Les techniques de caractérisation en ligne ont été complétées par des prélèvements sur filtre et une analyse par spectrométrie de masse, mettant en évidence la présence de HAP, d'hydrocarbures oxygénés, de composés soufrés et azotés. En utilisant des méthodes semi-quantitatives, il a été possible de mettre en relation la composition chimique (intensité relative de soufre et de HAP) avec la formation de vPM et leur répartition dans les phases particulaires et gazeuses des émissions.

Mots-clés: Emissions aéronautique, particules volatiles (vPM) et non-volatiles (nvPM), formation de particules, chambre atmosphérique, nucléation homogène, carburant aéronautique, brûleur de laboratoire pour carburant liquide.

NUCLEATION MECHANISMS OF VOLATILE PARTICLES IN AIRCRAFT ENGINE EMISSIONS AND THEIR LINKS WITH FUEL COMPOSITION

ABSTRACT

One of the actual concerns of the aviation industry is to reduce fuel consumption and environmental footprint. Indeed, aviation emissions impact air quality in and around airports. As other transport sectors, aviation effluents need to be addressed to reduce greenhouse gases contribution (2% of these emissions are related to air transport worldwide), volatile and non-volatile Particulate Matter (vPM and nvPM) and indirect impact as condensation trails.

To reduce these emissions, different approaches have been investigated, in particular the use of Sustainable Aviation Fuels (SAF). Aims of SAF are to decrease the net CO_2 emissions and nvPM. However, combustion of these fuels may lead to new pollutants that can react with atmosphere by formation of secondary aerosols. As part of the UNREAL project (Unveiling Nucleation mechanism in aiRcraft Engine exhAust and its Link with fuel composition), the objective of this work was to study the different molecular mechanisms of new particle formation from the exhausts of aircraft engines fed by fuels with different composition, from the standard Jet A-1 to 100 % SAF fuel.

The physicochemical characterisation of the particulate emissions from aircraft engines in real conditions is challenging both from the technical and economical point of view. Thus, a mini-CAST burner, suitable for the combustion of aeronautic liquid fuels, has been used as an alternative to obtain emissions comparable to some extent to those from aircraft engines. A decrease in nvPM emissions (number concentration, mass concentration and size distribution) can be observed in correlation with the quantity of aromatic compounds in the fuel. Moreover, the analysis by mass spectrometry revealed a decrease in the relative intensity of PAHs when alternative fuels were employed. Emissions from the burner have been injected, with and without soot filtration, into an atmospheric chamber for ageing (CESAM chamber reproducing atmospheric conditions at ground level – LISA). For all fuels tested formation of vPM by homogeneous nucleation has been observed in the atmospheric chamber in absence of nvPM. This phenomenon is particularly highlighted for fuels with high amounts of sulphur in their compositions. However, in real cases (presence of soot), the formation of vPM is only observed for the fuels containing high amounts of sulphur. The concentration of gaseous precursors formed for other fuels was not enough to produce vPM after being adsorbed on soot surface (heterogeneous nucleation). On-line characterisation techniques were completed by filter sampling and off-line mass spectrometry analysis, highlighting the presence of PAHs, oxygenated hydrocarbons, sulphur and nitrogen compounds. By employing semi-quantitative methods, it was possible to link the relative chemical composition (sulphur and PAH relative intensity) with vPM formation and their repartitions in particulate and gaseous phases.

Keywords: Aeronautic emissions, volatile (vPM) and non-volatile (nvPM) Particulate Matter, formation of particles, atmospheric chamber, homogeneous nucleation, aeronautical fuels, liquid laboratory burner.